FINAL REPORT

Title: Ultra-High-Performance Concrete (UHPC) Use in Florida Structural Applications

FDOT Contract Number: BDV31-977-105

Final Report

Submitted to

The Florida Department of Transportation Research Center
605 Suwannee Street, MS 30 Tallahassee, FL 32399

c/o Dr. Harvey DeFord, Ph.D.
Steve Nolan, P.E.

Submitted by:

Dr. Kyle A. Riding (kyle.riding@essie.ufl.edu) (Principal Investigator)
Dr. Christopher C. Ferraro (Co Principal Investigator)
Dr. Trey Hamilton (Co Principal Investigator)
Dr. Joel Harley (Co Principal Investigator)
Raid S. Alrashidi
Megan Voss
Daniel Alabi
Rami Zamzami
Engineering School of Sustainable Infrastructure and Environment
University of Florida
Gainesville, Florida 32611

September 2022

Engineering School of Sustainable Infrastructure and Environment

College of Engineering

University of Florida

Gainesville, Florida 32611

DISCLAIMER

The opinions, findings, and conclusions expressed in this publication are those of the authors and not necessarily those of the State of Florida Department of Transportation or the U.S. Department of Transportation.

Prepared in cooperation with the State of Florida Department of Transportation and the U.S. Department of Transportation.

SI (MODERN METRIC) CONVERSION FACTORS (FROM FHWA)

Symbol	When You Know	Multiply By	To Find	Symbol
Length				
in	inches	25.4	millimeters	mm
ft	feet	0.305	meters	m
yd	yards	0.914	meters	m
mi	miles	1.61	kilometers	km
Area				
in^2	square inches	645.2	square millimeters	mm^2
ft^2	square feet	0.093	square meters	m^2
yd^2	square yard	0.836	square meters	m^2
mi^2	square miles	2.59	square kilometers	km^2
Volume				
fl oz	fluid ounces	29.57	milliliters	mL
gal	gallons	3.785	liters	L
ft^3	cubic feet	0.028	cubic meters	m^3
yd^3	cubic yards	0.765	cubic meters	m^3
NOTE: volumes greater than 1000 L shall be shown in m^3				
Mass				
oz	ounces	28.35	grams	g
lb	pounds	0.454	kilograms	kg
Temperature (exact degrees)				
°F	Fahrenheit	5 (F-32)/9 or (F-32)/1.8	Celsius	°C
Illumination				
fc	foot-candles	10.76	lux	lx
fl	foot-Lamberts	3.426	candela/m^2	cd/m^2
Force and Pressure or Stress				
lbf	pound-force	4.45	newtons	N
lbf/in^2	pound-force per square inch	6.89	kilopascals	kPa

TECHNICAL REPORT DOCUMENTATION

1. Report No.	2. Government Accession No.	3. Recipient's Catalog No.
4. Title and Subtitle Ultra-High-Performance Concrete (UHPC) Use in Florida Structural Applications		5. Report Date September, 2022
		6. Performing Organization Code
7. Author(s) Kyle A. Riding, Christopher C. Ferraro, Trey Hamilton, Joel Harley, Raid S. Alrashidi, Megan Voss, Daniel Alabi		8. Performing Organization Report No.
9. Performing Organization Name and Address Department of Civil and Coastal Engineering Engineering School of Sustainable Infrastructure & Environment University of Florida 365 Weil Hall P.O. Box 116580 Gainesville, FL 32611-6580		10. Work Unit No. 11. Contract or Grant No. BDV31-977-130
12. Sponsoring Agency Name and Address Florida Department of Transportation 605 Suwannee Street, MS 30 Tallahassee, FL 32399		13. Type of Report and Period Covered Final Report 14. Sponsoring Agency Code
15. Supplementary Notes – N/A		

16. Abstract

In order for UHPC to be implemented in Florida structures and realize its potential benefits, research was needed to develop specifications for UHPC materials not supplied as prebagged materials. The research objective of this project was to establish mixing, placing, curing and durability requirements and test methods necessary to produce durable, non-proprietary UHPC, made using locally-sourced raw materials, for different classes of structural use and exposure conditions. This research program was performed using four different concrete mixture designs with different fiber contents and three different curing methods to investigate the range of material properties possible and their impact on strength, durability, and applicability of methods. As part of this work, a new modified double punch test was developed and is recommended for use in quality control, with direct tension testing recommended for mixture qualification. All mixtures with compressive strength above 15 ksi performed excellent in freeze-thaw testing. Steam curing was found to differentiate between good and worse performance of concrete microstructure for transport property testing. It is recommended that the UHPC fresh chloride limit be raised by 25% from 0.4 lb/yd^3 to 0.5 lb/yd^3. A modified rapid chloride migration test is recommended to be used on steam-cured samples with a chloride intrusion limit of 5 mm after 7 days. Steam curing samples gave conservative results at 28 days compared to the long-term test results and is recommended for acceptance testing purposes. A nondestructive electromagnetic sensor based on inductive principles quantify the fiber orientation in UHPC can be used in both lab and fields.

17. Key Word	18. Distribution Statement
Ultra-High-Performance Concrete, Durability, Tensile Strength, Construction	No restrictions.

19. Security Classif. (of this report)	20. Security Classif. (of this page)	21. No. of Pages	22. Price
Unclassified.	Unclassified.	419	

ACKNOWLEDGEMENTS

The Florida Department of Transportation (FDOT) is acknowledged for their funding and contributions to this study. Special acknowledgement is given to Steve Nolan and Dr. Harvey DeFord for their guidance and assistance throughout the project. The assistance of Ronald Simmons with use of the saltwater tanks at the FDOT State Materials Office and Clifford Craig in performing the low temperature differential scanning experiments is appreciated and acknowledged. The authors would also like to thank Richard DeLorenzo, Ghulam Mujtaba, Jose Armenteros, David Cerlanek for their advice and support in this project. The authors would also like to thank Michael Thomas for useful discussions on chloride threshold and rapid chloride migration testing for UHPC.

EXECUTIVE SUMMARY

1.1. Background

Ultra-high-performance concrete (UHPC) is a class of high compressive strength and durability concrete made with fibers to provide high tensile strength and toughness [1][2]. UHPC has commonly been used for repair applications, road overlays, and closure strips between precast panels but is increasingly being used or considered for use in full-scale members and structures [3–5]. While proprietary UHPC blends dominated early UHPC applications, the industry has had increasing interest in the use of non-proprietary UHPCs for larger-scale applications. While non-proprietary UHPCs come with added challenges of mix development, quality assurance, and quality control, they also provide the opportunity of greatly reduced cost of materials and shipping. For companies such as precast concrete plants, developing a non-proprietary UHPC mix to be used in large volumes in production makes strong financial sense.

UHPC has the potential to provide a very long service life for reinforced concrete structures, providing an alternative to polymer or stainless-steel reinforcement in extremely aggressive environments. The improved mechanical and durability characteristics of UHPC are due to its very dense microstructure and high volumes of well-distributed fibers that keep crack widths very small. The low porosity of UHPC is obtained by use of low water-cementitious materials ratios (w/cm) and high particle packing densities.

Fiber dispersion and orientation is a large concern with UHPC. Fibers can segregate due to poor material rheological properties and construction practices [6], leaving zones of high and low fiber content. Poorly distributed fibers that are preferentially oriented in an undesirable direction during member fabrication could lead to structural weaknesses and critical failures [7], [8]. Most methods of analyzing fiber distribution and alignment are time consuming and destructive. Ideal methods that are inexpensive, simple to perform, and nondestructive are needed to validate fiber orientation and density at critical member locations to ensure the safety and sustainment of many future concrete constructions.

1.2. Research Objectives

The research objective of this project was to establish mixing, placing, curing and durability requirements and test methods necessary to produce durable, non-proprietary UHPC, made using locally-sourced raw materials, for different classes of structural use and exposure conditions. In order to accomplish the research objectives of this project, a combined experimental and numerical approach was used. This research program was performed using four different concrete mixture designs with different fiber contents and three different curing methods to investigate the range of material properties possible and their impact on strength, durability, and test methods. The mixture designs developed for this project were not intended to be used as standard mixture designs at different precast concrete plants around Florida because the different locally available materials at each plant will require mixture customization to achieve optimum particle packing and strength. This research program included measurement of concrete mechanical-related properties, concrete transport-related properties, concrete durability properties, and development of a methodology to non-destructive method to measure fiber density and orientation.

1.3. Main Findings

Project findings can be summarized as follows:

- Tensile test methods currently in use for UHPC should use post-cracking characteristics such as toughness in addition to peak strength to describe the overall tensile behavior of the concrete. Simplified test methods such as the modified double punch test presented in Chapter 5 and the ASTM C1609 flexure test are useful methods for quality control, but the stress vs. strain relationship measured from a direct tension test is ideal for initial mix qualification.

- In field applications, UHPC elements that must be cast using more than one batch should have time intervals between placements of 20 minutes or less. Rodding the interface between the layers can help improve the bond strength.

- All mixtures with compressive strength above 15 ksi performed excellent in freeze-thaw testing. Steam curing was found to affect the freeze-thaw performance at the lowest strength level tested.

- Significant chloride leaching was found to occur in EN 480-14 during curing and testing, resulting in misleading chloride threshold values. The fresh chloride limit was recommended to be raised by 25% from 0.4 lb/yd^3 to 0.5 lb/yd^3. The ACI 318 water-soluble chloride limits as a % by mass of cementitious materials were found to be higher than that required for corrosion initiation for two of the UHPC mixtures tested and should be re-examined for UHPC.

- The steel fibers did not noticeably affect the chloride ingress in bulk diffusion experiments and had only a small effect on the chloride ingress measured in the modified rapid chloride migration test due the disconnected pore structure of the UHPC samples. The modified rapid chloride migration test was found to work for UHPC samples with fibers up to 2% by volume. A limit of 5 mm of chloride intrusion after 7 days was found to be a good limit to differentiate chloride diffusion performance. Steam-curing provided accelerated curing at 28 days that compared well to long-term test results and is recommended for acceptance testing purposes. MIP

- A nondestructive electromagnetic sensor based on inductive principles to characterize and quantify the fiber orientation in UHPC can be used in both the lab and field.

1.4. Recommendations

Based upon the findings from this study, the following recommendations are made:

- It is recommended that the direct tension test be used for mix design acceptance.
- The modified double-punch test is recommended to be used a quality-control test for UHPC.

- The modified rapid chloride migration test is recommended to be used as a quality-control test for the long-term durability of UHPC. For steam-cured samples, a chloride intrusion less than 5 mm for 7 days of testing could be used as an acceptance criterion.
- The fresh chloride limit was recommended to be raised by 25% from 0.4 lb/yd^3 to 0.5 lb/yd^3.
- The use of the nondestructive electromagnetic sensor developed to quantify the steel fiber percentages and orientation in UHPC is recommended.

1.5. Future work

- A quantitative method should be developed to determine if the results of a direct tension test were affected by eccentricity of the sample loading in the test frame
- Research should be undertaken to develop procedures to minimize or eliminate the formation of a stiffened surface layer (elephant skin) before surface finishing can be completed or before the placement of another layer on top of the first.
- Development of a resistivity meter with a range sufficient to measure the resistivities of all UHPC samples.
- The modified rapid chloride migration test used in this research shows potential as a quality-control test for UHPC durability. This test should be investigated further by testing samples with steel fibers above 2% at one year and compare the results to bulk diffusion test results
- Improve the portability of the electromagnetic sensor, the portability of the design is desired to be improved on so that it can be easily produced for mass markets. It is also desired to be able to make it very easy to carry and operate by technicians out in the field. In addition, future optimizations can be made to the sensor design (e.g., switching to a soft iron core) and circuitry/analysis algorithms (e.g., leveraging multiple frequency information) that should allow for better penetration depths and more reliable measurements. Sensor calibration can also be done to output the same values as seen in the CT scans.

TABLE OF CONTENTS

LIST OF FIGURES

LIST OF TABLES

1. INTRODUCTION

1.1. Background

Ultra-high-performance concrete (UHPC) is a class of high compressive strength and durability concrete made with fibers to provide high tensile strength and toughness [1][2]. UHPC has commonly been used for repair applications, road overlays, and closure strips between precast panels but is increasingly being used or considered for use in full-scale members and structures [3–5]. While proprietary UHPC blends dominated early UHPC applications, the industry has had increasing interest in the use of non-proprietary UHPCs for larger-scale applications. While non-proprietary UHPCs come with added challenges of mix development, quality assurance, and quality control, they also provide the opportunity of greatly reduced cost of materials and shipping. For companies such as precast concrete plants, developing a non-proprietary UHPC mix to be used in large volumes in production makes strong financial sense.

UHPC has the potential to provide a very long service life for reinforced concrete structures, providing an alternative to polymer or stainless-steel reinforcement in extremely aggressive environments. The improved mechanical and durability characteristics of UHPC are due to its very dense microstructure and high volumes of well-distributed fibers that keep crack widths very small. The low porosity of UHPC is obtained by use of low water-cementitious materials ratios (w/cm) and high particle packing densities.

Fiber dispersion and orientation is a large concern with UHPC. Fibers can segregate due to poor material rheological properties and construction practices [6], leaving zones of high and low fiber content. Fiber orientation can change during concrete placement, typically aligning with the direction of the concrete flow. Poorly distributed fibers that are preferentially oriented in an undesirable direction during member fabrication could lead to structural weaknesses and critical failures [7], [8]. Companies and regulatory bodies have no means to mitigate these hidden weak zones once the concrete member is fabricated unless they know they are present. Most methods of analyzing fiber distribution and alignment are time consuming and destructive. Ideal methods that are inexpensive, simple to perform, and nondestructive are needed to validate fiber orientation and density at critical member locations to ensure the safety and sustainment of many future concrete constructions.

Specifications for a nonproprietary mix will need to be stricter than specifications for a proprietary mix. Most proprietary mixes have significant history and research to support their performance. They also can benefit from significant quality control at the manufacturing plant where the product is pre-bagged. Non-proprietary mixes may be developed without the decades of performance history that many of the proprietary UHPC mixtures have. This becomes especially important when the mixing, placing, and curing processes are considered. Proprietary mixes are often mixed and placed with direct supervision by a representative of the proprietary company. Mixes designed by a precast plant, or an engineering firm may not have personnel with multiple years of UHPC experience. Recommendations for production and testing personnel qualifications are needed.

This research was done to investigate the UHPC construction methods to examine potential process requirements to achieve durable concrete and prevent material weakness from preferential fiber orientation or segregation. Durability, mechanical property test methods, and performance were also investigated to identify candidate test methods and gaps in knowledge to help guide the experimental research program. A non-destructive method that could be used to quantify fiber orientation and distribution of UHPC in structural members is proposed. Recommended specifications for UHPC materials and construction is also made.

1.2. Research Objectives

The research objective of this project was to establish mixing, placing, curing and durability requirements and test methods necessary to produce durable, non-proprietary UHPC, made using locally-sourced raw materials, for different classes of structural use and exposure conditions.

1.3. Research Approach

In order to accomplish the research objectives of this project, a combined experimental and numerical approach was used. This research program was performed using four different concrete mixture designs with different fiber contents and three different curing methods to investigate the range of material properties possible and their impact on strength, durability, and test methods. The mixture designs developed for this project were not intended to be used as standard mixture designs at different precast concrete plants around Florida because the different locally available materials at each plant will require mixture customization to achieve optimum particle packing and strength. This research program included the following work:

- Measured concrete mechanical-related properties using the following techniques:
    - Direct tension test developed by the Federal Highway Administration [9,10]
    - Four-point bending test (ASTM C1609) [11]
    - Simplified double-punch test UNE 83515 [12]
- Measured concrete transport-related properties using the following techniques:
    - Modified NT Build 492 rapid chloride migration (RCM) [13]
    - Bulk resistivity (AASHTO TP119) [14]
    - Surface resistivity (AASHTO T 358) [15]
    - Water absorption [16]
    - Mercury intrusion porosimetry (MIP)
    - Bulk diffusion (ASTM C1556) [17]
- Specimens were also made for the following tests:
    - Modified version of the accelerated test EN 480-14 [18] to measure the chloride threshold for fresh concrete
    - Freeze-thaw (ASTM C666) [19]
    - Low temperature differential scanning calorimetry (DSC)
    - Creep and shrinkage (ASTM C512) [20]

    - Bond testing
- Samples were made for outdoor exposure in seawater at both the Treat Island, ME and Seahorse Key, FL sites to link the laboratory testing to the field performance of structures.
- Measured chloride profiles for samples exposed to 16.5% NaCl solution for one year and compared to accelerated laboratory tests. Two samples of each mixture were left in the saltwater tank for later measurements.
- Electromagnetic sensor system was designed and optimized to be used as a non-destructive method for steel fiber characterization in both labs and fields.

2. LITERATURE REVIEW

2.1. Introduction

Ultra-high-performance concrete (UHPC) is a material with high compressive strength, high tensile strength, and ductility from the use of fibers. It has the potential to provide a very long service life for reinforced concrete structures, providing an alternative to polymer or stainless-steel reinforcement in extremely aggressive environments. The improved mechanical and durability characteristics of UHPC are due to its very dense microstructure and high volumes of well-distributed fibers that keep crack widths very small. The low porosity of UHPC is obtained by use of low water-cementitious materials ratios (w/cm) and high particle packing densities. Particle packing methods are used to optimize space filling and reduce the need for water to fill space and provide lubrication. Large quantities of different blends of cementitious materials and fine sands are used to optimize particle packing. Some of the properties that make UHPC such an excellent material for transportation infrastructure also necessitate in some cases different quality control test methods and field procedures to ensure that expected durability and mechanical property performance are achieved.

A review was made of UHPC construction methods to examine potential process requirements to achieve durable concrete and prevent material weakness from preferential fiber orientation or segregation. Durability, mechanical property test methods, and performance were also reviewed to identify candidate test methods and gaps in knowledge to help guide the experimental research program. A review of non-destructive methods that could be used to quantify fiber orientation and distribution of UHPC in structural members was also made.

2.2. UHPC Materials and Mixture Proportions

The formulation of non-proprietary UHPC mixtures requires particle size optimization through the use of several different cementitious materials and fine aggregates. Portland cements with a lower content of C_3A, sulfate, alkali content, and fineness are preferred because they have less negative impact on the workability and consequent entrapped air content [21]. Large quantities of supplementary cementitious materials are used, particularly silica fume and often slag cement. Silica flour can also be used [22]. A fine sand is used for the aggregates. Very high dosages of high-range water-reducing admixture are used, along with in some cases hydration stabilizers. Fibers are used to give the concrete a high tensile strength and, in some cases, give the UHPC strain-hardening properties. Steel is usually used between 1 and 4 percent by volume, however glass or PVA fibers are sometimes used for non-structural architectural panels [23]. Some examples of constituent material and mixture designs used for UHPC are presented in

Table 1.

Table 1: Typical material constituent and mixture designs for UHPC

Reference	Powder lb/yd3 (kg/m3)	Chemical admixture (SP) lb/yd^3 (kg/m^3)	Fine aggregate lb/yd^3 (kg/m^3)	Water lb/yd^3 (kg/m^3)	Fiber lb/yd^3 (kg/m^3)
FHWA[24]	1846 (1095) (Class H oil well CEM + SF)	24 (14)	1655 (982)	278 (165)	416 (247) (steel)
Meng et al.[25][26]	1807 (1072) (Type III CEM+FA+SF)	20 (12)	1704 (1011)	288 (171)	263 (156) (steel)
	1807 (1072) (Type III CEM+FA+SF)	22 (13)	1610 (955)	288 (171)	209 (124) (steel + synthetic)
	1896 (1125) (Type III+CEM+SL+SF)	22 (13)	1682 (998)	281 (167)	263 (156) (steel)
Wille et al.[27]	2048 (1215) (Type I CEM+SF+GP)	7 (4)	1761 (1045)	300 (178)	332 (197) (steel)
Park et al.[28]	1910 (1333) (Type I CEM+SF+GP)	98 (58)	1595 (946)	290 (172)	265 (157) (steel) (micro + macro)
Yu et al.[29]	1938 (1150) (Type I CEM +FA+SF)	56 (33)	1603 (951)	334 (198)	263 (156) (steel)
El-Tawil et al.[30]	1633 (969) (Type I CEM +SL+SF)	39 (24)	1971 (1169)	264 (157)	265 (157) (steel)
	1633 (969) (Type I CEM +SF)	17 (10)	2056 (1220)	278 (165)	

2.3. Fabrication Methods

Enhanced quality control is required to ensure members made with UHPC have the desired structural properties. Like normal-strength concrete, the quality of UHPC can be highly affected by the mixing and placement methods used. Because of the low w/cm and high fiber volume, UHPC requires more mixing energy than normal-strength concrete. UHPC is designed to be self-consolidating, but planning is needed to prevent fiber orientation and segregation problems, cold joints, and achieve an acceptable finish. UHPC curing will affect the hydration rate and type of product formed, greatly affecting strength, dimensional stability, and durability.

2.3.1. Mixing

Compared to conventional concrete, a higher energy is required during the mixing of UHPC. In order to obtain this amount of mixing energy, the mixing time is often increased. UHPC mixing time is often longer than 10 minutes. It can be reduced by carefully optimizing the mixture proportions, increasing the speed of the mixer, or using a high-shear mixer [5]. The UHPC mixing sequence is an important factor to ensure uniformity and consistency. Dry ingredients are usually added first to disperse ingredients and break down agglomerations by the shear action. The admixtures and water are then added, and the mixing is continued until fluidity is optimized.

The fibers are sometimes added at the beginning if a high shear mixer is used. The actual mixing procedure may vary.

2.3.2. Placement Method

The placement method may affect the mechanical properties of UHPC. The strength and tensile performances are highly influenced by the fiber orientation [31]. Fibers tend to orient themselves in the direction of concrete flow [31]. The degree of preferential orientation depends significantly on the placement methods, concrete viscosity, and flow distance [32–34]. Consequently, the placement process is a primary consideration when planning UHPC member fabrication.

The rheological properties of UHPC are affected by the content, material, and type of fibers. As the fiber content increases, the viscosity and yield stress increase leading to a decrease in workability and an increase in the probability of fiber interlock. When the fiber content exceeds a critical fiber concentration, the fibers can form clumps and balls, which make it hard for placement operations. Fiber balls can also result from locally high fiber concentrations from poor mixing [6]. Fiber agglomeration usually results in an unworkable mix; therefore, as UHPC mixes tend to stiffen rapidly, the placement should be done quickly. Internal vibrators are not allowed for UHPC because they can cause preferential orientation or even sedimentation of the fibers. Limited external vibration could be used for 1 or 2 seconds to facilitate release of entrapped air [5,35].

Placement techniques can influence the amount of preferential fiber orientation. While there is a concern that preferential orientation could cause weak zones or directions, preferential orientation of fibers can be used to increase the UHPC tensile strength where desired and increase the efficiency of the fibers [32,36,37]. Crack bridging by preferentially-oriented fibers reduces the widths of transverse cracks and increases the composite tensile strength in the direction of orientation. Strengths perpendicular to the direction of orientation are lower due to the reduced number of fibers oriented primarily in the transverse direction. The effect of concrete placement speed on fiber orientation was evaluated by moving a chute at 5 in./s, 10 in./s and 20 in./s. Wille and Parra-Montesinos [11] found that increased speeds created thin ribbon-like layers in the UHPC that would give a preferred fiber orientation along the length of the beam and better flexural strength results in beams tested according to ASTM C1609 samples [10]. Another study looked at two placement methods: a direct method, and use of an L-shaped device to control the flow of UHPC and provide fiber orientation [39]. The results of flexural strength, toughness, and modulus of rupture were compared. The UHPC specimens prepared by the L-shape device exhibited higher mechanical properties, 64.3%, 65.1%, and 77.1%, respectively, compared with specimens prepared by a direct-cast method. The effect of two different placement methods, placing the concrete at the center and the corner of the UHPC specimen, on the ultimate flexural strength was investigated (Yoo et al., 2014). The specimens with concrete placed in the center showed higher flexural strength because of better fiber dispersion with more fibers at the crack plane [40]. Another study examined the effects of fiber orientation on reinforcing bar pullout strength and used a casting device (chute) with sixteen channels to control the flow of UHPC [41]. The measurements were taken using pullout specimens with perpendicular, parallel, and random fiber orientation. The results showed that the specimens with fibers orientated

perpendicular to the load direction recorded the highest pullout forces, followed by the random orientation, and then the parallel orientation [41].

While studies have shown that fibers can be preferentially oriented on purpose, planning is critical to prevent problems. Concentrating the fibers in one direction requires that the member will have a lower percentage in other directions, giving lower tensile strength in that direction. Most studies on concrete fiber orientation control have been conducted on small specimens or slabs. For long-line prestressed members, work is needed to determine how to prevent fibers from preferentially orienting in the direction of the prestressing.

2.3.3. Curing Methods

Curing methods greatly affect UHPC microstructural development, which has a large impact on mechanical and durability properties. The most popular methods of curing to provide a necessary environment for the concrete are water curing, hot air curing, steam curing, and autoclave curing. In addition to accelerating cementitious material hydration, higher curing temperatures are used to change the type and microstructure of hydrates formed.

In UHPC, there is a strong relationship between curing temperature and the development of strength. For a precast UHPC plant, standard steam curing can be used to ensure rapid strength development. For one UHPC pedestrian bridge tested, the early strength was reduced from 215 to 147 MPa when the 194°F (90°C) steam curing was lowered to 158°F (70°C) [42]. Koh et al. showed that while concrete cured at ambient temperatures can attain a 90-day strength similar to that of steam-cured concrete, the strength during the first week is significantly lower [43]. Florida precast concrete producers, however, do not like to use steam because of the cost. The high ambient temperatures in Florida, the use of insulation, and the high heat of hydration of UHPC mixtures can still lead to high in-place temperatures and rapid strength gain without added heat. Yazici investigated the effect of curing condition on the mechanical properties of UHPC and concluded that steam curing was effective for increasing the compressive strength; however, it caused a reduction in flexural strength compared to standard curing at 28 days. This was thought to be because of the decreased bond strength between matrix and fibers [44].

Arunachalam and Vigneshwari found that oven-curing increased UHPC compressive strength [45]. However, in a study done Gu et al., it was observed that oven curing led to lower chloride and freeze-thaw resistance when compared to standard and steam curing. This thought to be because of internal micro-cracks that formed [46]. When oven curing is used, the coupled effects of both mechanical and environmental loads will play a role in determining the durability of UHPC structures [46]. More work is needed to examine the impact of curing temperatures on concrete durability properties.

The particular phases that form under ambient and elevated temperature curing will depend on the particular composition of UHPC used. Curing UHPC under lab temperature gives similar types of hydration products as normal-strength concrete. This includes calcium-silicate-hydrate (C-S-H), calcium hydroxide (CH), alumina, ferric oxide, monosulfate phases (AFm) and alumina, ferric oxide, trisulfate (AFt) phases. Differences in the quantities of hydration products will occur because of the pozzolanic reactions from high amounts of SCMs. The pozzolanic

reaction that happens when silica fume reacts with calcium hydroxide to form calcium silicate hydrate (C-S-H) is activated under high temperature [47,48]. C-S-H has been found to stay amorphous up to at least 194°F (90°C) [47].

Microstructural studies of autoclaved UHPC have found that phases, hydration product crystallinity, and porosity change as the temperature increases above 212°F (100°C) and the pressure increases. One study found that porosity reached a minimum when the concrete was cured between 302° and 392°F (150° and 200°C). When there are pozzolans to provide silica to react with calcium hydroxide, the Si/Ca ratio in crystalline calcium-silicate-hydrate phases formed also increases [49]. Heat treatment leads to phases such as foshagite, xonotlite, and jaffeite with portlandite still present. Autoclaving leads to the disappearance of portlandite. Afwillite, foshagite, and xonotlite can form at pressure above 72.5 psi (5 bars) temperatures above 302°F (150°C). Afwillite, foshagite, tobermorite, and xonotlite can form at pressures of 218 psi (15 bars) and temperatures above 392°F (200°C) [49]. Crystalline calcium-silicate-hydrate fill in porosity that normally would be empty, giving much higher compressive strength for UHPC when autoclaved [49]. Calcium hydroxide content is significantly reduced from pozzolanic reactions under autoclave conditions. The bound water content of hydrates also changes, altering hydration product density and space-filling ability [50].

2.4. Fresh Concrete Properties

The low water-cementitious material ratio, high paste content, and use of high volumes of fibers impart different fresh properties on UHPC than are typical for normal-strength concrete. A review of the causes of these properties and test methods used is provided.

2.4.1. Use of Chemical Admixtures

The superior mechanical and durability of UHPC is due mainly to the use of very low water-cementitious material ratios (w/cm). The low water mixture content of UHPC can give the mixture poor workability; therefore, high dosages of high-range water-reducing admixtures or superplasticizers are needed to achieve its fluidity. In order to understand concrete fresh properties, a discussion of the role of superplasticizers is helpful. Superplasticizers are used to reduce the concrete yield stress. Most superplasticizers do very little to the concrete viscosity, resulting in very sticky mixtures [51]. Superplasticizers improve the workability of concrete by adsorbing onto cement particles and providing electrostatic repulsion and steric hindrance to reduce particle flocculation [52]. Different types and dosages of superplasticizer will show different effects on the fresh and hardened properties of UHPC. Plank et al. [26] used two different types of superplasticizers, methacrylic-acid-ester-based and allyl-ether-based, in UHPC mixes having cement and silica fume. They reported that methacrylic-acid-ester-based superplasticizers interacted well with cement but not with silica fume, and the allyl-ether-based superplasticizers were more effective with silica fume. Using both of them resulted in better dispersion and interaction [53]. The incorporation of chemical admixtures is known to affect the total porosity and the pore size distribution [47]. Insufficient dosages of superplasticizers would make the fluidity of UHPC low and lead to a higher percentage of porosity. Courtial et al. studied the effect of different dosages of polycarboxylates on the microstructure of UHPC. They found that when the addition of polycarboxylate was modified from 1.8% to 2%, the belite phase content significantly decreased [54]. Wille et al. studied 38 UHPC mixtures and concluded that

based on the best spread value of the paste and entrapped air content, the optimum amount of superplasticizer (polycarboxylate ether-based) ranged from 1.4% to 2.4% of cement by weight [55].

It was reported that the workability of concrete is usually controlled by the density of the side chain of superplasticizers, whereas the retardation time is mainly influenced by the length of the side chain [56]. Hirschi et al, investigated eight types of polycarboxylate-based superplasticizers on the setting time and strength of UHPC [57]. The setting time had some variation but showed a good indication for the development of early compressive strength [57]. Mixtures having superplasticizers with long side-chain length showed the highest early strength compared to those which had medium side length [57]. Clearly, superplasticizer selection and dosage will greatly impact UHPC flow and setting properties.

2.4.2. Rheology

Compared to conventional concrete, UHPC has a higher viscosity. This is owed to the very low w/cm and use of large dosages of superplasticizers that often do little to lower the viscosity. Therefore, its rheological properties should be assessed during trial batches and structural member mockups to ensure it can be placed. Rheological evaluation of the cement paste helps in understanding the flow characteristics and the development of the early-age structure in pastes. The flow and pumping performance can be evaluated by rheological behavior as well [58]. Many test methods have been used to evaluate the yield stress and/or plastic viscosity of UHPC, such as mini-slump, mini V-funnel flow test, modified slump test, portable vane test, and inclined plane test [6]. However, among these test methods, the mini-slump test is the easiest way to characterize the flowability of the fresh paste of UHPC as it is inversely related to yield stress.

The flow test is typically used to measure the place ability of mortar in its fresh state. Since UHPC does not typically use coarse aggregates, the flow test with some modifications has become a widely used test for fresh UHPC. When used with UHPC, it is usually referred to as the mini-slump test and can be performed in the field for quality control testing. ASTM C1856 “Standard Practice for Fabricating and Testing Specimens of Ultra-High Performance Concrete [59]” modifies ASTM C1437 “Standard Test Method for Flow of Hydraulic Cement Mortar [60]” for UHPC to account for its unique properties. ASTM C1856 does not allow tamping in the mold or table-dropping to aid flow because UHPC is designed to be self-consolidating. This allows for the flow table to be taken off of the concrete pedestal normally used, making it field-portable, as shown in Figure 1. The brass cone mold is filled with UHPC in a single layer without tamping, as shown in Figure 2. The excess concrete is screeded using a small rubber bar [59]. Once filled and screeded, the cone is lifted to allow UHPC to spread evenly on the table. Spread measurements are taken after 120 ± 5 s to allow the self-consolidating UHPC time to stop flowing [59]. A flow between 8 and 14 in. (203 and 366 mm) is typically recommended to ensure concrete flowability [5]. Figure 3 shows UHPC at the end of a flow test with measurement of 8.5 inches (216 mm).

Figure 1: Flow table at the field

Figure 2: Filling the mold with UHPC

Figure 3: Static flow test with measurement of ~8.5 in

A method to calculate concrete fundamental rheological properties from the mini-slump test has been developed. Roussel et al. proposed a theoretical approach to estimate the yield stress of the cement paste from the mini-slump test by using a viscometer. Their approach used the final spread diameter of the mini-slump test, the surface tension of the fluid, and the contact angle between the fluid and the test surface to model the rheological properties [61]. A study done by Tregger et al. made different mixtures to measure the viscosity and yield stress by using a rheometer, plus the mini-slump test was performed simultaneously [62]. They confirmed good correlations between the yield stress and mini-slump flow and between the final spread time and viscosity/yield stress ratio [62]. Choi et al. proposed a more accurate method by considering the changes in final diameter according to the time measured at the mini-slump test [63]. A computational fluid dynamic analysis was used to simulate the mini-slump test and compared it to mini-slump experiments on four different UHPC mixtures. It was concluded that by applying the mini-slump test, the UHPC rheological properties could be easily estimated [63].

The very low water-cementitious ratio (w/cm) of UHPC can cause problems with slump loss due to evaporation leading to a big impact on the consistency of the mix. Therefore, many U.S. states require UHPC to be placed continuously and monolithically to avoid problems at the interface between placements as well as cold joint problems that may occur from the formation of elephant skin [64,65]. Cold joints may occur when having two placements of UHPC as elephant skin forms quickly on the surface of UHPC and hinders bonding of the layers as shown in Figure 4. Cold joints as a result of delays during concretes placement may occur quickly and randomly in unexpected locations and can lead to cracking. Lee et al. studied the effect of placement delays up to 60 minutes on the bonding shear performance. The results showed that a good bond could be developed if the delay was kept to 15 minutes or less, with only an 8% reduction in shear strength expected. After 15 minutes, however, a large drop in the bond strength was found [66].

It is recommended that a form liner or mesh be used to create a fluted surface to increase interlock and bond strength between adjacent placements of concrete. [67]

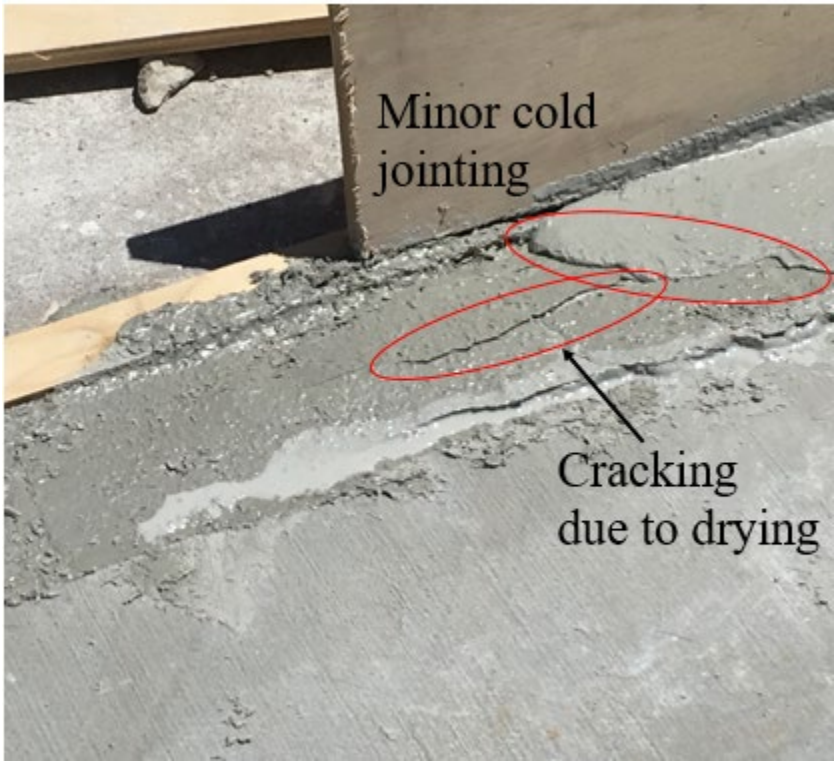

Figure 4: Defects in a UHPC joint due to placement procedure

2.4.3. Setting Time

UHPC will often have longer initial and final setting times than normal concrete because of the large quantities of high-range water-reducer used. UHPC initial and final time of set is usually measured by penetration standard method ASTM C403 "Standard Test Method for Time of Setting of Concrete Mixtures by Penetration Resistance [68]" or by Vicat Needle method ASTM C191 "Standard Test Methods for Time of Setting of Hydraulic Cement by Vicat Needle [69]" with some alterations mentioned by ASTM C1856. In the ASTM C403 standard method, a penetration needle is pressed into mortar in a rigid container with dimensions at least 6 in. (152 mm) in width and 6 in. (152 mm) in height. The penetration needle is attached to a press with a load cell or other device to measure the force and with a dial gauge to record the penetration distance into the concrete. The maximum force when the needle penetrates at least 1 . (25 mm) into the UHPC sample is recorded periodically [68]. The time when the pressure required to insert the needle 1 in. (25 mm) reaches 500 psi is considered the time of initial set and the time when it reaches 4000 psi is considered the time of final set.

ASTM C1856 modifies ASTM C191 for use on UHPC with only minor changes. In this test, UHPC instead of cement paste is placed into a conical ring without consolidation. The sample is

made to the specified flowability for the project instead of a normal consistency as is typically used. A 0.039-in. (1-mm) diameter needle with a 0.66 lb (300 ± 0.5 g) weight attached on top is dropped onto the sample inside a conical ring. The test is repeated periodically on different spots on the sample. In between tests, the sample is stored in a moist room, limiting applicability of this test to laboratory use and material prequalification. The initial setting time is taken as the elapsed time between mixing and when the weighted needle penetrates 1 in. (25 mm) into the surface. When no penetration is observed, the elapsed time from molding to that point is the Vicat final setting time [69].

To illustrate the effect that high admixture doses can have on the concrete time of set, some cases in the literature are highlighted. In one study, four different UHPC mixtures were tested using the penetration resistance test. The initial setting times ranged from 70 minutes to 15 hrs, and final setting times were between 5 hours and 20 hours [5]. In some UHPC mixes, based on the type and dosage of chemical admixtures, the UHPC can have an initial set time as low as 90 minutes and final setting time of 7 hours [70]. The difference in setting time can be attributed to differences in superplasticizer type and dosage, and in some cases the use of accelerators.

Due to the thixotropic properties and low w/cm of some UHPC mixes, the initial and final set times can be difficult to measure accurately. In one study, Graybeal tested the setting times of six different UHPC mixes and reported that one of them could not be measured due to the needle not being able to penetrate the sample. If left undisturbed, UHPC can form a strong surface layer called an elephant skin that can inhibit needle penetration. The rest of the mixtures tested had initial set times ranging from 4.3 hours to 9 hours and final set times from 7 hrs to 24 hrs [24].

2.5. Mechanical Properties

UHPC has high compressive strength; however, without fibers it has very brittle behavior. Fibers between 1 and 4% are commonly used to increase its ductility, with many mixtures exhibiting strain-hardening characteristics. If the UHPC tensile toughness can be provided reliably in concrete structural members, this could lead to a reduction in mild steel reinforcement requirements.

Testing is needed to verify concrete tensile properties to assure good structural performance. Several test methods have been proposed for quantifying the concrete tensile properties. These tests can be classified as flexural, panel, splitting, compact tension, or direct tension tests. Each type of test has its advantages and drawbacks. Variations of each type of test have been developed for plain or fiber-reinforced concrete to try to solve some of these issues for specific purposes. Instead of reviewing the dozens of variations of these tests in detail, this review will focus on tests that have been suggested for quality control testing, and that show the greatest promise. Consequently, panel tests will not be considered because of the size sample required and difficulty for labs to routinely test. Although compact tension tests can provide important fracture toughness information, they are difficult to run, require specialized equipment, and have a high coefficient of variation, so they will not be described in detail in this report [71].

2.5.1. Flexural Tests

Several flexural tests have been developed to indirectly measure concrete tensile properties. These tests attempt to measure the concrete deflection or crack opening under load as a measure of the concrete ductility and toughness. They are typically based on three- or four-point bending tests, with some beams made with notches [72]. This review will focus on two that have a history of use in the United States and have the most potential for adoption as a quality control test if modified.

ASTM C1018 "Standard Test Method for Flexural Toughness and First-Crack Strength of Fiber-Reinforced Concrete (Using Beam with Third-Point Loading)" [73] measures the concrete beam middle deflection when placed under third-point loading. The tensile stress-strain response of UHPC can be divided into four sequential phases: elastic behavior, brittle behavior - formation of many cracks in the UHPC matrix that are perpendicular to the direction of applied stress, crack straining where the individual cracks widen, and the localization stage where the individual cracks reach the strain limit [5]. The concrete toughness is defined as the area under the load-deformation curve up until a specified beam deflection [73]. This test was discontinued in 2006 and has only been used sparingly for UHPC. One study found a small difference in performance when steam curing was used. The modulus of rupture values for the first cracks were 1.3 ksi for the untreated specimens and between 1.3 ksi to 1.5 ksi for steam-cured specimens [5].

ASTM 1609 "Standard Test Method for Flexural Performance of Fiber-Reinforced Concrete (Using Beam with Third-Point Loading)" [11] has become a common method to use for measuring the flexural performance of UHPC. In this method, a simply supported beam is tested under third-point loading as shown in Figure 5. An example of a specimen in the test machine is shown in Figure 6. The size of the UHPC specimen tested is based on the maximum fiber length. Longer fiber lengths require larger cross-sections [59]. The deflection of the sample middle compared to the supports is measured by securing a jig onto the sample above the supports and measuring the distance between a bar connecting the two points above the supports to the top of the sample middle. The sample is loaded using deflection control and not displacement or force control. The loading rate is kept between 0.002 to 0.004 in./min until a net deflection of L/900 of a specimen is reached. Assuming linear-elastic response up until the first-crack occurrence, the first peak deflection can be estimated using Equation 1:

$$\delta_1 = \frac{23P_1L^3}{1296EI}\left[1 + \frac{216d^2(1+\nu)}{115L^2}\right] \qquad \text{Equation 1}$$

Where: δ_1 is the first peak deflection in inches
P_1 is the first peak load in lbf
L is the total beam span length in inches.
E is the estimated modulus of elasticity in psi.
I is the cross-sectional moment of inertia in inches
d is the average depth of the specimen at fracture in inches
ν is Poisson's ratio

After a deflection of L/900 is reached, the loading rate can be increased between 0.002 and 0.008 in./min until reaching a net deflection of L/150 [11]. The residual first-peak strength values can be used to calculate the strength of the concrete by using Equation 2:

$$f = \frac{PL}{bd^2} \qquad \text{Equation 2}$$

Where: f is the residual first-peak strength, psi
P is the first-peak load, lbf
L is the span length, in.
d is the depth of the specimen at the point of failure, in.
b is the average width of the specimen at point of failure, in.

Using the first-peak strength f_1, the equivalent flexural strength-to-toughness of the material can be determined from Equation 3:

$$R^D_{T,150} = \frac{150T^D_{150}}{f_1 bd^2} \times 100\% \qquad \text{Equation 3}$$

Where: $R^D_{T,150}$ is the equivalent flexural strength
T^D_{150} is the area under the load vs. net deflection curve 0 to L/150

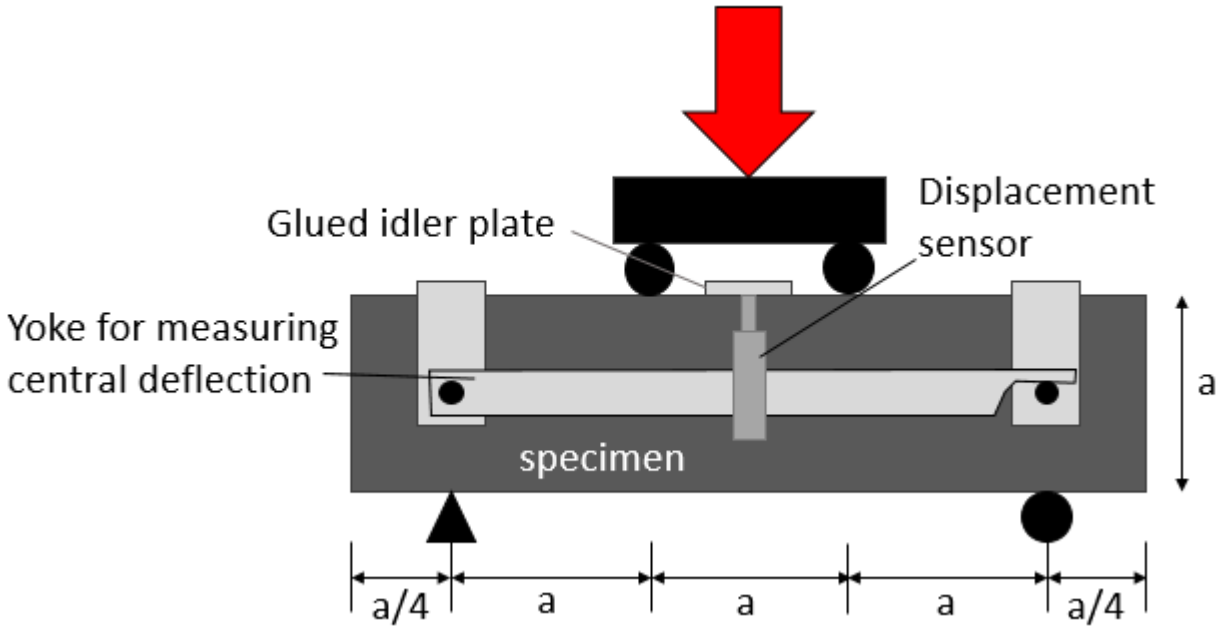

Figure 5: ASTM C1609 test schematic

Figure 6: Sample at University of Florida during testing according to ASTM C1609

ASTM C1609 may need some modifications in order to be used for quality control because many laboratories lack the ability to use deflection control to control the loading rate. Modifications may be possible to change the loading rate control method and deflection measurement method to simplify the test and widen the base of labs that could use it.

When loaded in flexure, the concrete beam section will have some regions in compression and some in tension. While the strain distribution with depth for the beam section may be linear, the stress distribution will not be because the UHPC tensile stress-strain relationship is not linear until failure. Inverse calculations are required to obtain the tensile stress-strain relationship. This requires either direct measurement of the concrete bottom strain, or assumption of the shape of the stress-strain curve [10,74]. Assuming the shape of the stress-strain curve can result in non-conservative values [10]. Flexural tests have been shown to have a high coefficient of variation of up to 20% for fiber-reinforced concrete [72]. This might be because of the span length-to-depth ratio may not be high enough.

2.5.2. Splitting Tensile Strength Test

ASTM C496 “Standard Test Method for Splitting Tensile Strength of Cylindrical Concrete Specimens [75]” is commonly used to assess the tensile strength of concrete indirectly. In this

test method, a cylinder is placed in a loading machine tested under a compressive load of 100 to 200 psi/min that is applied continuously along its side. The compressive force causes a split of the cylinder into halves. The tensile strength then can be calculated using Equation 4:

$$T = 2P/\pi ld \qquad \text{Equation 4}$$

Where: T is the ultimate splitting tensile strength (psi)
P is the ultimate load (lbf)
l is the specimen length (in.)
d is the specimen dimeter (in.)

This test is generally applicable for concrete, and since it includes assumption of mechanical behaviors that are not likely to be consistent with strain hardening fiber reinforced concrete, it needs to be modified to be applicable for UHPC. Graybeal proposed some modifications to ASTM C496 to allow it to be used with UHPC. These modifications include increasing the loading rate from 150 to 500 psi/min (1 to 3.5 MPa/min) due to the higher tensile strength of UHPC [76]. Also, since the initial cracking of UHPC occurs much earlier than the maximum tensile strength, the modified version includes using LVDTs across the middle of the cylinder, and spring-loaded clamps fitted onto the outside of the cylinder to transfer the transverse deformations to the transducers as shown in Figure 7 [76]. This allows for capturing the tensile cracking and post-cracking behavior electronically, thus calculating the tensile strength and ductility [76]. A downside of this test is it tends to inflate the tensile capacity of UHPC specimens due to differences in fiber pull-out behavior. Since cylinders are loaded in compression, it increases the normal force and friction on fibers preventing pull-out. Therefore, under this bi-axial stress state the fibers are able to hold a greater load before pulling out of concrete [76]. In fact, the discrepancy between splitting tensile strength and direct tension strength was shown to increase from 39% for plain concrete to 77% for UHPC with 3% by volume of steel fibers [77]. These discrepancies prevented widespread adoption of this test method.

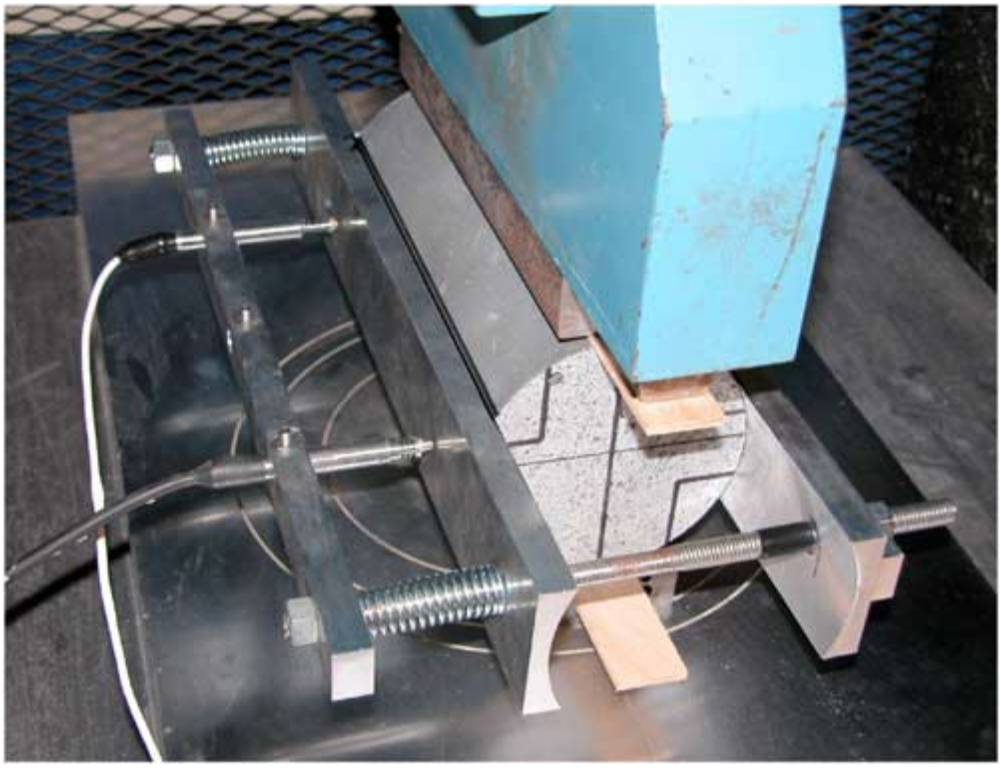

Figure 7: Splitting tensile test set-up, figure from [76]

Compared to conventional concrete, UHPC splitting tensile strength is much higher. A study was done by Ozyildirim by testing UHPC beams for splitting tensile strength (Ozyildirim, 2011). The average splitting tensile strength was measured after the initiation of the first crack, which is considered to be the discontinuity in the load-displacement curve [76]. The results showed an average value of 1.47 ksi of splitting tensile strength with a standard deviation of 0.37 ksi, and an average apparent ultimate strength of 3.21 ksi with a standard deviation of 0.27 ksi (Ozyildirim, 2011). Haber et al. made 20 UHPC mixtures to be tested for splitting tensile. All these mixes exhibited approximately the same initial cracking strength of 1.0 ksi [24]. Another study on 15 UHPC mixes showed an average of 1.08 ksi for the initial cracking strength [10].

2.5.3. Double-Edge Wedge-Splitting Test

A double-edge wedge splitting test has been developed to force the center of a sample to undergo tension perpendicular to the direction of a load application. While different dimensions have been used on samples for this test [33,71,79], the concept is the same. Figure 8 shows a schematic of the sample cross section used in the test, which is typically square [71,79]. A roller is used on the top and bottom notches to apply a normal force on each side of the notch. It can be run with and without the sawcut below the angled notch. This creates a tensile force perpendicular to the vector connecting the notches. The splitting force F_{sp} can be calculated using Equation 5 [79]:

$$F_{sp} = \frac{P \cdot (\cos\theta - f \sin\theta)}{2 \cdot (\sin\theta + f \cos\theta)}$$ Equation 5

Where: P is the load (lb)
θ is the notch angle (°)
f is the friction coefficient of the roller-concrete interface

The displacement is monitored using linear variable differential transformers (LVDTs) placed near the tip of the top notch, in the middle, and near the tip of the bottom notch as shown in Figure 8. These displacements are used to get the crack opening displacements (COD) and rotations along any axes [79]. The test can be run using displacement control at a rate of 0.051 in./s until 0.078 in. of displacement is reached, after which the loading rate is doubled until 0.157 in. of displacement is reached. At that point, the displacement rate is doubled again until the test is complete and the specimen is split in half [71].

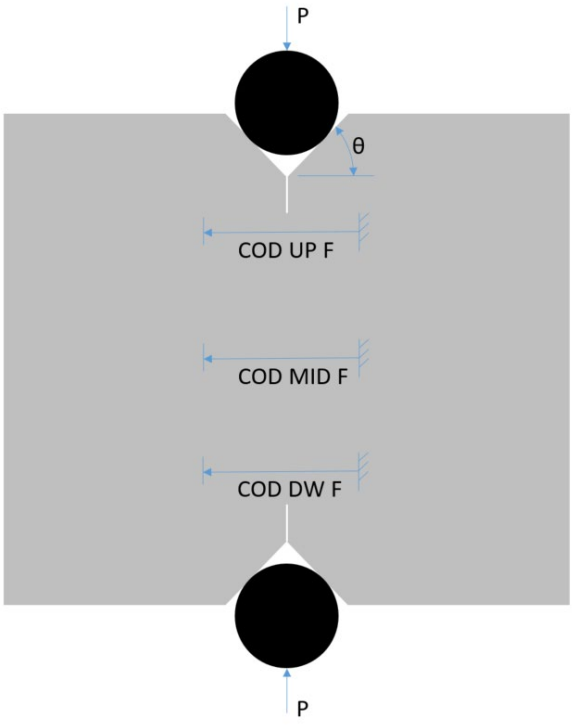

Figure 8: Schematic of double-edge wedge-splitting test, figure after [79]

This test is designed to avoid some of the drawbacks of the splitting tensile test. In the splitting tensile test, the concrete in the center of the sample will have compression in the vertical direction and tension in the horizontal direction, giving a biaxial state of stress. The compression force can add friction to fibers during pullout, changing their mode of failure. If friction can be eliminated between the concrete and the roller, this test can avoid that problem by placing forces

at an angle and separated at the notch to eliminate the compression force in the concrete at the center [79]. This test method has a coefficient of variation of 14% [71].

While this test method could provide good information about the tensile stress-strain behavior of UHPC, implementation at precast plants and local testing labs would be difficult. It requires significant instrumentation to measure the displacement at three locations using LVDTs. The displacement rates required for this test would likely be difficult to control in a simple compression machine. Finally, the sample geometry is unconventional and would require new molds or time-consuming saw cutting.

2.5.4. Double-Punch Test

The double-punch test, also known as the Barcelona test, is a relatively simple test used to find tensile properties of fiber-reinforced concrete. It has been standardized as UNE 83515 in Spain [12], but is otherwise used mainly for research purposes. This specification is based on the original double-punch method developed over 50 years ago [80]. This original double-punch test was used to calculate a single tensile strength value of normal concrete. It was meant to be a replacement for the split-cylinder test, which is comparatively difficult to set up [80]. This test can be run with a cylinder with a 6-in. diameter and 6-in. height or with a 6-in. cube. A punch with a 1.5-inch diameter and 1-inch height is placed at the center of the specimen on both the top and bottom, as shown in Figure 9.

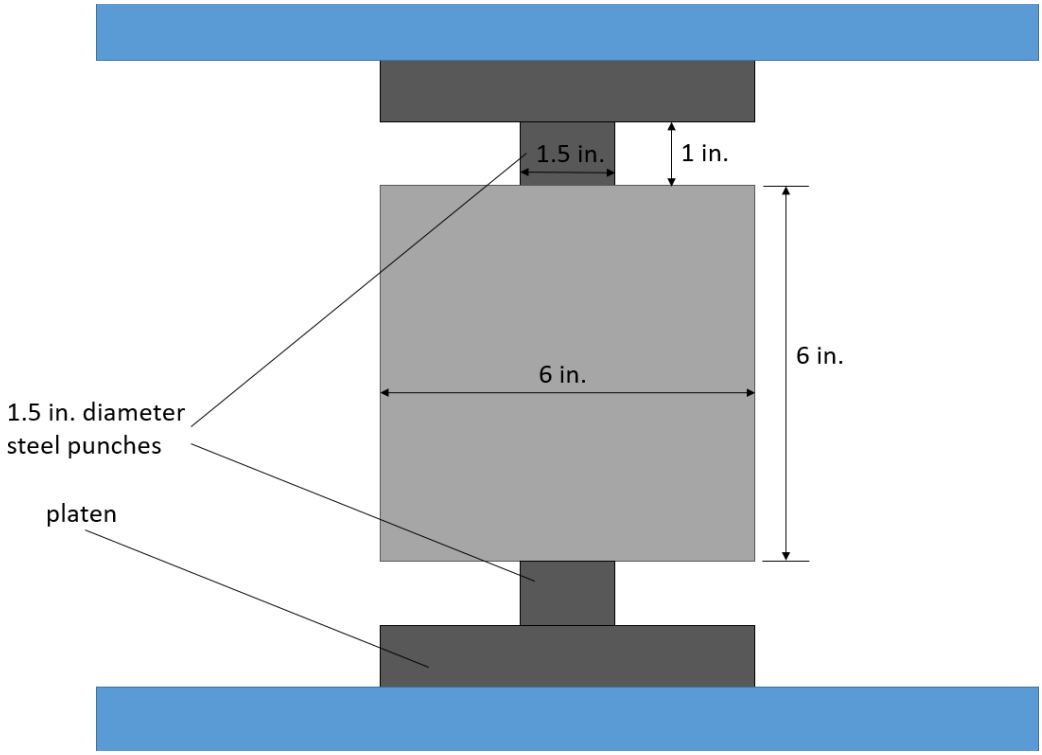

Figure 9: Double-punch test setup

The tensile strength from this test can be computed using Equation 6 as proposed by Chen (1973). It should be noted that in his 1969 paper, Chen uses a constant of 1.30 instead of 1.20 in the denominator [80].

$$f'_t = \frac{Q}{\pi(1.20 * bH - a^2)} \qquad \text{Equation 6}$$

Where: f'_t is the tensile stress (psi)
Q is the applied load (lb)
b is the radius of the cylinder (in.)
H is the height of the cylinder (in.)
A is the radius of the punch (in.)

Chen stated that this equation is valid when either *b/a* or *H/2a* is less than or equal to 5 [80]. The ASTM draft ballot for standardization of the double-punch test adds a safety factor of 0.75 multiplied in the numerator of Equation 6 to convert load to stress [81].

At the end of testing, the specimen will usually have 3-4 cracks propagating from the edge of the punch outward. Figure 10 shows a schematic of a typical specimen after failure.

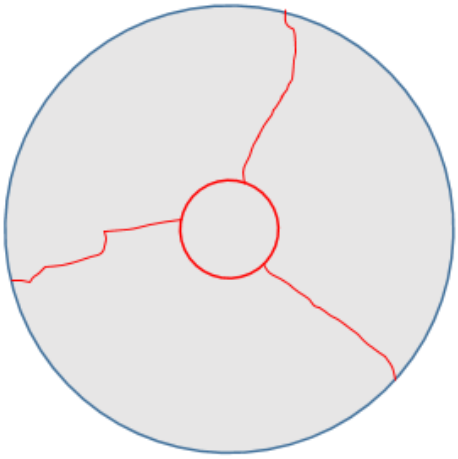

Figure 10: Typical double-punch failure

In order to modify this test method for fiber-reinforced concrete, crosshead displacement measurements were added. If a cylindrical specimen is used, the total circumferential opening displacement (TCOD) can be measured with a chain extensometer [82–84]. A typical load vs. displacement relationship is shown in Figure 11. This gives a curve of load vs. TCOD. Due to the cost and complexity associated with measuring the TCOD, some researchers have measured the axial displacement instead [82–84]. This can be done by measuring the distance between the top and bottom surfaces on the machine or by using the crosshead displacement output on the

machine used for testing. A typical result of this method is shown in Figure 12 [82–84]. As shown in this figure, there is an extended period of displacement without load in the beginning of the load vs. axial displacement graph. This region occurs when there is local crushing at the punch location, but full cracks have not yet formed in the specimen. When axial displacement is plotted vs. TCOD, a result similar to that depicted in Figure 13 is formed [82–84].

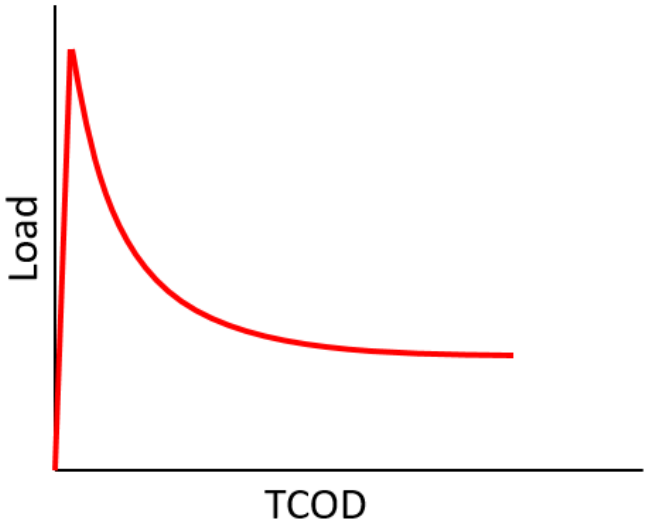

Figure 11: Typical load vs. circumferential displacement curve, figure after [82–84]

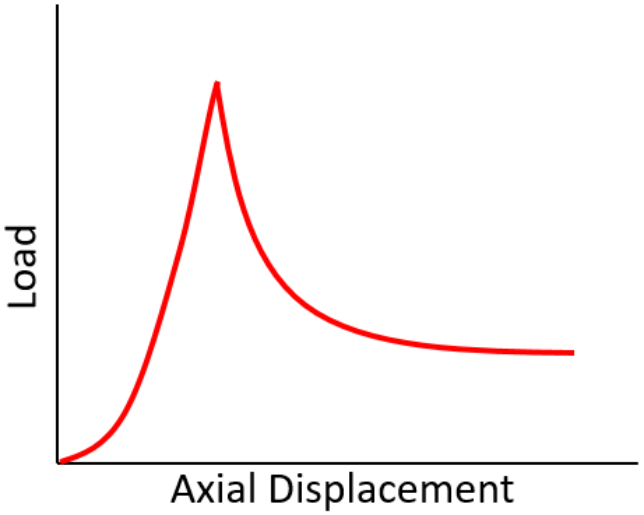

Figure 12: Typical load vs. axial displacement curve, figure after [82–84]

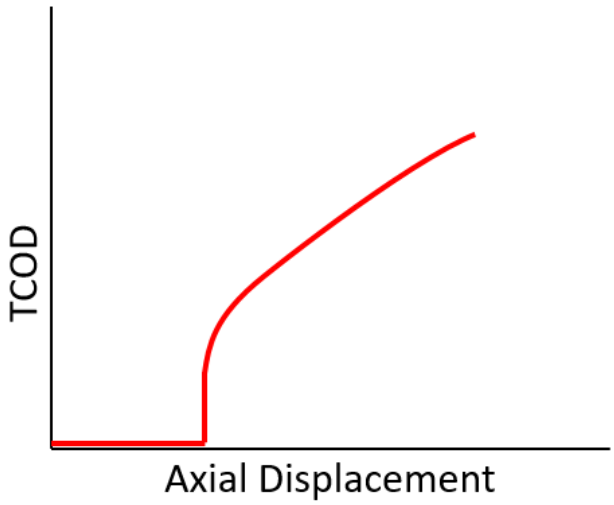

Figure 13: Typical circumferential displacement vs. axial displacement curve, figure after [82–84]

From the load vs. displacement data, multiple characteristics can be determined. In addition to the peak strength, as originally used by Chen [80], users of this test can also determine ductility of the sample. This can be done in multiple ways. First, the user could find the strength at a particular displacement past where the peak load occurs. Or, the user could find the displacement at which the strength drops below a particular load value. The residual strength (strength of fiber bridging after cracking) can also be found [84]. This value would occur after the concrete cracks and the load declines, beginning to level out. While defining the exact value of residual strength may be difficult due to the sloping load curve [84], it can be useful for comparison as it would increase with a higher dosage of fibers or better fiber pullout strength. This test can also be used to measure toughness [84], which is especially of interest for impact resistance.

The overestimate of tensile strength measured by the double punch test over that measured by direct tension testing has been shown to decrease with increasing fiber content, from 11% with plain concrete to 4% with 3% steel fibers [77]. The double punch test has also been shown to have a low coefficient of variation of between 9 [72] and 12% [85].

2.5.5. Direct Tension Test

Direct tension test methods can more realistically predict the tensile strength and ductility behavior than indirect test methods. Many different test methods have been proposed to test direct tension with different geometries (for example, notched and unnotched prism or cylinders, dog-bone or dumbbell shape) and various types of gripping or attachment systems (e.g. fixed or rotating boundary condition) [86]. More than 25 different configurations have been identified for UHPC direct tension testing [9,86]. There is no standard method however for direct tension testing of UHPC.

After several iterations of improvement, the Federal Highway Administration (FHWA) has recommended a direct tension test method for UHPC [9,10]. The test method uses a dog-bone shaped specimen with a dimension of 2 × 2 × 17 in. Aluminum plates are epoxied to each side on both ends as shown in Figure 14. Hydraulic grips of the universal testing machine are used to grip the samples and apply the tensile force to the specimens. The aluminum plates are added to the sample ends to reduce the crushing of the specimens during gripping and strengthen the sample where gripping forces and stress concentrations occur. This helps ensure that the cracks and sample failure occur in the sample center where the strain is measured. Some modifications were proposed to help prevent test failure around the end of the plates. These modifications were to use a small compressive force in the tapered portion of the aluminum plates and to use some clamps to prevent the plates from delaminating during loading as shown in Figure 15 [64].

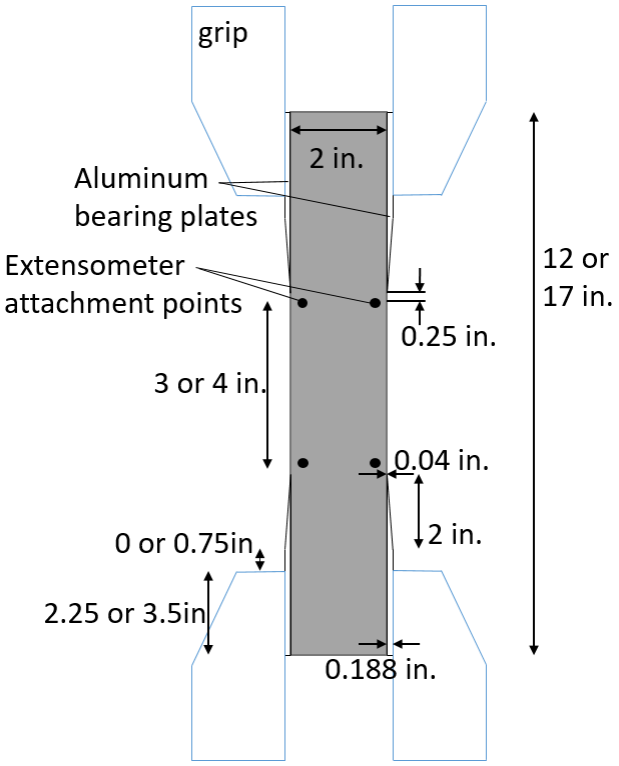

Figure 14: Schematic of direct tension UHPC test specimen

Figure 15: Tensile test before gripping with the C-clamps attached

While direct tension tests provide important information needed for structural design obtained during the material prequalification, none of the direct tension tests developed to date show promise for use in project quality control operations. The direct tension test proposed by FHWA [10] and that recommended by Riding et al. [64] are too complicated for use by precast plants and local testing labs and require expensive equipment, limiting their utility to qualification testing. Direct tension test methods possibilities that are simple such as briquette tests have been found to be too variable, difficult to get the sample aligned and avoid bending [64], or subject to fiber alignment issues [86].

2.5.6. Compressive Strength

The compressive strengths of mortar and concrete are typically used as an initial indication of their quality. UHPC strengths have been reported to exceed 150 MPa and are governed by many factors such as curing method, fiber shape and content, and testing methods. In the U.S., UHPC compressive strength is usually tested in accordance with ASTM C39 "Standard Test Method for Compressive Strength of Cylindrical Concrete Specimens" [87], along with ASTM C1856. One major change that ASTM C1856 makes to the ASTM C39 method is the reduction of specimen size (3 × 6 in. instead of 4 × 8 in.). This is partially due to limitations on the loading capacity of some compression testing machines. It also serves to reduce the amount of expensive UHPC that is wasted for testing. Because UHPC has a very small maximum aggregate size, the specimen size reduction does not affect results as much for UHPC as it would for normal

concrete. As described in ASTM C39, the loading rate for normal a concrete cylinder would be 35 ± 7 psi/s, but since UHPC has a significantly higher compressive strength, ASTM C1856 specifies a loading rate of 145 ± 7 psi/s in order to decrease the testing time (ASTM C1856-17, 2019). Both ends of UHPC specimens need to be ground because elastomeric pads are not suitable for use above 12 ksi, and bonded sulphur caps are weaker than the UHPC concrete.

2.6. Durability

UHPC is reported to have excellent performance against deterioration mechanisms that involve water or ion ingress into concrete. These mechanisms include freeze-thaw deterioration, deicer-salt scaling, abrasion, alkali-silica reaction, sulfate attack, chloride penetration, and carbonation. This durability is thought to come from the very low connected porosity of UHPC [88,89].

2.6.1. Freeze-Thaw Resistance

Air entrainment is typically used in concrete to provide protection against freeze-thaw deterioration. It is precluded from being used in UHPC however because it would unacceptably reduce the strength. In contrast to normal-strength concrete without air entrainment, UHPC has been shown to have excellent freeze-thaw durability. The low permeability and porosity of UHPC are thought to keep the concrete from becoming critically saturated [90].

Several studies have been conducted to investigate the freeze-thaw performance of UHPC. Ahlborn et al. performed freeze-thaw cycling on UHPC in accordance with ASTM C666, procedure B (freezing in air, thawing in water) for 300 cycles with no degradation measured [91]. Similarly, Acker and Behloul reported that UHPC showed no degradation after 400 cycles of freezing and thawing [92]. Russell and Graybeal showed that untreated UHPC specimens and UHPC specimens subjected to steam curing showed at least a 96% relative dynamic modulus of elasticity after 690 cycles of freeze-thaw conducted according to ASTM C666 procedure A-freezing and thawing in water [5]. Another study measured the resistance of UHPC to freeze-thaw in the presence of a NaCl solution, conducted according to CEN/TS 12390-9, that showed an extremely low mass loss after 112 freeze-thaw cycles [93]. Another study performed on UHPC with 2.5% steel fibers found a 15.8% increase in loading capacity after 600 freeze and thaw cycles [94]. Freeze-thaw testing of concrete made with locally produced materials having a 14,100-psi compressive strength showed no freeze-thaw damage up to 600 cycles. Between 600 and 1500 cycles, minor damage was observed, resulting in exposed steel fibers and reduced first-cracking strength [95].

UHPC has been found to have excellent field durability in cold climates. At the Cattenom power plant in France, UHPC was used to replace some of the beams. After six years of exposure in the aggressive environment with natural freeze-thaw cycles, there was no noticeable degradation of the beams [96]. In another case, UHPC samples were placed at the Treat Island, Maine exposure site maintained by the U.S. Army Corps of Engineers. Tide levels vary by as much as 22 feet at this site with the temperature during the winter ranging from -10 to -37°F (-23 to -38°C), making this site an ideal place to test UHPC performance. After several years of exposure and hundreds of freeze-thaw cycles, no evidence of deterioration or mass loss was seen on any samples [97].

While theories exist on the mechanism responsible for UHPC freeze-thaw durability, testing is needed to validate these theories. This will provide guidance to mixture design and test methods required for freeze-thaw performance. UHPC testing performed to date has mostly focused on concrete with compressive strength above 22 ksi. It is also not known at what strength level UHPC transitions to excellent freeze-thaw performance. ASTM C1856 requires UHPC freeze-thaw testing to be conducted according to ASTM C666 Procedure A for at least 300 cycles or until its relative dynamic modulus of elasticity reaches 90%. ASTM C666 requires the concrete to be cured in limewater for 14 days before testing, or 2 days if saw-cut from hardened concrete. No changes are recommended for UHPC curing or saturation level. If UHPC freeze-thaw durability comes from the low degree of saturation, this may not be reliable long term.

2.6.2. Scaling Resistance

UHPC has been shown to have excellent deicer-salt scaling resistance. The mechanism is not known, but it is possible that the high material tensile strength could help resist fractures that occur in the surface from the glue-spall effect [98]. Graybeal tested the salt scaling resistance of UHPC mixes and found no damage after 215 cycles [99]. Another study compared UHPC and normal-strength concrete. The mass loss due to surface scaling was > 1000 g/m^2 for normal-strength concrete compared to 7 g/m^2 for UHPC mixes after 1000 freezing and thawing cycles [96]. Another study showed that UHPC exhibited 100 g/m^2 mass loss after 56 cycles, or only 6.7% of the test limit [100]. Salt scaling performance has been measured for some non-proprietary UHPC mixes that were subjected to 50 cycles of freezing and thawing, and there was no visible deterioration observed, resulting in a zero rating [101].

2.6.3. Resistance to Alkali-Silica Reactivity

Concrete can experience deterioration from Alkali Silica Reaction (ASR) when reactive aggregates are used in concrete with a sufficiently high alkali loading. Due to the high content of cement and consequent alkali loading in UHPC mixes, it is important to evaluate the risk of ASR. One study with very-high-strength concrete made without SCMs found that ASR could occur, even at 0.2 w/cm. That study found however that when the mixture used fly ash, it was able to suppress the reaction. UHPC made with silica fume has shown excellent ASR resistance [102]. The ASR risk of UHPC was tested in one study in accordance with ASTM C 1567 "Standard Test Method for Determining the Potential Alkali-Silica Reactivity of Combinations of Cementitious Materials and Aggregate (Accelerated Mortar-Bar Method)" [103]. In this test, UHPC samples are immersed in a 1 N NaOH solution at 176°F (80°C). No expansion or deterioration of UHPC was found in this testing [93]. Graybeal also used an accelerated mortar bar test to measure ASR risk and found expansion below the nonreactive threshold limit of 0.10% [5]. Moser reported that no increase in expansion for UHPC samples could be measured after 600 days, and the expansion was below the threshold limit [104]. Sawab et al. tested some UHPC mixes containing quartz sand and compared the specimens with controls containing river sand. The results indicated that the control specimens fell into the potentially deleterious category, while UHPC specimens showed no expansion [105]. In summary, the results from several studies indicate that UHPC made with SCMs should not experience ASR, especially if steam-curing is applied.

2.6.4. Sulfate Resistance

Very limited research has been conducted on UHPC sulfate resistance, mainly because UHPC risk to sulfate attack is generally considered minimal. One study was performed, however. Three UHPC prisms of 1.6 × 1.6 × 6.3 in. (40 × 40 × 160 mm) were immersed in a sodium sulfate solution Na_2SO_4 (16 grams of SO_4^{2-} per liter) for 500 days, and the length was measured regularly. The results indicated no expansion or deterioration of the samples. [93]. These results demonstrate how the very low permeability of UHPC keeps sulfate ions out of the concrete, significantly reducing the risk of deterioration from external sulfate attack.

2.6.5. UHPC Transport Properties

The ability of concrete to resist fluid ingress through the specimen is an important indicator of its durability. Penetration of concrete by fluids containing deleterious ions occurs through pores and the capillary connections between the pores. Ion transport occurs inside concrete by different mechanisms such diffusion due to concentration gradients, pressure gradients from external sources, and capillary action (sorptivity) [106].

2.6.5.1. Electrical Tests

Electrical properties of concrete have been used for many years as a quality indicator. Electrically conductive pore solution can fill concrete pores, making it electrically conductive. The concrete electrical resistivity, or inverse of conductivity, is dependent on both the pore system and the pore solution conductivity, and can be normalized by the pore solution resistivity ρ_0 (Ω·m) to give an empirical material pore system index called the formation factor F, as shown in Equation 7 [107]:

$$\frac{\rho_T}{\rho_0} = F \qquad \text{Equation 7}$$

Where: ρ_T is the concrete electrical resistivity (Ω·m)

The formation factor is independent of specimen size or shape, and it is related to the pore system as the inverse of the product of the concrete porosity volume $\emptyset$ and connectivity β, as shown in Equation 8 [108,109]:

$$F = \frac{1}{\emptyset\beta} \qquad \text{Equation 8}$$

The Nernst-Einstein relationship can also be used to relate F and the concrete electrical resistivity to the concrete bulk effective diffusion coefficient D (m^2/s), as shown in Equation 9 [107,110]:

$$\frac{\rho_T}{\rho_0} = F = \frac{D_o}{D}$$ Equation 9

Where: D_0 is the self-diffusion coefficient (m^2/s)

Equation 9 shows how the concrete resistance against chloride penetration can be proportional to the concrete electrical properties. This relationship is what allows concrete electrical tests to be used for concrete quality tests.

The concrete pore system, pore solution conductivity, and consequently electrical resistivity are highly dependent on the concrete mixture characteristics such as cementitious material composition, water-to-binder ratio, and degree of hydration [109]. As the concrete hydrates with time, the microstructure and pore solution can also be significantly changed due to environmental conditions [109].

One study attempted to measure the formation factor on UHPC using a resistivity meter. They cured the samples in a simulated pore solution after 7 days of sealed curing. They assumed that the sample pore solution came into equilibrium with that of the simulated pore solution. This is questionable because of the very low transport properties of UHPC. Additionally, it is unlikely that the UHPC was saturated during that period of time, potentially giving unconservative transport properties. Twenty-eight-day results showed that the formation factors they measured are considerably higher than normal-strength concrete. In addition, the results indicated an estimated time for corrosion initiation of 210 years for UHPC mixes [111]. Steel fibers are electrically conductive and greatly alter the measured values, even though they would not change the actual transport properties.

2.6.5.2. Surface and Bulk Resistivity

In order to calculate the formation factor, the concrete electrical resistivity must be measured. Surface resistivity can be used to evaluate the electrical resistivity of a saturated concrete cylinder to provide an estimation of its permeability [15]. One of the most common techniques for measuring the surface resistivity is a four-probe technique. In this technique, four equally-spaced electrodes are located on the concrete surface to measure the potential difference caused by the applied current [112]. The Surface electrical resistivity can be calculated by using Equation 10:

$$\rho = K \times R = K \times \left(\frac{V}{I}\right)$$ Equation 10

Where:

ρ is the concrete surface resistivity (Ω-cm)
R is the measured resistance (Ω)
V is the voltage measured between two inner probes (V)
I is the applied current by the two exterior probes (A)
K is the geometry factor

It is very important to apply an appropriate geometry factor K that converts the resistance to a resistivity. Many commercial surface resistivity meters such as the Proceq Resipod automatically apply a correction factor of 2πa. The geometry correction factor to obtain the resistivity can be calculated using the Equation 11:

$$K_{surface} = \frac{2\pi a}{1.10 - \frac{0.730}{d/a} + \frac{7.34}{\left(d/a\right)2}} \qquad \text{Equation 11}$$

Where: a is the probe tip spacing (cm)
d is the specimen diameter(cm)
L is the specimen length(cm)
$K_{surface}$ is the geometry correction, and it is only valid for specimens with $d / a \leq 4$ and $L / a \geq 5$

The bulk resistivity test uses the same equipment (4-pronged Wenner probe) as surface resistivity to measure the resistance of the cylinder with the probe tips attached to conductive plates placed on the end of the cylinder [14]. Saturated sponges or conductive gel are typically used between the conductive plates and the ends of the cylinder, as shown in Figure 16. The bulk resistivity can be calculated using Equation 12:

$$\rho = R_{cylinder} \times K \qquad \text{Equation 12}$$

Where: ρ is the resistivity of the concrete (Ω·cm)
$R_{cylinder}$ is the calculated bulk resistance (Ω)
K is the geometry factor, which is the ratio of the cross-sectional area A (cm^2) to the length of the specimen L (cm)
a is the probe tip spacing (cm)

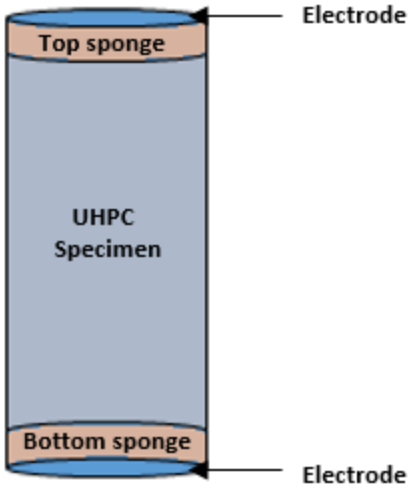

Figure 16: Bulk resistivity set-up

UHPC resistance to chloride penetration was evaluated using the surface and bulk resistivity test methods. The electrical resistivity measurements were within the ranges of very low to negligible at 28 days. This is due to the very dense microstructure of UHPC [24]. The results illustrated that these tests might be able to be used with mixes having fibers since the fibers most of the time do not touch to create a conductive path along the entire length of the specimens since they are randomly dispersed except when some alignment due to material flow during placement cannot be avoided.

2.6.5.3. Rapid Chloride Permeability Test

ASTM C1202 "Electrical Indication of Concrete's Ability to Resist Chloride Ion Penetration" [113] has been commonly used for determining the transport properties of UHPC. This test method, typically referred to as the rapid chloride penetration test (RCPT), involves at least two days of specimen preparation after the desired curing procedure. The samples need to be cut into 2-in. thick slices and placed in a vacuum desiccator with both ends exposed. The vacuum is maintained for three hours in the desiccator, and then the desiccator is filled with de-aired water and maintained for an additional hour. After that, the samples should be allowed to soak for 18 ± 2 hours. The exposed sides of 2-in. thick samples are sealed to avoid any moisture loss, and then placed inside a testing cell with one side of the cell filled with 3.0% sodium chloride (NaCl) and the other side filled with 0.3M sodium hydroxide (NaOH) solutions, as shown in Figure 17. The electrical charge passed between the electrodes is integrated with time using readings taken every 30 minutes during the six-hour testing period [16]. Even though this test has been adopted as a standard test, there have been number of criticisms of this technique related to the high voltage used, temperature rise of the specimen, and the effect of admixtures that may mislead the results [114,115].

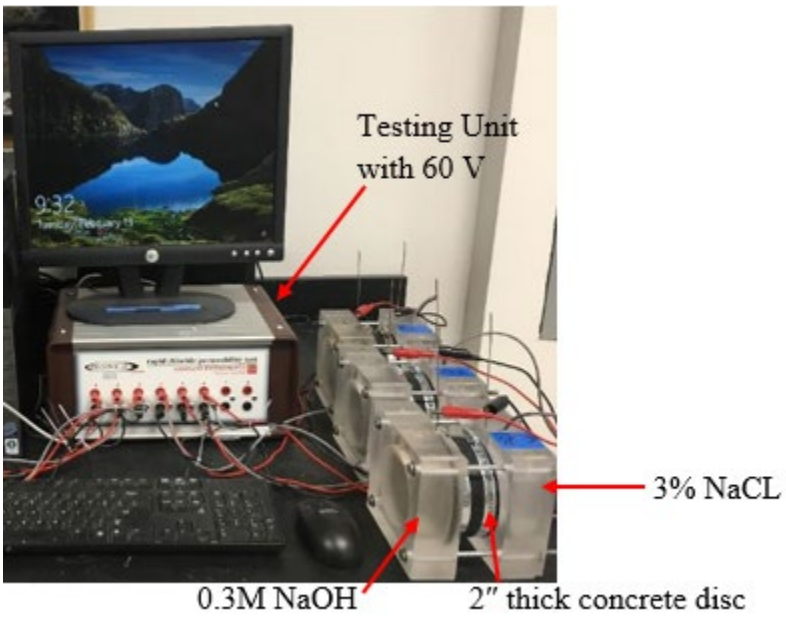

Figure 17: RCPT test set-up

ASTM C1856 requires that ASTM C1202 only be used with UHPC that does not contain metallic fibers [59] because the fibers will conduct electricity but not significantly change the chloride ingress. ASTM C1856 also warns that UHPC that has been heat-cured may give values very close to zero Coulombs. It is unknown what a measurement close to zero means in terms of pore connectivity. Additionally, since most UHPC is reinforced with steel fibers, the applicability of this test for qualification or quality control testing may be limited unless it can be shown otherwise. Graybeal tested some UHPC mixes with steel fibers, and the results showed a possibility of using this test provided no conductive path is created between the two ends of the specimens [24]. More work is needed to determine how much an effect the fibers actually have on the measured values.

Studies conducted on UHPC with ASTM C1202 have shown that the electrical conductivity is low. El-Tawil et al. tested two UHPC mixes with three different fiber volume contents (0.5%, 1.0%, and 1.5%), and reported that the penetration of chlorides was negligible [101]. Graybeal tested some UHPC mixes having different percentage of steel fibers (2 – 4.5% by volume) using ASTM C1202 and applied two different curing regimes: lab temperature and steam curing. The charge passed was found to be negligible for both steam-cured and untreated specimens after 56 days [99]. In samples made using 0.2 w/cm and 20% replacement of cement with silica fume, it was observed that only 64 Coulombs was passed, which is considered to be negligible according to ASTM C1202 [116].

2.6.5.4. Rapid Chloride Migration Test

NT Build 492 test uses an electrical voltage to accelerate chloride migration into a concrete specimen [117]. In this test method, a 2-in. thick concrete sample is exposed to a 10% NaCl

solution on one side and a 0.3 N NaOH solution on the other, as shown in Figure 18. The test is set for 30 Volts, then the voltage and test duration can be adjusted based on the initial current. After the test is done, the concrete specimen is split in half, and 0.1 M silver nitrate is applied to measure the chloride penetration. The non-steady state migration coefficient is calculated using Equation 13:

$$D_{nssm} = \frac{0.0239(273+T)L}{(U-2)t}\left(x_d - 0.0238\sqrt{\frac{(273+t)Lx_d}{U-2}}\right) \qquad \text{Equation 13}$$

Where: D_{nssm} is the non-steady-state migration coefficient, $\times 10^{-12}$ m^2/s
U *is the* absolute value of the applied voltage, V
T is the average value of the initial and final temperatures in the anolyte solution, °C
L is the thickness of the specimen, mm
x_d is the average value of the penetration depths, mm
t is the test duration, hour

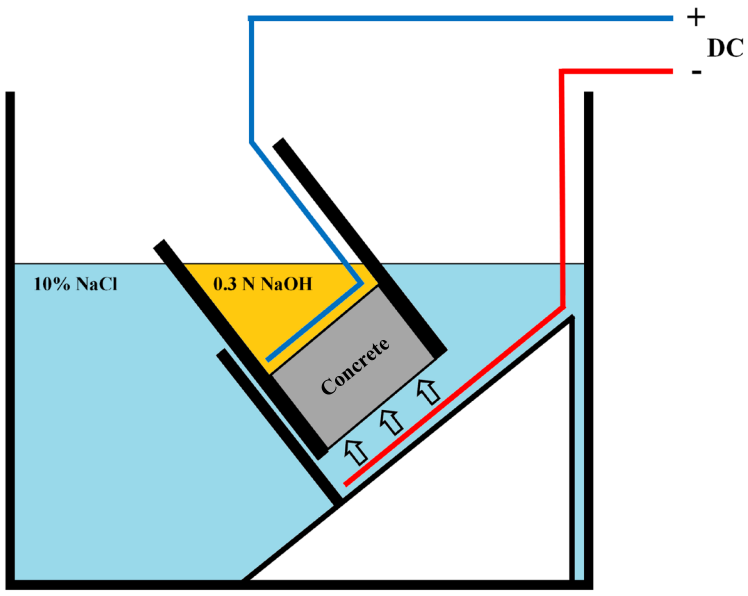

Figure 18: NT Build 492 test set-up

This test has been modified to measure the chloride penetration through UHPC samples. Vincler et al. have modified the test; these modifications include increases in the volume of the solution to 2.7 L and the voltage to 70 V [118]. These modifications reduce the heat issues and accelerate the test time. Based on the results, the depth of chloride penetration for the UHPC samples did not reach 0.2 in. (5 mm), and the diffusion coefficient was 10^{-15} m^2/s. They concluded that the proposed test gives accurate results for the diffusion coefficients when compared to 5-year

chloride exposure. Mosavinejad et al. tested the durability of some UHPC mixes using NT Build 492 [119]. They ran the test for 96 h since the initial current was below 5 mA. The results showed the UHPC has an extremely high resistance to chloride penetration. Rafiee compared the results of UHPC, HPC, and ordinary concrete tested using NT Build 492 [120]. There was no chloride penetration for UHPC, compared to 7.5 mm for HPC, and 31 mm for the ordinary concrete.

NT Build 492 shows excellent promise for qualifying UHPC mixtures based on their resistance to chloride penetration. Testing is needed to determine the effect of steel fiber inclusion on the results, and how to interpret results with such a low chloride intrusion.

2.6.6. Chloride Ion Diffusion

Chloride penetration in UHPC has been found to be much lower than high-performance concrete (HPC) and normal-strength concrete [121]. ASTM C1556 "Standard Test Method for Determining the Apparent Chloride Diffusion Coefficient of Cementitious Mixtures by Bulk Diffusion" [17] is a common method for determining the concrete chloride diffusion coefficient. In this method, concrete specimens are split into two parts, the 3-in. top part of a 4 × 8 in. cylinder is sealed with epoxy from all sides except the finished surface and vacuum-saturated with $Ca(OH)_2$ for at least 18 hours, then submerged in sodium chloride solution for at least 35 days. Most high-performance concrete are exposed to chlorides for much longer time, usually one year. The bottom part of the specimen is used to measure the concrete initial chloride concentration. The chloride content for both the top and bottom parts are measured using titration as described in ASTM C1152 [122]. The chloride diffusion coefficient can then be calculated by fitting a calculated chloride profile to the measured chloride profile.

Bulk chloride diffusion testing on UHPC has shown that it has excellent resistance to chloride penetration. In one study UHPC mixes were exposed to chloride solution for 90 days, and then the top surface of the specimens was ground off. The depth of chloride penetration was found to be 0.08-0.12 inches (2-3 mm), and the chloride diffusion was found to be as low as 1×10^{-13} m^2/s compared to normal concrete at 5×10^{-12} m^2/s to 5×10^{-11} m^2/s [123]. This test may prove to be impractical for routine UHPC testing because of the length of time required for the concrete to be ponded for any measurable amount of chlorides to penetrate.

2.6.7. Water Absorption

When water is absorbed into partially saturated concrete, it can bring with it chlorides or other aggressive ions [124]. ASTM C1585 "Standard Method for Measurement of Rate of Absorption of Water by Hydraulic- Cement Concrete [125]" is commonly used to determine concrete water absorption. In this method, 2- × 4-in. concrete disks are conditioned for not less than 18 days. The conditioning period begins with placing the samples in a chamber maintained at a temperature of 122°F (50°C) and a relative humidity of 80% for three days. After that, the samples are placed in a sealed container at a controlled temperature of 73 ± 3.6°F (23 ± 2°C) for at least 15 days to allow the sample moisture content to come to a constant value throughout the sample thickness. The sample bottoms are then exposed to water by placing them on supports in water, with the water depth at 0.079 ± 0.039 in. (2 ± 1 mm) from the sample bottom. The

samples are weighed periodically for 8 days to measure the water uptake. The absorption of the samples can be determined using Equation 14:

$$I = \frac{m_t}{A \times d} \qquad \text{Equation 14}$$

Where: I is the absorption (mm)
m_t is the change in mass of the specimen (g) at time t
A is the exposed area of the specimen (mm^2)
d is the density of the water (g/mm^3)

The slope of absorption can be determined for the primary and secondary absorption rates. The primary absorption rate is the slope of the best-fit line to the absorption for the first 6 hours. The secondary absorption rate is the slope of the best-fit line to the absorption for the first week of the test.

BS EN 12390-8 is a common method used for determining the depth of water penetration under pressure in hardened concrete [126]. According to this method, after demolding, the surface of specimens that are going to be exposed to water pressure should be roughened and cured at least 28 days. A water pressure of 72 ± 7 psi (500 ± 50 kPa) is applied for 3 days, then the specimens are split into halves, and allowed to dry slightly until the water penetration front can be clearly seen. The maximum depth of penetration is then measured to the nearest mm.

The relative humidity of the samples considerably affects the results and can lead to misinterpreting the actual absorption behavior. In fact, samples conditioned at a 50% relative humidity showed almost six times of total absorption higher than samples conditioned at 80% relative humidity. Therefore, the sample curing history and conditioning should be taking into account for more reliable and less variations in the results- especially for field samples [127]. A comparison was made between conditioning samples with two different procedures, conditioning the samples as mentioned in ASTM C1585, and placing the samples in an oven at 140°F (60°C) until constant mass. It was concluded that drying the samples at 140°F (60°C) gave more reliable measurements for the sorptivity testing [128].

UHPC has been shown to have very low water absorption, mostly because it has such low porosity. UHPC has only 1-2% capillary pores by volume [129]. Roux et al. made two UHPC mixes: one was table-vibrated, and the other was produced with a pre-set pressure of 8.7 ksi. The water absorption values for both mixes were observed to be less than 4.5×10^{-4} lb/in.^{2}. This is due to the absence of capillary porosity [124]. A similar trend was observed when comparing the water absorption of UHPC to HPC (Dili & Santhanam, 2004). O'Neil et al. compared UHPC and HPC water absorption and reported that for UHPC, the rate of water absorption according to the EN 13369 standard was seven times lower [130]. Another study looked at the effect of micro fillers on UHPC water absorption. At an age of 90 days, very-high-strength concrete made with coarse aggregates and ultra-high-performance concrete mixes had low water absorption due to the low level of capillary pore connectivity. The water absorption values measured according to

the EN 13369 standard are presented in Table 1, where the silica fume gives the lowest values for both mixes (0.7%, and 3.3%) [131].

Table 2: Water absorption (%) of UHPC and VHPC at age of 90 days [131]

	Silica fume	Metakaolin	Phonolith	Pulverized fly ash	Limestone micro filler	Siliceous micro filler
UHPC	0.7	1.9	2.2	3.2	2.8	1.6
VHPC	3.3	4.0	4.2	4.3	4.2	4.1

Fibers have been found to influence the water absorption amount. The high content of steel fibers in UHPC tends to decrease water absorption, unlike polypropylene fibers, which tend to increase the water absorption [132].

Overall, water absorption shows significant promise for use as a qualification test for UHPC because it includes the effects of pore connectivity and tortuosity. If pressurized in some way like the EN 12390-8 test, it could be performed in just a few days and could differentiate UHPC where chlorides cannot penetrate more than 0.39 in. (10 mm) at a slow rate.

2.7. Mercury Intrusion Porosimetry (MIP) Test

MIP is a common test used for characterizing the porosity and the size distribution of capillary pores in cement paste specimens. The test procedure usually involves breaking the samples into small pieces, stopping the hydration through a solvent exchange, removing the moisture by vacuum until a constant weight is achieved, and using high pressure to fill the pores with mercury [133].

MIP is based on the physical phenomenon that as a non-wetting liquid, no capillary absorption will occur. Mercury encases the sample and will only penetrate capillaries when high pressure is applied. Pore size can be determined from the applied pressure, using an assumed pore geometry [134,135]. The pore shapes are assumed to be cylindrical, and the relationship between the pore size and the applied pressure is given by Washburn equation, as shown in Equation 15 [134,135]:

$$\Delta P = \frac{2\,\gamma\,cos\,\theta}{r_{pore}} \qquad \text{Equation 15}$$

Where: ΔP is the pressure difference across the curved mercury interface (Pa)
γ is the surface tension of mercury (N/m)
θ is the contact angle between the solid and mercury
r_{pore} is the resultant pore size (m)

MIP has some drawbacks. The assumed cylindrical pore shape is much different than the shape of the actual pores. During drying, the pore walls could be damaged, and under high pressure the mercury could break through thin or damaged walls and alter the pore structure [133,136].

Vincler et al. have performed MIP on some UHPC mixes with 1% fibers. For most of the samples, the intruded pore sizes were about 2 nm [118]. A study by Cheyrezy et al. used MIP to demonstrate the very low porosity of reactive powder concrete (RPC). The cumulative porosity ranged primarily from 3.75 nm to 100 μm and did not exceeded 9% in volume [50]. Kang et al. used MIP on some UHPC samples with different heat curing. They concluded that the increase in temperature made the UHPC pore structure finer, less than 100 nm [137]. The incorporation of nano-SiO_2 in UHPC was found to lead to a decrease in the amount of capillary pores as measured by MIP [138]. UHPC in another study was found to have a total porosity of 7.88%, compared to 12.69% for normal concrete, confirming that UHPC has a really small open-pore volume [139]. This pore system difference measured by MIP seen could serve as a good measure of the concrete's ability to keep out water and chlorides.

2.7.1. Carbonation

Carbonation is the reaction of cement hydration products with carbon dioxide (CO_2). The reaction of carbon dioxide from the atmosphere with calcium hydroxide in solution forms calcite ($CaCO_3$), as shown in Equation 16.

$$Ca(OH)_2 + CO_2 \rightarrow CaCO_3 + H_2O \qquad \text{Equation 16}$$

This reaction can reduce the alkalinity of concrete, leading to the destruction of the passive layer on reinforcing steel. However, since the UHPC has a very low w/cm and has a very dense structure, UHPC carbonation rates are extremely low. It was found that there was no carbonation of UHPC specimens that were exposed to 5% CO_2 for 42 days and to 100% CO_2 for 90 days, but some penetration was reported in later ages of exposure [140]. In another study, UHPC prisms with a cross-section of 4 × 4 in. (100 × 100 mm) were oven-dried at 120°F (50°C) for the first two weeks and then stored in a 1% CO_2 atmosphere for accelerated aging. The results indicated that the carbonation depth was 0.06 to 0.08 inches (1.5 mm to 2 mm) after one year of exposure [123]. In one study, composite reinforced concrete (CRC) beams were made by Aarlborg Portland. These beams had a low w/cm between 0.15 and 0.2, 6% by volume of steel fibers, and 20-25% cement replacement by silica fume. After being exposed for 16 years to Madrid's climate, where the temperature ranges between 20 and 90°F (-6 to 32°C), the carbonation depth was measured. The results showed that the beams were very resistant to carbonation penetration, and the depth of carbonation recorded was less than 0.039 inch (1 mm) from the surface. [141]. Carbonation performance of Ductal® with 2% of steel fibers was compared to that of very high-performance concrete. It was reported that after four months of an accelerated carbonation test, the carbonation penetration depth of Ductal® was below the limit of detection of around 0.020 inch (0.5 mm) [131].

2.7.2. Abrasion Resistance

Abrasion resistance is the "ability of a surface to resist being worn away by rubbing and friction" [142]. UHPC has excellent abrasion resistance and has begun to be used in hydraulic structure repair because of its excellent abrasion resistance [143,144]. Abrasion resistance is a function of the material surface hardness and material elasticity to prevent brittle cracking [145]. Materials with high hardness are brittle and abrasion can induce brittle cracking of the surface leading to

high wear. The matrix has to have some elasticity/plasticity so that it can hold aggregate particles in place without fracturing. The very-high-strength of UHPC and steel fiber reinforcement contributes to this resistance [146].

Several test methods have been developed to measure abrasion resistance for normal-strength concrete. ASTM C418 measures the concrete wear after sandblasting to simulate air- and water-born abrasive damage [147]. ASTM C1138 was developed by the U.S. Army Corps of Engineers originally and uses steel ball agitation in water to measure concrete resistance to erosion-abrasion [148]. ASTM C944 simulates concrete wear under steel-tire impact. In this method, a rotating cutter is used to abrade the surface of concrete samples in a given time. The cutter has a 22 ± 0.2 lb weight placed on it as it rotates to increase the friction force [149]. ASTM C1856 modifies ASTM C944 for the high UHPC strength and abrasion resistance. For UHPC, it is recommended to use 44 ± 0.4 lb instead of the normal load to accelerate the test. It was shown that the mass loss for UHPC was linear with the weight, allowing for this test acceleration without affecting the results [101].

Several studies have been performed to demonstrate the benefits of UHPC on abrasion resistance. Reactive powder concrete (RPC), a predecessor material to UHPC, was examined for use in overlays. It was found that the RPC had eight times the abrasion resistance of normal-strength concrete and four times that of high-strength concrete when cylinders were tested for 1000 cycles [150]. The type of curing has been found to affect UHPC abrasion resistance. Graybeal and Tanesi compared UHPC abrasion resistance after four types of curing: steam, ambient air, tempered steam, and delayed steam curing. The results indicated that the values for ambient air-cured specimens were between 1.1 g to 2.1 g of weight loss, which is high compared to 0.1 to 0.3 g weight loss for the steam-cured specimens [151]. The steam-curing treatment dramatically enhances the abrasion resistance of UHPC due to increasing the degree of hydration and the strength [151]. Aggregates also play a significant role in the UHPC abrasion resistance. When comparing different UHPC mixes, it was found that UHPC with coarser aggregate showed a 50% higher abrasion loss than UHPC with no coarse aggregate [152].

2.7.3. Field Performance

In 1995, UHPC was used for the first time in North America, on a bridge in Quebec, Canada. The 197-foot (60-m) long bridge showed no deterioration, despite exposure to aggressive marine environment [153]. In 1997, three UHPC samples were subjected to daily tides and freeze-thaw cycles at Treat Island to monitor long-term durability. They measured the chloride penetration and found that chlorides did not penetrate farther than 0.39 inch (10 mm) into the concrete, even after 15 years of exposure [97].

2.8. Non-Destructive Evaluation Methods

Non-destructive evaluation (NDE) which is also commonly referred to as non-destructive testing (NDT) or non-destructive inspection (NDI), is an approach for testing materials or structural members. The process is used to determine the health or characteristics of the material that is being studied. This approach contrasts with widely-used destructive testing, where the structure is placed under load or in other adverse conditions for study or to determine causes of failures [154]. As a result, NDE/NDT/NDI is necessary when the structure is intended to remain in use. It

allows the health of the system to be evaluated and maintenance or rehabilitation of such structure to be carried out [155,156]. NDE is also used to estimate the life expectancy of structures, such as bridges and buildings, for the purpose of planning and improvement [156]. NDE could provide a way to inspect structural members made with UHPC to ensure fiber distribution and orientation specifications are met. A discussion of NDE methods applicable to concrete is given.

The oldest and still most common NDE method is visual inspection [155], where the structure is physically examined for cracks and faults that can be seen on the surface. This approach is relatively inexpensive and requires relatively little training. The method is useful as cracks on the surface, or even delaminations, that are observable from visual inspection are a clear sign of problems in the inspected structure [155]. The disadvantage, however, is the fact that many faults are not visually observable on the surface of the material. Many serious faults often start deeper in the material [157].

For concrete, there are some challenges associated with the visual inspection, such as the existence of microcracks that are not easily visible. Also, the person inspecting needs to know what exactly to look for [157]. In addition, some of the areas that need inspection are often not accessible or are only accessible from one side of the concrete structure. The possibility of damage from an inaccessible surface means visual inspection cannot accurately assess the structure.

To address the disadvantages of visual inspection, various NDE methods have been developed and continue to be developed as the need for more robust and more informative inspections grow. In this document, five broad categories of non-destructive evaluation will be discussed: electrical [154], electromagnetic [155], thermographic [157], radiographic [157], and sonic/ultrasonic [155]. How each of these analytical methods are used to inspect concrete, their advantages, and their disadvantages will be described. A rigorous review of ultrasonic inspection techniques, which are a focus of this project, will be performed.

2.8.1. Sonic and Ultrasonic Nondestructive Evaluation Methods

These methods involve the transmission and receiving of mechanical stress waves through a material at sonic (20 Hz – 20 kHz) and ultrasonic (typically greater than 20 kHz) frequencies. They are generally non-invasive contact or non-contact methods that analyze sounds and sound echoes/reflections and how different materials respond to them.

2.8.1.1. Impulse-Response Method

The impulse response method is the sonic/ultrasonic method that requires the fewest devices to implement and is commonly used in practice. Its use is codified in ASTM C1740 [158]. The method uses a calibrated rubber-ended hammer with a load cell [158] connected to the data acquisition system that induces elastic waves in the structure under test. This is used to generate the force spectrum. The elastic wave propagation in the structure is picked up by a geophone [155] (pickup microphone) that generates a velocity spectrum output of the received signal due to the impact force from the hammer and subsequently amplifies it before signal processing is performed [159]. The signal processing is done by taking the fast Fourier transform (FFT) of the

signal and the resulting velocity spectrum divided by the force spectrum to get a transfer function called the mobility of the test, which is given in (m/s)/N [159]. The mobility is plotted against frequency, which is a measure of the flexibility and the elastic modulus of the structure/material.

One of the sewer tunnels west of the pumping stations in St. Louis, Missouri [159] was tested with impulse-response at four test points after the flooding from the Mississippi river in 1993. It was successfully shown that three points were in good condition with no voiding behind the brick lining and one was very weak and was subsequently reinforced by replacing the defective portion.

The advantage of this method is the ease with which it can be implemented because of the simplicity of the equipment involved. One major drawback is the poor defect location precision and the complexity of interpreting the results that requires some understanding of how the material should respond [154].

2.8.1.2. Impact-Echo Method

The impact-echo is similar to the impulse-response method. In fact, some literature consider them the same [155].The two methods are different in that the impact-echo method typically operates at a much higher frequency range, typically around 10 kHz to 150 kHz [154,160]. The higher frequencies occur from the impact because of the diameter of the impacting device is reduced [154]. When the data is collected, an FFT is performed on the received elastic wave from the pickup device. A frequency response function is made from the signals, and the resonant frequency peaks correspond to the thickness or depth of the faults in the structure. If the depth of the structure is known, incorrect depths will correspond to a fault.

This is a widely accepted and used method because of its ease of testing, since very simple tools are needed for the impact, and success with identifying voids in ducts [155]. Its use is codified in ASTM C1383 [161].

Recently, artificial neural networks have been used in the impact-echo analysis [162]. The impact-echo method trains the network with a set of input-output data, where the input is impact-echo data and the output is the presence of cracks in the structure. The neural network is then able to give appropriate output data for every input variable after training with back propagation [162]. Concrete conditions have also been determined using extreme learning machines [163] using techniques that learn from the impact-echo data obtained.

The advantage of this method is that it is a simple way of testing without the need of coupling the sensor to the base because the pickup microphone is air-coupled [154]. The drawback, however, might arise from the inability to sometimes interpret the results accurately because of possible sensitivity issues in the transducer or even low frequencies resulting in the indistinguishability of the defect areas [155,162].

2.8.1.3. Ultrasonic Method

The ultrasonic method uses ultrasonic waves (typically greater than 20 kHz frequency) to probe concrete structures. Its use is codified in ASTM B548 [164].This data is gathered in three

different forms: A-scans, B-scans, and C-scans. A-scans show a one-dimensional image of the structure by measuring reflected signals over time from the structure and plotting it against its amplitude [165]. If the wave velocity is known, the time axis can be converted into depth into the material. A B-scan is a "slice" of the vertical profile of the structure [166]. The B-scan shows a two-dimensional image across time and location. The color of the image usually corresponds to the amplitude at the time and location. A C-scan provides the surface "snapshot" of the structure. The C-scan shows a two-dimensional image across horizontal locations and vertical locations. The color of the image usually corresponds to the maximum amplitude across some time range (or gate).

The three different scans of the structure can also be combined in a number of ways to form a 3-D analysis of structures [165]. This method has gained a lot of attention and research over the years because of its versatility in showing defects deep inside the structure. A piezoelectric transducer is used to generate sounds that are greater than 20 kHz or the threshold of human hearing. This generated wave excites the structure typically using bulk waves. The waves are then transmitted through the structure and then reflected. The reflected signal is then processed using different algorithms, one famous algorithm being the synthetic aperture focusing technique (SAFT) algorithm [167]. A color map is then generated based on the different densities that the structure is made of. Faults and delaminations can then be seen as these typically have an earlier arrival [168] than the back of the structure for example, and these will stand out in the image of the structure that is generated.

The advantage of this method is that a lot of details can usually be obtained from the scan of the structure revealing things like flaws and voids with proper interpretation [154,155]. Impedance matching ensures that the intensity of the wave is not attenuated by the air gap that exists between the transducer and the structure without proper coupling. One major drawback of this method is its time consuming nature, which limits the speed at which tests can be carried out [166].

2.8.1.4. Ultrasonic Pulse Velocity Method

The ultrasonic pulse velocity method [169] is one of the oldest and most widely accepted sonic/ultrasonic methods for concrete testing. Its use is codified in ASTM C597 [170]. It is effective for non-destructive testing and evaluation of the quality and uniformity in concrete samples. It is typically used to determine compressive strength and the elastic modulus of concrete [171]. Figure 19 shows an example of setup. The setup uses a transmitter to send an ultrasonic wave, a receiver to receive the wave, a pulse generator that generates the wave, and a device to amplify and display the received signal. The amplification device can be standalone or coupled with other devices. When a time-varying mechanical force excites a semi-infinite solid like a concrete surface, three types of waves are typically propagated, the fastest of which is the longitudinal wave, also called P-wave or compression wave [172,173]. The secondary wave is called the shear, also called S-waves [173,174]. The third wave is the surface wave [175]. The time of arrival is recorded as the difference between the time when the excitation begins and when the first wave arrives. This is used to calculate the compression wave velocity by dividing the path length of the wave through the concrete by the time of travel through the concrete. From the compression wave velocity, we can compute the Young's modulus [155] and other desired

properties [171]. The health or quality of the concrete can also be linked to the velocity of the wave through the concrete, where generally we want values greater than 3500 m/s to indicate at least a good quality concrete.

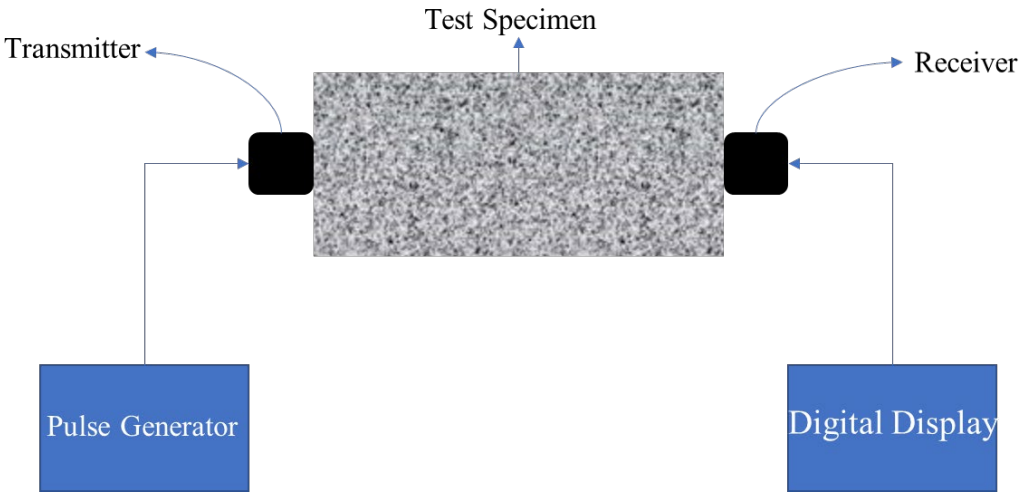

Figure 19: Ultrasonic Pulse Velocity (UPV) setup

The ultrasonic pulse velocity method continues to be improved through ongoing research. For example, some researchers have used the ultrasonic pulse velocity method to monitor the development of cracks in a concrete structure when under heating conditions, demonstrating the versatility of the method to evaluate structural integrity[176,177]. The compressive strength of a concrete structure was also predicted through artificial neural networks using the densities and the velocity of waves traveling through the medium as input data [171], showing how the behavior of structures over time can be determined based on their ultrasonic pulse velocities.

The advantages of this method are that it has a simple evaluation procedure, it is easily deployed, and has a relatively low cost of use. One major drawback according to [172] is that there is a tendency for the S and P-waves to be indistinguishable in thin specimens.

2.8.1.5. Ultrasonic Phased Array Method

The ultrasonic phased array method [177] uses multiple transducers for the purpose of scanning a surface using different configurations. Its use is codified in ASTM E2700 [178] A typical phased array system consists of multiple transducers [164,177] that can be set up to all transmit at the same time then receive at the same time, to all transmit and receive at different times, or set so that some transmit while others are receiving simultaneously. The user usually has a bit of freedom in choosing the configuration of the phased array system to get specific results. A phased array system can be used to get many A-scans at once that are then interpreted using different algorithms, such as the 3D SAFT [179], to detect faults or even to check the health of a given structure. The basic phased array system is comprised of a set of transducers, a pulse generator, a receiver system, an amplifier, and typically a computer for signal processing.

The ultrasonic phased array method continues to be improved through ongoing research. For example, the phased array transducers have been reported to use flexible transducers that have the capability to stretch up to 50% to be able to access hard-to-reach surfaces for imaging purposes [180].

The advantages of this method are that it provides a means of improving the performance of low-frequency ultrasonic investigations and it can also be very useful because of its fast data acquisition. One major drawback is the possibility of having dead zones where the transmitter signals may be larger than the echo and thus suppress it, making it disadvantageous for very shallow flaws, like the case in [154] where the tendon ducts were not very visible.

2.8.1.6. Nonlinear Ultrasonic Method

The nonlinear ultrasonic method [181] measures the nonlinear response of solid structures from the excitation of linear ultrasonic sources. A strong nonlinear response typically occurs near deterioration of the structure or occurs due to microstructures that gives rise to nonlinear attenuation, amplitude-dependent phase delay [182] and resonance frequency shifts [183]. Typically, these are detected using Fourier analysis, which provides low amplitude signals below the noise level. Authors in [184,185] propose a method called the scaling method to enhance the detection of such nonlinear ultrasonic properties.

The nonlinear ultrasonic method continues to be improved through ongoing research. For example, the scaling subtraction method [182] was introduced to replace the typical Fourier analysis of the nonlinear properties of the ultrasonic wave interaction [184] which is easier to implement and less dependent on the quality of the equipment used. [182].

The advantage of this method is that it provides a way of quantifying and detecting nonlinearity properties from the interaction of linear ultrasonic wave interaction with materials [184]. It can be used to monitor damage evolution [182]. In general, this can all be accomplished without a known baseline signal since the nonlinear components do not overlap with the excitation. One major drawback is that the method requires a high input signal amplitude, which requires a lot of power to generate [182].

2.8.1.7. Ultrasonic Guided Wave Method

The ultrasonic guided wave method [186] utilizes a different approach from the bulk wave method where only a localized area under the probes is insonified [156] per time. This is the area that can be scanned at a time. The probes also need to be moved to cover the entire length. Ultrasonic guided waves on the other hand, use a single probe station [187] and a considerable length of a structure/device is scanned at once. The guided wave methods uses a transducer coupled to a wedge [187] to give an angle-beam excitation through a structure to insonify the structure and collect data from the interaction of the waves with the structure, where reflections from cracks and delaminations [186] can be seen and analyzed [156]. This method makes use of the sample sides for propagation because the waves are constantly bouncing back and forth in the structure creating overlaps between the waves and creating some form of interferences (constructive or destructive) [188]. A plot of the constructive interferences against the frequency exciting this gives a dispersion curve for the structure forming a wavenumber-frequency pair that

shows what frequencies need to be excited to get certain velocities, hence, helping to design experiments that are specific for each structures as needed [156].

The advantage of this method is that it is inexpensive to implement since only a small amount of equipment is needed for implementation, saving cost on transducers and overall equipment size [189]. A major drawback is that the waves are dispersive meaning that the phase velocities are generally a factor of frequency [156] implying that each frequency used has a unique mode corresponding to it, hence limiting the use over a broader frequency band.

2.8.2. Sonic and Ultrasonic Nondestructive Evaluation Equipment

The most important sonic and ultrasonic nondestructive evaluation equipment are the transducers. The transducers perform the transmission and receiving in order to perform non-destructive testing.

2.8.2.1. Contact Ultrasound Transducers

Contact ultrasonic transducers are transmitters and receivers that send and receive ultrasonic waves to and from a structure when they are in contact with the surface of the element. They work by converting electrical signals into acoustic signals and vice versa through a device [156]. Contact ultrasound transducers usually require some form of couplant to reduce acoustical leakage into the areas surrounding the test structure, preventing a reduction in the efficiency of the transmission.

There are some advantages associated with the use of contact ultrasound transducers such as the ability to use them across most material types. For example, contact ultrasound is applicable to both reinforced and non-reinforced concrete structures. Yet, the downside is the need of a couplant to be able to use this transducer effectively.

2.8.2.2. Electromagnetic Acoustic Transducer (EMAT)

Electromagnetic acoustic transducers (EMAT) are electromagnetic devices to convert electrical energy to acoustic energy in the presence of a magnet [190]. It uses a coil that the electrical signal passes through that lies on a typically permanent magnet (sometimes electromagnets are used) to create a bias field that induces an acoustic signal in a conductive surface, which then transmits through the structure under test. The reverse happens at the receiving side, where the acoustic signal picked up from the structure is picked up and this induces an electric field in the coil in the presence of a magnetic field [191].

EMAT devices stand out due to a couple of facts. First, the devices do not require coupling to the surface being inspected. As a result, it is easier to use with rough surfaces and even curved surfaces. The second difference is that the magnetic component in the EMAT only enables it map out existing ferromagnetic parts of a structure. This makes the application of EMAT niche because it can only be used successfully with electrically conductive structures. Concrete structures with no metallic fibers or reinforcements may not be an applicable use for EMAT transducers. The use of EMAT transducers is codified in ASTM E1962 [192].

2.8.3. Radiography Methods for Concrete

An x-ray instrumentation system [193] employs electrically powered linear accelerators to generate x-rays, which are then beamed into the structure. This test is applied in a similar way to how medical x-rays are used to characterize bones and tissue. Soft x-rays, i.e. x-rays with lower frequencies and longer wavelengths (about 0.2 – 8 nm) [194] are used for medical practice [195]. In the case of inspecting structures, hard x-rays, x-rays with higher frequencies and shorter wavelengths (about 0.01 – 0.2 nm) , are used to better penetrate the structure [196]. As a result, protective measures are needed to prevent the exposure of humans to hard x-rays [197]. This is one reason why the x-ray method is most suited for enclosed spaces, where adequate protective measures can be put in place to ensure safety of the operator. There are lower-powered portable versions for use in the field [198].

While the x-ray method renders images in two-dimensions (2D), a computed tomography scan, or CT scan, is a three-dimensional (3D) scan [199] that uses x-ray radiation to determine the internal structure of materials, for example UHPC [200]. The CT scan method is very useful in determining the fiber orientation in the UHPC and as such is very useful for this UHPC project. One of the downsides to CT scanning however, is the fact that we can only scan a small sample at a time [200–202].

The gamma-ray method [203] can be the safer form of the x-ray method if the nuclear probe is carefully handled. The gamma-ray method uses a nuclear source with a probe that is in contact with or in a hole drilled into the structure under test. The gamma-ray method, however, requires more processing time than the X-ray method for the same size of structure [155].

2.8.4. Electrical Methods for Concrete NDE

The electrical impedance tomography method [204] tests the resistivity of concrete with electrodes that are spaced in a pattern, typically in a straight line according to the Wenner method as shown in Figure 20 [205]. The resistance between these electrodes is then measured. The electrodes must maintain good contact with the structure by drilling small holes into the structure. The resistivity method is usually good for testing electron mobility in the concrete, which is usually a measure of corrosion and chloride infiltration of the concrete structure or beam [155]. The main drawback is the need to always maintain a good electrical contact with the structure. This test method helps in determining the durability of concrete - even in the presence of reinforcement; there is research that has shown the resistivity values of UHPC are very low, and this method may be promising for use with UHPC for the Florida Department of Transportation (FDOT) [25,206].

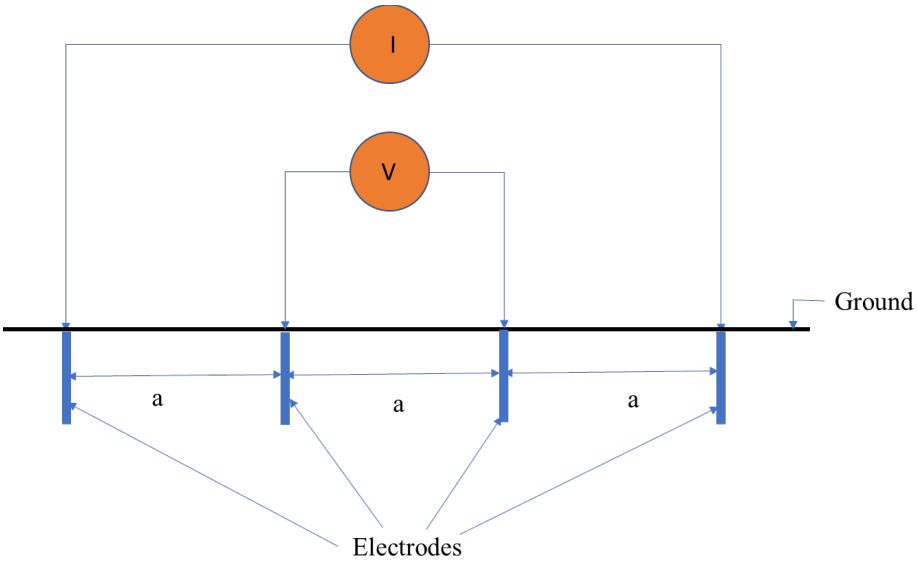

Figure 20: Wenner method

2.8.5. Half-cell Potential Measurement

Half-cell potential [155,207] creates a contour map of concrete for detecting levels of corrosion damage. It typically entails comparing the potential of the steel reinforcement in a concrete structure to a reference half-cell electrode on the surface of the beam or structure. It is usually helpful in comparing regions that have been identified as having corrosion to those that are yet to be determined. A uniformly low potential typically indicates a corrosion risk. Also, a high potential gradient suggests localized corrosion [155]. It is standardized by ASTM C876 [208]. The main drawback is similar to that of the resistivity method in that you also need to drill a hole to contact the reinforced steel. It has been used to experimentally show that UHPC had lower corrosion probability when compared to some other concrete materials [209].

2.8.6. Galvanostatic Pulse Technique

The galvanostatic pulse technique is one of the oldest methods of corrosion testing in concrete reinforcement [210]. It was introduced for field application in response to the problems associated with the interpretation of corrosion risk assessment using the half-cell potential measurements of reinforcements. The method is a transient polarization method in the time-domain, where a short pulse is applied galvanostatically through a counter electrode to the concrete. This results in a change in the electrochemical potential of the steel reinforcement, which is recorded by a reference electrode that is typically situated at the center of the counter electrode. The ohmic resistance must be evaluated based on the result received from the experiment. The corrosion level of the steel reinforcement can then be inferred from the calculation of the ohmic resistance of the steel reinforcement. This technique is codified as ASTM C876-91 [211].

2.8.7. Electromagnetic Methods for Concrete NDE

Electromagnetic methods have shown some promise for use in detecting steel fibers in concrete because of their magnetic properties. This test method is based on measuring the magnetic properties of steel fibers and is not applicable to polymer fibers.

2.8.7.1. Inductive Methods

Inductive methods have been shown to be useful for measuring the fiber content and orientation in test samples without macro-reinforcement [212,213]. The steel fibers in UHPC give off a magnetic field. A coil wrapped around the concrete will pick up a difference in the magnetic field from the concrete in the form of an electrical signal. This inductance can be correlated with the volume of steel fibers in the concrete. Since steel fibers are long and slender, the magnetic field measured will be different depending on the direction of the fiber. By changing the axis about which the coil is wrapped around the sample, the orientation of the fibers can be measured to within 8.4 lb/yd^3 (5 kg/m^3) [212]. This method is often combined with the double punch test to determine sample strength and any contributions to the strength from fiber alignment. Application of this method to large structural members may be more difficult; however, as it would require a large coil, the ability to lift a structural member through the coil, the ability to change the axis of the structural member measured, and the ability to take into account any effects of reinforcing steel bars or steel prestressing strand.

2.8.7.2. Ground Penetrating Radar (GPR) Method/Impulse Radar Method

The ground penetrating radar method utilizes electromagnetic waves in the MHz to GHz region [214] from antennas to scan a concrete structure as shown in Figure 21. These waves are usually in the short-wavelength range, with frequencies ranging from 15 MHz to 3 GHz and can be tuned to achieve a desired resolution by selecting the right frequencies to use. For example, longer wavelengths are typically better for evaluating the insides of a masonry structure. The waves travel into the material, reflect and are then measured at the receiving antenna. The main difference between the GPR and the impulse radar method is that the impulse radar method typically uses higher frequencies than the GPR [154], whereas GPR uses lower frequencies compared to the impulse radar. The main drawback of this method is the high rate of absorption by the medium, making it difficult to achieve high resolution and excellent depth penetration simultaneously [215]. The method is useful for the evaluation of masonry arch bridges and harbor dock walls [155] and can be used to inspect structures that are built using UHPC.

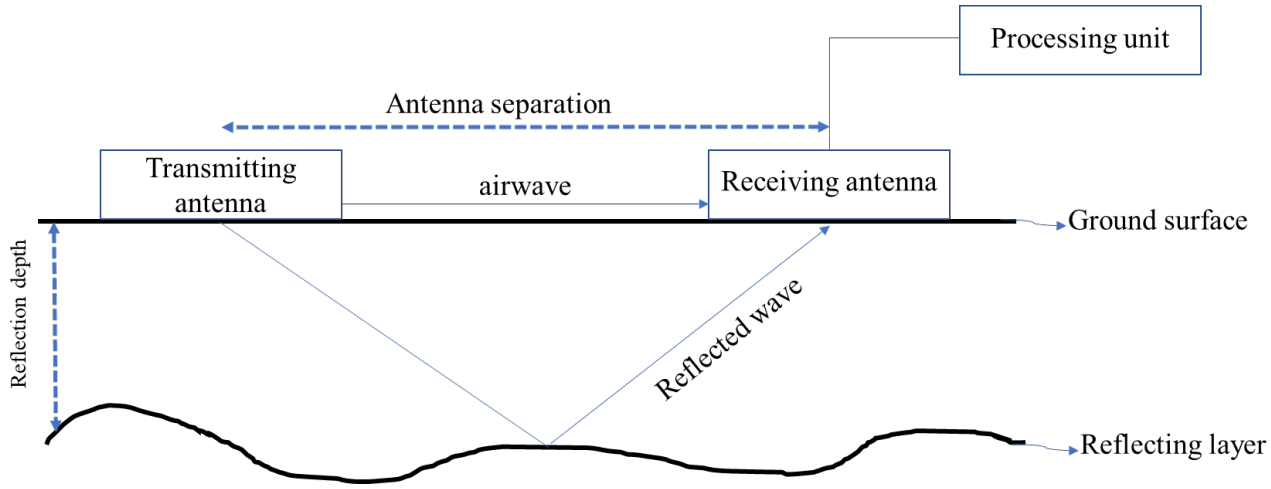

Figure 21: Ground Penetrating Radar

2.8.7.3. Cover Meter

A cover meter [155] is used to determine the location of steel rebar and the thickness of the concrete covering the rebar, as shown in Figure 22. The meter consists of two coils that are placed on an iron-cored inductor, and current is passed through one coil, which in turn induces a current in the second coil that is amplified and measured [155]. The magnitude of the induced current in the second coil is determined by the size of the steel bars and the thickness of the concrete cover. This is a good approach for measuring how thick concrete covering a reinforcement is because the magnitude of the induced current is influenced by the thickness of the concrete cover. With some adaption, there may be the possibility of adapting this technology to steel fiber detection in UHPC.

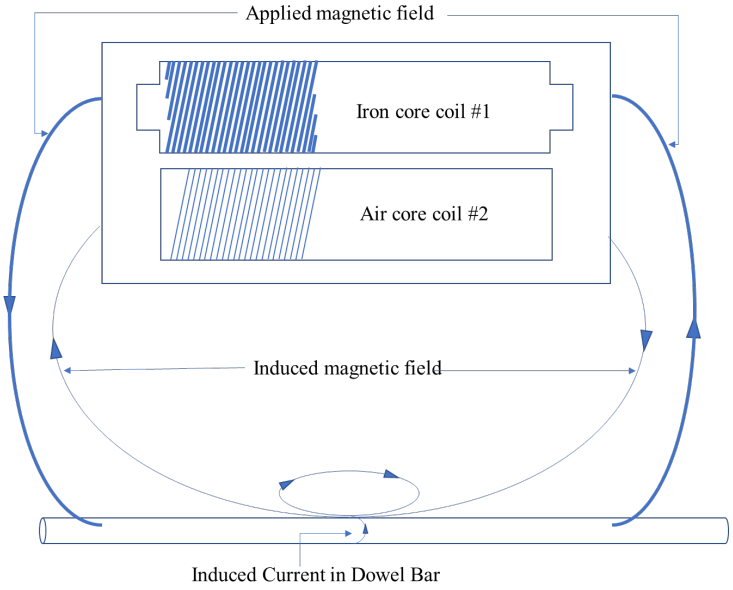

Figure 22: Cover meter basic operation

2.8.8. Thermography Methods for Concrete NDE

Infrared thermography [216] is a method that measures heat from infrared rays emitted by the concrete surface with specialized cameras. These signals are converted into a temperature map and a color scale indicates the relative temperature differences of that surface. For concrete structures, an even surface and homogeneous thickness produce a uniform temperature signature. In contrast, structures tend to heat up faster in those regions that have delaminations or other defects, creating a difference from the homogeneous regions [155] . This is a particularly good diagnostic method for large structures where the heatmap can be easily observed and the regions with defects can be monitored and inspected further.

2.9. Summary

UHPC has many unique properties that make it an excellent candidate material to make structural members that are stronger, longer, and more durable than those under current practices. In order to use UHPC, quality control test methods are needed to measure its true properties and ensure that it has the expected durability and tensile strength everywhere desired. A review of potential test methods for plant quality control use was performed, showing that many test methods exist, and that with some adaption may be used for UHPC.

3. UHPC TENSILE STRENGTH CLASSES AND QUALITY CONTROL TESTING

3.1. Introduction

Ultra-high-performance concrete (UHPC) has become increasingly popular in the United States in the past decade. Many states and private companies are now looking to develop their own non-proprietary UHPC mixtures to save money in large-scale projects. With an increase in the number of suppliers and mix designs for UHPC comes the added difficulty of determining mix approval and quality control requirements. This is especially true when it comes to testing tensile strength and behavior of UHPC. Because traditional concrete without fiber-reinforcement does not have tensile strength after cracking, there are no widely used quality control tensile tests for concrete that capture the entire failure behavior. Flexure tests can give an indirect measure of tensile behavior but require displacement sensors and data logging systems that are not available in most concrete testing laboratories. Direct tension testing of concrete often requires uncommon specimen shapes and expensive gripping equipment in addition to a sophisticated data logging system.

This study compared three different tension testing methods: the direct tension test developed by the Federal Highway Administration (FHWA), the flexural test described in ASTM C1609, and a simplified double-punch test based on the Spanish norm UNE 83515 [9,12,217]. Two different types of steel fiber were each tested at 5 different doses to see how well the simpler test methods would reflect the results of the direct tension test. Recommendations are made on how the simpler test methods could be used for quality control testing.

3.2. Materials and Methods

All specimens were made using the same concrete mix design with changes only to the type and amount of fiber used. The fiber types are described in Table 3. The mix proportions are shown in

Table 4. A plot of particle size distribution for the dry materials is shown in Figure 23.

Table 3: Fiber Properties

Geometry	**Material**	**Coating**	**Length Inches (mm)**	**Diameter Inches (mm)**
straight	steel	brass	0.50 (13)	0.008 (0.20)
twisted	steel	none	0.50 (13)	0.02 (0.50)

Table 4: Mixture Proportions

Material	Weight (lb/yd^3)
Sand	1585
IL Cement	1597
Slag	309
Silica Fume	155
Water	240
High-range water-reducing admixture	30.9
Water-reducing and workability-retaining admixture	30.9
Surface-enhancing admixture	5.2

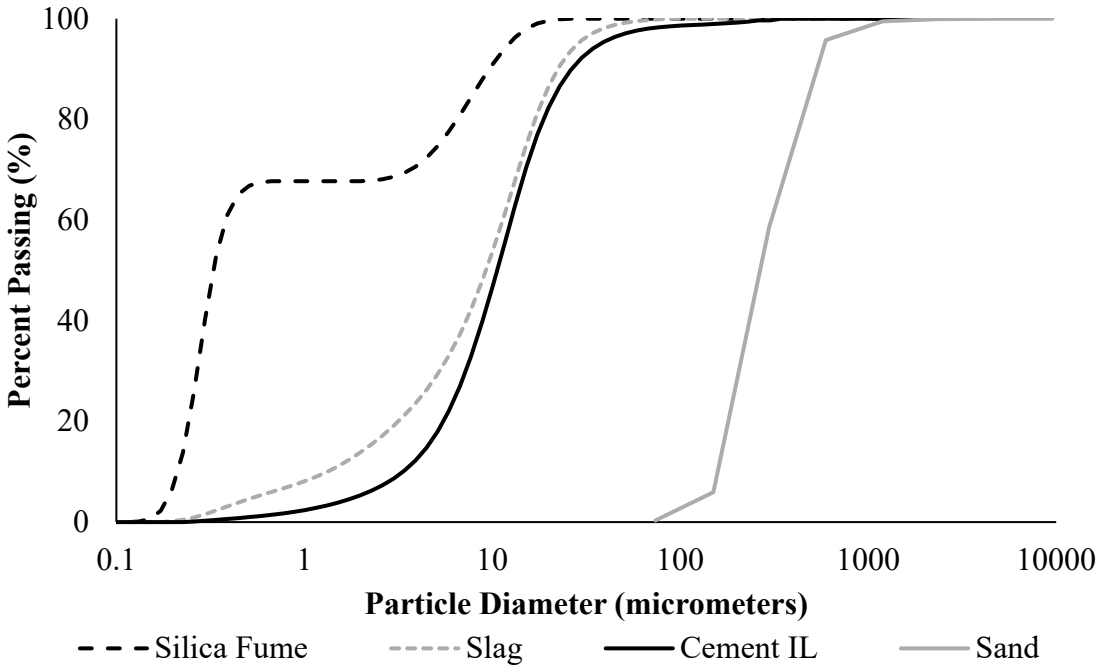

Figure 23: Particle size distribution of aggregate and cementitious materials used

It should be noted that there are two key differences between the fibers: geometry and diameter. While the fibers will be referred to as “straight” or “twisted” in this report for simplicity, the results cannot be used to indicate a preferred geometry for performance. In fact, the difference in diameter likely makes a larger contribution to post-cracking behavior as this affects the fiber aspect ratio significantly. The purpose of using two different fiber types is to show how the test methods characterize mixes with different post-cracking behaviors and to show that minimum fiber percentage cannot be the sole metric by which UHPC mixes are approved for tensile behavior. Each of the two types of fibers were evaluated at five different dosages. The target volume percentages for fibers were 1.0%, 1.5%, 2.0%, 2.5%, and 3.0%. However, actual fiber percentages were each 7% lower than the targets due to a mix volume calculation issue. For

example, the mix targeting a 1.0% of fibers by volume actually had only 0.93%, and the mix targeting 3.0% actually had 2.79%. For simplicity, the original target percentages will be referred to in this report.

The mixes were made using a vertical shaft high-speed mixer with a 1-ft^3 capacity. Dry materials were added to the mixer as it mixed with a slow speed of less than 10 rpm to homogenize the materials. After homogenization, the water was added slowly, followed by the admixtures. Mixing speed was increased to a medium speed of approximately 30 rpm for roughly 3 minutes, followed by fast mixing at 50 rpm for the remainder of the mixing time. The concrete was mixed for at least 30 minutes before fibers were added, followed by 5 minutes of mixing to disperse the fibers. Because of the limited mixer capacity, two separate batches were made for each mix. The flexure specimens were made from one batch, and the double-punch and tension specimens were made from the other. Compression cylinders were made from each batch as a quality control measure and to see if fiber percentage and type impacted compressive strength and by extension, the tensile, flexure, and double punch strength.

Six specimens were made for direct tension testing for each fiber type and dosage. The direct tension test method from the FHWA was followed, with the addition of added C-clamps at the top and bottom of the specimen at the tapered portion of the aluminum plates [9]. This addition was found to reduce the number of specimens that cracked outside of the region where expansion was measured. Specimens that failed outside of this measured region were excluded from the analysis because an accurate stress vs. strain graph could not be produced. Fabricating six specimens from each mixture design ensured that there were at least three valid tests for each mixture design. A schematic of the specimen and test set up in the grips is shown in Figure 24. Beam test specimens were made from steel molds 2 × 2 × 17 in. From the direct tension test, the following values were calculated: the maximum stress, the stress at a strain of 0.005 in/in, and the toughness (area under the curve) up until 0.005 in/in of strain.

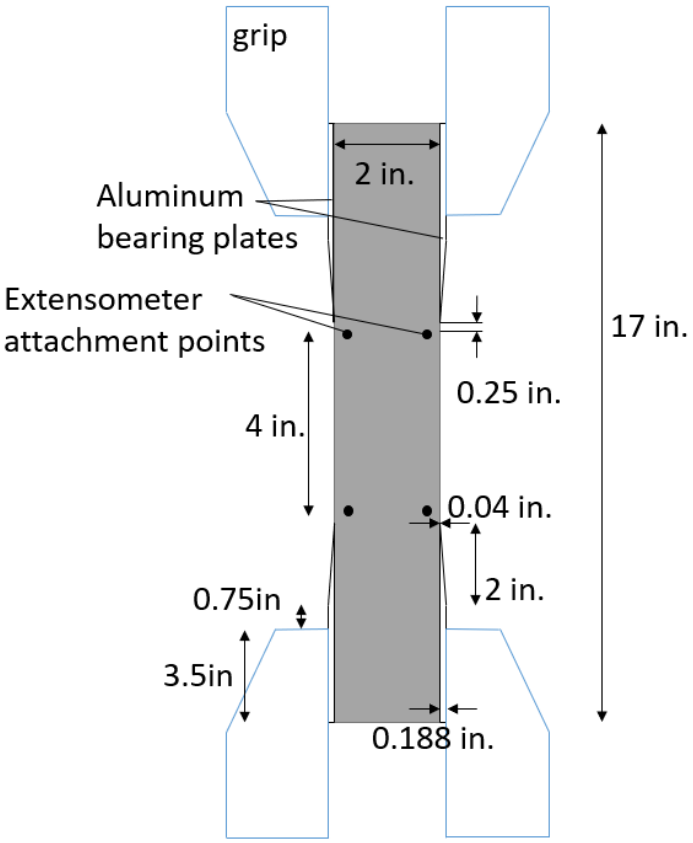

Figure 24: Direct tension testing set-up

Four 4 in. × 4 in. × 14 in. flexural specimens were made for each mixture design, ensuring that at least 3 of each were successful. Figure 25 shows a schematic of the test set-up. The value "a" in Figure 25 is equal to 4 inches for this test. The test was performed according to ASTM C1609. The values calculated and used for analysis were the maximum bending stress, also referred to as the "modulus of rupture," the stress at a deflection L/600, the stress at a deflection of L/150, and the toughness (area under the curve) up until the deflection of L/150 was reached.

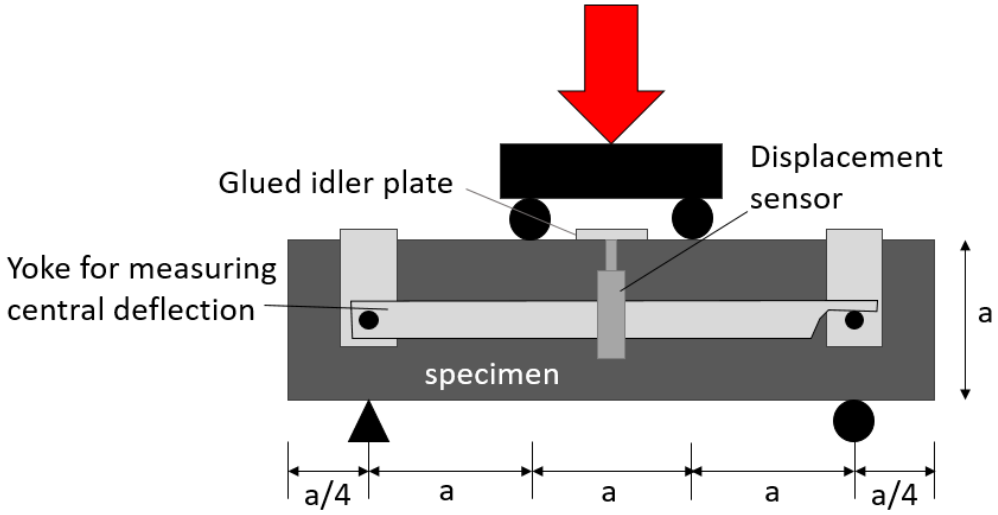

Figure 25: Flexure testing set-up

The double punch test used for this study was a modified version of UNE 83515, commonly known as the "Barcelona Tests" [12]. Three 6-in. diameter × 6-in. tall cylindrical double-punch specimens were made from plastic molds for each mix. This test was simplified so it could be performed in a standard compression testing machine with simple mechanical displacement gauges. A schematic of the simplified test method is shown in Figure 26. While the original test method used a circumferential extensometer to measure displacement, this method used a dial gauge to measure vertical displacement of the specimen. Circumferential and vertical displacement-measuring techniques have been shown to be related to each other in the double-punch test [83,84]. To further simplify the testing, a dial gauge was used as the displacement-measuring device, and readings of load vs. displacement were taken manually by the technician at set displacement intervals. For the first 0.10 inches of displacement, readings were taken every 0.01 in. From 0.10 in. – 0.30 in., load was recorded every 0.02 in. Testing of concrete specimens made from the same batch of concrete showed that taking discreet readings at increments less than or equal to 0.025 in. did not alter the overall toughness results by more than 2 percent. A load rate was selected to give a displacement rate similar to that used in UNE 83515. After the specimen neared failure, no adjustments were made to the machine load rate dial for the remainder of the test. Specimens were loaded at a load rate between 200-600 lb/sec during the linear portion of the load vs. displacement curve. Testing on specimens made from the same batch of concrete showed that a load rate between 200 and 800 lb/sec produced no statistically significant change in toughness or peak strength results for the double-punch test. From the double-punch data collected, the loads were converted to stresses using Equation 17:

$$f'_t = \frac{4 * Q}{9 * \pi * a * H} \qquad \text{Equation 17}$$

Where f'_t is the tensile stress, Q is the applied load, a is the diameter of the steel punches, and H is the height of the cylinder [12]. The maximum stress was reported, along with the stress at a displacement of 0.14 in. and the toughness calculated as the area under the stress vs. displacement curve. The displacement of 0.14 in. was selected as a point at which strengths would be compared because the peak load consistently occurred before this displacement. This ensures that the stress at 0.14 in. is a post-cracking stress, which would be a better measure of toughness and fiber matrix strength than the peak stress, which is often a measure of cementitious matrix strength in more brittle specimens. Any displacement that consistently occurs past the peak stress of all specimens could be used for comparison as long as it is consistent. The toughness was calculated for the entire 0.30 in. of vertical displacement.

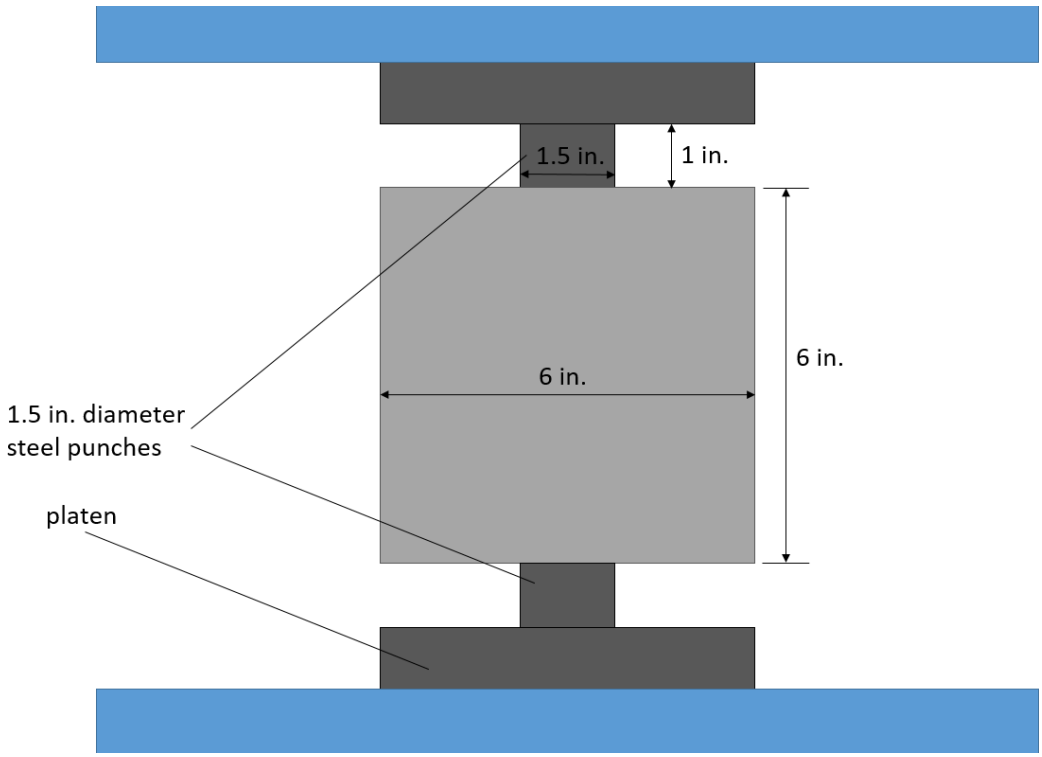

Figure 26: Simplified double-punch test set-up

3.3. Results

Because of the large amount of data collected for this study, graphs of every successful trial of every test are presented in Figure A-1 to Figure A-30, which are contained in Appendix A. Trials where the specimen cracked in a location unacceptable for data analysis were not plotted and were not considered in the calculation of average values. Graphs showing average values include error bars representing the standard deviation of the replicates for the particular mix.

Figure 27 through Figure 29 show the average maximum stress values calculated from direct tension, flexure, and double-punch testing for each mix, respectively. Of the three types of values

calculated from each test (maximum stress, stress at specified point, toughness), the maximum values were the least affected by both fiber type and fiber dose. This is because even specimens with low amounts of fiber could have a relatively high strength in the cementitious matrix alone. Many specimens with low doses of fibers had very high cracking strengths in flexure or tension, followed by a sharp decrease in load right after cracking. As fiber dosage increased and specimen behavior became strain-hardening, trends relating fiber percentage and maximum stress were more apparent. This can be especially noticed in the straight fiber specimens with 2-3% fibers. Values from these mixes were higher than values from the other seven mixture designs, for which maximum stress values ranged from 750-1000 psi. It can reasonably be assumed that concrete with a compressive strength of 17,000 psi could have a tensile strength in this range, even without any fiber reinforcement. Equation 18 is often used as an estimate of when concrete will crack in tension.

$$f_t' = 7.5\sqrt{f_c'} \qquad \text{Equation 18}$$

where f'_t is the tensile strength and f'_c is the specified compressive strength [218]. Concrete with a specified compressive strength of 17,000 psi would then have an estimated tensile strength of 978 psi. In strain-hardening specimens, the maximum stress of the concrete exceeded the stress exhibited during the first crack because the fiber matrix was stronger than the uncracked cementitious matrix. As fiber content increases, the post-peak strength and toughness increase due to a greater number of crack-bridging fibers. Specimens made with 2-3% straight fibers exhibited strain-hardening behavior, while the specimens made with twisted fibers did not. For all specimens, as strain increases, fiber pullout begins and the strength of the specimen decreases. In direct tension testing, initial cracking stresses were highly variable because they depended on specimen alignment. A specimen that was slightly misaligned would have a lower initial cracking stress than a perfectly aligned specimen. If the specimen were strain-hardening, it could compensate for these misalignments after cracking by bending and redistributing load. However, the more brittle specimens could not regain strength after cracking, causing very high standard deviations to be calculated for these specimens.

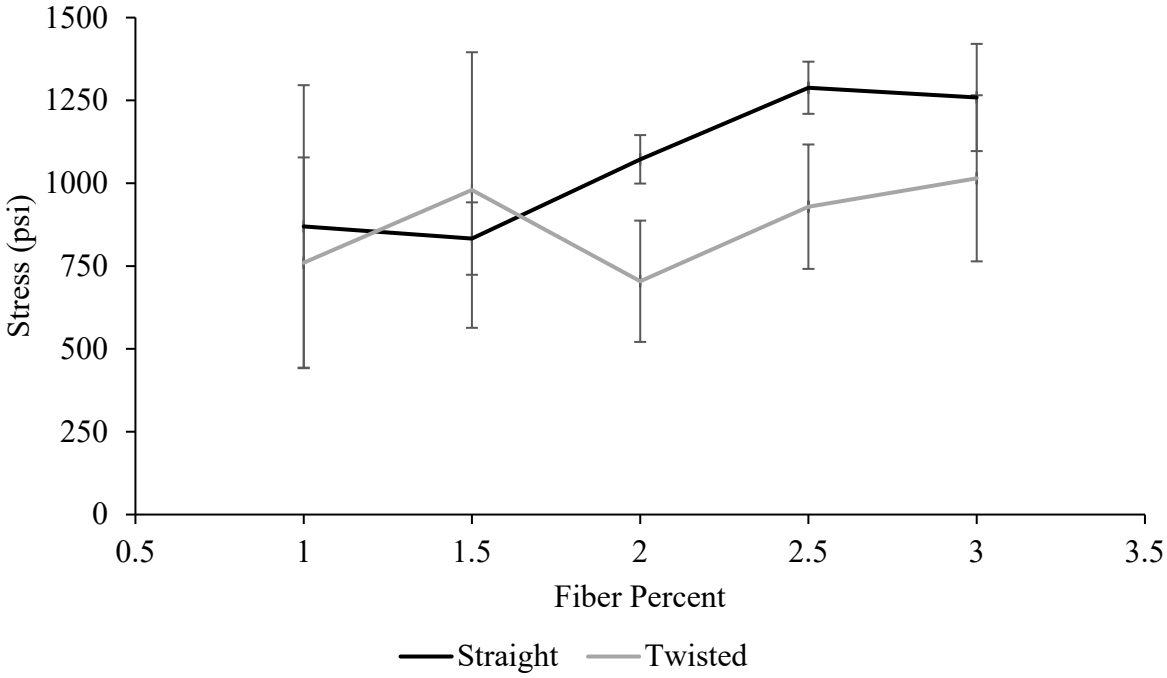

Figure 27: Average maximum stresses from direct tension testing

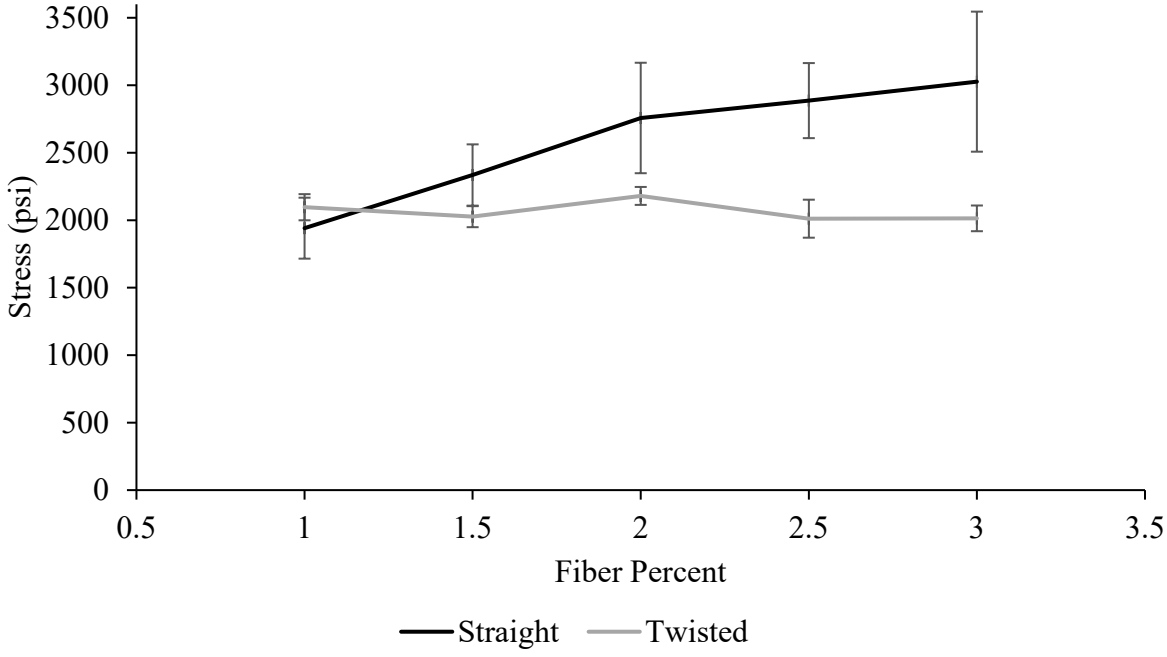

Figure 28: Average maximum bending stresses (moduli of rupture) from flexure testing

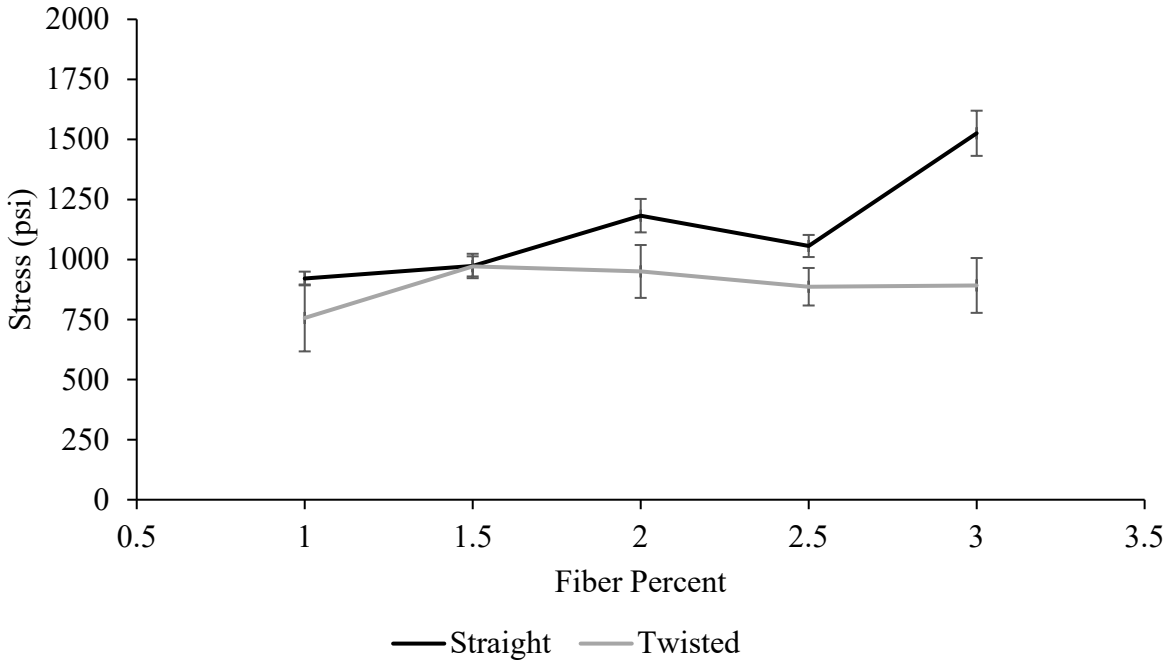

Figure 29: Average maximum tensile stress from double-punch testing

The results from flexure and double-punch testing showed similar trends in their maximum stress values. No relation was found between maximum stress and fiber percentage for the twisted fiber mixes, and a slight increase for straight fiber mixes. For all three tests, the R^2 value for maximum stress was below 0.1 for Helix mixes. The R^2 value was between 0.5 and 0.7 for straight fiber mixes. These R^2 values were calculated using all the trial values for each test, not only the averages. From the error bars plotted in the average graphs, the double-punch test had the lowest standard deviation in maximum stress. This was especially true for the twisted fiber mixes and the less-ductile straight fiber mixes, which had especially high coefficients of variation (standard deviation normalized with average value) in the direct tension test. This makes sense as the direct tension test is most susceptible to effects caused by misalignment of the specimen. Additionally, the double-punch test has a large volume over which the specimen can fail, as cracks can form anywhere in the specimen. It also produces a very large failure plane of 36 $in.^2$ compared to the 4 $in.^2$ direct tension failure plane. The direct tension and four-point flexure tests both have a 4 in. length over which failure can occur. The failure plane for a flexure test is 16 $in.^2$, but the maximum stress occurs only at the bottom surface of the specimen. For these reasons, defects and discontinuities such as air voids or fiber clumps will be more common in the large double-punch specimens, but each defect will have a relatively small effect on the results because it will comprise a small portion of the stressed volume and eventual failure plane.

Some specifications used in the United States for UHPC require only a maximum stress value to be reported for either flexure or direct tension testing [219,220]. Colorado only requires that the maximum value be greater than the first peak value of the ASTM C1609 flexural test [221], and Florida only requires a strength of 1,200 psi to be reached in the ASTM 1609 flexural test [219].

While Florida's Dev927UHPC only applies to proprietary concrete mixes, and specimens tested for this research were made from non-proprietary UHPC, every mix tested in this study would meet the tensile requirements for Florida's current specification. This could be inadequate because it does not consider post-peak performance such as relative post-peak maximum strength and toughness, and while the specimens made with twisted fibers reached a stress of higher than 1,200 psi, the mixes with lower fiber contents were not able to maintain that load after cracking. For this reason, it is recommended that at least one additional property specification be included that relates to the post-peak performance. This is similar to Canadian and Swiss requirements that use a minimum ratio of maximum stress to first peak stress in conjunction with a minimum first peak strength to approve UHPC mixes [222,223]. While this may be difficult to determine in specimens that do not have an obvious first crack, it does a better job of taking the entire tensile behavior into account than simply using the maximum strength value.

Some states that do not have any tensile requirements at all choose instead to require a minimum amount of fiber to be included in a mix [224,225]. While this may be a useful requirement in conjunction with other tensile requirements or with a list of specific approved fibers, the results from this research show that fiber content by itself does not ensure desired behavior. A fiber's aspect ratio, thickness, and geometry may influence its effectiveness in transferring load to the cementitious matrix.

For this research, the additional parameters studied to help represent behavior were toughness and stress at a specified displacement. Figure 30 through Figure 32 show how the average toughness changed with respect to fiber type and amount. While this change is still only slightly evident in the twisted fiber mixes, it is clear that the straight fiber mixes gained toughness as fiber percentage increased. One large discrepancy can be seen in Figure 32, where the specimens made with 2.5% straight fibers had a low double-punch toughness compared to what would be expected in the trend. The cause for this is unknown, as the double-punch specimens were made in the same mix as the direct tensile specimens, and no abnormal behavior was seen in the toughness of the 2.5% straight fiber direct tension tests. Peak stress was also low for the 2.5% straight fiber double-punch specimens, as shown in Figure 29.

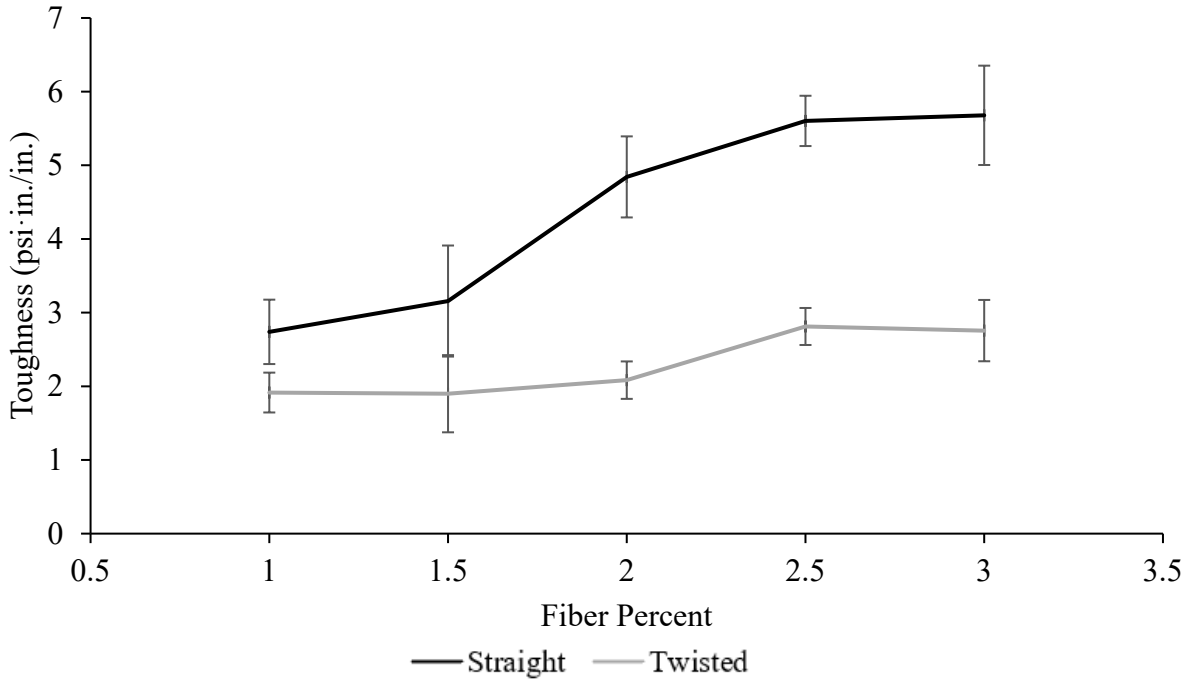

Figure 30: Average toughness from direct tensile testing

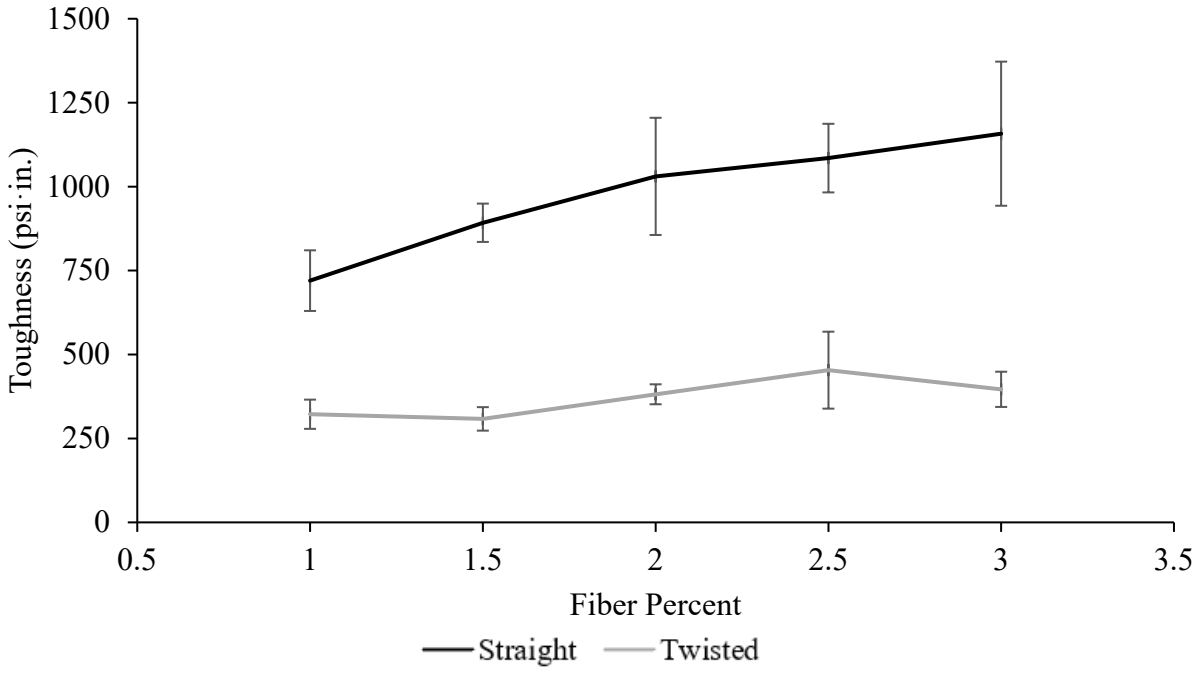

Figure 31: Average toughness from ASTM C1609 flexural testing

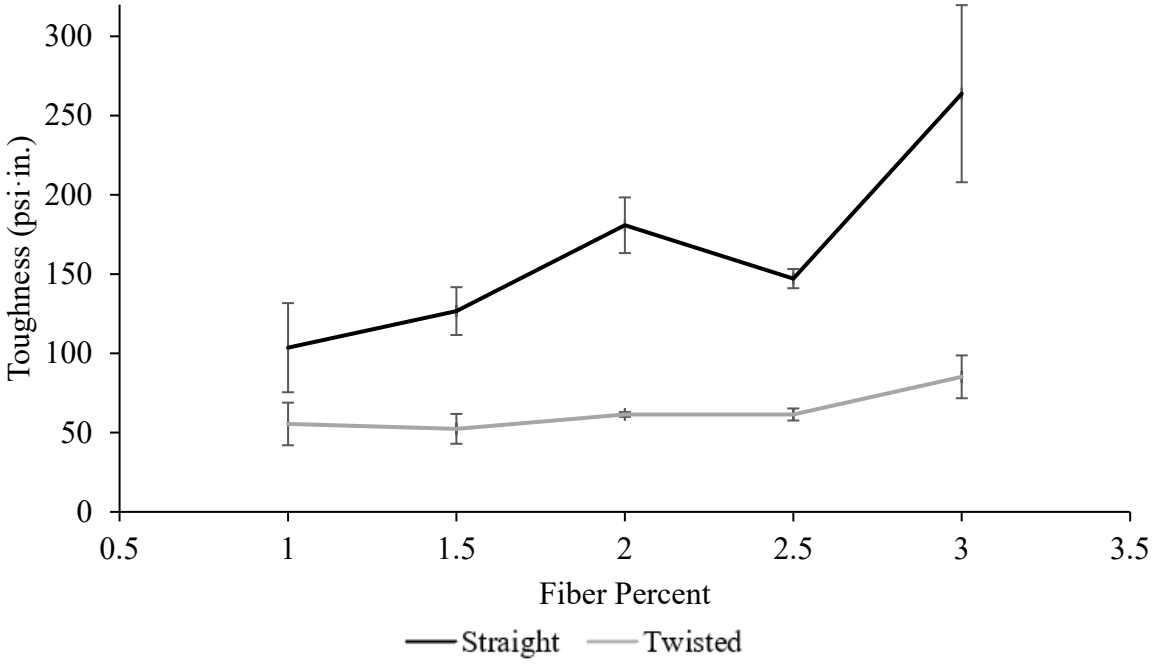

Figure 32: Average toughness from double-punch testing

The final parameter studied for each test method was the stress at a specified strain. ASTM C1609 requires that the flexural stress be reported at specified deflections of L/600 and L/150, so both of these values were investigated [217]. For a span (L) of 12 inches, these deflections corresponded to 0.02 in. and 0.08 in., respectively. For the tension tests, a specified strain of 0.005 in./in. was chosen. This was chosen because it is the lowest tensile strain at which a reinforced concrete member is considered tension-controlled [218]. Therefore, a structural engineer may be interested in the tensile strength of the concrete at this point. In addition, this strain is large enough that the first crack will always occur before it, ensuring that it is truly a measure post-cracking tensile strength. Some of the 1% twisted fiber specimens did not reach this strain, so their values were not used for the calculation of the average. For the double-punch test, a displacement of 0.14 in. was chosen. This value was chosen to be large enough so that it would occur after the peak stress for each mix. A larger value was not chosen because at increased displacements, the twisted fiber specimens had very low strengths, making the results more difficult to differentiate at higher displacements. However, as long as the displacement chosen for comparison is consistent for all specimens and occurs after the peak strength, the value chosen would not make a large difference for comparison.

The average values for stresses at specified strains are presented in Figure 33 through Figure 36. An upward trend was clearly visible for the straight fiber specimens as fiber content increases, while the twisted fiber specimens showed less of a change. The 2.5% straight fiber double-punch specimens had surprisingly low stress values. It is thought that this could be a result of material non-homogeneity during placement. Selecting a specific deflection or strain at which to compare stresses can be a useful tool to measure specimen ductility. However, it is important that the

location be determined so that the stress value is taken from the same portion of every specimen's response curve. For example, a very ductile double-punch specimen may not experience peak stress until after 0.10 inch of displacement; therefore, the displacement selected must take this into account so that the comparison is not made between a pre-peak value of one specimen and a post-peak value of another. This issue was present when finding the flexural stress values at a deflection of L/600, as this value was measuring a value before the maximum stress for most of the straight fiber specimens but a post-peak value for all the twisted fiber specimens. In addition, for the low-fiber content twisted fiber flexure specimens, the initial crack often caused a large displacement of over 0.02 in. to occur almost instantaneously, meaning there were no data points taken at a deflection of 0.02 in. In these cases, a weighted average was taken of the points before and after a 0.02 in. deflection was reached to determine the stress at 0.02 in. However, this was not necessarily equivalent to the flexural stress that the specimen would hold at 0.02 inches; it was likely an over-estimate. The stress readings at a deflection of L/150 (0.08 inches for this study), all occurred after the peak stress had been reached, giving a more comparable number between fiber types. When comparing the readings at 0.08 in. to those at 0.02 in. of deflection, it can be seen that the twisted fiber specimens exhibited a large decrease in strength, typically a decrease of 65-80 percent. The straight fiber specimens lost about 15% of their strength for the 2%-3% specimens. The 1% and 1.5% specimens had higher stresses at a 0.08 in. deflection than at a 0.02 in. deflection. Similar trends are found when comparing the stress at 0.08 in. of deflection to the maximum stress, or modulus of rupture. Twisted fiber specimens lost 75-90% of their maximum stress, while straight fiber specimens lost only 10-25 percent. A metric like this could be used to confirm specimen toughness, but it would penalize specimens that had a higher maximum stress, all else being equal. A single value at a specified displacement may be preferred, especially in direct tensile testing where stresses at known strains may be desired for design calculations. One downside of directly transferring tensile behavior from the direct tensile test to a design scenario is the gauge length over which strain is measured. The 4 in. region may have multiple cracks form in it, but typically only one or two of these cracks are responsible for the majority of the strain measured. The strain is really an average strain over the arbitrarily determined 4 in. distance. While this test has been widely accepted in the UHPC research community, a researcher using a different direct tension test may see different results simply because of the length over which the strain is measured because of sample size effects. If a 2-inch region is used and the localized crack forms within it, the strain readings would be roughly twice as large as those calculated from a 4-inch region, which could make it appear to be more ductile than it is.

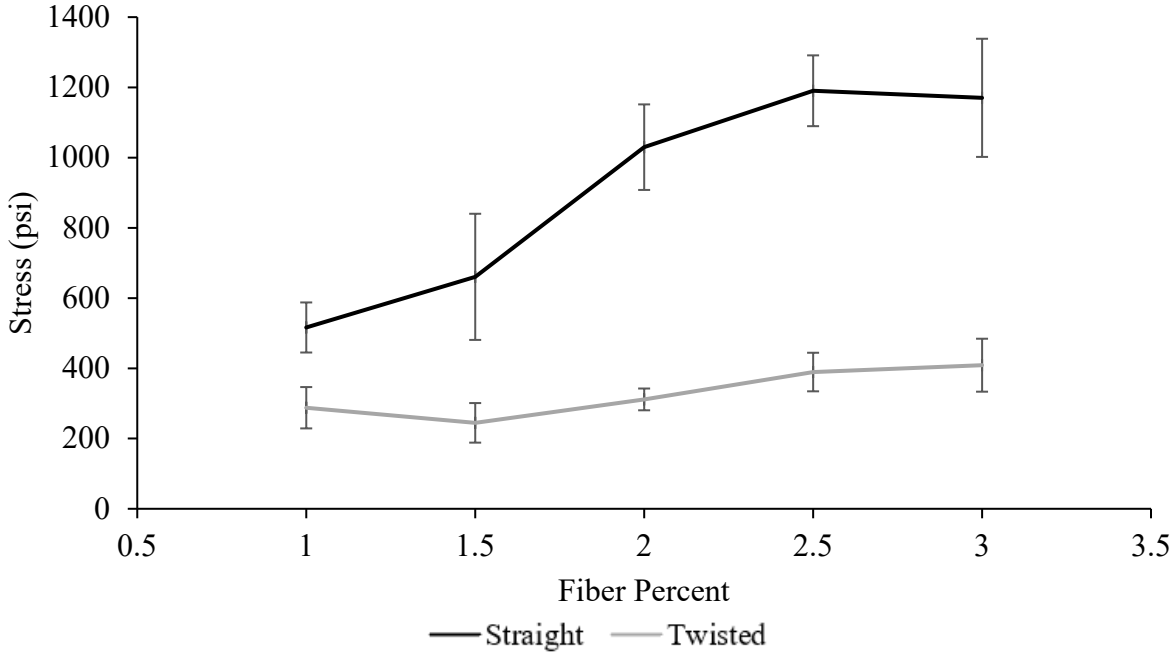

Figure 33: Average direct tensile stress at 0.005 in./in. strain

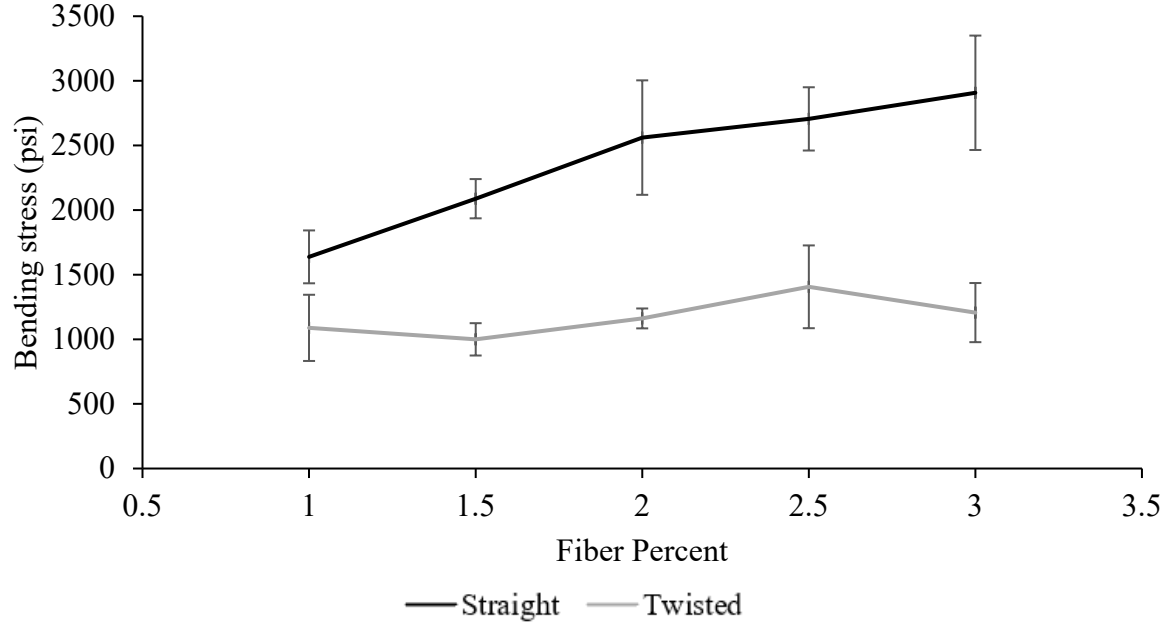

Figure 34: Average flexural stress at a deflection of L/600

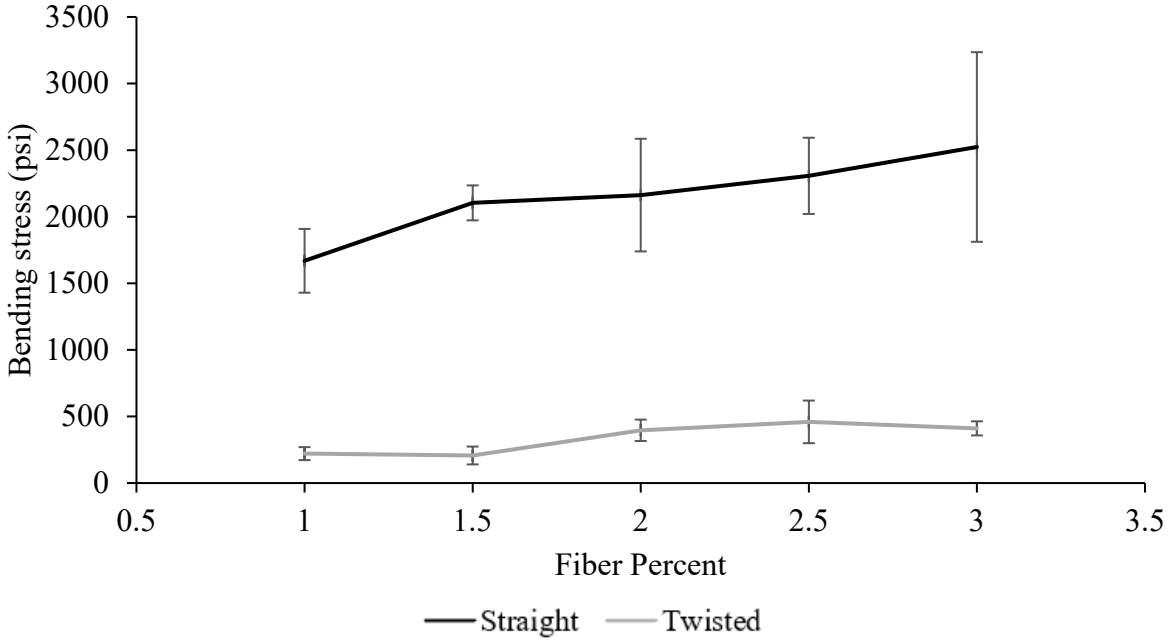

Figure 35: Average flexural stress at a deflection of L/150

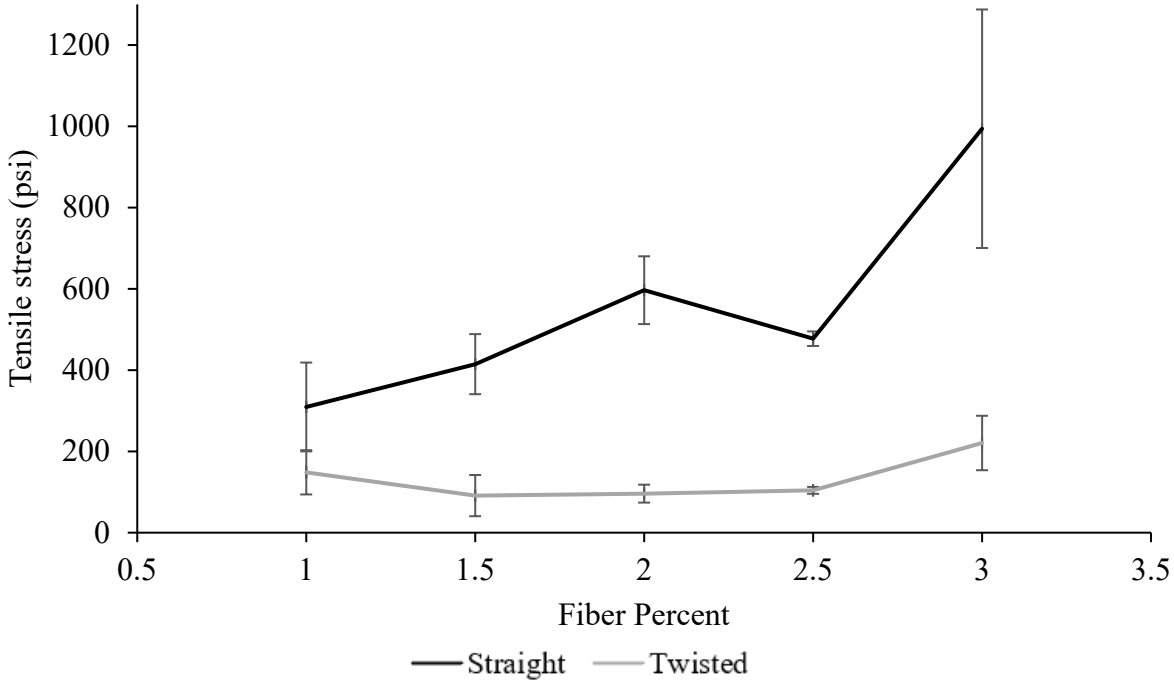

Figure 36: Average double-punch tensile stress at a vertical displacement of 0.14 inches

A purpose of this study was to determine whether the results of simpler methods (third-point flexure and modified double-punch) would reliably reflect the results of the more-complicated direct tensile method. Establishing this relationship is imperative to being able to use one of the simplified methods as a quality control test. Figure 37 and Figure 38 show the relationships of the results of ASTM C1609 and the modified double punch test to the results of the direct tension test, respectively. The results were compared by plotting direct tension values on the independent (x) axis and the simplified methods on the dependent (y) axis. An equation for the best-fit linear trendline and R^2 value were calculated for each comparison.

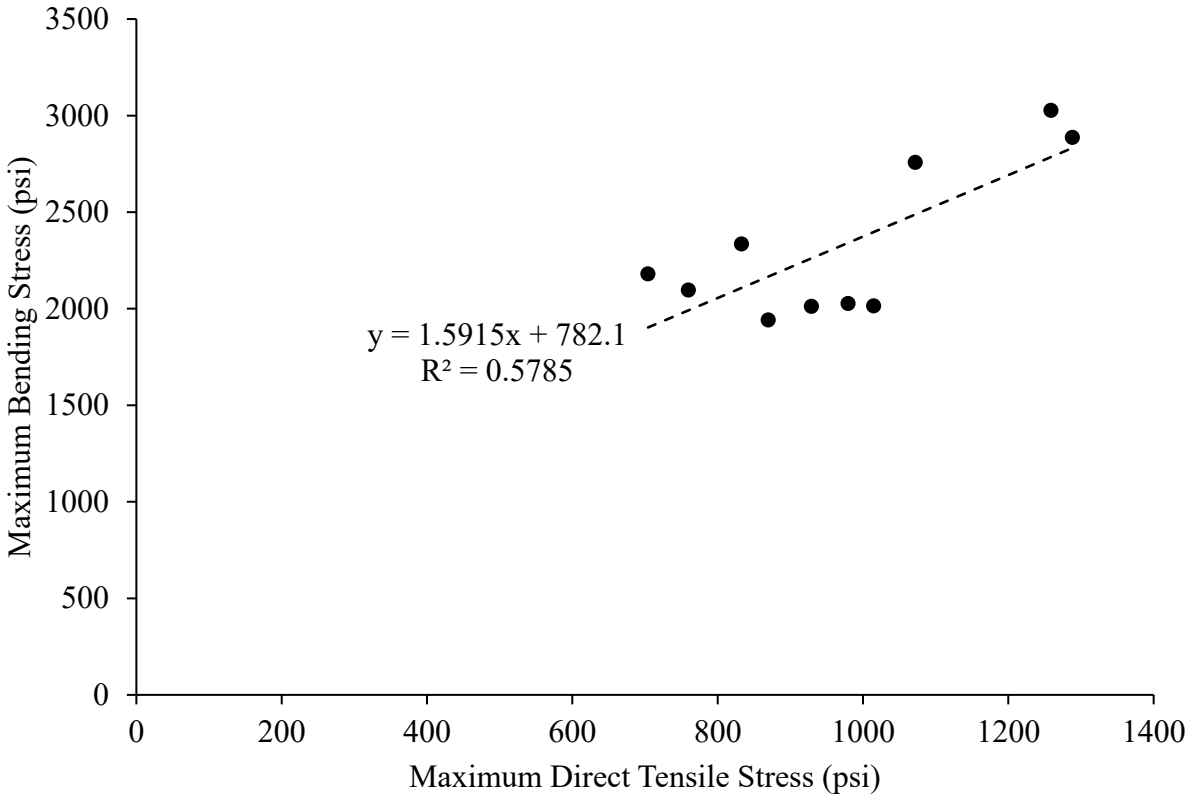

Figure 37: Relationship between maximum bending stress in ASTM C1609 and maximum direct tensile stress for specimens tested

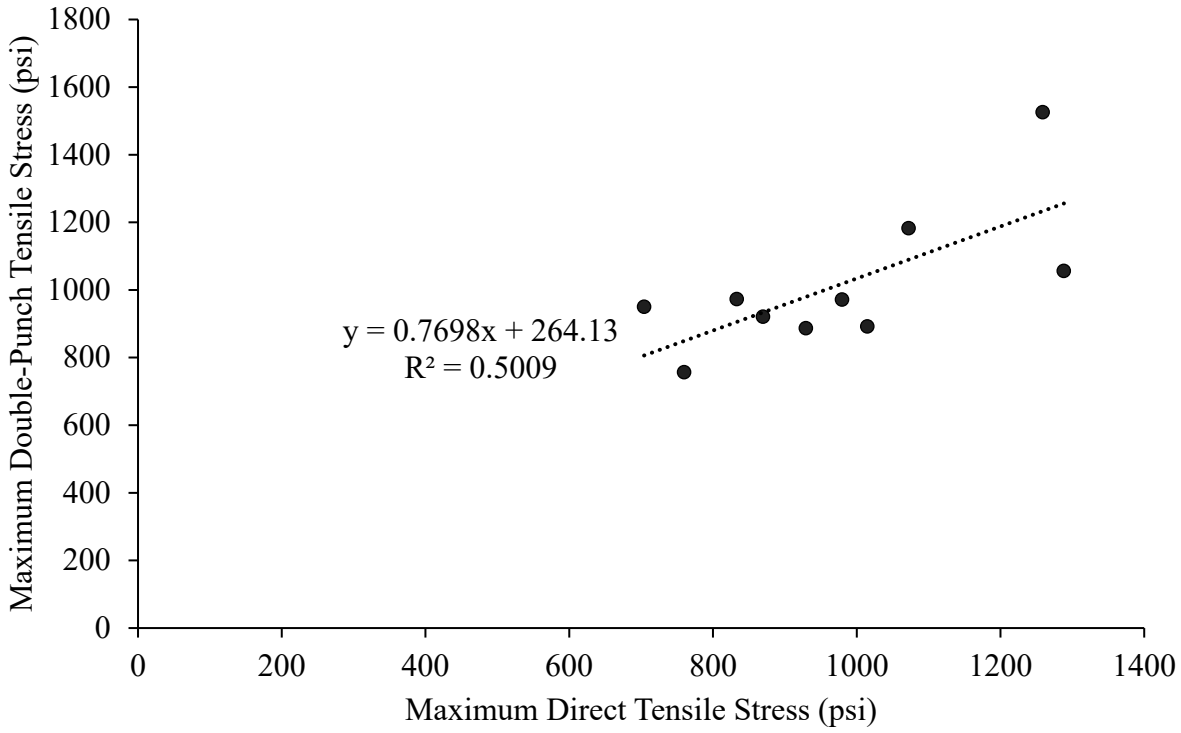

Figure 38: Relationship between maximum double-punch tensile stress and maximum direct tensile stress for specimens tested

As expected, there was not a high correlation between the maximum stresses of each test, as the maximum stresses within each test method were highly variable. The trendline equations do, however, provide useful information about the relationship between results of the tests. As seen in Figure 37, the bending stresses from ASTM C1609 are consistently higher than the direct tensile stresses from FHWA's test. Using the trendline equation, a mix with a direct tensile strength of 1,000 psi would be expected to have a maximum stress in the flexure test of roughly 2,370 psi. Because ASTM C1609 produces results as a bending stress, these values can't directly be compared with direct tension values; higher stress requirements must be set for specimens tested with ASTM C1609. Therefore, it is important that the current Florida requirements for UHPC in flexure be increased, preferably to 2,300 psi or higher for UHPC. An alternative option would be to require the use of inverse calculations to obtain the direct tension stress-strain relationship from the ASTM C1609 results. The results from the double-punch test comparison are closer in value to the direct tension results from corresponding mixes. The trendline and equation in Figure 39 show the relationship between the maximum double punch tensile stress and direct tensile maximum strength. Using the equation calculated, at the lower bound of direct tensile stresses measured, a direct tensile stress of 700 psi would predict a double-punch tensile stress of roughly 800 psi. At the upper end, a direct tensile stress of 1300 psi would predict a double punch test strength of 1,260 psi. The similarity of these values show the reliability of Equation 17 at calculating a tensile stress from double-punch load, and it makes comparisons

between results of the double-punch test and direct tension test more intuitive. However, as with the third-point flexure test, care should be taken not to regard results from this test as being of equal value to results from the direct tension test.

Toughness values showed a much higher correlation between tests than the maximum values did, as shown in Figure 39 and Figure 40. Both the flexure and double-punch tests showed an R^2 value of higher than 0.8, indicating a good correlation. Toughness values for both flexure and double-punch testing showed a larger gap between the twisted fiber and straight fiber mixes than the direct tensile toughness did. In direct tension, the 1% straight fiber specimens had lower toughness than the 2.5% and 3% twisted fiber specimens. However, it showed higher toughness in the double-punch test than all twisted fiber specimens, and the difference in the flexure test was even more pronounced. Looking at the actual direct tension curves for these mixes, at the strain of 0.005, the straight fiber specimens with 1% fiber content had higher strength than the equivalent specimens made with twisted fibers, which also seemed to lose strength with displacement at a faster rate. This suggests that if the toughness calculation for the direct tensile test was changed to be over a range longer than 0.005, the 1% straight fiber specimens would have shown a higher toughness than those made with twisted fibers. While tensile behavior preference will change based on the application of a concrete, the behavior of the 1% straight fiber specimens will usually be preferable to that made with 3% twisted fiber, as the stress retained after cracking is more reliable. Using 1% of straight fiber would also likely cost less than using 3% twisted fiber. For a strain-hardening mix, neither of these options would be approved; however, this comparison shows the importance of making a toughness determination over a greater portion of the stress vs. strain curve. It is suggested that if a toughness value were to be used for determining tensile class, it be calculated at an end-point strain of 0.01 in./in.

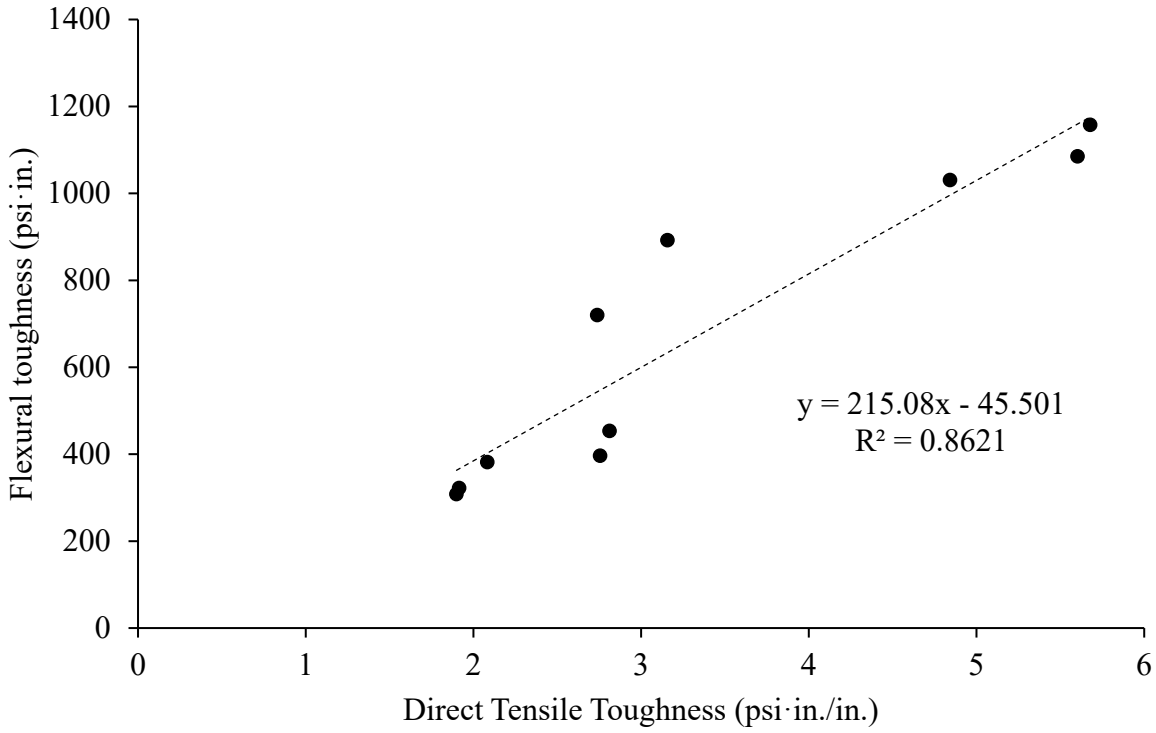

Figure 39: Relationship between flexural toughness and direct tensile toughness

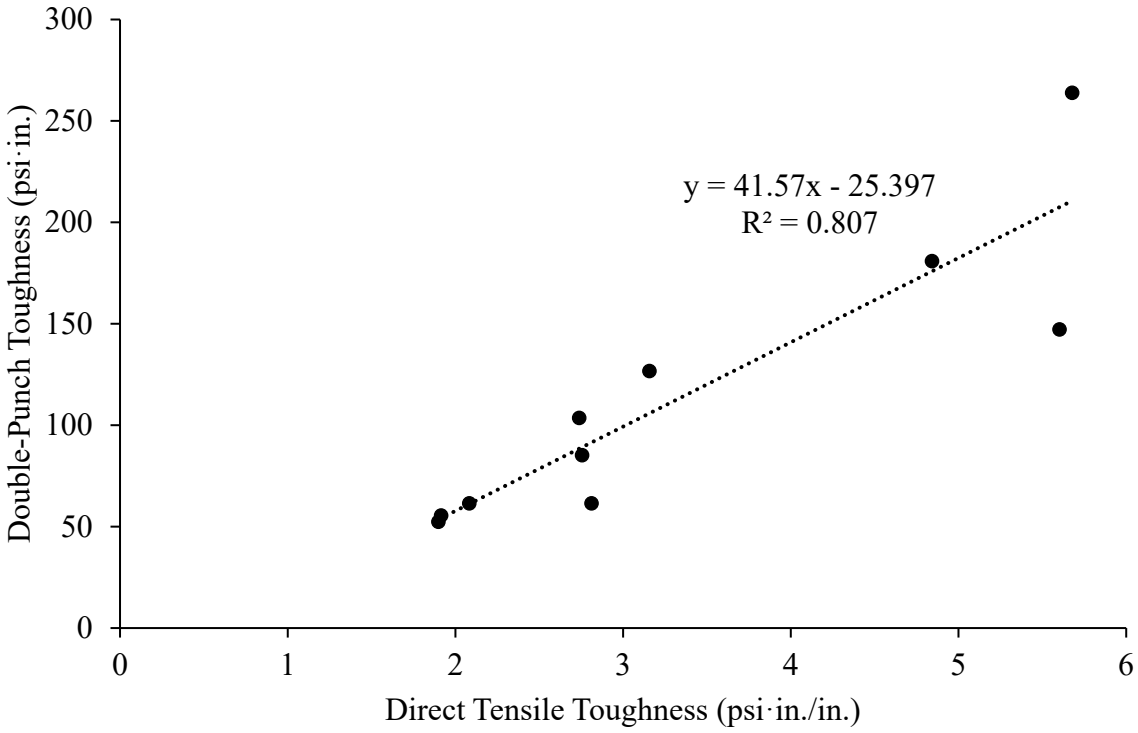

Figure 40: Relationship between double-punch toughness and direct tensile toughness

Comparison of the stresses at specified displacements of the flexural or double punch specimens with that of the direct tension specimens had R^2 values near or above 0.8 as shown in Figure 41 through Figure 43, which were similar to the toughness correlations. Once again, the flexure test had higher correlation than the double punch test, although it is likely that a replicate of the 2.5% straight fiber double punch mix would improve its values. The flexure stress at a deflection of L/600 had an extremely high correlation with the tensile stress at 0.005 strain, with an R^2 value higher than 0.97. When the flexure stress at L/150 was compared, the correlation decreased. This appears to be due to the high stress values achieved by the 1% and 1.5% straight fiber specimens at this deflection. As mentioned earlier, they averaged a higher stress at the larger deflection than at the smaller one. These correlations show that either the flexure or double punch test could be reliably used for quality control testing in place of direct tension testing.

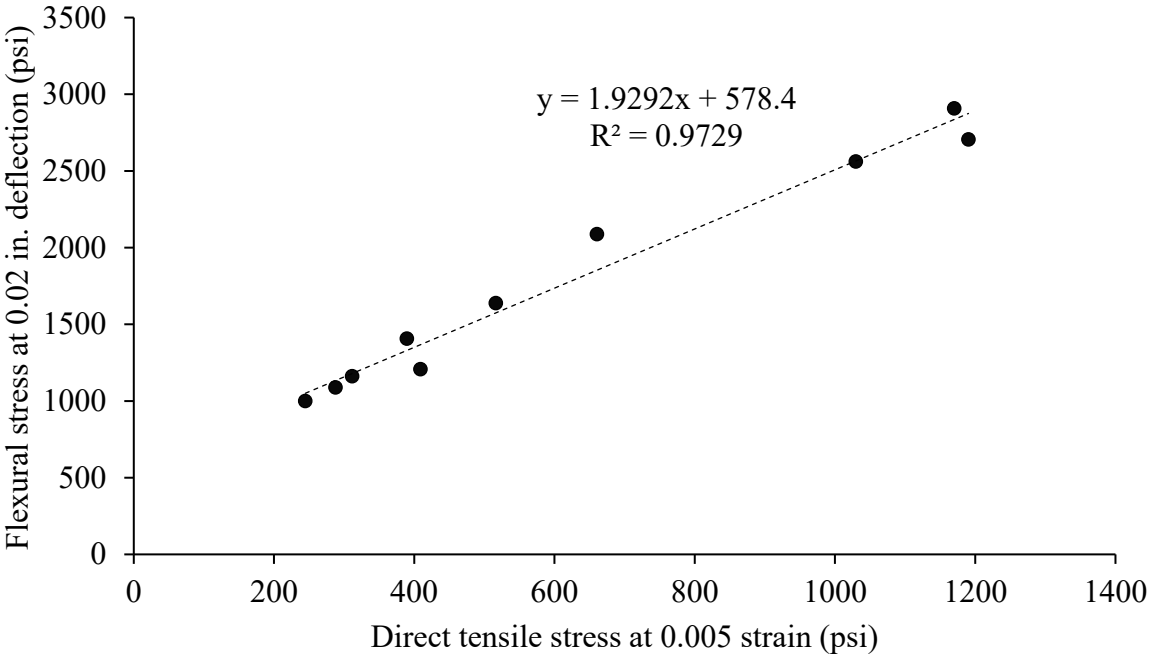

Figure 41: Flexural stress at L/600 (0.02 in.) vs. direct tensile stress at 0.005 strain

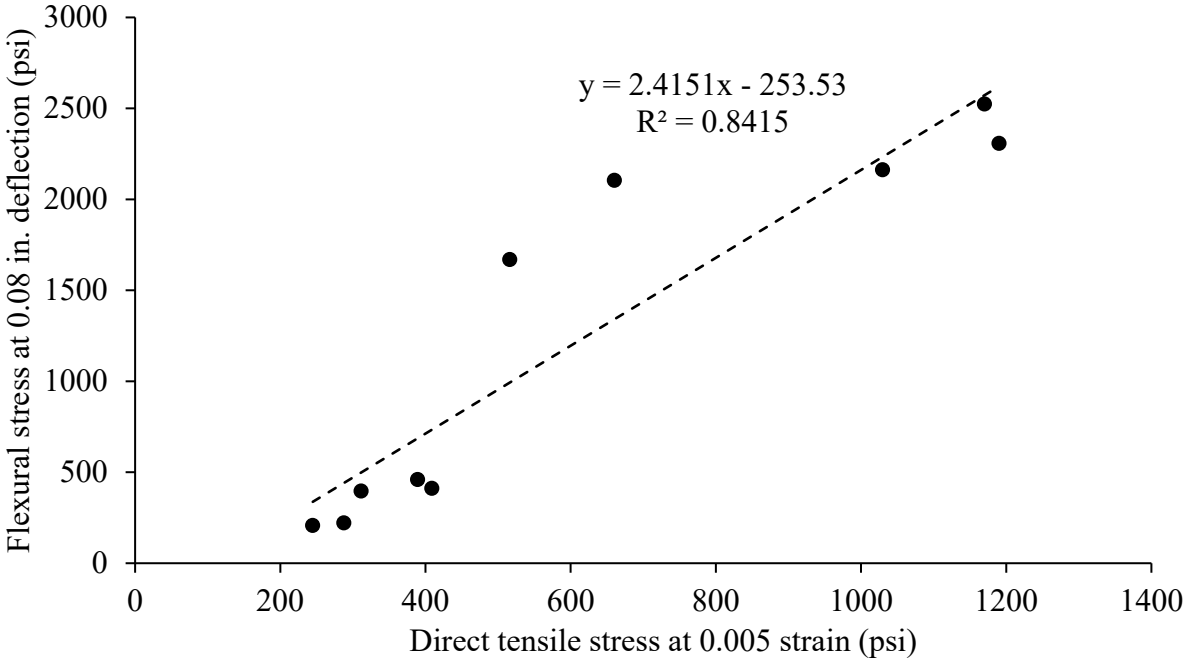

Figure 42: Flexural stress at L/150 (0.08 in.) vs. direct tensile stress at 0.005 strain

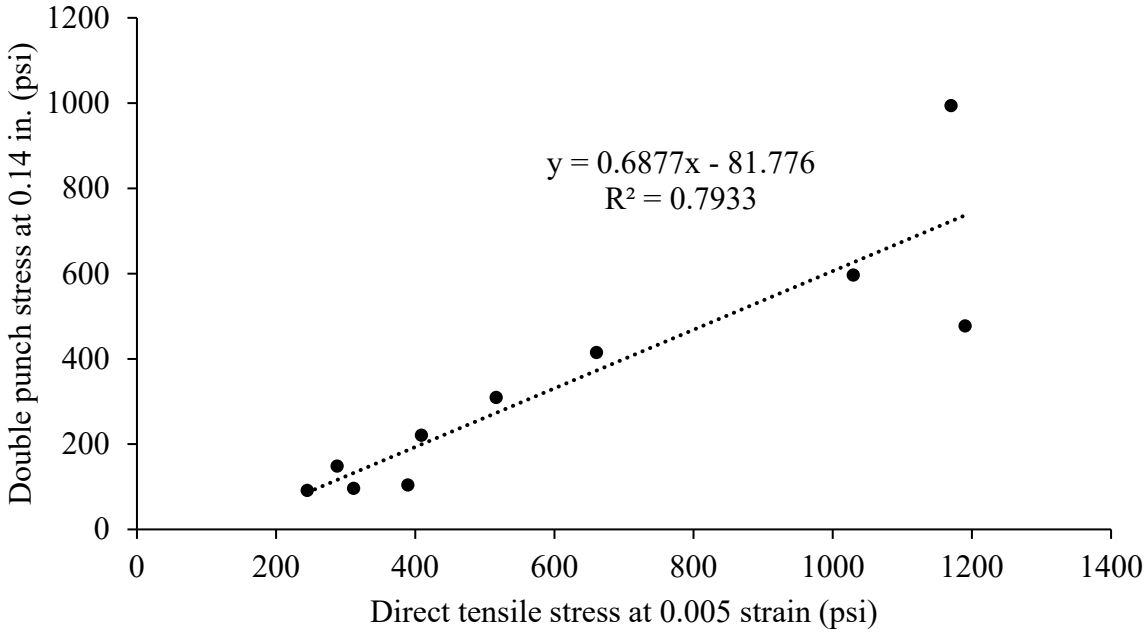

Figure 43: Double-punch stress at 0.14 in. vs. direct tensile stress at 0.005 strain

Tensile strength classes were developed to be used in Florida for non-proprietary UHPCs. The preferred test method to use when establishing the UHPC strength class is the direct tensile test. While researchers have proposed inverse analysis techniques to characterize UHPC tensile behavior [226–228], they rely on assumptions of the stress vs. strain behavior and/or the curvature of the cracked specimen [229]. Many specification agencies use a ratio of maximum stress to peak stress to approve a mix or determine a mixture tensile class [222,223].The downfalls of this method are that it can require a subjective determination of the first cracking stress and that a higher initial cracking stress can lead to the rejection of an otherwise adequate mix. For these reasons, it is recommended that Florida Department of Transportation (FDOT) use stress at a specified displacement to determine a mixture's appropriate tensile class. Mixtures with at least 2% of the straight steel fibers tested tend to be strain hardening, while mixes with 1 or 1.5% appear strain softening or elasto-plastic. All of the mixes with twisted fibers exhibited a steady decline in tensile strength as strain increased. Specifying a stress at a particular strain ensures that mixes with high maximum tensile stresses but low toughness would not be approved as a strain-hardening UHPC. A value of 900 psi at 0.005 strain is approximately equal to the average value for the 2% straight fiber specimens tested minus one standard deviation. If this were used as a criterion for a strain-hardening tensile strength class, the 2%, 2.5%, and 3% straight fiber mixes would be approved, while the 7 others would not. Because some specimens are still increasing in strength at 0.005 strain and may not yet have reached their maximum strength, (such as the1.5% straight fiber trial 1 and 2% straight fiber trial 4), it should be acceptable to use the best strength value reached after a strain of 0.005.

3.4. Summary and Recommendations

It is recommended that direct tension tests be used for mix design acceptance because it does the best job of showing overall stress vs. strain behavior. Some mixes that are not strain-hardening, such as the mixtures made with 1% and 1.5% straight fiber, will appear strain-hardening in a flexure test, although a direct tension test will show that they are clearly not. In addition, the direct tension test will give results that are most easily correlated to design, as the stress values in the flexure test are not direct tensile stresses, but bending stresses, which are usually over twice as large, as seen in Figure 37. The suggested minimum requirements for tensile strength classes based on this research are shown in Table 5. This table uses two criteria to determine strength class: the maximum stress the specimen reaches and the stress the specimen has at 0.005 strain. A third category is present for the enhanced strain-hardening class, to ensure materials characterized in this class maintain a high strength even at 0.01 strain. Figure 44 shows a schematic of the results from a direct tension test and which points would be used for mix qualification. The direct tension results shown in the figure would qualify as enhanced ductility UHPC because all three points are above the required values. A mix design being tested for qualification would need to have multiple specimens tested in this way, with the average in each category exceeding the tensile class requirement. It is suggested that at least 6 specimens be used in testing for qualification of a mix, with no more than 3 excluded for cracking outside of the area used to measure specimen strain. Using Table 5, the mixes made in this study would be classified as follows: mixtures made with 2.5% and 3% straight fibers could be classified as enhanced ductility, 2% straight fibers would be strain-hardening, and mixes 1% and 1.5% straight fibers, as well as 3% twisted fibers would qualify as strain-softening. The remainder would be non-tensile UHPC. Based on this table, most projects with structural members made from UHPC would likely specify a strain-hardening material. This would include highway closure strips which are designed to reduce the development length needed for mild steel reinforcement, columns or piles designed to experience bending stresses, and pretensioned members. Strain-softening materials could be used in non-structural cases where crack width should remain small, such as in architectural applications, coatings for enhanced durability in seawater, or road overlays. The enhanced ductility class could be used if the designing engineer wants to rely heavily on the UHPC tensile strength in design. Because of the added cost, the enhanced ductility class would likely be used sparingly and on a case-by-case basis with the design structural engineer specifying desired values at specified stresses. This would ensure that the mix has been designed to perform well for its exact application.

Table 5: Recommended UHPC tension classes

Tensile Class	Maximum tensile stress (psi)	Maximum direct tensile stress after 0.005 in./in. strain (psi)	Maximum direct tensile stress after 0.010 in./in. strain (psi)
Non-tensile	-	-	-
Strain-softening	800	400	-
Strain-hardening	1000	900	-
Enhanced ductility*	1200	1100	900

*This class may also be used with specific requirements set by the structural engineer.

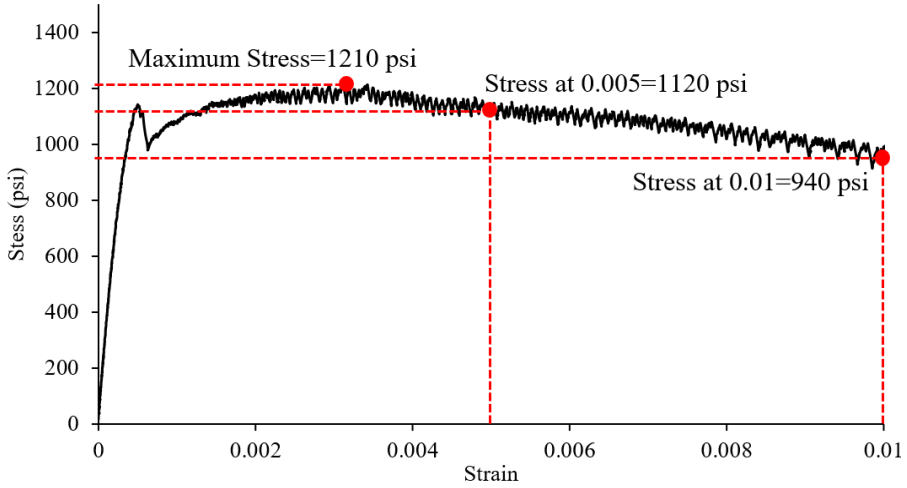

Figure 44: Example of qualification values taken from a direct tension test

The double punch or ASTM C1609 could be used as a suitable tensile strength quality control test for UHPC because both adequately correlated to the direct tension. The flexure test provided better correlation to the direct tension test, but it is more time consuming and requires more expensive equipment than the double-punch test. Therefore, suggested quality control requirements for both tests are presented in Table 6, with the idea that only one test would be used, at the discretion of either the DOT or the testing lab. It is recommended that at least 3 specimens be required for testing and the average taken. The requirements for quality-control testing are slightly more lenient than the requirements for the quality-approval testing to account for testing variability because any mix design being tested in QC will already have been tested and approved with the more stringent QA direct tension test. For example, the mixture with 1.5% straight fibers would pass as a strain-hardening material if it were tested with the flexure test in quality control. However, it would not have been approved as a strain-hardening UHPC initially in the direct tension test. The purpose of the QC requirements is to be able to detect errors that may have occurred in a mix to cause a reduced tensile strength and toughness from what was expected. For example, the 2.5% straight fiber double-punch specimens were much weaker than expected based on the trends of other straight fiber double-punch tests. If the double-punch quality control test were performed on this mix, it would show that this mix could not be classified as enhanced ductility, even though the original mix design would have been approved for the enhanced ductility class by the direct tension test.

Table 6: Recommended UHPC quality-control requirements for tension classes

Tensile Class	Maximum Flexural Stress (psi)	Flexure stress at L/150 (psi)	Maximum Double-punch stress (psi)	Double-punch toughness (psi·in.)
Non-tensile	-	-	-	-
Strain-softening	1800	1000	800	90
Strain-hardening	2300	2000	1000	130
Enhanced ductility	2500	2200	1200	200

4. NON-PROPRIETARY UHPC DIRECT TENSILE STRENGTH

4.1. Introduction

One of the most unique and valuable characteristics of ultra-high-performance concrete (UHPC) compared to normal concrete is its strength and ductility in tension. This is due to the steel microfibers mixed into the UHPC, which help to bridge cracks in the concrete and transfer significant tensile stresses even after cracking. Once the concrete has cracked, the fibers begin to straighten and slide through the concrete matrix as they pull-out from the concrete adjacent to the crack. The friction generated between the fiber and concrete matrix is the mechanism that simultaneously transfers tensile stress across a crack and generates tensile ductility.

Intuitively, adding fiber to a UHPC mix increases its strength and toughness in tension. The present research, however, focused on how the curing temperatures and mix design of the concrete matrix affect the strength and ductility in tension. The tensile strength of unreinforced normal-strength concrete has historically been estimated based on empirical relationships between the concrete tensile strength f'_t (psi) and compressive strength f'_c (psi) [230–232]. Equation 19 shows the relationship used in ACI 318-14 [218]:

$$f'_t = 6.7\sqrt{f'_c} \qquad \text{Equation 19}$$

Research by Graybeal developed a relationship between compressive strength and initial cracking strength of concrete specifically for UHPC [5]. These relationships are shown in Equation 20 for steam cured specimens and Equation 21 for untreated specimens:

$$f_{ct} = 8.3\sqrt{f'_c} \qquad \text{Equation 20}$$

$$f_{ct} = 6.7\sqrt{f'_c} \qquad \text{Equation 21}$$

Where

f_{ct} =initial tensile cracking strength of fiber-reinforced concrete, in psi

These equations, however, do not give information about post-cracking strength or toughness of the specimen, which is an important characteristic that the present research has addressed.

As reliance on the tensile strength of UHPC in structural applications increases, it is imperative that the effect of curing methods on that tensile strength be well-understood. To that end, the present research investigated the tensile behavior of UHPC cured under simulated field conditions.

The present research also evaluated the behavior of high-strength concrete mixes that would typically not be considered UHPC; concrete with a compressive strength under 17,000 psi is not considered UHPC by most specifications [59,223,233,234]. Concrete mixtures with compressive strengths from 12-ksi to 18-ksi were designed and tested to evaluate their strain-hardening

behavior relative to that of UHPC mixtures. This may encourage specifications to allow for reliance on fiber-reinforced concrete tensile strength even if the concrete is not classified as UHPC.

4.2. Materials and Methods

The materials used for this research included a fine masonry sand, as well as multiple different cementitious materials and a filler material to improve particle packing. The particle size distribution of the fine materials was measured using laser particle size analysis and is shown in Figure 45. The particle size analysis of the sand is also shown in this figure, but it was measured using sieve analysis performed according to ASTM C136 [235]. Material oxide composition on the cementitious materials was determined using X-ray fluorescence and are shown in Table 7. The two portland cements used were also analyzed with X-Ray diffraction and Rietveld refinement to find their phase compositions. A voltage of 45kV was used with a current of 40mA. The scan was performed from 8° to 80° 2Θ with a step size of 0.016° 2Θ. Table 8 shows the XRD results.

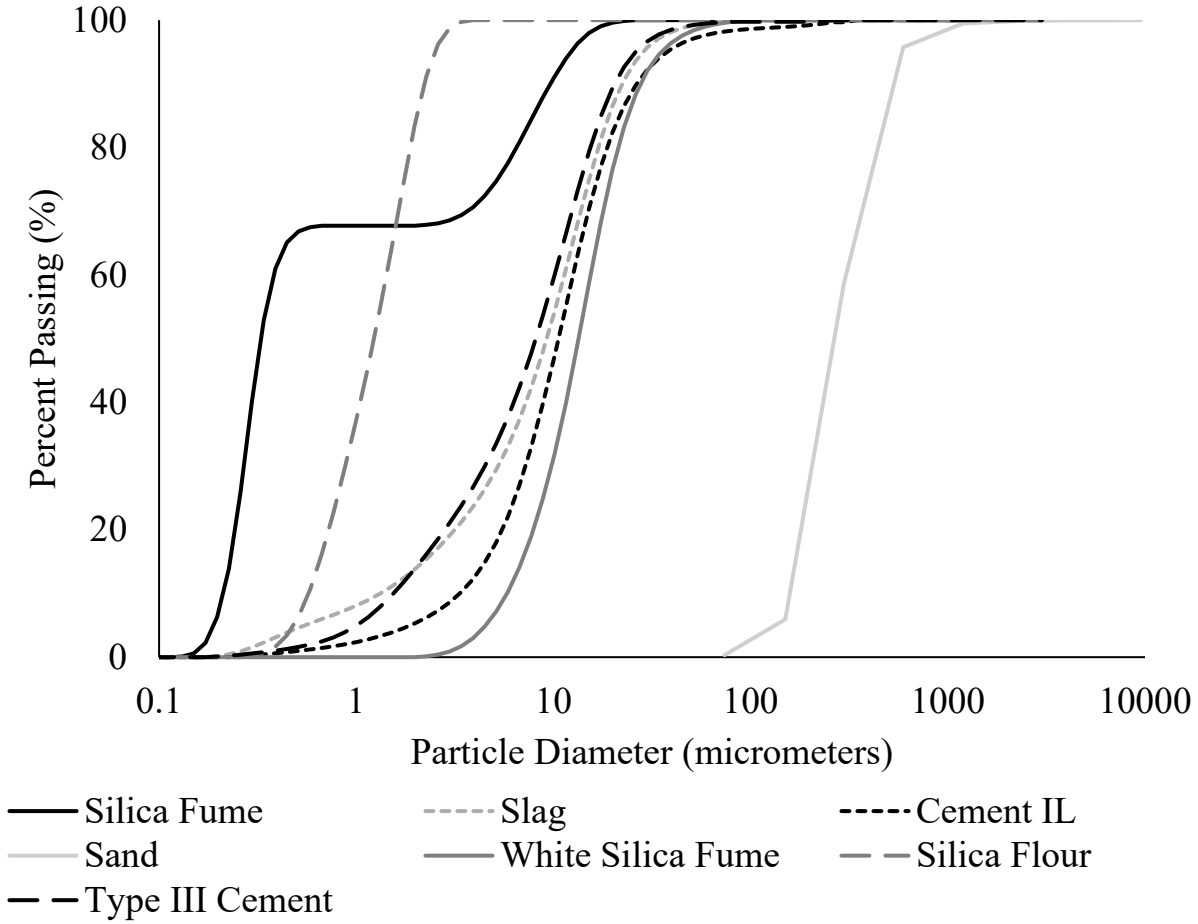

Figure 45: Particle size distribution of materials

Table 7: XRF results for materials, percent

Parameter	Type IL Cement	Type III Cement	Slag	Silica Fume	White Silica Fume	Silica Flour
SiO_2	18.82	20.00	34.79	80.45	96.49	98.88
TiO_2	0.22	0.22	0.64	0.02	0.02	0.01
Al_2O_3	4.79	4.90	13.17	0.48	1.37	0.17
Fe_2O_3	3.10	3.30	0.78	4.78	0.16	0.01
MnO	0.06	0.13	0.32	0.44	0.00	0.01
MgO	0.80	1.00	4.66	10.43	0.01	0.01
CaO	62.85	63.30	43.71	0.95	0.00	0.01
Na_2O	0.08	0.12	0.19	0.18	0.07	0.01
K_2O	0.25	0.38	0.41	0.77	0.02	0.02
P_2O_5	0.41	0.49	0.04	0.03	0.23	0.01
SO_3	3.02	3.70	3.00	0.07	0.00	0.01
ZnO_2	0.00	0.05	0.00	0.00	0.43	0.00
LOI	5.45	2.44	0.02	2.93	0.66	0.27

Table 8: XRD results for materials, percent

Phase	Type IL Cement	Type III Cement
Alite	44.3	53.0
Belite	23.2	16.4
Aluminate	4.2	4.1
Ferrite	11.2	13.8
Bassanite	0.5	5.2
Gypsum	5.1	1.1
Calcite	11.7	2.3
Anhydrite		1.6
Arcanite		0.5
Syngenite		0.9
Thenardite		0.5
Quartz		0.6

Four different non-proprietary mix designs were developed in order to have mixes with varying compressive strengths. Samples from each of the four mix designs underwent one of three different curing methods in order to investigate how this would impact the compressive and tensile strength. The temperature vs. time of the three curing methods is shown in Figure 46. The first curing method was called fog curing, with specimens being cured between 68 °F and 78 °F (20°C and 26°C) in the molds during the first day and 73.5°F ± 3.5°F (23.0°C ± 2.0°C) and >95% relative humidity as specified in ASTM C31 [236] from demolding at day 1 until testing at day 28. The second curing method was called steam curing, where samples cured in their molds at room temperature for one day were then demolded and placed above a water bath in a sealed container in an oven at 194°F (90°C) for 48 hours. After removal from the oven, the samples

finished curing in the moist room until 28 days of age. The final method was named precast curing as it was designed to represent the temperatures that would occur in a concrete member made at a precast concrete facility. For precast-cured members, samples were initially cured in their molds at room temperature for 4 hours and then placed in an oven in their molds with lids on at 158°F (70°C) until they had reached 22 hours since water addition. They were then removed from the oven and allowed to cool. At 24 hr they were demolded and placed in the moist room until they were 28 days old.

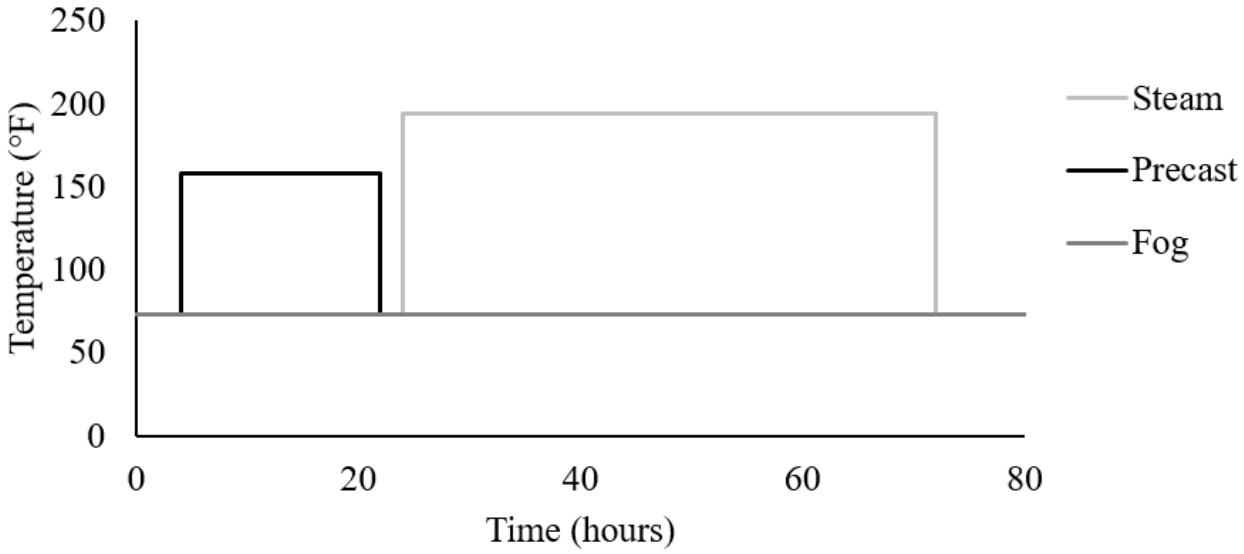

Figure 46: Curing temperatures for first three days

The target compressive strengths ranged from 12-ksi to 21-ksi in order to include mixes across the spectrum of high-strength concrete to UHPC. The mix designs used were named for their target strength, but the actual strengths of the samples varied due to the different curing methods used.

Table 9 shows the mix designs for the 3 lower-strength mixes. They were designed to use standard materials commonly available in the local market. Table 10 shows the mix design for the mix targeting compressive strength over 21 ksi. Achieving the higher strengths required better particle packing employing materials not typically used in precast plants, such as silica flour and white silica fume. The water contents of the admixtures were determined by drying them in an oven for 24 hours, and the weight of water lost was added to the mix water amounts in

Table 9 and Table 10 to get the total water amount. For example, the mix shown in Table 10 had 288 lb/yd^3 of water. Of this 288 lb/yd^3, 72 lb/yd^3 came from the admixtures.

Table 9: Mix proportions for lower strength mixes

Material	12-15 ksi lb/yd^3	15-18 ksi lb/yd^3	18-21 ksi lb/yd^3
Fine Masonry Sand	1856	1815	1588
IL Cement	1583	1404	1597
Slag	-	272	309
Silica Fume	83	136	155
Water	417	362	335
HRWR admixture	10.9	16.4	30.9
HRWR and workability-retaining admixture	10.9	16.4	30.9
Surface-enhancing admixture	2.1	3.4	5.2
Fines-to-Sand Ratio	0.90	1.00	1.30
Total Cementitious Material	1666	1812	2061
w/cm	0.250	0.200	0.163

Table 10: Mix proportions for the UHPC >21-ksi mix design

Material	21+ ksi lb/yd^3
Sand	1361
Cement, Type III	1477
Silica Flour	369
White Silica Fume	369
Water*	288
HRWR admixture	46.1
HRWR and workability-retaining admixture	40.4
Corrosion inhibitor admixture	23.1
Fines-to-Sand Ratio	1.63
Total Cementitious Material	1846
Admixture Water	72.4
w/cm	0.156

*After re-adjusting water amount to account for liquid admixtures, 75% of the water by volume was added as ice

**Does not include silica flour content

The concrete mixes were made in a high-shear mixer using 0.81 ft^3 batches. Eighteen tension samples from each mix design were made to have six samples for each curing method. Three compression samples for each curing method were also made from 3-in. × 6-in. plastic cylinder molds. The tension samples were 2-in. × 2-in. × 17-in. prisms cast horizontally in steel molds.

The test method used was the direct tension test developed by the FHWA for UHPC [9]. This method used the rectangular-prism UHPC specimens and tapered aluminum plates with the

dimensions shown in Figure 47. The tapered aluminum plates helped to reduce localized crushing of the concrete at the location of the grips and encourage cracking to occur in the center of the specimen. An extensometer with one LVDT on each side of the sample was attached to the top and bottom of the central 4 inches to measure expansion. The testing procedure began with a compression phase that applied a 4000-lb load to the specimen, producing a stress of approximately 1000 psi. This was followed by the tension phase, where the stress was applied using a crosshead displacement rate of 0.0001 in./s (0.00254 mm/s). One modification made to the original procedure was the addition of C-clamps placed on the tapered portions of the aluminum plates to help prevent cracking between the plates. Figure 48 shows this set-up.

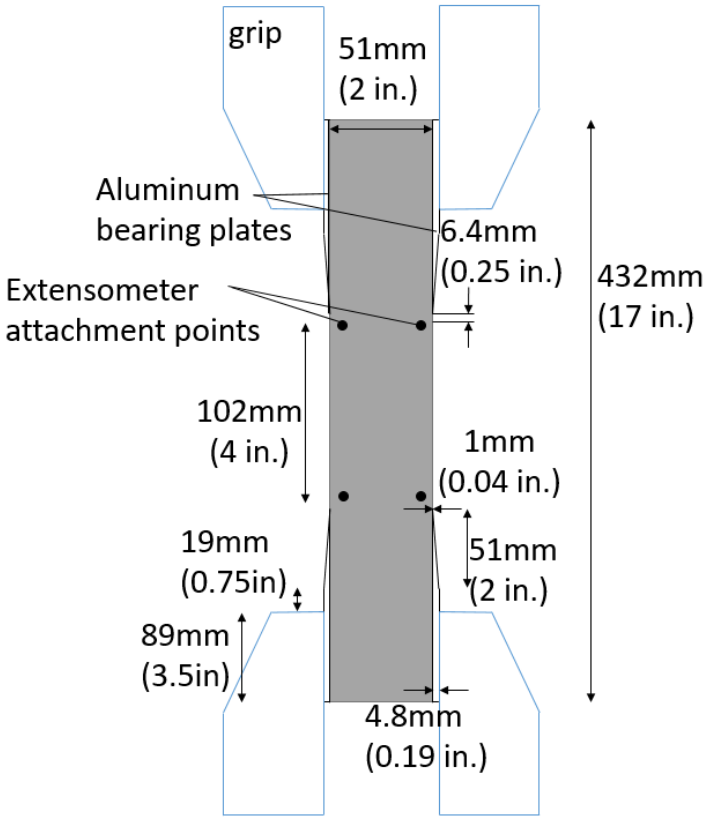

Figure 47: Schematic of tensile specimen with plates in grips

Figure 48: Image of tensile testing setup including c-clamps

After testing, the specimens' cross-sectional dimensions were measured above and below the largest localized crack to find the cross-sectional area of the member. The load vs. expansion data were converted to stress vs. strain data by dividing load by the measured cross-sectional area and dividing the elongation by the gauge length of 4 inches. If the largest localized crack formed outside of the 4 in. span measured by the extensometer, the stress vs. strain data for that specimen was not plotted, but the maximum stress value was used to find the average of the sample group. If fewer than three of the six specimens tested for a mix had valid failures (failures inside of the extensometer region), the mix was re-done with more specimens. After graphing the stress vs. strain data for all successful runs up to a strain of 0.015, an average of the successful runs was calculated and graphed as well. Figure B-1 through B-12 in the Appendix B show the graphs for all successful specimens. In addition to plotting the stress vs. strain data, specific values were also taken from each test run. These included modulus of elasticity, calculated as the

slope of the stress vs. strain data from a stress of -500 psi to a stress of 500 psi. The maximum stress was also noted, as well as the effective cracking stress, defined as the stress at which the 0.02% offset line intersects the specimen's stress vs. strain curve, as described in the AASHTO direct tension test. In addition, the toughness of each specimen was calculated as the area under the curve from a strain of 0 until 0.005 strain. The stress at 0.005 strain was also recorded, to provide an idea of the specimens' strength after cracking. A strain of 0.005 was chosen as it is the strain at which a reinforced concrete member is considered to be tension-controlled. Figure 49 shows these values on a direct tension stress vs. strain graph.

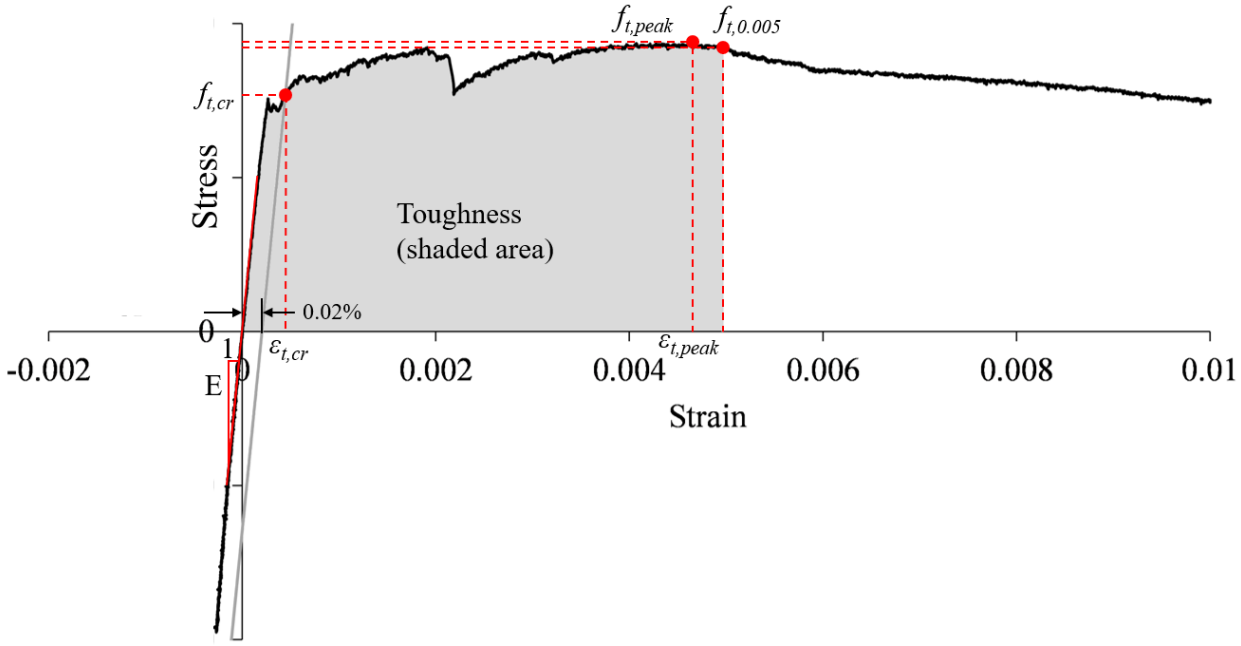

Figure 49: Quantitative values calculated from each tensile test

In addition to noting quantitative data from each test, specimens were also given a qualitative categorization to describe their tensile behavior. This classification was done for each specimen in accordance with the balloted AASHTO method for Uniaxial Tensile Response of Ultra-High-Performance Concrete. The values $f_{t,cr}$, $\epsilon_{t,cr}$, $f_{t,peak}$, and $\epsilon_{t,peak}$ as shown in Figure 49 were used to determine the sample classification. Tensile response classification involved some subjective determinations, as well as some insights into potential drawbacks of the classifications. The first classification is type H-1. This classification indicates that a test specimen had a maximum tensile stress, $f_{t,peak}$, that was at least 20% greater than its cracking stress, $f_{t,cr}$. In addition, the peak stress must have occurred at a higher strain than the cracking stress, or $\epsilon_{t,peak} > \epsilon_{t,cr}$. The second classification, H-2, has the same requirements as for an H-1 classification except that the peak stress exceeds the cracking stress by less than 20%. For both H-1 and H-2 classifications, the test specimen's crack localization must occur inside the central 4 in. measured by the extensometer. If the cracking occurred outside the central span, the specimen is classified as H-3. The H-4 classification indicates that the testing apparatus imparted an eccentricity to the specimen. The occurrence of eccentricity that is great enough to affect the test results is typically revealed by an early change in elastic modulus as the specimen is in tension, or by a large difference between the 4 LVDTs on the extensometer, each of which measures elongation on a

different face of the specimen. It was found that determining whether or not a specimen should be classified as H-4 was the most subjective step in the process. The AASHTO draft specification currently in the ballot process states that for an H-4 classification, the testing apparatus imparts “non-negligible bending during the initial loading of the test specimen.” Determining what constituted non-negligible bending required judgment. Figure 50 through Figure 53 show examples of stress vs. strain results for specimens classified as H-1, H-2, H-3, and H-4, respectively.

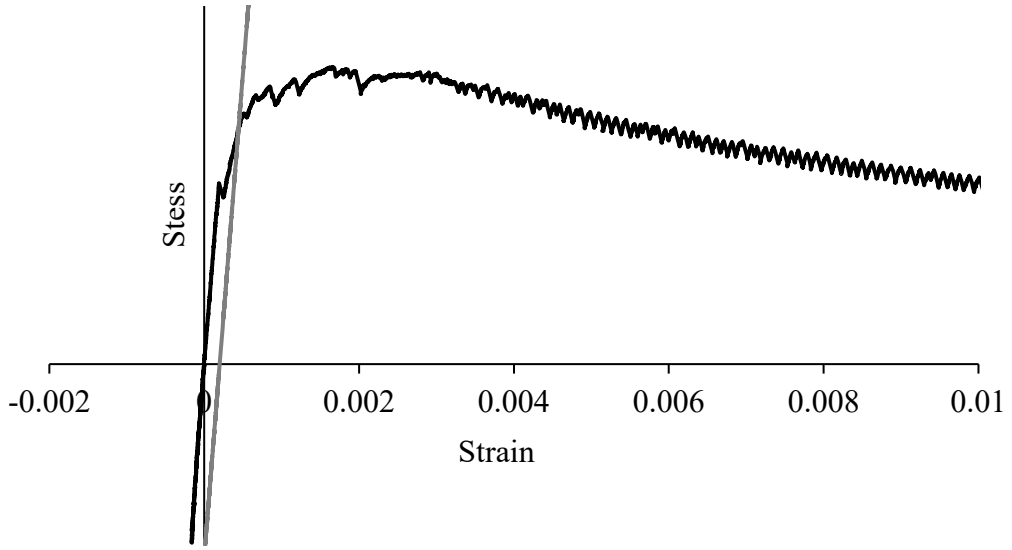

Figure 50: Example of a type H-1 result

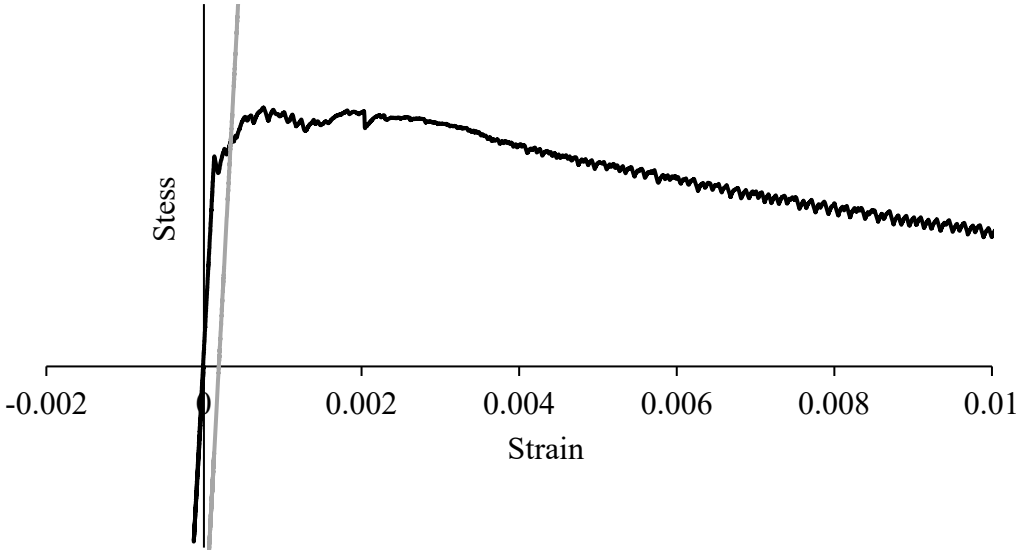

Figure 51: Example of a type H-2 result

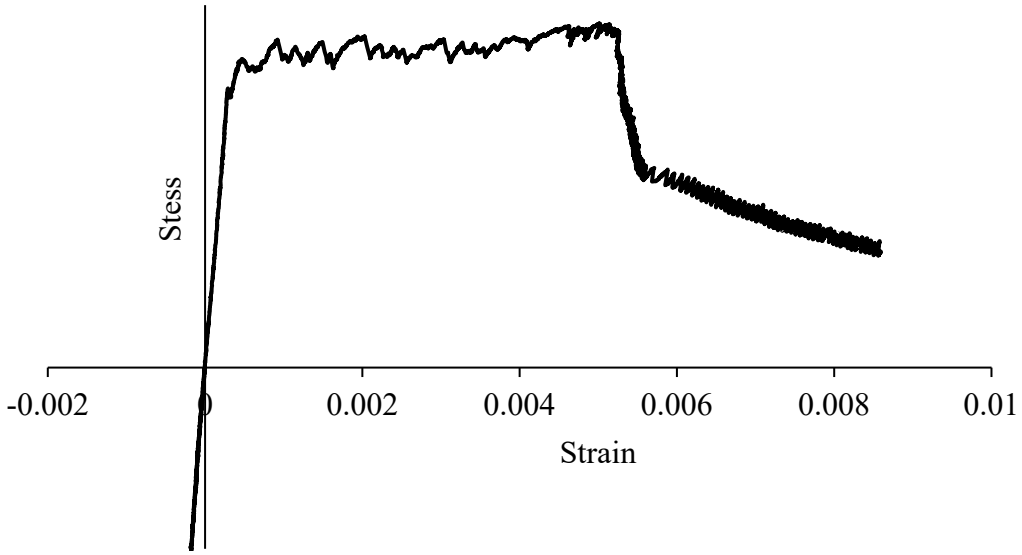

Figure 52: Example of a type H-3 result

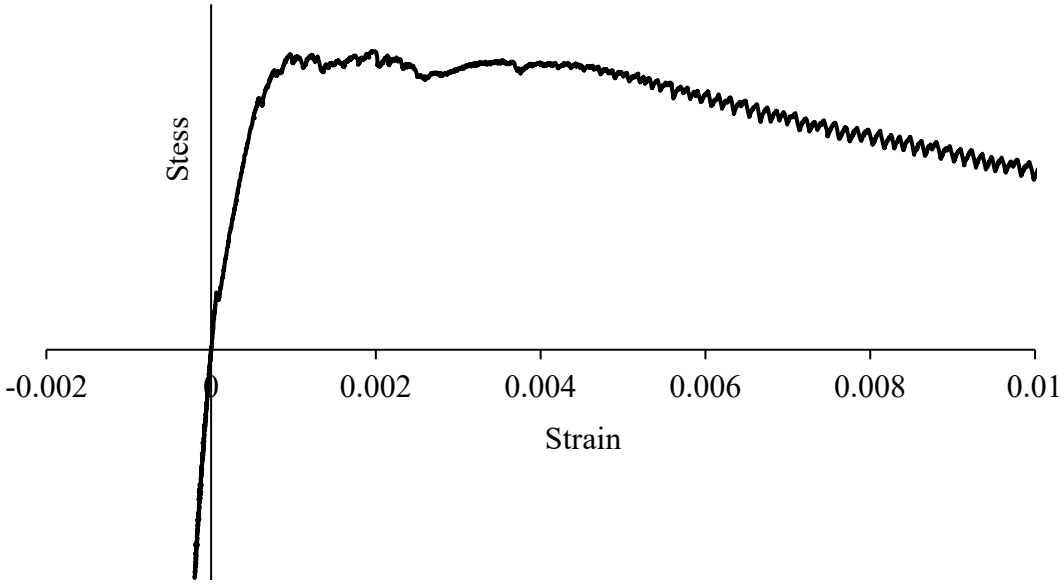

Figure 53: Example of a type H-4 result

In addition to the four H categories describing tensile behavior, there is also a Type-S designation defined by AASHTO. This is a strain-softening response, where the load prior to cracking exceeds the specimen's load after cracking. Figure 54 shows an example of a type S result. It was found that many specimens in this research were considered type-S because they did not meet the H-1 and H-2 requirement that $\epsilon_{t,peak} > \epsilon_{t,cr}$. Even if specimens could maintain or increase in strength after $\epsilon_{t,cr}$, a higher strength occurring before $\epsilon_{t,cr}$ meant that a specimen could not be classified as H-1 or H-2. Figure 55 shows an example of this scenario. For this specimen, the maximum stress of 1,212 psi occurred at a lower strain than did the effective cracking stress

of 995 psi. Even though the specimen achieved a stress of 1,162 psi after cracking, it could not be classified as H-2. The final classification is type N, which describes a test where minimal, if any, post-cracking strength is shown. None of the specimens tested for this research were classified as type N.

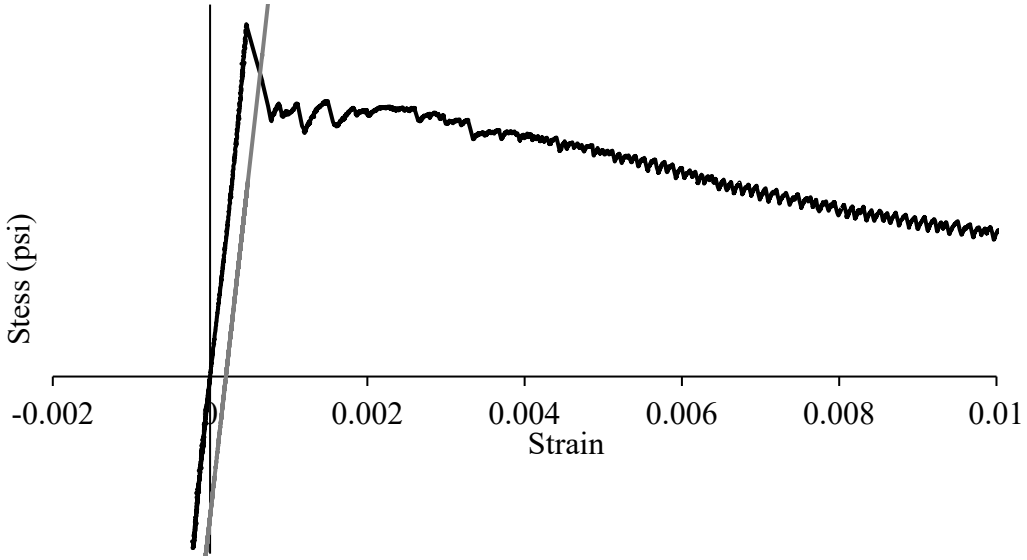

Figure 54: Example of a type S result

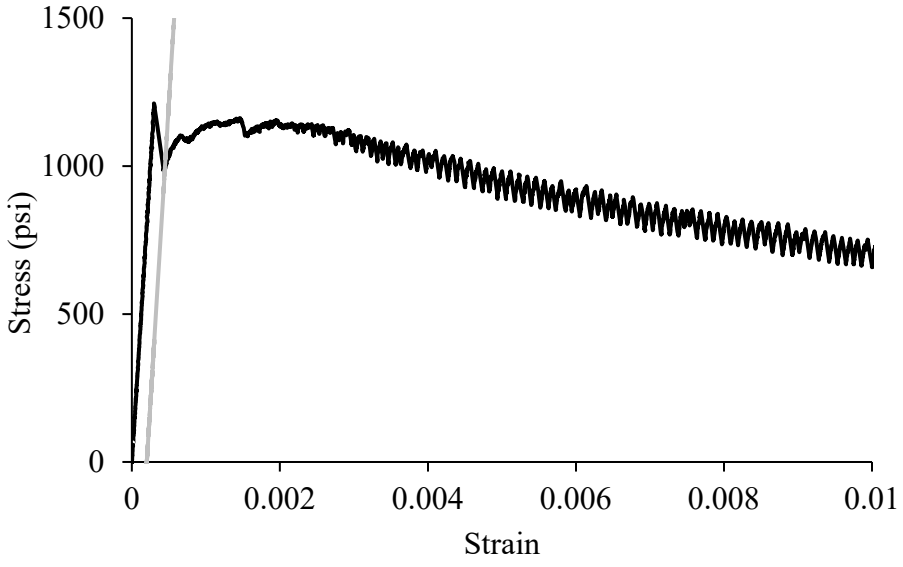

Figure 55: Response classified as S due to high strength before effective cracking stress

For each category of combined mix design and curing method, an average of the quantitative values was taken. However, not all values from all tests were included in the average. For specimens with a tensile response classified as H-3, no values relying on post-cracking strain value were used. Therefore, only peak stress and modulus were used from H-3 specimens. For specimens with an H-4 classification, elastic modulus was not used because the eccentricities could cause premature cracking, reducing the calculated elastic modulus. The standard

deviations of the averaged values were also calculated and are presented in the Appendix. The average values were used to plot against various mix design parameters. Included in these were the 28-day compressive strength values of cylinders made in the same batch and cured in the same way. Cylinders from mixes expected to have compressive strengths above 17,000 psi were tested at a load rate of 145 ± 7 psi/s (1.0 ± 0.05 MPa/s) according to ASTM C1856 [59], while cylinders expected to have a compressive strength below 17,000 psi were tested at a load rate of 35 ± 7 psi/s (0.25 ± 0.05 MPa/s) according to ASTM C39 [87]. All cylinders were cast with dimensions of 3 in. by 6 in. and were later ground on the ends before testing to ensure the surfaces were plane. The data were also plotted against the mixes' water-cementitious materials ratio (w/cm) and the fines-to-sand ratio in the mix. Fine filler materials such as the silica flour used in the 21+-ksi mix were classified as "fines" along with the cementitious material but not as cementitious material in the w/cm ratio. While the sand used did have some material passing through a No. 200 sieve that may be considered "fines", due to the very small amount, none of the sand weight was classified as fines in the calculations.

In addition to plotting the quantitative tensile testing values against the mix parameters, the values were also compared against each other using two-sample t-tests. These tests helped to compare each of the 12 mix combinations to every other combination to see if there were statistical differences. This was especially useful to determine if differences due to curing method were statistically significant.

4.3. Results

The compressive strength values for each sample set are shown in

Table 11 Not all of the fog-cured mixes met the target compressive strength for the mix, but all of the steam-cured mixes did fall into the target range. The precast and steam curing methods did significantly affect the compressive strength of the mixes, as expected. The benefit of steam curing was more pronounced for mixes with a higher compressive strength, which also had a lower w/cm than the lower strength mixes. This is not surprising, as the weaker mixes would not be considered UHPC in most cases, and the 28-day strength of normal concrete is adversely affected by high temperatures early in curing. This effect is known as the crossover effect because while early age strengths are improved due to heat treatment, later age strengths are reduced, resulting in a strength vs. time curve that intersects the curve of an un-heated specimen's curve [237]. In all cases, the steam-cured concrete met the target strength, and for most mixes, either the precast or fog-cured concrete did as well. Overall, the compressive strengths provided a very good range over which to compare, with the lowest compressive strength average at 12,400 psi and the highest at 24,100 psi. The mixes were often referred to by the lower bound of their target strength; for example, the mix designed for a 15- to 18-ksi compressive strength would be referred to as the 15+-ksi mix.

Table 11: Average Compressive Strengths for each Mix

Mix Target (ksi)	Curing	Strength (psi)	Std. Dev. (psi)	COV
12-15	Steam	14,057	1,197	8.52%
12-15	Precast	12,389	505	4.08%
12-15	Fog	17,062	676	3.96%
15-18	Steam	16,553	1,242	7.50%
15-18	Precast	13,205	1,090	8.25%
15-18	Fog	16,475	3,047	18.49%
18-21	Steam	18,949	765	4.04%
18-21	Precast	14,346	236	1.64%
18-21	Fog	18,852	796	4.22%
21+	Steam	24,094	1,155	4.79%
21+	Precast	19,525	642	3.29%
21+	Fog	17,267	1,866	10.81%

The first step in data analysis was to plot the data and classify the tensile response. Table 12 shows the number of specimens for each category that was designated to each tensile response classification. Most mix design and curing method categories had a wide range of tensile responses, making it difficult to classify the overall behavior of the sample group using this method. However, the classifications were useful in determining which of the quantitative values from each specimen to include in the averages.

Table 12: Tensile response classifications

Mix Design	Curing	H-1	H-2	H-3	H-4	S
12+	Fog	1	2	2	0	1
12+	Precast	3	1	1	1	0
12+	Steam	2	2	0	2	0
15+	Fog	0	0	0	4	2
15+	Precast	0	1	1	0	3
15+	Steam	1	1	1	1	2
18+	Fog	0	1	1	1	3
18+	Precast	1	4	0	0	1
18+	Steam	1	2	1	0	2
21+	Fog	0	3	2	1	0
21+	Precast	1	3	2	0	0
21+	Steam	1	4	0	0	1

The modulus of elasticity, as determined with the best-fit line from -500 psi to 500 psi, was found to be in the range of 3,000,000 to 7,000,000 psi for most specimens. The modulus varied significantly within each mix design and curing method combination, with coefficients of variation above 25% for half of the groupings. It is likely that slight variations in specimen alignment during testing affected the modulus results, even if they were not large enough to cause premature cracking. For this reason, it is suggested that the modulus of elasticity value taken from direct tensile testing not be used in place of the ASTM C469 method [238]. Figure 56 through Figure 58 show the relationship between the elastic modulus and the three mix design indicators (compressive strength, w/cm, and fines/sand), and very low R^2 values can be seen, indicating no correlation.

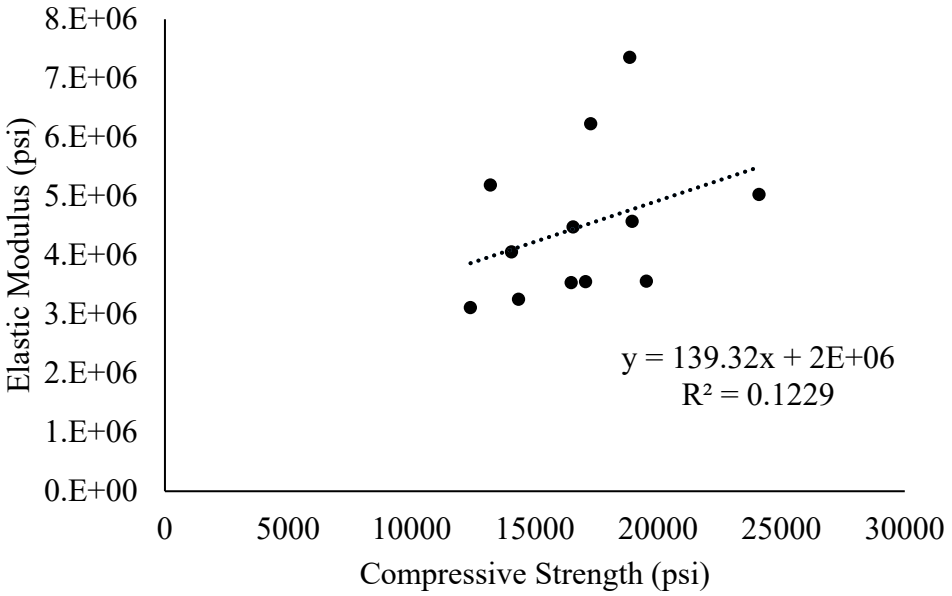

Figure 56: Elastic modulus vs. concrete compressive strength

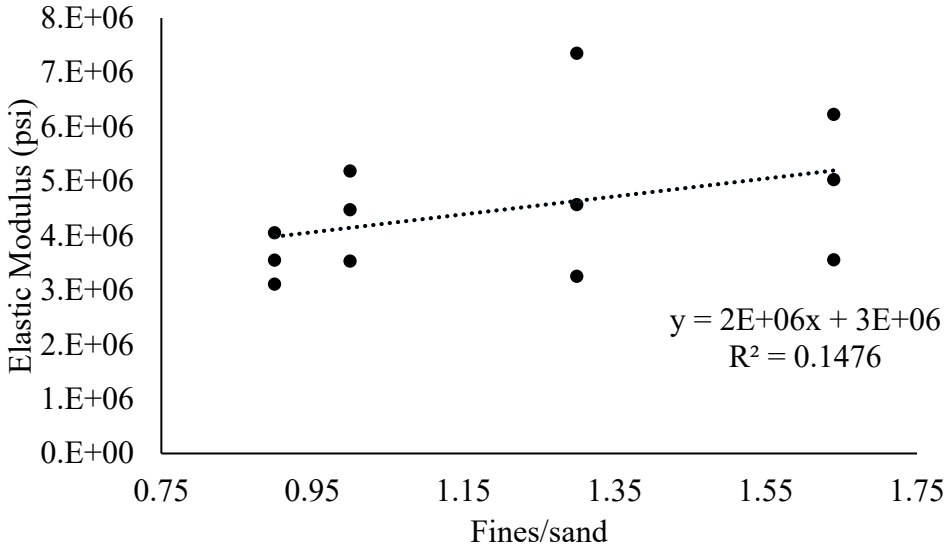

Figure 57: Elastic modulus vs. fines/sand ratio

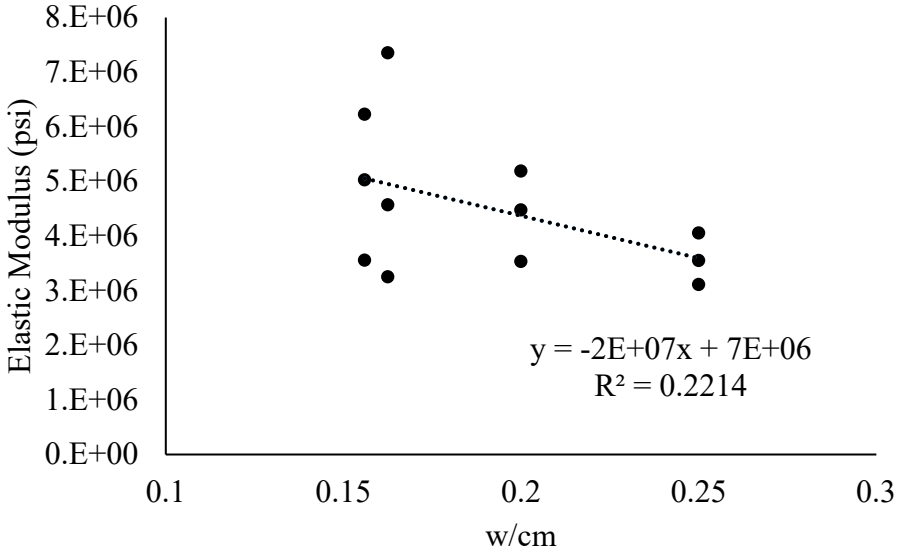

Figure 58: Elastic modulus vs. w/cm

The effective cracking stress, determined by finding the intersection of the specimen's stress vs. strain graph with a 0.02% offset line, was determined for all specimens except the H-3 specimens, as cracking outside of the extensometer region could cause the 0.02% offset line to intersect a point in the stress vs. strain data that was too late into the specimen's post-cracking behavior. Tests that were classified as H-4 did tend to have lower effective cracking stresses than other specimens. There are two factors contributing to this. The first is that the H-4 specimens were eccentrically loaded, which resulted in uneven stress distribution across the cross-section of the test specimen and likely a lower actual cracking stress. The second factor is a result of how the effective cracking stress is calculated. The H-4 specimens had an early decrease in elastic

modulus, which caused the 0.02% offset line (drawn parallel to the portion of the curve that typically occurred before this modulus decrease) to intersect the stress vs. strain data at a lower stress value compared to the maximum stress. Figure 59 through Figure 61 shows the relationship between effective cracking stress and the three mix parameters for each specimen type. Effective cracking stress had better correlation to the various mix design parameters than did elastic modulus. The ratio of fines to sand had the best correlation, with an R^2 value of 0.75.

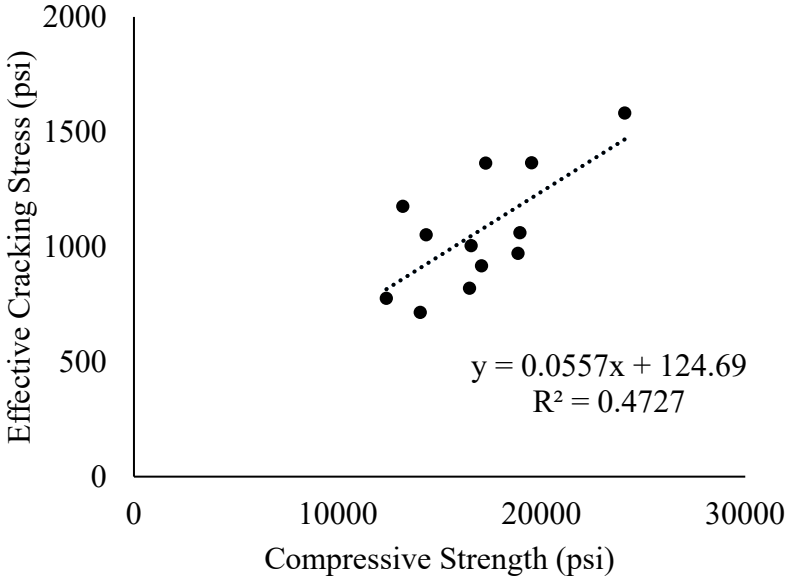

Figure 59: Effective cracking stress vs. compressive strength

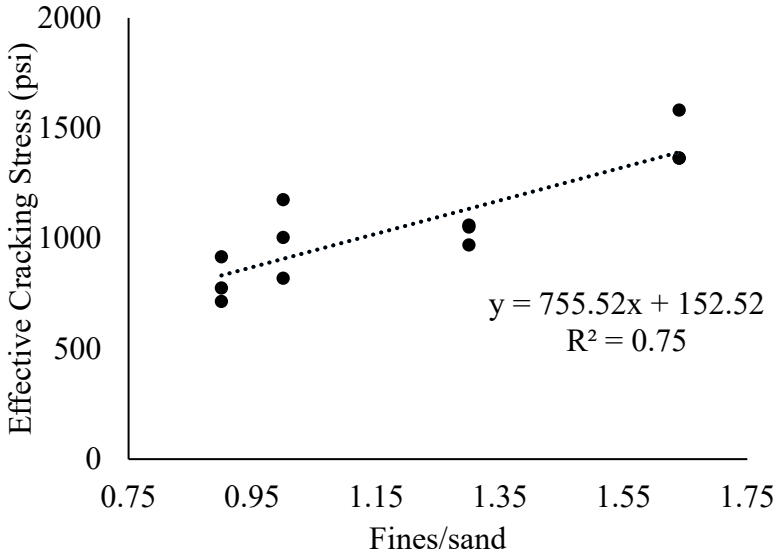

Figure 60: Effective cracking stress vs. fines/sand ratio

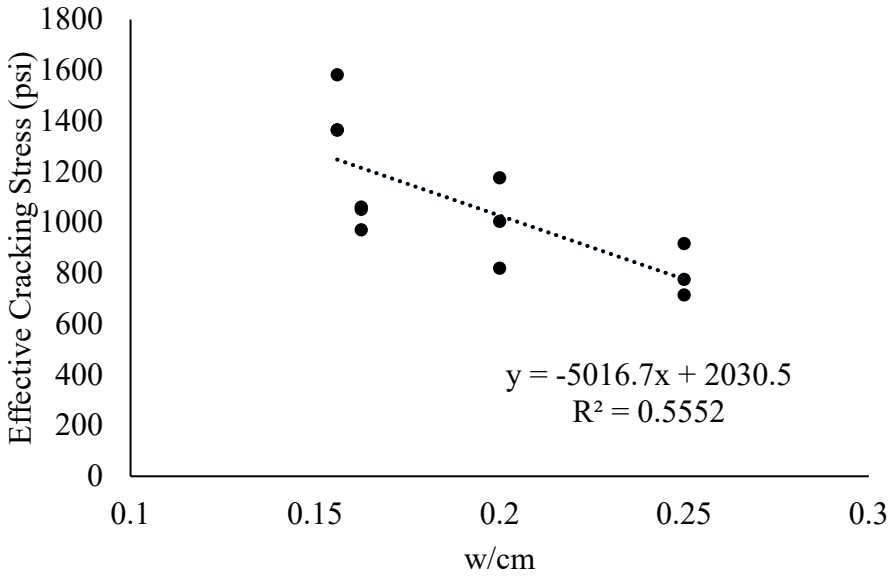

Figure 61: Effective cracking stress vs. w/cm

Comparisons between the specimens' peak stresses and mix properties showed results very similar to those from the effective cracking stress. For some specimens, the peak stress occurred at the initial rupture of the concrete before the fibers were fully engaged in tension. For other specimens, the peak stress occurred after cracking as the pull-out resistance of the fibers increased the specimen's tensile strength. The R^2 values for peak stress are all slightly higher than those for effective cracking stress, with the fines/sand ratio once again having the best correlation. Figure 62 through Figure 64 shows these relationships. Notably, each of the three 21+ sample groups had significantly different peak stress when compared with each of the other 9 groups.

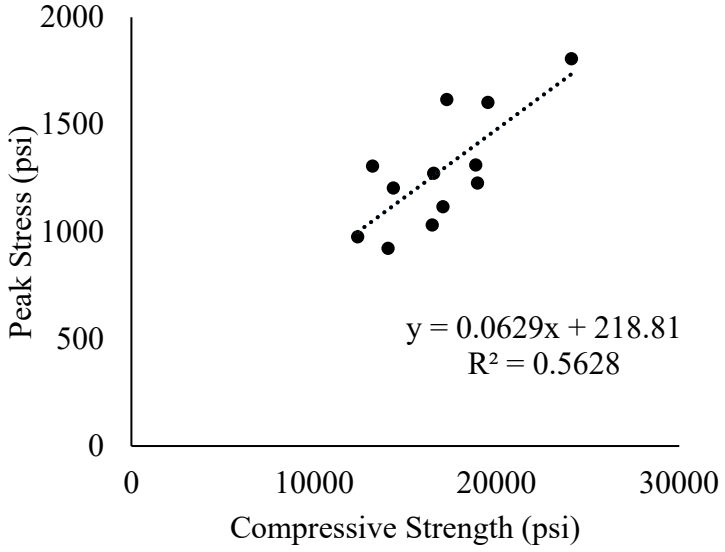

Figure 62: Peak stress vs. compressive strength

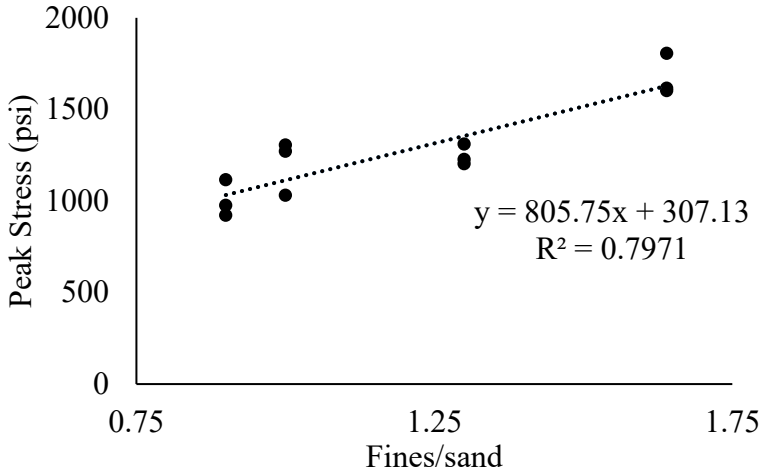

Figure 63: Peak stress vs. fines/sand ratio

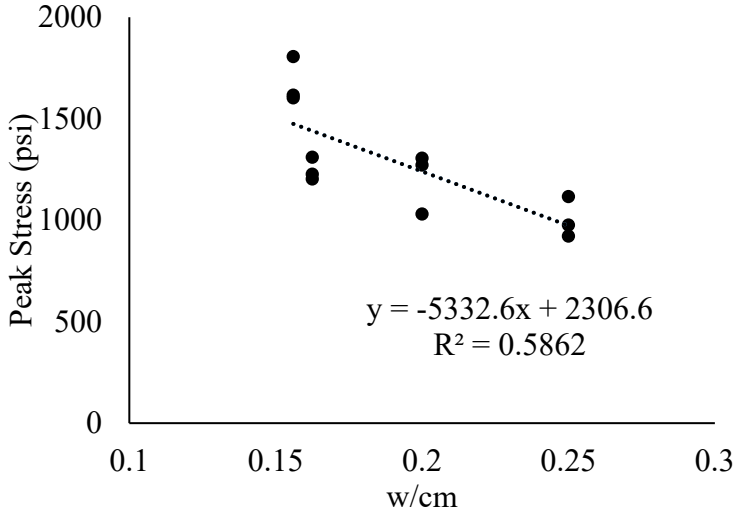

Figure 64: Peak stress vs. w/cm

The toughness calculated as area under the curve from a strain of 0 until 0.005 showed some of the highest regressions to the mix characteristics. Figure 65 through Figure 67 show the plots of tensile toughness vs. the three mix parameters.

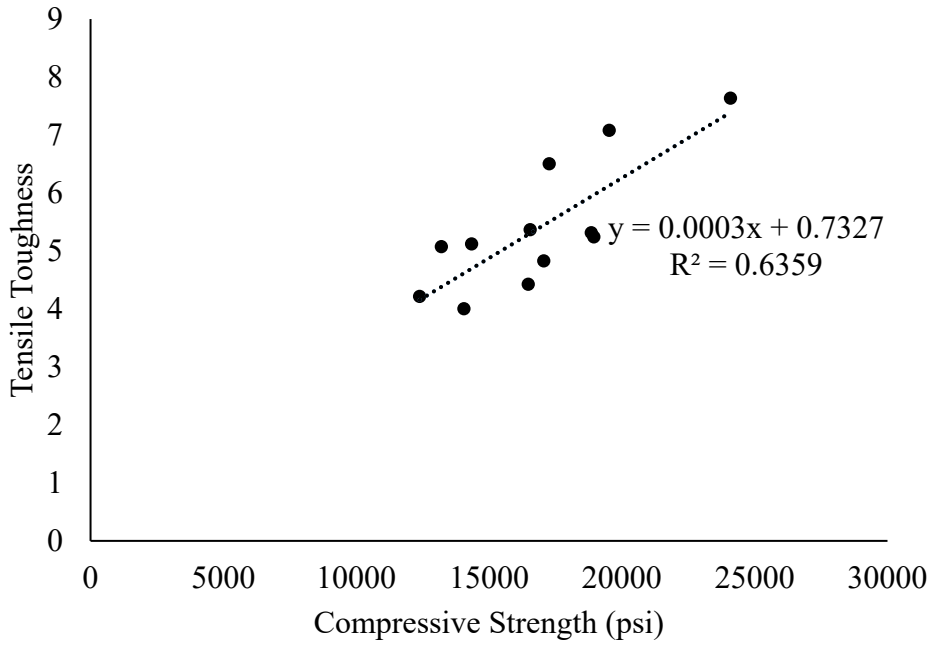

Figure 65: Toughness vs. compressive strength

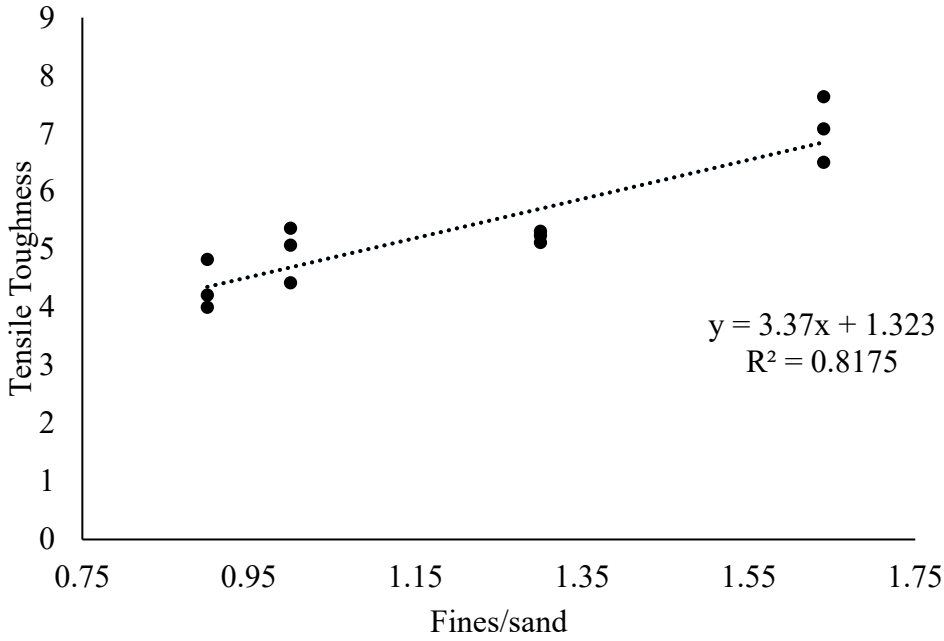

Figure 66: Toughness vs. fines/sand ratio

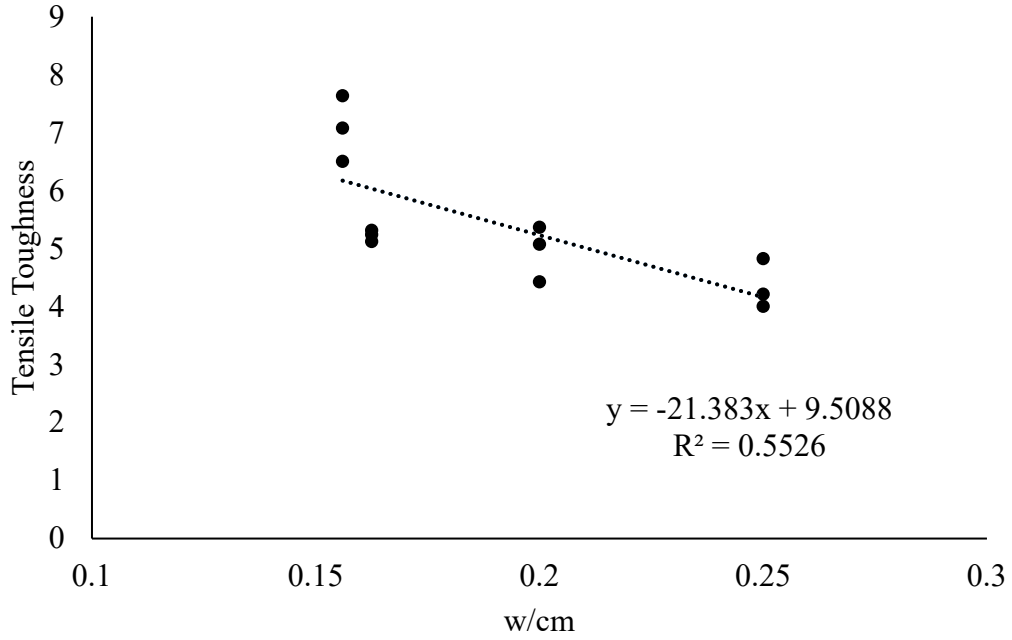

Figure 67: Toughness vs. w/cm

The post-cracking stress of each specimen was measured at a strain of 0.005. This strain value was selected as it is the tensile strain at which a reinforced concrete specimen transitions from being compression controlled [218]. Therefore, it is reasonable to assume that most reinforced concrete members will be designed to undergo a strain of at least 0.005 in some portion of the member. The results shown in Figure 68 through Figure 70 once again indicate that the best correlation was with the fines/sand ratio.

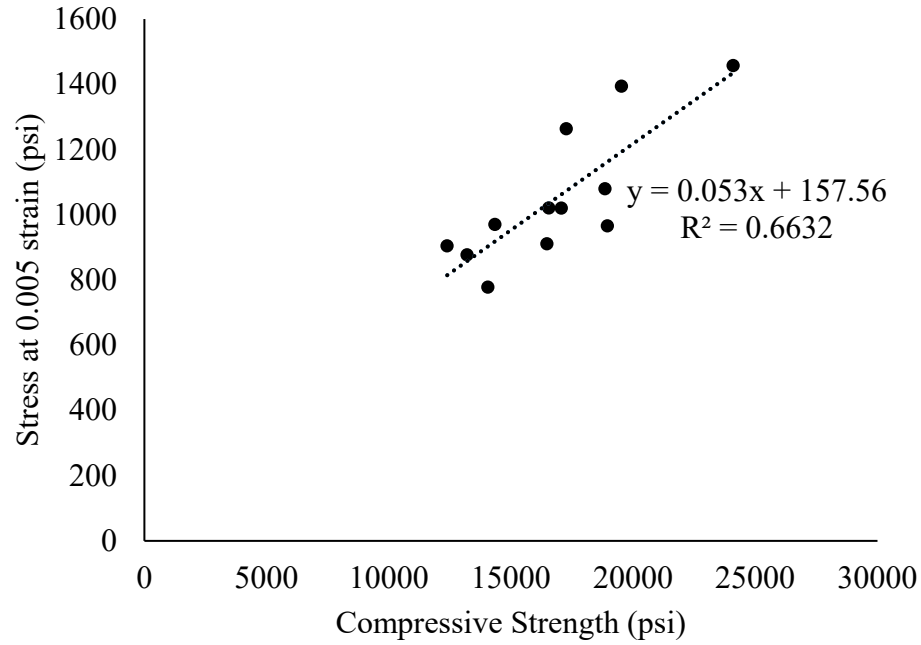

Figure 68: Post-cracking tensile strength vs. compressive strength

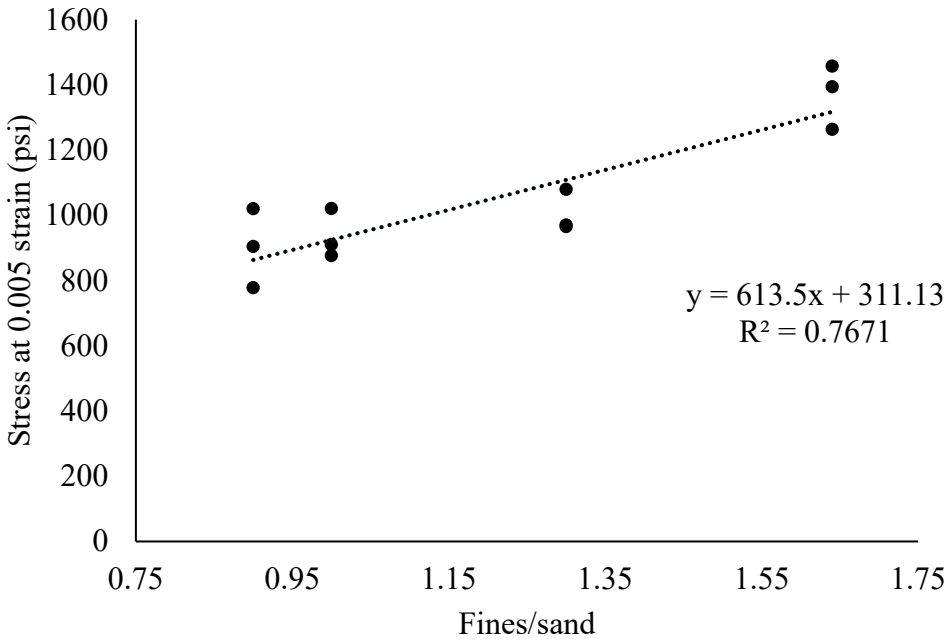

Figure 69: Post-cracking tensile strength vs. fines/sand ratio

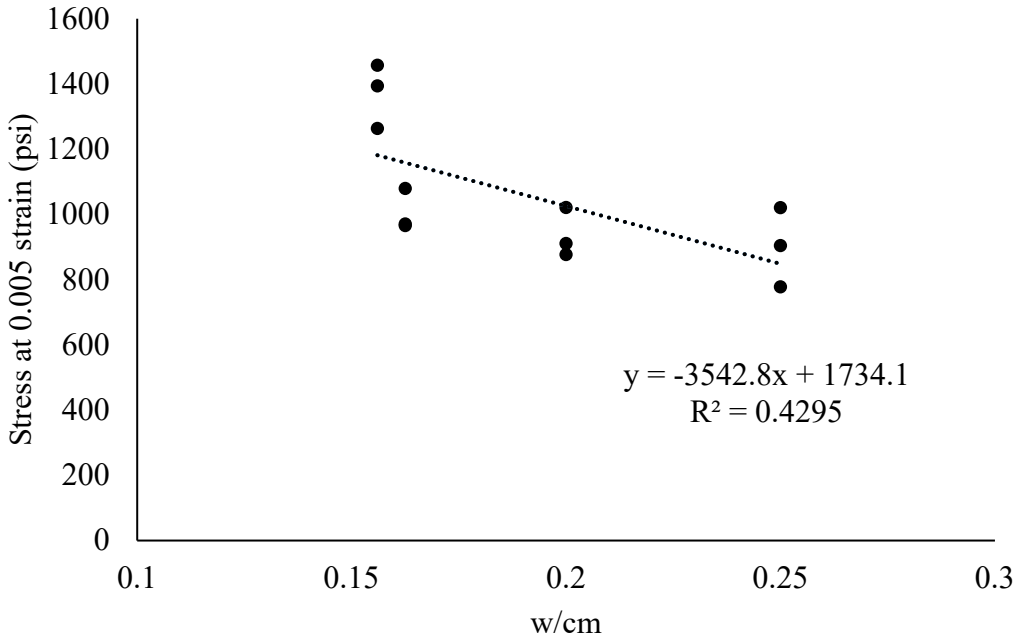

Figure 70: Post-cracking tensile strength vs. w/cm

Table 13 through Table 17 show P-values calculated from 2-factor t-tests comparing results of each sample group to each other group. The tables compare results from compression tests, effective cracking stress, peak stress, tensile toughness, and strength at a strain of 0.005. P-values less than 0.05 are highlighted to show a statistical significance between the two groups using a 95% confidence interval. Some P-values may be listed as 0.000, indicating that the P-value was less than 0.0005 and was therefore rounded down. The diagonal lines from top left to bottom right shows all 1.000 values, as these are the comparisons with any given mix and itself. In the 3 cell by 3 cell boxes following the same diagonal, comparisons within the same mix design but with different curing methods can be made. Most values in these "same mix design boxes" for Table 17 shows statistically non-significant p-values, showing that curing method did not have a large effect on the tensile properties of the concrete. In contrast, Table 13 shows 7 of the 12 comparisons between different curing methods and the same mix design are statistically significant, showing that compressive strength is often influenced by curing method.

Table 13: P-values of two-factor t-tests comparing compressive strength of sample groups

	12			15			18			21		
Mix type	Fog	Pre.	Steam	Fog	Pre.	Steam	Fog	Pre.	Steam	Fog	Pre.	Steam
12 fog	1.000	0.002	0.032	0.775	0.014	0.577	0.059	0.022	0.049	0.875	0.020	0.003
12 precast		1.000	0.156	0.149	0.361	0.033	0.001	0.026	0.001	0.049	0.001	0.004
12 steam			1.000	0.329	0.429	0.087	0.010	0.722	0.009	0.087	0.006	0.002
15 fog				1.000	0.222	0.971	0.321	0.351	0.306	0.727	0.232	0.056
15 precast					1.000	0.039	0.005	0.218	0.005	0.047	0.003	0.001
15 steam						1.000	0.074	0.094	0.065	0.620	0.067	0.005
18 fog							1.000	0.011	0.889	0.309	0.337	0.007
18 precast								1.000	0.010	0.115	0.006	0.005
18 steam									1.000	0.285	0.392	0.008
21 fog										1.000	0.186	0.013
21 precast											1.000	0.009
21 steam												1.000

Table 14: P-values of two-factor t-tests comparing effective cracking stress of specimens

	12			15			18			21		
Mix type	Fog	Pre	Steam	Fog	Pre	Steam	Fog	Pre	Steam	Fog	Pre	Steam
12 fog	1.000	0.250	0.143	0.411	0.075	0.513	0.694	0.274	0.326	0.017	0.015	0.001
12 precast		1.000	0.217	0.348	0.011	0.058	0.105	0.000	0.045	0.013	0.006	0.000
12 steam			1.000	0.071	0.004	0.024	0.046	0.000	0.019	0.003	0.002	0.000
15 fog				1.000	0.009	0.096	0.178	0.001	0.064	0.005	0.003	0.000
15 precast					1.000	0.155	0.113	0.164	0.356	0.104	0.120	0.004
15 steam						1.000	0.790	0.620	0.670	0.018	0.019	0.001
18 fog							1.000	0.435	0.514	0.015	0.016	0.001
18 precast								1.000	0.935	0.021	0.021	0.000
18 steam									1.000	0.044	0.048	0.003
21 fog										1.000	0.992	0.059
21 precast											1.000	0.077
21 steam												1.000

Table 15: P-values of two-factor t-tests comparing peak stress of specimens

	12			15			18			21		
Mix type	Fog	Pre	Steam	Fog	Pre	Steam	Fog	Pre	Steam	Fog	Pre	Steam
12 fog	1.000	0.159	0.060	0.364	0.060	0.164	0.101	0.355	0.327	0.002	0.001	0.000
12 precast		1.000	0.411	0.418	0.001	0.008	0.005	0.006	0.022	0.000	0.000	0.000
12 steam			1.000	0.100	0.000	0.002	0.002	0.001	0.009	0.000	0.000	0.000
15 fog				1.000	0.001	0.018	0.011	0.020	0.052	0.001	0.000	0.000
15 precast					1.000	0.679	0.952	0.107	0.373	0.019	0.001	0.000
15 steam						1.000	0.711	0.421	0.666	0.014	0.004	0.000
18 fog							1.000	0.245	0.445	0.028	0.012	0.001
18 precast								1.000	0.791	0.004	0.000	0.000
18 steam									1.000	0.009	0.003	0.000
21 fog										1.000	0.902	0.122
21 precast											1.000	0.033
21 steam												1.000

Table 16. P-values of two-factor t-tests comparing tensile toughness of specimens

	12			15			18			21		
Mix type	Fog	Pre	Steam	Fog	Pre	Steam	Fog	Pre	Steam	Fog	Pre	Steam
12 fog	1.000	0.304	0.189	0.479	0.657	0.431	0.403	0.593	0.462	0.033	0.011	0.006
12 precast		1.000	0.339	0.396	0.012	0.055	0.002	0.007	0.002	0.003	0.001	0.000
12 steam			1.000	0.083	0.003	0.040	0.001	0.001	0.000	0.006	0.001	0.000
15 fog				1.000	0.035	0.100	0.007	0.024	0.007	0.005	0.002	0.000
15 precast					1.000	0.562	0.379	0.865	0.502	0.020	0.006	0.000
15 steam						1.000	0.916	0.626	0.797	0.083	0.020	0.004
18 fog							1.000	0.477	0.759	0.035	0.009	0.000
18 precast								1.000	0.631	0.023	0.003	0.000
18 steam									1.000	0.026	0.007	0.000
21 fog										1.000	0.271	0.037
21 precast											1.000	0.231
21 steam												1.000

Table 17: P-values of two-factor t-tests comparing post-cracking tensile stress of specimens

	12			15			18			21		
Mix type	Fog	Pre	Steam	Fog	Pre	Steam	Fog	Pre	Steam	Fog	Pre	Steam
12 fog	1.000	0.392	0.119	0.416	0.296	0.997	0.643	0.700	0.662	0.162	0.050	0.018
12 precast		1.000	0.035	0.918	0.621	0.256	0.026	0.357	0.275	0.046	0.009	0.000
12 steam			1.000	0.028	0.061	0.046	0.001	0.015	0.002	0.019	0.008	0.000
15 fog				1.000	0.549	0.273	0.027	0.403	0.325	0.032	0.010	0.000
15 precast					1.000	0.162	0.013	0.183	0.103	0.036	0.015	0.001
15 steam						1.000	0.553	0.618	0.554	0.110	0.025	0.005
18 fog							1.000	0.162	0.083	0.174	0.042	0.005
18 precast								1.000	0.944	0.062	0.018	0.001
18 steam									1.000	0.067	0.024	0.001
21 fog										1.000	0.392	0.183
21 precast											1.000	0.630
21 steam												1.000

4.4. Discussion

With the exception of the elastic modulus values, which showed little correlation to any of the mix characteristics used for comparison, the fines-sand ratio in the mix design consistently had the best correlation to the tensile properties of the sample groups. It is hypothesized that the concrete mixes with the most fines had a denser microstructure from good particle packing. This could create more friction during fiber pullout, and therefore, a tighter bond, between the concrete matrix and the fibers. Research by Garas et al. shows scanning electron microscopy (SEM) scans of fiber-matrix interfaces for UHPC cured by different methods used for tensile creep testing. They proposed that the heat-treated UHPC had denser microstructures and decreased porosity. Their SEM images showed a porous zone surrounding the fibers of the non heat-treated specimens, which had higher tensile creep than their heat treated specimens [239]. While the results of this study do not indicate a correlation between tensile behavior and curing method, the fines/sand ratio does indicate a correlation between tensile behavior and the density of the matrix.

The effective cracking stresses measured did not have a strong correlation to Equation 19 through Equation 21 as presented earlier in this paper, even when accounting for the curing method used. This could be partially because the equations were developed for the actual cracking stress, but the effective cracking stress is determined by a 0.02% offset intersection. The actual first crack stress was not determined for this research due to the subjectivity required to determine the value for many samples; however, it is possible that this parameter would have had a better relationship with compressive strength. When plotting tensile characteristics against compressive strength, R^2 values ranged from 0.47 for cracking stress to 0.66 for stress at a post-cracking strain of 0.005. However, many empirical equations for the relationships between cracking strength and compressive strength, including Equation 19 through Equation 21, use the square root of the compressive strengthas the independent variable. In order to see if this would improve the correlation of the tensile values to compressive strength, the data in the results section were re-plotted against the square root of compressive strength. In every case, this actually reduced the R^2 value for correlation, although the change was never larger than 5% of the R^2 value. This shows that even if the coefficients in Equation 19 through Equation 21 were adjusted for concrete in the compressive strength range of 12-24 ksi, the square root of compressive strength would still have an unreliable predictor of effective cracking tensile strength for this particular set of data.

When looking at the tensile results compared to the w/cm, the best fit line consistently under predicts the tensile strength or toughness of the 21+ ksi mix. One way to improve the correlation would be to include the silica flour in the cementitious material to calculate the ratio. While there is some debate about how reactive a material must be in order for it to be considered "cementitious," silica flour and other similar filler materials are typically not included in this calculation. However, making this adjustment to include silica flour as cementitious material would change the w/cm of the 21+-ksi mix from 0.156 to 0.13, keeping the w/cm for all other mixes the same. The change in R^2 values for comparing tensile properties against w/cm that would result are shown in Table 18. The correlations improve for all cases when the silica flour is included as cementitious material. In including the filler material as a "cementitious material,"

the w/cm parameter becomes more confounded with the fines/sand ratio, as the "cementitious material" and "fines" designations would include all of the same material. However, the w/cm still would not provide a better correlation than the fines/sand ratio. For this reason, and to align with the industry standard of excluding low-reactivity filler materials in the calculation of w/cm, the silica flour was excluded from "cementitious material" for the graphs in the results section.

Table 18: R^2 values comparing tensile properties to w/cm

Tensile Property	Without silica flour	With silica flour
Effective cracking stress	0.555	0.702
Peak Stress	0.586	0.741
Toughness	0.553	0.720
Stress at 0.005	0.430	0.605

In many of the P-value tables shown in Table 13 through Table 17 of the results, there is a consistent significant difference between the results of the 21+-ksi mix and the other three mixes. The incidence rate of significant difference the fog and precast-cured 21+-ksi mixes being significantly different from the other 9 mixes was much higher for tensile properties than for compressive strength. The mix design for the 21+-ksi mix did differ greatly from the other three mix designs. In order to achieve the target strength, specialized materials had to be used, including different admixtures, silica flour for filler material, a Type III cement instead of a Type IL cement, and white silica fume in place of the standard silica fume used for the other mixes. This mix also had a lower w/cm and replaced 75% of the mix water with ice. These differences in mix composition can make a large difference in the bond between the cementitious matrix and the fibers, even if the compressive strengths were not statistically different.

Improvements can be made to the AASHTO tensile classifications to make them more consistent. One issue with the current classification method is there is a disadvantage to mixes with a high cracking strength. If two mixes have the same post-cracking strength and behavior but one cracks at a higher load, that mix is less likely to be classified as H-1 or H-2. This seems counterintuitive, as a high cracking strength is indicative of a strong concrete and a well-aligned test specimen. An additional problem with the tensile classification categories is the subjectivity with which a specimen is determined to be H-4, or misaligned. While some specimens have an obvious change in elastic modulus due to an eccentricity, many other specimens show a slow, gradual decrease in elastic modulus as strain increases and they near cracking. Due to the previously stated advantages of eccentrically loaded specimens showing lower cracking strengths in the results and therefore, being more likely to be classified as strain-hardening, a less-subjective method of determining which test specimens have non-negligible eccentricities is desired. One method of doing this would be to give guidelines on allowable differences in the readings of LVDTs on opposite sides of the specimen. These guidelines would have to control for differences in extensometer set-ups, as the extensometer attachment points would affect the differences in their readings. However, this could solve some of the subjectivity with classification. A final improvement that could be made to the classification system would be to change the two classifications for imperfect tests to not require strain hardening. Currently, there is not a classification for specimens that either crack outside of the extensometer or are loaded

eccentrically but are not strain-hardening. Figure 71 shows an example of a specimen that has both these characteristics, making classification difficult.

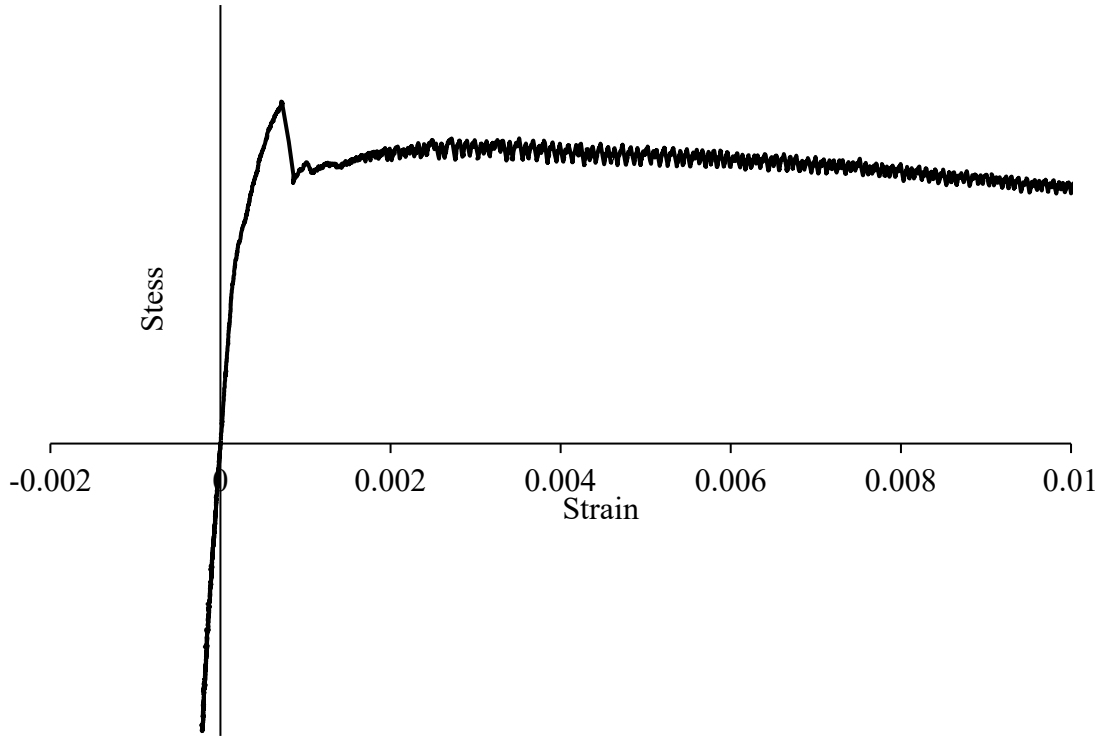

Figure 71: Stress vs. strain results of an eccentrically loaded, strain-softening specimen

4.5. Conclusions

The following conclusions were drawn based on this research.

1. The modulus of elasticity as measured by the direct tension test is highly variable and did not show a strong relation to any of the mix design parameters.
2. Effective cracking stress, peak stress, post-cracking stress, and toughness showed relatively high correlation (0.75-0.82 R^2 values) to the ratio of fines/sand in the mix, and low to moderate correlation (0.42-0.67 R^2) values when compared to w/cm or compressive strength. The two-factor t-tests showed that overall, compressive strength did make a difference in tensile results, but in most cases, curing method did not. Curing method did impact concrete compressive strength for 7 of the 12 comparisons on the same mixture. Curing method was only statistically significant for 1 of the 12 comparisons for effective tensile strength, however. This finding is reassuring as it means tensile tests done on samples cured in a laboratory environment will not give significantly different 28-day tensile results compared to concrete undergoing different curing temperatures in the field.

Based on experience conducting the direct tension test and the results reported, the following recommended changes should be made to the FHWA strength classes for adoption of use by the FDOT.

1. Allow the maximum stress after cracking to be used as $f_{t,peak}$ for determining tensile strength class. Due to the variability of cracking stress and the theoretical correlation between high cracking stresses and low eccentric load applied during testing, it is recommended that a specimen with a high strength before the effective cracking strain should not be penalized in classification. If it is decided that the maximum post-cracking stress be used for classification, then the reported $f_{t,peak}$ should also be the post-cracking stress.
2. Add a category for classifying test results that do not exhibit strain hardening but still can show tensile strength results affected by imperfect alignment or cracks forming outside of the extensometer region. Alternatively, re-name categories H-3 and H-4 and re-define them to include specimens that are type S or N.
3. Sub-classify category S with respect to post-cracking strength. This could be done similarly to the 20% strength gain differentiation between H-1 and H-2, but instead could be defined as, “a specimen losing 20% of its cracking strength or less before a strain of 0.005 is categorized as S-1. S-2 specimens lose between 20-50% of their effective cracking stress by 0.005 strain, and S-3 specimens lose more than 50% of their effective cracking stress.” This improvement is especially seen as important if improvement 1 is not made.

5. MODIFIED DOUBLE PUNCH TEST ROUND-ROBIN STUDY

5.1. Introduction

UHPC tensile property measurements for quality control go beyond what the split cylinder test can measure. The split cylinder test only produces a single strength value as a result and does not take into account post-cracking behavior that is critical for UHPC performance. Previous research for this project has compared tensile results between a direct tension test, a modified double-punch test, and a flexure test. This research showed that the double-punch test and flexure tests could produce results that correlated with the direct tension test, even though these were indirect test methods. Due to the lack of expensive, specialized apparatus required to run the modified double-punch test and correlation to the direct tensile test, the modified double punch test was selected as an ideal quality control test method for UHPC tensile performance. Because the modified double-punch test used in this study was a revised version of a specified double-punch test, further information about the test method was desired. This task report shows the results of a round-robin study done to investigate the single-operator and between-laboratory variance of this revised double-punch test.

5.2. Materials

Two different concrete mixes were used for the samples in the round robin study. The mix designs are shown in Table 19. The mixes are named A, B, and C based on their water-cementitious material ratio (w/cm) and steel fiber content.

Table 19: Mix designs

Material (w/cm)	Mix C (0.20 w/cm) lb/yd^3	Mix A & B (0.1625 w/cm) lb/yd^3
Fine Masonry Sand	1815	1588
IL Cement	1404	1597
Slag	272	309
Silica Fume	136	155
Water	362	335
HRWR admixture	16.4	30.9
HRWR and workability-retaining admixture	16.4	30.9
Surface-enhancing admixture	3.4	5.2

The dry materials used were analyzed for particle size distribution. The sand was analyzed using sieve analysis according to ASTM C136 [235]. The cementitious materials particle size distributions were measured using laser particle size analysis and are shown in Figure 72.

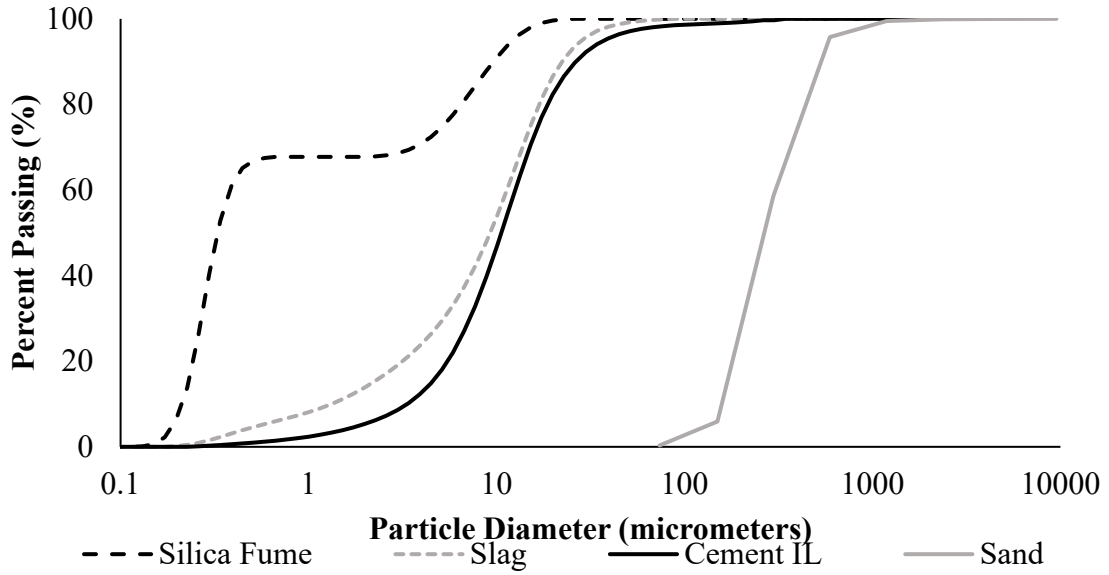

Figure 72: Particle size distribution of materials

The cementitious materials were also analyzed using X-ray fluorescence (XRF) to determine material oxide composition, and the cement was analyzed using X-ray diffraction (XRD) and Rietveld refinement according to ASTM C1365 [240] to determine its phase composition. The XRF results are shown in Table 20, and the XRD results are in Table 21.

Table 20: XRF results for cementitious materials

Parameter	Cement IL	Slag	Silica Fume
SiO_2	18.82	34.79	80.45
TiO_2	0.22	0.64	0.02
Al_2O_3	4.79	13.17	0.48
Fe_2O_3	3.10	0.78	4.78
Mn_2O_3	0.06	0.32	0.44
MgO	0.80	4.66	10.43
CaO	62.85	43.71	0.95
Na_2O	0.08	0.19	0.18
K_2O	0.25	0.41	0.77
P_2O_5	0.41	0.04	0.03
SO_3	3.02	3.00	0.07
ZnO	0.00	0.00	0.00
SrO	0.00	0.00	0.00
Cr_2O_3	0.00	0.00	0.00
LOI	5.45	0.02	2.93

Table 21: XRD results for cement

Phase	Type IL Cement
Alite	44.3
Belite	23.2
Aluminate	4.2
Ferrite	11.2
Bassanite	0.5
Gypsum	5.1
Calcite	11.7

The fibers used were high-strength straight, brass-coated steel fibers that were 0.50 in. (13 mm) long and 0.0079 in. (0.20 mm) n. diameter. The three mixes tested used a combination of different fiber percentages and mix designs, as shown in Table 22.

Table 22: Material properties used for study

Mix	Concrete Mix (w/cm)	Fiber Content (% volume)	Batch Size (ft^3)	56-day Compressive Strength (psi)
Practice Samples	0.1625	1.5	3.5	-
Material A	0.1625	1.5	3.5	19,600
Material B	0.1625	2.5	3.5	18,300
Material C	0.20	3.0	4.0	18,400

The compressive strength of the mixes was measured at the age of testing using 3-in. × 6 in. cylinders, in accordance with ASTM C39, modified by ASTM C1856 [59,87]. The results are shown in Table 22. The three mixes were each made in single batch to ensure specimen variation was kept to a minimum. The 3-in. × 6-in. cylinders made for compressive strength measurements were made from the same batch as the double-punch test samples. The double-punch test samples made were cylinders with a diameter of 6 in. and a height of 6 in Molds were fabricated by cutting a 6-in. inner-diameter PVC pipe in 6 in. lengths and cutting a slit down the side of each one. A wooden base was then cut and covered with a plastic liner to ensure the easy release and eliminate moisture loss from absorption. The pipe was attached to the base using silicone. Additionally, some molds for the final mix were made by cutting the top 6 in. off of a 12- in. × 6-in. plastic cylinder mold. The size of each sample was roughly 0.10 ft^3, which limited the number of samples that could be made from a single batch. Because of this, only 10 labs were chosen for Mix A and B, and no spare test samples were given to the labs. This amounted to 30 samples per mix. The size of Mix C was increased to 4.0 ft^3 to allow for 11 labs to participate, but shipping problems hindered one lab from receiving samples. Overall, 13 different labs were included in the study, as not every lab participated for every mix.

5.3. Methods

The samples were placed by filling buckets with UHPC directly from the mixer and then placing the concrete from the buckets into the molds. The molds were labeled in numerical order to distinguish the sample made first from those made at the end of the placement. The samples were then struck 30 times with a mallet and then the top was finished. They were cured under a plastic sheet at room temperature for at least 20 hours. The samples were then removed from the molds and labeled with their mold number. The samples from Mix A, Mix B were steam-cured for 48 hours beginning 24 hours after mixing. They were wrapped with wet towels and plastic wrap that was taped shut to prevent moisture loss. Figure 73 shows the wrapped samples. The oven temperature used for steam curing was 194°F (90°C). After the samples were removed from the oven and allowed to cool, they were unwrapped and placed in a moist-cure room for at least 28 days. The samples from Mix C were not heat-treated in any way but were instead kept in a moist-cure room at 73.5 ± 3.5°F for at least 28 days.

Figure 73: Specimens wrapped for steam treatment

After the 28 days had passed and before 56 days, the samples were delivered to participating labs. Samples for Mix A and B were stored in plastic containers and driven to participating labs, where the participants were instructed to store them in a moist environment until testing. Samples from Mix C were wrapped in wet towels and sealed in large plastic bags and mailed to participating labs, who were instructed to store them in a moist environment until testing. All samples were tested at 56 days, ± 1 day, in accordance with the tolerances for testing ages in ASTM C39, section 8.3 [87]. The 3 samples for each lab were selected to ensure each lab received a sample from the first, middle, and last third of placement time after mixing. This would help ensure variations in fiber content or orientation due to settlement or concrete stiffening would not disproportionately affect a given lab's results.

The labs tested the 3 samples for each mix according to the specification presented in Appendix A. Each lab was to report the following information: specimen identification, average measured height and diameter of the specimen, the raw data pairs of displacements and loads, and the maximum load. Calculations to convert load into stress were performed by the laboratory running the study after the data was submitted. Equation 1 in Appendix A shows how the stresses were calculated based on load and the specimen's height. The peak stress and toughness for each specimen was then recorded. Equation 2 in Appendix A shows how the toughness was calculated.

Discrepancies in the data were addressed in the following ways:

- If a lab did not report the height and width of the sample, they were assumed to have a height of 6.00 in. and diameter of 6.00 in.
- If a lab skipped a reading or did not take them frequently enough to meet the specification (0.01 in. at the start of the test and 0.02 in. after 0.10 in. of displacement), the data was used as reported. Previous research showed that readings taken at intervals of 0.05 in. could consistently reproduce the toughness of a specimen to within 4% of the toughness calculated with complete data, meaning the specification requirements of data collection interval are higher than necessary to produce good results.
- If a lab did not report data for a full 0.30 in. and was missing no more than 0.02 in. of data (corresponding to the last data point), the last data point was extrapolated by assuming the slope from the previous two data points continued until 0.30 in.
- If a lab did not report data for a full 0.30 in. and was missing more than 0.02 in. of data (corresponding to more than one data point), the data from this test sample was not included in the 0.30 in toughness results. This occurred from some testing machines stopping before the full test had been completed.
- If a lab reported data for more than 0.30 in. of displacement, the load at 0.30 in. was interpolated, if necessary, from the previous and subsequent data points to ensure toughness was only calculated for 0.30 in. of displacement for all specimens.
- If a lab did not report the peak load for a sample, the peak strength was estimated as the highest load reported in the load vs. displacement pairs. These estimated peak strengths are shaded in Table 23.

- If a lab did not submit three usable results for a given material, all data from that lab was not included in the statistics for lab averages or for precision statement calculations according to ASTM C802 [241]. If one or two usable results were submitted, those were used to calculate overall statistics.

5.4. Results

Table 23 shows the results of peak stress for each lab. The highlighted numbers have been estimated by taking the maximum value reported from the incremental load vs. displacement pairs. Table 24 shows the toughness results calculated until a vertical displacement of 0.30 in.

Table 23: Peak stress results (psi)

Laboratory	Replicate	Mix A (1.5% fibers)	Mix B (2.5% fibers)	Mix C (3.0% fibers)
1	a	1037	1439	1323
	b	1017	1179	1253
	c	1196	1313	1846
2	a	1226	1274	1432
	b	1285	1380	1244
	c	1245	1516	1284
3	a	1285	1674	1453
	b	1139	1430	1479
	c	1068	1276	1423
4	a	1173	1485	
	b	949	1361	
	c	1238	1795	
5	a	1034	1557	1347
	b	1290	1343	1298
	c	1506	1289	1453
6	a	1347	1260	1708
	b	1200	1478	1219
	c	1169	1605	1240
7	a	1371	1463	
	b	1069	1505	
	c	1035	1325	
8	a	1076	1305	1117
	b	1066	1275	1790
	c	1247	1572	1616
9	a	1220	1312	
	b	1153	1578	
	c	1428	1463	
10	a	1192	1308	1745
	b	1259	1446	1331
	c	1390	1293	1367
11	a			1134
	b			1487
	c			1376
12	a			1905
	b			1541
	c			1371
13	a			1474
	b			1256
	c			1581

Table 24: Toughness results (psi·in.)

Laboratory	Replicate	Mix A (1.5% fibers)	Mix B (2.5% fibers)	Mix C (3.0% fibers)
1	a	119.4	210.1	210.5
	b	149.1	151.7	176.4
	c	186.1	136.4	336.4
2	a			191.5
	b	181.4		162.1
	c	150.0		162.9
3	a	169.5	235.9	203.0
	b	151.4	228.8	183.1
	c	132.8	197.8	219.3
4	a	134.1	203.9	
	b	116.6	160.0	
	c	175.3	183.9	
5	a	127.2	234.9	210.3
	b	148.3	157.2	264.7
	c	209.7	153.3	170.3
6	a	146.5		327.6
	b	149.8	208.0	144.3
	c	163.8	200.6	168.4
7	a	125.4	201.7	
	b	134.6	180.6	
	c	114.8	156.4	
8	a	105.4	189.2	
	b	165.0	155.2	
	c	161.8	241.2	
9	a	129.1	143.9	
	b	148.9	217.1	
	c	181.2	181.8	
10	a	161.2	202.3	309.4
	b	181.4	145.5	152.8
	c	213.9	179.3	206.9
11	a			185.2
	b			174.8
	c			136.8
12	a			354.9
	b			
	c			
13	a			248.7
	b			142.1
	c			254.5

Analysis was done on the lab averages for each material to ensure that a particular lab did not produce results that were statistically different from the overall average. This was done by calculating the h-value for each lab according to ASTM C802, which finds how many standard deviations each lab's average is from the overall average for a given material [241]. The critical h-value for a round-robin test with 10 labs is 2.29 [241], which was not exceeded for any lab or material in peak stress, as shown in Figure 74. Figure 75 shows the h-values for toughness, which had a fewer number of labs due to some laboratories being unable to get complete data for the full 0.30 in. displacement required. The number of labs whose toughness data was complete was 9 for Mix A and 8 for Mix B and C. The h-value for 9 labs (Material A) is 2.23, and the value for 8 labs (Materials B and C) was 2.15. Laboratory 3 did produce an h-value of 2.158 for Mix B, which is slightly higher than its critical value. This is not seen as highly problematic because the other materials from laboratory 3 did not show results that were largely positive compared to the other laboratories.

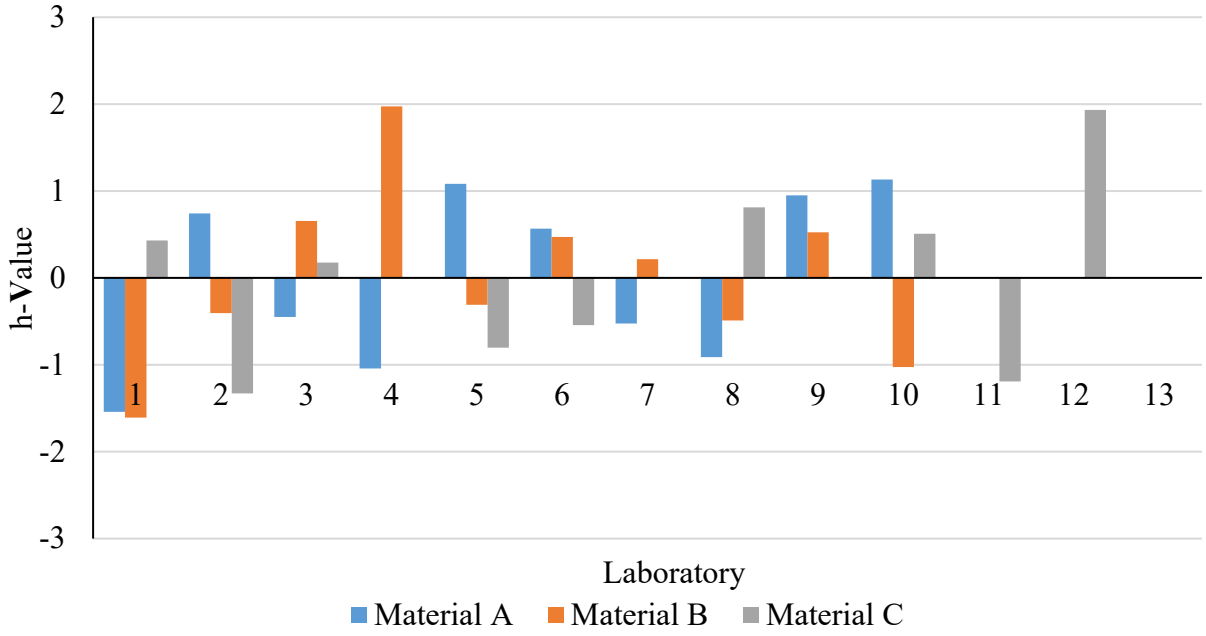

Figure 74: H-values for peak stress

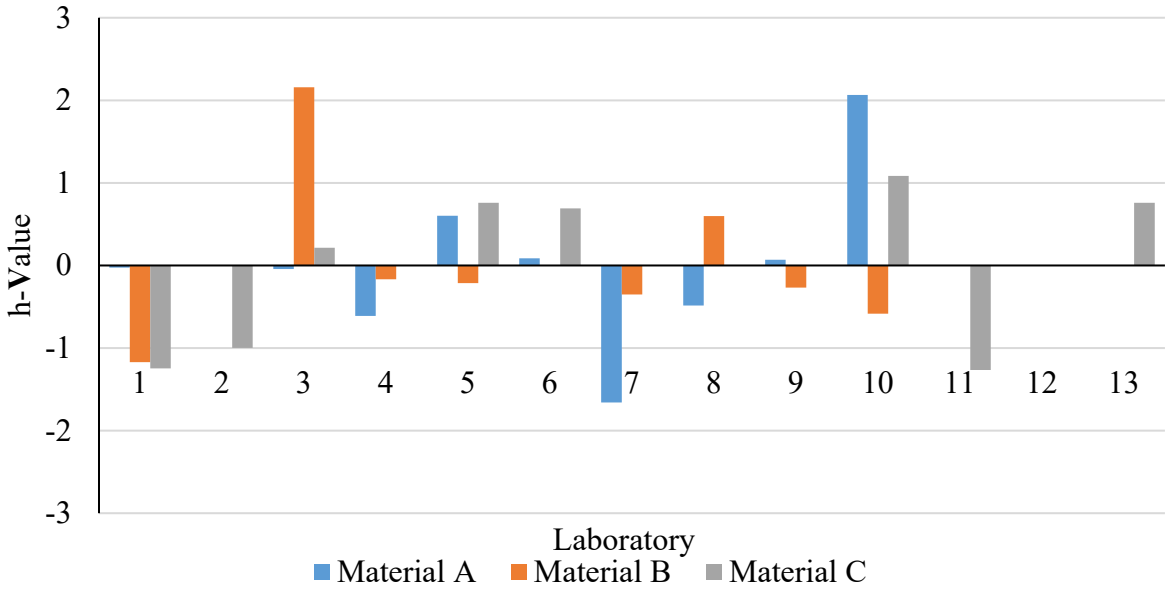

Figure 75: H-values for toughness

The k-values for each lab and material were also calculated according to ASTM C802. The k-values show how the variability within one laboratory's test results compare to the pooled results for the material from all laboratories. This is done using the standard deviations of each lab's data and dividing it by the pooled standard deviation, calculated as the square root of the average of each lab's variance. Higher k-values show that the given laboratory had more variance for the given material than average. The critical k-value for peak stress is 2.11 for all materials, as 10 labs were used with 3 materials each. The critical k-value for toughness is 2.09 for Mix A (9 labs) and 2.06 for Mixes B and C (8 labs). Figure 76 shows the peaks stress values, and Figure 77 shows the toughness values. No k-values exceeded the critical value for any lab or material in either peak stress or toughness.

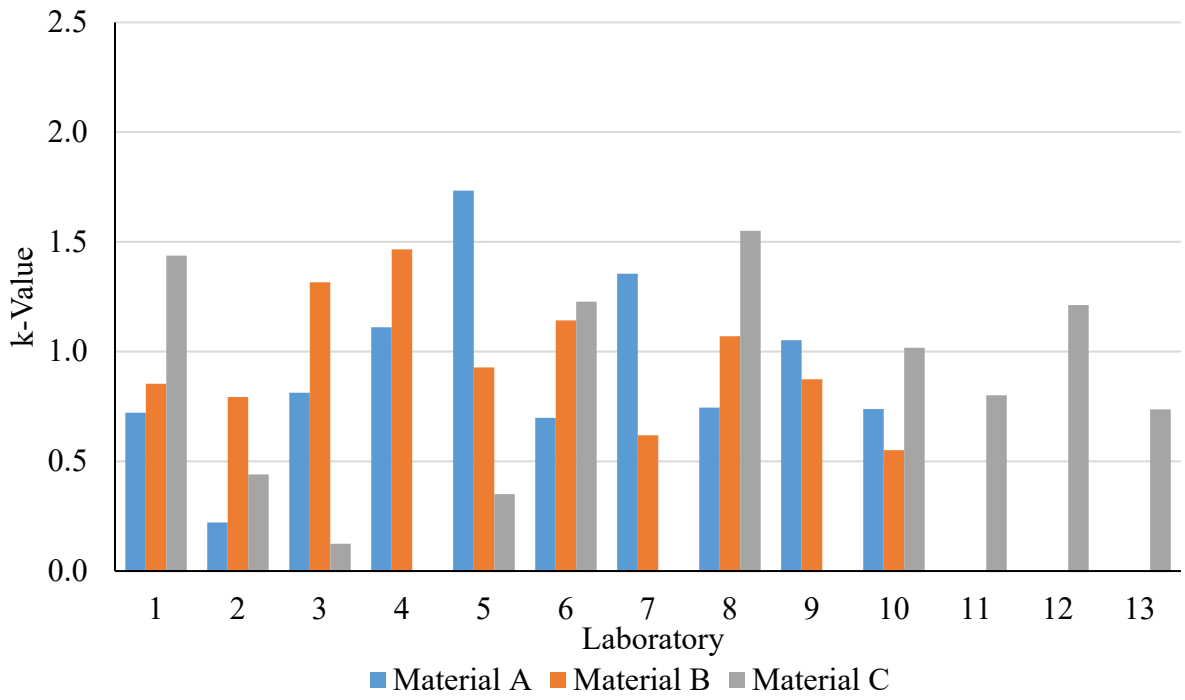

Figure 76: K-values for peak stress

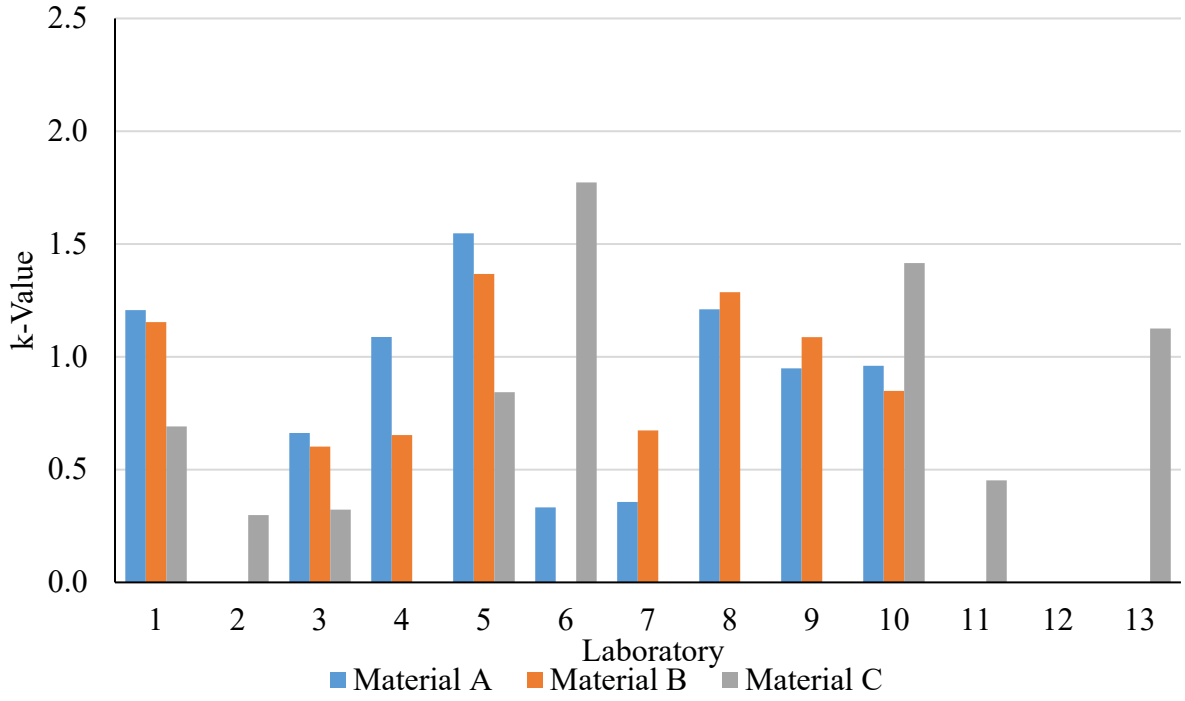

Figure 77: K-values for toughness

The components of variance were calculated in accordance with ASTM C802 and are shown in Table 25 and Table 26. For almost all cases, the material between-laboratory variance calculation was negative, which is taken as a between-laboratory component of variance of zero. The exception to this was the toughness for Mix A, which had a relatively low between-laboratory component of variance. Because multilaboratory variance is the sum of the single-operator and between-laboratory components, the single operator variance is equal to the multilaboratory variance for peak stress for all materials and for toughness in all but Mix A.

Table 25: Variances and components of variance for peak stress

		Components of Variance		Variance	
Mix	Average	Single-Operator	Between-Laboratory	Single Operator	Multilaboratory
A	1,197	18,555	0	18,555	18,555
B	1,417	23,300	0	23,300	23,300
C	1,436	50,735	0	50,735	50,735

Table 26: Variance and components of variance for toughness

Mix	Average	Components of Variance		Variance	
		Single-Operator	Between-Laboratory	Single Operator	Multilaboratory
A	152	767	9	767	776
B	185	1,134	0	1,134	1,134
C	197	3,159	0	3,159	3,159

The variance values from Table 25 and Table 26 were used to calculate the standard deviations shown in Table 27 and Table 28, where the standard deviations are the square roots of the variances. The standard deviations were then divided by the material averages to produce the coefficients of variation. Once again, the single operator and multi-laboratory coefficients of variation (CV) were identical or very close for every material, due to the low between-laboratory components of variation.

Table 27: Standard deviations and coefficients of variation for peak stress

Mix	Average	Standard Deviation		Coefficient of Variation	
		Single-Operator	Between-Laboratory	Single Operator	Multilaboratory
A	1,197	136	136	11.4	11.4
B	1,417	153	153	10.8	10.8
C	1,436	225	225	15.7	15.7

Table 28: Standard deviations and coefficients of variation for toughness

Mix	Average	Standard Deviation		Coefficient of Variation	
		Single-Operator	Between-Laboratory	Single Operator	Multilaboratory
A	152	27.7	27.9	18.23	18.33
B	185	33.7	33.7	18.17	18.17
C	197	56.2	56.2	28.60	28.60

Due to the highly variable nature of tensile tests for concrete, tensile tests are usually reported as the average of multiple tests. Should the double-punch test shown in Appendix D be used for a quality control test, the specifying agency will likely require the results of at least three test specimens to be reported. Because the specification in Appendix D was written for a single specimen and does not state that three specimens must be run, the statistics presented in Table 25 through Table 28 used each test specimen as a separate result and calculated variation for a single test. However, to give an idea of variation for an average of three samples, Table 29 through Table 31 show statistics calculated for each lab's average. In cases where a lab did not

report three complete results, the lab's average was not included. However, the lab's individual results were included in the statistics under "All tests." The number of values included for the statistical calculations is shown in parentheses in each column heading. The inclusion of values from labs that did not report three complete test results is one reason the values in the "All tests" columns for Table 29 through Table 31 vary slightly from those presented in Table 26 and Table 28. These tables show that the coefficient of variation significantly decreases when the lab averages are compared, as expected.

Table 29: Statistics for Mix A

	All tests		Lab averages	
	Peak Stress (30)	Toughness (29)	Peak Stress (10)	Toughness (9)
1.50%	psi	psi·in	psi	psi·in
average	1196.9	152.9	1196.9	151.9
std.dev	133.6	27.4	73.7	16.3
CV (%)	11.2	17.9	6.2	10.7
variance	17,848	750	5425	265

Table 30: Statistics for Mix B

	All tests		Lab averages	
	Peak Stress (30)	Toughness (26)	Peak Stress (10)	Toughness (8)
2.50%	psi	psi·in	psi	psi·in
average	1416.7	186.8	1416.7	187.5
std.dev	141.9	31.3	66.1	16.6
CV (%)	10.0	16.8	4.7	8.9
variance	20,137	981	4370	277

Table 31: Statistics for Mix C

	All tests		Lab averages	
	Peak Stress (30)	Toughness (25)	Peak Stress (10)	Toughness (8)
3.0%	psi	psi·in	psi	psi·in
average	1436.4	211.9	1436.4	205.9
std.dev	205.2	63.5	87.5	25.5
CV (%)	14.3	29.9	6.1	12.4
variance	42,125	4,026	7,661	648

5.5. Discussion

For both peak stress and toughness, the between-laboratory components of variance were either zero or close to zero for all three materials. This is likely because the single-operator component

of variance tended to be high. One reason for this is tensile tests for concrete are usually quite variable. Another reason that seemed to be present for Mix C was that there was a slight trend between a specimen's strength and its order of placement among the specimens, with specimens placed later in the order tending to have higher strength and toughness. The selection of specimens for each lab was controlled so each lab would receive a specimen from the beginning, middle, and final third of the specimens placed. This was done to minimize the effect of possible variation in specimen characteristics based on their order of placement; however, it also shifted variation from between laboratories to single operator. Figure 78 shows this trend between peak stress and sample order number for the Mix C samples. The relationships for Mixes A and B had R^2 values of 0.26 and 0.10, respectively, which shows a much smaller relationship. However, these materials also had larger peak stresses as sample number increased.

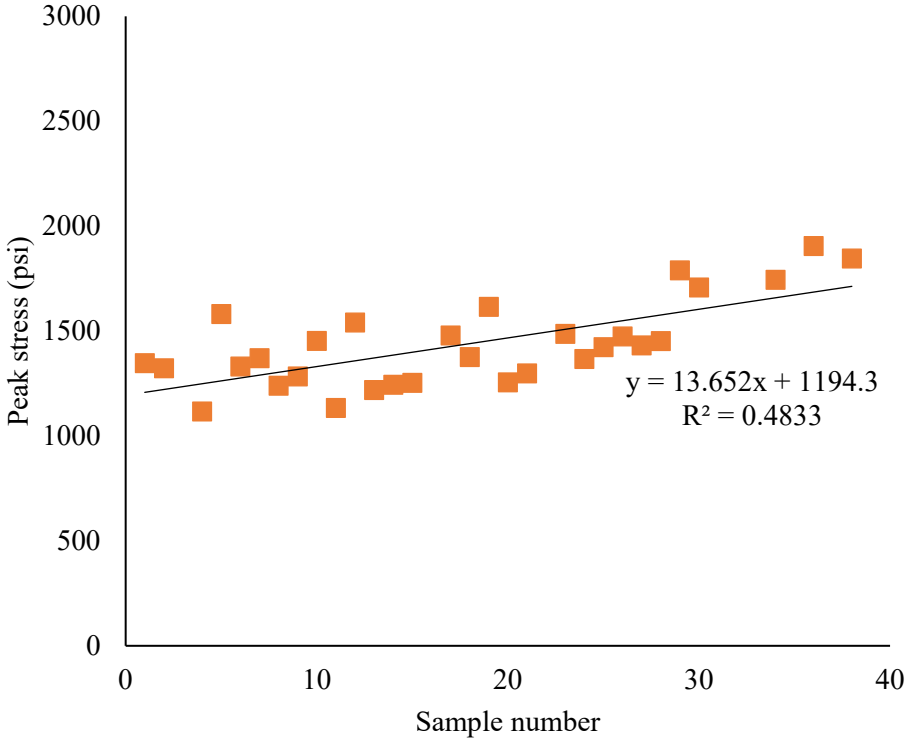

Figure 78: Peak stress vs. sample number for Mix C samples

Figure 78 shows that for Mix C, the samples with the largest 5 numbers had higher peak stress values than any of the other samples. These specimens may have been made with concrete containing a higher percentage of fibers by volume, or the concrete could have stiffened later in mixing, making placement of the samples take longer. Previous research for this project has shown that the double-punch test gives higher strength and toughness results if the specimen has been placed in multiple layers. While the fabrication was done with the goal of placing each specimen in a single placement from the bucket, cylinders placed with very stiff concrete likely needed to be made by scraping the stiff concrete out of a bucket in multiple lifts, which could have formed vertical planes of fibers. In order to see how these five higher values affected the results, the statistics in Table 31 were repeated without these 5 values. The new values are shown in Table 32. Unlike the statistics in Table 29 through Table 31, the "Lab Averages" statistics in

Table 32 do include labs that did not have 3 complete results, in order to include the 5 laboratories that tested the higher-number samples in the data. The exclusion of these 5 data points from the statistical calculations reduced the coefficients of variation substantially for individual tests to similar values seen for Mixes A and B. There is a smaller reduction for the lab averages. Figure 79 shows that the relationship between sample number and peak stress for Mix C without these 5 values is much weaker, with an R^2 value of only 0.105.

Table 32: Statistics for Mix C excluding largest five sample numbers

	All tests		Lab averages	
	Peak Stress (25)	Toughness (20)	Peak Stress (10)	Toughness (8)
3.0%	psi	psi·in	psi	psi·in
average	1364.0	189.0	1359.6	187.4
std.dev	130.5	36.6	73.3	22.4
CV (%)	9.6	19.4	5.4	11.9
variance	17,043	1,338	5,369	501

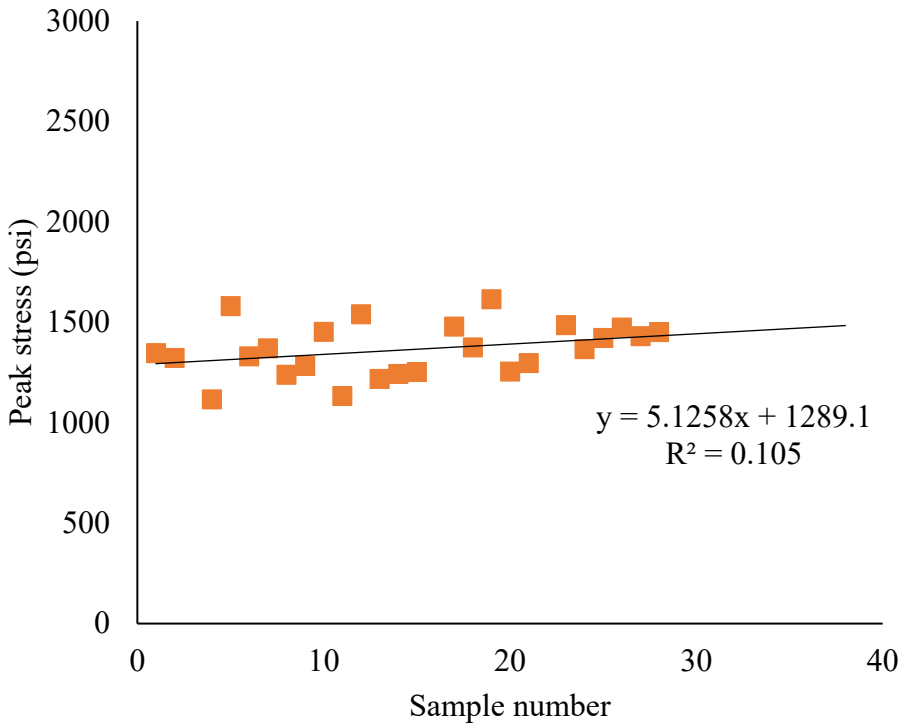

Figure 79: Peak stress vs. sample number for Mix C excluding largest five sample numbers

The results for all materials show that the modified double-punch test does not have high between-laboratory variation, meaning that different equipment and technicians do not have a

large effect on the test results. There is large variation in the results between individual samples, but this is common for tensile tests. For comparison, the third point flexure test described in ASTM C1609 reports coefficients of variation of 9.2 for peak stress and 17.3 for toughness, and these were calculated using the mean of three or four identical specimens as a single test result [217]. The specimens used were likely weaker and not as well fiber-reinforced as the ones used in this study, as UHPC is stronger than most fiber-reinforced concretes. This would likely increase the variability of the results, but using an average of multiple samples as the mean of a set would decrease variability.

One of the concerns that prompted this round robin study was that the manual adjustment of load rate described in the procedure in Appendix D could cause large variations in results, especially with different technicians and different machines. This did not prove to be the case, as a wide range of compression machines was used in this study, and between-laboratory variance was shown to be low. In order to ensure that the round-robin study fully showed variation as a result of poorly regulated loading rate, no lab was allowed to use a displacement-controlled test machine, even though many did have the capability to do this. It is recommended that the test method in Appendix D be modified to allow for the use of a displacement-controlled loading system that would load a specimen at 0.02 in/min; however, the variation for this has not been tested in the study.

5.6. Conclusions and Recommendations

Based on the results of this study, the following recommendations are made:

1. The modified double-punch test can reliably be used for a quality control test of UHPC tensile behavior.
2. The double-punch test showed multilaboratory coefficients of variation (CVs) ranging from 10.8%-15.7% for peak stress and 18.17%-28.60% for toughness for a single test specimen.
3. The variation in the double-punch test was shown to be almost entirely due to single-operator variation, as the multilaboratory component of variation was zero or very low. This is likely due to high variability in tensile strength between samples.
4. The double-punch test shows coefficients of variation lower than that of the ASTM C1609 flexure test when a sample is taken as an average of three test specimens.
5. If the double-punch test is adopted, at least three specimens should be required to be tested.

6. BOND STRENGTH OF UHPC FROM DIFFERENT BATCHES

6.1. Introduction

The introduction of ultra-high-performance concrete (UHPC) into mainstream infrastructure projects has brought opportunities for faster construction, improved durability, and thinner section sizes. One difficulty with introducing UHPC into the construction industry is that methods for UHPC mixing, testing, and placing are very different from those used with normal concrete. When determining placement methods, engineers and contractors must consider how the techniques could affect the orientation and dispersion of the steel fibers in the UHPC. Research has shown that fibers tend to orient themselves in the direction of concrete flow [31,234,242]. Concrete flowing around barriers such as rebar may deposit more fibers upstream from the barrier and contain a section of concrete downstream with reduced fiber content [242]. Additionally, while normal concrete is often consolidated with internal vibration, this has been proven to increase fiber settlement and cause preferential fiber orientation [234]. Another unique quality of UHPC is the elephant skin that quickly forms on the concrete's surface after it has been placed [65]. This "elephant skin" is a rough crust that can form on the surface exposed to the ambient environment within minutes after casting [243]. The combination of low water content and high amounts of superplasticizer results in early desiccation and stiffening of this skin. In addition to causing difficulties with surface finishing and trapped air, this elephant skin has the potential to cause a weak interface between concrete placed at different times or at different locations of a large specimen. The stiffness of the elephant skin on the first layer could prevent subsequent layers from intermixing and fibers from bridging the interface between the two layers. This is especially a concern if the specimen being placed requires multiple batches of UHPC. The Canadian guidelines for UHPC recommend that in cases where UHPC cannot be placed monolithically and the intersections of multiple wave fronts of UHPC cannot be avoided, an "L" shaped rod or a propeller on a shaft should be inserted through the full depth of the concrete and twisted as it is pulled out [234].

The purpose of this research is to determine how the strength of the bond between two separate placements of UHPC changes with the amount of time between placements and the fresh properties of the concrete. The concrete placement in this study was very rapid, giving little difference in time between placements and from the start of placement of the first layer and completion of the second layer placement. This research has applications for precast concrete producers who want to make full-sized concrete specimens out of UHPC. These specimens often require multiple batches of concrete. Because specialized mixers are often used for UHPC, one mixer is used for multiple batches with a significant waiting time in between, leaving time for the elephant skin to form and thicken. While significant research has been performed on the proper construction techniques for binding UHPC to hardened concrete or UHPC [244–246], this research focuses on the best methods to ensure fresh UHPC binds well to UHPC that has stiffened after placement but not yet reached initial curing. This research could also be applicable to 3-D printed concrete structures, for which UHPC has many admirable rheological properties, which require good bond strengths between many layers of concrete.

6.2. Materials and Methods

The materials used for this study included ASTM C595 Type IL cement [247], slag, silica fume, and a fine masonry sand. The sand particle size distribution was measured according to ASTM C136 [235]. The cementitious materials were analyzed using a HORIBA laser particle size analyzer. Figure 80 shows the results of the particle size analysis. The silica fume showed a bimodal distribution even after 30 minutes of sonication and the inclusion of a surfactant to the solution. It is likely that agglomerated particles caused the bimodal distribution.

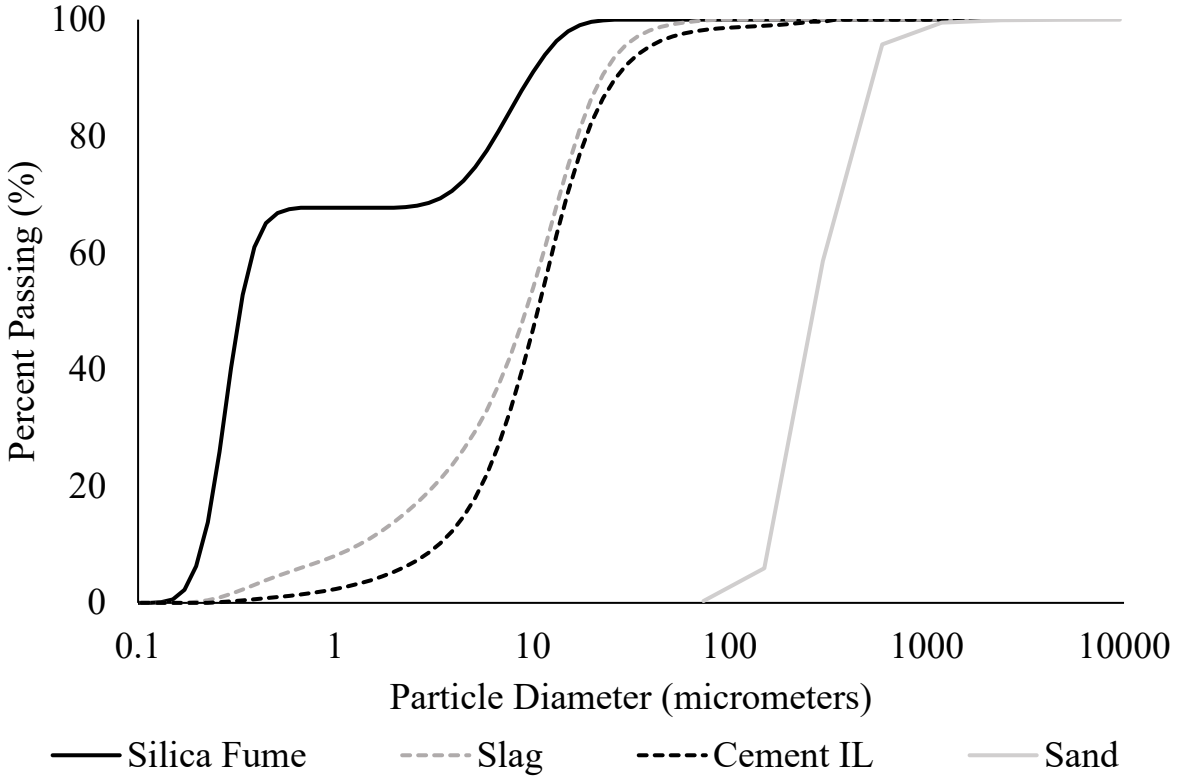

Figure 80: Particle size analysis of materials

The cementitious materials were analyzed using X-ray fluorescence (XRF) to find the chemical composition. In addition, the Type IL cement was analyzed using X-ray diffraction (XRD) with Rietveld refinement [240] to find the cement crystalline composition.

Table 33 and Table 34 show the results of the XRF and XRD analysis, respectively.

Table 33: XRF results for cementitious materials

Parameter	Type IL Cement	Slag	Silica Fume
SiO_2 (%)	18.82	34.79	80.45
TiO_2 (%)	0.22	0.64	0.02
Al_2O_3 (%)	4.79	13.17	0.48
Fe_2O_3 (%)	3.1	0.78	4.78
MnO (%)	0.06	0.32	0.44
MgO (%)	0.8	4.66	10.43
CaO (%)	62.85	43.71	0.95
Na_2O (%)	0.08	0.19	0.18
K_2O (%)	0.25	0.41	0.77
P_2O_5 (%)	0.41	0.04	0.03
SO_3 (%)	3.02	3	0.07
LOI (%)	5.45	0.02	2.93

Table 34: Type IL cement phase composition

Phase	Percent
Alite	44.3
Belite	23.2
Aluminate	4.2
Ferrite	11.2
Bassanite	0.5
Gypsum	5.1
Calcite	11.7

Two different mix designs were used for this research. The mix designs were selected to ensure there were different flow properties between the mixes without much change in tensile performance.

Table 35 shows the mix proportions used for the two mixes. They are labeled with their target compressive strength, as determined by previous trial mixes. Water in the admixtures is included in the water content shown in Table 35. For example, the 335 lb/yd^3 of water shown includes water in the admixture and water added as batch water. All mixes used high-strength steel fibers with a 13-mm length and 0.2-mm diameter at a 2.0% volume addition.

Table 35: Mix design proportions for bonding tests

Material	15-18 ksi lb/yd^3	18-21 ksi lb/yd^3
Sand	1815	1588
IL Cement	1404	1597
Slag	272	309
Silica Fume	136	155
Water	362	335
HRWR admixture	16.4	30.9
HRWR and workability-retaining admixture	16.4	30.9
Surface-enhancing admixture	3.4	5.2
Fines-to-sand ratio	1.00	1.30
Total cementitious material	1812	2061
w/cm	0.200	0.163

The test method used to measure interlayer tensile strength was based on ASTM C1583 [248]. Specimens were made by placing a 2.5-in. thick layer of concrete initially and then waiting a prescribed amount of time until adding an additional 1.5 in. of concrete on top. Samples were not covered or troweled between placement of the first and second layers. The concrete for the second layer was dyed red to help visually find the interface between the layers. The molds in which the layers were placed were 4 in. × 4 in. × 14 in. steel rectangular prism molds. Three cores were drilled 2.5 in. deep into each prism, resulting in three test specimens that met the spacing requirements in ASTM C1583. Figure 81 shows a diagram of a prism with the three cores drilled in it. Three compression cylinders measuring 3 in. × 6 in. were made for the concrete in each layer. Figure 82 shows two specimens after being cored.

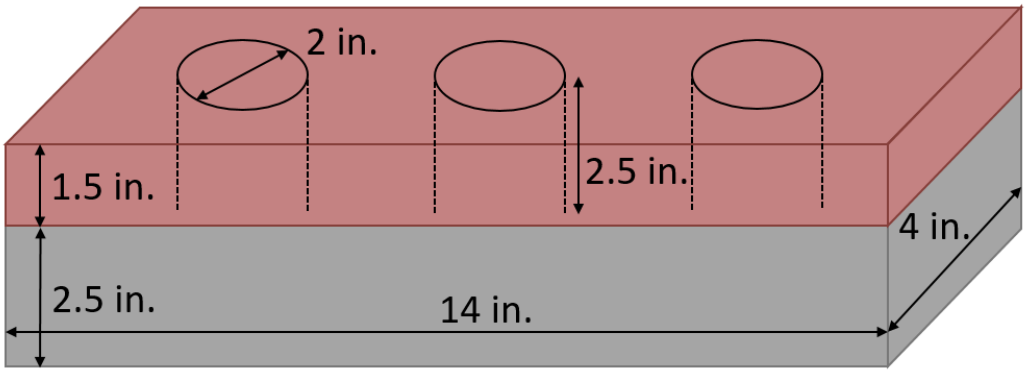

Figure 81: Dimensioned diagram of test specimens

Figure 82: Cores in layered prisms

Testing was performed to determine how different UHPC fresh properties, times between layers, and consolidation methods affected the bond strength between layers. For each mix design and time interval used, three different consolidation methods were applied. The control placement method used no consolidation. The second consolidation method was external vibration. Vibrated specimens were cast on a vibrating table that was turned on for 10 seconds after the second layer was placed. The final consolidation method was rodding. This method used a tamping rod pushed vertically through both layers of concrete after the second layer had been placed. Each rectangular prism was rodded 6 times in a zig-zag pattern to space out the locations and cover the entire area of interface. All specimens were finished with a trowel after consolidation and covered to prevent evaporation.

The flow diameter of each concrete batch was tested in accordance with ASTM C1856 at the time of placement [59]. In addition, at the time of placement of the top layers of concrete, the stiffness of the bottom layer was measured by placing a Vicat needle attached to a lightweight shaft as shown in Figure 83 on top of the concrete surface. Weights were then slowly added to the Vicat needle until it pierced through the elephant skin. The weight of the needle plus any added weights was then recorded. The combined weight of the needle and the shaft attached to it was 1.0 oz (28 g). The needle had a diameter of 0.079 in. (2.0 mm) and a length of 2.04 in. (51.8 mm). The weights added were metal with holes through the center so they could be balanced on the metal holder atop the needle shaft. A combination of larger weights weighing 1.6 oz (45 g) and smaller weights weighing 0.3 oz (9 g) each was used in order to get a more precise measure of the stiffness. A stand was fabricated to keep the needle vertical while it rested on the elephant

skin. A base with a diameter of slightly less than 4 in. was used to prevent the base from indenting the elephant skin but allow the stand to fit in the 4 in.-wide prism mold. A 0.25-in. hole in the middle of the base allowed the needle to fall through without touching the base, while preventing the threaded portion of the Vicat needle from embedding into the concrete. A clear tube with an inner diameter of 0.53 in. was used to align the 0.41 in.-diameter plastic shaft vertically and keep the needle perpendicular to the concrete surface. While this was not a standard method for measuring surface stiffness, the results could be compared to find the relative stiffness of the elephant skin when the second layer of concrete was placed in order to see how this influenced the results.

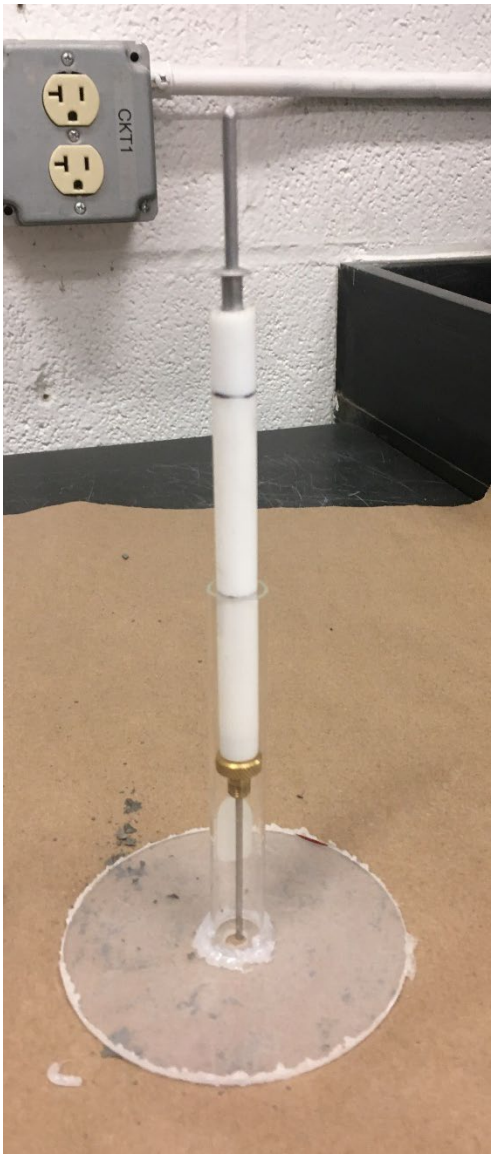

Figure 83: Vicat needle used to test concrete and elephant skin stiffness

The first specimens were made in a 2 ft^3 batch, with all the concrete for both layers mixed at the same time. This allowed one batch of concrete to be used to test multiple time differences

between layer placement, as some concrete could continue mixing in the machine as the first layer was dispensed and placed. One large drawback of this method, however, was that the concrete mixing in the machine stiffened as it was mixing, resulting in much lower flow measurements for concrete that had been mixed for 20 or 30 minutes. This, combined with the increased elephant skin thickness of the first layers that had been waiting for 20 or 30 minutes, provided two factors that could influence the bond strength. To address this, subsequent specimens were made by using two separate mixers for the first and second layers. The first layers were made from a high shear mixer in batches of 0.81 ft^3. The second layers were made in a Calmetrix Pheso rheometer using an attritor propeller. The mix designs were identical except for red powdered dye added to the second layer mix. Using this method, the increased time between placement only affected the thickness of the elephant skin and not the stiffness of the concrete. This method was more representative of field conditions, as a company needing multiple batches of UHPC to fill formwork would place the second batch as soon as it was finished mixing. For these subsequent mixes, each batch of concrete was only used to test one time difference, but all three consolidation methods were performed on specimens from the same batches. One drawback of this method was that the two different mixers produced concretes with different fresh properties due to different batch sizes and mixing energies.

After the prisms had cured for 1 day, they were demolded and left to cure in a moist curing room with a temperature between 70.0°F and 77.0°F (21.0°C - 25°C) as specified in ASTM C31 [236]. Specimens were briefly removed from the curing environment to be cored. Coring was done with a 2.5 in. outer diameter bit, resulting in a 2 in. core. At approximately 26 days, specimens were removed from the curing environment so they could dry prior to the attachment of aluminum pull-off discs to the surface of each core. The pull-off discs were attached with Sika 31 epoxy and left to cure for two days at laboratory temperature.

On day 28 after mixing, the compression cylinders were tested according to ASTM C1856 and interlayer specimens were tested using a pull-off test based on ASTM C1583 [248]. The set-up for pull-off testing is shown in Figure 84. A 30,000 lb capacity universal testing machine was used to perform the test. The machine measured load and crosshead displacement, but an additional data collection system was used to measure crack width with two LVDTs. One LVDT was attached by securing the holder to either side of the rectangular prism containing the cores using hot glue. The LVDT plungers faced upwards and bore against an aluminum plate attached to the top of the aluminum pull-off disk epoxied to the top of the core. Figure 85 shows a close-up view of the LVDT on one side of the specimen.

Figure 84: Pull-off testing setup

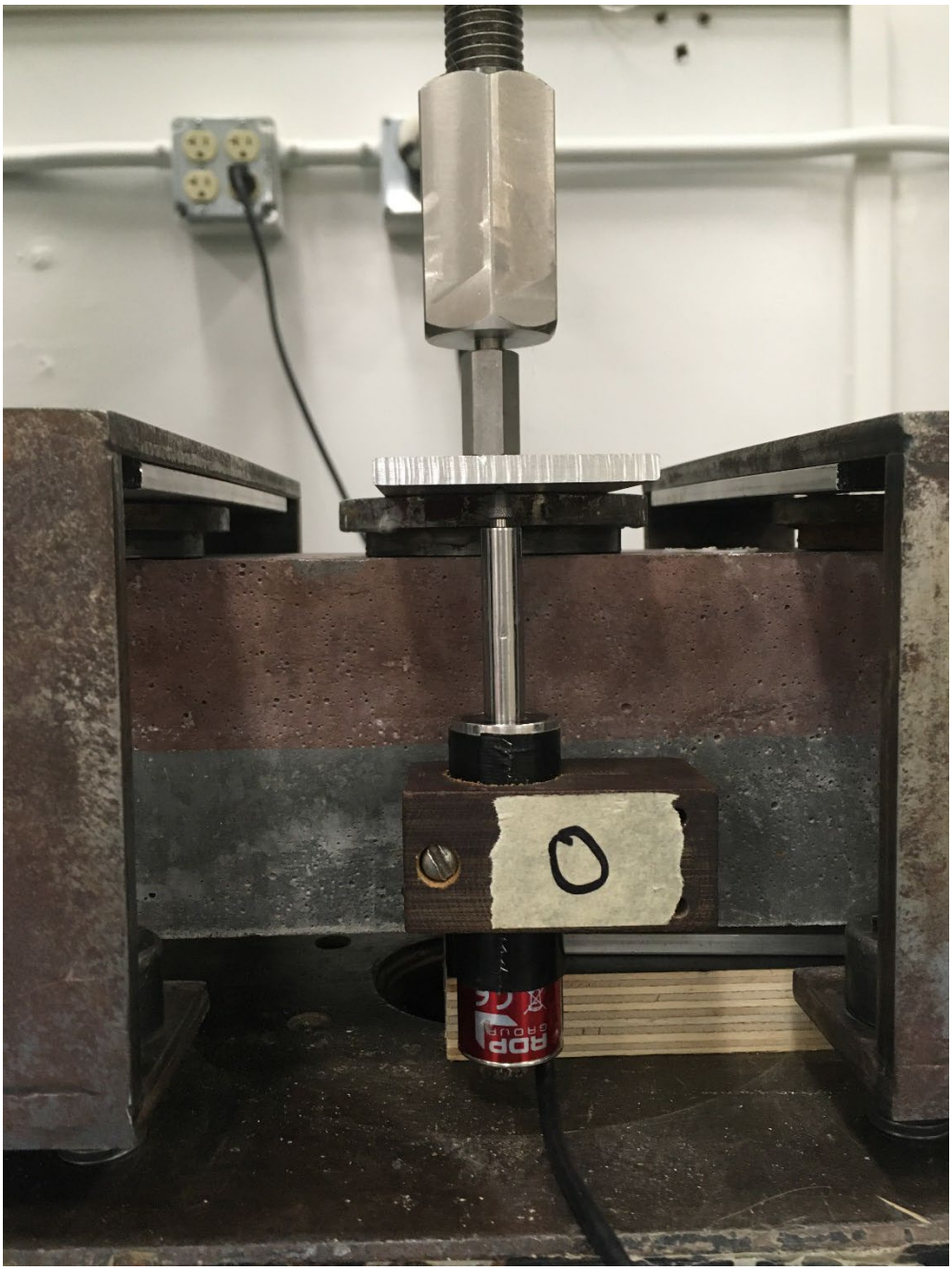

Figure 85: LVDT attached to prism bearing on plate above pull-off disk

6.3. Results

Table 36 shows the mixes from which prisms were made using the various consolidation methods. It shows the mass required for the Vicat needle to puncture through the Layer 1 elephant skin in the “Layer 1 stiffness” column. The needle for the 15-ksi mix at a 35-minute interval with concrete from different batches required all the available weights and still did not puncture through the elephant skin. Therefore, this value is denoted as 8.92+ oz (253+ g), with 8.92 oz (253 g) being the maximum load that could be added to the needle. Qualitatively, it

should be noted that the amount needed would have been significantly higher than 8.92 oz (253 g). The 18-ksi mix with a 30-minute time interval was not tested at all for core strength because the process of drilling the cores caused a break between the two layers of concrete.

Table 36: Mixes used and fresh properties

Mix Design (ksi)	Time Interval (min)	Batches for layers	Layer 1 stiffness (oz)	Layer 2 flow (in.)
18	10	same	1.0	7.9
15	10	different	1.3	7.1
18	10	different	1.3	9.5
18	20	same	2.9	6.6
18	20	different	1.5	9.4
18	30	same	5.4	4.1
15	35	different	8.9+	5.5
18	35	different	5.7	9.8

The location of each break was recorded as being either in the bottom layer, the interface between the layers, the top layer, or near the epoxy attaching the metal pull-off disk to the top of the core. Figure 86 shows some broken cores after being tested. The specimen on the top had failures from left to right at the interface, epoxy, and bottom of the core. The specimen on the bottom had all interface failures. No breaks occurred in the top layer of concrete. Most breaks, including those that occurred in the bottom layer of concrete, were brittle and therefore did not produce useful stress vs. strain data. Figure 87 shows the stress vs. strain data for a sample that broke in the bottom layer of concrete. This sharp decline in strength after cracking followed by very low strength for the remainder of testing was typical for specimens breaking in the bottom layer. Specimens breaking at the interface or at the epoxy showed an immediate drop to zero after cracking. Figure 88 the stress vs. strain data for an interface failure. Based on these results, the predominant data used to compare the specimen results were the peak stress and location of failure.

Figure 86: Concrete cores after testing

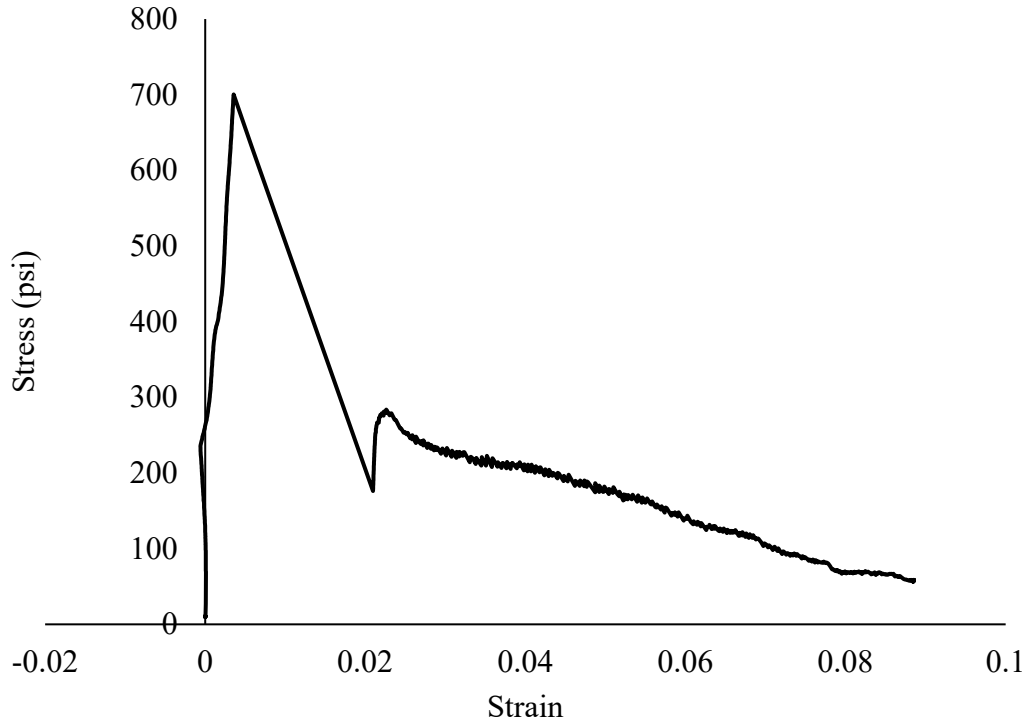

Figure 87: Stress vs. strain data for a specimen failure in the bottom concrete layer

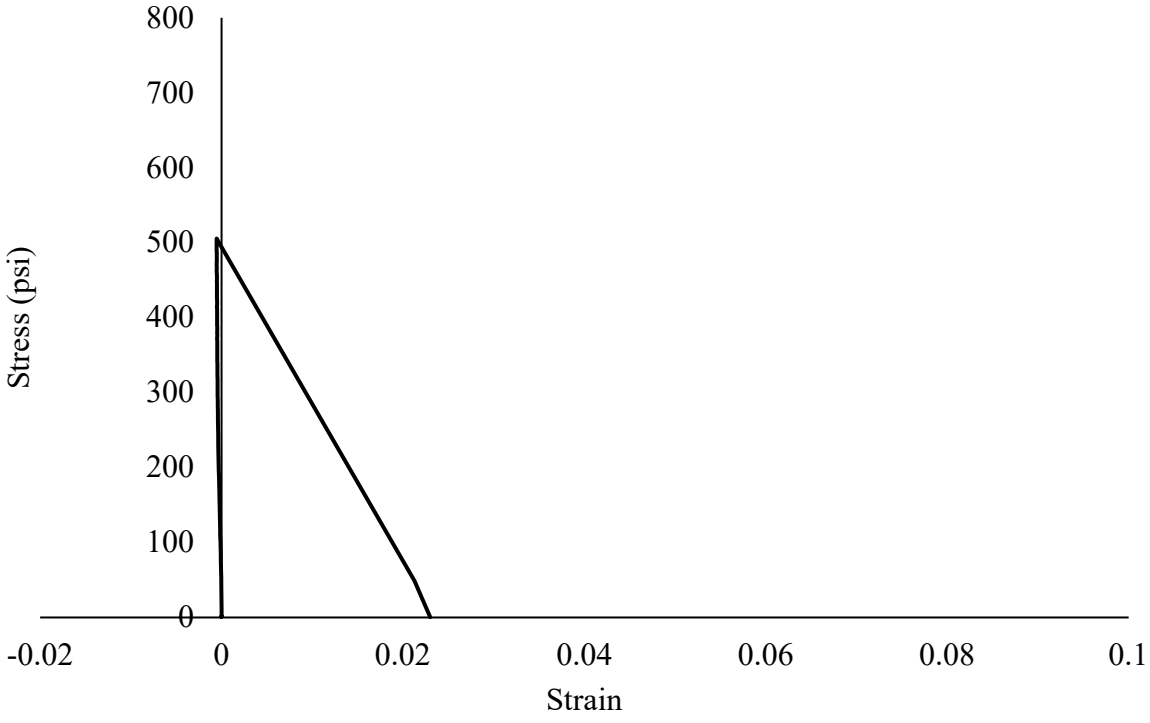

Figure 88: Stress vs. strain data for specimen failure at layer interface

The peak stress of each core is plotted in Figure 89 through Figure 91. The shape and color of each data point indicates the consolidation method used, and the shading of each data point indicates the location of the break. Figure 89 plots the peak stress and failure method with respect to the amount of time in between the placement of the two concrete layers. Figure 90 plots the peak stress and failure method vs. the weight required for the Vicat needle to puncture the elephant skin (higher values show a stiffer bottom layer) at the time the second layer was placed. Figure 91 shows the peak stress values plotted against the flow in inches of the top layer.

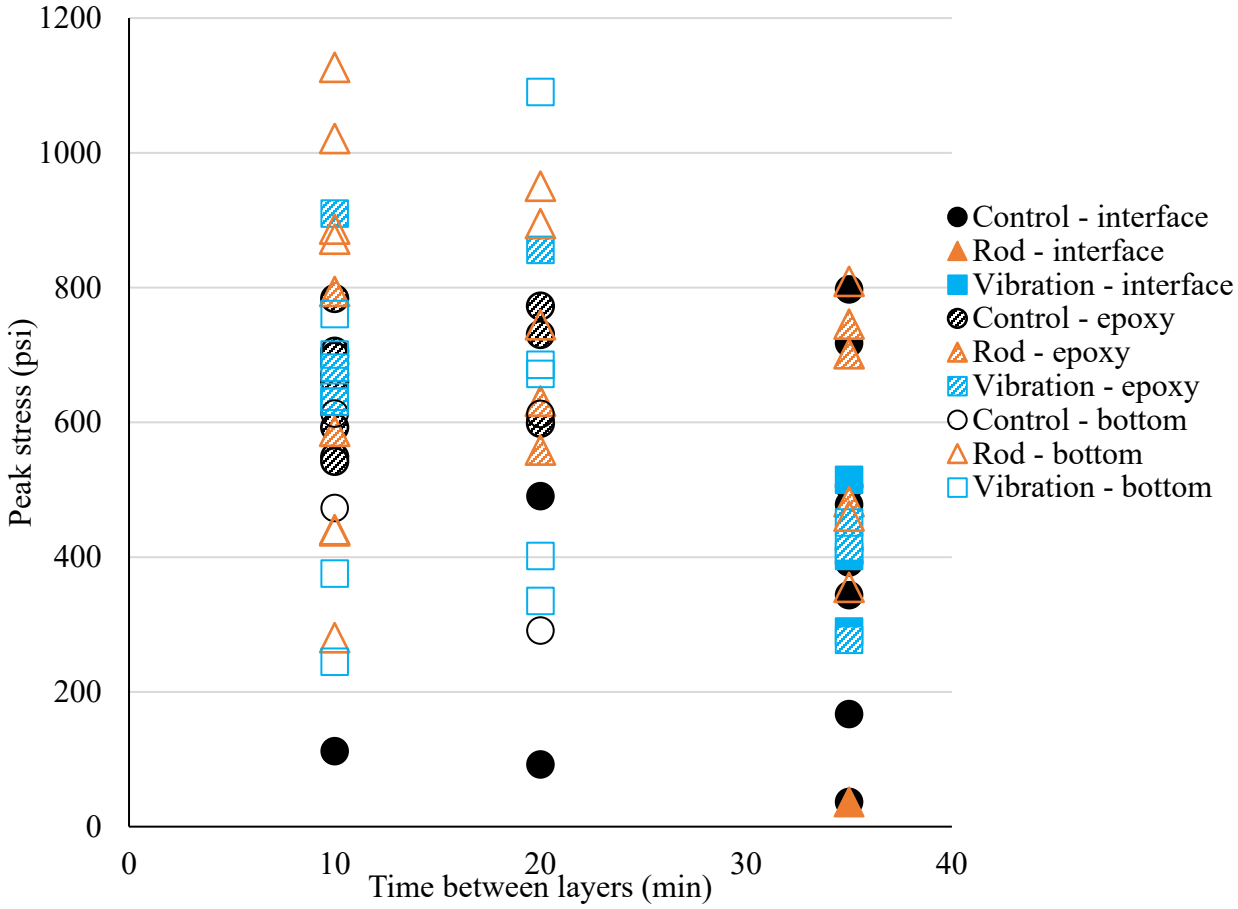

Figure 89: Core peak stress vs. time between layers

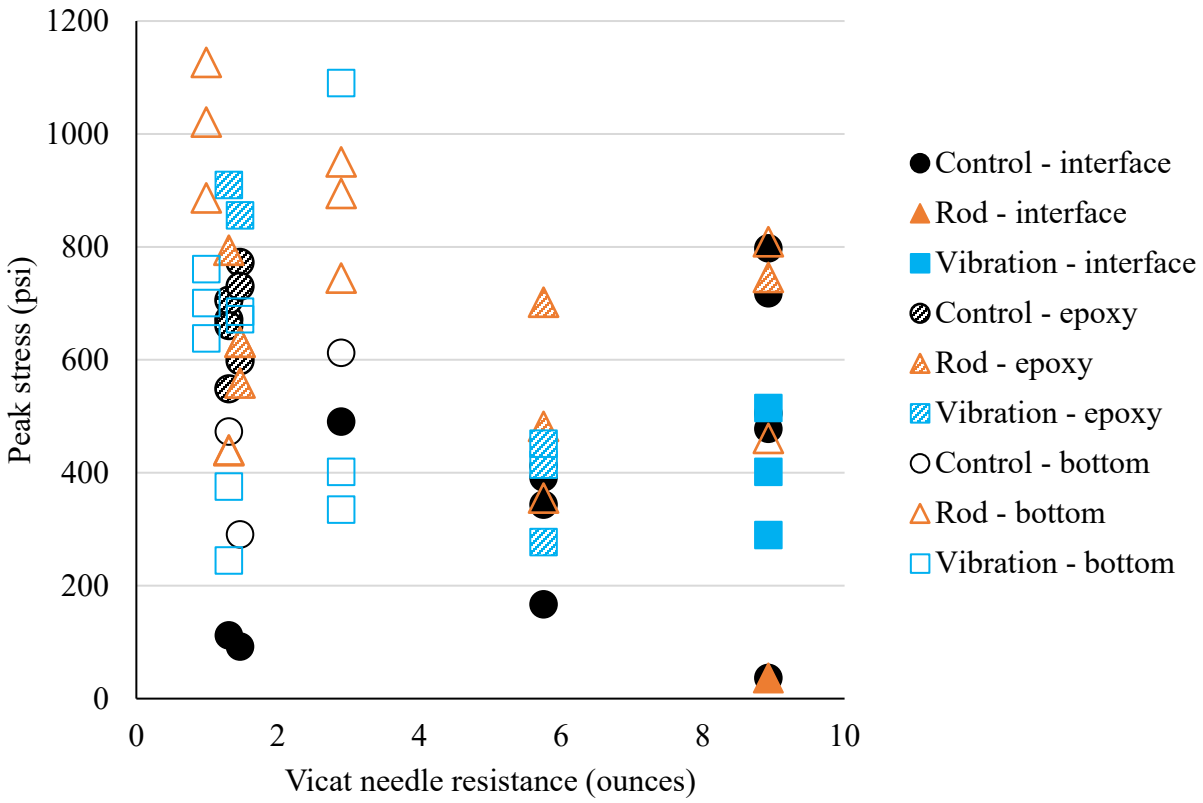

Figure 90: Core peak stress vs. first layer stiffness

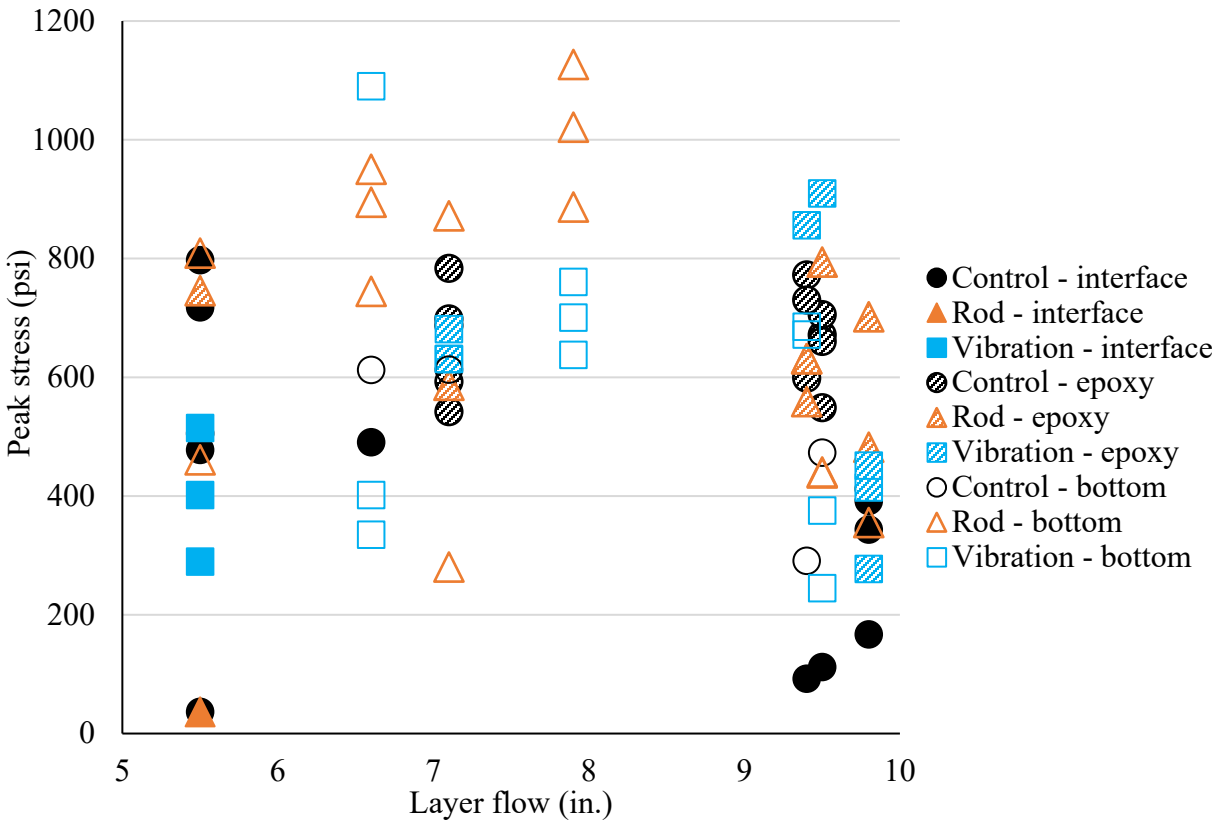

Figure 91: Core peak stress vs. flow of second layer

Figure 89 through Figure 91 show that the cracking stress for the cores was highly varied. Interface strengths ranged from 0-800 psi, epoxy strengths range from 275 psi to over 1100 psi (for specimens breaking in the concrete bottom layer, epoxy strength was higher than the specimen's maximum strength), and the strength of the concrete itself ranged from 250-1125 psi. This high variability made it difficult to draw conclusions on how the varying factors affected the bond strength. It was determined that failures in the epoxy only gave a lower-bound strength which both the interface and concrete layers would exceed. With this in mind, Figure 92 was created to give a better picture of the overall results and averages excluding specimens that broke in the epoxy. The median value for each category is shown by the horizontal line in the center of each box, while the "X" shows the mean. The box shows the interquartile range, calculated using an inclusive median.

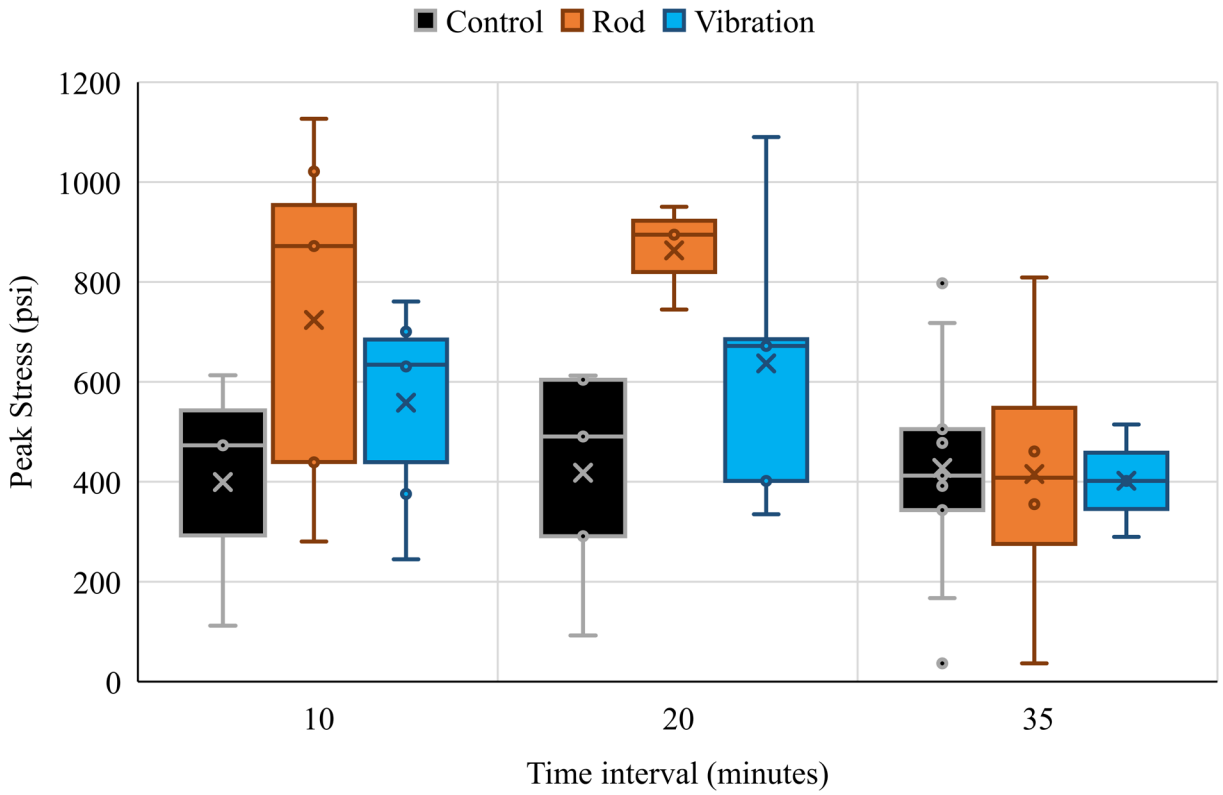

Figure 92: Box and whisker plot of non-epoxy failure strengths vs. time between layers

As Figure 57 shows, the specimens with layers placed at a 35-minute interval had the weakest average and median bond strengths. This was especially true for the specimens consolidated with rodding or external vibration. The control specimens had similarly low average breaks for all time intervals. The rodded specimens had higher strengths on average than the vibrated specimens.

Due to the very brittle nature of interface failures with low post-cracking strength, as shown in Figure 88, the percentage of core failures that occurred at the specimen interface was examined.

Table 37 shows the percentage of non-epoxy failures that occurred in the interface between layers for each combination of consolidation and time interval between layers. There are also overall statistics presented for each time interval and consolidation method. This table helps to show that at any time interval, interface failures were much more common for control specimens than they were for the rodded or vibrated specimens. In fact, none of the specimens that had been rodded or vibrated with either a 10- or 20-minute interval between layers failed at the layer interface. This table also shows a clear change in the control specimens as the time interval increased. Even though the mean and median breaking strengths for control specimens were relatively unaffected by time interval, as shown in Figure 92.

Table 37 shows how the failure locations were greatly affected by time.

Table 37: Percentage of concrete failures occurring in the interface between layers

Time interval	Control	Rod	Vibration	Overall
10 minutes	33%	0%	0%	10%
20 minutes	60%	0%	0%	23%
35 minutes	100%	25%	100%	81%
Overall	76%	7%	23%	38%

6.4. Discussion

In order to better understand the mechanisms affecting break strength and location, selected specimens were scanned using x-ray computed tomography (CT). This scanning produced multiple images of the specimens using differences in density to differentiate fibers, concrete, and air. Three-dimensional images were also produced of the specimens. The 3-D images are shown with only the fibers visible to see through a larger portion of the specimen. Most specimens scanned were cores that had already been tested, but larger sections of the prisms were used for rodded specimens to see how individual rodding motions would affect different areas of the panels.

For mixes using 2% fibers by volume, the stress vs. strain data showed surprisingly low post-cracking tensile strengths. For failures occurring at the interface, this was due to very few, if any, fibers bridging the interface between the layers. Figure 93 shows a CT scan of one of the cores after testing. A clear interface can be seen where the layers meet, and the fibers near it are preferentially oriented parallel to the interface. For failures occurring at the bottom of the core, there are three potential contributors to the low post-cracking strength: fiber orientation, edge effects from cut surfaces, and slack in the testing set-up. Fiber orientation effects from casting are believed to be the largest contributor. Previous tensile testing data from concrete with the same mix design and fiber percentage are shown in **Error! Reference source not found.** and Fi. These results showed much better toughness and post-peak strength for the same mixes, but the direct tension tests used specimens that were cast in a way to encourage fibers to align parallel to the tensile stresses. The cored specimens, on the contrary, were cut into prisms that likely preferentially oriented the fibers in a direction perpendicular to the eventual tension stresses. Research by Duque et al. on tensile tests of concrete with preferential fiber orientation showed specimens with fibers perpendicular to flow had an average post-cracking stress more than 50% lower than the average for specimens with parallel fibers [31]. Preferential fiber orientation in the horizontal direction can be clearly seen in Figure 93, especially at the layer interface. This contributed to lower stresses, especially after cracking.

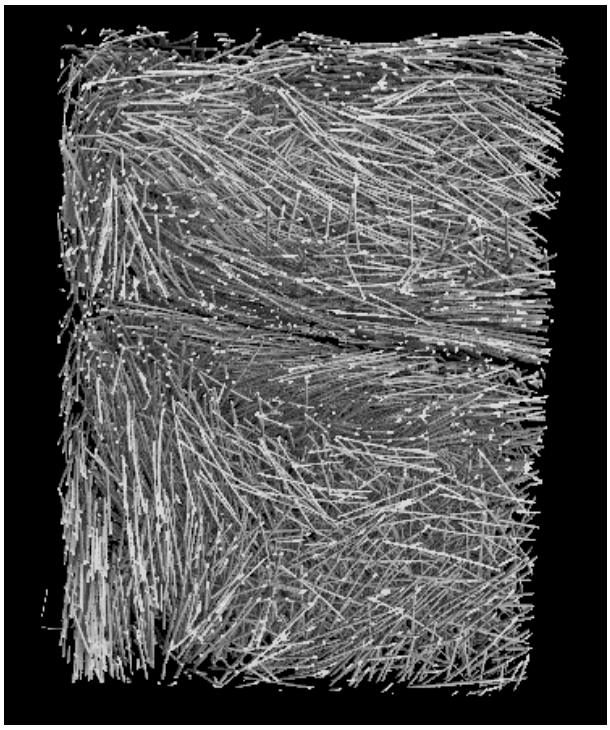

Figure 93: 3D CT scan of control specimen

An additional reason for low post-cracking tensile strengths for non-interface failures could be the fact that the fibers were being cut around the perimeter of each specimen. The French specification for flexure testing of UHPC prisms makes a point to account for fiber edge effects when calculating the cross-sectional area of a specimen [233]. This step in the calculation applies a factor of 1.2 to any area that is less than a half-fiber's length away from an edge that has been cast, to account for increased fiber alignment in the area. It applies a factor of 0.5 to any area less than half a fiber's length away from a saw-cut edge, to account for fibers being shorter on average in this region [233]. For the 2-in. diameter cores in this study, this would amount to an effective area change from 3.14 $in.^2$ to 2.45 $in.^2$, or an approximately 22% decrease in area. This area adjustment is logical to make if the strength of the concrete is due to the fibers. However, in many of the specimens tested, the failure occurred at an interface where few fibers were located, making the initial cracking strength in this study largely due to the cementitious matrix itself, for which the cross-sectional area should not be reduced due to fiber edge effects. If the area change was applied to post-cracking stress but not pre-cracking stress, a higher residual stress would be shown. If the edge effects were accounted for in the entire stress vs. strain curve, a higher overall strength would be seen, but the percentage of peak stress maintained after cracking would be the same.

The final reason for large drops in strength after cracking could be due to the tension set-up. The method for connecting the metal disk on top of the core to the testing machine involved multiple hinge connections allowing rotation in different directions, as well as two threaded connections to include the load cell and two threaded connections to attach the disk to the hinge joints. In addition, the metal straps holding the specimen down as the crosshead moved upwards did allow some movement of the specimen. These combined connections allowed a considerable amount

of crosshead displacement to occur where the majority of strain was imparted on the connections. This expansion in the connections could have released a large amount of energy to the specimen when the initial crack occurred and the straps and hinges relaxed. Figure 94 shows the data from Figure 87, but it is plotted vs. displacement instead of strain and has the addition of the machine compliance to the sample strain. When comparing the two graphs, it can be seen that a large amount of crosshead displacement occurred early in the testing that did not increase the LVDT readings of specimen expansion. This means that the crosshead displacement was adding strain to other portions of the test set-up, such as the screw and hinge connections and the metal specimen straps. When the specimen cracked, a slight drop in stress would have resulted in relaxation of the deformation in the connection components. The concrete's reduction in modulus due to cracking transferred deformation from the machine's components to the concrete specimen. This sudden increase in elongation to the concrete could have caused a shock load to the specimen, increasing the loss in stress at the time of cracking. While a strain-hardening specimen would not be as affected by this, a specimen that is already somewhat brittle would be more affected by the lack of rigidity of the setup.

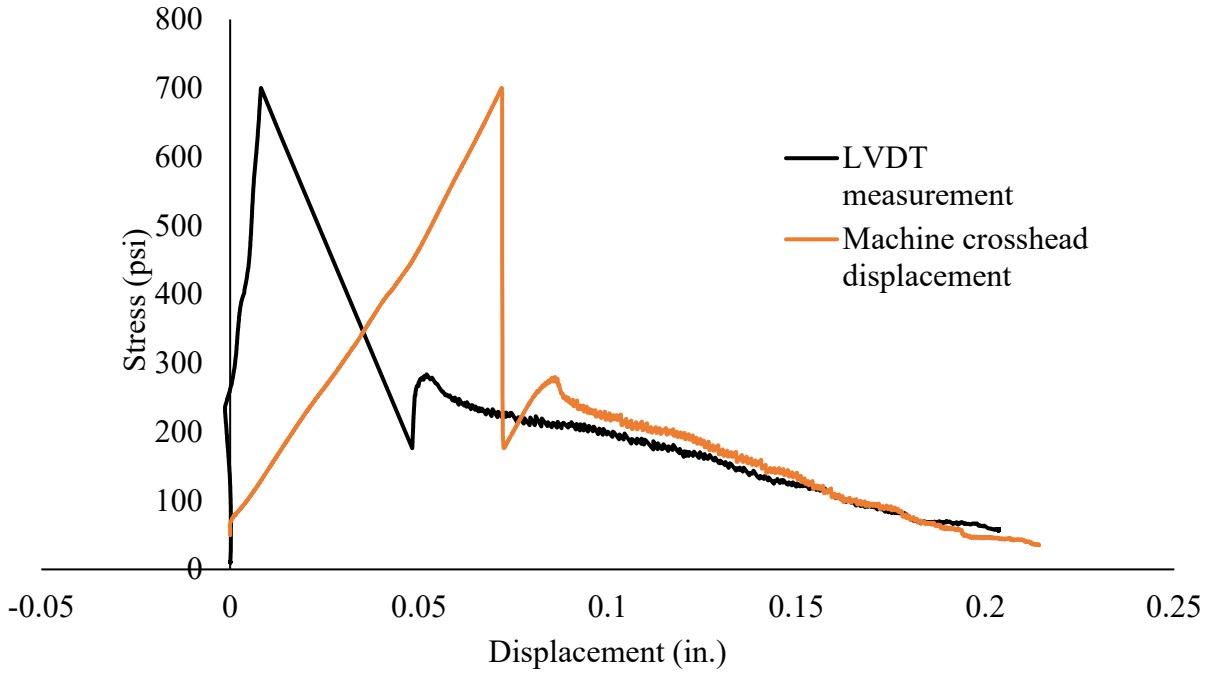

Figure 94: Comparison between displacement in machine crosshead and specimen crack width

It is possible that the strength of the epoxy bond to the concrete surface on a given day could have affected the results in Table 37 and Figure 92. It was noticed that no epoxy failures occurred the first day of testing, but subsequent testing days had epoxy failures, possibly due to variability in surface preparation. This change in the epoxy strength could have a slight influence on results because specimens with a higher epoxy bond strength would likely show a lower percentage of interface failures. The reason for this is that interface failures were typically,

although not always, lower strength failures than epoxy bond failures. Therefore, increasing the strength of the epoxy bond would likely not increase the number of interface failures as much as it would increase the number of failures in the bottom of the cores. In contrast, lower strength epoxy bonds would break before the load had a chance to reach the required breaking strength of the concrete layer. This would mean that instead of being able to record the concrete's strength, this value would be thrown out of the averaging and would not be able to count as a non-interface break. The results of interface failures seen at the different time intervals and with different consolidation methods, however, show large variations that were consistent across multiple mixes. Therefore, it is unlikely that a change in epoxy bond strength from day to day or between specimens would affect the results enough to change any conclusions.

For specimens with layers 10 and 20 minutes apart, the rodded specimens had the highest average strength. For the 35-minute specimens, average strengths were roughly equal, but the rodded specimens had a lower percentage of breaks occurring at the interface. It is theorized that this was due to the rodding motion re-orienting fibers in a vertical direction and forcing the layers to intermix. Figure 95 shows a CT scan of a specimen that has been rodded. It can be seen in the circled section that the fibers are oriented much more vertically in the location of rodding than in the surrounding sections. Figure 96 also shows this with two rodded locations (circled in red and yellow on the bottom right) that have more vertically oriented fibers. These fibers would be parallel to the tensile direction in the pull-off test, helping to increase the strength of the specimen. This would increase not only the strength at the interface, but also the strength of the individual layers of concrete, which can explain why the strength of core bottom failures increased as well with rodding. In both figures, it should be noted that the region over which the rodding affected fiber distribution was very small. Even with a rodding motion for every 9 $in.^2$ of interface area, there was still a substantial amount of space between the rod locations that were unaffected. For a larger-scale specimen, it is likely that rodding would not occur as frequently, although it is also likely that large-scale specimens will have only a small region where two separate concrete flows intersect and must be mixed. Figure 97 through Figure 99 show a large air void introduced into the concrete at the rodding location circled in red in Figure 96, for three different angle views as well as the 3-D image. A large air void was also present for the second rodded location for this specimen but is not shown in these figures. These rod air voids were only present in the shown specimen, which was rodded at 35 minutes. This particular mix had the highest Vicat needle resistance at over 253 g, so it is understandable that the stiff lower layer of concrete was too stiff to flow into the void created by the rod. While this shows a potential problem that could result from rodding a specimen, it should not be an issue if the concrete is still fluid.

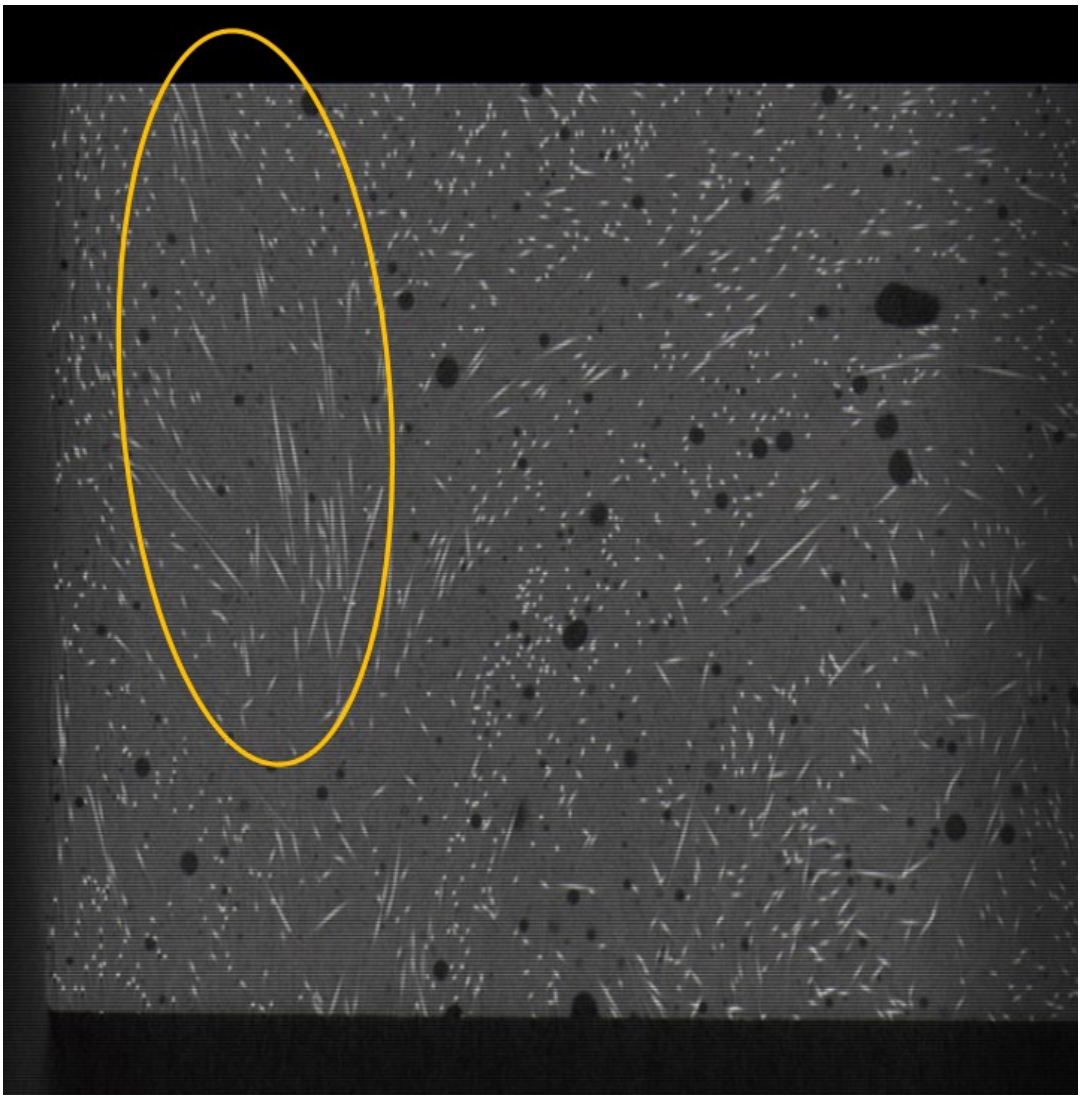

Figure 95: 2-D cross-section from CT scan of rodded specimen

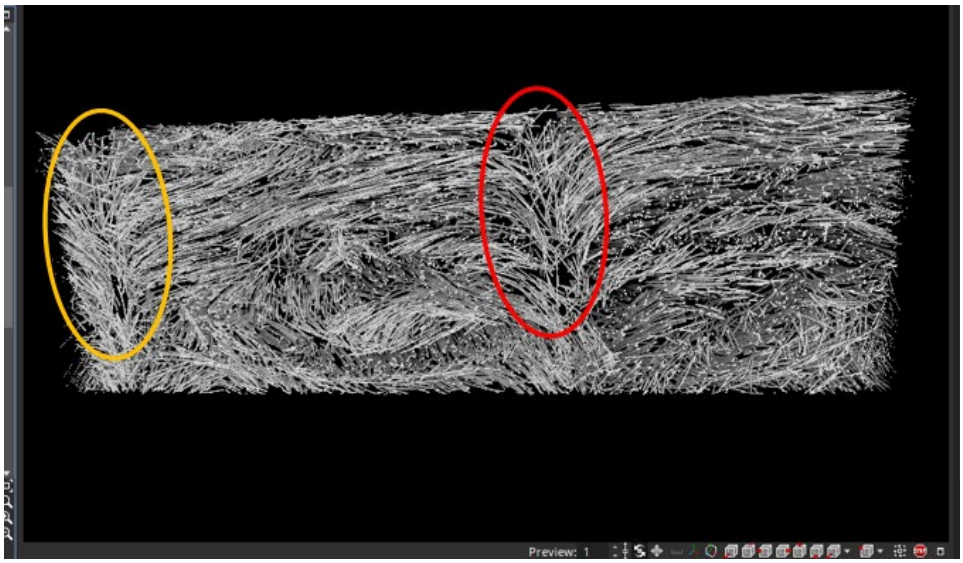

Figure 96: Changes in fiber orientation occurring at locations where concrete was rodded.

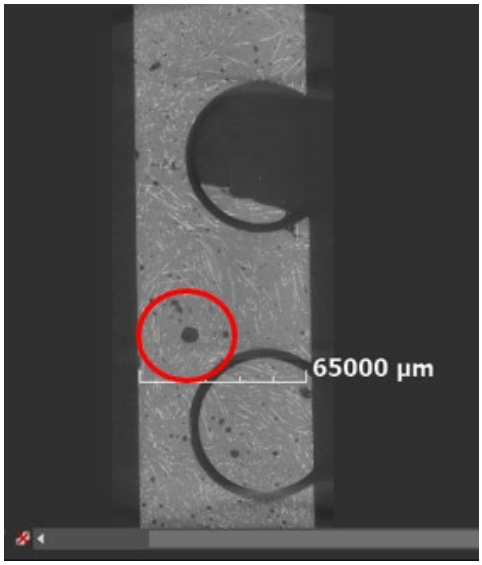

Figure 97: 2-D view (top) of large air void at location where concrete was rodded from Figure 96

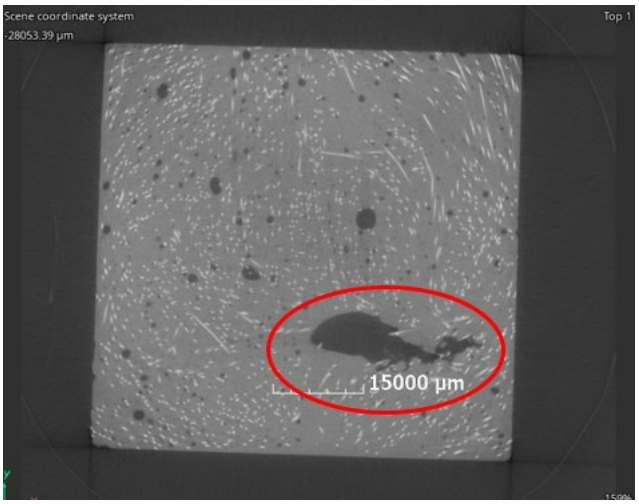

Figure 98: 2-D view (side) of large air void at location where concrete was rodded from Figure 96

Figure 99: 2-D view (front) of large air void at location where concrete was rodded from Figure 96

Figure 100 shows another defect seen in the 35-minute specimens with high layer 1 stiffness. The interface failures from this specimen showed large amounts of air trapped between the layers of concrete. While UHPC typically has significant volumes of entrained air, these voids occurred between the layers and had a flat, irregular shape instead of being spherical. As with the air in the rodded regions, these interface air voids were only seen in the 35-minute specimen with the highest layer stiffness. Surprisingly, the samples that were vibrated still had these voids, which

shows how detrimental stiff concrete can be. In addition to a stiff lower layer at the time of placement, the top layer of concrete used also had a very low flow, likely due to overmixing in a mixer different from the one used for the lower layer.

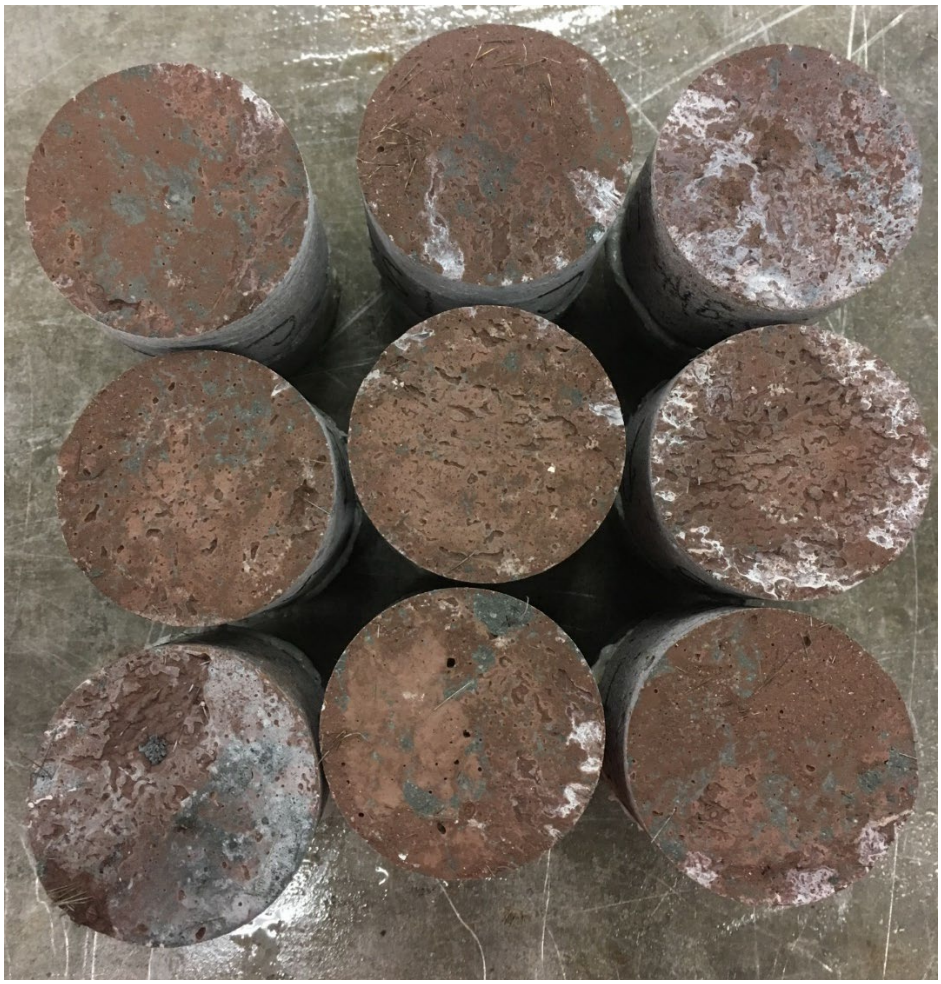

Figure 100: Cored, vibrated, and rodded specimens with air trapped between interfaces. 15-ksi and 35-minute mix

While most specimens did not experience air void defects, all of them had issues with fibers bridging the interface. Figure 93 shows a clear break in the middle of the core where the two layers meet and no fibers cross. This was common for specimens of all time intervals and consolidation methods. Figure 96 shows that rodded specimens typically had a clear “V” shape of few fibers seen in the CT scans at locations where the rod was used. Figure 101 shows a cut of a sample at the location of rodding where it is clear that the rod pushed the interface downwards instead of pushing fibers through the interface. Vertical fibers near the center of the V (circled) are clearly seen where the specimen was rodded. However, these fibers did not intersect the interface. Even without fiber bridging, however, this interface would be stronger than a horizontal interface, as it is angled with respect to the tensile force and has a larger surface area of bond.

Figure 101: Cut prism shows interface deformation due to rodding

Based on the results from this research, the researchers recommend that specification agencies limit either the time between layers or the stiffness of the bottom layer at the time of a second placement. It should be noted that there was a good correlation between the time the concrete layer was resting and its resistance to the Vicat needle, as shown in Figure 102. This correlation is logical, as increased time would increase both desiccation of the elephant skin and curing of the concrete beneath it. However, this research tested only two different mix designs, and different UHPC mixes may have different consistencies at later times. This is one advantage of using a surface stiffness test such as the Vicat needle one used here – the results are specific to the mix itself as well as any environmental factors such as temperature and humidity that could affect stiffness. While a time limit between placements would not require testing of the specimen surface, it could be difficult to determine, as one batch placement can take 15 minutes by itself to complete. A similar problem arises if a surface stiffness test is introduced, as a large concrete member could have different concrete stiffness measurements in different locations.

Table 37 shows that time difference of over 30 minutes between placements is detrimental to the integrity of the bond between those placements, especially if no consolidation method is used. For the needle test, a stiffness limit of 200 g or less of needle weight could be required to allow a second concrete placement on a specimen. For needle weights between 100 – 200 g, a consolidation method could be required after the second placement has been made.

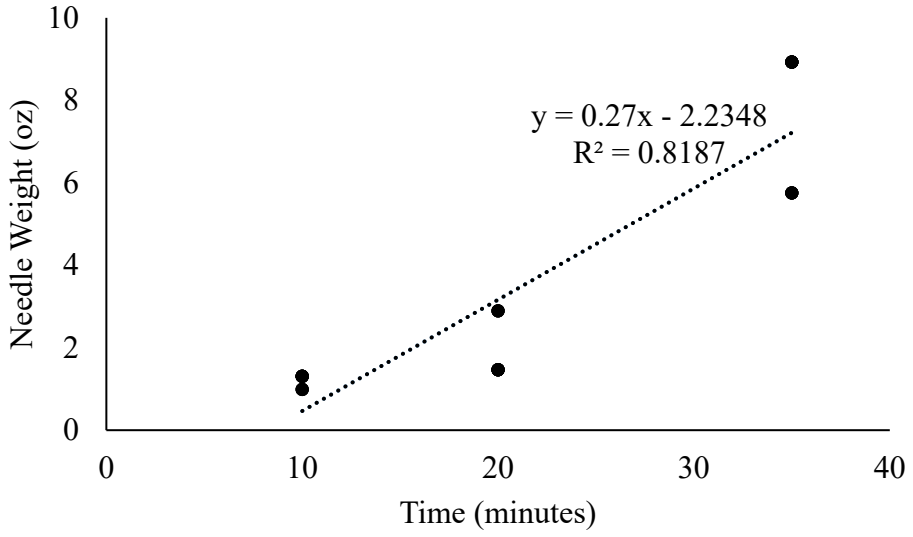

Figure 102: Relation between first layer stiffness and time

There were no apparent trends in the data comparing strength or failure location to the flow of the top layer of concrete; therefore, it is not recommended that this be specified in any way to ensure good bond. Most UHPC specifications do have a designated flow range for quality control purposes, and this should be sufficient for bond between layers as well.

6.5. Conclusions

The following conclusions were drawn from this research:

1. Concrete placed in multiple batches should be rodded or otherwise mechanically mixed at the interface between the two batches to increase bond strength and to reduce fiber alignment. Timing of rodding was found to be important; rodding after concrete stiffening, in some cases, introduced air voids into concrete.
2. Any layer effect will have fiber preferential alignment and reduced fiber content crossing layer interfaces. Concrete placed in multiple layers will ideally be placed within 20-minute of each other to improve bond strength and increase the strength in the interface.
3. A needle test used to measure surface stiffness correlated well to the amount of time between placements and helped to quantitatively indicate elephant skin thickness and/or stiffness. A similar method could be used in the field to specify limits and determine when consolidation is needed for different environmental conditions.
4. The flow of the second layer of concrete had little impact on bond strength when compared to the stiffness of the lower layer's elephant skin.

The following recommendations are being made based on the research results.

1. Concrete should be placed continuously and in a manner to minimize the area of overlap between two flows of concrete, as fibers may not bridge these interfaces even with short elapsed times.
2. Rodding should be used at locations where two layers intersect to increase strength of the interface bond.
3. A modified Vicat needle test with reduce weight, such as the method described in this research, can be used to determine when elephant skin is too stiff to mix with a subsequent placement. It is recommended that if such a test is adopted, any layer resisting a Vicat needle with more than 200 g is unacceptable for binding with subsequent layers. A lab test should be developed and used to determine acceptable resistance values for placement for individual mixtures before the concrete is placed onsite.

7. CREEP BEHAVIOR OF NON-PROPRIETARY UHPC MIXES

7.1. Background

Ultra-high-performance concrete (UHPC) is a class of high strength and high durability concrete made with fibers to provide tensile strength and toughness. UHPC has commonly been used for repair applications, road overlays, and closure strips between precast panels but is increasingly being used or considered for use in full-scale members and structures [3–5]. While proprietary UHPC blends dominated early UHPC applications, the industry has had increasing interest in the use of non-proprietary UHPCs for larger-scale applications. While non-proprietary UHPCs come with added challenges of mix development, quality assurance, and quality control, they also provide the opportunity of greatly reduced cost of materials and shipping. For companies such as precast concrete plants, developing a non-proprietary UHPC mix to be used in large volumes in production makes strong financial sense.

The creep behavior of a concrete mix has an especially influential effect on prestressed concrete member design. Deformation due to creep will increase prestress losses, thus decreasing the amount of beneficial compression that the prestressing strands add to the member. For concrete with high creep or shrinkage, this decrease in prestressing compression result in a higher net tensile stress for a flexural specimen, making it easier for cracks to form. Consequently, additional prestressing steel must be used to offset the losses, thus adversely impacting the economy of the system. For these reasons, it is important to make sure that the creep behavior of the concrete used is known and minimized.

Previous testing of UHPC creep has shown good performance, with creep coefficients in the range of 0.3-1.2 [24,99,234]. Thermally-treated UHPCs typically have lower creep coefficients in the range of 0.3-0.7 [99]. Creep tests are usually performed beginning at 28 days at a load equal to 40% of a specimen's compressive strength, but to better represent the higher loads applied to prestressed members at younger ages, researchers have also investigated UHPC creep in different loading conditions. Haber et al. found creep coefficients in the range of 0.8-2.5 for specimens loaded at 65% of their compressive strength at 7 days or less [24]. Flietstra tested proprietary UHPCs cured with multiple different methods, including one designed to mimic the conditions of a precast environment. The specimens were loaded at 60% of their compressive strength and showed low creep coefficients (0.80-1.3), although measurements were only done for 30 days [249]. Garas et al. tested proprietary UHPCs in tension and compression and found that heat treatments both 60°C and 90°C reduced tensile and compressive creep, with a stronger influence seen in tension [239].

The research presented in this paper focuses on the creep behavior of concrete cylinders placed under high loads only 2 days after mixing. The early-age loading was selected to reflect a typical age at which prestressing load is added to concrete members. The mixes used for this study were all non-proprietary UHPC mixes. They were designed to show a wide range of compressive strengths, some of which may not be classified as UHPC. A primary focus of this research was to determine if lower strength non-proprietary UHPCs would show creep coefficients similar to those reported for higher strength proprietary UHPCs; this comparison will help precasters evaluate the potential savings against the increased creep. As with many previous UHPC creep

studies, multiple curing methods were investigated in the present study. The effects of heat treatment on the behavior of non-proprietary UHPC mixes was especially of interest.

7.2. Materials and Methods

The creep cylinders were made from four different concrete mixes that used a wide variety of cementitious materials, as is common for UHPC. A fine masonry sand was used for aggregate; no coarse aggregate was used. The particle size distribution for the sand was tested using ASTM C136 [235]. The particle size distributions for the cementitious and filler materials were measured using laser particle size analysis, as shown in Figure 103. The silica fume showed two distinct particle size peaks, which is likely due to agglomerated particles being categorized as larger particles. The silica fume was dispersed with an ultrasonic wand for 7.5 minutes prior to analysis. The results agree well with particle size distributions from other studies following the use of dispersion techniques [250].

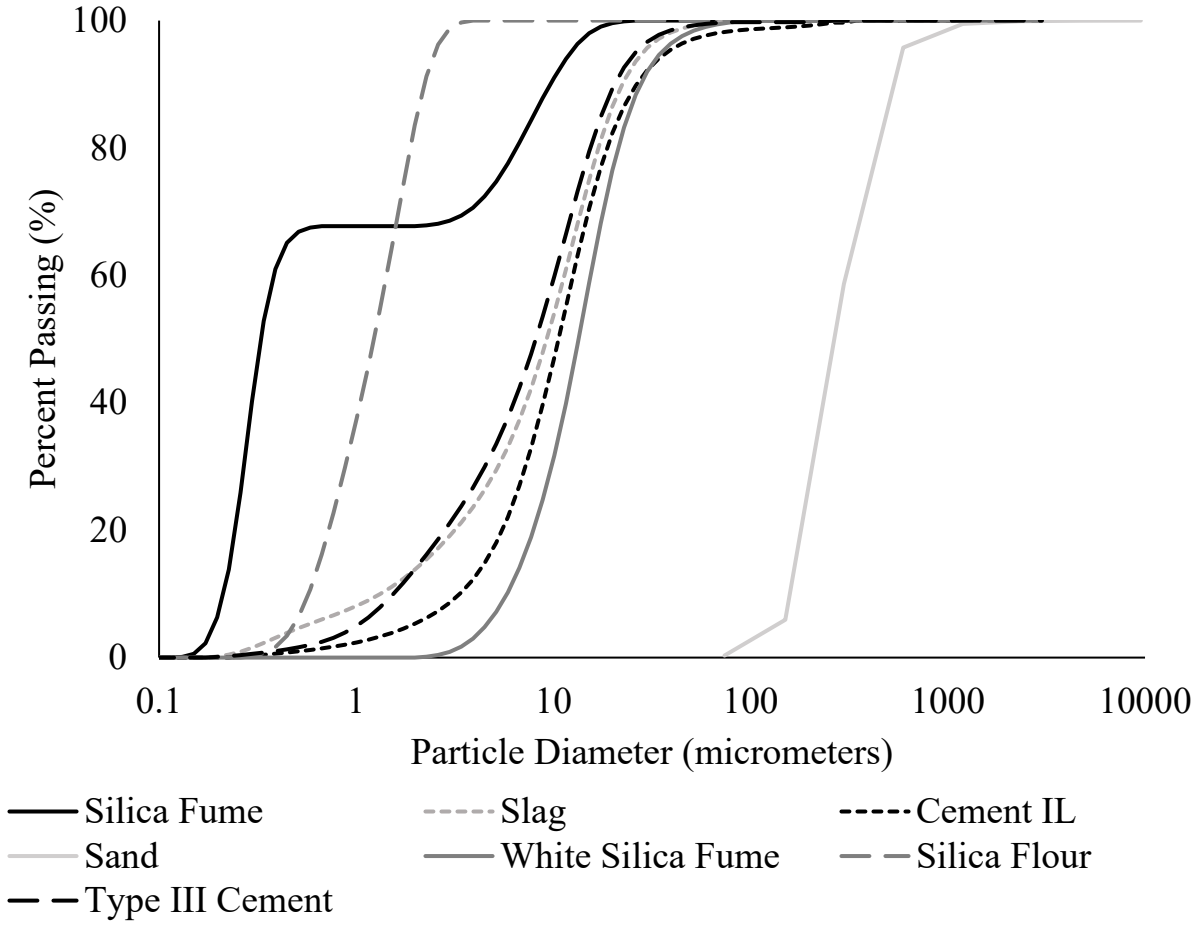

Figure 103: Particle size distribution

The cement phase composition was quantified using X-ray diffraction (XRD). A PANalytical X'Pert powder diffraction machine was used for scanning, and the software Profex was used for analysis with Rietveldt refinement. The scans were run using a maximum step size of 0.016 with each step lasting at least 10 seconds. The scans were performed over a 2θ angle range of 8°-80°

with a current of 40mA and a 45kV voltage. Table 38 shows the results of the analysis for the two cements used.

Table 38: Percent Cement phase compositions from X-ray diffraction

Phase	Type IL Cement	Type III Cement
Alite	44.3	53.0
Belite	23.2	16.4
Aluminate	4.2	4.1
Ferrite	11.2	13.8
Bassanite	0.5	5.2
Gypsum	5.1	1.1
Calcite	11.7	2.3
Anhydrite		1.6
Arcanite		0.5
Syngenite		0.9
Thenardite		0.5
Quartz		0.6

X-ray fluorescence (XRF) was used to measure the oxide composition of the cementitious and filler materials used in the mixes. Table 39 shows the results of this analysis.

Table 39: XRF material composition, percentages

Parameter	Type IL Cement	Type III Cement	Slag	Silica Fume	White Silica Fume	Silica Flour
SiO_2	18.82	20.00	34.79	80.45	96.49	98.88
TiO_2	0.22	0.22	0.64	0.02	0.02	0.01
Al_2O_3	4.79	4.90	13.17	0.48	1.37	0.17
Fe_2O_3	3.10	3.30	0.78	4.78	0.16	0.01
MnO	0.06	0.13	0.32	0.44	0.00	0.01
MgO	0.80	1.00	4.66	10.43	0.01	0.01
CaO	62.85	63.30	43.71	0.95	0.00	0.01
Na_2O	0.08	0.12	0.19	0.18	0.07	0.01
K_2O	0.25	0.38	0.41	0.77	0.02	0.02
P_2O_5	0.41	0.49	0.04	0.03	0.23	0.01
SO_3	3.02	3.70	3.00	0.07	0.00	0.01
ZnO_2	0.00	0.05	0.00	0.00	0.43	0.00
LOI	5.45	2.44	0.02	2.93	0.66	0.27

Four different mix designs were used for creep samples, each with a different target strength. The mixes were developed to reach their target strength ranges by 28 days with standard lab curing methods. The mix designs and their target strengths are shown in

Table 40 for the mixtures up to 21 ksi in strength, and Table 41 for the mixture above 21 ksi in strength. The industry standard is to not include silica flour in UHPC w/cm calculations. Consequently, the w/cm given in Table 41 did not include silica flour in the cementitious material calculations.

Table 40: Mix proportions for lower strength mixes

Material	12-15 ksi lb/yd^3	15-18 ksi lb/yd^3	18-21 ksi lb/yd^3
Fine Masonry Sand	1856	1815	1588
IL Cement	1583	1404	1597
Slag	-	272	309
Silica Fume	83	136	155
Water	417	362	335
HRWR admixture	10.9	16.4	30.9
HRWR and workability-retaining admixture	10.9	16.4	30.9
Surface-enhancing admixture	2.1	3.4	5.2

Table 41: Mix proportions for 21+ ksi mix design

Material	21+ ksi lb/yd^3
Fine Masonry Sand	1361
Cement, Type III	1477
Silica Flour	369
White Silica Fume	369
Water*	288
HRWR admixture	46.1
HRWR and workability-retaining admixture	40.4
Corrosion inhibitor admixture	23.1

*After adjusting water added to account for admixture water and SSD sand, 75% of the water by mass was added as ice.

The mixes were made in a vertical-shaft high-shear mixer with batch sizes of 0.81 ft^3. All mixes used 0.50 in. (13 mm) long and 0.008 in. (0.2 mm) diameter straight high-strength steel fibers at 2.0% by volume.

Specimens from each of the four mix designs were cured with three different methods designated as *lab*, *precast*, and *steam* curing, resulting in 12 different combinations of mix designs and curing methods. *Lab* curing is defined as curing at 68°F to 78°F (20°C to 26°C) in the molds for the first day, followed by removal from the molds and storage at 72°F to 75°F (22°C to 24°C) with 46% to 54% relative humidity until testing. Because loading occurred at 2 days and the specimens needed to be dry in order to attach the gauge points before testing, curing in a moist condition until the age of 7 days according to ASTM C512 was not done [20]. *Precast* curing was designed to mimic the conditions a large precast UHPC member would experience in the field. For this method, specimens were cured for 4 hours in the molds and then placed (still in

their molds) inside a sealed container in an oven at 158°F (70°C). They were then removed at 22 hours and left to cool, followed by storage in a shrinkage room at 72-75°F (22-24°C) and 46-54% relative humidity. Steam-cured specimens were cured in the molds at 68-78 °F (20- 26°C) for 24 h. Molds were then removed, and the specimens were placed in sealed containers above a water bath in an oven at 194°F (90°C) for the following 24 h; this created a high humidity environment that simulated steam curing. While most UHPC heat treatment is done for 2 days, this study only steam-cured specimens for 1 day after demolding to allow the specimens to be loaded on the second day. Figure 104 shows a graph of temperature vs. time to depict the different curing procedures.

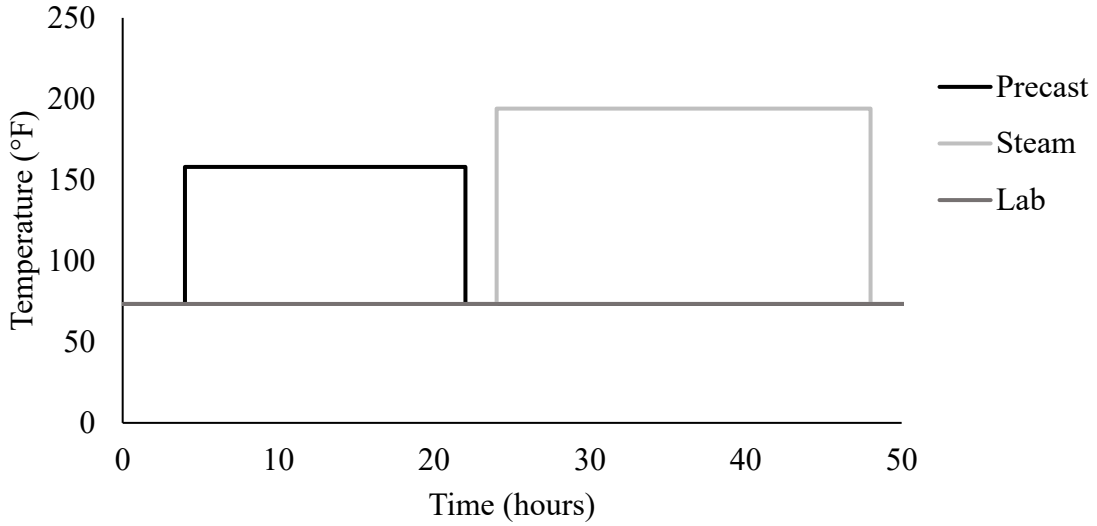

Figure 104: Curing method temperatures

Nine cylinders from each mix design were made for each curing method, totaling 27 cylinders for each mix. Of these cylinders, 2 were used for creep testing, 2 were used as control cylinders, and 3 were tested in compression at the time of loading. This is in accordance with ASTM C512, which requires at least 2 cylinders for creep, control, and compression [20]. The remaining two cylinders were spare cylinders kept in case cylinders were damaged during loading; however, no spare cylinders were needed for any of the 12 mixes. In accordance with ASTM C1856, the cylinders made were 3 in. in diameter by 6 in. long, and the ends were ground prior to testing [59].

After grinding, positive gauge points were applied to the surface of each creep and control cylinder. Three gauge lines spaced at 120° increments around the circumference of the cylinders were used. The gauge lengths were 4.1 in. An aluminum template with notches for gauge points was fabricated to consistently apply the gauge points to the cylinders' surfaces at the same interval. Figure 105 and Figure 106 show the gauge point application procedure. The control cylinders were covered on the top and bottom ends with epoxy to prevent moisture loss during the loading period.

Figure 105: Gauge points with epoxy are placed in template notches

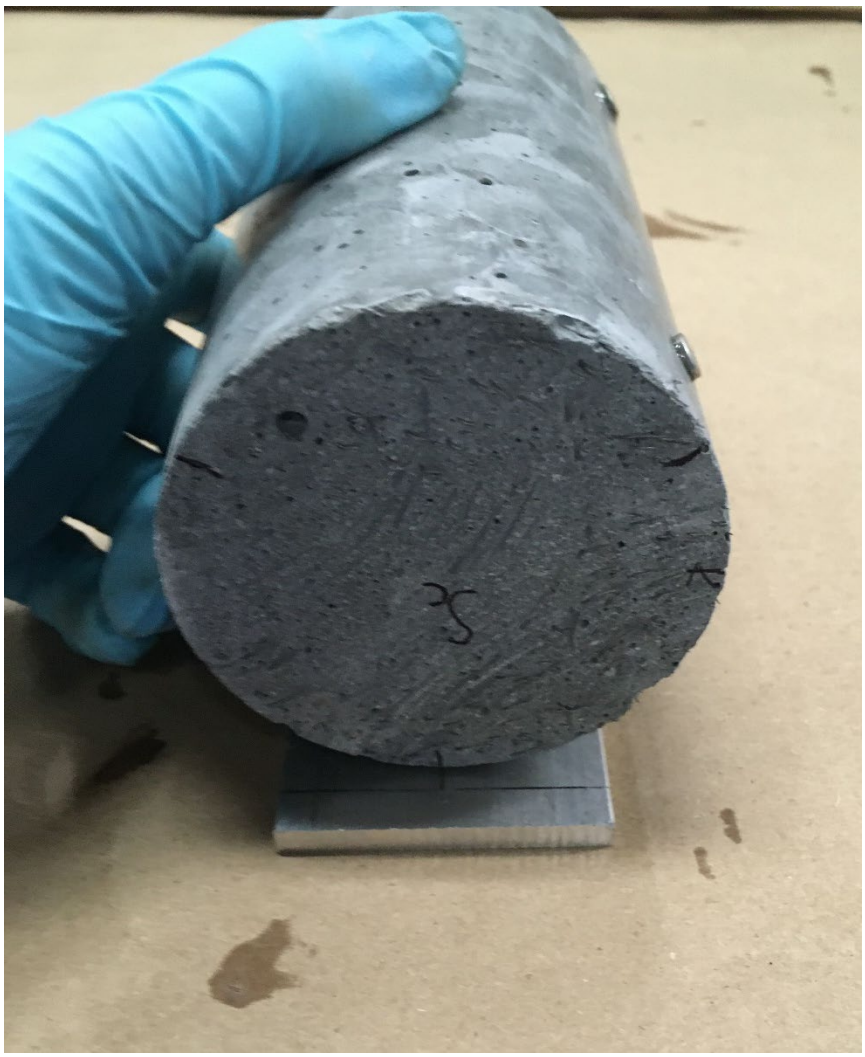

Figure 106: Cylinder is lined up on template to adhere gauge points

The concrete cylinder compressive strengths were determined before loading. Instead of loading the creep cylinders to 40% of their tested compressive strength, the testing was designed to mimic the methods used to fabricate prestressed concrete members. In this procedure, specimens were tested to see if they had met a certain pre-determined target compressive strength. The target used was 10,000 psi. If the specimens had an average compressive strength of at least 10,000 psi, they were then loaded at 65% of this strength in the creep frames, or 45,950 pounds. While ASTM C512 specifies loading creep specimens to 40% of their compressive strength [20], many concrete members are stressed at percentages much higher than this, thus a 65% load was used. For specimens that did not meet the required 10,000 psi compressive strength at 2 days, a load of 65% of 8,000 psi was used instead. This was applied to the 12-ksi mix specimens. While the 12-ksi precast and steam specimens did reach 10,000 psi compressive strength at 2 days, the control cylinders did not. Therefore, all 3 curing methods for the 12-ksi mixture were loaded at 65% of 8,000 psi, or 36,760 pounds.

The frames used for creep testing were spring-loaded, as shown in Figure 108. Each frame had two creep cylinders placed in line with half-length cylinders at either end to reduce stress concentrations. Milled steel platens were placed above and below the stack of concrete and the steel loading plates to ensure a uniform compressive stress over the cylinder cross-section. A spherical washer as depicted in Figure 107 was placed between the loading plate on the bottom and the lower platen to reduce eccentricities in loading. The load was increased using a hydraulic jack in line with a digital load cell which could ensure the load was within 2% of the target during measurements. After loading, bolts were hand tightened to transfer load from the jack to the four threaded rods of the frame. The jack was then released. Multiple strain readings taken while the cylinders were loaded with the bolted threaded rod connection show that there was little change in load between when the frames were bolted and when they were unbolted and being loaded completely through the jack. Readings were taken according to ASTM C512, with readings before and after loading, 2-6 hours after loading, daily for the first week, weekly for the first month, and monthly for the first year. Strain readings were also taken of the 2 control cylinders right before every reading of the creep cylinders. Before every creep reading, the load in the creep frame was transferred from the threaded rods to the jack by jacking the top plate down to within 2,000 lb of the target load, releasing the bolts, and adjusting the jack as necessary according to the load cell readings. This was done to ensure the load was maintained as the specimens deformed and to ensure readings were always being taken when the specimens were within the required 2% of the target load.

Figure 107: Milled steel platen and spherical washer

Figure 108: Two creep frames, one being loaded with hydraulic jack

Strain readings were taken with the portable strain-measuring device shown in Figure 109 and Figure 110. The strain-measuring device had a precision of 0.0001 inches. It was calibrated before each set of four cylinders (2 creep and 2 control) was measured using gauge points embedded into a metal plate, shown in Figure 110.

Figure 109: Strain-measuring device

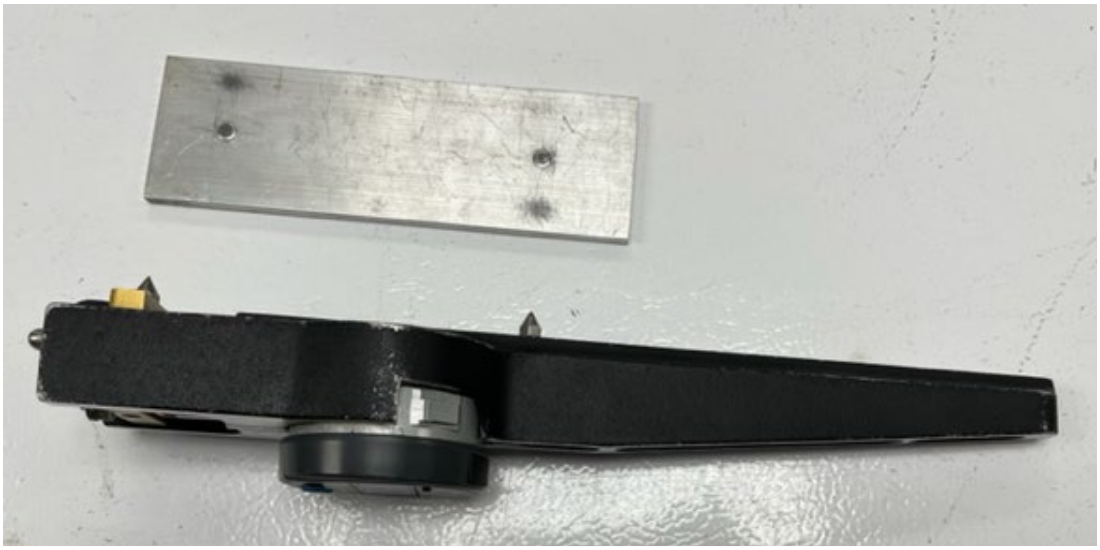

Figure 110: Side view of strain-measuring device with calibration plate

After 1 year of loading and measurement, the load was released. The specimen strains were measured immediately after unloading to measure the elastic recovery. Creep recovery readings were also taken for the first three months after the load was removed, after which additional creep recovery was negligible.

7.3. Results

The average 2-day compressive strengths for each mix design and curing method are shown in Table 42. During the initial loading of the samples, an elastic modulus was calculated by dividing the applied stress by the strain of the specimens. Table 42 also shows the elastic modulus calculated as the average of the two loaded specimens. It also shows the creep rate and creep coefficient, discussed later in this section.

Table 42: Two-day compressive strengths and creep results

Mix design (ksi)	Curing Method	Average 2-day compressive strength (psi)	Elastic Modulus (psi)	Creep Rate (10^{-8} /psi/ln(days+1))	Creep Coefficient
12+	lab	9,933	3.75E+6	5.60	1.55
12+	precast	11,303	4.64E+6	3.69	1.00
12+	steam	14,489	4.82E+6	3.15	0.87
15+	lab	10,990	2.71E+6	4.07	0.85
15+	precast	13,878	5.75E+6	2.36	0.84
15+	steam	15,042	7.54E+6	1.43	0.80
18+	lab	10,135	2.96E+6	4.00	0.92
18+	precast	16,389	5.51E+6	2.60	0.89
18+	steam	19,442	6.06E+6	1.31	0.61
21+	lab	14,390	6.18E+06	2.69	1.28
21+	precast	19,442	5.94E+06	1.48	0.48
21+	steam	21,664	7.24E+06	0.71	0.44

Figure 111 through Figure 114 show the strain due to shrinkage as measured from the control cylinders. It also shows the strain due to creep, which was calculated as the measured strain on the creep cylinders minus the measured strain on the companion control cylinders. The strain due to creep does not include the strain due to initial loading. The measurement taken immediately after loading was set as the zero point.

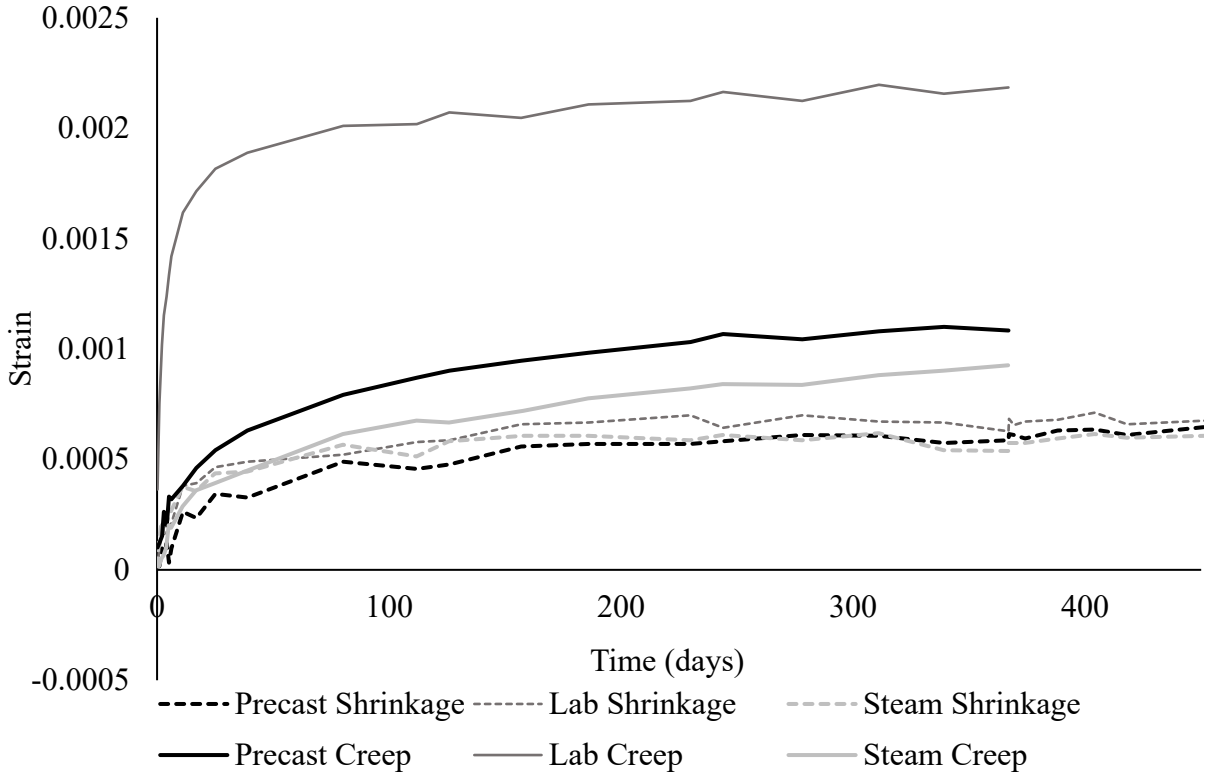

Figure 111: Post-loading strain in 12-ksi cylinders

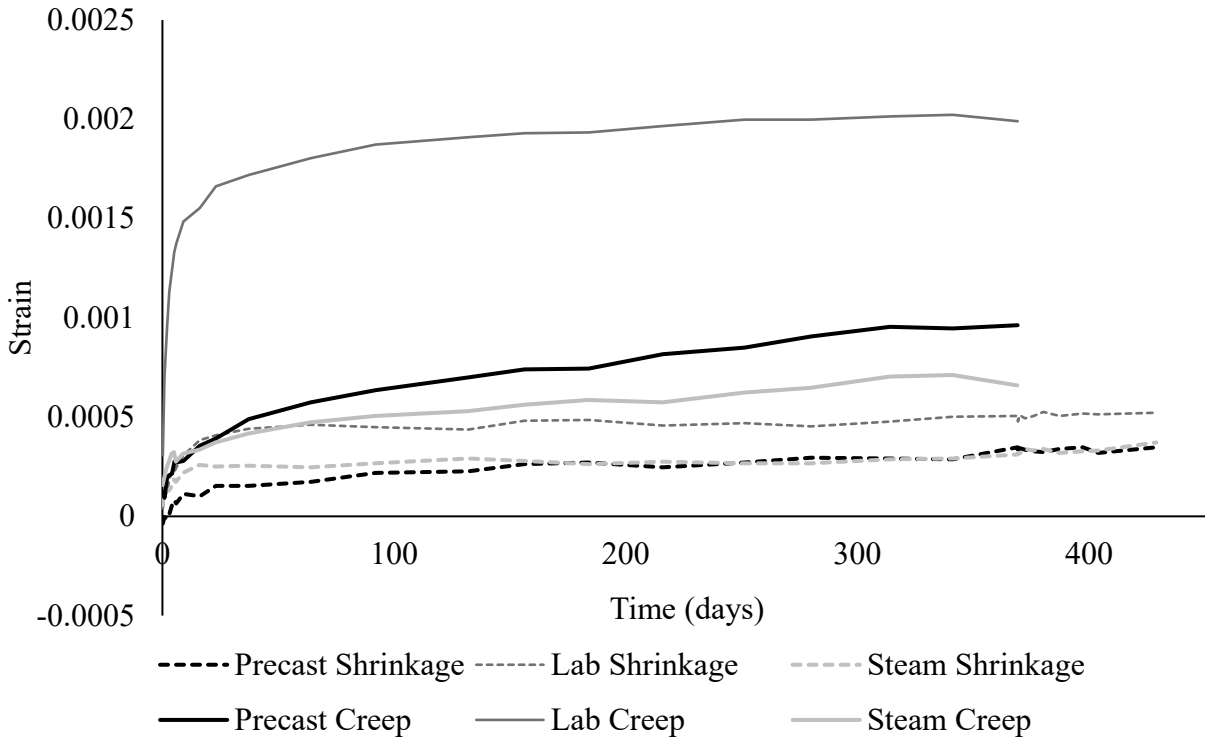

Figure 112: Post-loading strain in 15-ksi cylinders

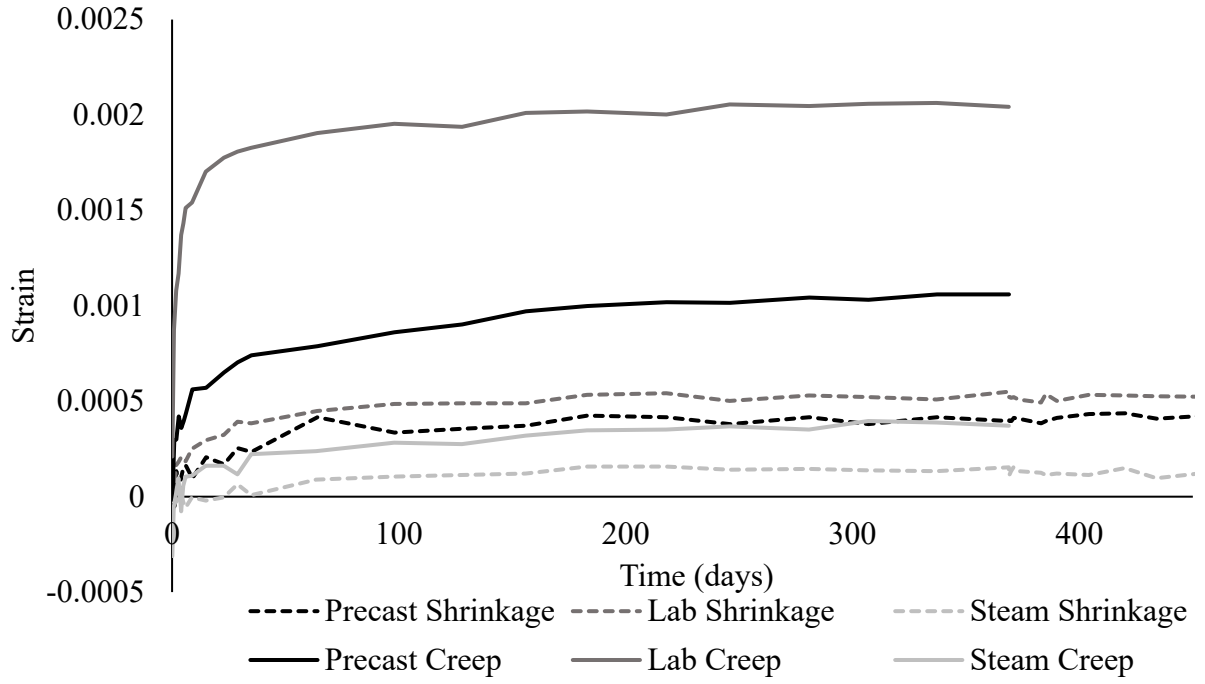

Figure 113: Post-loading strain in 18-ksi cylinders

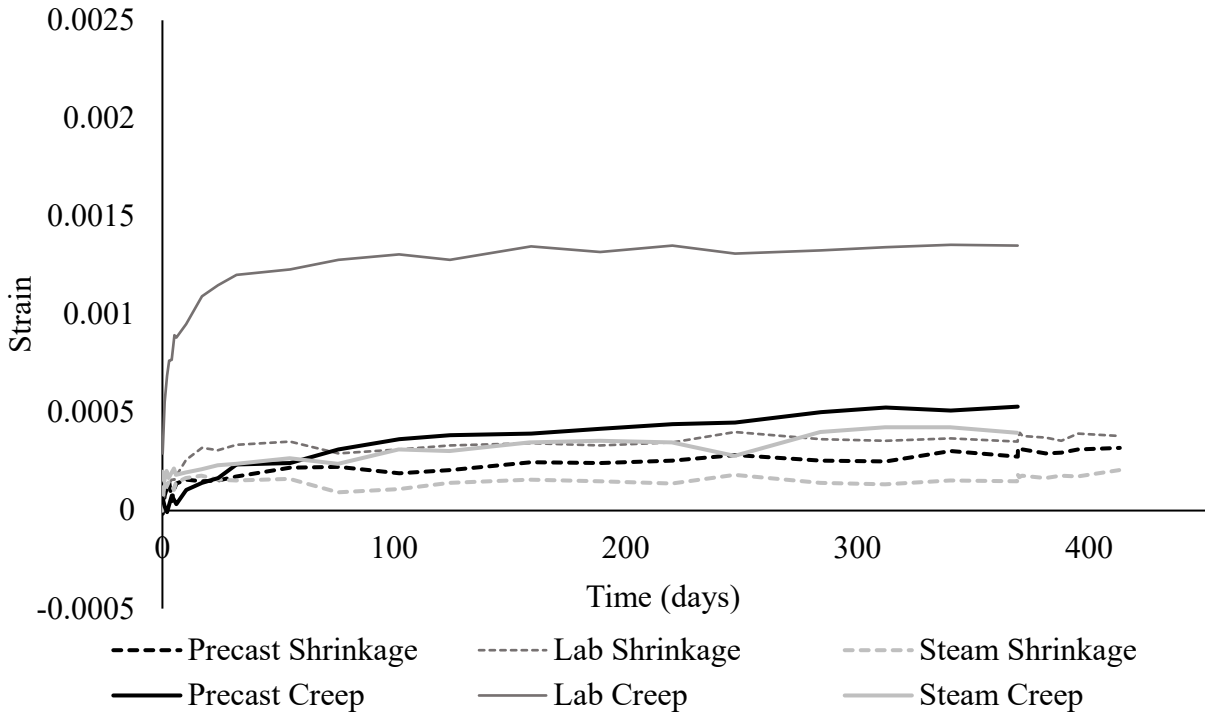

Figure 114: Post-loading strain in 21-ksi cylinders

Figure 115 illustrates and labels the distinct strain types according to their portion of the strain vs. time curve. Figure 116 through Figure 119 show the strain change over time for the creep cylinders. Included in these figures are the elastic and time-dependent strain due to loading and unloading.

Table 43 provides a tabulation of these values for each mix. Cylinders were unloaded after a full year to measure creep recovery. Figure 116 through Figure 119 show that the full initial elastic strain was not recovered; this was especially the case for the fog-cured specimens. As in Figure 111 through Figure 114, the strain measured from the control cylinders was subtracted from the strain measured in the loaded creep cylinders to account for shrinkage due to drying.

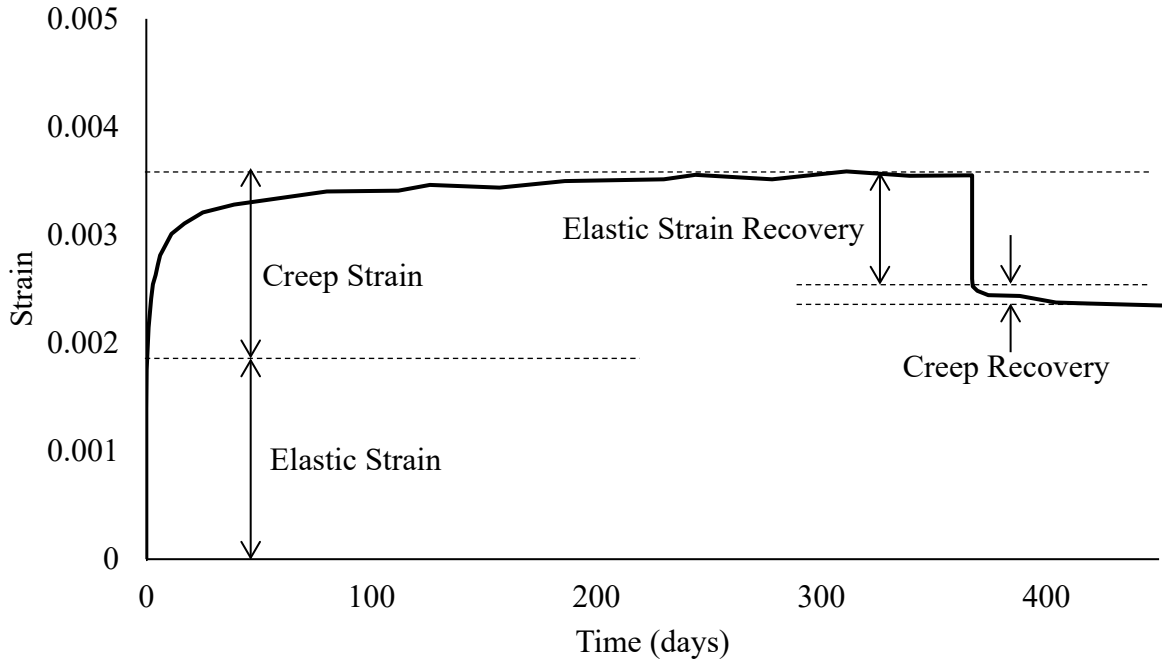

Figure 115. Strains due to creep, loading, and unloading

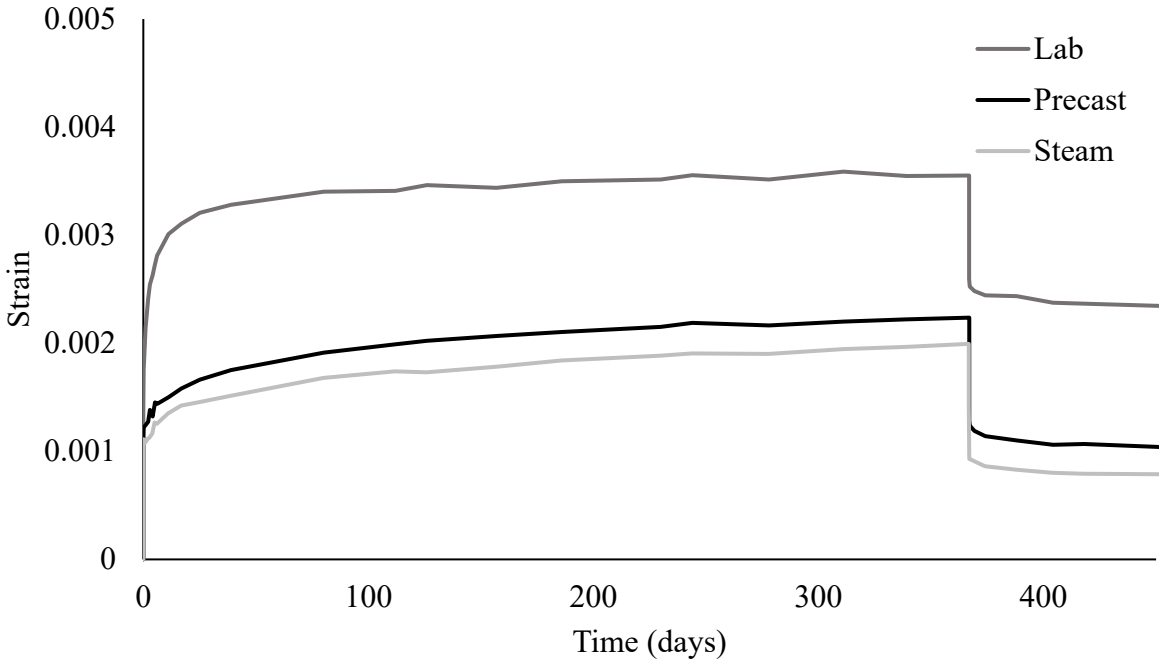

Figure 116: Strain over time for 12-ksi loaded cylinders

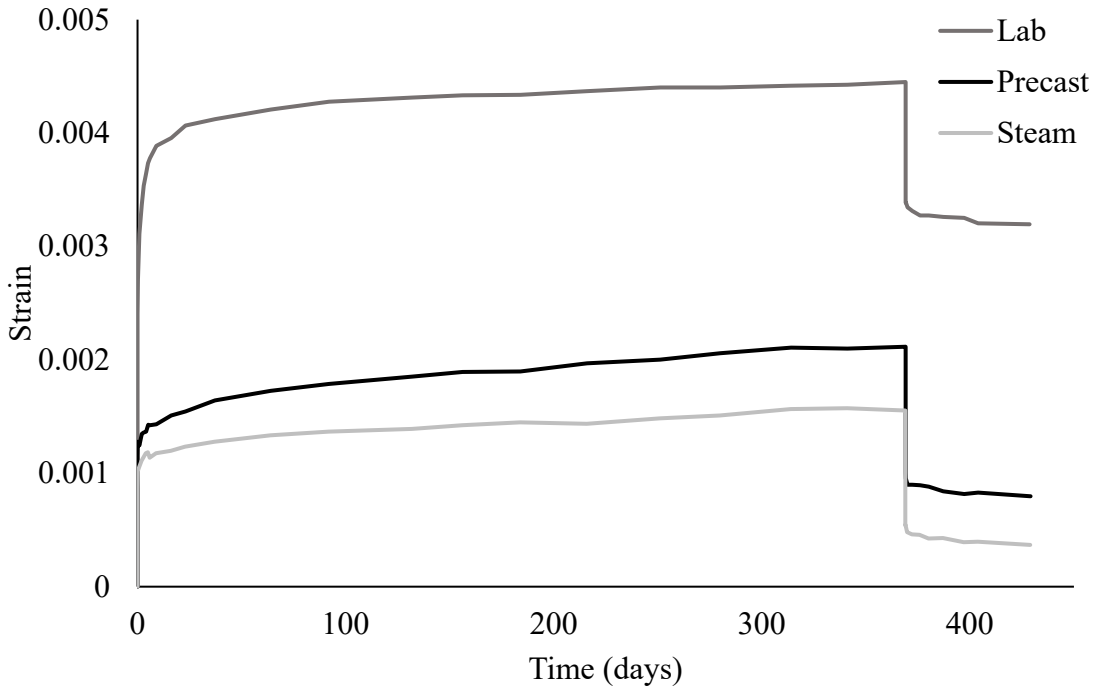

Figure 117: Strain over time for 15-ksi loaded cylinders

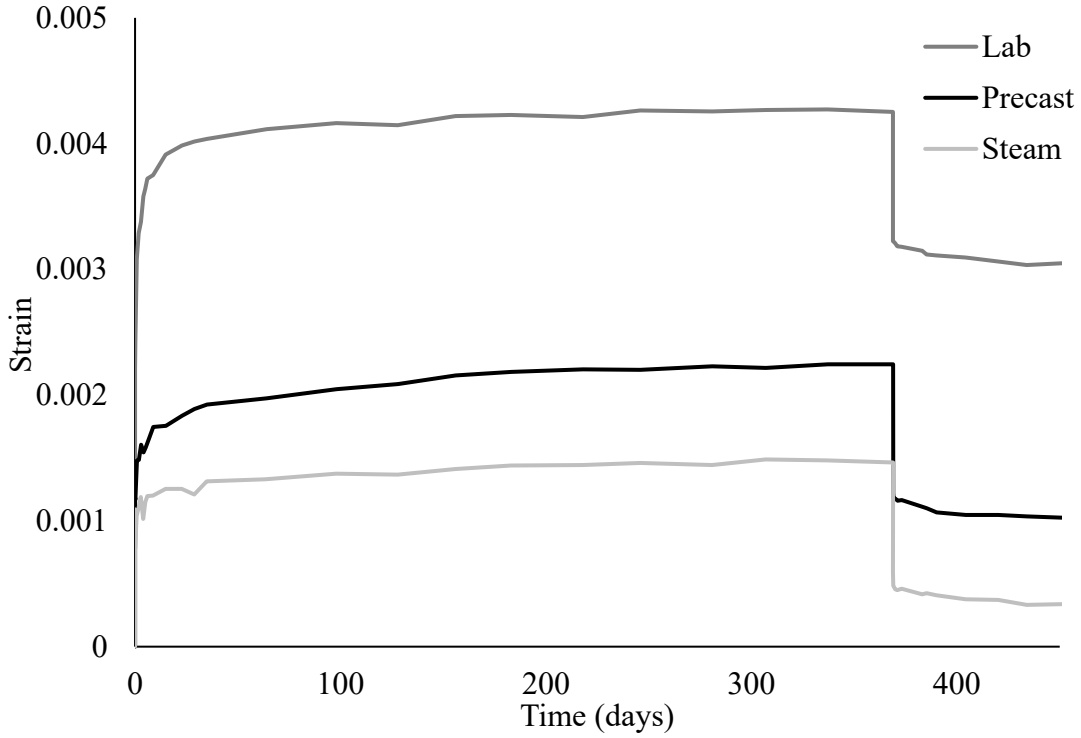

Figure 118: Strain over time for 18-ksi loaded cylinders

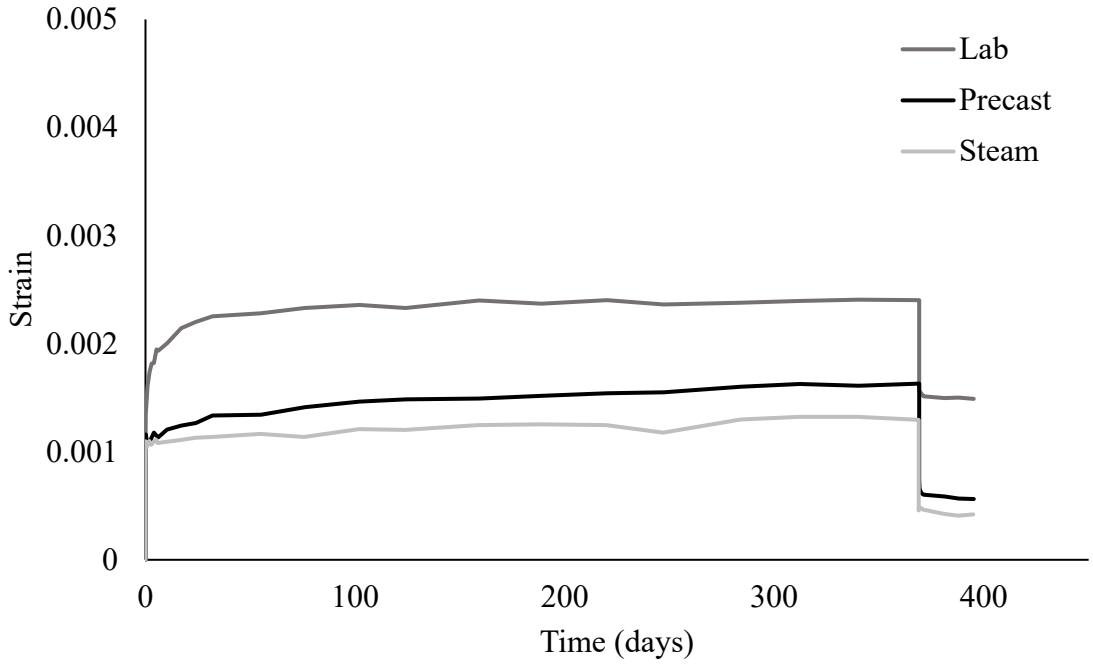

Figure 119: Strain over time for 21-ksi loaded cylinders

Table 43: Creep recovery strains compared with loaded strains

Mix design (ksi)	Curing Method	Initial loading (- microstrain)	Loading + Creep (-microstrain)	Unloading (microstraion)	Unloading + Creep Recovery (microstrain)	Unloading Strain Recovery (%)	Total Strain Recovery (%)
12+	Lab	1,392	3,552	959	1,148	27	32
12+	Precast	1,121	2,237	951	1,169	43	52
12+	Steam	1,064	1,994	587	1,169	29	59
15+	Lab	2,403	4,450	1,064	1,254	24	28
15+	Precast	1,153	2,117	1,112	1,319	53	62
15+	Steam	862	1,834	1,011	1,185	55	65
18+	Lab	2,209	4,252	1,028	1,218	24	29
18+	Precast	1,185	2,245	1,023	1,226	46	55
18+	Steam	1,092	1,464	874	1,165	60	80
21+	Lab	1,052	2,403	829	914	34	38
21+	Precast	1,100	1,630	890	1,104	55	68
21+	Steam	898	1,295	898	894	69	69

Figure 120 through Figure 123 show semilog plots with the strain per unit stress plotted against the natural log of time. This was done to find the creep rate according to ASTM C512 using Equation 22 [20].

$$\epsilon = \frac{1}{E} + F(K) \times \ln(t+1) \qquad \text{Equation 22}$$

Where: ϵ is the total strain per unit stress, [in.·(in.·psi)$^{-1}$]
E is the instantaneous elastic modulus, (psi)
$F(K)$ is the creep rate, calculated as the slope of a straight line representing the creep curve on the semilog plot, [psi·ln(day)]$^{-1}$
t is the time after loading, (days)

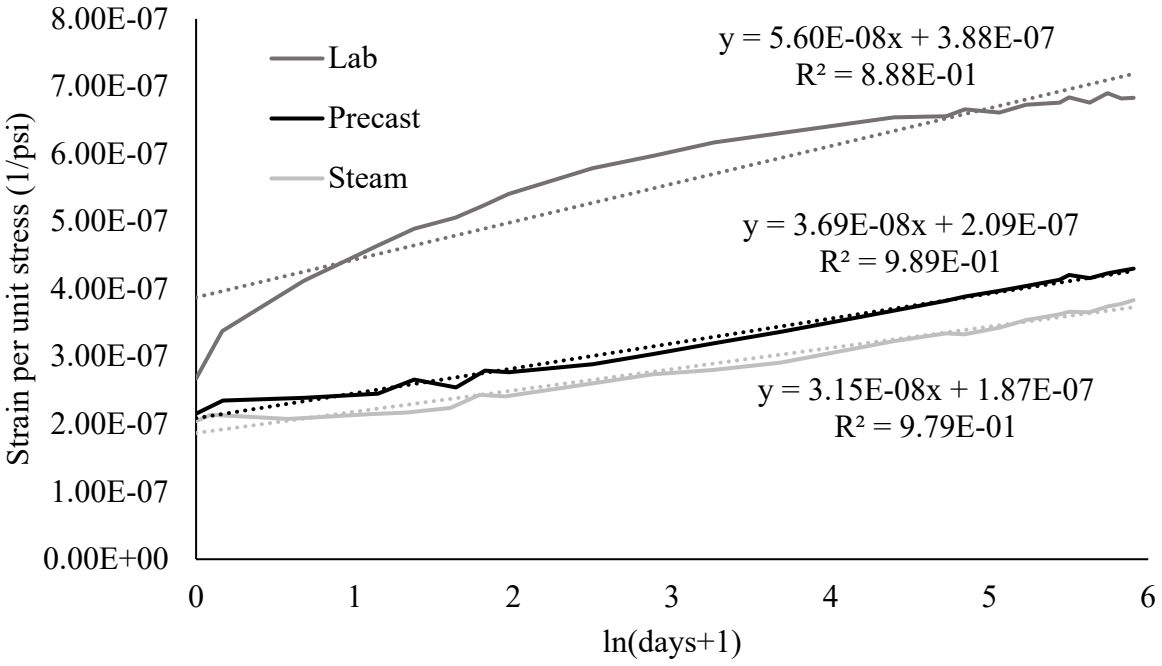

Figure 120: 12-ksi specimens semilog plot of strain per unit stress vs. time

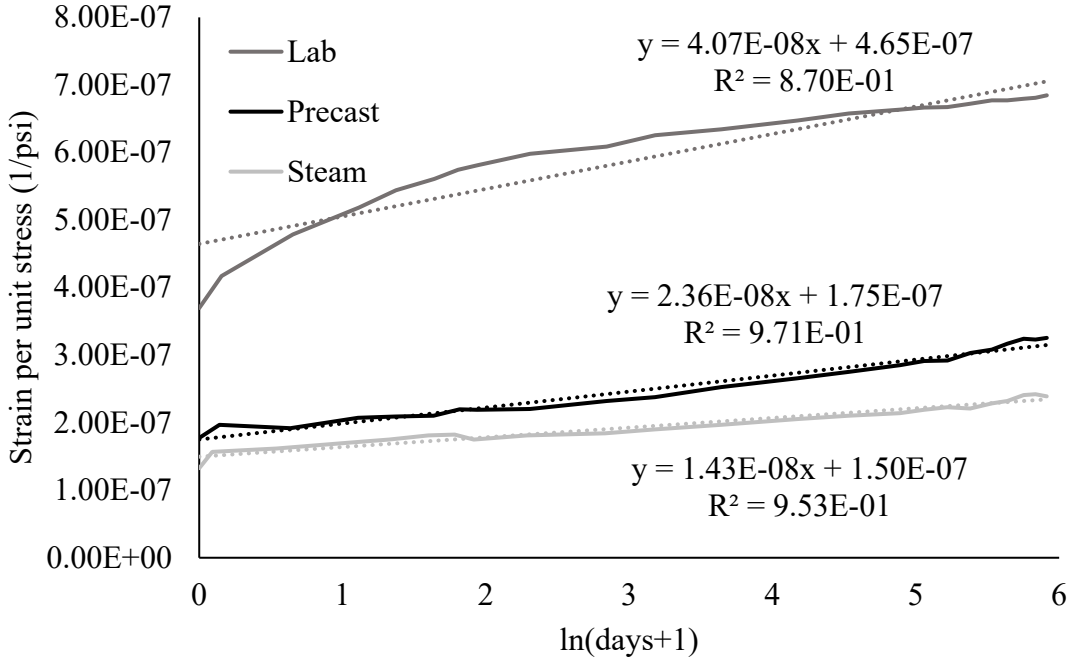

Figure 121: 15-ksi specimens semilog plot of strain per unit stress vs. time

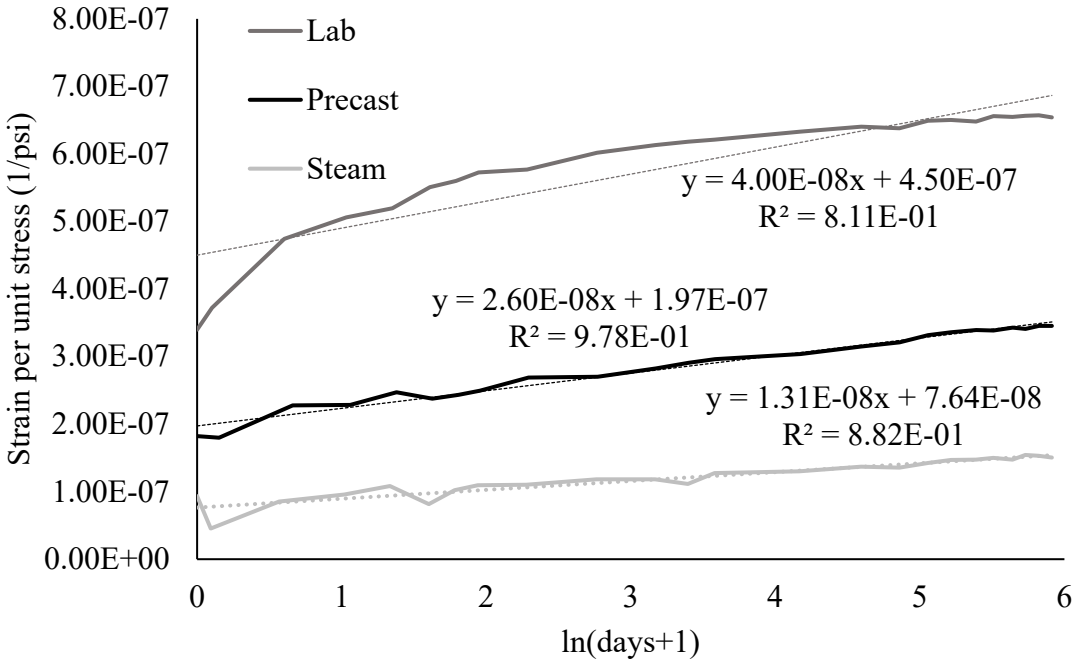

Figure 122: 18-ksi specimen semilog plot of strain per unit stress vs. time

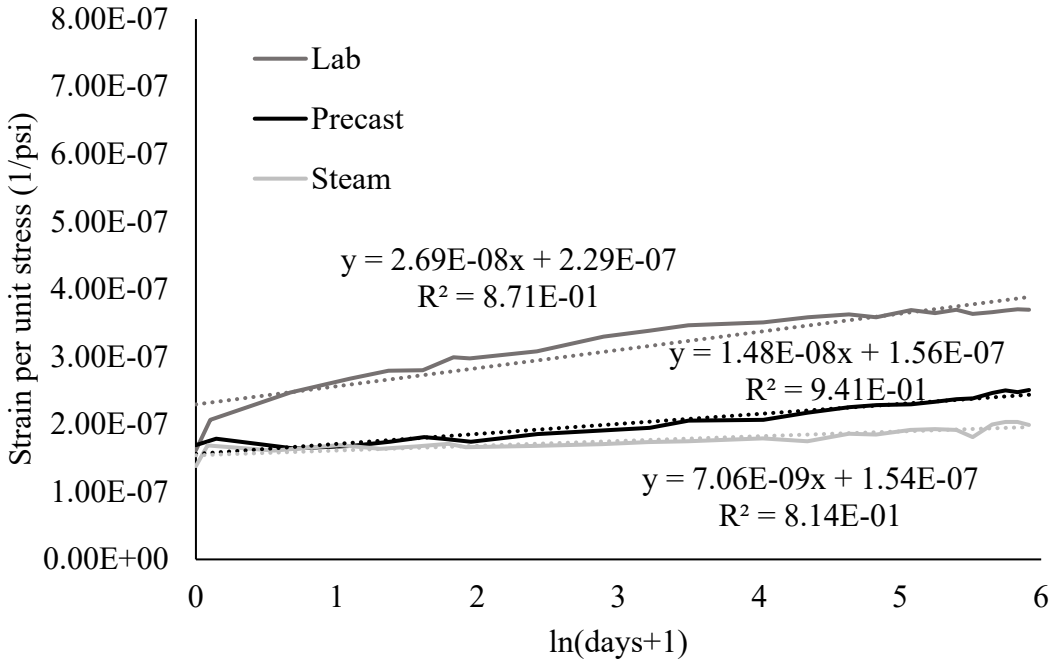

Figure 123: 21-ksi specimen semilog plot of strain per unit stress vs. time

The creep rate for each specimen is organized in Table 42. The creep rate values were taken from the slopes of the best fit lines in Figure 120 through Figure 123. Creep rate is a useful metric to compare creep behavior across mixes because it is normalized for both the load applied and the time over which a specimen is tested. Figure 124 compares the creep rate of each specimen group to its compressive strength at the time of loading. Unsurprisingly, the specimens with higher compressive strengths show significantly lower creep rates for the higher strength UHPC specimens, in some cases decreasing the creep rate by a factor of four.

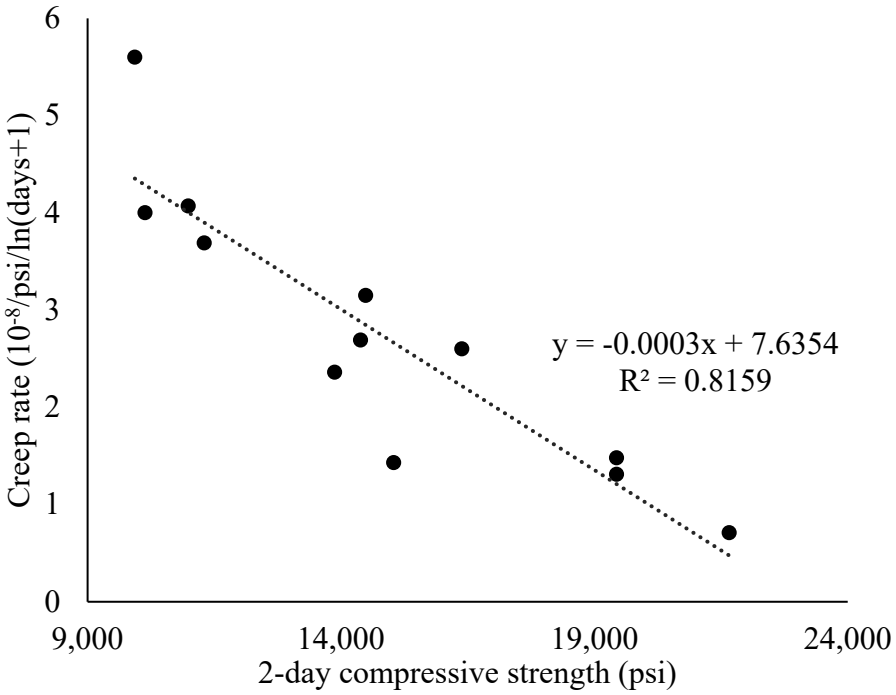

Figure 124: Creep rate vs. compressive strength

Table 42 also shows the creep coefficient for each specimen. The creep coefficients were calculated using Equation 23:

$$\phi(t, t_0) = \frac{\epsilon_{creep} - \epsilon_{control}}{\epsilon_{loading}} \qquad \text{Equation 23}$$

Where: ϕ is the creep coefficient, dimensionless
t is the age of the concrete, (days)
t_0 is the age of the concrete at the time of loading, (days)
ϵ_{creep} is the measured time-dependent strain after loading on the loaded cylinders at time t, dimensionless
$\epsilon_{control}$ is the measured strain on the control cylinders at time t, dimensionless
$\epsilon_{loading}$ is the initial (elastic) strain on the cylinders at the t_o, dimensionless

Unlike creep rate, the creep coefficient does depend on the amount of time over which the test is run. If both creep and elastic modulus change linearly with load, then the creep rate remains constant. However, this is not always the case, especially when loads are above 40% of the concrete's compressive strength. The creep coefficients reported in the present research were calculated using the creep at one year. Other researchers may use different test lengths or may calculate a projected final creep and report an ultimate creep coefficient.

7.4. Discussion

The elastic moduli of the mixes were compared to multiple models used to predict the elastic moduli of concrete based on their compressive strength, with emphasis on models developed for UHPC. The models are shown in Equation 24 through Equation 28. Equation 24 is used in the American Concrete Institute's building code for normal-weight concretes [218]. Equation 25 was developed by Kakizaki et al. from research with high-strength concretes [251]. The concretes used had compressive strengths ranging from 12 to 20 ksi, which fits well with the compressive strengths used in the present research. Equation 26 is used in ACI 363 for high strength concretes with strengths up to 12ksi [252]. Equation 27 was developed by Ma et al. for UHPC without coarse aggregate with compressive strengths of 21.5-26.5 ksi [253]. This equation is similar to the equation by El Helou et al. in the proposed AASHTO UHPC guide specification that shows a good fit with their data on mechanical behavior of UHPC. Equation 28 was developed by Graybeal to estimate the elastic moduli of concretes with compressive strengths of 19 ksi and below [99].

Figure 125 shows the data points from the present research plotted against these models. When comparing these equations to the data from this research in Figure 125, all models overestimate the modulus for the lowest-strength lab-cured mixes. This is likely because the amount of time required for loading and taking the initial measurements could have allowed for some deformation due to very early creep being measured, thus decreasing the measured modulus of elasticity. A better comparison would be made if separate samples had been produced and tested for modulus, rather than using the creep loading data to calculate the modulus. Of the equations used, the Kakizaki equation did the best at predicting the modulus, with an R^2 value of 0.51. Using a straight line of best fit resulted in an R^2 value of 0.59, suggesting that the data from these mixes is closer to being linear than to fitting any of the modulus equations used. However, an R^2 value of 0.59 is still relatively low, indicating that a straight line is not a particularly good predictor of modulus based off of compressive strength. In addition, the concrete mixes tested only had a range of compressive strengths from 9,900 psi – 21,600 psi, so the best-fit line would likely not be applicable to concretes with compressive strengths outside of this range.

$$E_c = 57{,}000\sqrt{f'_c} \qquad \text{Equation 24}$$

$$E_c = 43{,}980\sqrt{f'_c} \qquad \text{Equation 25}$$

$$E_c = 40{,}000\sqrt{f'_c} + 1{,}000{,}000 \qquad \text{Equation 26}$$

$$E_c = 524{,}500\left(\frac{f'_c}{10}\right)^{\frac{1}{3}} \qquad \text{Equation 27}$$

$$E_c = 7{,}100{,}000e^{\left(-\frac{1}{2}\left(\frac{\ln\frac{f'_c}{44{,}000}}{1.7}\right)^2\right)} \qquad \text{Equation 28}$$

Where: E_c is the modulus of elasticity in psi
f'_c is the specified compressive strength in psi

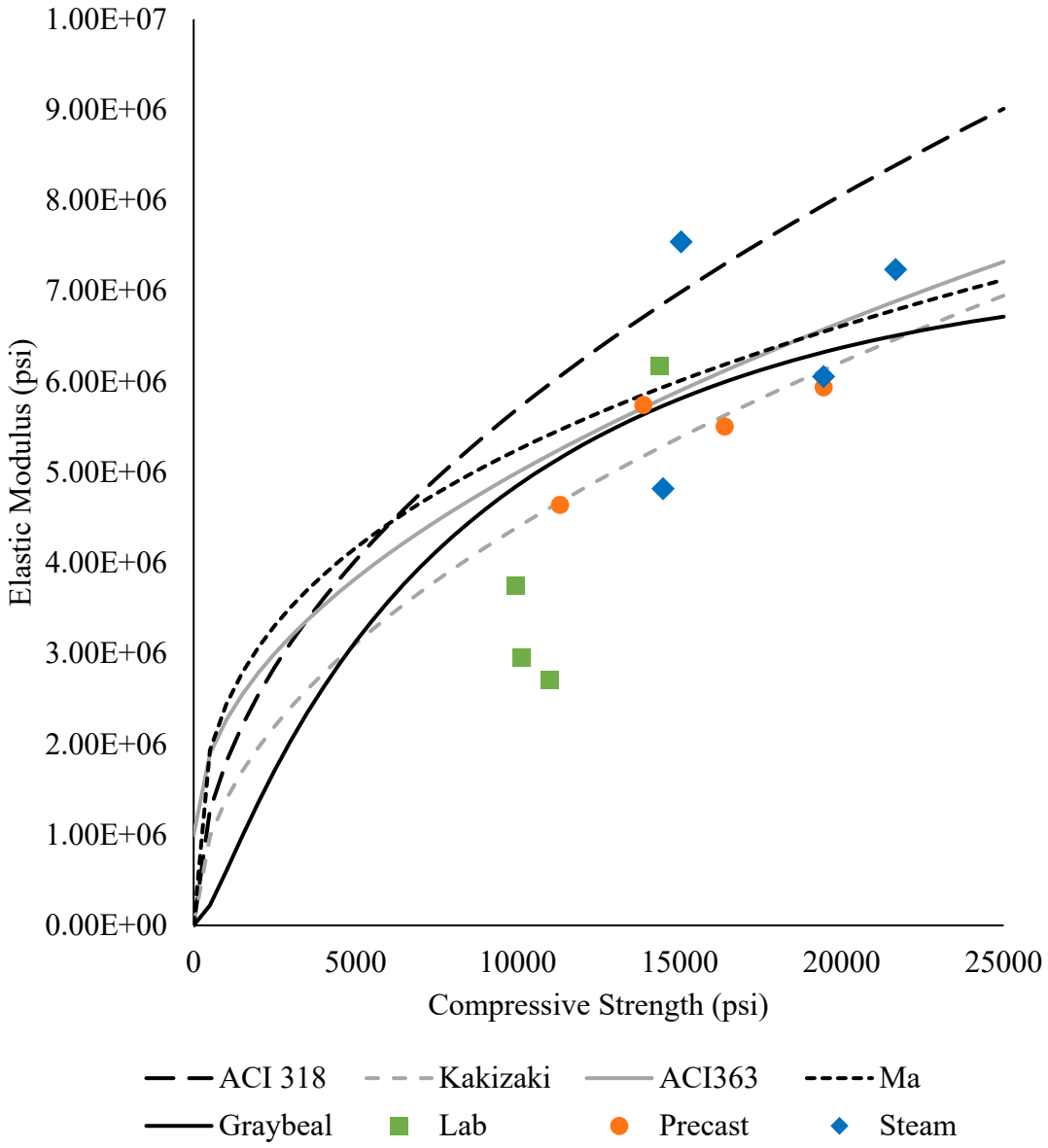

Figure 125: Elastic modulus comparison with models

The trends in shrinkage were similar to the trends in creep, as the highest strains occurred in the lab-cured specimens, followed by precast, and finally steam-cured specimens. This is expected as shrinkage after the first 48 hours of curing was largely due to drying. The lab-cured specimens likely had more unreacted water than the precast and steam specimens, allowing for more evaporation to occur. For all mixes, the shrinkage strain was significantly lower than the creep strain, amounting to 23-29% of the creep strain for lab-cured specimens and 30-48% of the creep strain for most heat-treated specimens at the end of one year. The exception to this was the 12-ksi samples, for which shrinkage strain in the precast and steam specimens was 54% and 58% of the creep strain for the precast and steam specimens, respectively. This could be a result of these

specimens being loaded at a reduced stress compared to the other mixes, but when comparing the creep loads to the specimens' compressive strengths, the ratios for the 12-ksi mix were similar to those for the 15- and 18-ksi mixes. Another likely reason that a higher proportion of post-loading strain was due to shrinkage for the heat treated 12-ksi samples was that they had a higher water-cementitious material ratio (w/cm). The 12-ksi samples had a w/cm of 0.25, while the next highest was 0.20 for the 15-ksi samples. Even with heat treatment, there was likely unreacted water in the 12-ksi samples that resulted in higher drying shrinkage.

The creep recovery in Figure 116 through Figure 119 showed very similar values for all samples, regardless of the curing method used or the initial strain due to loading. Table 43 showed the strain due to unloading and creep recovery and compared it with the strain due to loading and creep. Table 43 showed that the amount of recovered strain from combined unloading and creep recovery was very similar for all samples. However, when recovery was reported as a percent of loaded deformation, the heat-treated specimens performed better. Little research on creep recovery of UHPC was found in the literature. For the present research, however, it is assumed that as the lab and precast specimens aged, their elastic moduli increased due to continued hydration. The 18-ksi+ and 21-ksi+ steam-cured specimens, which had completed most of their strength gain during heat treatment, had very similar values of strain increase and reduction during loading and unloading, respectively. It is likely that the lab-cured and precast-cured specimens had also reacted almost fully in the year of loading, making their moduli during unloading similar to those of the steam-cured specimens. This is supported by the data in Figure 120 through Figure 123, which shows the slope of the lab-cured specimens decreasing with time. The precast and steam specimens are more linear on the semi-log plot with generally higher R^2 values. The 15+ steam specimens had lower strain during loading than during unloading, which could be because these cylinders were initially loaded before the epoxy on the locator points had hardened. They were then released and reloaded, but they may have retained strain from the initial loading that wasn't measured during the second loading after the epoxy had cured.

The creep coefficients from the present research ranged from 0.45-1.55 and are similar to those presented by other researchers [24,99,234,254]. Mohebbi and Graybeal developed a model for predicting UHPC creep coefficient based on age and strength at loading, relative humidity, and time [254]. The creep coefficients from the present research are lower than the Mohebbi and Graybeal model predict. While the reason is unclear, one possibility is that the model does not account for variation in the applied load; many specimens in the present research were loaded at a lower percentage of strength than the ones used to develop the model. Another possibility is that the model does not account for the paste content in the mixes. Creep occurs primarily in the concrete paste, and it is likely that the non-proprietary UHPCs developed for this research had a lower paste content and more aggregate than the stronger proprietary ones used to develop the model.

7.5. Summary

These results show that the heat generated during curing of large members with a high cementitious material content can result in an increase in elastic modulus and decrease in creep strain. Mixes with strengths lower than the UHPC threshold of 17 ksi that were heat treated exhibited good creep performance with low creep coefficients compared to those expected for

normal strength or high performance concrete. It is recommended that the determination of a mix's creep behavior be done using the actual curing temperatures that the large-scale specimens will experience, as this can make a large difference in both the creep and shrinkage behavior. Conclusions are summarized as follows:

1. The non-proprietary UHPC mixes tested in the present research showed creep coefficients in the range of 0.47-1.55, which are similar to the results of other testing where the specimens were loaded at early ages [24]. While mixes with lower compressive strengths (<15,000 psi) had higher creep coefficients (0.82-1.55) than the higher strength mixes (0.47-0.89), they were still comparable to the results of testing on proprietary UHPCs found in literature.
2. Elevated temperatures during curing for the precast-cured and steam-cured concrete reduced both the creep and shrinkage strain of all mix designs.
3. The elastic modulus measured at the time of loading was lower than the predictions of multiple models for lower-strength mixes but correlated reasonably well for the majority of specimens.
4. The length change due to unloading was similar for cylinders of all curing conditions and was much lower than the length change due to loading for lab-cured cylinders. This suggests that the elastic modulus of the lab-cured specimens increased as the cylinders continued to cure in their first year.

8. FREEZE THAW AND LOW TEMPERATURE DIFFERENTIAL SCANNING CALORIMETRY TESTING

8.1. Introduction

Air-entraining admixtures are added to normal strength concrete to prevent freeze-thaw damage. Because entrained air reduces the strength of concrete, air-entraining admixtures are omitted from UHPC mixtures. To date, most researchers have focused on testing UHPC with compressive strength above 21 ksi (150 MPa), for which the freeze-thaw performance against the freeze-thaw cycling was found to be excellent. Testing was conducted to determine if this excellent performance extended to the lower strength levels considered in this study.

Four ultra-high-performance concrete (UHPC) mixes with different mixture proportions, including different water-cementitious material ratios (w/cm), were made to test the performance of UHPC against freeze-thaw cycling. The mixtures were designed for multiple strength classes and curing methods. Four compressive strength classes of 12-15 ksi, 15-18 ksi, 18-21 ksi, and 21+ ksi were used to measure the concrete freeze-thaw durability. The UHPC samples were made for three different curing regimens; limewater curing in a fog room, simulated precast beam curing (hereafter called precast curing), and steam curing. Samples for freeze-thaw durability were made and tested using 1.5% steel fibers for all the different strength classes. The samples were tested for up to 330 cycles to determine at which strength level the UHPC F-T performance becomes acceptable without the use of air entrainment.

Samples were made for low temperature differential scanning calorimetry (DSC) from the same mixture designs used for freeze-thaw tests to determine the temperature at which water freezes in UHPC pores and determine if the freezing point depression is sufficient to prevent ice formation at temperatures experienced by UHPC in service. A mortar mix was also made at a 0.40 w/cm for comparison. Companion samples to those evaluated with differential scanning calorimetry were evaluated with mercury intrusion porosimetry (MIP).

8.2. Materials and Methods

A fine masonry sand was used in the UHPC mixtures, with properties shown in Table 44. Cementitious materials used for this study included ASTM C595 Type IL cement [247], ASTM C150 Type III cement [255], slag cement (slag) [256], an ASTM C1240 dark gray silica fume [257], a white silica fume, and silica flour. The compositions of the cementitious materials were measured by x-ray fluorescence using a Rigaku Supermini x-ray fluorescence (XRF) machine and are shown in Table 45. The cements' phase compositions were determined using quantitative X-ray diffraction (XRD) [240] and are provided in Table 46.

Table 44: Properties of fine aggregates (sand)

Properties	Value
Specific Gravity	2.66
Absorption	0.20%

Table 45: XRF results for materials (%)

Parameter	Type IL Cement	Type III Cement	Slag	Silica Fume	White Silica Fume	Silica Flour
SiO_2	18.82	20.00	34.79	80.45	96.49	98.88
TiO_2	0.22	0.22	0.64	0.02	0.02	0.01
Al_2O_3	4.79	4.90	13.17	0.48	1.37	0.17
Fe_2O_3	3.10	3.30	0.78	4.78	0.16	0.01
MnO	0.06	0.13	0.32	0.44	0.00	0.01
MgO	0.80	1.00	4.66	10.43	0.01	0.01
CaO	62.85	63.30	43.71	0.95	0.00	0.01
Na_2O	0.08	0.12	0.19	0.18	0.07	0.01
K_2O	0.25	0.38	0.41	0.77	0.02	0.02
P_2O_5	0.41	0.49	0.04	0.03	0.23	0.01
SO_3	3.02	3.70	3.00	0.07	0.00	0.01
ZnO_2	0.00	0.05	0.00	0.00	0.43	0.00
LOI	5.45	2.44	0.02	2.93	0.66	0.27

Table 46: Cement composition

Phase	Type IL Cement (%)	Type III Cement (%)
Alite	44.3	53
Belite	23.2	16.4
Aluminate	4.2	4.1
Ferrite	11.2	13.8
Bassanite	0.5	5.2
Gypsum	5.1	1.1
Calcite	11.7	2.3
Anhydrite	-	1.6
Arcanite	-	0.5
Syngenite	-	0.9
Thenardite	-	0.5
Quartz	-	0.6

Twenty-four samples were made and analyzed for freeze-thaw testing from four different mix designs with four different strength classes that ranged from 12 to 21 ksi. Mixture proportions are provided in Table 47 for the mixtures with strengths up to 21 ksi and Table 48 for the mixture class above 21 ksi. The admixture water contents were included in the w/cm calculations. The mixture made with a 0.40 w/cm was only used for the low temperature DSC and MIP experiments.

Table 47: Mixture proportions for lower strength mixes

Mix	Weight (lb/yd^3)				Admixtures (lb/yd^3)			Calculated Values	
	Sand	Cement IL	Slag	Silica fume	HRWR[1]	WRWR[2]	SE[3]	w/cm	cm/s
0.40 w/cm	2628	955	0	0	-	-	-	0.40	0.36
12-15 ksi	1856	1583	0	83	10.9	10.9	2.1	0.25	0.9
15-18 ksi	1815	1404	272	136	16.4	16.4	3.4	0.20	1.0
18-21 ksi	1588	1597	309	155	30.9	30.9	5.2	0.1625	1.3

[1] high range water reducing; [2] water reducing and workability retaining; [3] surface enhancing

Table 48: Mixture proportions for specimens with strengths greater than 21 ksi

Mix	Weight (lb/yd^3)				Admixtures (lb/yd^3)			Calculated Values	
	Sand	Cement III	Silica Flour	White Silica fume	HRWR	Accelerator	RHRWR[1]	w/cm^2	cm/s^2
21+ ksi	1361	1477	369	369	46.1	23.1	40.4	0.13	1.63

[1] retarding high range water reducer; [2] silica flour is included as cementitious material

For the freeze thaw testing, all of the UHPC batches used 1.5 volume percent steel fibers with a length of 0.5 in. (13 mm) and diameter of 0.008 in. (0.2 mm). An IMER Mortarman 750 mixer, a large pan mixer with orbital mixing action, was used to make the UHPC for freeze-thaw tests. The samples were removed from the molds at 24 ± 2 hrs after mixing, and cured using three different methods: limewater curing in a fog room at lab temperature after demolding at 24 hrs, steam curing following demolding at 24 hrs, and precast curing during the first 24 hrs. The limewater-cured samples were put in a limewater bath in a moist curing room meeting ASTM C511 [258] that was kept between 70°F and 77°F (21°C and 25°C) and above 95% relative humidity after demolding. After demolding at 24 hrs, the steam-cured specimens were placed in a covered pan above water and put in an oven with a set temperature of 194°F (90°C) for two days of steam curing, followed by curing in limewater in the moist room until testing. Specimens cured using the precast curing method were first cured in their molds at lab temperature for 4 hrs. After 4 hrs, they were placed in a covered pan while they were still in their molds in an oven with a temperature of 158°F (70°C). They were then removed at 22 hours of age from the oven, demolded, and placed in the limewater in the moist curing room until they were ready for testing. Six samples were made for each strength class and curing method. Figure 126 shows target temperatures with time for the three curing regimes.

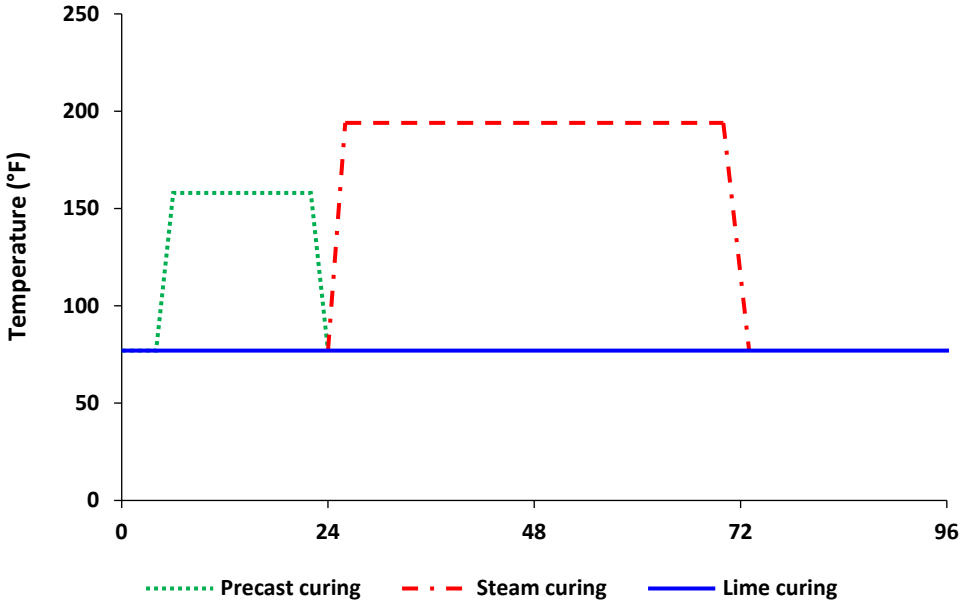

Figure 126: Target temperatures with time for the three curing regimes

For the low temperature DSC testing, all the mixes used the mixture proportions shown in Table 47 and Table 48, and they were made in a mortar mixer meeting ASTM C305 [259] with a batch size of 0.05 ft^3 with no fibers. The material properties of sand are given in Table 44. After mixing, 2 in. × 4 in. molds were filled and cured using the same three types of curing used for the freeze-thaw samples. The samples were stored in limewater until they reached 14 days of age to give curing equivalent to that of the freeze-thaw samples. The same 2 in. × 4 in. specimens were sampled for both DSC and MIP.

8.2.1. Compressive Strength

Four different non-proprietary mix designs with three curing methods were used to study UHPC freeze-thaw behavior. The UHPC mixtures were designed to range in compressive strength from 12 ksi to 21 ksi at 28 days in order to investigate how the F-T performance would be impacted. The compressive strength was measured according to ASTM C39 with a load rate of 35 ± 7 psi/s (0.25 ± 0.05 MPa/s) for samples that were expected to have a compressive strength below 17 ksi (120 MPa) [87]. ASTM C1856 was followed with a load rate of 145 ± 7 psi/s (1.0 ± 0.05 MPa/s) for samples that were expected to have a compressive strength above 17 ksi (120 MPa) [59]. Three specimens with a dimension of 3 in. × 6 in. for each strength class and curing method were tested at 14 days to follow the same curing age for the F-T samples.

8.2.2. F-T Testing Procedure

ASTM C666 procedure A was used to determine the resistance of concrete specimens against repeated cycles of freeze-thaw [19]. Two 3 in. × 4 in. × 16 in. (75 mm × 100 mm × 400 mm) concrete specimens were made for each curing method for each UHPC concrete mixture.

Prior to testing, the specimens were brought to a temperature within -2°F and +4°F (-19°C and -16°C) of the target thaw temperature of 39°F (4°C), and tested for fundamental transverse frequency according to ATM C215 [260]. The specimens were then weighed, and the cross-section dimension were measured. The specimens were then placed in the stainless-steel trays used to hold the samples during freeze-thaw testing, with clean water added to cover the specimens from all sides as shown in Figure 127.

Figure 127: Freeze thaw chamber

A 0.039 in. to 0.12 in. (1-3 mm) water-filled space was maintained around all sides of the specimens during testing. The specimens were removed from the machine during thawing every 33 cycles, and the transverse frequencies were measured after weighing. The specimens were then returned to the machine to continue testing until they reached the target 330 cycles. The concrete relative dynamic modulus of elasticity (RDME) was calculated using Equation 29 [19]:

$$P_N = \left(\frac{n_N}{n_0}\right)^2 \times 100 \qquad \text{Equation 29}$$

Where: P_N is the relative dynamic modulus of elasticity at N cycles, (%)

n_N is the resonant frequency at N cycles of freezing and thawing, (Hz)

n_0 is the resonant frequency at 0 cycles of freezing and thawing, (Hz)

8.2.3. DSC Testing Procedure

UHPC samples were tested using low-temperature differential scanning calorimetry (DSC) at the FDOT State Materials Office to determine the temperature at which water freezes in UHPC to test the hypothesis that the pores in UHPC are too small for water in them to freeze at temperatures used in freeze-thaw testing. DSC is a thermal analysis technique in which the heat flow into or out of a sample is measured. When the water freezes (exothermic phase transition) inside the sample pores, the phase change is measured as heat flowing out of the sample. The pore size at which a freezing event is occurring in after 1 cycle of freezing can be calculated using Equation 30 [261][262]

$$r_p = \frac{64.67}{\Delta T} + 0.57 \qquad \text{Equation 30}$$

Where: r_p is pores radius, nm

ΔT is the change in liquid freezing temperature for the freezing point depression or undercooling from the liquid in the pore

After the DSC samples were cured, they were cut into ~5 mm × 5 mm × 1 mm thick samples to fill the crucible. Prior to testing, the samples were weighed, and silver iodide was sprinkled on top as an ice nucleation agent [261]. The samples temperature profile cycled from + 15°C to -60°C and back to + 15°C at a rate of 1°C per min.

8.2.3.1. MIP Procedure for the DSC Samples

MIP is a common test used for characterizing the porosity and the size distribution of capillary pores in cement paste specimens [263][264]. For each curing method, the samples were cut into small pieces using a wafer saw with maximum dimensions of 0.12 in. × 0.98 in. × 0.39 in. (3 mm × 25 mm × 10 mm). After that, the samples were immersed in a 2 in. × 4 in. plastic container with a large volume of isopropanol for 7 days. The isopropanol exchange was used to diffuse into the paste and replace the pore solution. The samples were then placed in a vacuum desiccator to remove the isopropanol and store the samples without carbonation until testing. The testing was conducted using a Quantachrome PoreMaster 60 at a pressure range of 135 kPa to 415 MPa. The relationship between the pore size and the applied pressure is given by the Washburn equation, as shown in Equation 31 [134,135]:

$$d = \frac{-4\,\gamma\,cos\,\theta}{P} \qquad \text{Equation 31}$$

Where: d is the pore diameter (m)

γ is the surface tension of mercury (N/m)

θ is the contact angle between the solid and mercury

P is the applied pressure (N/m^2)

Analysis using the Washburn assumes the pore shapes to be cylindrical, and the surface tension of mercury γ to be 0.48 N/m. The contact angle θ has often been assumed to be 140°. However, based on the work presented by Muller and Scrivener using a comparison between MIP results and NMR relaxometry, the assumption for the angle is most likely overestimated. Therefore, 120° was suggested for use, and was used in this research. [265]

8.3. Results and Discussion

8.3.1. Compressive Strength for F-T samples

The average compressive strength, standard deviation, and coefficient of variation for each mix are presented in Table 49. Even though the mixes were designed to meet the strength target for 28 days of curing, most of the limewater cured samples and all of the steam cured samples met the target strength at 14 days. The steam curing increased the compressive strength for all mixtures except for the lowest strength class mix. The precast curing lowered the concrete strength for all mixtures, showing the importance of the pre-curing before steam curing in forming a good microstructure [266].

Table 49: Average compressive strengths for each mix

Mix Target (ksi)	Curing	Strength (psi)	Std. Dev. (psi)	COV
12-15	Limewater	13815	1,345	9.74%
12-15	Steam	12429	2,392	19.24%
12-15	Precast	12703	1,358	10.69%
15-18	Limewater	16958	525	3.10%
15-18	Steam	18188	1,307	7.19%
15-18	Precast	13675	555	4.06%
18-21	Limewater	16459	746	4.53%
18-21	Steam	18443	1,912	10.37%
18-21	Precast	13994	1,111	7.94%
21+	Limewater	19882	1,696	8.53%
21+	Steam	22096	761	3.45%
21+	Precast	16308	1,773	10.87%

8.3.2. Freeze-Thaw

ASTM C666 [19] was followed to study the freeze-thaw durability under the effect of four different strength classes, and three different curing methods. The UHPC relative dynamic modulus of elasticity (RDME) with increasing cycles is shown in Figure 128 and the mass change in Figure 129. Table 50 summarizes the overall mass loss and relative dynamic modulus of elasticity measurements after 330 cycles. After 330 cycles, the 12-ksi mixture showed higher mass gains of 0.03%, 0.25%, and 0.44% for the limewater-cured, steam-cured, and precast-cured samples, respectively. This could indicate internal cracks that absorbed water during the testing [267]. The RDME likely increased because of continued hydration [267] [268].

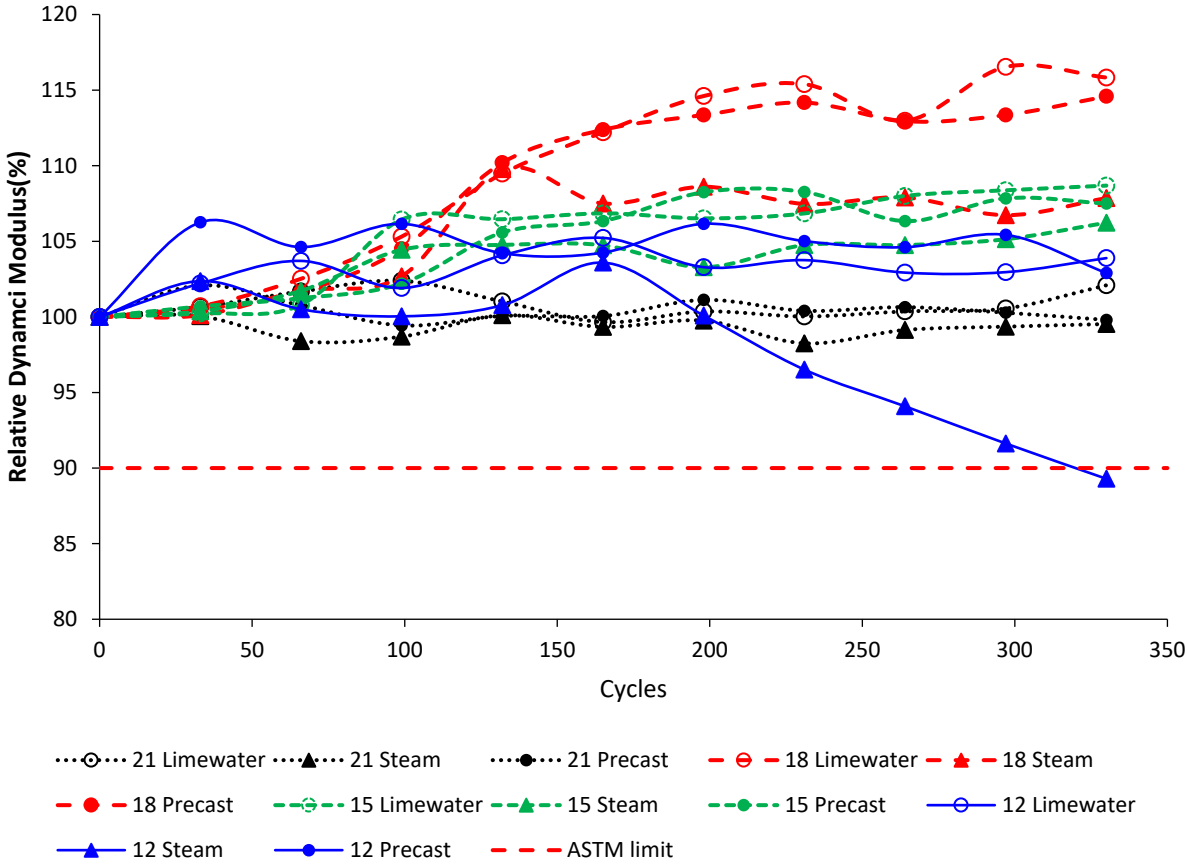

Figure 128: Relative dynamic modulus of freeze thaw samples.

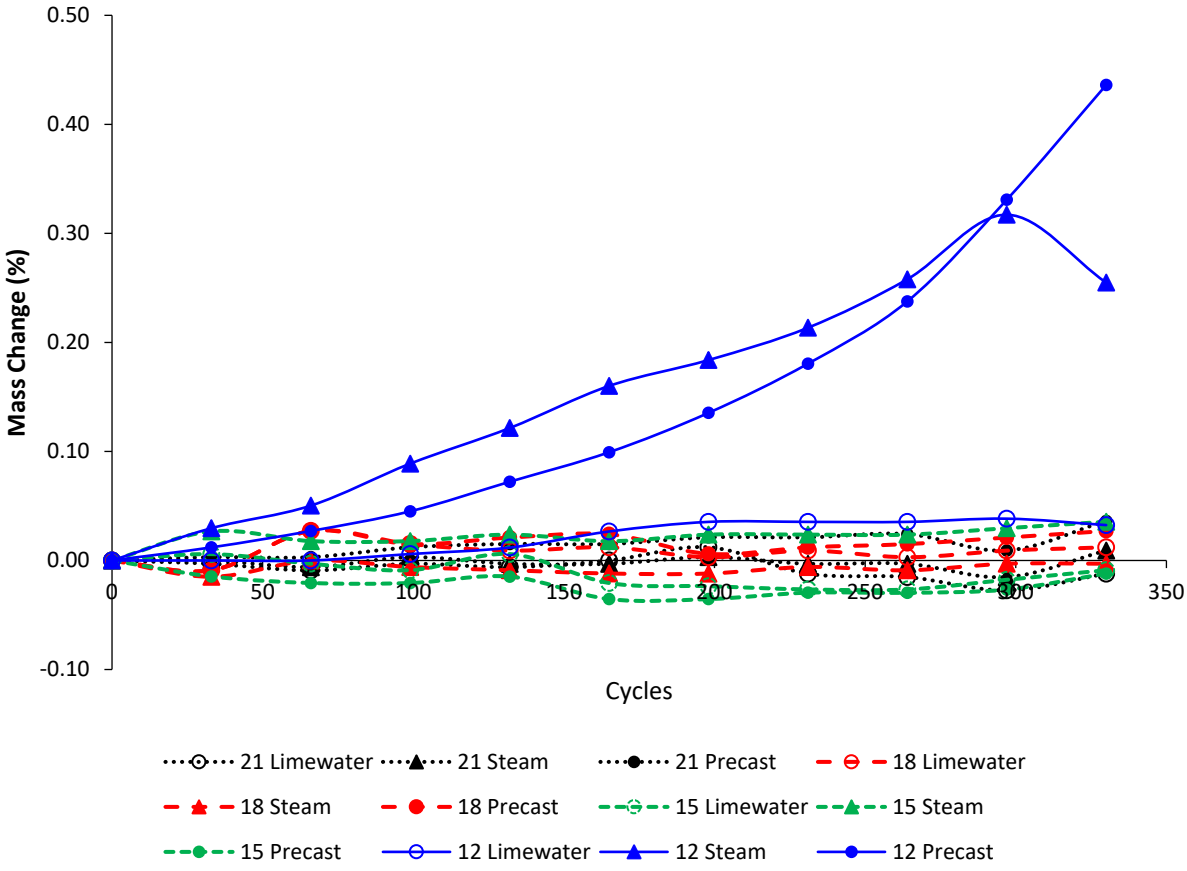

Figure 129: Mass change of samples during freeze-thaw testing

Table 50: Percent of mass change and relative dynamic modulus of the mixes

Mix (ksi)	Mass change after 330 cycles			RDME% after 330 cycles		
	Limewater	Steam	Precast	Limewater	Steam	Precast
12-15	0.03	0.25	0.44	103.9	89.3	102.9
15-18	-0.01	0.04	-0.01	108.7	106.2	107.5
18-21	0.01	0.00	0.03	115.8	107.9	114.6
21 +	-0.01	0.01	0.04	102.1	99.5	99.8

In general, an increase in the relative dynamic modulus was observed for all mixes cured in limewater. This expected increase is because of increased hydration with exposure to moisture during the test and is in agreement with many researchers [267] [268] [269]. The steam-cured samples showed the lowest values with cycling because the steam curing likely increased the degree of reaction, leaving less space available for additional hydration. The precast-cured samples showed RDME in between that of the limewater-cured and steam-cured samples. The steam-cured specimens for the lowest strength class started to show a decrease in the relative

dynamic modulus by 165 freeze-thaw cycles, and were close to falling below the ASTM C1856 limit of 90% at the 300 cycles [59]. This was manifest mainly in some light surface scaling. The 12-ksi samples had the highest initial water content - 15%, 24%, and 45% more than the 15-ksi, 18-ksi, and 21+ ksi samples, respectively. The surface scaling might be from an interfacial liquid layer, high in cementitious material, between the UHPC and the sides of the cylinder mold. Figure 130 shows a picture of a 12-ksi steam-cured sample at the end of the testing, clearly showing surface scaling. A study was done by Lee Ming showed a similar trend to this observation as they found that compared to the standard curing, the steam-cured samples had slightly lower relative dynamic modulus [270] [271]. Another study was done by Graybeal showed that the RDME decreased slightly for the steam-treated specimens compared to a significant increase for the untreated specimens as the untreated UHPC had more unhydrated cementitious particles, and space available for continued hydration [272]. In general, this indicates that the steam-cured samples exhibited higher levels of hydration before testing.

Figure 130: photo of the 12 ksi steam-cured specimen after 330 cycles

8.3.3. Low Temperature DSC

The measured heat flow curves of freezing of the limewater, steam and precast cured samples for each strength class are shown in Figure 131, Figure 132 and Figure 133 respectively. The highest strength class mix, the 21-ksi mix, showed the lowest heat flow (around 0.01 W/g) for all the three types of curing. This indicates the very low volume of pores in the concrete and the small pore sizes present. For the limewater-cured samples shown in Figure 131, there is a peak close to -40 °C for the 0.40 w/cm, 12-ksi, and 15-ksi samples, which most likely correspond to pore water. The highest strength class mixes, showed no peaks, except for is a small peak around -20 °C for the 18-ksi mix, which could be from voids near the surface [273].

The steam-cured and precast-cured samples showed a similar pattern as the limewater-cured samples, except that the 21-ksi steam cured sample had a peak around -45 °C instead of -40 °C which also indicates the homogeneously nucleated pore water. There were multiple exothermic peaks located between -10 °C and -20 °C for the 12-ksi precast cured samples and a peak close to -25 °C for the 0.4 w/cm sample which indicates many pores for these samples. The 12-ksi mixture is the only mixture with significant freezing events above ~ -35°C in the steam-cured and precast-cured concrete. This may explain the mass gain and beginning of damage seen in those two sets of concrete samples, while no other concrete samples showed significant mass gain or RDME decrease during freeze-thaw cycling.

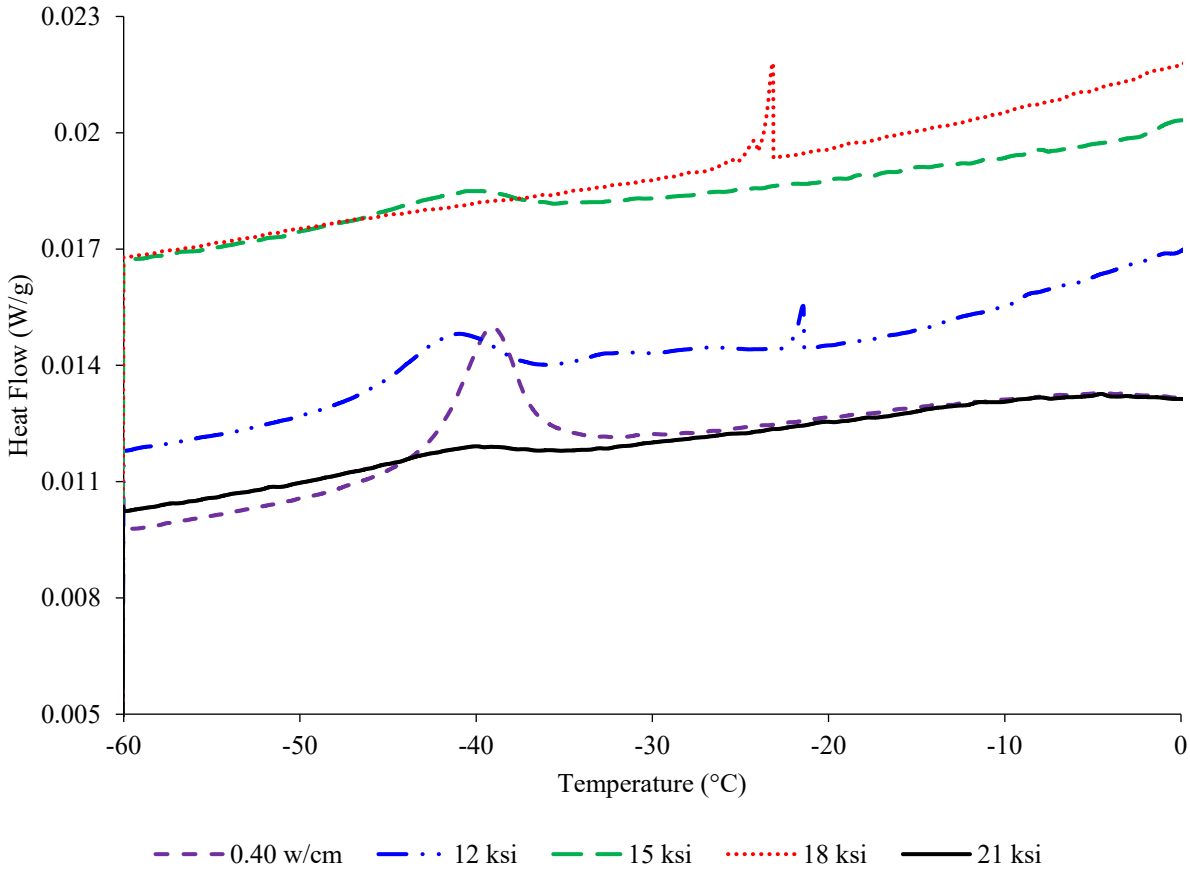

Figure 131: Measured heat flow curve of freezing of the limewater-cured samples

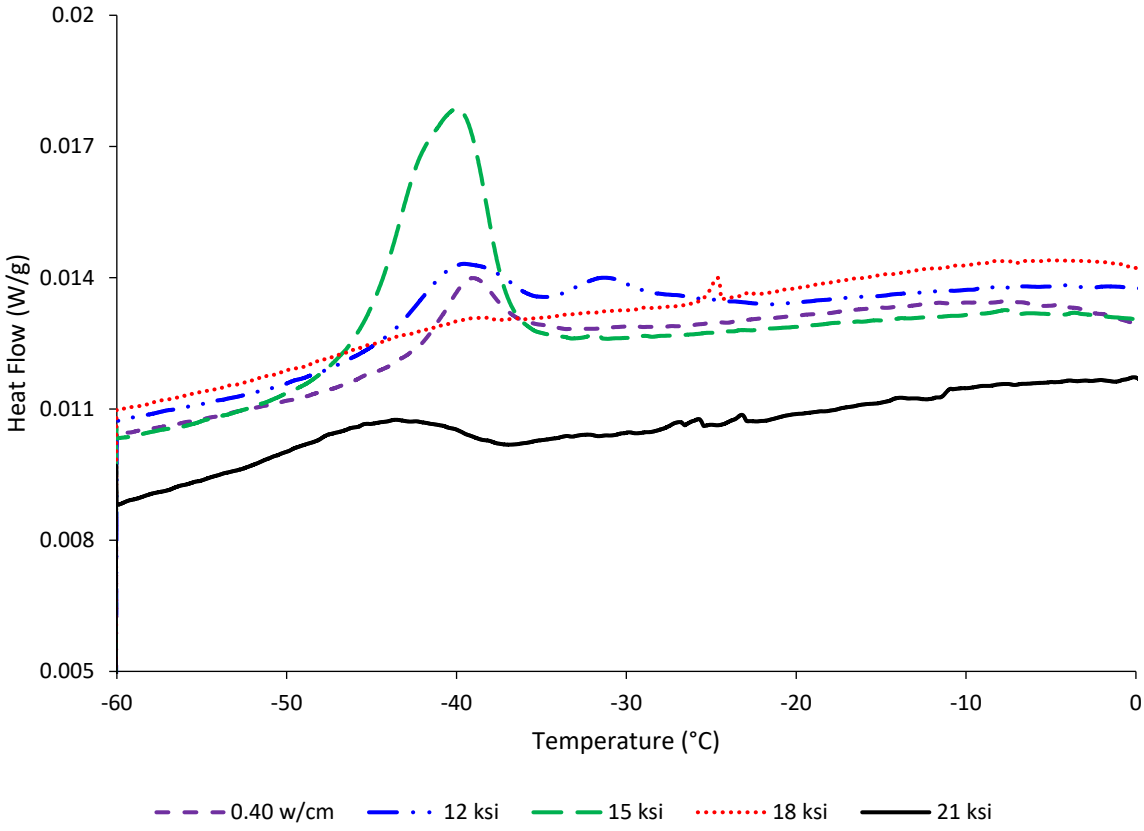

Figure 132: Measured heat flow curve of freezing of the steam-cured samples.

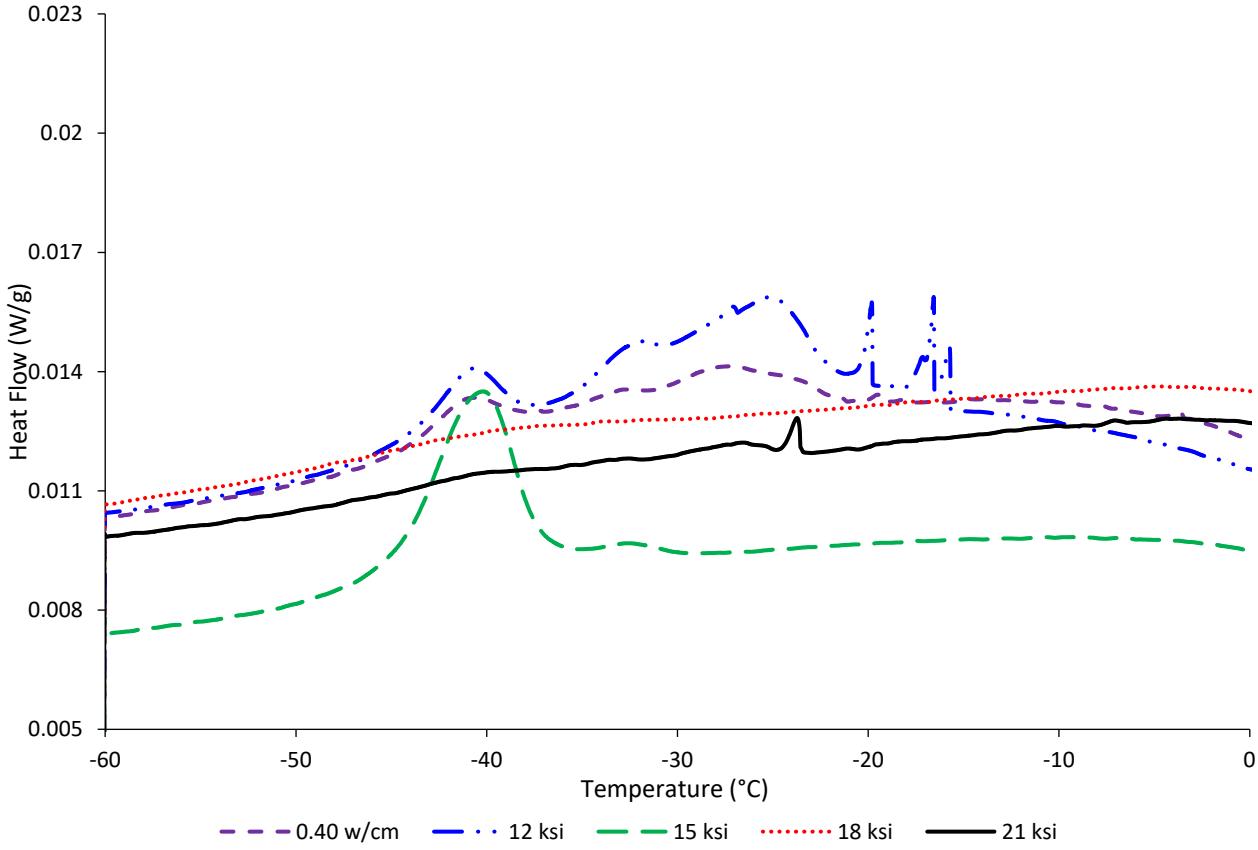

Figure 133: Measured heat flow curve of freezing of the precast-cured samples.

8.3.4. Mercury Intrusion Porosimetry

MIP was measured for all the mixes and compared to a normal concrete mix with a 0.40 w/cm. The cumulative pore volume and pore size distribution of the limewater, steam, and precast-cured samples are shown in Figure 134, Figure 135, and Figure 136 respectively. It can be clearly seen that the UHPC mixes for all the strength classes had lower porosities than the normal concrete mix which confirms the refinement of their pore structures.

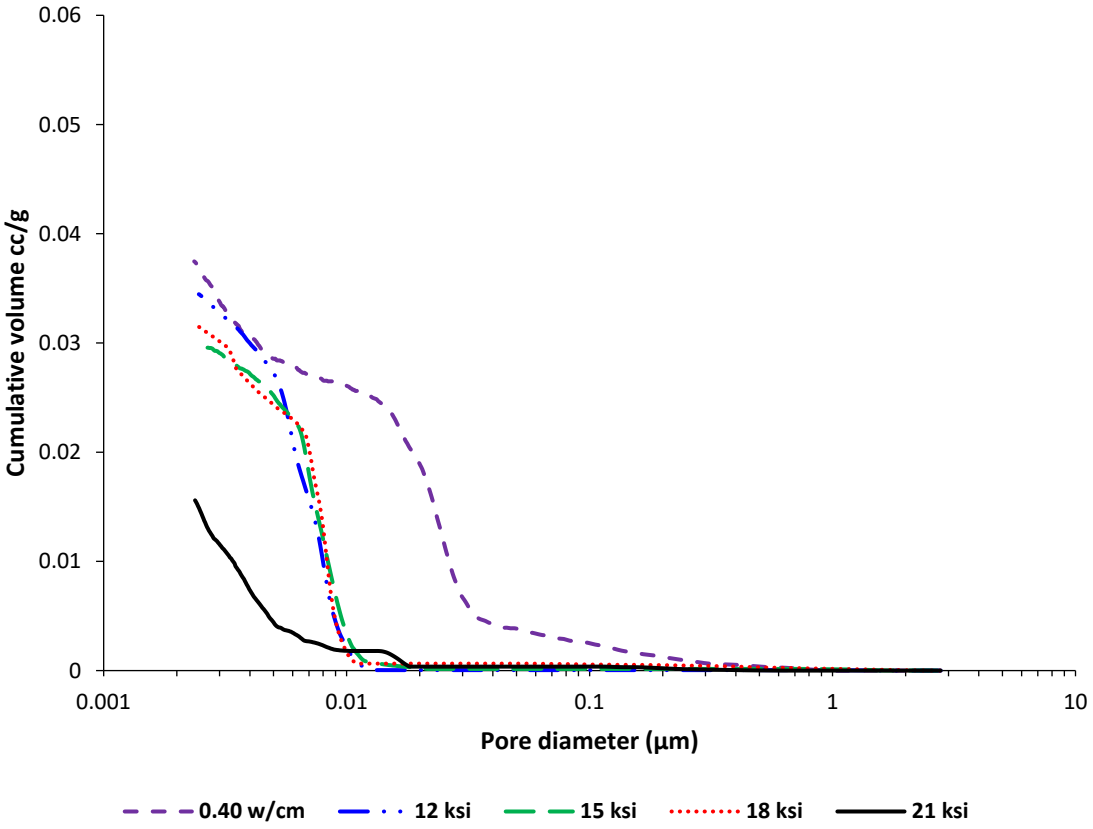

Figure 134: MIP cumulative pore volume of the limewater cured samples at the age of 14 days.

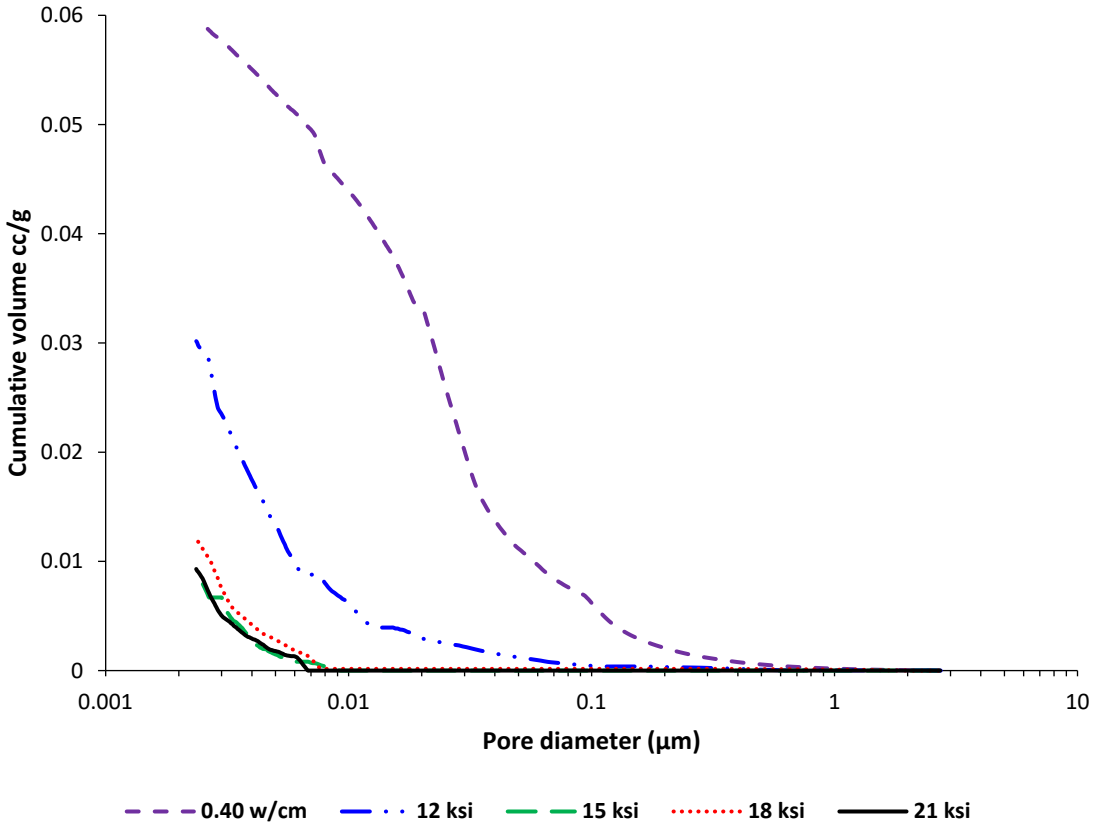

Figure 135: MIP cumulative pore volume of the steam cured samples at the age of 14 days.

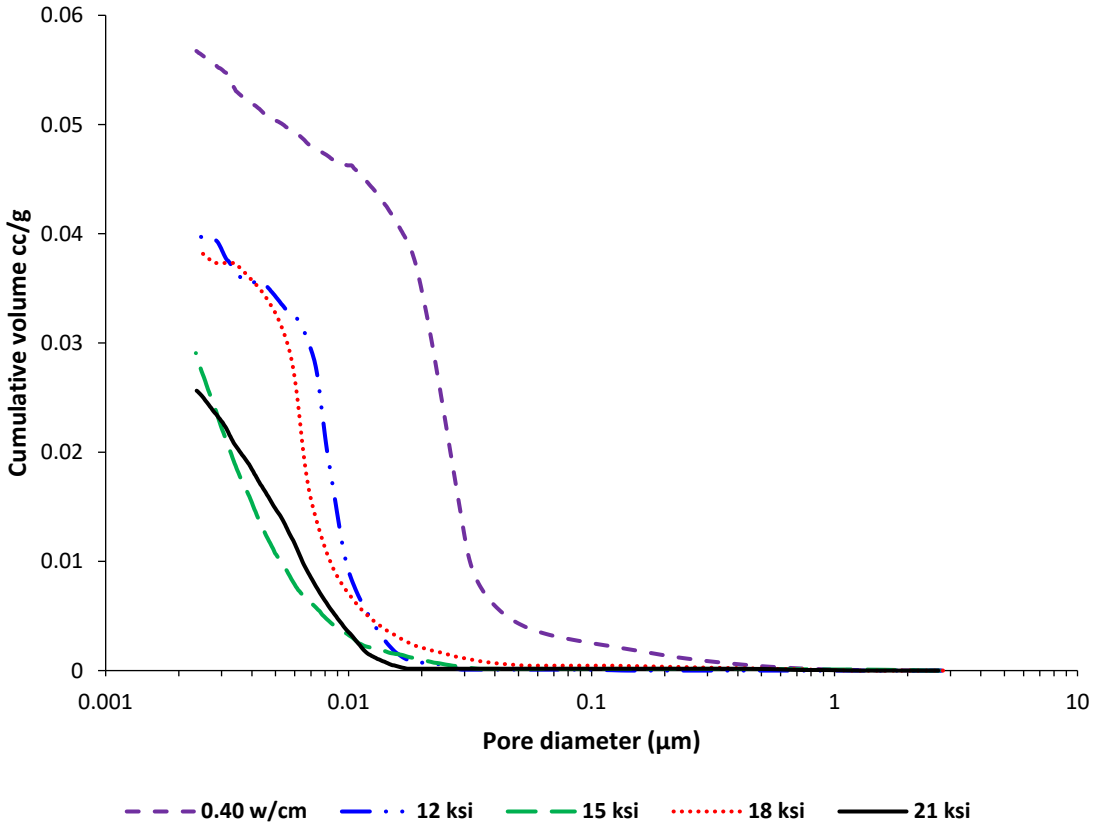

Figure 136: MIP cumulative pore volume of the precast cured samples at the age of 14 days.

The critical pore diameter (d_c) reflects the pores connectivity as it is the smallest pore size diameter of the subset of the largest pores which creates a connected path throughout the whole sample, and it can be obtained from the derivative of the pore distribution curve (the maximum of the dV/dP curve) [274]. The low strength class mixes, 0.4 w/cm and 12 ksi, showed a conventional curve with a well-defined inflection point, while most of the higher strength UHPC mixes showed a flatter porosity curve making it difficult it to establish the critical pore diameter. However, it can be clearly seen that the pore size curve of the UHPC mixes for all of the strength classes shifted towards the smaller pore diameters when compared to the normal concrete. Therefore, the critical pore diameters for the 0.4 w/cm concrete limewater-, steam-, and precast-cured samples (0.027 µm, 0.03 µm, and 0.032 µm) were almost two times greater than the critical pore diameters of the UHPC mixes which consists of lower permeability or penetrability of the UHPC samples.

It can be seen from the cumulative mercury intrusion data for all the curing types used that the strength was inversely related to the volume of intruded mercury. Samples for the highest strength mix, 21 ksi, had intruded volumes that were about one-third of those obtained for the 0.4 w/cm control concrete mix (0.02 cm^3/g and 0.06 cm^3/g, respectively, which was expected as a

higher water content leaves more void space as the free water is consumed by hydration or lost through evaporation.

Limewater-cured and precast-cured specimens showed a similar trend with respect to their pore sizes. The steam-cured specimens also showed lower porosity for the higher strength mixes, 21, 18, and 15 ksi compared to the other two curing methods. However, for the steam-cured 12-ksi specimens showed a higher porosity and critical pore diameter than the samples cured by the other two methods which could explain why the steam cured samples from that mixture showed some damage during freeze-thaw testing.

In general, when compared to normal concrete, the test results showed the UHPC samples had very small pore size diameters, less than 0.01 μm, confirming their dense microstructure [275] [137] [276]. For the concrete mixes in this study, samples with higher strengths had lower mercury intrusion volumes and lower volumes of pores. When looking at the effect of curing methods on the samples, limewater and precast curing methods showed similar trends for their critical pore diameters. The precast curing method lowered the strength slightly, showing the negative effect of high temperature after placement. The steam curing method showed a positive effect in forming a good microstructure for all of the mixes, except for the 12-ksi mix, for which the samples permeabilities increased and the strengths decreased at later ages. Lower strengths and higher permeabilities are a typical consequence of high temperatures on normal and high strength concretes. Therefore, the 12-ksi mixture may have suffered from the cross-over effect typically seen with normal strength concrete that experiences high temperature curing, with some pores with diameters in the 0.01 to 0.1 micrometer range. This is in line with some of the results of other studies conducted for UHPC with higher strengths than used in this study [272][277].

8.4. Summary

Samples were made with 1.5% by volume of steel fibers for each strength class examined in this study and were subjected to freeze-thaw testing for up to 330 cycles. All the samples were found to be freeze-thaw resistant and showed no damage, except for the 12-ksi steam-cured samples that were below the ASTM limit of 90% of RDME. The 12-ksi mixture was affected negatively by the steam curing as it was the only mixture with a lower steam-cured 14-day compressive strength than limewater cured samples. This could be because only a small amount of additional hydration would be expected after the steam curing and during the freeze-thaw testing to offset a decrease in the RDME from microcracking. The 12-ksi steam cured and precast cured concrete showed water freezing above -35°C, which would indicate larger pore sizes than seen in the other higher strength mixtures. The MIP results showed that the 12-ksi mixture had some moderate sized pores with diameters in the 0.01 to 0.1 micrometer range that could have contributed to some damage seen in the freeze-thaw testing. All mixtures with compressive strengths above 15-ksi performed excellently in freeze-thaw testing.

9. FRESH CHLORIDE LIMIT TESTING

9.1. Introduction

Concrete reinforcing steel corrosion is most often initiated by the presence of chloride ions in the concrete near the steel surface. The chloride threshold is the chloride concentration at the steel required to initiate corrosion. Threshold chloride concentration values depends on several factors and varies from concrete to concrete. The chloride threshold values can be influenced by the type and content of cement, total cementations materials and chemical admixtures used, the water-to-cementitious ratio (w/cm), degree of hydration, time of exposure, type of steel, steel-concrete interface, and the chlorides source whether mixed internally or penetrated later into concrete [278–283]. Fresh concrete chloride limits are typically specified to prevent corrosion from beginning in new concrete right after construction. The ACI 318 Building Code Requirements for Structural Concrete and the ACI 222R Guide to Protection of Reinforcing Steel in Concrete Against Corrosion provide recommendations for limits on admixed chlorides present in new concrete and are shown in Table 51 and

Table 52, respectively. The chloride limits are given as a mass percentage of the cementitious materials because a portion of the chlorides can be bound by cement hydration products during curing, effectively removing them from the pore solution [284][285]. The acid soluble limits give the total chloride content allowed in the concrete, whereas the water-soluble limits give the amount allowed in the pore solution. The acid soluble chloride content is higher because some of the chlorides are assumed to be bound by the cement hydration products to form Friedel's salt [286][287].

Table 51: ACI-318 Maximum water-soluble chloride ion (Cl-) content in concrete, percent by mass of cementitious materials

Exposure Class	Non-prestressed Concrete	Prestressed Concrete
Concrete in Dry Environment (C0)	1.00	0.06
Concrete in Wet Environment, no External Chlorides (C1)	0.30	0.06
Concrete in Wet Environment with External Chlorides (C2)	0.15	0.06

Table 52: ACI 222R recommended chloride limits for new concrete [285]

Concrete Type	New Construction Chloride Limit (Percent Chlorides by Mass of Cementitious Material)	
	ASTM C1152 Acid-Soluble Chloride Content	ASTM C1218 Water-Soluble Chloride Content
Prestressed	0.08	0.06
Reinforced Concrete in Dry Environment	0.30	0.25
Reinforced Concrete in Wet Environment	0.20	0.15

The Florida Department of Transportation specification 346-3.4.2 limits the acid-soluble chloride content of new concrete in moderately or extremely aggressive environments to 0.40 lb/yd^3, irrespective of the cementitious material content [288]. Trace chlorides present in cementitious materials or admixtures typically result in very low fresh chloride contents and should not be difficult to meet for normal-strength concrete mixtures. Ultra-high-performance concrete mixture designs however use much higher dosages of cementitious materials and admixtures than normal strength concrete that can result in non-negligible total fresh chloride contents. While the UHPC chloride content may be low when calculated on a mass basis of cementitious materials, the mixture may exceed the 0.40 lb/yd^3 limit. These high chloride values are likely to occur more frequently in the future as more UHPC mixtures are made with locally available materials and alternative cementitious materials and may result in concrete mixtures failing to meet specifications for fresh chloride content limits that are based on mixture proportions used in normal-strength concrete mixtures. SCMs are known to reduce the chloride threshold because they consume the concrete hydroxyl content near the steel. The high SCM content used in UHPC, coupled with lack of data in the literature on the chloride threshold of UHPC means that data showing that UHPC has a higher chloride threshold than normal-strength concrete is needed before a higher limit can be allowed for UHPC, without sacrificing the higher durability afforded by the low diffusivity of UHPC.

UHPC samples without fibers were made to measure the chloride threshold in new concrete. Four different UHPC mix designs with four different strength classes, 12-15 ksi, 15-18 ksi, 18-21 ksi, and 21+ ksi were used in these experiments. Their chloride thresholds and corrosion rates once corrosion began were compared to control concrete samples made with a water-cementitious ratio (w/cm) of 0.44. NaCl was added to the concrete mixtures at increasing amounts to measure the corrosion threshold for admixed chlorides. The chloride threshold for fresh concrete is measured in this study using a slightly modified version of the accelerated test EN 480-14 [18]. The concrete water-soluble and acid-soluble chloride ion contents were measured according to ASTM C1218 and Florida Method FM 5-516 to determine the bound chlorides and fresh chloride limits for corrosion [289][290].

9.2. Materials and Methods

9.2.1. Materials

Materials used for the 0.44 w/cm mix included ASTM C595 Type IL cement [247], natural silica sand, and ASTM C33 No. 89 crushed limestone [291]. The aggregate properties used in the control concrete mixture are shown in Table 53.

The particle size distributions of the cements and the cementitious materials were determined using HORIBA LA-950 laser particle size analysis, and the results are shown in Figure 137. The silica fume was sonicated for 7.5 minutes prior to testing and showed a bimodal distribution which is likely due to agglomerated particles being categorized as larger particles [292].

Table 53: Properties of aggregates

Properties	Values	
	No. 89 Limestone	Silica sand
Specific Gravity	2.45	2.60
Absorption (%)	5.44	0.20

Cementitious materials used for UHPC mixes included fine masonry sand, ASTM C595 Type IL cement, ASTM C150 Type III cement [255], ASTM C989 slag [256], an ASTM C1240 gray silica fume [257], an ASTM C1240 white silica fume, and silica flour. The chemical composition of the cementitious materials was measured using x-ray fluorescence (XRF) and the results are presented in Table 54 [240].

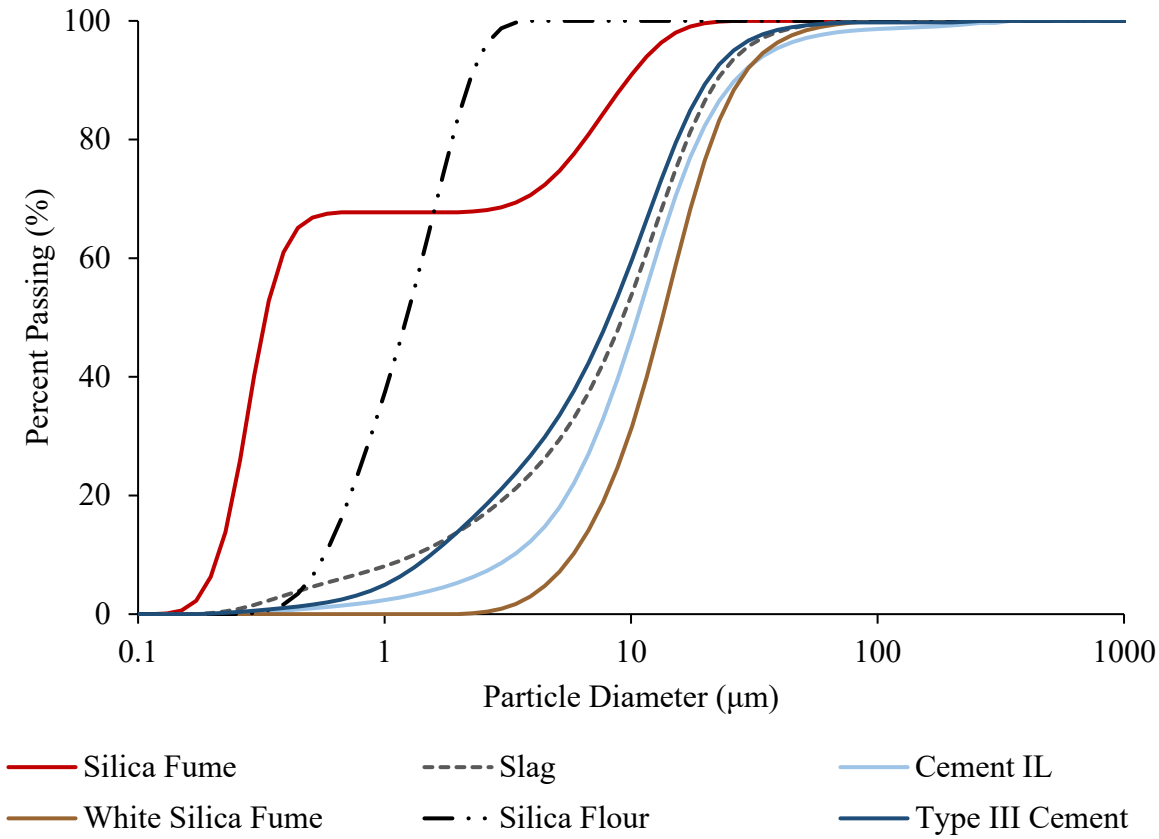

Figure 137: Particle size distribution

Table 54: XRF results for materials (%)

Parameter	Cement IL	Cement III	Slag	Silica Fume	White Silica Fume	Silica Flour
SiO_2	18.82	20	34.79	80.45	96.49	98.88
TiO_2	0.22	0.22	0.64	0.02	0.02	0.01
Al_2O_3	4.79	4.90	13.17	0.48	1.37	0.17
Fe_2O_3	3.10	3.30	0.78	4.78	0.16	0.01
MnO	0.06	0.13	0.32	0.44	0.00	0.01
MgO	0.80	1.0	4.66	10.43	0.01	0.01
CaO	62.85	63.30	43.71	0.95	0.00	0.01
Na_2O	0.08	0.12	0.19	0.18	0.07	0.01
K_2O	0.25	0.38	0.41	0.77	0.02	0.02
P_2O_5	0.41	0.49	0.04	0.03	0.23	0.01
SO_3	3.02	3.70	3.00	0.07	0.00	0.01
ZnO_2	0.00	0.05	0.00	0.00	0.43	0.00
LOI	5.45	2.44	0.02	2.93	0.66	0.27

UHPC samples were made and analyzed for fresh chloride threshold testing from four different mix designs with four different strength classes, 12-15 ksi, 15-18 ksi, 18-21 ksi, and 21+ ksi and compared to normal strength concrete samples with a total cementitious materials content of 700 lb/yd^3 and water-cementitious ratio of 0.44. Mixture proportions are provided in Table 55 and Table 56 for the UHPC mixes and Table 57 for the control mixture.

Table 55: Mixture proportion for lower strength mixes

	Weight (lb/yd^3)				Admixtures (lb/yd^3)			Calculated Values	
Mix (ksi)	Sand	Cement IL	Slag	Silica fume	HRWR[1]	WRWR[2]	SE[3]	w/cm	cm/s
12-15	1856	1583	0	83	10.9	10.9	2.1	0.25	0.9
15-18	1815	1404	272	136	16.4	16.4	3.4	0.20	1.0
18-21	1588	1597	309	155	30.9	30.9	5.2	0.1625	1.3

[1]: high range water reducing; [2]: water reducing and workability retaining; [3]: surface enhancing

Table 56: 21 ksi mixture proportion

	Weight (lb/yd^3)				Admixtures (lb/yd^3)			Calculated Values	
Mix (ksi)	Sand	Cement III	Silica Flour	White Silica fume	HRWR	Accelerator	RHRWR[1]	w/cm[2]	cm/s[2]
21+	1361	1477	369	369	46.1	23.1	40.4	0.13	1.63

[1]: retarding high range water reducer; 2: silica flour is included as cementitious material

Table 57: Mixture proportion for the 0.44 w/cm mix

	Weight (lb/yd3)			
Mix	Sand	No. 89 Limestone	Cement IL	w/cm
0.44 w/cm	955	1781	700	0.44

9.2.2. Methods

9.2.2.1. Modified EN 480-14 Specimens Preparation and Experimental Setup

Prior to mixing, all the materials were weighed, and the steel bar (working electrode) was cut to a 5-inch length and cleaned using a grade 0000 steel wool. The cleaned steel bar was coated with epoxy for 1.8 inches, starting 2.2 inches above the end that comes into contact with the concrete. The samples were prepared in accordance with the EN 480-14 standard "Part 14: Determination of the effect on corrosion susceptibility of reinforcing steel by potentiostatic electro-chemical test" with some modifications [18]. Small modifications in sample geometry were made to use U.S. customary units. These differences were made to accommodate dimensions of commonly

found containers and materials used in the Florida rather than those specified for commonly available containers and materials available in Europe. The differences include sample diameter and height, wire diameter and length, and length of the wire embedded in the concrete. Sample geometry used including the steel bar dimension, preparation, and centering are shown in Figure 138. The king (center) wire of an ASTM A416 steel strand was used for the working electrodes in this study.

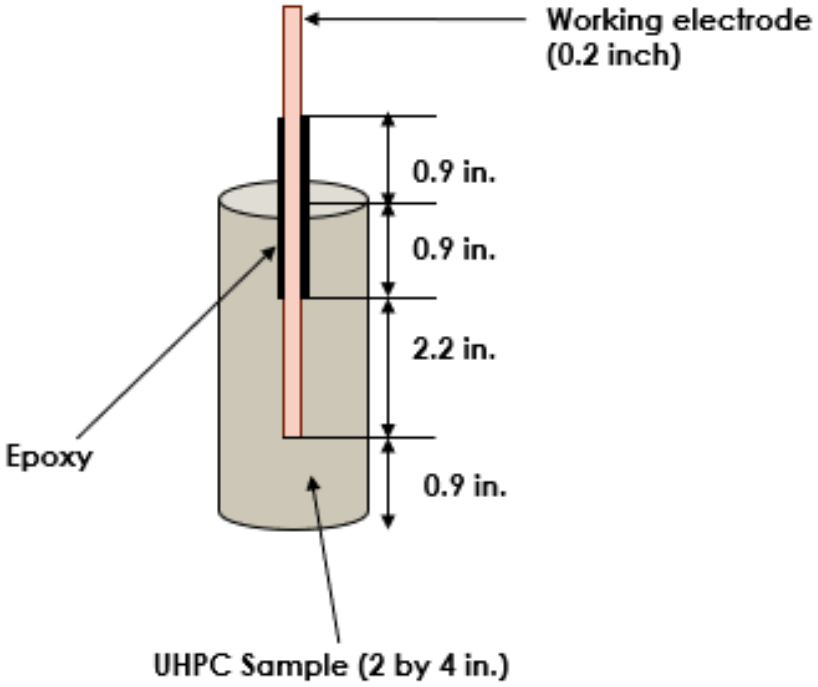

Figure 138: Preparation setup of UHPC specimen

All the UHPC mixes with different strength classes were made in a mortar mixer meeting ASTM C305 [259] with a batch size of 0.05 ft^3 and no fibers. The results were compared to those from the control concrete mixture. NaCl was added to the mixtures to boost the chloride concentration to determine the level at which corrosion would occur. The samples were made with different chloride contents ranging from 0.2 to 16 lb/yd^3. The mixes were each compared to a reference mix with the same mix design with no added chlorides, including the normal concrete that had a 0.44 w/cm. The mixing time varied depending on the type of the mix. The mixing times used for each mixture are given in

Table 58.

Table 58: Mixing time for each type of threshold chloride mixes

Mix type	Mixing Time (mins)
0.44 w/cm	5.0
12 ksi	10.0
15 ksi	15.0
18 ksi	20.0
21ksi	25.0

After the mix was done, a 2 in. × 4 in. cylinder was filled with the concrete and the steel bar (working electrode) was embedded in the center of the cylinder. Half of a separate 4 in. × 8 in. cylinder was filled to be used to later measure the water and acid soluble chloride content and was demolded 2 days after placement for testing. The 2 in. × 4 in. cylinder was removed from the mold 24 hours ± 1 hour after mixing, and then placed in a lime solution for another 24 hours. A 0.4 in. section from the top surface of the cylinder was kept dry, as contact with the solution may lead to errors in the test results. After the 24 hour equilibration period, the working electrode (steel bar), reference electrode (silver chloride), and counter electrode (stainless steel) were connected to a potentiostat at a potential of 500 ± 5 mV, and the current change over time was measured for 24 hours. The potentiostatic test was carried out as described in PN-EN 480-14 standard [18]. The testing set up is illustrated in Figure 139.

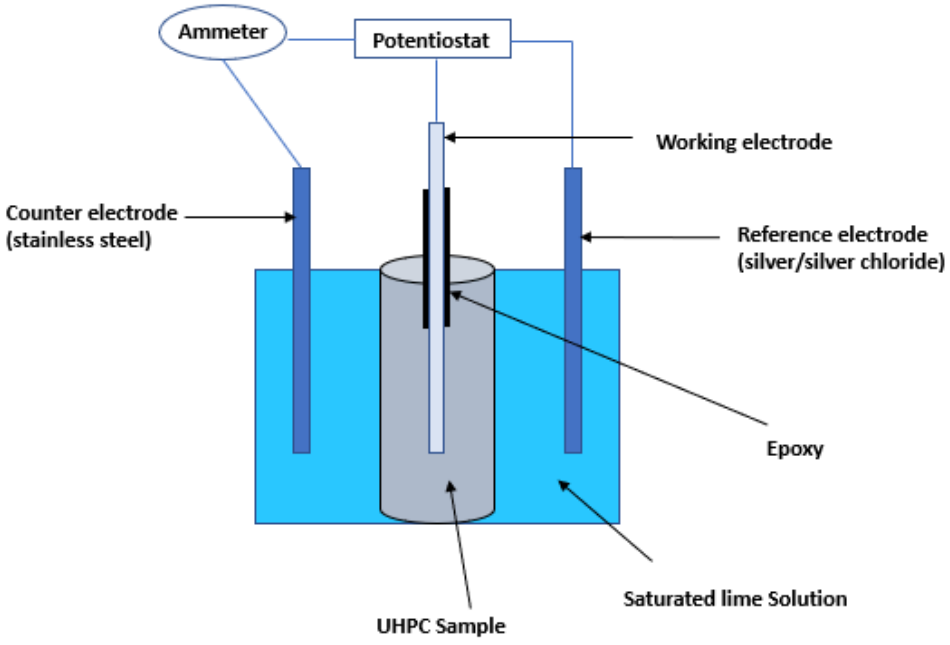

Figure 139: Threshold chloride test set up

After the test was completed, the specimen was split open, and the working electrode was examined for corrosion, as shown in Figure 140. The appearance of visible corrosion is usually

accompanied by a sharp current increase. The test was repeated if the working electrode had crevice corrosion or if there was evidence that the corrosion happened as a result of the voids. The mixing and testing were continued for each strength class until the corrosion was visually observed.

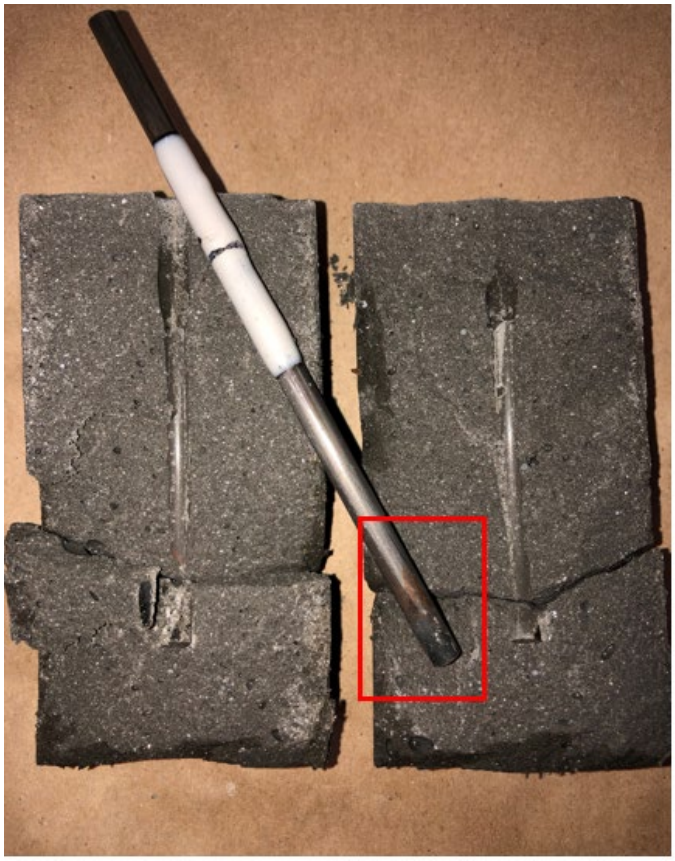

Figure 140: UHPC specimen after getting cracked open

A sample of limewater was taken before placing the UHPC sample in the solution and after the test was done to measure any chloride leaching. The companion samples were also tested for both acid and water-soluble chlorides.

9.2.2.2. Acid and Water Soluble-Chlorides

After the 2-day lab curing, the companion chloride samples were pulverized into a powder, sieved using #50 and #20 sieves, and dried in a 221°F (105 °C) oven for 24 hours. The powders were sealed in a bag and placed in a desiccator to prevent moisture intrusion. Later, the samples were tested for acid- and water-soluble chloride concentrations in accordance with Florida Method FM 5-516, and ASTM C1218, respectively [289] [290].

9.3. Results and Discussions

9.3.1. Modified EN 480-14 Measurements

The modified EN 480-14 European method was followed to determine the admixed chloride threshold for new concrete [18]. The sample current flow was measured during the first 24 hours of testing, and the maximum current density was calculated by dividing the maximum current flow by the unit area of the working electrode (was 9.54 cm^2). The reference samples with no added chlorides showed a current density less than 0.8 $\mu A/cm^2$. The current measured did not appreciably change when additional chlorides were added until the chloride threshold was reached. When the admixed chloride threshold was reached, a sharp current increase was observed, as shown for the 18-21 ksi mixture in Figure 141. The differences between samples with active corrosion and samples with chloride contents below the chloride threshold are easily seen and noted. After the test was complete, a sample autopsy, as shown in Figure 142 was performed to determine if corrosion had occurred.

Table 59 gives the current measured for the 18-21 ksi mixture with replicates for different chloride contents. It can be seen that up to 9 lb/yd^3, the corrosion current density remained less than 0.85 µA/cm^2; however, at 10 lb/yd^3, the corrosion current density increased to 36 µA/cm^2 indicating active corrosion. In general, when the w/cm of the mix decreased, the corrosion current density decreased, as expected. The values of the average corrosion current density at 24 hours for the UHPC samples compared to the samples with no added chlorides at 1 hr are presented in Table 60. UHPC samples had a corrosion current density more than an order of magnitude lower than the normal concrete mix. The 21+ ksi mixture had a current density of 15.8 µA/cm^2 at 24 hours while the normal-strength concrete mixture had a measured current density of 421 µA/cm^2 at 1 hr. This is likely caused by the higher electrical resistivity of the UHPC.

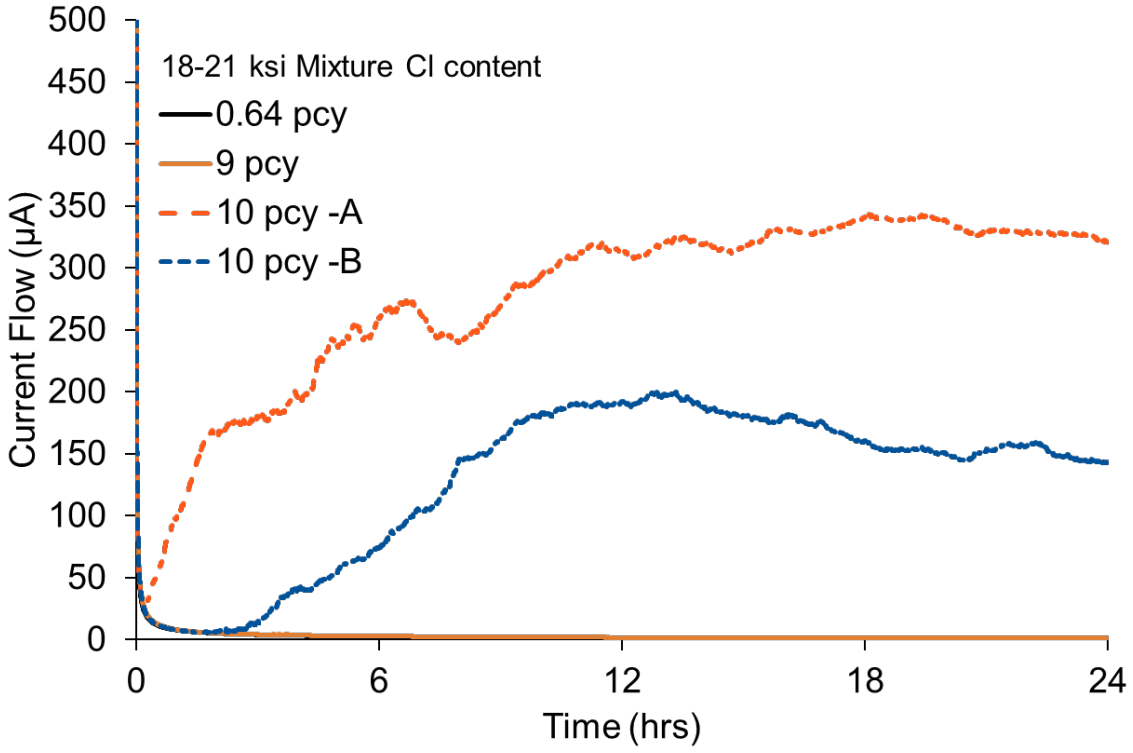

Figure 141: Current flow for corroded samples of 18-21 ksi mixture compared to non-corroded samples

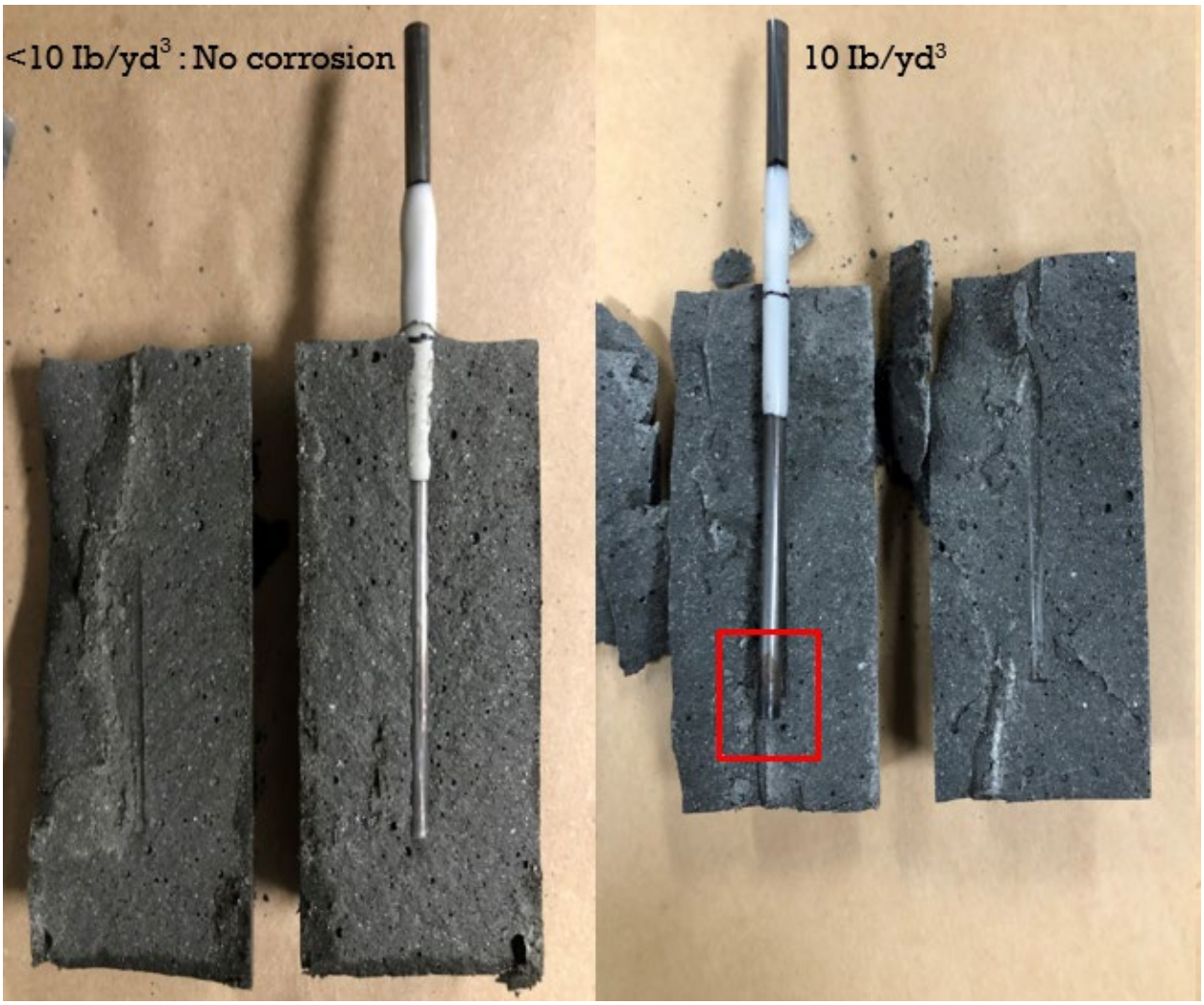

Figure 142: Sample without corrosion compared to sample with corrosion for 18-21 ksi mixture

Table 59: 18-21 ksi mixture corrosion current flow and density

Mix	Total Cl content (lb/yd^3)	Maximum current (μA)	Maximum Current density ($\mu A/cm^2$)
0-A	0.64	7.8	0.82
0-B	0.64	8.3	0.87
5-A	5	7.8	0.82
5-B	5	7.8	0.82
8-A	8	4.6	0.48
8-B	8	4.6	0.48
9-A	9	8.1	0.85
9-B	9	4.4	0.47
10-A	10	200	21
10-B	10	343	36

Table 60: Concrete current density compared to the reference mixes

Mix	Total added Cl content (lb/yd^3)	Test time when stopped (hr)	Average current density when test stopped ($\mu A/cm^2$)
0.44 w/cm	0	24	0.39
	12	1	421.0
12-15 ksi	0	24	0.56
	13	24	105
15-18 ksi	0	24	0.46
	16	24	87
18-21 ksi	0	24	0.82
	10	24	28.4
21+ ksi	0	24	0.21
	13	24	15.8

The mixes corrosion rate with time is shown in Figure 143. As seen in the graph, there is a large difference in the corrosion rate between mixes. Even though the maximum amount of added chlorides was similar for the mixtures, the normal concrete mix exhibited significantly higher corrosion current density. The corrosion rate increased as the time increased and decreased as the strength of the mix increased. The 21+ ksi mix showed a steady corrosion rate indicating its higher electrical resistivity compared to the normal concrete, in which it showed a rapid increase in current, and reached the maximum current density in less than 1 hour. This indicates that if the chlorides were to penetrate the 18 – 21 ksi and 21+ ksi mixes, the corrosion rate would most probably remain almost constant with time or even negligible due to significant reduction in the oxygen diffusion, water diffusion, and low electrical conductivity associated with the low-porosity UHPC structure [293].

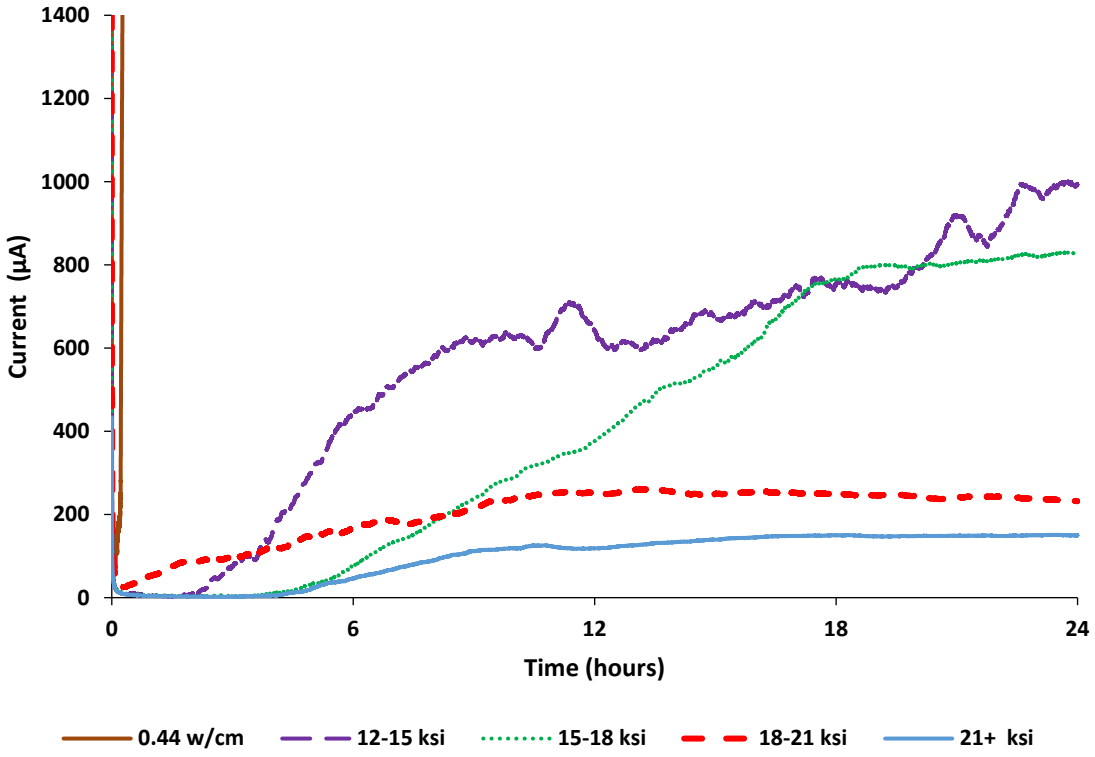

Figure 143: Mixture corrosion current flow versus time

9.3.2. Acid- and Water-Soluble-Chlorides

Chloride ion concentration can be measured using acid-soluble (total) chlorides or water-soluble (free) chlorides. The acid-soluble chlorides represent the total amount of chlorides, including the chemically and physically bound chlorides ions in the hydrated cementitious materials that are potentially available for future corrosion in the concrete. The water-soluble chlorides represent the chloride ions in the concrete that are available for initiating corrosion [294].

FM 5-516 method and ASTM C1218 were followed to determine the amount of acid- and water-soluble chlorides in the concrete samples [289][290]. Bound chlorides were estimated by calculating the difference between the acid- and water-soluble chlorides. Chloride tests were done for the companion samples. The chloride contents in the limewater before and after use in the tests were also measured. The measured chloride contents for the companion samples from each strength class with the amount of added NaCl to initiate corrosion were compared to samples with no added NaCl in The 21+ ksi mixture used a different type of silica fume and different chemical admixtures, resulting in lower initial chloride content than the 18-21 ksi mixture. When looking at the amount of chlorides that were internally added to the mixtures to initiate corrosion, the mixes had similar chloride contents, ranging from 10 to 13 lb/yd3. However, the measured acid-soluble chlorides per mass of cementitious materials indicates that the normal concrete mixture with a 0.44 w/cm had a higher chloride ratio, 1.60%, which was about two to three times higher than the UHPC mixes with chlorides of 0.79%, 0.74%, 0.51%, and 0.60% for the 12-15, 15-18, 18-21 and 21+ ksi mixtures, respectively. The water-soluble

chlorides per mass of cementitious materials were close to zero for all the mixes with no added chlorides. The water-soluble chloride content as a percentage of the cementitious materials required to initiate corrosion decreased as the strength of the mixes decreased.

Table 61. The total of the acid-soluble chlorides of the UHPC reference samples with no added chlorides were almost two times higher than the normal concrete reference samples, with the 18-21 ksi mixture containing more than the allowed 0.4 lb/yd^3 of chlorides allowed by FDOT. This could be because of the high amount of the different cementitious materials that were used and the high amount of chemical admixtures, as shown in Figure 144. The 21+ ksi mixture used a different type of silica fume and different chemical admixtures, resulting in lower initial chloride content than the 18-21 ksi mixture. When looking at the amount of chlorides that were internally added to the mixtures to initiate corrosion, the mixes had similar chloride contents, ranging from 10 to 13 lb/yd^3. However, the measured acid-soluble chlorides per mass of cementitious materials indicates that the normal concrete mixture with a 0.44 w/cm had a higher chloride ratio, 1.60%, which was about two to three times higher than the UHPC mixes with chlorides of 0.79%, 0.74%, 0.51%, and 0.60% for the 12-15, 15-18, 18-21 and 21+ ksi mixtures, respectively. The water-soluble chlorides per mass of cementitious materials were close to zero for all the mixes with no added chlorides. The water-soluble chloride content as a percentage of the cementitious materials required to initiate corrosion decreased as the strength of the mixes decreased.

Table 61: Measured chloride contents for companion samples at 2 days

Mixes	Target chloride content lb/yd^3	Total chlorides (acid-soluble) lb/yd^3	Total chlorides (acid-soluble) Percent of Cementitious Material	Water-soluble chlorides lb/yd^3	Water-soluble Percent of Cementitious Materials
0.44 w/cm	0	0.23	0.03	0.02	0.00
	12	11.26	1.60	6.43	0.91
12-15 ksi	0	0.30	0.02	0.19	0.01
	13	13.21	0.79	8.60	0.52
15-18 ksi	0	0.38	0.02	0.26	0.01
	13	13.39	0.74	9.35	0.52
18-21 ksi	0	0.51	0.02	0.00	0.00
	10	10.45	0.51	5.70	0.28
21+ ksi	0	0.14	0.01	0.07	0.00
	13	13.13	0.60	5.60	0.25

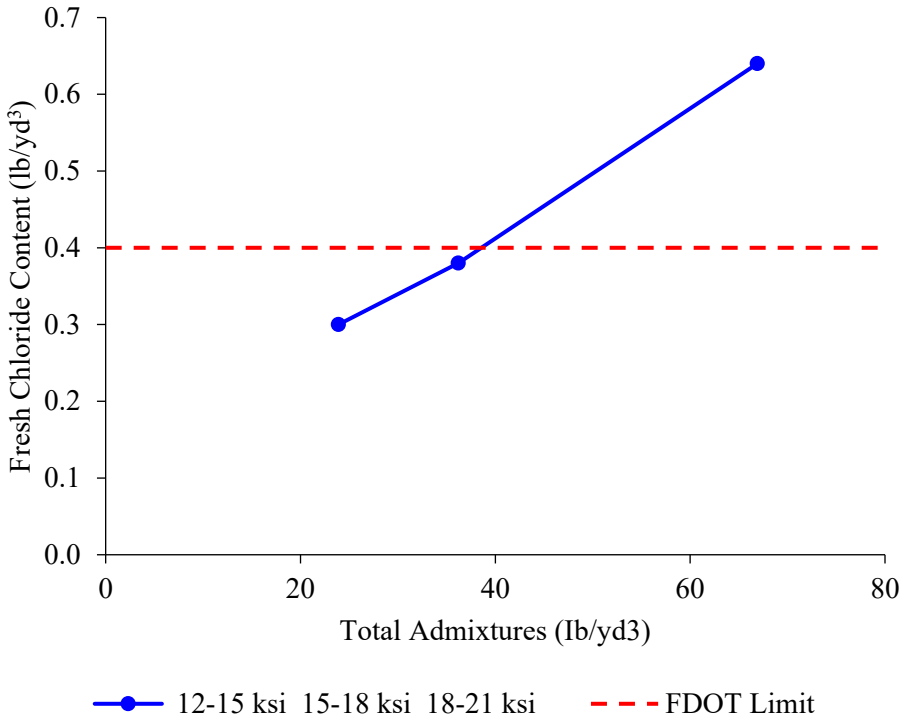

Figure 144: Fresh chloride content of the admixtures used for the 12 to 21 ksi UHPC mixes

Limewater samples before and after testing were analyzed for chloride content to determine the chloride content leached out of the concrete, after which the concrete chloride contents present when corrosion occurred were calculated by subtracting the leached amount from the concrete chloride concentration before leaching, referred to as the residual concrete chloride corrosion thresholds. The measured chloride content for the samples that had corrosion are reported in The ratios of the acid-soluble chlorides to the water-soluble chlorides were almost double for the lower-strength mixes and almost three times for the higher-strength mixes (18-21 ksi and 21+ ksi mixes). The normal-strength concrete bound less chloride than the UHPC mixes, likely because of the high cementitious material content used for UHPC. The leached chloride content of the normal-strength concrete mix was almost 4 times higher than the content found for UHPC during testing. This resulted in total chloride threshold contents, after accounting for leaching, that were ~25% higher for UHPC than normal-strength concrete. This shows that the concrete chloride limit could be increased by 25% to 0.5 lb/yd3 without changing the factor of safety against corrosion. While this test method could identify corrosion initiation as confirmed by the test specimen autopsies, the chloride content leached into the limewater during curing and testing needs to be accounted for when calculating the residual concrete chloride threshold content that initiates corrosion.

Table 62. The ratios of the acid-soluble chlorides to the water-soluble chlorides were almost double for the lower-strength mixes and almost three times for the higher-strength mixes (18-21 ksi and 21+ ksi mixes). The normal-strength concrete bound less chloride than the UHPC mixes, likely because of the high cementitious material content used for UHPC. The leached chloride

content of the normal-strength concrete mix was almost 4 times higher than the content found for UHPC during testing. This resulted in total chloride threshold contents, after accounting for leaching, that were ~25% higher for UHPC than normal-strength concrete. This shows that the concrete chloride limit could be increased by 25% to 0.5 lb/yd^3 without changing the factor of safety against corrosion. While this test method could identify corrosion initiation as confirmed by the test specimen autopsies, the chloride content leached into the limewater during curing and testing needs to be accounted for when calculating the residual concrete chloride threshold content that initiates corrosion.

Table 62: Chloride content calculations for concrete with reinforcing steel corrosion

Mixes	Cementitious Materials lb/yd^3	Total chlorides (acid-soluble) lb/yd^3	Water-soluble chlorides lb/yd^3	Leached chlorides after testing lb/yd^3	Bound chlorides lb/yd^3	Total chlorides in concrete after leaching (lb/yd^3)
0.44 w/cm	704	11.26	5.38	3.87	2.01	7.39
12-15 ksi	1666	13.21	5.13	0.94	7.14	12.27
15-18 ksi	1802	13.39	6.34	1.27	5.78	12.12
18-21 ksi	2060	10.45	3.73	0.66	6.06	9.79
21+ ksi	2203	13.13	4.95	0.85	7.33	12.82

A big difference was observed between the residual chloride contents that initiate corrosion for normal concrete and UHPC when expressed as percentages of cementitious materials (

Table 63). The calculations assume that the leaching does not affect the bound chloride content. It can be seen that UHPC had a similar amount of bound chlorides by mass of cementitious materials, however the chloride content required to initiate corrosion in the concrete decreased with increasing strength level. This may be because the high percentage of SCMs in the UHPC lowers the hydroxyl content and pH.

Table 63: Residual chloride thresholds

Mixes	Cementitious material content lb/yd3	Acid-soluble chlorides for corrosion as a percent by mass of cementitious material	Water-soluble chlorides for corrosion as a percent by mass of cementitious material	Bound chlorides as a percent by mass of cementitious material
0.44 w/cm	704	1.05	0.76	0.29
12-15 ksi	1666	0.74	0.31	0.43
15-18 ksi	1802	0.67	0.35	0.32
18-21 ksi	2060	0.48	0.18	0.29
21+ ksi	2203	0.56	0.22	0.33

ACI-318 limits the water-soluble chloride content to the values shown in Table 51. When comparing the results to the ACI-318 limits, it seems that the ACI limits as a percentage of cementitious material for the higher-strength UHPC mixes, 18-21 ksi and 21+ ksi, are non-conservative and can result in corrosion, especially for non-prestressed concrete with C1 category of exposure. The 18-21 ksi and 21+ mixes had 0.18, and 0.22 percent of water-soluble chlorides, compared to the 0.30% maximum chloride limit for exposure C1 for non-prestressed concrete in ACI-318. Also, the lower UHPC strength classes, 12-15 ksi and 15-18 ksi, almost reached the maximum limits by the ACI 318, in which they were 0.31% and 0.35% respectively. While these limits may be non-conservative in terms of chloride content required to initiate corrosion, the corrosion rates were extremely low and concrete at these chloride contents may still have a long service life.

9.4. Summary

UHPC and normal concrete samples were made without fibers and with increasing levels of internally admixed chlorides for four different levels of strength to determine chloride thresholds for internally added chlorides. A slightly modified version of EN 480-14 was used to monitor corrosion rates of samples with admixed chlorides. The normal concrete mix exhibited significantly higher corrosion current density and current flow than the UHPC mixtures, with the current flow rate decreasing as the strength increased. Significant chloride leaching was found to occur in EN 480-14 during curing and testing, resulting in misleading chloride threshold values. Once the leached chloride contents were accounted for, the chloride contents calculated showed that the UHPC had ~ 25% higher chloride threshold than the control mixture. This can justify raising the fresh chloride limit 25% from 0.4 lb/yd3 to 0.5 lb/yd3. Looking at the chloride results, the chloride binding of fresh chlorides in UHPC was similar to that measured in normal-strength concrete by percent of cementitious materials. The ACI 318 water-soluble chloride limits as a percent by mass of cementitious materials were found to be non-conservative for the two of the UHPC mixtures tested and should be re-examined for UHPC.

10. UHPC PERMEABILITY TEST METHODS

10.1. Introduction

Twelve ultra-high-performance concrete (UHPC) mixes with different mixture proportions, water-cementitious material ratios (w/cm), and fiber contents were made to test the chloride penetrability performance of UHPC. These mixtures were designed for different strength classes to determine the strength level at which the concrete forms a non-continuous pore structure and limit the chloride ingress into the concrete.

UHPC mixtures were made for multiple strength classes and used three different curing methods. Four compressive strength classes of 12-15 ksi, 15-18 ksi, 18-21 ksi, and 21+ ksi were used to measure the concrete structural and durability properties. The UHPC samples were made using lab-temperature curing in a moist (fog) room, simulated precast beam curing (hereafter called precast curing), and steam curing. The mixes were made with no fibers and with two percentages of steel fibers, 1.5% and 2%, to determine the effects of steel fiber inclusion on transport property measurements. Samples were made to test mixture performance in a modified NT Build 492 [13] rapid chloride migration (RCM) test to determine if this method could be suitable to determine the sample resistance to chloride intrusion. Measured chloride penetration in the modified RCM test was compared against the results of five other test methods: bulk resistivity [14], surface resistivity [15], water absorption [16], mercury intrusion porosimetry, and ASTM C1556 bulk diffusion [17].

10.2. UHPC Materials and Mixture Proportions

A fine masonry sand was used in the UHPC mixtures, with properties shown in Table 64. Cementitious materials used for this study included ASTM C595 Type IL cement [247], ASTM C150 Type III cement [255], slag [256], an ASTM C1240 dark gray silica fume [257], an ASTM C1240 white silica fume and silica flour. The particle size distributions of the cements and the cementitious materials were determined using a HORIBA LA-950 laser particle size analysis, with the results shown in Figure 145. The silica fume was sonicated for 7.5 minutes prior to testing and showed a bimodal distribution which it is likely due to agglomerated particles being categorized as larger particles [292].

Table 64: Properties of fine aggregates

Properties	Value
Specific Gravity	2.66
Absorption	0.20%

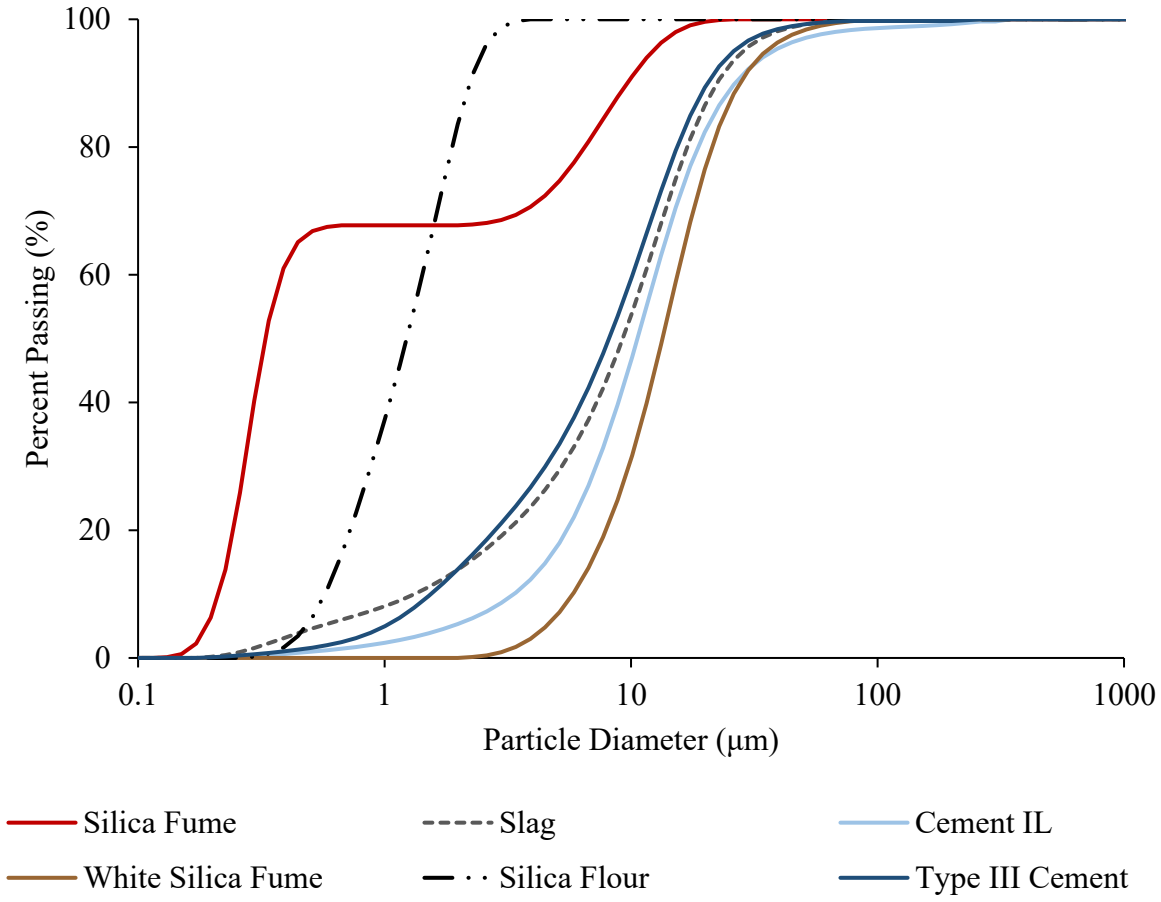

Figure 145: Particle size distribution

The compositions of the cementitious materials were measured by x-ray fluorescence and are shown in Table 45. Glass beads were made from the samples and used in the XRF testing. The cements phase compositions were measured using semi-quantitative X-ray diffraction (XRD) [240] and is provided in Table 46.

Table 65. XRF results for materials (%)

Parameter	Cement IL	Cement III	Slag	Silica Fume	White Silica Fume	Silica Flour
SiO_2	18.82	20	34.79	80.45	96.49	98.88
TiO_2	0.22	0.22	0.64	0.02	0.02	0.01
Al_2O_3	4.79	4.90	13.17	0.48	1.37	0.17
Fe_2O_3	3.10	3.30	0.78	4.78	0.16	0.01
MnO	0.06	0.13	0.32	0.44	0.00	0.01
MgO	0.80	1.0	4.66	10.43	0.01	0.01
CaO	62.85	63.30	43.71	0.95	0.00	0.01
Na_2O	0.08	0.12	0.19	0.18	0.07	0.01
K_2O	0.25	0.38	0.41	0.77	0.02	0.02
P_2O_5	0.41	0.49	0.04	0.03	0.23	0.01
SO_3	3.02	3.70	3.00	0.07	0.00	0.01
ZnO_2	0.00	0.05	0.00	0.00	0.43	0.00
LOI	5.45	2.44	0.02	2.93	0.66	0.27

Table 66: Cement composition

Phase	Type IL Cement (%)	Type III Cement (%)
Alite	44.3	53
Belite	23.2	16.4
Aluminate	4.2	4.1
Ferrite	11.2	13.8
Bassanite	0.5	5.2
Gypsum	5.1	1.1
Calcite	11.7	2.3
Anhydrite	-	1.6
Arcanite	-	0.5
Syngenite	-	0.9
Thenardite	-	0.5
Quartz	-	0.6

Twelve different UHPC samples were made for this study using mixtures designed for four different strength classes, 12-15 ksi, 15-18 ksi, 18-21 ksi, and 21+ ksi, respectively. Samples in the range of 15-18 ksi were repeated with a reduced chemical admixture dosage to reduce the possibility of fiber segregation. The mixes were often referred to by the lower bound of their target strength. Samples in the 15-18 ksi mixture class are referred to as 15 ksi and 15.2 ksi mixes and are mixture replicates. The samples were designed for three curing methods, moist-room, steam and precast. Type III cement was only used for the 21 ksi mixture to improve particle packing and achieve the higher strength, and 75% of the water used for this mix was ice to offset the temperature rise expected from the high mixing energy used. For each strength class, steel fibers with 0.008 in. (0.2 mm) diameter and 0.5 in. (13 mm) length were used at three

different percentages, 0%, 1.5%, and 2%. Table 67 shows the mixture proportions used for the 12-15, 15-18, and 18-21 ksi mixtures, while Table 68shows the mixture proportions used for the 21+ ksi mixture.

Table 67: Mixture proportion for lower strength mixes

Mix (ksi)	Weight (lb/yd^3) Sand	Cement IL	Slag	Silica fume	Admixtures (lb/yd^3) HRWR[1]	WRWR[2]	SE[3]	Calculated Values w/cm	cm/s
12-15	1856	1583	0	83	10.9	10.9	2.1	0.25	0.9
15-18	1815	1404	272	136	16.4	16.4	3.4	0.20	1.0
18-21	1588	1597	309	155	30.9	30.9	5.2	0.1625	1.3

[1]: high range water reducing; [2]: water reducing and workability retaining; [3]: surface enhancing

Table 68: 21-ksi mixture proportion

Mix (ksi)	Weight (lb/yd^3) Sand	Cement III	Silica Flour	White Silica fume	Admixtures (lb/yd^3) HRWR	Accelerator	RHRWR[1]	Calculated Values w/cm^2	cm/s^2
21+	1361	1477	369	369	46.1	23.1	40.4	0.13	1.63

[1]: retarding high range water reducer; 2: silica flour is included as cementitious material

10.3. UHPC Mixing and Samples Fabrication

All UHPC batches were made in the concrete mixing facilities at the University of Florida (UF). The IMER Mortarman 750 mixer, a large pan mixer with orbital mixing action shown in Figure 146, was used to make UHPC batches up to 4.0 ft^3 in volume. The Pheso Rheometer shown in Figure 147 was used to make trial batches.

Figure 146: IMER Mortarman mixer for UHPC batches up to 4.0 ft^3

Figure 147: Pheso Rheometer mixer for UHPC batches up to 0.13 ft^3

One day prior to mixing, the fine aggregate and cementitious materials were weighed and sealed in 5-gallon buckets. On the day of mixing, the mixer was rinsed with water to dampen the surfaces and drained, then all the dry materials were added and mixed for two minutes. While the mixer was running, the water and admixtures were slowly added over a period of about one

minute. After the mixture workability changed from appearing like a soil-cement to a viscous fluid with self-consolidating properties, the steel fibers were added and mixed for an additional five minutes. The total mixing time ranged from 20 to 35 minutes, depending on the mix.

After the mixing was done, 4-in, × 8-in. (100-mm × 200-mm), and 3-in. × 6-in. (76-mm × 152-mm) concrete cylinders were made according to ASTM C1856 [59]. The concrete was placed into the cylinder molds using a small bucket that was tapped 30 times with a mallet for consolidation. After placing and tapping the concrete, the samples were finished and capped to prevent moisture loss during the first 24 hours after mixing. Concrete specimens were removed from the molds 24 hours ± 2 hours after mixing. Three different curing methods were used, moist-room curing at lab temperature after demolding at 24 hours, steam curing following demolding at 24 hours, and precast curing during the first 24 hours.

The moist-room-room-cured specimens were demolded and stored in a moist-room-curing room meeting ASTM C511 [258] that was kept between 70°F and 77°F (21°C and 25°C) and above 95% relative humidity. The steam-cured specimens were demolded and placed in a covered pan above water and put in an oven with a set temperature of 194°F (90°C). After two days of steam curing, the samples were stored in the moist room until testing. Duct tape was used to seal the cover to the pan to prevent the samples from drying out and to prevent pressure build-up in the pan. The precast-cured specimens followed a regimen intended to simulate the temperature development of a beam made in a precast facility. The high heat of hydration provided by the high cementitious material content can significantly heat up the beam during curing, accelerating the curing and changing the concrete properties. For the simulated precast curing method, specimens still in their molds were placed, after four hours of precuring, in a covered pan without water at a temperature of 158°F (70°C). They were removed from the oven after 22 hours and allowed to cool, after which they were demolded and placed in the moist-room-curing room until they were ready for testing or further sample preparation. Figure 148 shows target temperatures with time for the three curing regimes.

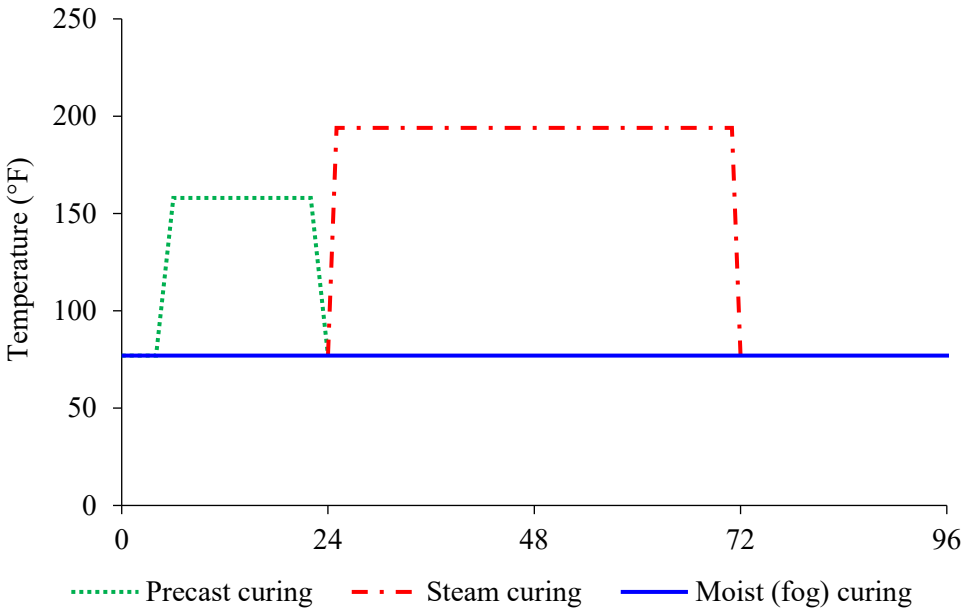

Figure 148: Curing method temperatures

10.4. UHPC Penetrability Testing Methodology

Four different non-proprietary mix designs, each cured by three different methods, were used to study UHPC resistance to chloride penetration. The following sections describe the test methods used to evaluate the UHPC penetrability resistance and compare results to determine the most suitable method for mix design approval.

10.4.1. Compressive Strength

The UHPC mixtures were designed to range in compressive strength from 12 to 21 ksi at 28 days in order to investigate how the UHPC chloride penetrability performance would be impacted, and at what level the chloride ingress would be limited. The compressive strength was measured according to ASTM C39 with a load rate of 35 ± 7 psi/s (0.25 ± 0.05 MPa/s) for samples that were expected to have a compressive strength below 17,000 psi (120 MPa) [87]. ASTM C1856 was followed with a load rate of 145 ± 7 psi/s (1.0 ± 0.05 MPa/s) for samples that were expected to have a compressive strength above 17,000 psi (120 MPa) [59]. Three specimens with a dimension of 3 in. × 6 in. for each strength class and curing method were ground prior to testing and tested at an age of 28 days.

10.4.2. Modified Rapid Chloride Migration Test

A modified version of the rapid chloride migration test (NT Build 492) test similar to one suggested for UHPC by Thomas and Moffatt of the University of New Brunswick was used to measure chloride ingress for the different mixtures. The test modification is based on the idea that pores in UHPC are only connected to the surface for a limited depth [295]. This test uses an electrical voltage to accelerate the movement of chlorides into the concrete specimen [117]. For each curing method, a total of two cylinders were made and sawcut into three 2 in. × 4 in. (50

mm × 100 mm) discs before testing. After sawcutting, the day prior to testing, the specimens were cleaned and placed in a vacuum desiccator for three hours followed by one hour in a saturated lime solution while they remained under vacuum. After that, they were kept submersed in the limewater at atmospheric pressure for 18 ± 2 hours. After the specimens were prepared, they were exposed to 10% NaCl solution on one side and 0.3 N NaOH on the other side and tested at an age of 28 days as shown in Figure 149.

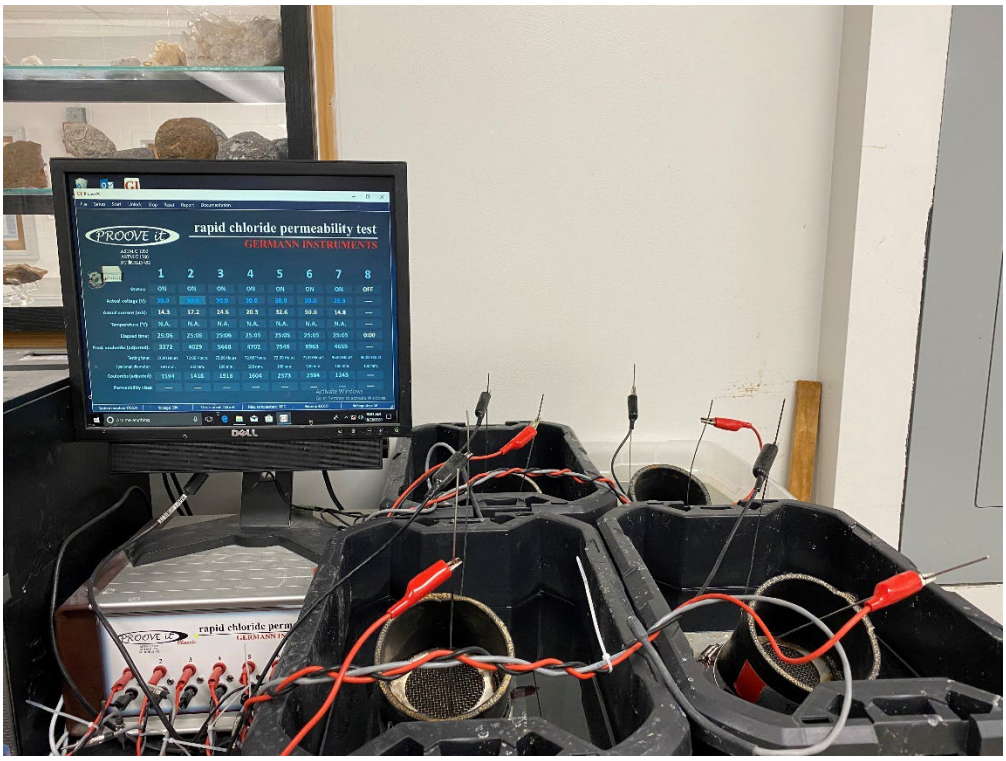

Figure 149: RCM testing set up

A 30 V sample driving potential was used for all specimens with or without fibers. Steel fibers are known to affect concrete electrical resistivity measurements, making it difficult to employ a purely electrical test method as a measure of fiber reinforced UHPC penetrability. The RCM test uses measures of the chloride penetration depth in the test to calculate a non-steady state migration coefficient, not a measure of electrical resistance. It was hypothesized that RCM chloride penetration depth measurements would have minimal-to-no change from the inclusion of fibersThree different test durations were used to determine if chloride penetration stops after an initial penetration during the first few days in UHPC, signifying a discontinuous pore structure with little pore connection between the surface and sample interior. After the test duration was complete, the concrete samples were cut into halves and sprayed with 0.1 M silver nitrate to determine the chloride penetration depths as shown in Figure 150. The non-steady state chloride migration coefficient was then calculated using the Equation 32.

$$D_{nssm} = \frac{0.0239(273+T)L}{(U-2)t}\left(x_d - 0.0238\sqrt{\frac{(273+t)Lx_d}{U-2}}\right) \qquad \text{Equation 32}$$

Where: D_{nssm}: non-steady-state migration coefficient, $\times 10^{-12}$ m^2/
U: absolute value of the applied voltage, V;
T: average value of the initial and final temperatures in the anolyte solution, °C
L: thickness of the specimen, mm
x_d: average value of the penetration depths, mm
t: test duration, hour

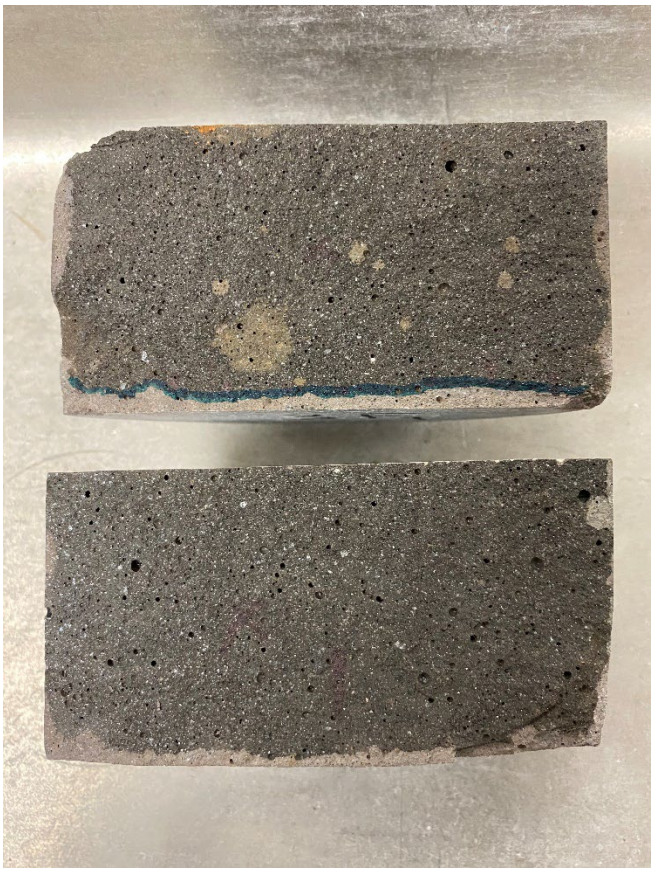

Figure 150:10-day RCM testing sample after sprayed with 0.1 M silver Nitrate

10.4.3. Surface and Bulk Resistivity Tests

After demolding, three 4-in. × 8-in. (100-mm × 200-mm) cylinders for each curing method were used for surface and bulk resistivity testing. These tests were used to provide a rapid indication of concrete resistivity to the chloride penetration. The higher the resistivity, the lower the

chloride penetration that would be expected. Comparison between mixes with and without fibers were made to see the effect of the steel fibers on the electrical properties of the specimens. Steel fibers were expected to affect the readings due to creating a conductive path that reduces resistivity, although the extent is not known. One study found that this test might be used with mixes having fibers because the fibers are usually randomly dispersed, and most of the time they do not touch to create a connected path along the entire length of the specimens, although they would shorten the path [5].

Concrete surface resistivity was measured according to AASHTO T 358, with the curing was performed in a moist-curing room. A Proceq Resipod meter was used to measure the resistivity [15] [14]. Prior to testing, the end faces of UHPC 4-in. × 8-in. (100-mm ×200-mm) cylinders were ground as shown in Figure 151. To measure the concrete surface resistivity, four marks were made at 0, 90, 180, and 270-degrees around the circumference of the samples. On the day of testing, the samples were removed from the moist room, and the measurements were taken using the resistivity meter as shown in Figure 152.

Figure 151: Grinding UHPC samples for resistivity measurements

Figure 152: Surface resistivity test set up

Bulk resistivity was measured according to AASHTO T 119 using the same samples used to measure the surface resistivity. To measure the concrete bulk resistivity, the probes of the Resipod were connected to two conductive plates placed on the ground ends of the specimens. Top and bottom saturated sponges were also used between the conductive plates and the end faces of the specimens to improve the electrical connection. Their resistances were recorded to provide a correction for the bulk resistivity readings. After recording the sponges' resistivities, the concrete specimen was placed between the plates and the readings were taken as shown in Figure 153. The infrared thermometer was used to measure the specimens' temperature. These steps were performed for the other two specimens, and they were then be returned to the moist room for further testing at a different age.

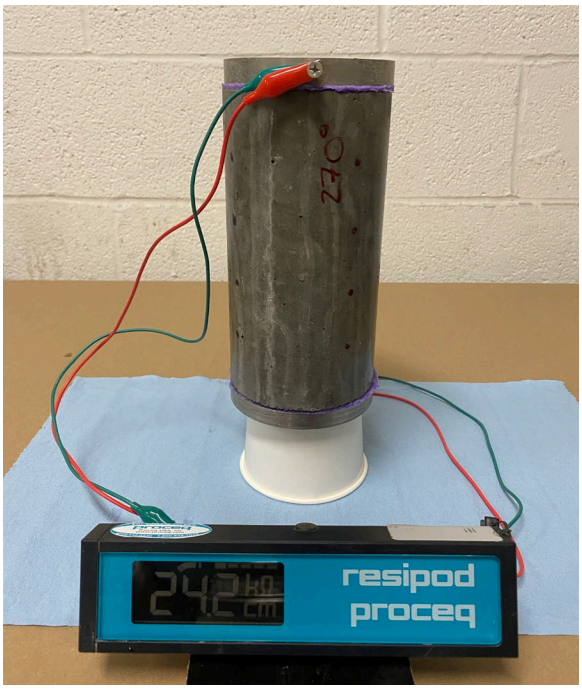

Figure 153: Bulk resistivity test set up

10.4.4. Mercury Intrusion Porosimetry (MIP)

MIP is a common test used for characterizing the porosity and the size distribution of capillary pores in cement paste specimens [263][264]. For each curing method, the samples were cut into small pieces using a wafer saw with maximum dimensions of 0.12 in. × 0.98 in. × 0.39 in. (3 mm × 25 mm × 10 mm). After that, the samples were immersed in a 2-in. × 4-in. (50-mm × 100-mm) plastic container with a large volume of isopropanol for 7 days to stop hydration. The isopropanol exchange was used to diffuse into the paste and replace the pore solution. The samples were then placed in a vacuum desiccator to remove the isopropanol and store the samples without carbonation until testing. The testing was conducted using a Quantachrome PoreMaster 60 at a pressure range of 135 kPa to 415 MPa. The relationship between the pore size and the applied pressure is given by the Washburn equation, as shown in Equation 33 [134,135]:

$$d = \frac{-4\,\gamma\,cos\,\theta}{P} \qquad \text{Equation 33}$$

Where: d is the pore diameter (m)

γ is the surface tension of mercury (N/m)

θ is the contact angle between the solid and mercury

P is the applied pressure (N/m^2)

Analysis using the Washburn equation assumes the pore shapes to be cylindrical, and the surface tension of mercury γ to be 0.48 N/m. The contact angle θ has often been assumed to be 140°.

However, based on the work presented by Muller and Scrivener using a comparison between MIP results and NMR relaxometry, the assumption for the angle is most likely overestimated. Therefore, they suggested using 120°, which was used in this research [265].

10.4.5. Water and Isopropanol Absorption

The ASTM C1202 vacuum saturation method [16] was used to measure UHPC absorption capacity by isopropanol. It is believed that the isopropanol molecule is too large to penetrate into gel pores [296]. The samples at 28 days were placed in a vacuum desiccator for three hours and then submerged with deaired water under vacuum for one hour. After that, the samples were open to air for 18 ± 2 hours. They were weighed and recorded as an initial weight. They were then placed in an oven for 24 hours at 212°F (100°C). Their weights were taken after the drying period. Then the samples were placed in the desiccator again under vacuum for three hours and submerged with isopropanol for one hour. They were then left in the isopropanol under atmospheric pressure for 18 ± 2 hours. The difference in mass was calculated for both water and isopropanol, and the measurements were compared. UHPC has been shown to have very low water absorption of only 1-2% by volume [129]. Therefore, the higher strength mixes were expected to have very low water absorption.

10.4.6. Bulk Diffusion

Samples were tested according to ASTM C1556 to determine the apparent chloride diffusion of UHPC mixes by bulk diffusion [17]. After 27 days of curing, three 4-in. × 8-in. (100-mm × 200-mm) cylinders were cut and epoxied from each mixture and curing method used. The cylinders were cut into three sections as shown in Figure 154. The bottom sections of the cylinders were epoxied on all sides except the cut surface to allow for one-dimensional chloride ingress.

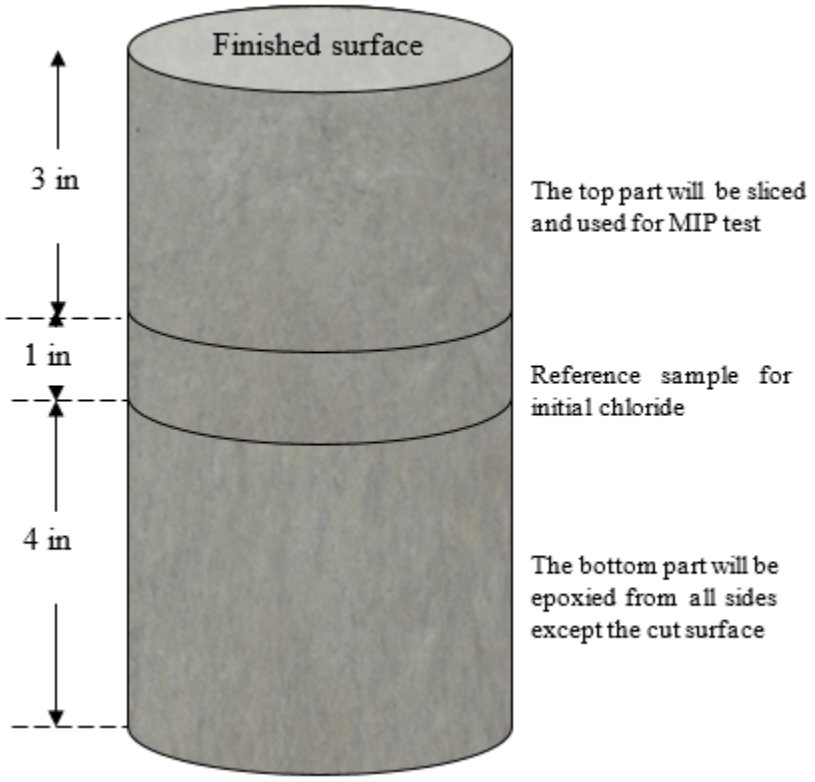

Figure 154: Bulk diffusion sample cut set up

Samples were soaked in tap water for 48 hours before submersion in tanks containing 16.5% NaCl solution at the Florida Department of Transportation (FDOT) State Materials Office (SMO) for one year of exposure as shown in Figure 155. Two samples for each strength class and each curing method used were left in the saltwater tank to be tested for a longer exposure period to see the if the chlorides diffused more with time.

Figure 155: Sodium chloride tank at FDOT

After the exposure period was complete, the samples were cut to remove the epoxy, then ground in layers for chloride profiling as shown in Table 69. The 1-in. (25-mm) thick slice taken from the sample middle was used to determine the initial chloride concentration. After grinding, each layer was placed in a container and dried for 24 hours at 212°F (100°C). The powders were then put in a Ziplock bag and stored in a desiccator to avoid moisture gain. The chloride content was tested using a Mettler Toledo EasyCl auto-titrator following FDOT FM-516 [290].

Table 69: Layers and thickness of the chloride profiling

Layer	Thickness (mm)	Depth (mm)
1	1	0-1
2	1	1-2
3	1	2-3
4	1	3-4
5	1	4-5
6	1	5-6
7	2	6-8
8	2	8-10
9	2	10-12
10	2	12-14

10.5. Results and Discussion

10.5.1. Compressive Strength

The average compressive strength, standard deviation, and coefficient of variation for each mix are presented in Table 70. All the mixes, except the 21+ ksi mixes, were designed to utilize locally available materials. The 21+ ksi mixes used materials such as silica flour and white silica fume to achieve higher strength through better particle packing. Not all the samples met the target strength range due to the variability in the test results and because these mixes were designed based on trial mixes in a different mixer. The steam curing increased the compressive strength for all mixes except for the lowest-strength class mix. This was because the higher temperatures would not aid the lower-strength class at later age [297]. The precast curing lowered the concrete strength compared to the steam-cured concrete, and compared to the moist-room cured samples except for the 21+ ksi mixture with 2% steel fibers, showing the importance of the extended pre-curing before steam curing in forming a good microstructure [266].

Table 70: Average compressive strengths for each mix

Mix ID	Strength (psi)			Std. Dev. (psi)			COV		
(fiber %)	Moist	Steam	Precast	Moist	Steam	Precast	Moist	Steam	Precast
21+ (0%)	16398	19002	12700	529	2871	334	3.2	15.1	2.6
21+ (1.5%)	17864	21109	15928	237	1175	1714	1.3	5.6	10.8
21+ (2%)	16555	20742	18545	2928	327	2329	17.7	1.6	12.6
18+ (0%)	14445	17175	13999	757	1415	830	5.2	8.2	5.9
18+ (1.5%)	17965	18585	14452	850	1196	1304	4.7	6.4	9.0
18+ (2%)	17174	16767	15704	1221	824	982	7.1	4.9	6.3
15+ (0%)	17544	19210	14745	1286	1516	965	7.3	7.9	6.5
15+ (1.5%)	18943	17943	15310	597	1672	358	3.2	9.3	2.3
15+ (2%)	17832	17118	15210	967	846	1057	5.4	4.9	7.0
15.2+ (0%)	16973	16349	12622	586	1900	974	3.5	11.6	7.7
15.2+ (1.5%)	15629	17296	13494	1579	864	2192	10.1	5.0	16.2
15.2+ (2%)	15630	16346	12687	1280	1272	1714	8.2	7.8	13.5
12+ (0%)	15568	13351	13017	1198	2893	953	7.7	21.7	7.3
12+ (1.5%)	16108	15755	14111	1030	605	563	6.4	3.8	4.0
12+ (2%)	15904	15688	13309	1226	691	409	7.7	4.4	3.1

10.5.2. Modified Rapid Chloride Migration Test

The non-steady state migration coefficients, D_{nssm}, were calculated using Equation 32 and are shown in Table 71 for each mix and fiber content. As presented in Table 71 the mix strengths were inversely related to the D_{nssm} coefficient. The chloride migration coefficient was extremely low for all of the mixes and decreased as the w/cm of the mix decreased. The 21+ ksi, 18-21 ksi, 15-18 ksi and 12-15 ksi mixes had chloride migration coefficients of 0.25×10^{-12}, 0.54×10^{-12}, 2×10^{-12}, and 3.8×10^{-12}, respectively. The 21+ ksi had almost 16 times lower chlorides coefficient

than the 12 ksi mix. The steam-cured samples and most of the precast-cured samples showed lower D_{nssm} coefficients when compared to the moist-room-cured samples because of the accelerated hydration. The 12 ksi steam-cured samples however showed a higher D_{nssm} coefficient than the moist-room-cured samples because of the crossover effect typically seen in normal-strength concrete indicative of a worse pore system from higher-density hydration products and lower bound water in the C-S-H [297][237].

Table 71: Rapid chloride migration coefficient of mixtures, $D_{nssm} \times 10^{-12}$ (m^2/s)

Mix ID (Fiber %)	3 days			7 days			10 days		
	Moist	Steam	Precast	Moist	Steam	Precast	Moist	Steam	Precast
21+ (0%)	0.21	0.04	0.13	0.21	0.03	0.05	0.25	0.04	0.07
21+ (1.5%)	0.22	0.13	0.24	0.12	0.07	0.12	0.16	0.08	0.12
21+ (2%)	0.19	0.07	0.19	0.08	0.03	0.08	0.07	0.03	0.06
18+ (0%)	0.37	0.12	0.21	0.29	0.05	0.05	0.28	0.04	0.14
18+ (1.5%)	0.33	0.07	0.36	0.61	0.04	0.17	0.54	0.03	0.13
18+ (2%)	0.28	0.24	0.38	0.43	0.15	0.28	0.43	0.14	0.21
15+ (0%)	0.52	0.14	0.42	0.56	0.14	0.40	0.52	0.16	0.41
15+ (1.5%)	2.01	0.10	0.39	1.10	0.28	0.43	1.23	0.34	0.53
15+ (2%)	0.38	0.18	0.50	1.04	0.34	0.69	1.22	0.46	0.62
15.2+ (0%)	0.98	0.21	0.66	0.75	0.18	0.41	0.81	0.16	0.50
15.2+ (1.5%)	0.22	0.22	0.31	1.91	0.20	0.47	1.45	0.23	0.70
15.2+ (2%)	0.70	0.27	0.52	0.94	0.21	0.53	1.05	0.18	0.60
12+ (0%)	1.07	2.81	3.94	0.99	3.04	3.80	0.95	2.62	2.60
12+ (1.5%)	1.25	1.74	3.15	0.96	1.31	2.97	0.86	1.34	2.68
12+ (2%)	1.78	1.73	1.19	-	-	-	-	-	-

Figure 156 through Figure 160 show the chloride penetration depth for the three-, seven- and ten-day tests for all mixes. The highest-strength mix, 21+ ksi, showed an extremely low chloride ingress, 6 mm at most for the moist-room-cured samples, and less than 3 mm for the steam-cured and precast-cured samples after ten days of testing. It seems that the chloride penetration did not go much further with time especially for the steam-cured samples and almost stopped after 3 days of testing. The 18-21 ksi steam-cured samples showed a similar type of results to the steam-cured samples of the 21+ ksi mix, whereas the moist-room-cured and precast-cured samples showed a slightly higher chloride ingress with time, up to 11 mm and 5 mm, respectively, at the end of the testing. The 15 and 15.2 ksi mixtures samples had higher chloride ingress, especially for the moist-room-cured samples that were about 5 times higher than the 21+ ksi mix. The steam-cured and precast-cured samples also showed higher chloride penetration. The 15-18 ksi mixture cured in the moist room showed higher chloride ingress in this test than the higher-strength mixtures, as expected. No consistent trend was seen with fiber content for the 18-21 ksi and 21+ ksi mixtures, indicating that the discontinuous pore structure controlled the chloride penetration through the samples and not the increased electrical current because of the lower electrical resistivity from the inclusion of steel fibers. The chloride ingress for the 12-ksi samples without fibers and with 1.5% fibers went completely through the samples by the end of testing.

The 12-ksi samples with 2% steel fibers failed the testing before the three days because the presence of the fibers increased the current flow in the sample and increased the chloride ingress.

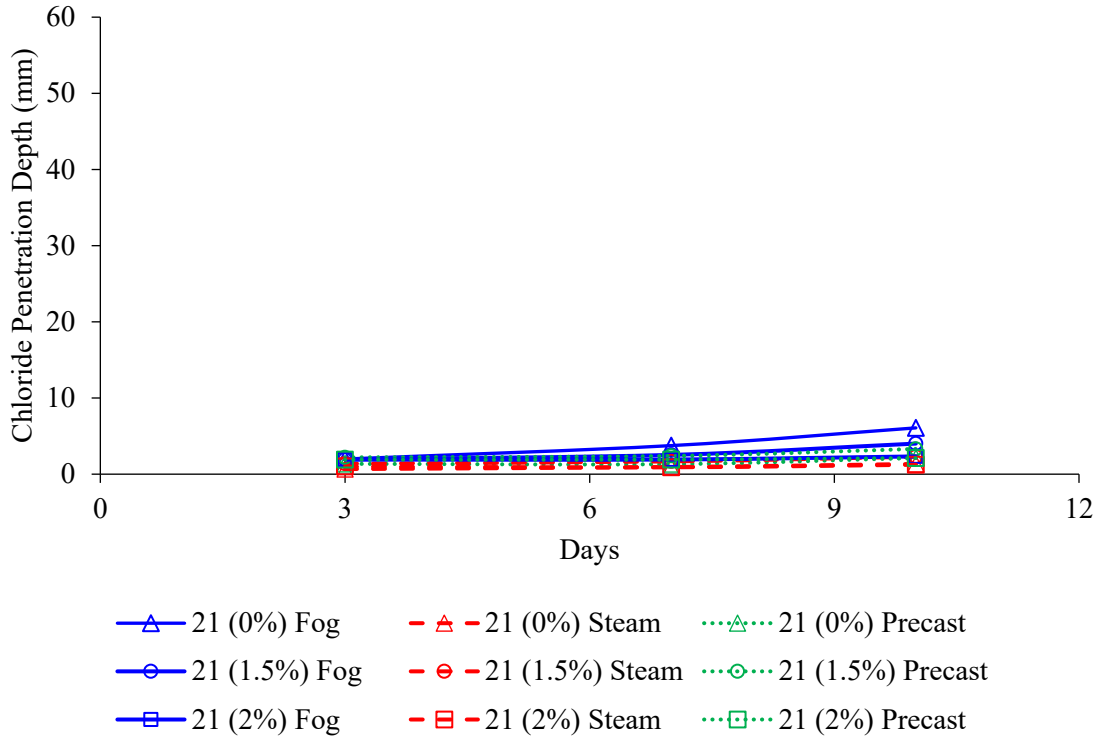

Figure 156: Chloride penetration depth of 21-ksi mixture after 3, 7, and 10 days of testing

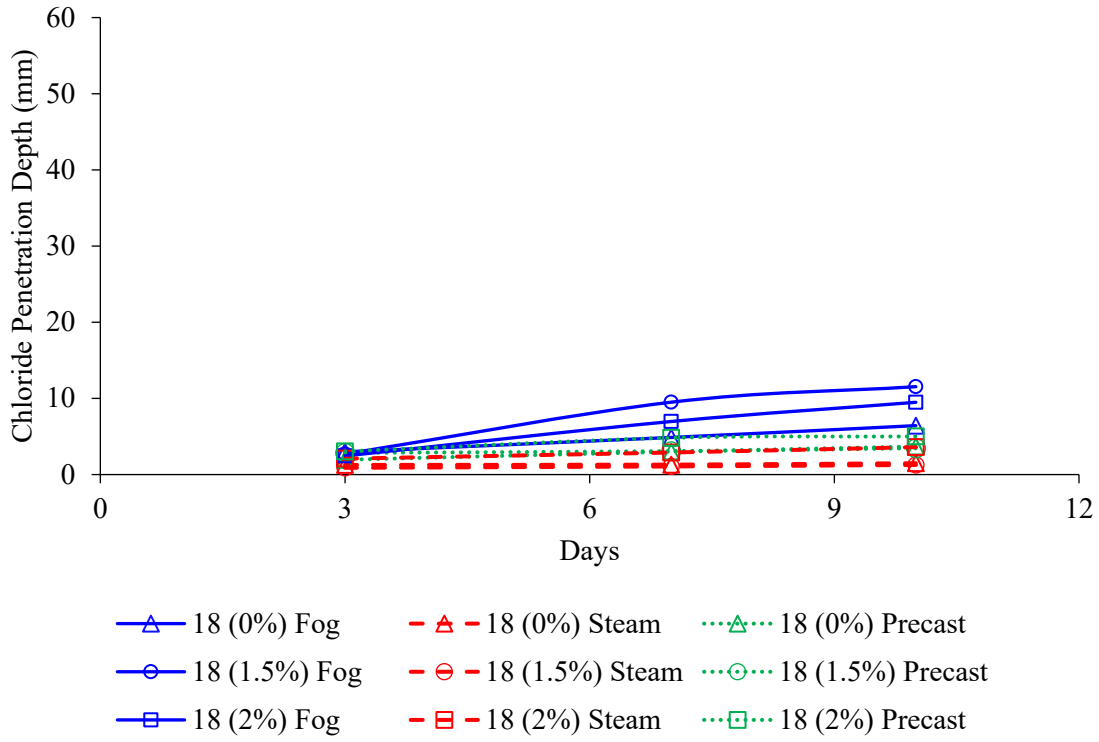

Figure 157: Chloride penetration depth of 18-ksi mixture after 3, 7, and 10 days of testing

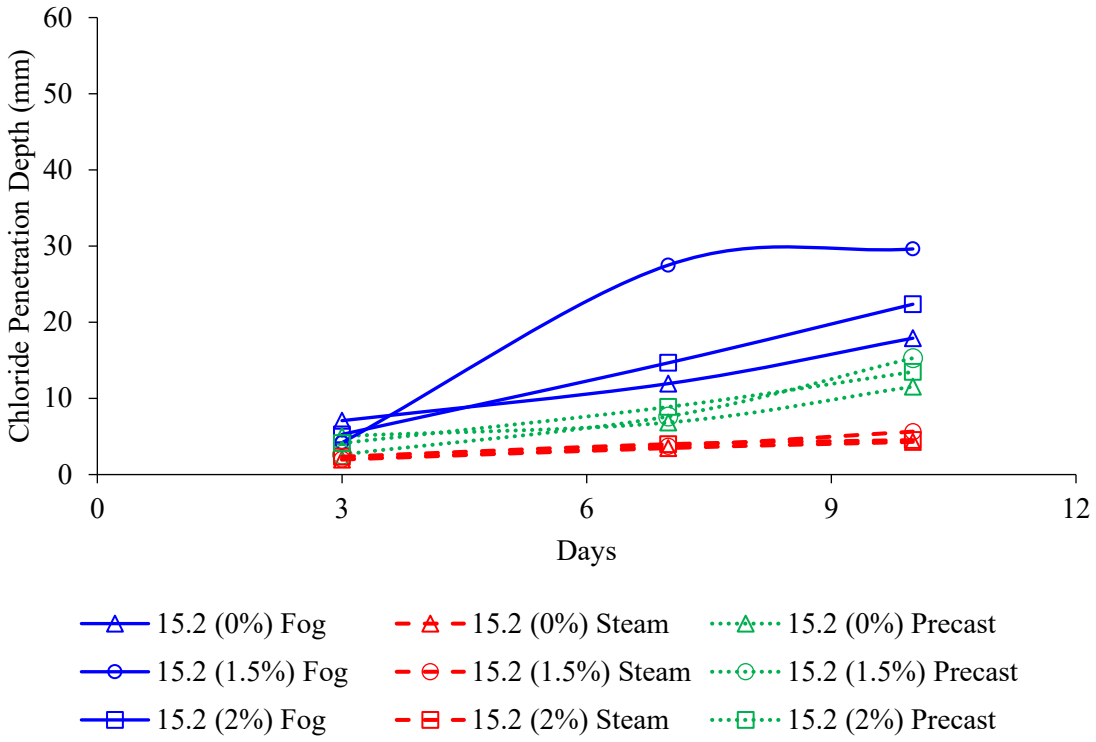

Figure 158: Chloride penetration depth of 15.2-ksi mixture after 3, 7, and 10 days of testing

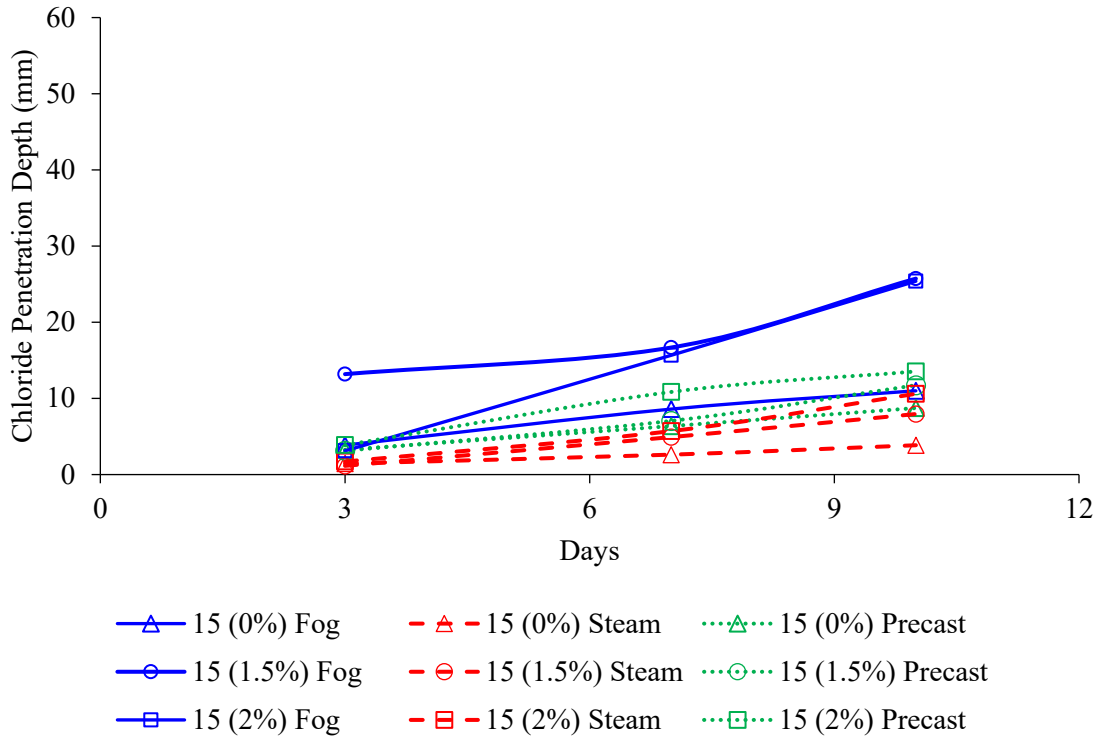

Figure 159: Chloride penetration depth of 15-ksi mixture after 3, 7, and 10 days of testing

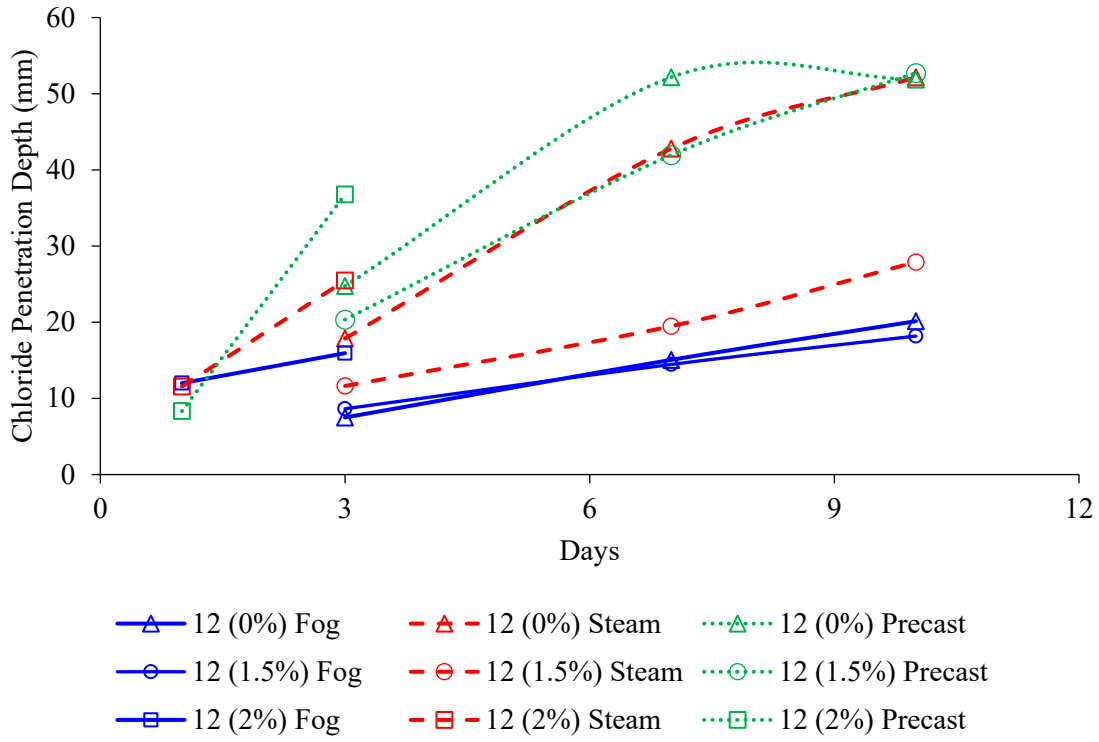

Figure 160: Chloride penetration depth of 12-ksi mixture after 3, 7, and 10 days of testing

The curing method used greatly influenced the measured results, however the differences decreased as w/cm decreased in these mixtures. The moist-room-cured samples showed higher chloride ingress when compared to steam-cured samples, except for the 12 ksi mix. The steam-cured-to-moist-room-cured and precast-cured-to-moist-room-cured chloride penetration depth ratios of all the samples without fibers are shown in Figure 161 and Figure 162, respectively. All of the mixes with strengths above 12 ksi had low ratios of steam-to-moist-room-curing penetration depth while the 12-ksi mix showed the highest ratio, indicating the impact of curing on microstructure and the strength cross-over effect. The 12-ksi and 15-ksi mixtures experienced significant cracking during the test with 1.5% steel fibers, as shown in Figure 163 for 15-ksi samples. The moist-room-cured samples had more cracks when compared to the precast- and steam-cured samples, which also corresponded to higher penetration depths. The cracking may have been caused by either corrosion of the steel fibers or differential shrinkage from sample heating during testing. For the 18-21 and 21+ ksi mixes, the steel fibers did not noticeably affect the chloride ingress or specimen appearance after the test. This could be because the pores were discontinuous and because the samples had extremely high resistivity, making the corrosion rate very small. This makes RCM a viable test for UHPC samples with ≤ 2% steel fibers because it measures the physical quantity of actual chlorides that penetrate through the samples and not just sample electrical properties.

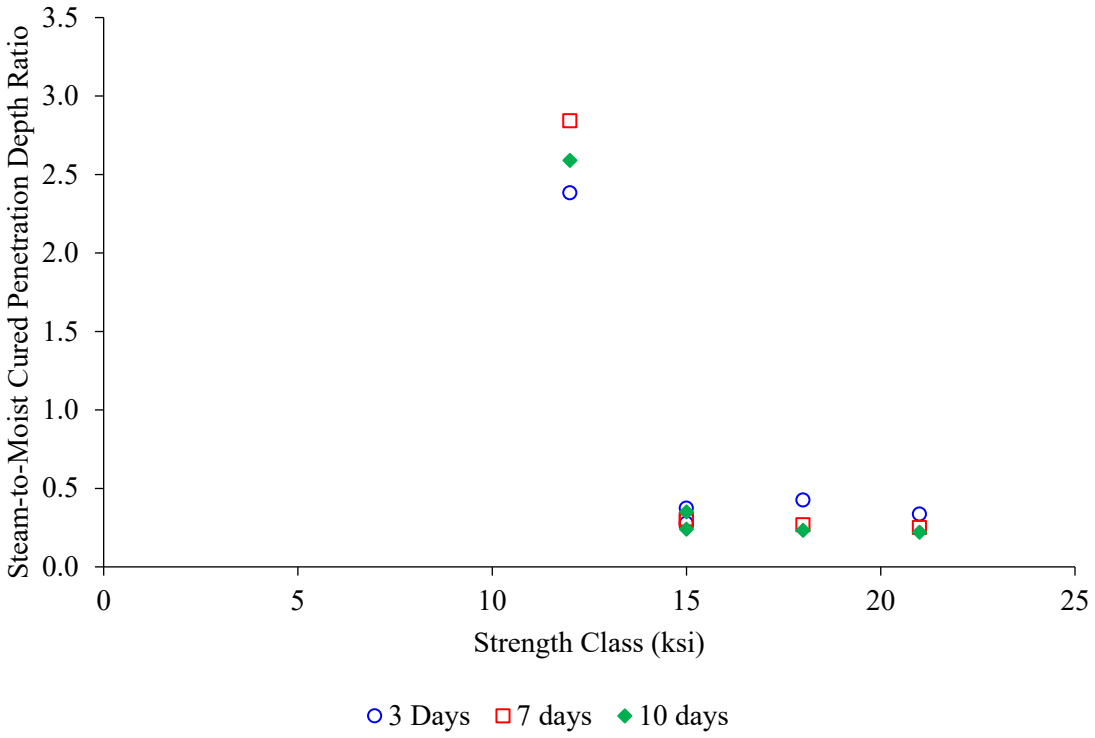

Figure 161: RCMT chloride steam-to-moist penetration depth ratio for samples without fibers

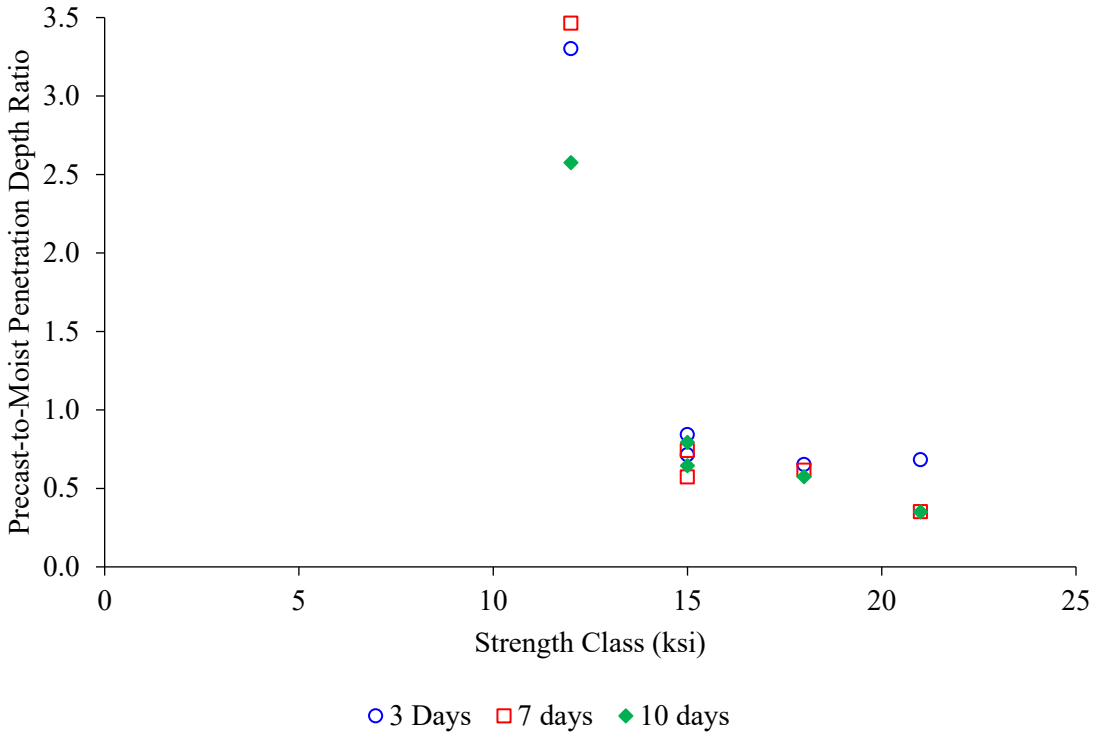

Figure 162: RCMT chloride precast-to-moist penetration depth ratio for samples without fibers

Figure 163: Mix 15 ksi samples with 1.5% of steel fibers at the end of 10 days of RCM testing

10.5.3. Surface and Bulk Resistivity Tests

The surface and bulk resistivity measurements were determined using a Proceq Resipod meter in accordance with AASHTO T 358 and AASHTO TP 119, except that the curing used was different than in the standards as explained in section 10.3 [15] [14]. The electrical resistivity testing can be significantly affected by the electrolytes in the pore structure and by any addition that improves the bulk conductivity, such as with the addition of steel fibers. The bulk electrical resistivity is a composite of the low-resistivity steel fibers, the higher-resistivity pore solution, and the low-diffusivity matrix, and ionic conduction will follow the path of least resistance at any given point in the sample. If the volume percent of steel fibers added is sufficient for the steel fibers to form a continuous path, essentially all the conduction will occur along the interconnected steel path [298].

The 28-day and greater than one year (the actual age is mentioned in Table 72) surface and bulk resistivity measurements for all mixes with or without steel fibers are presented in Table 72. The measurements were taken from the average values of three cylinders for each strength class for each curing method. It should be noted that due to the limited range of the Resipod meter, some of the resistivity values of the higher-strength mixes could not be obtained because they exceeded the upper range of the meter. The measurements that were out of range are noted with a dash (-) in Table 72 Based on the results, the resistivity values increased as the strength increased or as the w/cm of the mix decreased, as expected. The surface resistivity measurements of 21+

ksi moist-room-cured samples without fibers at 28 days were 8 times, 13-16 times and 23 times higher than resistivity measurements of the moist-room-cured samples without fibers of the strength classes of 18-21 ksi, 15-18 ksi, and 12-15 ksi, respectively. The incorporation of 1.5% of steel fibers by volume led to a considerable reduction in the 28-day electrical concrete resistivity of 70-80 %. Also, the 2% steel fibers led to a more significant reduction in agreement with literature [299] [300]. Looking at the effect of the curing methods, because of the increase of the curing temperature, the steam curing and the precast curing improved the resistivity of all of the mixes, except for the 12-ksi mix, indicating that elevated temperatures do not aid the low-strength mixes. The steam-cured and precast-cured samples had electrical resistances that were 2 to 11 times and 1 to 5 times higher, respectively, than the moist-room-cured samples. The over one-year (see the actual age in Table 72) electrical resistivity values of the moist-room-cured samples greatly increased with time due to the continued hydration. The precast-cured samples slightly increased with time, while steam-cured samples slightly increased or even decreased for 12-15 ksi and 15-18 ksi samples. This could be because they absorbed water near the surface, increasing the saturation and decreasing the resistivity.

Table 72: 28 day and over one-year surface and bulk resistivity measurements (kΩ-cm)

Mix ID (Fiber %)	Surface Resistivity 28 days			Surface Resistivity over 1 year			Sample Age (days) for Measurements Taken After 1 Year	Bulk Resistivity 28 days			Bulk Resistivity over 1 year		
	Moist	Steam	Precast	Moist	Steam	Precast		Moist	Steam	Precast	Moist	Steam	Precast
21+ (0%)	1075	-*	1036	-	-	-	435	-	-	-	-	-	-
21+ (1.5%)	319	931	273	1014	1273	1064	425	183	-	162	-	-	-
21+ (2%)	254	538	204	778	1093	823	414	134	-	128	-	-	-
18+ (0%)	133	-	-	1120	1099	794	531	92	-	-	-	-	-
18+ (1.5%)	36	190	103	290	284	189	517	24	93	59	158	77	98
18+ (2%)	35	250	73	274	226	136	489	18	129	37	146	126	75
15+ (0%)	81	524	236	697	417	241	503	29	-	73	-	-	139
15+ (1.5%)	16	128	46	125	81	46	477	9	46	20	91	39	30
15+ (2%)	13	126	43	82	80	41	463	6	47	11	54	40	29
15.2+ (0%)	65	628	248	707	396	268	446	35	-	133	-	-	158
15.2+(1.5%)	14	125	72	124	79	80	467	7	48	33	58	35	44
15.2+ (2%)	10	121	47	91	80	46	456	5	42	23	42	34	25
12+ (0%)	47	48	27	124	48	35	449	24	25	14	81	35	31
12+ (1.5%)	17	17	10	44	16	14	435	12	12	8	36	19	14
12+ (2%)	8	8	4	14	7	5	421	5	5	3	17	8	9

*Measurements with dash symbol indicates that the values were out of range and could not be detected by the Resipod meter

Based upon the AASHTO 358 classification system for surface resistivity testing, outlined in Table 73, the 15-18 ksi, 18-21 ksi steam-cured and precast-cured samples without fibers and all the 21+ ksi samples with or without fibers were classified as having “negligible” penetrability at 28-days curing age, whereas the 15-18 ksi, 18-21 ksi, and 12-15 ksi moist-room-cured samples without fibers were classified as having “very low” chloride penetrability.

Table 73: AASHTO 358 chloride penetrability classification for the surface resistivity test

Chloride ion permeability classification	28-day surface resistivity (kΩ-cm)
High	< 12
Moderate	12-21
Low	21-37
Very low	37-254
Negligible	> 254

A study was done by the Federal Highway Administration (FHWA) on UHPC samples without fibers and they observed that the minimum value of the bulk resistivity measurements was 215 kΩ-cm for all of the mixes. They recommended a resistivity threshold of at least 150 kΩ-cm at an age of 28 day for UHPC samples that use standard curing without fibers [301]. This value was based on preblended UHPCs, and not non-proprietary UHPCs. Figure 164 shows the 28-day bulk resistivity measurements of the moist-room-cured samples (standard) of all mixes with and without steel fibers compared to the value that was proposed by the FHWA (150 kΩ-cm), shown in a dotted red line. All the mixes were below the proposed bulk resistivity limit except the 21+ ksi samples without and with 1.5% steel fibers. The bulk resistivity of the 21+ ksi samples without fiber exceeded the maximum range of the Proceq Resipod. The bulk resistivity of the 21+ ksi samples with 1.5% steel fibers was higher than 150 kΩ-cm. Figure 165 and Figure 166 show the bulk resistivity measurements of the samples with 1.5% and 2% steel fibers respectively. It can be seen that the steel fiber addition led to a significant decrease in the electrical resistivity compared to the samples without fibers. Increasing the fiber content reduced the electrical resistivity.

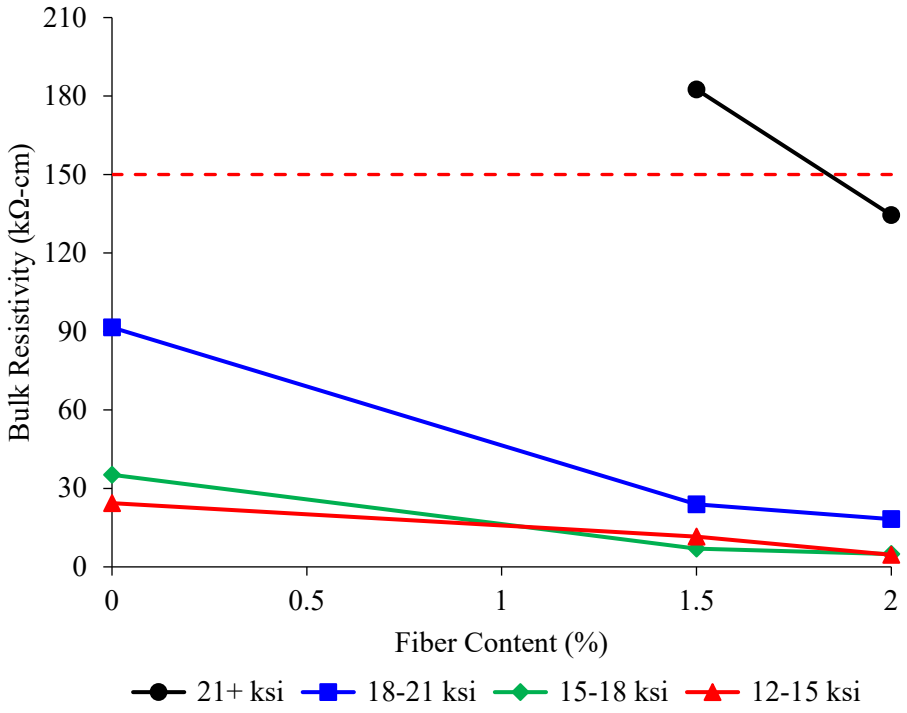

Figure 164: 28-day bulk resistivity measurements for the moist-room-cured samples

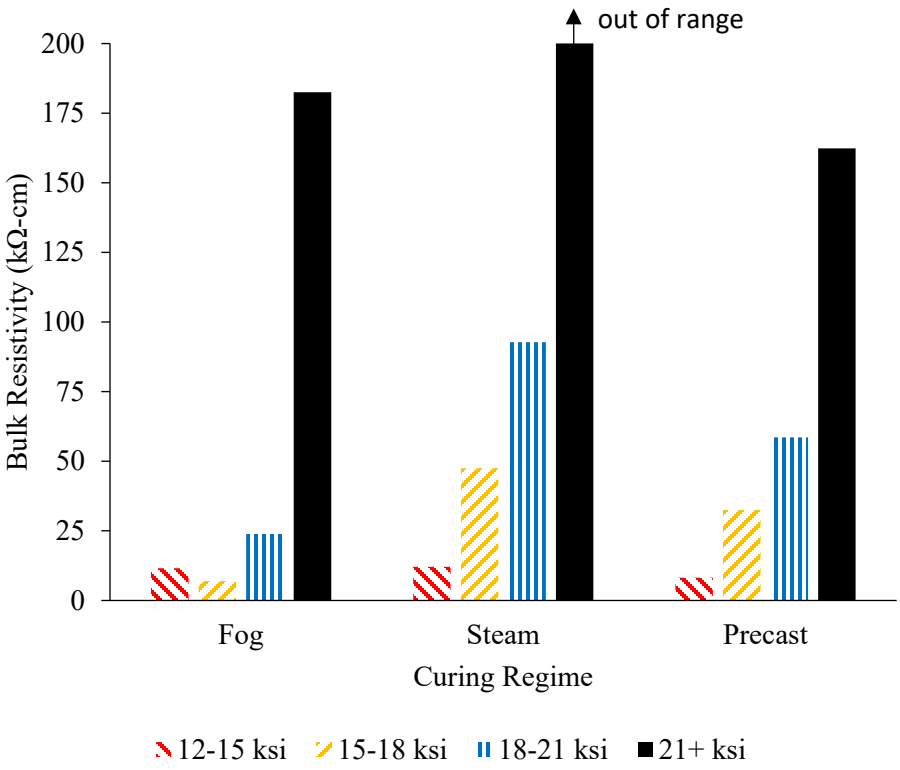

Figure 165: 28-day bulk resistivity measurements for all mixes with 1.5% of steel fibers

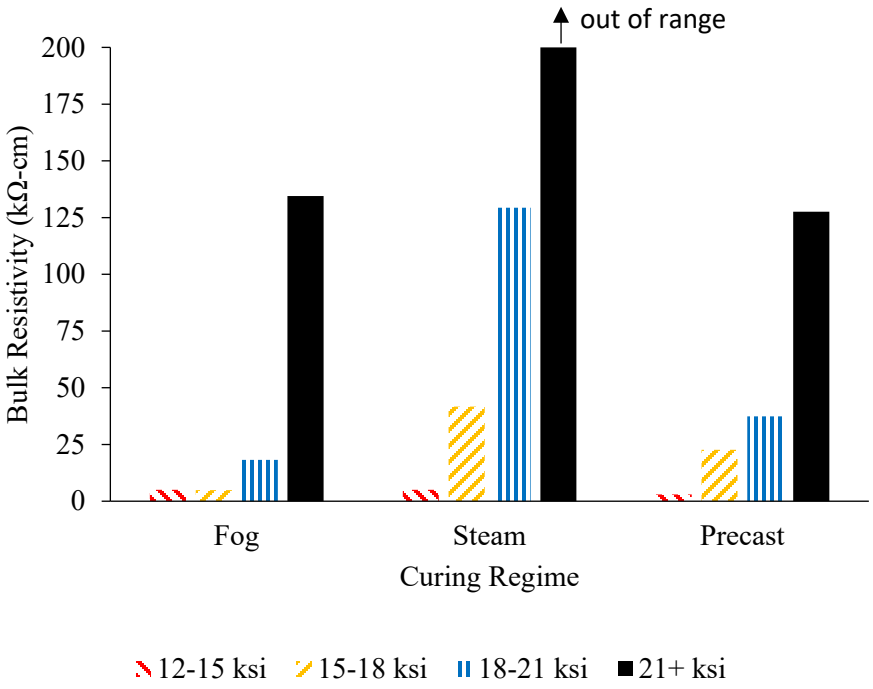

Figure 166: 28-day bulk resistivity measurements for all mixes with 2% of steel fibers

10.5.4. Water and Isopropanol Absorption Tests

The ASTM C1202 vacuum saturation method was followed to measure the UHPC absorption capacity by water and isopropanol [16]. Isopropanol was selected as it is believed that the larger molecule size of isopropanol cannot access the C-S-H gel pores [296].

The mass absorption for both water and isopropanol were calculated and shown in

Table 74. The absorption increased as the strength of the mixes decreased, as expected. The values of water absorption for the 12-15, 15-18, 18-21 ksi moist-room-cured samples with no fibers were four, three, and two times higher than values of the 21+ ksi moist-room-cured samples, respectively. The moist-room-cured and precast-cured samples showed a similar absorption rate, while the steam curing method produced the lowest absorption. The steam-cured samples had much lower absorption than the other curing methods likely because the steam-cured samples reached a high percentage of their ultimate degree of hydration by 28 days, giving less space to absorb water, while the moist-room-cured samples continued to hydrate and absorb more water with time. The isopropanol absorption showed a similar pattern to the water absorption. The isopropanol absorption values were 30-55% less than the values of the water absorption. This was expected as the isopropanol would mostly fill the larger (capillary) voids, and not the very fine (gel) pores [296].

Table 74: 28-day results of water and Isopropanol absorption (%)

	Water Absorption			Isopropanol Absorption		
Mix ID (Fiber %)	Moist	Steam	Precast	Moist	Steam	Precast
21+ (0%)	0.49	0.25	0.52	0.33	0.11	0.31
21+ (1.5%)	0.45	0.23	0.67	0.31	0.09	0.43
21+ (2%)	0.37	0.24	0.58	0.22	0.11	0.38
18+ (0%)	0.95	0.47	0.95	0.80	0.37	0.76
18+ (1.5%)	1.65	0.91	1.62	1.00	0.38	1.43
18+ (2%)	1.67	0.85	1.45	0.96	0.42	0.92
15+ (0%)	1.68	1.30	1.82	0.70	0.50	0.94
15+ (1.5%)	1.43	1.00	1.76	0.61	0.35	1.05
15+ (2%)	1.45	0.80	1.38	1.24	0.55	1.11
15.2+ (0%)	1.27	0.63	1.03	0.79	0.20	0.51
15.2+ (1.5%)	1.58	0.85	1.49	0.85	0.31	0.90
15.2+ (2%)	1.25	0.74	1.12	1.03	0.50	0.78
12+ (0%)	1.82	1.29	1.64	1.20	0.50	1.19
12+ (1.5%)	2.36	1.38	2.25	1.59	0.72	2.06
12+ (2%)	2.57	1.67	2.60	1.43	0.71	2.08

*Values were not adjusted for the relative density of isopropanol (0.786)

Figure 167 through Figure 169 show the water absorption capacity for samples with 0, 1.5% and 2% of steel fibers. The isopropanol absorption values for the samples with steel fibers and samples without fibers also were shown in Figure 170 through Figure 172. The steel fibers seem to slightly increase the absorption rate. The water absorption rate of 21 ksi mix seemed not to be affected by the presence of steel fibers.

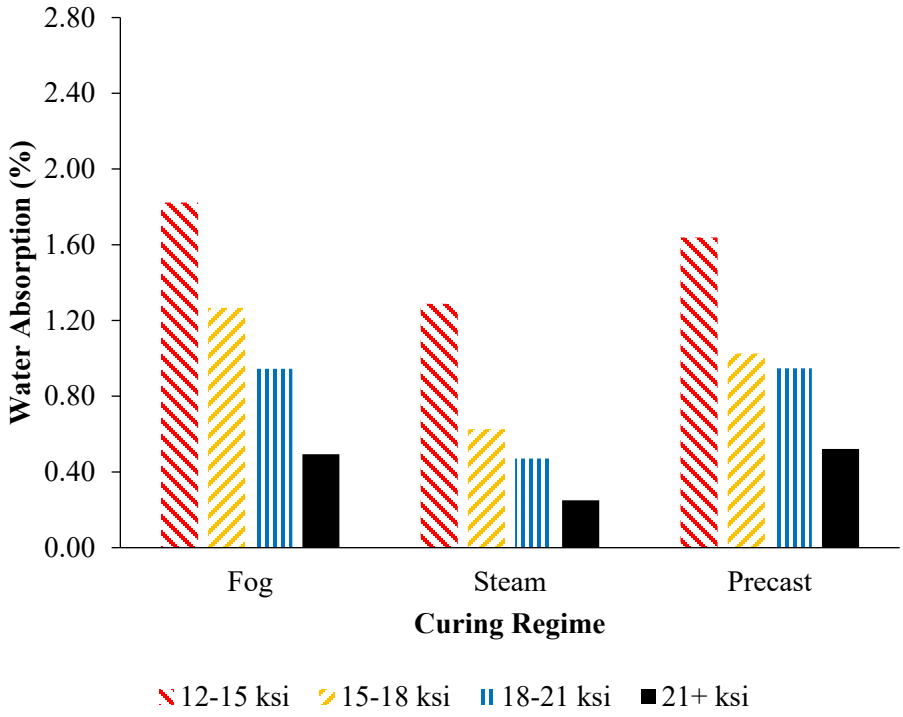

Figure 167: Water absorption rate for samples without fibers

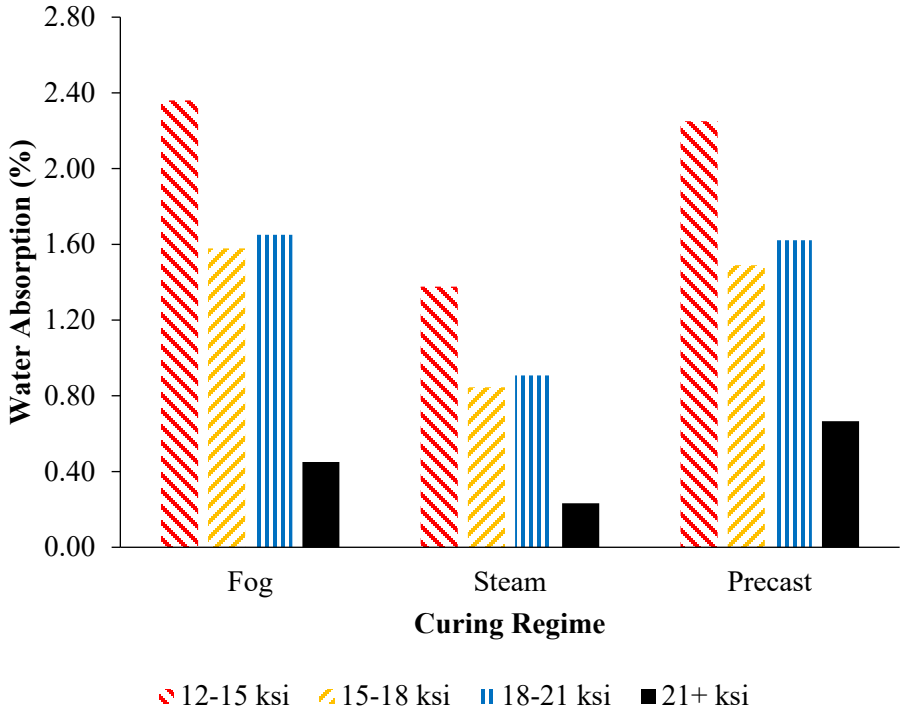

Figure 168: Water absorption rate for samples with 1.5% of steel fibers

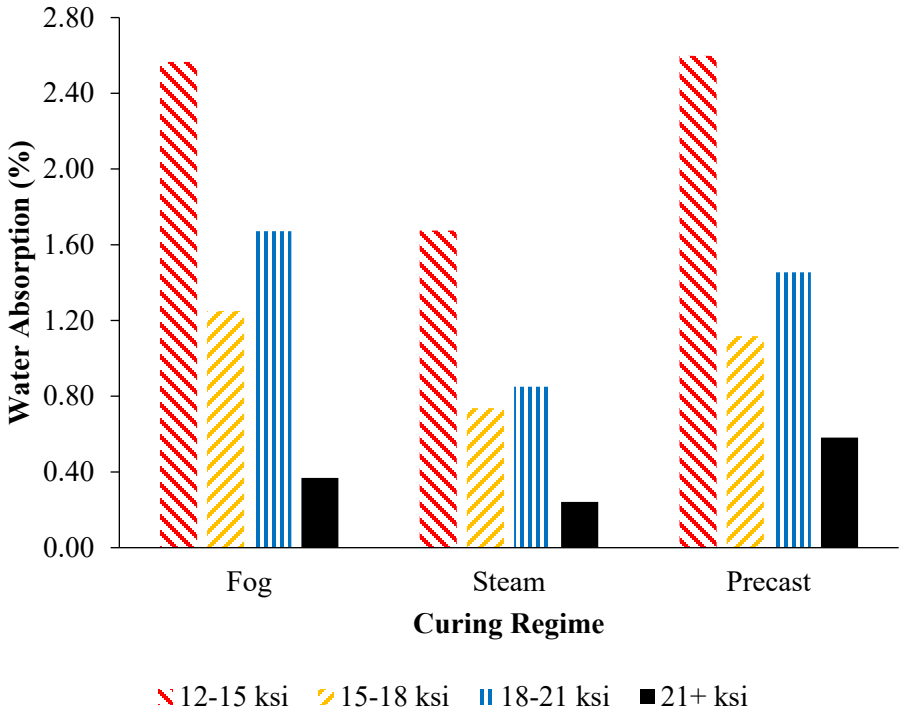

Figure 169: Water absorption rate for samples with 2% of steel fibers

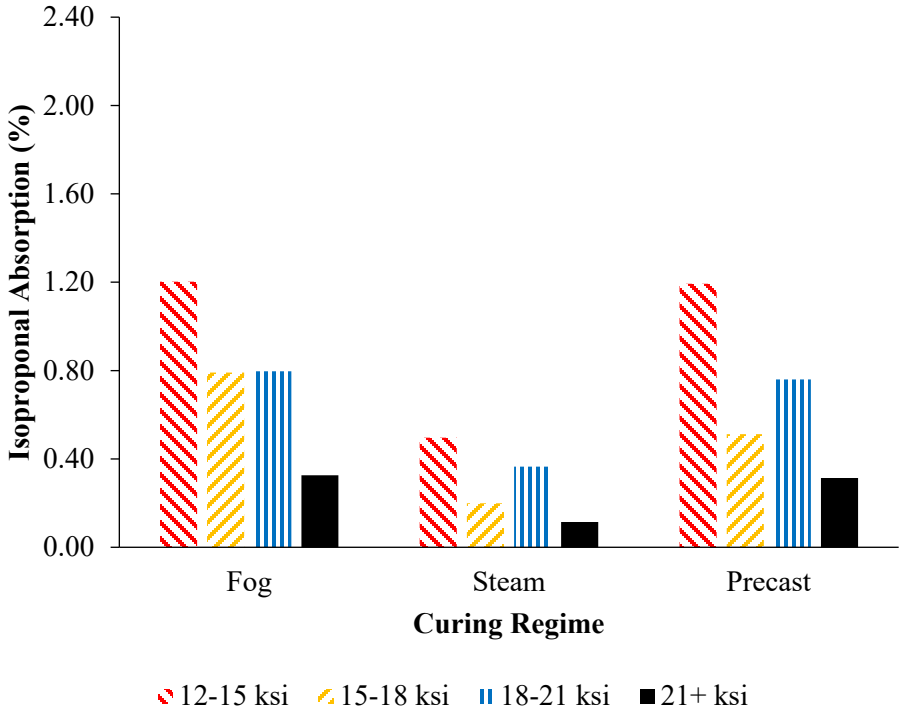

Figure 170: Isopropanol absorption rate for samples without fibers

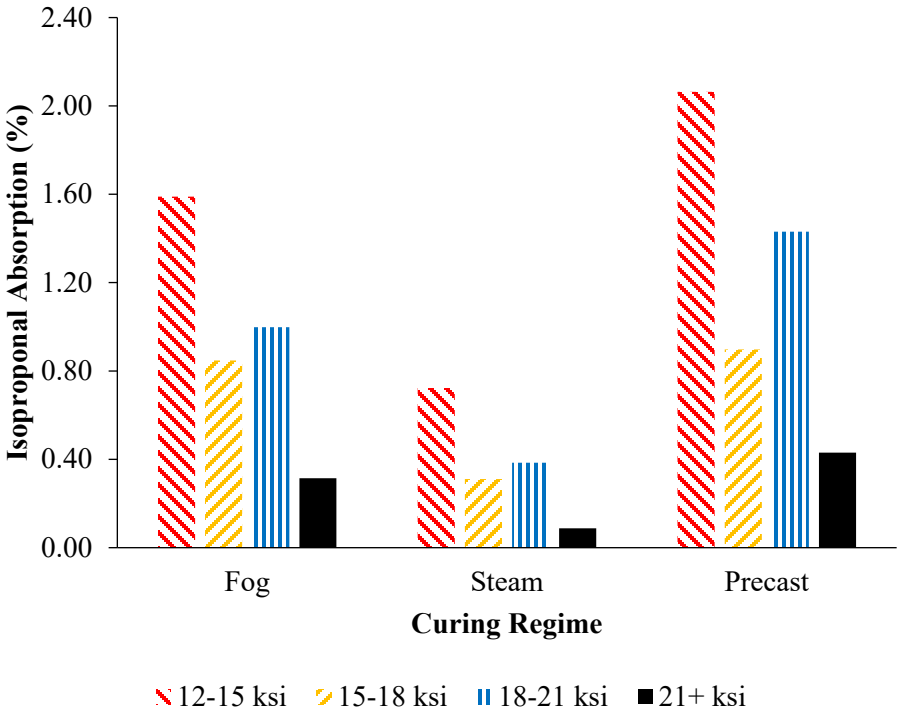

Figure 171: Isopropanol absorption rate for samples with 1.5% of steel fibers

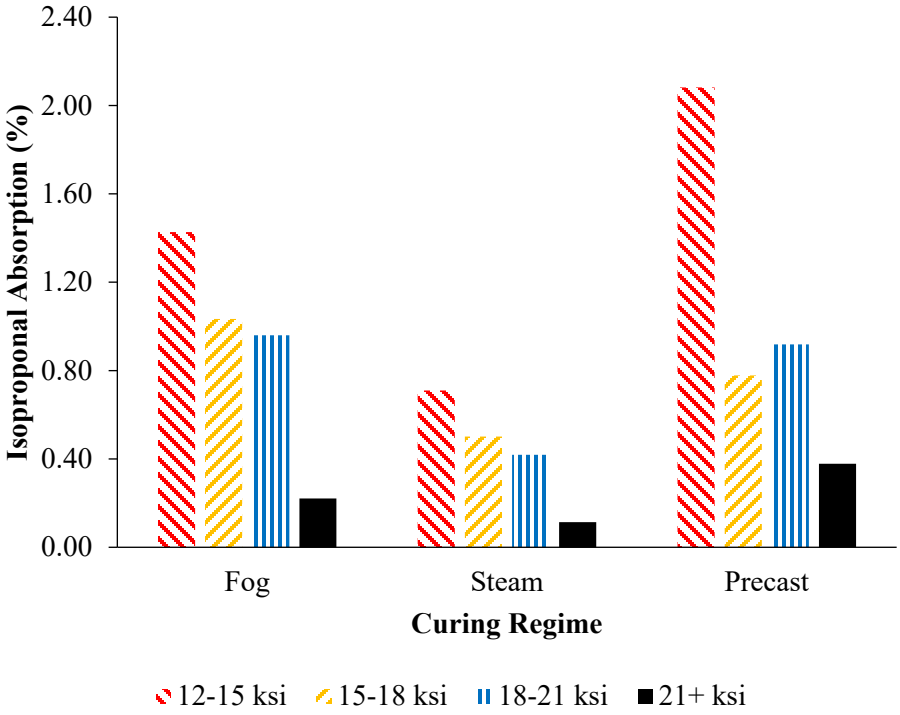

Figure 172: Isopropanol absorption rate for samples with 2% of steel fibers

10.5.5. Mercury Intrusion Porosimetry

MIP was used to measure pore size distributions for all the mixes with three different types of curing, with and without steel fibers. The Washburn equation was used to calculate the pore entry diameter based on the pressure applied, assuming the pores were cylindrical in shape [134,135]. The critical pore diameter and threshold diameter are also two important parameters that relate porosity to transport properties. The critical pore diameter reflects the pore connectivity as it represents the minimum diameter of pores that are geometrically connected continually throughout the whole sample [263]; it corresponds to the peak value of the differential pore volume in the distribution curve. The threshold diameter is the largest pore diameter at which the slope of the cumulative intrusion curve increases abruptly [302].

The cumulative pore volume versus pore radius for all the UHPC mixes with and without steel fibers are shown in Figure 173 through Figure 177. A gradual decrease in the cumulative pore volume is seen as the strength of the mixes increases and the w/cm decreases. The lowest strength class mixes, 12-15 ksi, had the highest mercury volume intruded while the highest strength class mixes, 21 + ksi, had the lowest pore volume measured. The 21 + ksi mixture showed almost two times less intrusion than the 12-15 ksi mixture, (0.021 cm^3/g and 0.045 cm^3/g) respectively, which was expected as higher water content leaves more void space that would need to be filled by hydration products to become solid space. Since the moist room cured samples did not go through heating, they exhibited a conventional curve with a well-defined inflection point in all mixtures except for the 21 + ksi mixture, whereas the precast-cured and steam-cured samples showed a flatter porosity curve, making it difficult to establish the critical pore diameter. The test results showed the UHPC samples had very small threshold pore size radii, less than 10 nm, 7nm, 5nm for the moist-room-cured samples of the 12-15, 15-18, and 18-21 ksi mixtures without steel fibers, respectively. Figure 178 shows the mercury intrusion curve for the moist-room-cured samples without steel fibers. The range of pore sizes seen for these mixes is in line with literature as it was suggested that the total porosity of UHPC not be more than 1-2% with pore size ranges between 2 nm and 10 nm [303][304]. The 21+ ksi samples had a porosity curve without the typical S-shape, therefore, the threshold diameter could not be detected. This most likely means that the 21+ ksi samples had small and discontinues pores that were difficult to be measured by MIP. MIP is capable of measuring volumes over a wide range of pore sizes, from 4 nm and up [265]. The mercury did not penetrate the fine pores smaller than 3 nm [305]. This would give an indication that the capillary pores responsible for transport properties are disconnected as MIP measures the pore entry sizes rather than measuring the real pore sizes [306]. As expected, the steam curing and precast curing methods showed a positive effect by reducing the pore size distribution and volume intruded. This is likely because of their higher degree of hydration, leaving less space of voids. Interestingly, steam curing reduced the pore size distribution for the 12-15 ksi mixture compared to the moist-room-cured sample, even though the other transport property tests showed that the transport properties were better with moist-room-curing.

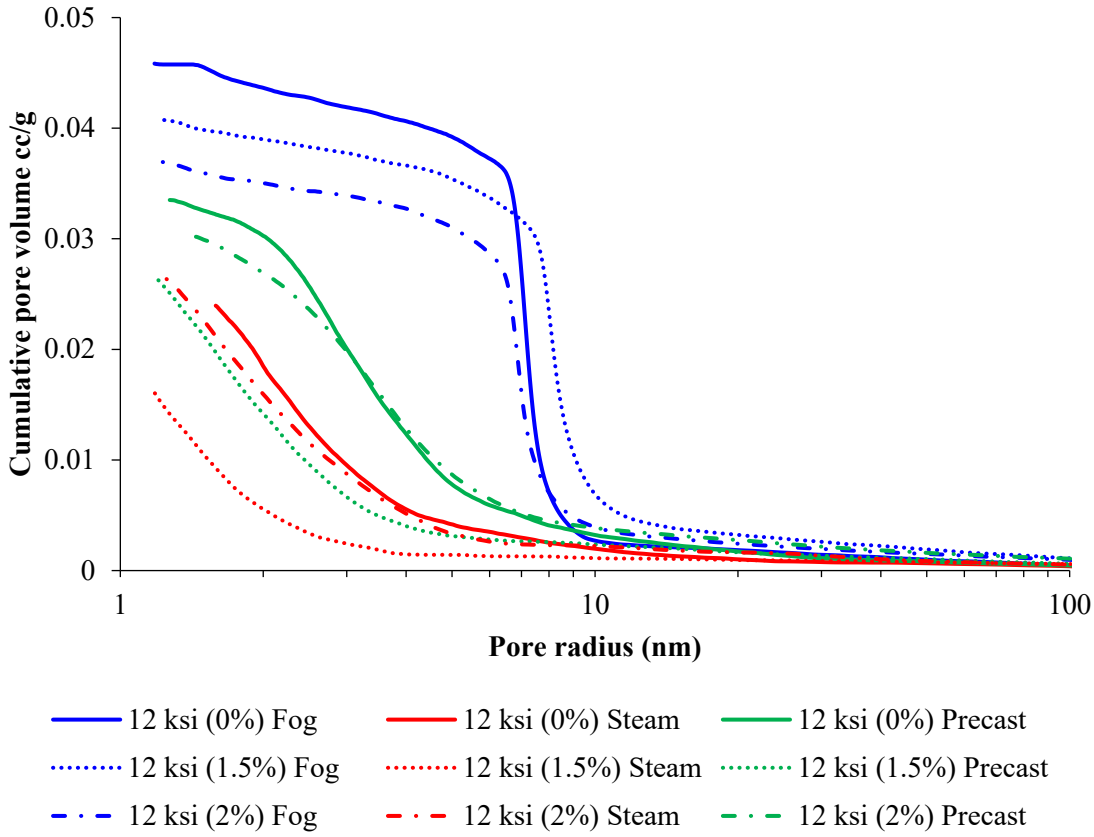

Figure 173: MIP cumulative pore volume of the 12 ksi mixture

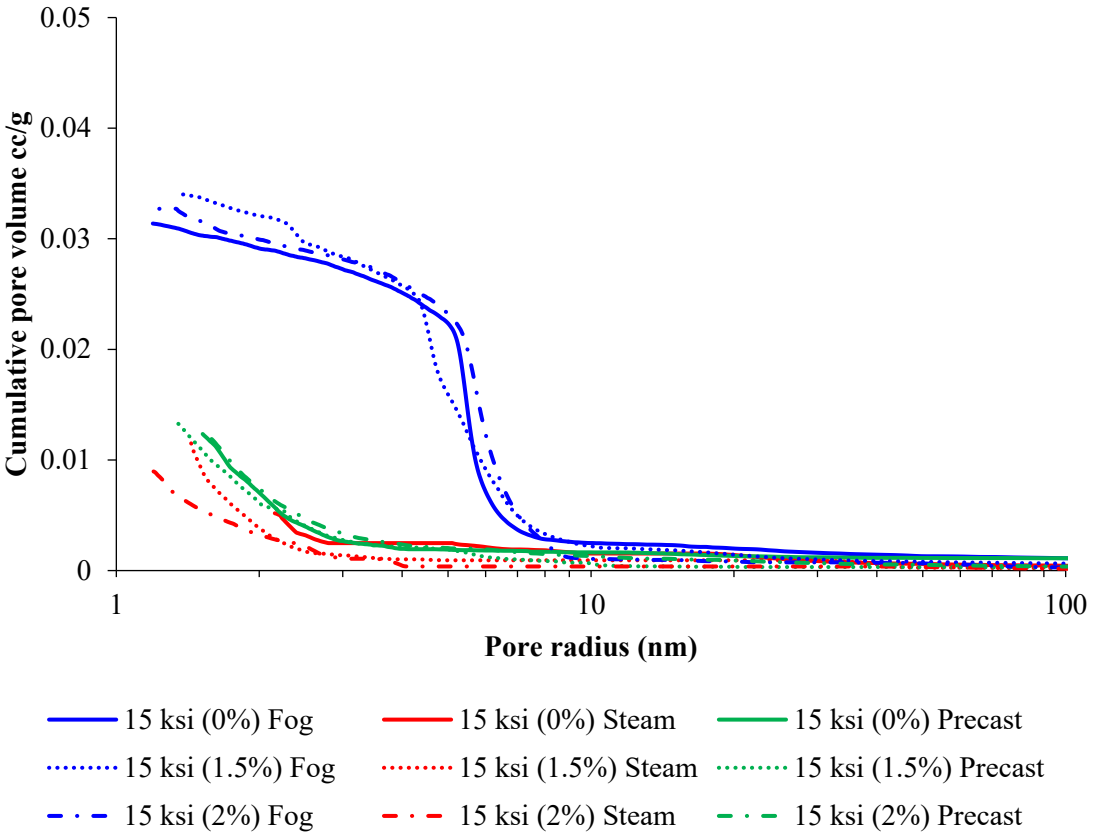

Figure 174: MIP cumulative pore volume of the 15 ksi mixture

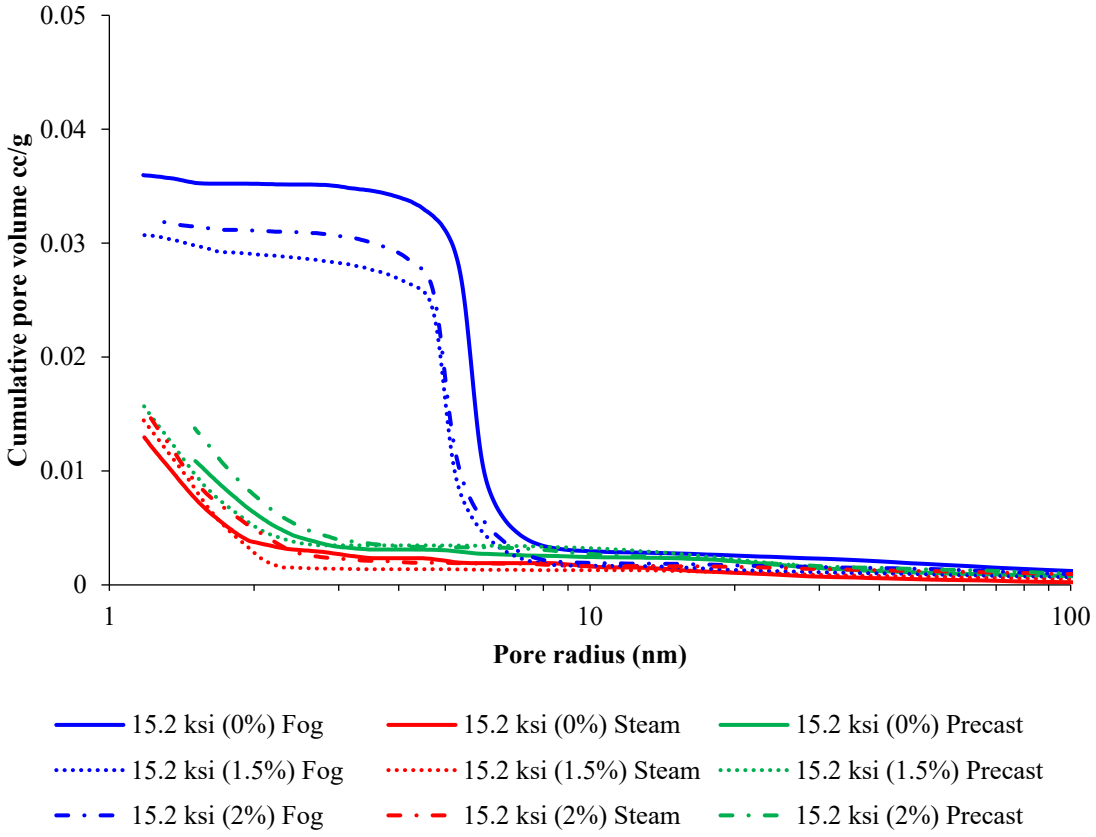

Figure 175: MIP cumulative pore volume of the 15.2 ksi mixture

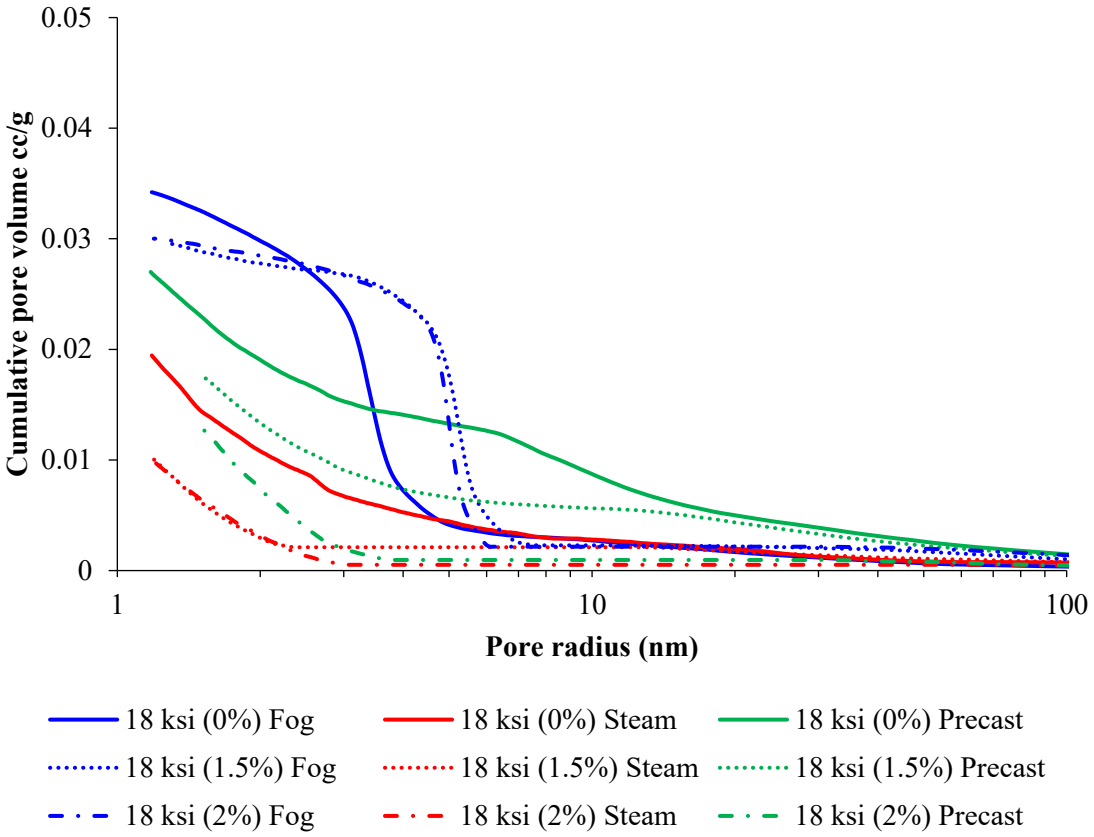

Figure 176: MIP cumulative pore volume of the 18 ksi mixture

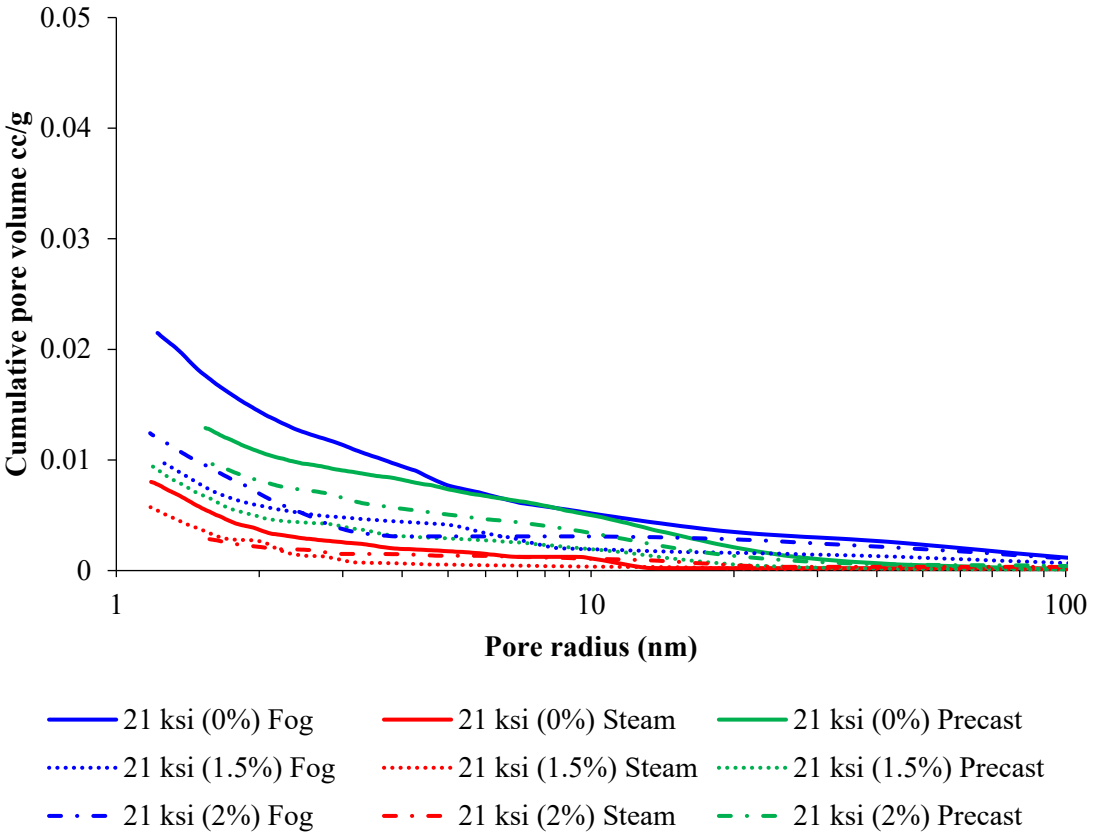

Figure 177: MIP cumulative pore volume of the 21 ksi mixture

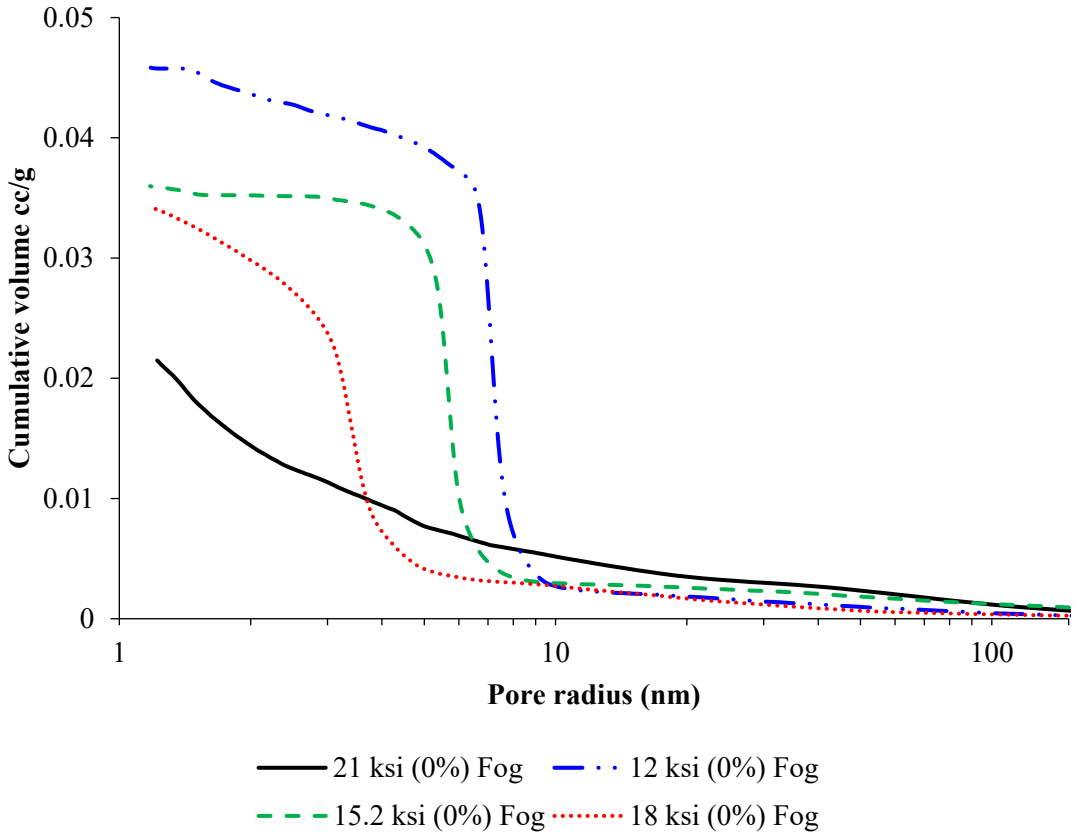

Figure 178: All mixes moist-room-cured samples without steel fibers

The steel fibers only minimally affected the pore size distributions measured. When compared to the samples without fibers, a slightly lower mercury intrusion was seen for those with fibers, but the threshold and critical pore size diameter were similar. This indicates that the fibers had a tight bond with the cementitious matrix and did not create pathways for fluid ingress.

10.5.6. Bulk Diffusion

Bulk diffusion samples were tested according to ASTM C1556 to determine the apparent chloride diffusion of UHPC mixtures [17]. The chloride content was tested using a Mettler Toledo EasyCl auto-titrator following the FDOT FM-516 standard procedure [290]. The apparent chloride diffusion coefficients calculated after one year of saltwater exposure for each mixture for each curing method are presented in Table 75. The apparent chloride diffusion coefficient increased as the w/cm increased for the mixes; this was expected as higher w/cm is known to lead to increase concrete penetrability [307][308]. The chloride diffusion coefficient was extremely low for all UHPC mixes when compared to the chloride diffusion of normal strength concrete seen in literature. Typical values for normal strength concrete are in the range from 5×10^{-12} to 50×10^{-12} m^2/s [123] The 21+ ksi moist-room cured-samples without fibers had an apparent chloride coefficient as low as 0.04×10^{-12} m^2/s, in which it was about 4 times, 4.5 times and 9.5 times lower than the 18-21 ksi, 15-18 ksi, and 12-15 ksi moist-room-cured samples. Elevated temperatures did not affect the chloride diffusion coefficients measured for the

21+ ksi mixture, but negatively affected the 12-15 ksi mixture. The cross-over effect seems to be more prevalent with the lower-strength mixtures. The 21+ ksi and 18-21 ksi mixtures did not see large differences in the diffusion coefficients based on curing method, likely because the chloride diffusion coefficient was very low already at 28 days when the samples were exposed to the chlorides. This kept the chloride ingress low as the microstructure densified from continued hydration in the moist-room-cured samples to the point that no appreciable difference was seen at one year in the ingress.

Table 75: Apparent diffusion coefficient at 1-year of exposure

Mix ID (Fiber %)	D_a (10^{-12} m^2/s)		
	Moist	Steam	Precast
21+ (0%)	0.07	0.07	0.04
21+ (1.5%)	0.04	0.05	0.06
21+ (2%)	0.04	0.07	0.03
18+ (0%)	0.28	0.21	0.33
18+ (1.5%)	0.33	0.21	0.15
18+ (2%)	0.19	0.26	0.40
15+ (0%)	0.32	0.23	0.95
15+ (1.5%)	0.39	0.44	0.53
15+ (2%)	0.27	0.51	0.87
15.2+ (0%)	0.29	0.18	0.38
15.2+ (1.5%)	0.25	0.21	0.15
15.2+ (2%)	0.19	0.16	0.30
12+ (0%)	0.67	2.71	4.62
12+ (1.5%)	0.25	2.19	2.14
12+ (2%)	0.54	1.67	6.82

Figure 179 and Figure 180 show the results for the measured chloride concentrations of all the moist-room-cured,steam-cured, and precast-cured samples without steel fibers, respectively. The 12-15 ksi, 15-18 ksi, and 18-21 ksi moist room cured samples showed chloride penetration 10 mm or above as compared to only 5 mm penetration of the 21 + ksi samples. The steam- and precast-cured samples showed similar trends as the moist-room-cured samples, except that the 12 ksi samples showed significantly higher chloride penetration than that in the moist room samples of deeper than 14 mm.

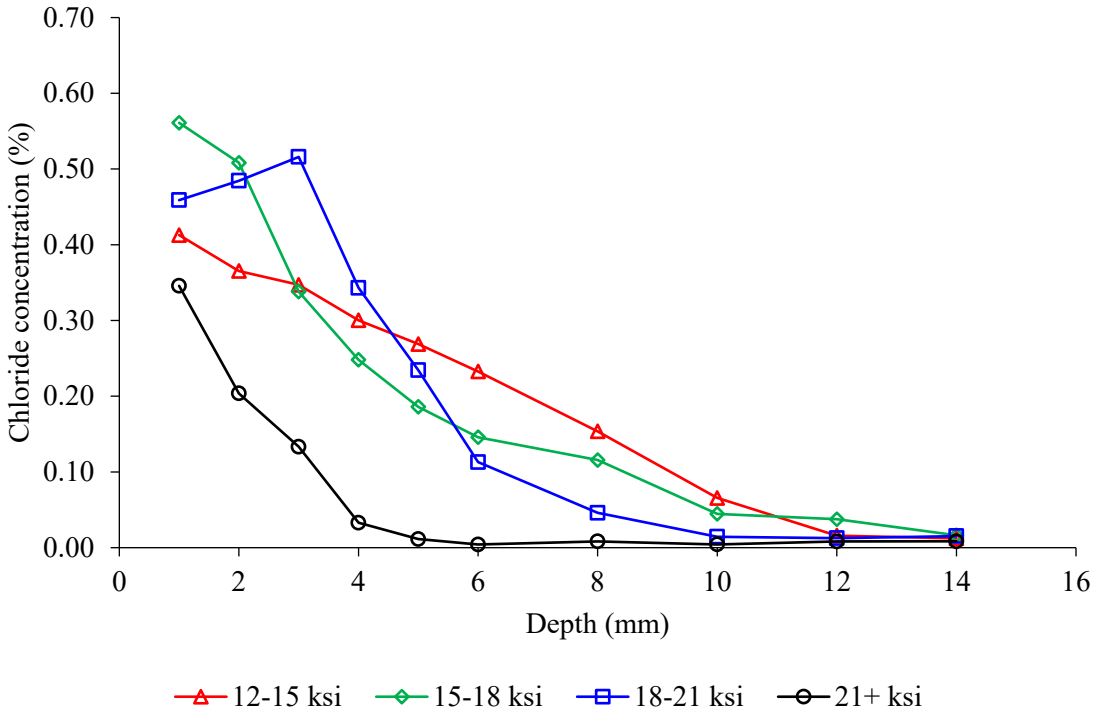

Figure 179: Chloride profile at 1-year of exposure for all the moist room cured samples without fibers

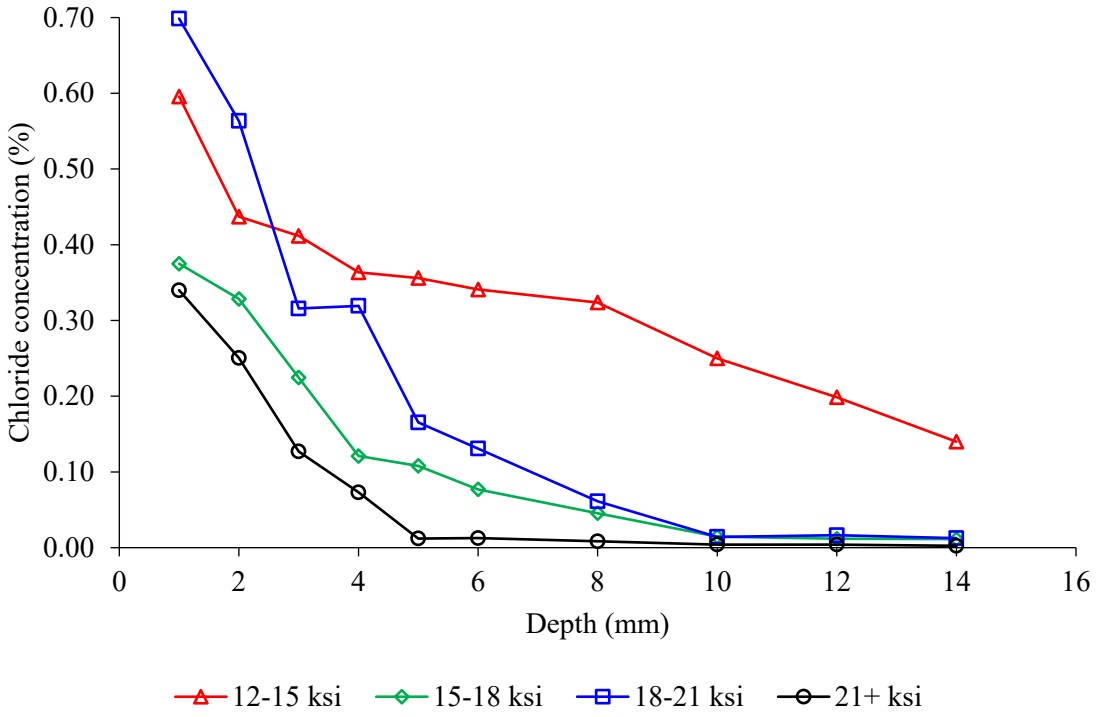

Figure 180: Chloride profile at 1-year of exposure for all the steam cured samples without fibers

10.6. Correlation Between Permeability Tests

10.6.1. Rapid Chloride Migration Test and Apparent Chloride Diffusion Coefficient

The relationship between the three, seven, and ten day modified RCM (NT Build 492) and bulk diffusion (ASTM C1556) results were evaluated for the all the mixtures with and without steel fibers as shown in Figure 181, Figure 182 and Figure 183. A good correlation between the RCM samples and the apparent chloride diffusion was seen for all the three durations. Among the three durations, the 7-day RCM testing showed the best correlation between the curing methods with coefficients of determination, R^2, of 0.91 and 0.90 for the steam-cured and precast-cured samples, respectively. The moist-room-cured samples had a lower 0.24 R^2. This could because the moist-room-cured samples were not fully hydrated at 28-days when compared to the steam-cured and precast-cured samples. Figure 184 showed the correlation between the 7-day RCM testing and chloride diffusion for the samples without fibers. It can be clearly seen the higher the strength of the mix, the lower the chloride penetration and chloride diffusion coefficient. All the samples showed very low chloride penetration except the 12-15 ksi. Samples with a chloride intrusion below 5 mm at 7 days showed very low chloride diffusion coefficients in testing and could be used as an acceptance criterion.

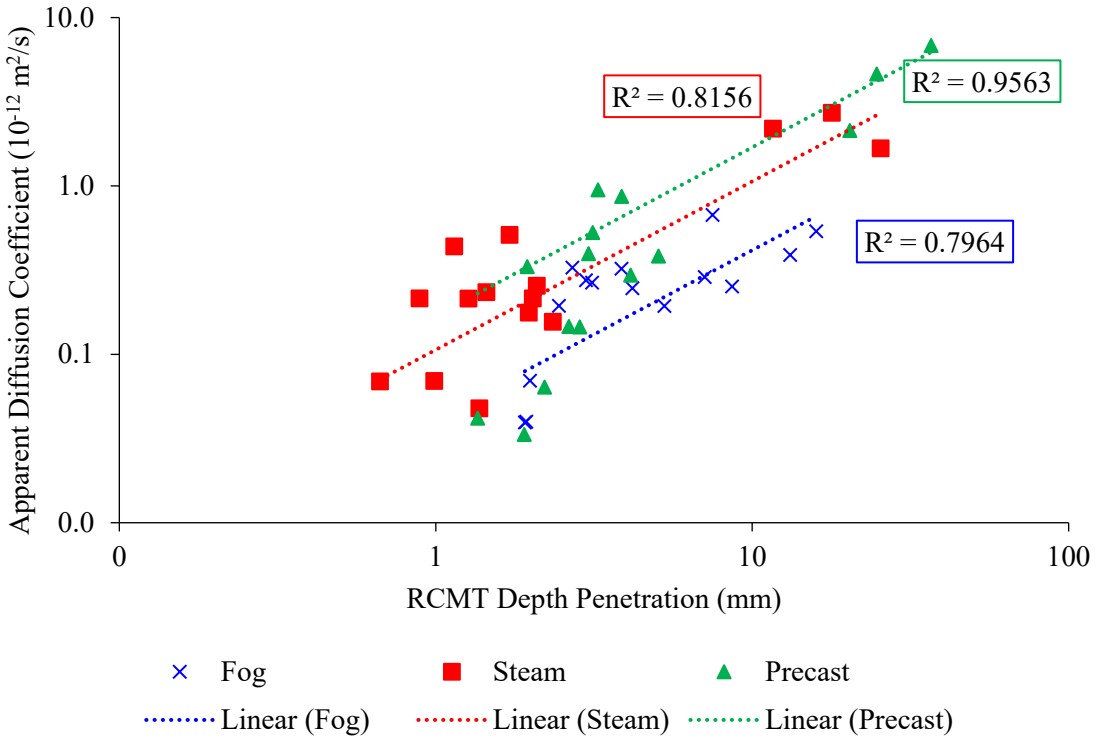

Figure 181: 3-day RCM chloride penetration depth versus the chloride diffusion coefficient

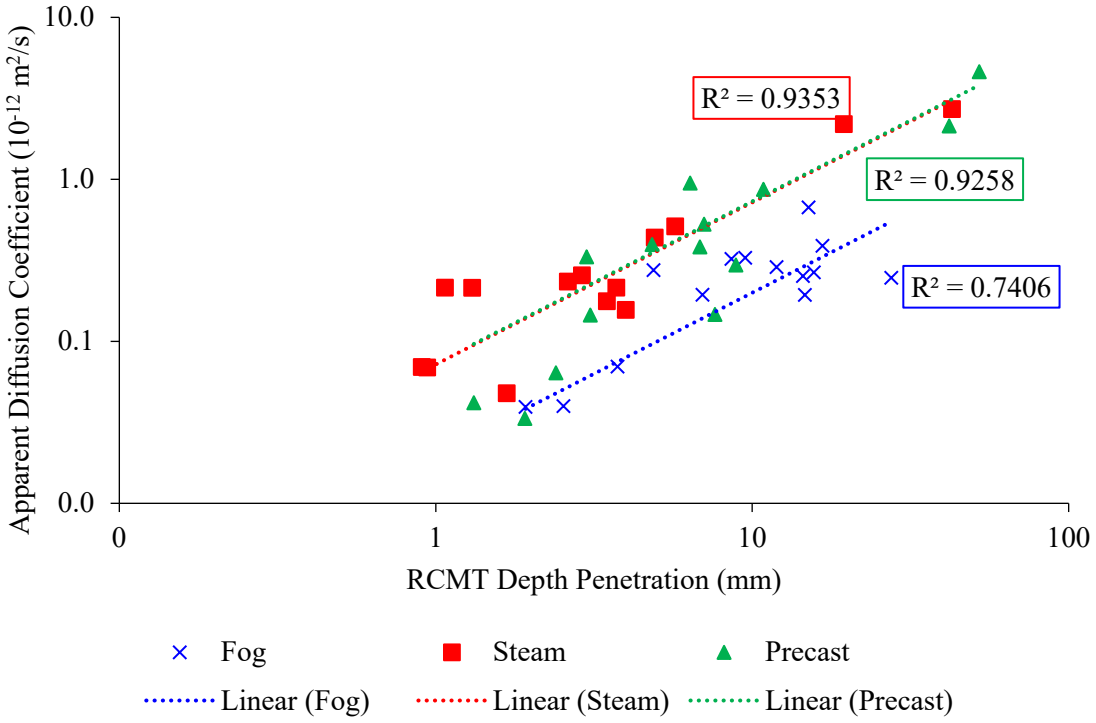

Figure 182: 7-day RCM chloride penetration depth versus the chloride diffusion coefficient

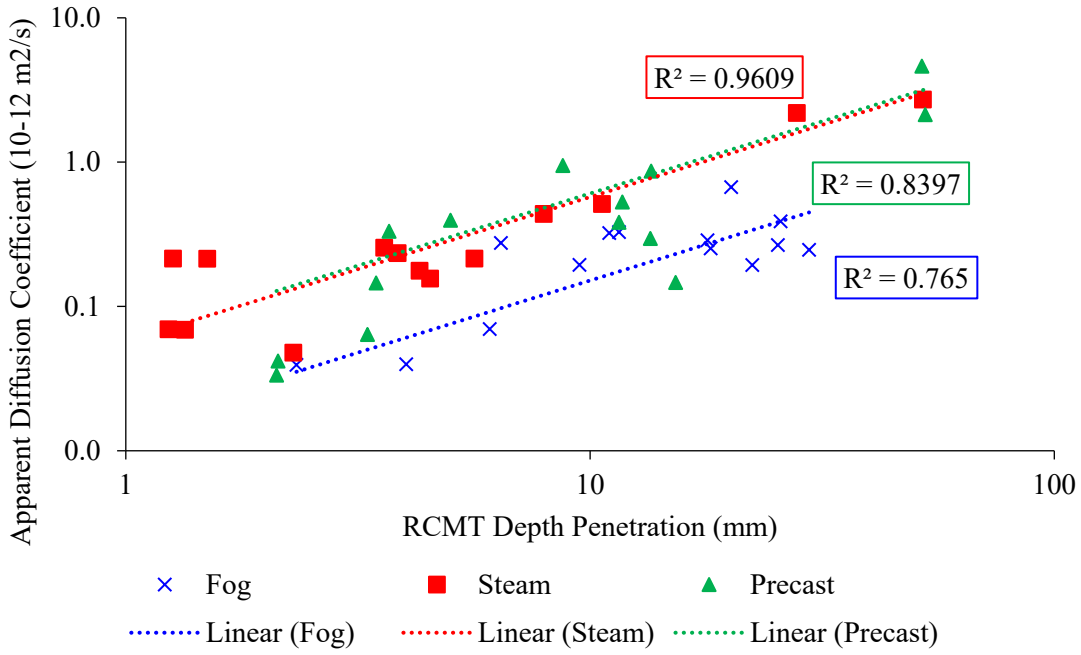

Figure 183: 10-day RCM chloride penetration depth versus the chloride diffusion coefficient

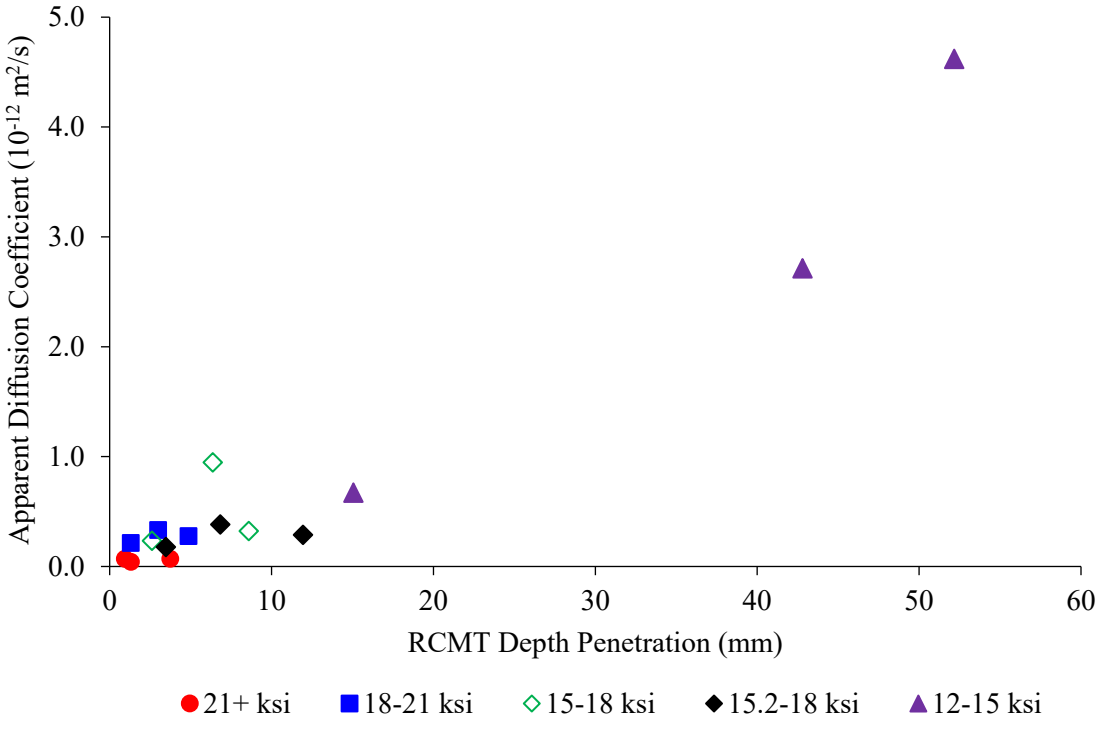

Figure 184: 7-day RCM testing for samples without fibers vs chloride diffusion coefficient

The steam-cured and moist-room-cured samples had similar bulk diffusion chloride penetration levels in all samples, except in the 12-15 ksi samples. The rapid chloride migration samples showed deeper penetration in the moist-room-cured samples in all but the 12-15 ksi samples. This is likely because the 15-18 ksi and higher samples had continued hydration past 28 days, contributing to the densification of the samples. Even though the chloride diffusion rate was higher in the moist-room-cured samples at 28 days as evidenced by the rapid chloride migration samples, the low initial concrete penetrability of all the samples kept the overall ingress low while the permeability was able to be reduced and catch up to that of the steam-cured samples, giving minimal overall differences in performance after a year of chloride exposure. The 12-15 ksi steam-cured samples likely suffered from the crossover effect, giving overall poorer performance, while the higher-strength mixtures did not. Because the 15-18 ksi and higher mixtures had similar chloride ingress values for a year in the saltwater exposure test independent of the curing method used, and the steam-cured 12-15 ksi mixture experienced higher chloride ingress, steam curing samples for testing at 28 days would be a conservative approach for mixture approval.

10.6.2. Electrical Resistivity and Apparent Chloride Diffusion Coefficient

The relationship between surface resistivity (AASHTO T 358) and bulk resistivity (AASHTO TP 119) for the moist-room-cured samples with and without steel fibers is shown in Figure 185. There is a strong relationship between them with $R^2 = 0.99$, this was expected as they both measure the same electrical resistance, only with different geometry factors. The steam-cured and precast cured samples showed higher resistivity measurements, especially for the 18-21 ksi and 21+ ksi mixtures, in which they were out of range, therefore the relationship between surface and bulk tests was not applied.

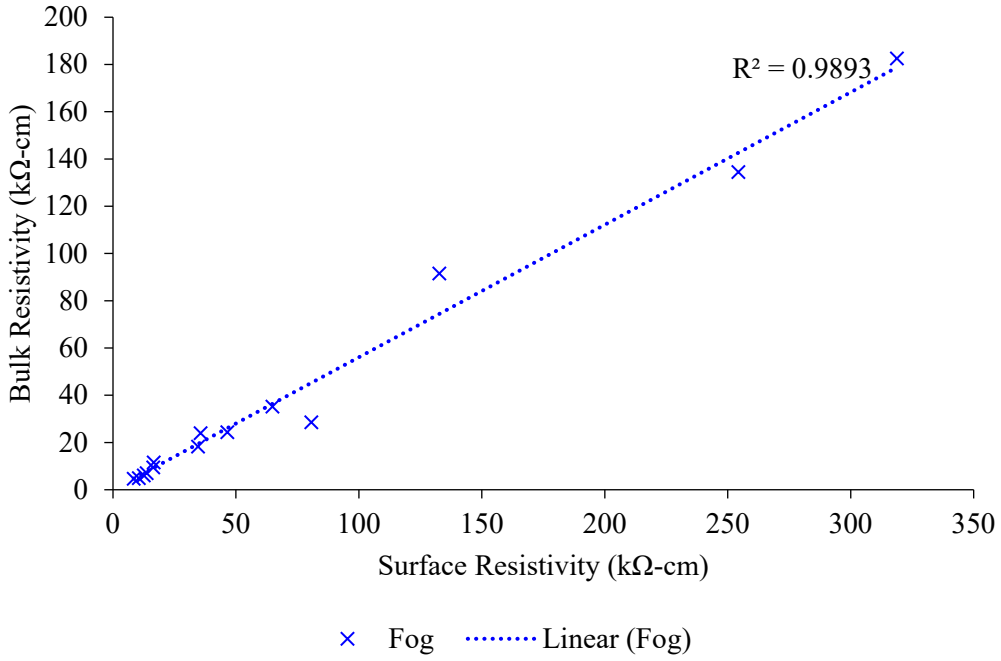

Figure 185: Surface resistivity vs bulk resistivity for all the moist-room-cured samples

The relationship between surface resistivity (AASHTO T 358) and bulk diffusion (ASTM C1556) was evaluated for the moist room cured samples without fibers with all type of curing at 28 days and slightly over 1-year are shown in Figure 186 and Figure 187. Even though some of the higher strength measurements were out of range for the higher strength mixes, it can be seen that higher surface resistivity readings for the higher strength mixes corresponded with lower apparent diffusion coefficient, in line with literature [310]. In general for UHPC, the electrical resistivity test was suggested to be used as a quality control predictor of the chloride ingress resistance [311].

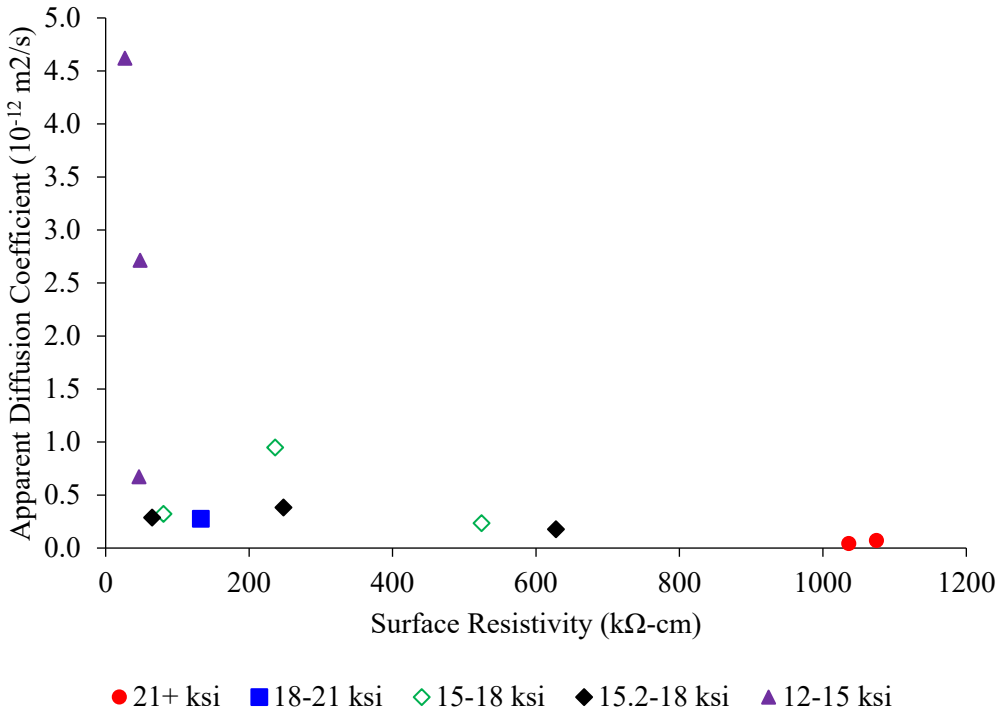

Figure 186: 28-day SR measurements for samples without fibers vs bulk diffusion coefficient

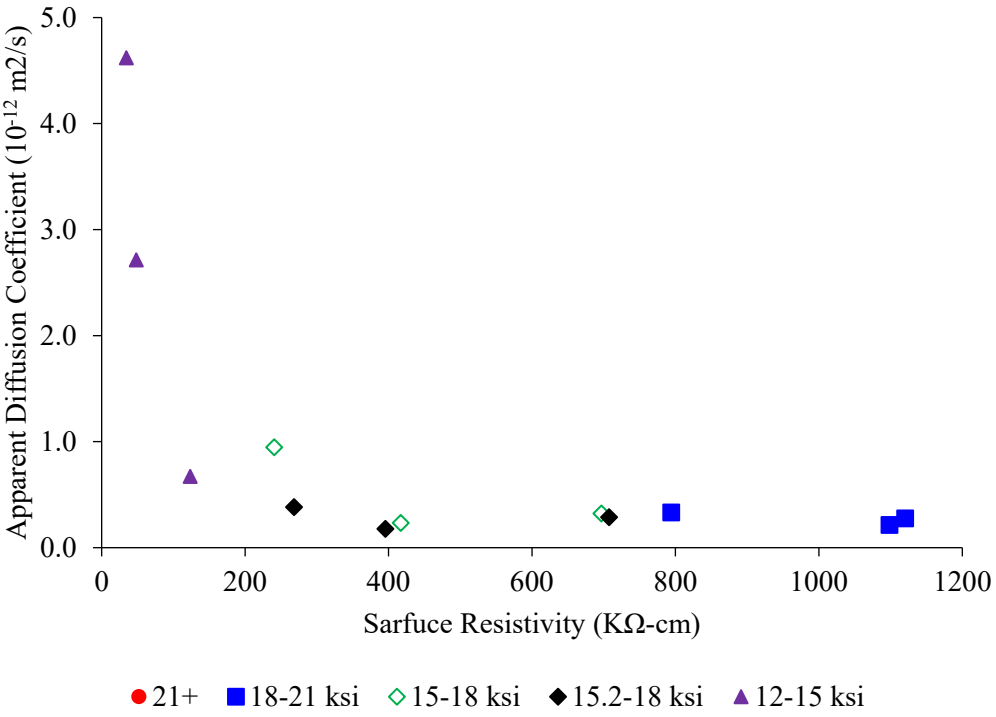

Figure 187: 1-year SR measurements for samples without fibers vs bulk diffusion coefficient

10.6.3. Absorption Rate and Apparent Chloride Diffusion Coefficient

The relationship with water and isopropanol absorption test showed a strong correlation for all the curing methods as shown in Figure 188. The moist-room-cured, steam-cured and precast-cured samples had an R^2 equal to 0.79, 0.77, and 0.87, respectively. This was expected as they both measure absorption capacity, with the isopropanol meant to measure the only the capillary voids. Figure 189 showed the results of the water and isopropanol absorption capacity for the samples without fibers for all the different curing methods. The trend is seen between the mixes, as the higher strength mixes showed lower absorption capacity.

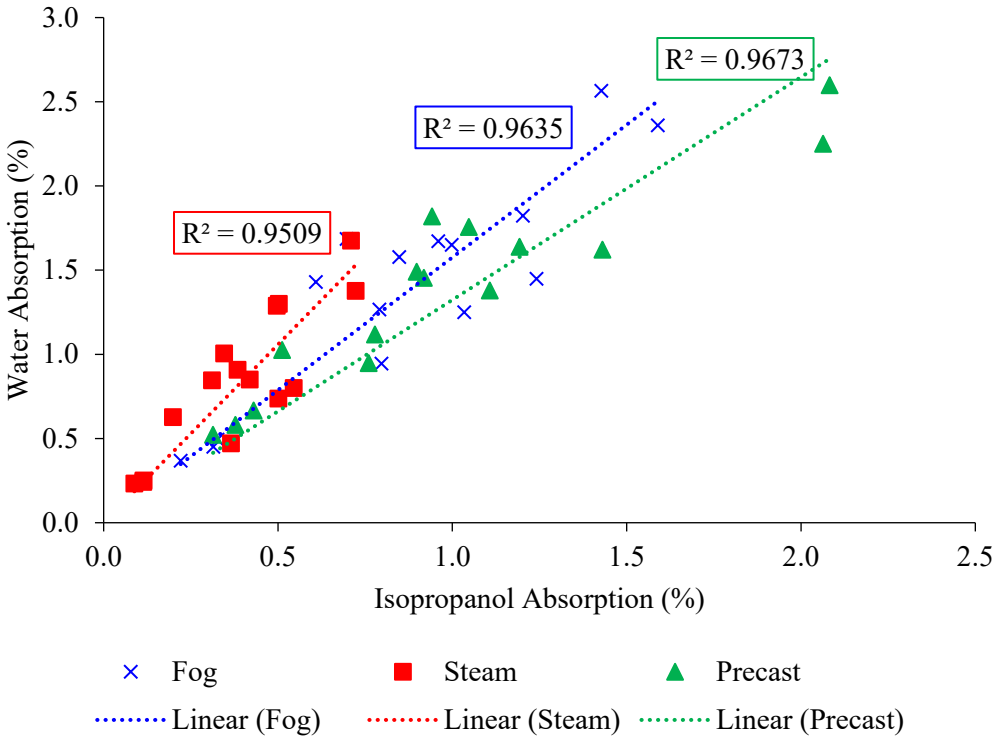

Figure 188: Water versus isopropanol absorption capacity for all the samples for all curing methods

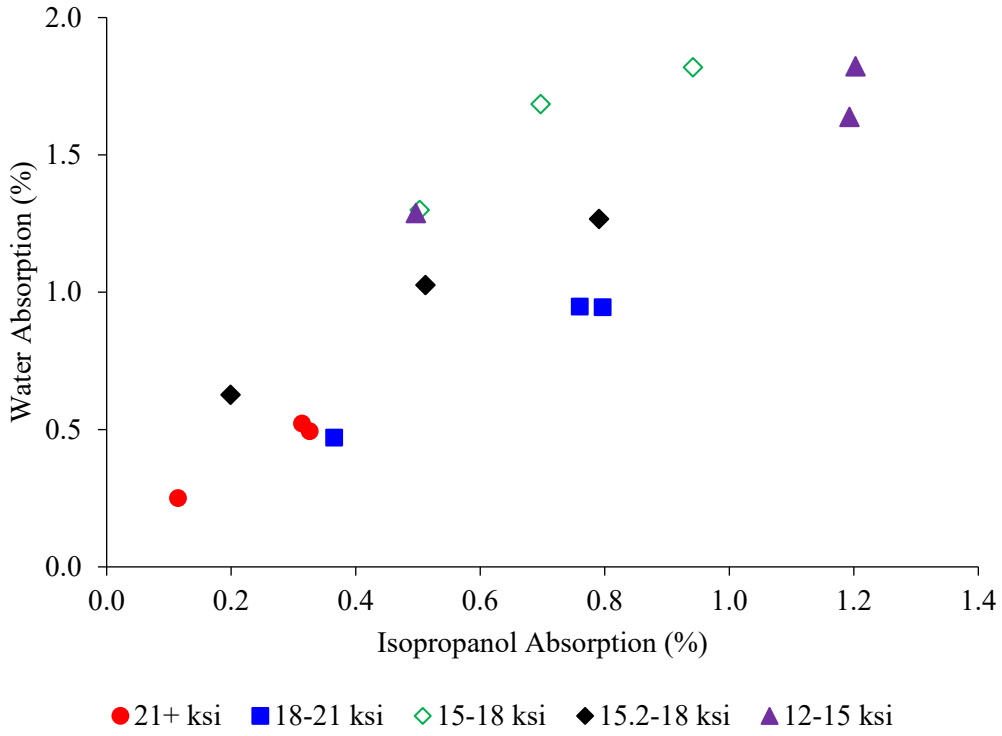

Figure 189: The absorption % for the samples without steel fibers with all curing methods

The water and isopropanol absorption test results also showed that there is a relationship between the absorption and apparent chloride diffusion coefficient. Figure 190 and Figure 191 show the relationship between the water absorption and isopropanol absorption for samples without fibers compared to the apparent chloride diffusion coefficient, indicating that the lower the absorption rate, the lower the apparent chloride diffusion coefficient. All the samples without fibers (excluding the 12-15 ksi steam-cured and precast-cured samples) had an apparent diffusion coefficient less than 1×10^{-12} m^2/s, with absorption rate lower than 1.8% and 1.2%, respectively for the water and isopropanol absorption measurements. The water absorption rate for all the samples with or without fibers versus the chloride diffusion is shown in Figure 192. There is a positive trend and a correlation, especially for the moist-room-cured samples.

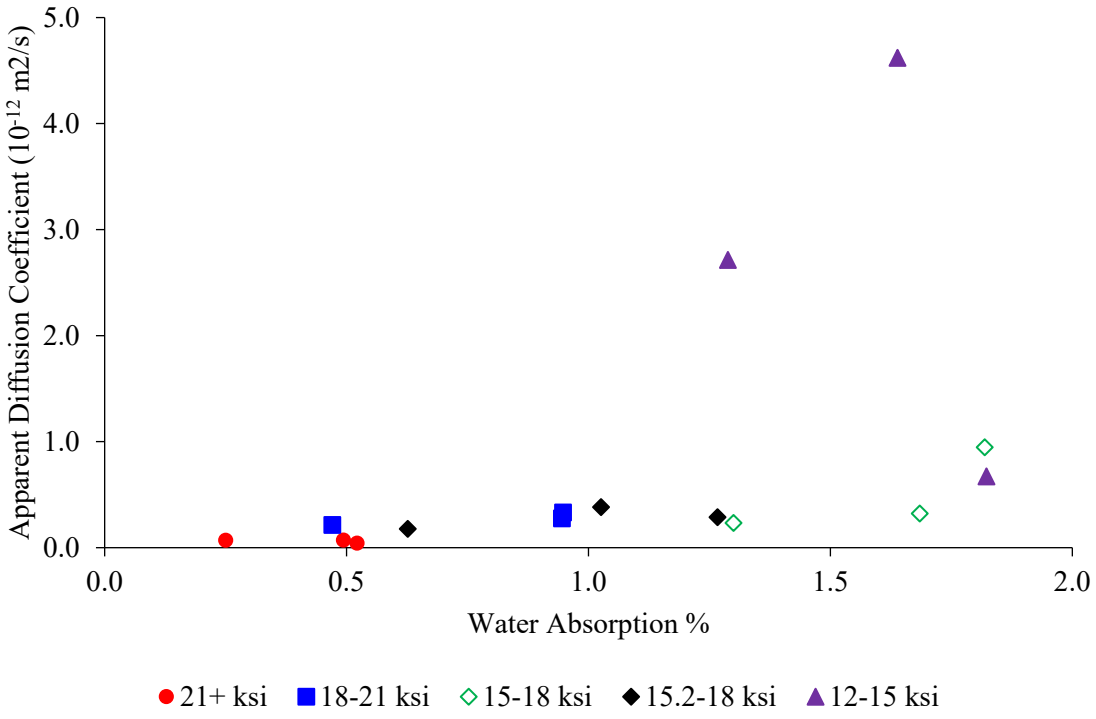

Figure 190: Water absorption rate vs chloride diffusion for all the samples without fibers

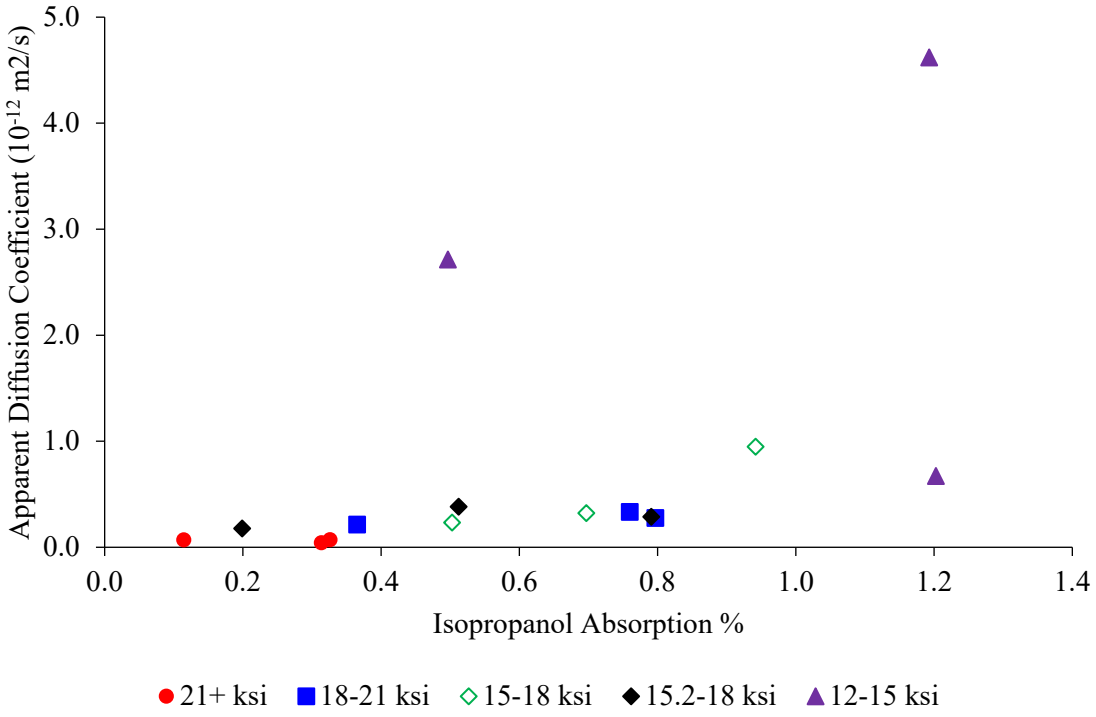

Figure 191: Isopropanol absorption rate vs chloride diffusion for all the samples without fibers

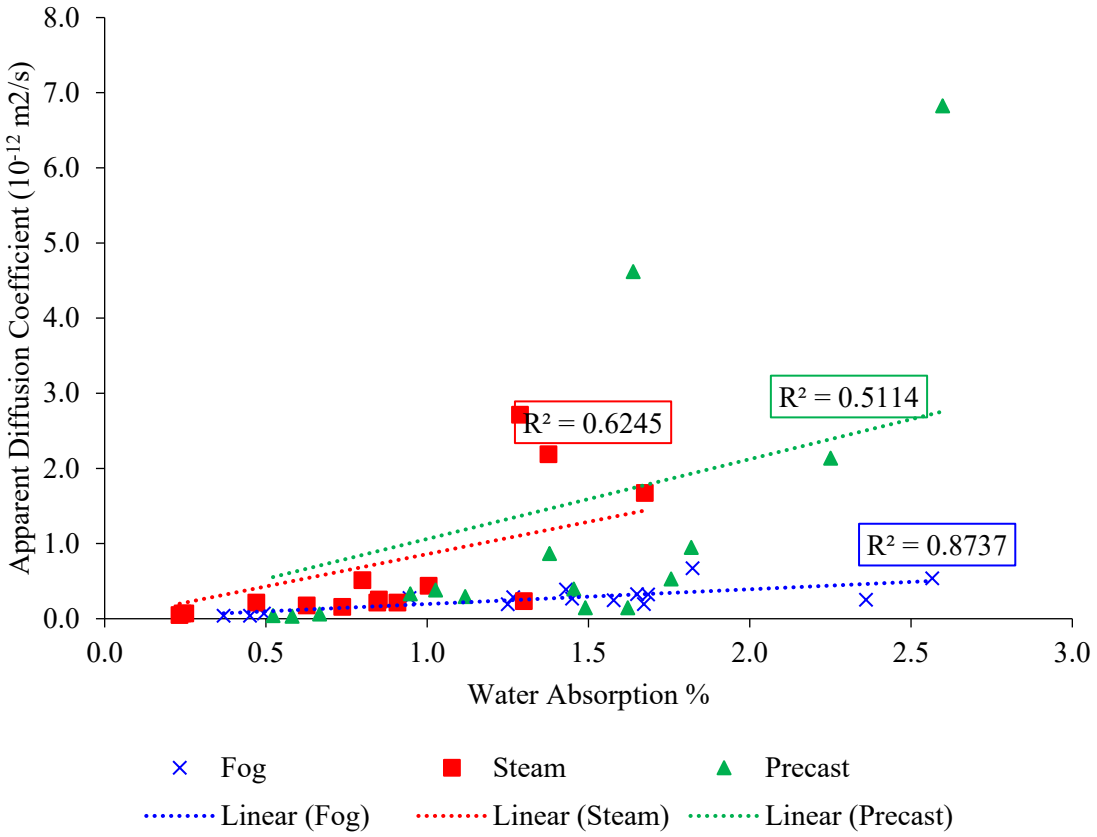

Figure 192: Water absorption vs chloride diffusion for all samples including fibers

10.7. Summary

Samples were made with 0%, 1.5%, or 2% fibers for the four UHPC mixture designs and three curing methods in this study. The modified rapid chloride migration results were compared to the bulk diffusion, MIP, absorption, and electrical tests. The steel fibers did not noticeably affect the chloride ingress in bulk diffusion experiments due the disconnected pore structure of the samples. The fibers had only a small effect on the chloride ingress measured in the modified rapid chloride migration test in the 15-18 ksi, 18-21 ksi, and 21+ ksi mixtures because of the discontinuous pore structures. Steam curing samples gave conservative results at 28 days compared to the long-term test results and is recommended for acceptance testing purposes. Very low porosity was seen in the MIP tests in the steam-cured samples, probably because pores were smaller than the smallest pore measurable in the MIP of 3 nm. The surface resistivity measurements showed a good relationship with the chloride diffusion results; however, the presence of steel fibers alters the measured results, making resistivity measurements difficult to use on as-produced concrete mixtures with fibers. The modified rapid chloride migration test was found to work for UHPC samples with fibers up to 2% by volume. A limit of 5 mm of chloride intrusion after 7 days was found to be a good limit to differentiate chloride diffusion performance.

11. DURABILITY SITE SAMPLES

11.1. Introduction

In order to evaluate UHPC durability in marine environment and eventually compare the accelerated lab tests data to the long-term durability field data, samples were made with 1.5% by volume of steel fibers for each strength class, 12-15 ksi, 15-18 ksi, 18-21 ksi, and 21+ ksi and placed at Seahorse Key, FL and Treat Island, ME. Companion samples placed at each site were made from the same batch of concrete. The mixture proportions used for the 12-15, 15-18, and 18-21 ksi class mixtures are shown in Table 76. Table 77 shows the mixture proportions used for the 21+ ksi mixture.

Table 76: UHPC mixture proportions

Mix (ksi)	Weight (lb/yd^3)				Admixtures (lb/yd^3)			Calculated Values	
	Sand	Type IL Cement	Slag	Silica fume	HRWR	WRWR[1]	SE[2]	w/cm	cm/s
12-15	1852	1583	0	83	10.9	10.9	2.1	0.25	0.9
15-18	1811	1404	272	136	16.4	16.4	3.4	0.20	1
18-21	1585	1597	309	155	30.9	30.9	5.1	0.1625	1.3

[1]water reducing and workability retaining; [2]surface enhancing

Table 77: UHPC mixture proportions

Mix (ksi)	Weight (lb/yd^3)				Admixtures (lb/yd^3)			Calculated Values	
	Sand	Type III Cement	Silica Flour	White Silica fume	HRWR	Accelerator	RHRWR[3]	w/cm*	cm/s*
21+	1359	1477	369	369	46.1	23.1	40.3	0.13	1.62

[3]retarding high range water reducer; *includes silica flour

11.2. Seahorse Key Site Samples

For the Seahorse Key site, a column and a base unit were made for each sample set. The size of the column was 8 in. by 8 in. by 3 ft, and it contains black reinforcing steel bars with 0.5 in and 1 in cover to determine the effect of cover depth. The black steel bars were threaded on the ends to couple them to short stainless-steel segments that protrude from the ends of the specimens to facilitate specimen fabrication, transport, and electrical connection for later non-destructive measurements. They also contain stainless steel inserts used to attach the column to the base, as well as a 316 stainless steel all-thread bar that runs the length of the specimen in the center that can be used as a counter electrode for linear polarization testing. The base unit was unreinforced, with stainless steel inserts cast into the concrete to attach the column and connect to adjacent base samples. The base units were designed to be 4” thick and 2’ 8” wide. Figure 193 shows a

schematic view of the column and base. Figure 194 shows a schematic of the assembled samples, and Figure 195 shows an isometric view of the sample design when assembled on-site.

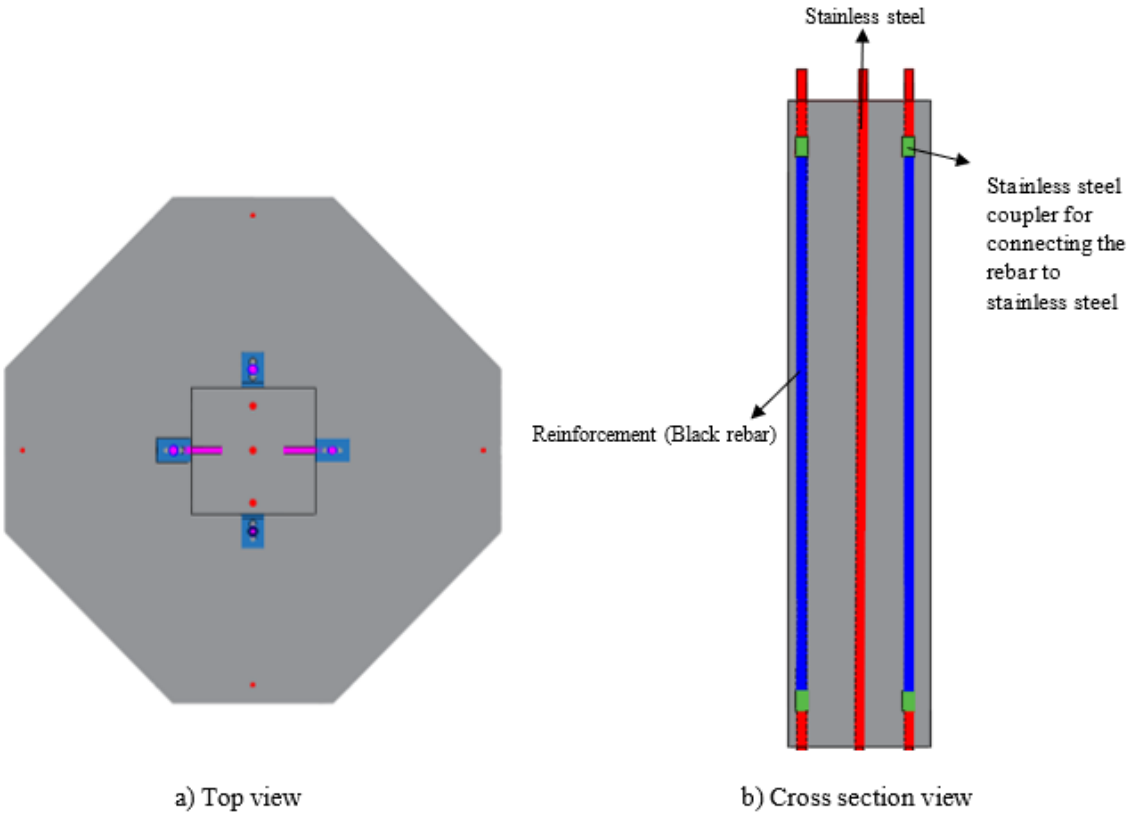

Figure 193: Schematic view of durability base and column section

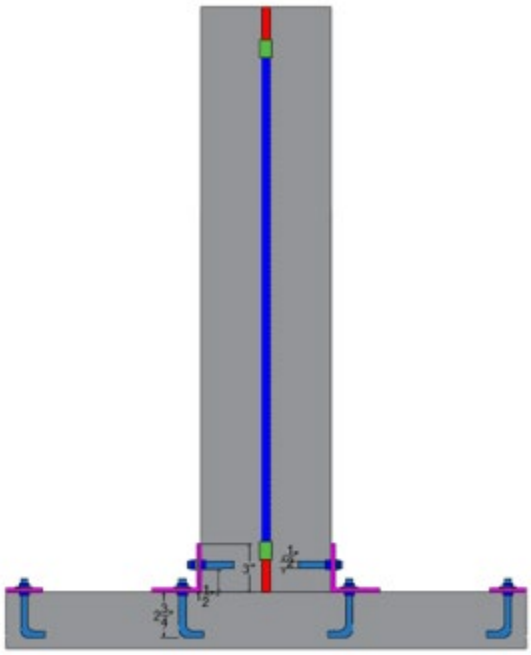

Figure 194: Schematic view of the assembled specimens

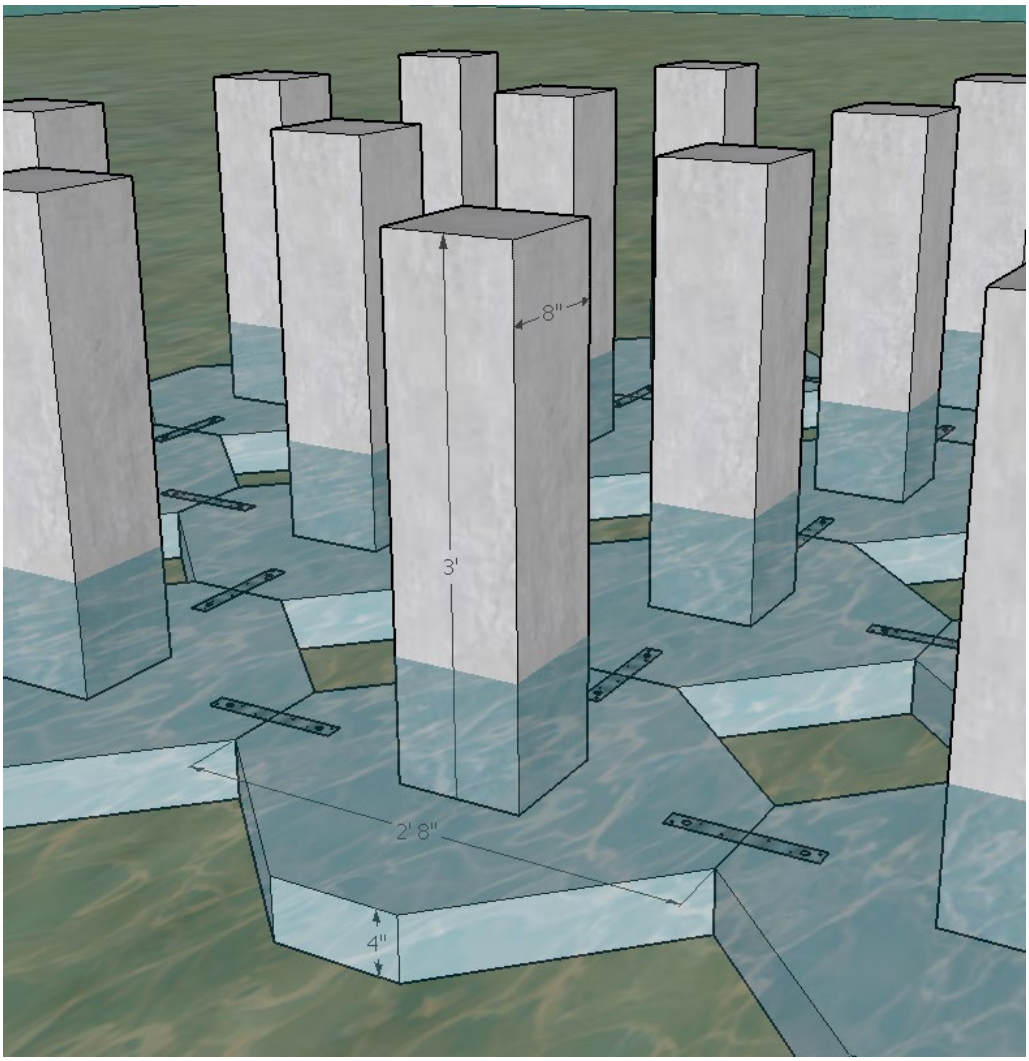

Figure 195: Isometric view of Seahorse Key durability sample design after assembled on-site

For 12-15 ksi, 15-18 ksi, and 18-21 ksi class mixtures, two columns were made for the Seahorse Key site using two different curing methods: moist-room curing after demolding at 1 day until 28 days of age and steam-curing. For the 21+ ksi mixture, only one durability sample was made for the Seahorse Key site because of limitations on the availability of white silica fume and silica flour needed for that mixture design. The 21+ ksi mixture sample for Seahorse Key was cured using the steam curing method. Steam curing is commonly used by manufacturers of prefabrication concrete products. It accelerates the hydration of cement and supplementary cementitious materials (SCMs), which lead to improved concrete properties at an early age. Steam curing was done by first demolding the column at 1 day, wrapping it with wet towels, followed by plastic wrap and duct tape to prevent evaporation. It was then placed for 48 hours in an oven that was set to 194°F (90°C). Figure 196 shows a chart with the curing temperature regimes used in this study. Figure 197 shows a picture of a column sample in the oven during steam curing. The base units for all mixtures were cured after demolding at 1 day in the moist room until 28 days of age.

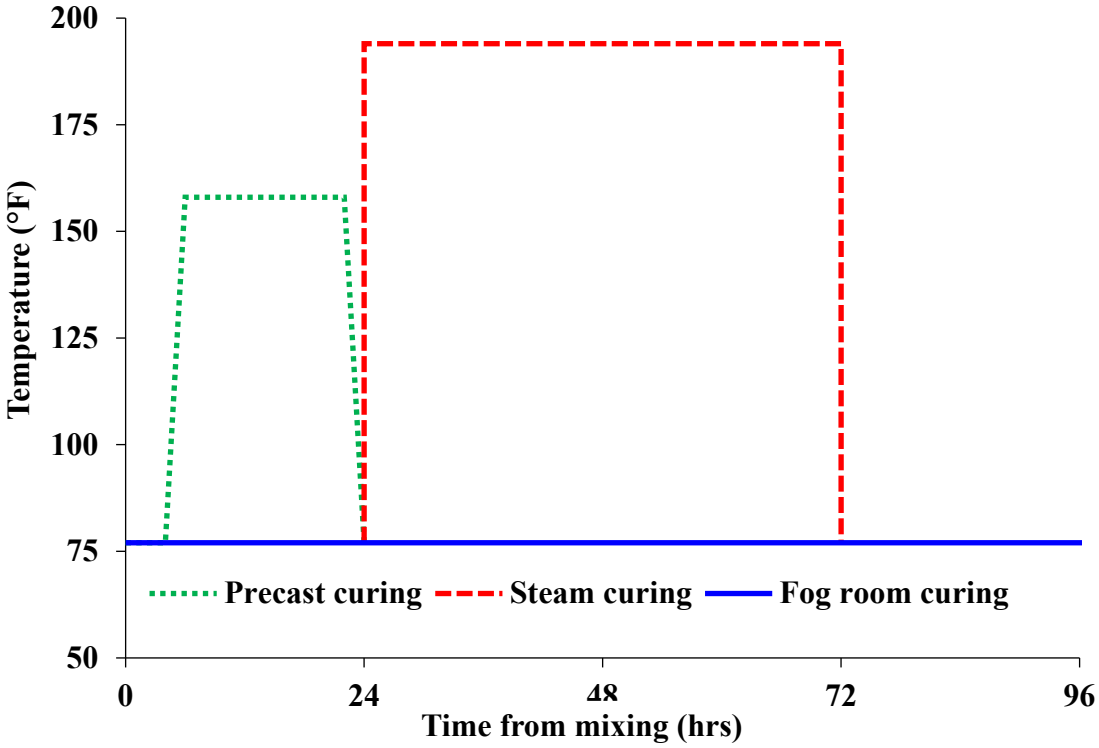

Figure 196: Curing temperatures used for each curing regime

Figure 197: Column specimen during steam curing

11.3. Treat Island Site Samples

For the Treat Island, ME site, 9 6-in. cubes were made for each mixture from the same batches of concrete used to make the steam-cured columns for exposure at Seahorse Key. Three samples were made for each of the three curing methods used, fog, steam, and precast as shown in Figure 196. Stainless steel labels were made for each sample with the date made, curing type, and mixture design and embedded into the concrete during sample fabrication, as shown in Figure 198. The fog room-cured specimens were stored in a moist curing room for 27 days after demolding. The steam-cured specimens were placed after demolding at 24 hours in a covered pan with water and put in an oven with a set temperature of 194°F (90°C) for two days of steam curing, followed by curing in the moist room until testing. Specimens cured using the simulated precast curing method were placed in a covered pan without water while they were still in their mold in an oven with a temperature of 158°F (70°C) after four hours of the mixing. They were removed from the oven after 18 hrs. of heat curing, demolded, and placed in the moist curing room until 28 days of age.

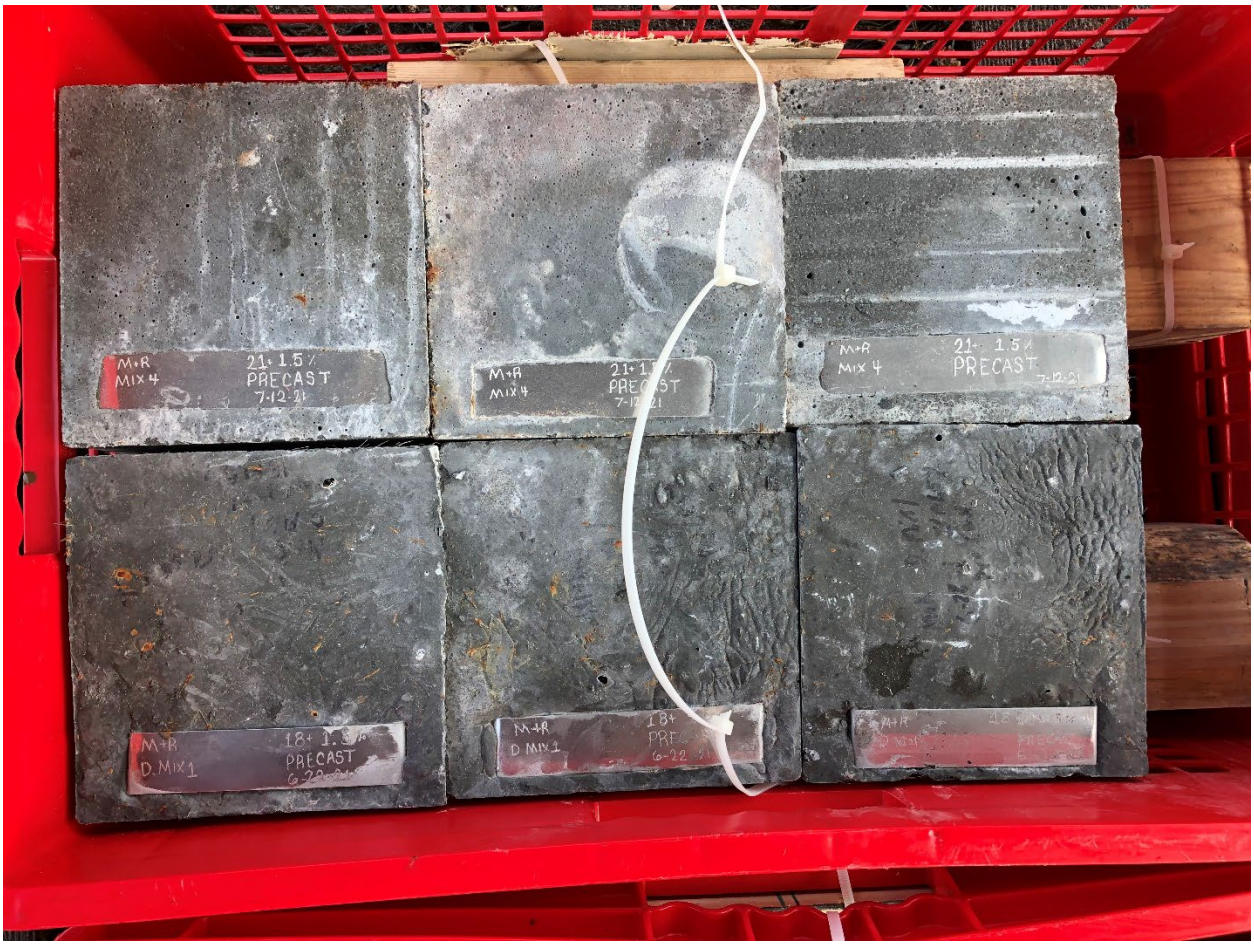

Figure 198: Concrete cube samples with labels

11.4. Initial Temperature Monitoring

Concrete columns were instrumented with thermocouples to measure the temperature profile experienced and deviation from the curing environment temperatures due to the concrete heat of hydration. Immediately after the concrete was placed, thermocouples were embedded in the center of the columns. For the 12-15 ksi mix, the temperature for both the column and a cube cured in the moist room were measured for comparison. It can be seen from Figure 199 the temperature for the 12-15 ksi and 15-18 ksi mixes reached the peak temperatures at around 14 hours. The temperature rises for the 18-21 ksi and 21+ ksi mixtures were significantly retarded because of the very high superplasticizer dosages that were used to achieve the low water-cementitious material ratios (w/cm) used. The high temperatures above 125°F reached during curing by the 12-15 ksi and 15-18 ksi mixtures are not surprising given the amount of cementitious material in each mixture and wood forms used, even with the relatively small member cross section. The cube sample only reached 93°F because of the smaller size sample used. Figure 200 shows that the column steam temperature reached an equilibrium after 8 hours of curing in the 194°F oven.

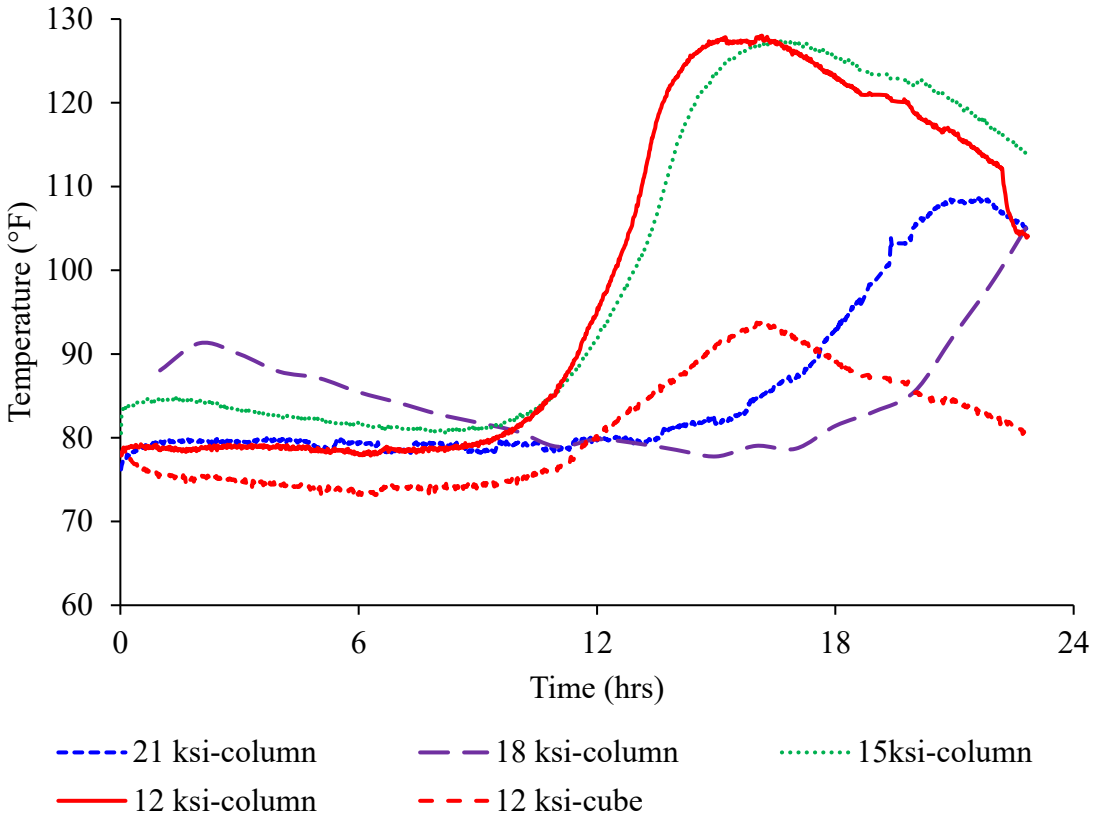

Figure 199: Concrete sample temperature measurements during the first 24 hours after mixing

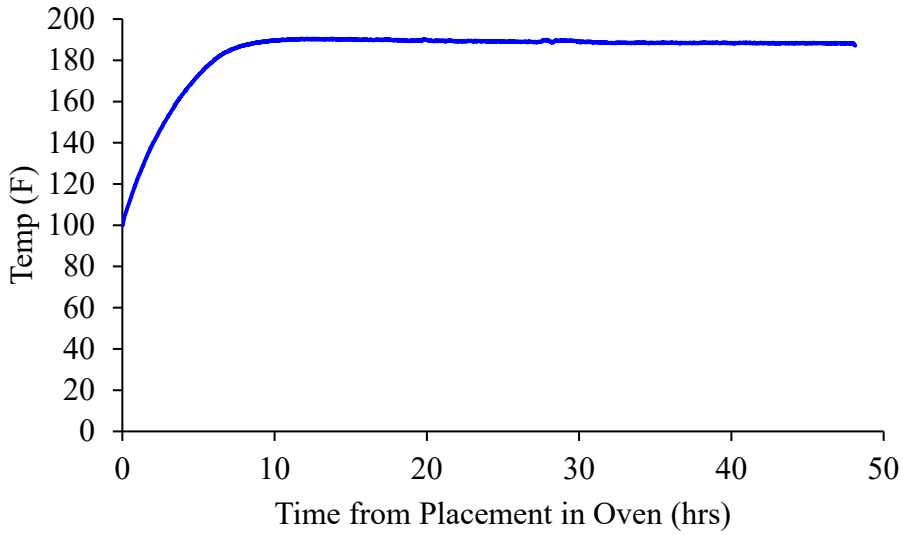

Figure 200: Steam cured column sample measured temperature while in the oven

11.5. Site Sample Installations

Column samples were placed at the Seahorse Key site as shown in Figure 201, while cube samples were placed on the mid-tide dock at Treat Island, as shown in Figure 202 and Figure 203. Table 78 shows the mixing date and date placed on site for all of the samples. It is anticipated that as part of future work of a future project, the research team will retrieve one cube from the Treat Island site for each mixture/curing regime at three different ages to determine the chloride diffusion coefficient with age and compare the results to the bulk diffusion samples.

Figure 201: UHPC samples placed at Seahorse Key

Figure 202: UHPC samples placed at Treat Island

Figure 203: Treat Island, ME mid-tide dock showing location of samples in red containers

Table 78: Mixing date and site placement date

	Seahorse key (FL)				Treat Island (ME)	
	Fog column		Steam column		Fog/steam/precast cubes	
Mix	Mix date	Site placement date	Mix date	Site placement date	Mix date	Site placement date
12-15 ksi	3/17/2021	5/12/2021	7/15/2021	09/28/2021	7/15/2021	08/16/2021
15-18 ksi	7/29/2020	9/23/2020	6/29/2021		6/29/2021	
18-21 ksi	7/22/2020	9/23/2020	6/22/2021		6/22/2021	
21+ ksi	-	-	7/12/2021		7/12/2021	

11.6. Compressive Strength

Three 3-in. × 6-in. UHPC samples were made for each strength class for each curing method from the same batches used to make the 6-in. cube samples. The compressive strength data were measured according to ASTM C1856 [59] at 28 days for all the different curing methods. As shown in Figure 204, the steam cured samples had the highest measured 28-day compressive strengths followed by fog room curing and then simulated precast curing.

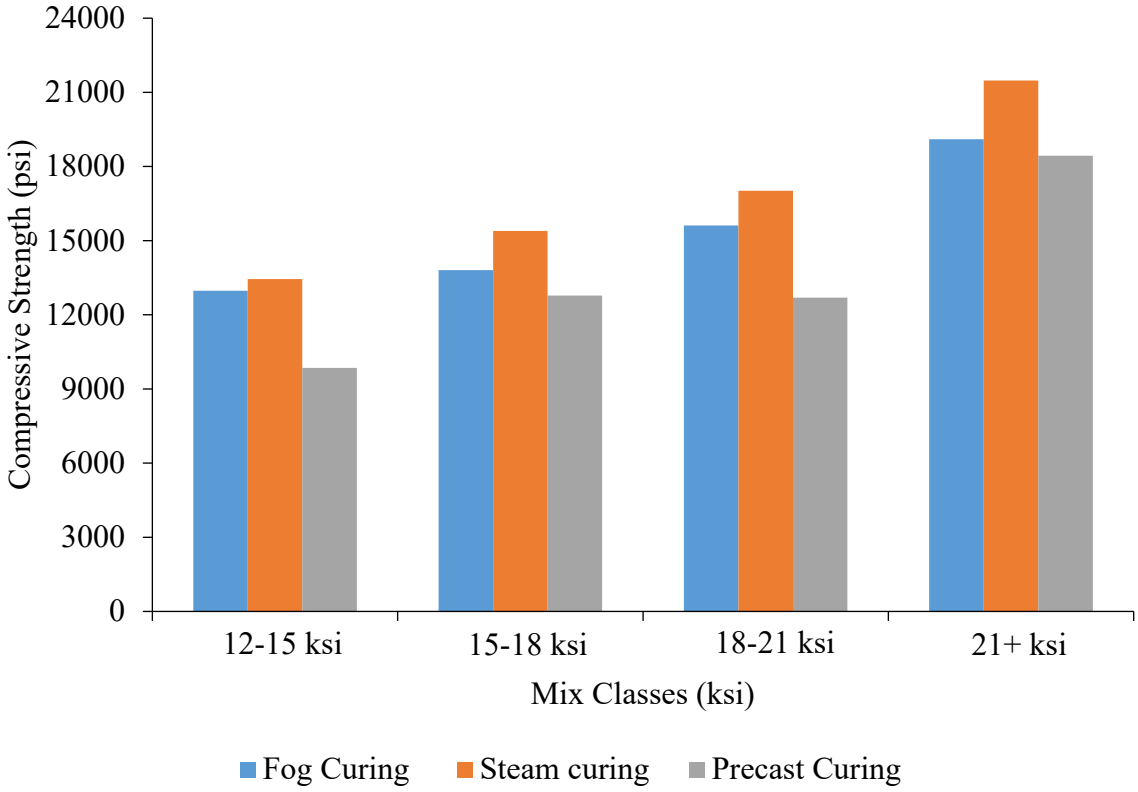

Figure 204: 28-Day compressive strength for the mixtures used to make the Treat Island cubes and Seahorse Key steam-cured columns

11.7. Summary

Samples were made with 1.5% by volume of steel fibers for each strength class examined in this study and were placed at Seahorse Key, FL and Treat Island, ME. For the Seahorse Key site, a column and a base unit were made for each sample set. The base units were made using the fog room curing method, and the columns were made using two different curing methods, fog and steam, except that the 21+ ksi mixture sample set was only made using the steam curing method due to the limited availability of white silica fume and silica flour required for that mixture. For the Treat Island site, 6-in. cubes were made for each mixture from the same batches of concrete used to make the steam-cured columns for exposure at Seahorse Key. Three samples were made for the Treat Island site using each of the three curing methods.

12. NON-DESTRUCTIVE METHODS FOR FIBER DISTRIBUTION AND ORIENTATION

12.1. Introduction

Ultra-high performance concrete (UHPC) is a form of concrete with unprecedented durability and opportunities for new types of and longer structural members because of the tensile strength [1] and ductility [2] provided by steel fibers included in the mixture. Yet, fibers can segregate due to poor material rheological properties and construction practices [6], leaving zones of high and low fiber content. Fiber orientation can change during concrete placement, typically aligning with the direction of the concrete flow. Poorly distributed fibers that are preferentially oriented in an undesirable direction during member fabrication could lead to structural weaknesses and critical failures [7], [8]. Companies and regulatory bodies have no means to mitigate these hidden weak zones once the concrete member is fabricated unless they know they are present. The technology described is designed to validate fiber orientation and density at critical member locations to ensure the safety and sustainment of many future concrete constructions.

In the field of nondestructive evaluation, ultrasound is currently one of the most used approaches for assessing concrete members [155]. However, ultrasound is problematic for assessing fiber content for several reasons. First, the ultrasound internally scatters in the concrete material, leading to a strong attenuation and dispersive responses from the fibers [155]. As a result, coherent ultrasound reflections distinguishing fibers cannot be obtained. Second, while the steel fibers have a higher wave speed relative to concrete, the fibers are only a small percentage of the volume (usually 1% to 3% of the total volume). Hence speed variations, the basis of pulse velocity testing [312][313], due to the fibers are small compared to the overall bulk signal. This makes the steel fibers difficult to distinguish from the aggregates of the UHPC. In addition, wave speed variations may be due to potentially larger variations in the aggregate rather than the fibers. There has been a recent feasibility study characterizing UHPC with ultrasound [314], but no variation specifically due to the fibers is evident. Third, conventional ultrasound (which has no directional dependence) has no means for estimating the orientation of the fibers without some form of financially and computationally expensive tomography system [167], [315].

Relative to other nondestructive testing modalities, electromagnetic methods have been used in literature to quantify the presence of metals in concrete. Eddy current testing is one of the most prominent methods that have been applied for years [316]. In [317], an eddy current method is used to test for the presence of steel rebars in reinforced concrete structures. This method relies on the conductivity of steel rebars to be able to detect the presence and location of steel rebar in reinforced concrete structures. The method works by generating a magnetic field by passing an electric current through a search coil. This magnetic field induces a current in the steel rebars. The current then creates a magnetic field that opposes the magnetic field generated by the search coil [318]. The magnitude of this induced magnetic field is proportional to the thickness of steel rebars that are present in the reinforced structure. Eddy current testing has, however, not been used for quantifying the volume and orientation of fibers in the field due to various shortcomings. First, the high magnetic permeability of ferromagnetic materials restricts the eddy currents to only penetrate the surface of the material [319]. In addition, eddy current testing requires high voltage and high frequencies for operation [316], [319].

Electrical resistivity methods have been used to quantify the volume of steel fibers in SFRC and UHPC [320][321][322]. These methods place electrodes on or around a concrete sample while passing relatively high currents through it. The current measurements are used to determine the resistivity of the sample, measuring its ability to resist the current flow. Because steel fibers are conductive, the resistivity of the sample should be lower in proportion to the number of fibers in the concrete sample. However, this method is not reliable for various reasons. First, there have not been reliable field tests, only [321] and [322] have been able to show lab tests where resistivity has been used. Second, the resistivity of the samples is highly dependent on the concrete degree of saturation, pore system, temperature, and pore solution conductivity [155]. Overall, most traditional non-destructive evaluation methods are insufficient for characterizing fiber content in UHPC because their ability to quantify the amount of fiber is dependent on many other factors and they can only account for the fiber content but not the fiber orientation.

This report considers an alternative approach based on a low frequency, inductance-based electromagnetic approach for UHPC testing. This quantitative inductive sensor uses one or more electromagnets to generate magnetic fields. The fields generate currents in metals that oppose the magnetic field and increase the electromagnet's inductance, which is measured. The denser the metal, the greater the inductance change. This technology operates on different principles than existing non-destructive evaluation methods (e.g., ultrasound, thermography, etc.), and while similar to eddy current probes, it operates at a much larger scale and with different materials. For example, eddy current probe ranges are usually < 10 mm (compared to the 120 mm size of this new sensor), and are less effective for ferromagnetic materials, like steel.

Unlike other inductive sensors (e.g., proximity sensors [323] and some metal detectors [324]), this new type of inductive sensor extracts quantitative information on fiber percent and orientation. Metal detectors operate on related, but different, principles that ensure good depth penetration and detection sensitivity but have a coarse spatial resolution and cannot quantify metal density and orientation information. Most metals detectors are specifically designed to ignore dispersed metal (such as steel fibers) since they often represent mineralization in the soil. Inductive proximity sensors utilize the same fundamental theories as these sensors but usually only detect metals less than a centimeter away. In addition, they are generally designed for crude metal detection and sometimes distance estimation in manufacturing. Since greater penetration depth and completely different information are required in this application, the sensor design is a radical departure from the traditional inductive sensor.

This new electromagnetic sensor system was designed and optimized for steel fiber characterization. The system is low power and consumes less than 20 mW of power at 0.6 V and can be safely used in the field. It is able to identify fiber quantity and orientation. Similar ideas have been demonstrated in the literature before [325], [326]. This work expands on these studies by focusing on design that can be used in real-time in the lab and field for fiber quantity and orientation measured. How to optimize the design of these magnetic sensors to ensure high penetration in the concrete and high accuracy in its measurements is discussed in this report.

Detailed in this report is the overall design of the inductive sensor system and its calibration. The system's capabilities are demonstrated with experimental data taken from the lab and field data taken from full-size UHPC members fabricated for the Florida Department of Transportation.

The results demonstrate that the estimation of fiber orientation in both lab and field specimens can be successfully obtained, and fiber density in the lab.

12.2. Inductive Sensor System Design

Outlined in this section are the various components of the electromagnets that were refined and optimized to make the sensor. It details the parameters and procedures that were taken into consideration in the design of the sensor.

12.2.1. Electromagnet Shape

The shape of a magnet will determine the shape of the generated magnetic field, the penetration of the magnetic field, the directionality of the magnetic field generated, and the spread of the magnetic field. One of the most common shapes used in electromagnetics is the pancake coil. It is easy to design and implement as it is a loop of wires in a two-dimensional array. It is most commonly used for eddy current testing [316] because of its simple design and its ease of use. The spacing between the wires in the coil can also be used to determine the frequency in a pulse setting application.

The magnetic field generated in a pancake coil is shown in Figure 205(a). It can be seen from Figure 205(a) that the magnetic field is shaped around the pancake coil in a way that it spreads in all directions. In a case such as this, where specific directionality is desired to best penetrate the UHPC specimen volume for proper fiber detection over varying depths, a different shape of coil is desirable to direct the field in the desired direction.

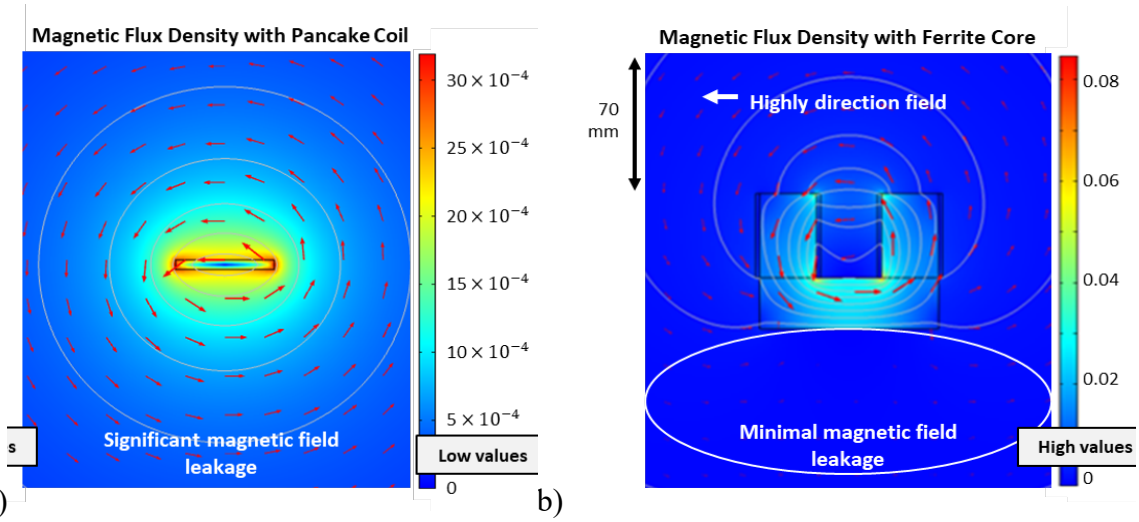

Figure 205: COMSOL Multiphysics simulations of the (a) a pancake coil more traditionally used in metal detectors and inductive proximity sensors and (b) the ferrite core magnetic sensor used in this new device.

Directionality can be achieved by placing a reflective surface on one side of the pancake coil to direct all the fields in one direction. Another way to create directionality is to use a core that has a high permeability, such as a soft iron or ferrite core. Soft iron cores typically have one of the

highest permeabilities, but the downside is that they are also conductive, requiring more input energy. Ferrite cores, on the other hand have high permeability and low conductivity (approximately infinitesimal) that will be almost as effective as soft iron cores while keeping the energy costs lower overall. The ferrite would help keep the magnetic field from spreading and channeling it in the desired direction, helping to determine the approximate fiber volume and fiber orientation.

Ferrite cores come in different shapes, sizes, and permeability. In this study, a U-shaped N87 core that had a relative permeability of 1950 was used. The high permeability helped to contain the generated field within the core, mimicking the traditional horseshoe magnet. The generated field in this arrangement is shown in Figure 205(b). With this configuration, the magnetic field can be channeled in a direction that is useful and has low energy waste at the same time. The magnetic field penetration is also improved in this way, helping to detect steel fibers that are below the surface of the UHPC specimen.

Figure 206 shows an experimental demonstration of the two magnets using a test frequency of 1000 Hz. Specifically, the change in inductance (relative to the inductance of air) created by placing the corresponding sensor some height away from a UHPC specimen is shown. The figure shows that the U-magnet has approximately 100 times greater change in inductance compared with the pancake coil when placed near a UHPC specimen for fiber detection. This enables higher sensitivity and higher resolution with less energy consumption.

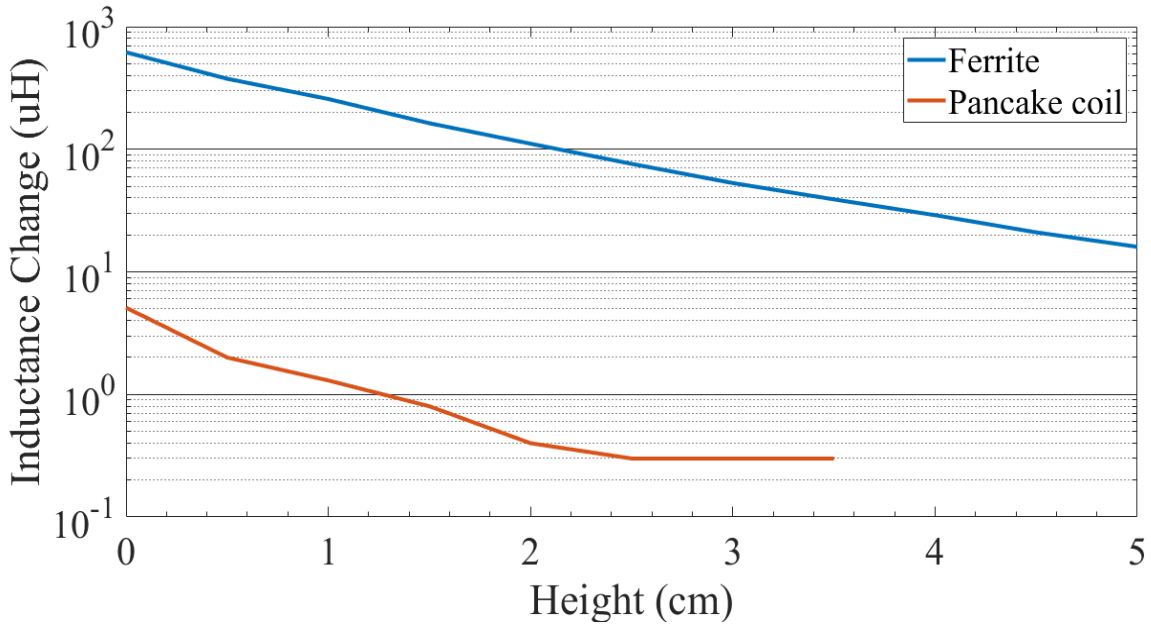

Figure 206: A semi-log Plot showing the Inductance Change of the U magnet (Ferrite) in the sensor system compared with that of a pancake coil at 1000 Hz and this is measured over an incremental height of 0 to 5 cm from the surface of a UHPC specimen

12.2.2. Electromagnet Size

One of the factors considered for the design of the electromagnet is its size and how it affects the sensing performance. The electromagnet has two size-related components: its length and effective cross-sectional area near the surface of the specimen. The effects of these two components on the inductance and resistance of the device can be mathematically described through electromagnetic theory. In general, a high inductance (to have greater sensor sensitivity) and low resistance (to minimize losses) is desired. The inductance L of an infinitely long solenoid is represented in Equation 34 through Equation 37:

$$L = \mu \frac{N^2}{l} \quad \text{Equation 34}$$

$$\mu = \mu_r \mu_0 \quad \text{Equation 35}$$

$$L = \mu \frac{(l/w_{coil})^2}{l} A \quad \text{Equation 36}$$

$$L = \mu \frac{l}{w_{coil}^2} A \quad \text{Equation 37}$$

where μ is the permeability, μ_r is the relative permeability and μ_0 is the permeability of free space also known as the magnetic constant, N is the number of turns of wire, l is the length, w_{coil} is the diameter of the wire/coil, and A is the cross-sectional area. The resistance is defined in Equation 38:

$$R = \frac{\rho l}{A} \quad \text{Equation 38}$$

where ρ is the resistivity of the material, l is the length of the wire, and A is the cross-sectional area of the wire.

A high inductance is desired to improve the sensitivity of the sensor. Specifically, a high inductance enables the best utilization of the resolution and range of the inductance measurement device and minimizes noise in the data. Based on Equation 34 through Equation 38, a core with a large cross-sectional area, small length, and the high number of turns provides a high inductance and therefore good sensor sensitivity. However, the small length of magnets practical for field use usually restricts the number of possible turns. A large magnet cross-sectional area can help increase the number of possible turns by providing an extra surface to wrap the wires around. Therefore, the length and cross-sectional area of the core were optimized considering Equation 36 and by testing different sizes of cores to provide many turns and high inductance.

A low resistance is desired to minimize loss in the system and ensure the system is safe. Specifically, the power loss P_{loss} is defined by Equation 39:

$$P_{loss} = I^2 R \qquad \text{Equation 39}$$

where I is the current. The power is lost principally as heat. This shows that the amount of heat is proportional to the resistance, which can be reduced by using a thicker coil. Therefore, a low resistance is achieved by a large cross-sectional area. This objective aligns with maximizing the inductance.

12.2.3. Number of Turns

As shown in Equation 34, the number of turns in the electromagnet has a squared relationship with the inductance. This relationship indicates that the maximum possible number of turns for the sensor should be used. However, other factors need to be considered. First, more turns lead to a higher sensor resistance and, by extension, higher losses. Loss as a result of the coil is a function of the current squared and resistance as shown in Equation 38. Therefore, the higher the resistance, the more loss incurred on the overall system. There is an increase in the overall heating of the system because of the power losses because most of the loss occurs in the form of heating. This will increase the overall cost, complexity, and efficiency of the system since a cooling system would have to be put in place. The number of turns is limited by the maximum practical weight since the mass increases with the number of turns.

In light of the restrictions already discussed, insulated American wire gauge (AWG) 25 magnetic wire was used for each of the magnets. The AWG 25 was chosen because it is thick enough to prevent breakage during winding and thin enough to provide tight packing of wire, which maximizes the number turns as possible in the available space. The other advantage of a thicker gauge over thinner gauges is less resistance per unit length.

In the first iteration of the sensor, 320 turns were used, resulting in a single layer of coil covering the core. This was done to reduce the parasitic capacitance, which can be caused by overlapping coils [327]. For the second iteration of the sensor, a multilayered coil of 200 turns on each leg was created for a total of 400 turns. This represents a cumulatively coupled series inductor, which produces a higher inductance due to the mutual coupling between the windings [328][329][330]. This successfully reduced the amount of coil that would have been needed had the wire been wrapped around the legs and the limb of the core. Results like those for the first iteration were achieved but with a smaller core, allowing the coils to be placed as close as possible to the test surface without jeopardizing the integrity of the coil. The effect of the parasitic capacitance was countered by engaging some winding techniques like interweaving the layers as suggested in the literature [323]. Figure 207a shows a COMSOL Multiphysics simulation that compares coils wound around each side of the core and having the coils wound at just the legs and connected in a cumulatively coupled series configuration as shown in Figure 207b. It can be seen from the figure that the same magnetic field density was achieved in both cases, but with slightly better directionality because some of the field shown was concentrated

around the u-magnet limb. The magnetic flux is seen to be very directional with minor leakage around the top where there is additional winding.

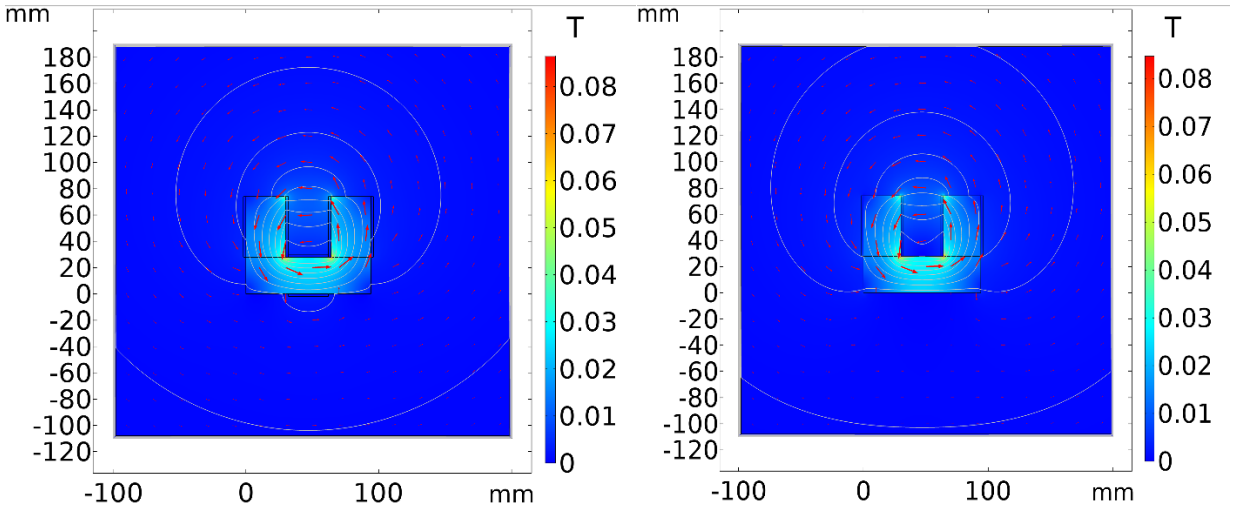

a) b)

Figure 207: The magnetic flux at 1000 Hz for the U magnet designed with a) coils wrapped around the two legs and the top, and b) coils wrapped around the two legs

12.2.4. Excitation Frequency

One of the most important factors in designing the sensor is the selected excitation frequency [155]. The higher the frequency, the less penetration attained with ferromagnetic materials due to their high permeability [8]. Figure 208 plots the impedance response of the electromagnet, showing the different impedance, and the corresponding resistance versus frequency. The resistance and the inductance are shown on the same plot versus the frequency. The resistance is in Ohms, the inductance is in mH, and the frequency is in Hertz (Hz). An increase in the inductance up to a maximum of about 10.6 mH can be seen at about 10 kHz. The maximum resistance of 1600 Ohms occurred at the self-resonant frequency of about 28 kHz, where the inductance approached zero.

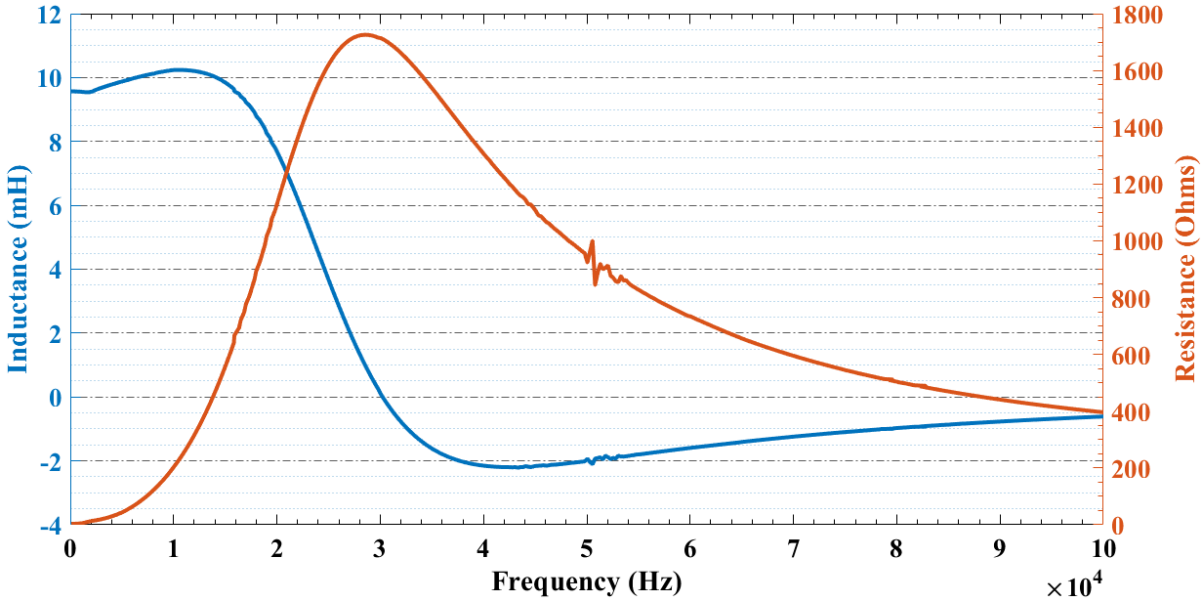

Figure 208: Impedance response of the 100 mm long magnet with a 250 turn. The orange plot shows the resistance in Ohms, while the blue plot is the inductance in mH. The x axis is the frequency in Hertz

Furthermore, as the frequency increases, the quality factor (or Q-factor) increases linearly when the resistance and inductance are constant (typically at lower frequency), which in Figure 208 is the region of inductances that are less than 10 kHz. The Q- factor is defined in Equation 40:

$$Q = \chi/R = 2\pi f \frac{L}{R} \qquad \text{Equation 40}$$

Where Q is the quality factor, and X is the reactance. This shows that a lower Q represents a higher R which is an increase in the loss in the system, increasing the energy cost. The higher frequencies that are applied above the resonant frequency corresponds to a lower Q, hence a higher loss. One of the major considerations in selecting the frequency was to stay below the self-resonant frequency.

Inductors are typically made by winding a conductor around an axis, with or without a core, giving rise to some self-capacitance [327]. This can become what is called 'parasitic capacitance' at high frequencies. This parasitic capacitance is due to the difference in voltage (very small) between the coil windings, leading to some capacitive effect that becomes pronounced as the frequency increases, leading to a reduction in the quality of the inductor. This effect can be reduced by optimizing the way the coils are wound to reduce the capacitive effect and thereby increase the quality factor of the inductor [323]. A low operating frequency should be selected to minimize parasitic capacitance.

12.2.5. Sensing Height Calibration

Sensing depth significantly affects the accuracy of this device. The change in inductance relative to air is larger when the sensor is close to the ferromagnetic material. Determining how the inductances change with depth enables the estimation of fiber depth. A lift-off test was employed to measure the change in inductance as a function of height from a ferromagnetic material, which in this case was a steel rebar. The sensor was incrementally lifted off the surface at 0.2 in. (5 mm) increments. The inductance was measured against the incremental height and fit to a curve to quantify the measurement decay, as shown in Figure 209. These measurements were used to calibrate measurements of the distance between the sensor and the sample.

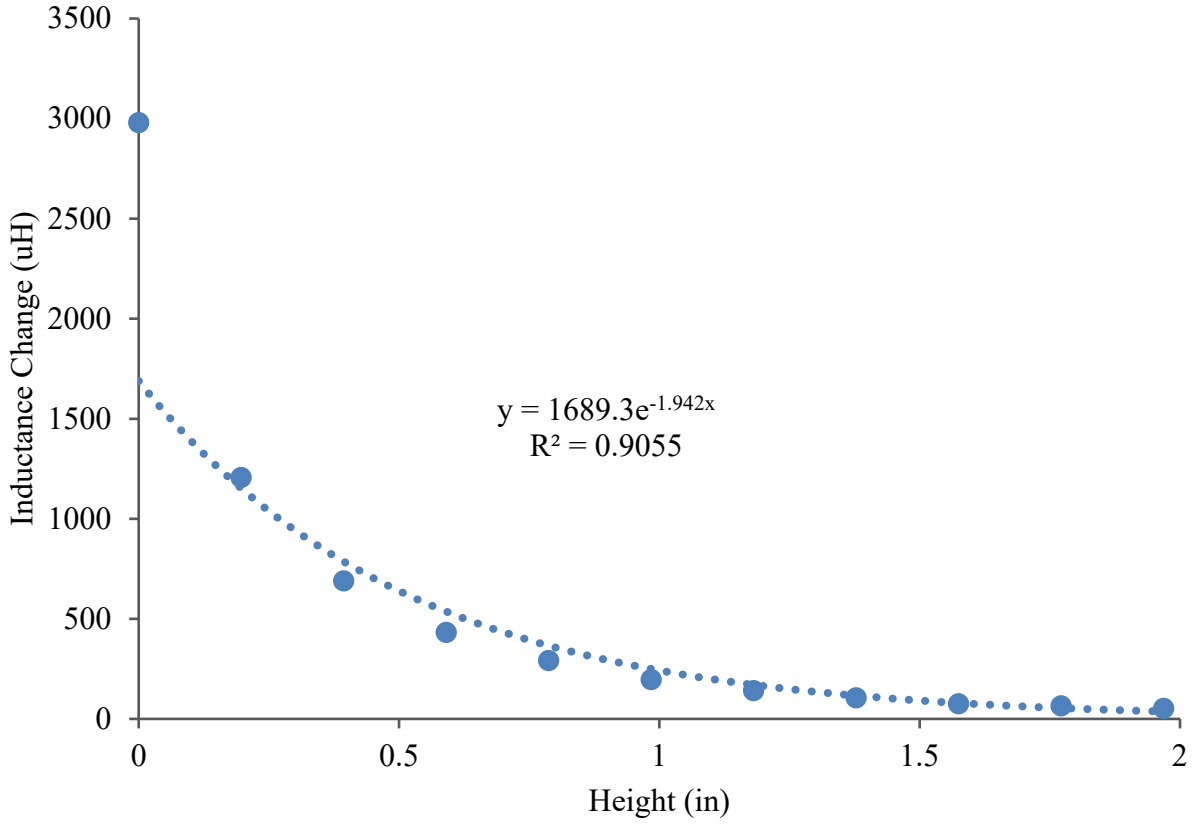

Figure 209: Showing the inductance change versus height for a ferromagnetic material, which is a steel rebar in this case

12.2.6. Electromagnet Arrangement

To measure the fiber alignment in all possible directions would effectively require a rotating magnetic system and significant computational resources. This would make the sensor system bulky, impractical, and slow. Therefore, two orthogonal electromagnets were used to measure the relative alignment of the fibers. This enabled the estimation of the relative alignment of the

steel fibers with minimal hardware and software. The alignment, θ, of the fibers was determined, using Equation 41, from the respective amplitudes observed for each sensor.

$$\theta = \boldsymbol{atan}(L_x \,/\, L_y) \qquad \text{Equation 41}$$

where L_x and L_y are the measured inductances from the orthogonal sensors. For simplicity, the ratio of inductances was used as a surrogate metric.

12.3. Prototype Sensor Package Design

Four prototypes were made, called version 1, version 2, version 3, and an automated version. Figure 210, Figure 211, Figure 212, and Figure 213 show the different prototype versions.

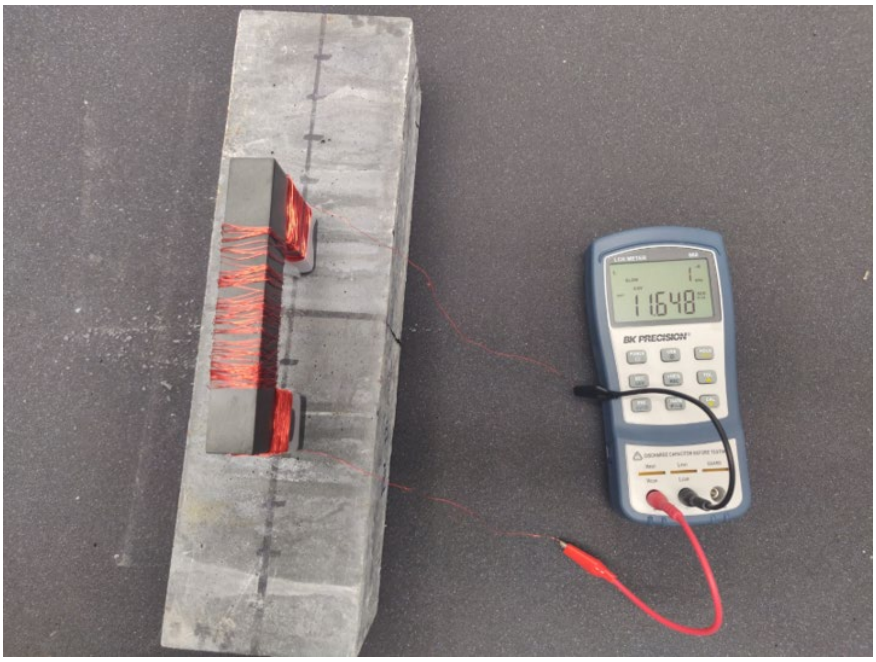

Figure 210: Initial inductive sensor system consisting of the electromagnets and LCR meter

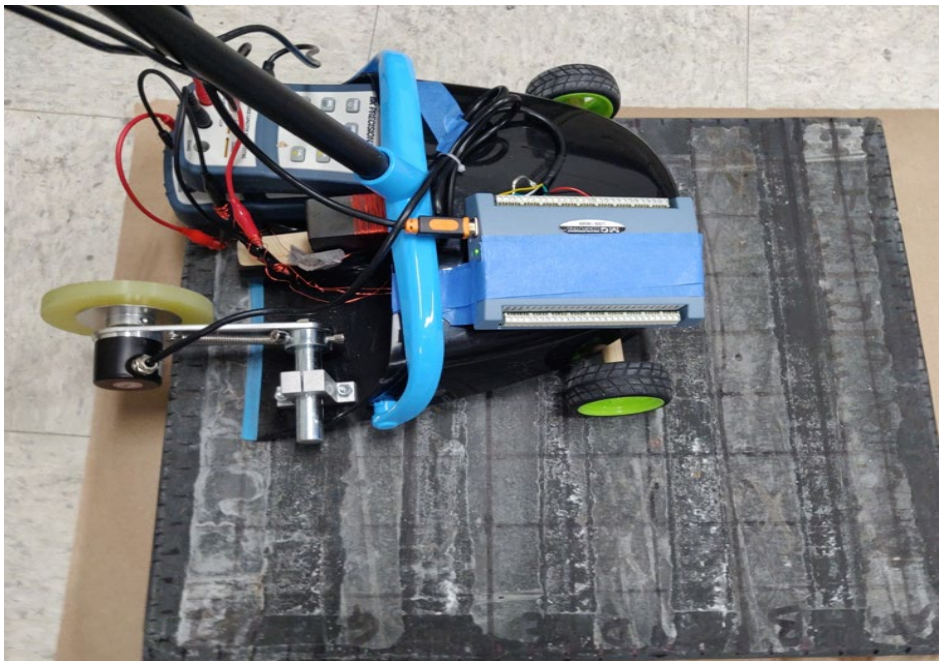

Figure 211: Second prototype with two electromagnets, LCR meters, an encoder for location measurement, and data acquisition system all enclosed in a dustpan with wheels

Figure 212: Third prototype with two electromagnets, LCR meter, encoder for location measurement, and data acquisition system, all enclosed in a 3D printed case with a wooden handle and wheels

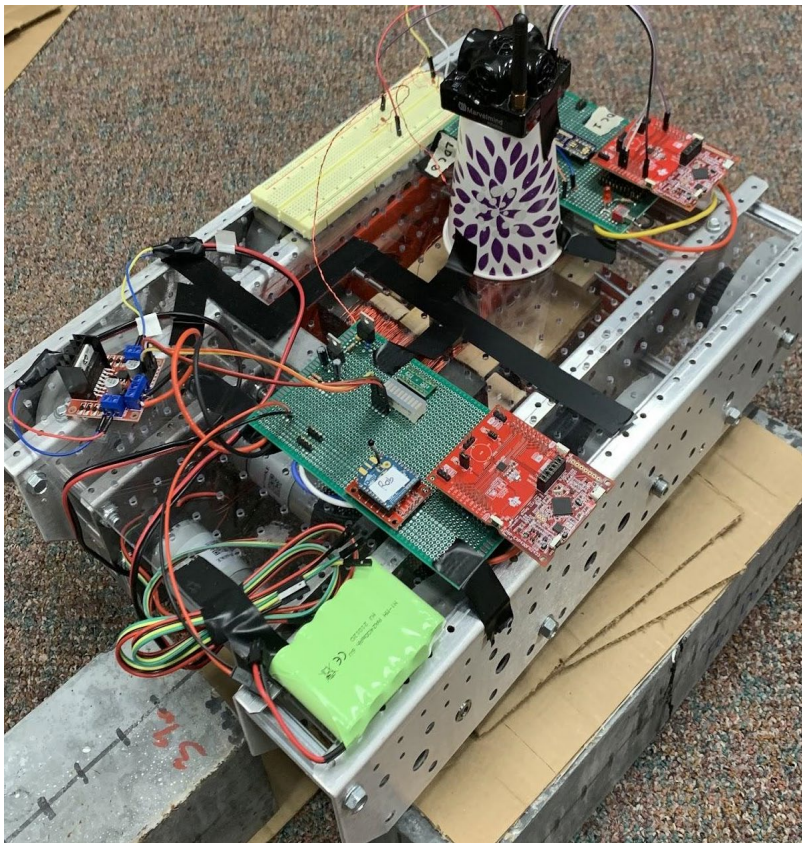

Figure 213: Image of the automated robotic system that uses a localized GPS to record its position while acquiring inductance data

12.3.1. Version 1: Sensor Only

The initial system was a single-sensor system. It comprises one magnet measuring 96 mm in length, 28 mm by 30 mm in cross-sectional area, wound with AWG 25 wire individually. Circuitry and other components are also necessary for the sensor system. The magnets are not self-exciting and need an excitation circuit. The BK Precision 880 Dual-Display Handheld inductance, capacitance, and resistance (LCR) meter was used as both the exciter and the reader. The LCR meter sends about 50 mA of current through the magnet coils to create a magnetic field. When the magnetic field interacts with the steel fibers, the interaction changes the magnetic field and consequently changes the inductance read by the LCR meter and stored on the computer.

The electromagnet is connected to an LCR meter and placed directly on the test specimen and multiple readings are taken and recorded, by either writing the data on a paper/pad, or by connecting the LCR meter to a computer for direct acquisition with the accompanying software. First, the LCR meter is turned on, and the ‘PRI/AUTO’ button on the bottom-left corner of the LCR meter is pressed until the display shows ‘L’ on the top-left corner of the display. The ‘L’ stands for inductance reading, and ‘C’ stands for the capacitance measurement that is displayed on the screen when the LCR meter is first turned on. The frequency of choice can be selected by

pressing the ‘FREQ/REC’ button at the middle of the buttons, until the desired frequency is shown on the display, the frequency choices on this particular LCR meter are 100, 120, 1000, 10 000, and 100 000 Hz.

12.3.2. Version 2: Dual Sensor System

This was the first two-sensor system. It comprises two magnets measuring 96 mm in length, 28 by 30 mm in cross-sectional area, with 210 turns of AWG 25 individually connected to an LCR meter each. Two wheels, an encoder, and data acquisition system are all mounted on a dustpan with a long handle. The system directly connects to a Dell workstation. The dual magnets are shown in Figure 214. Figure 211 shows the full setup.

This system introduced an encoder and the data acquisition system. The encoder allows the collection of accurate data relating to the position of the magnet with time. The encoder is connected to a wheel that revolves as the sensor is moved, and the data acquisition system enables the collection of the encoder data while logging it onto the computer. This provided an indication of where each data point was collected to make an accurate log of the position versus the inductance change observed. The term inductance change was used to describe the difference in the inductance measured in air and that measured on a UHPC prism or specimen. This was used to determine the quantity of ferromagnetic steel fibers present.

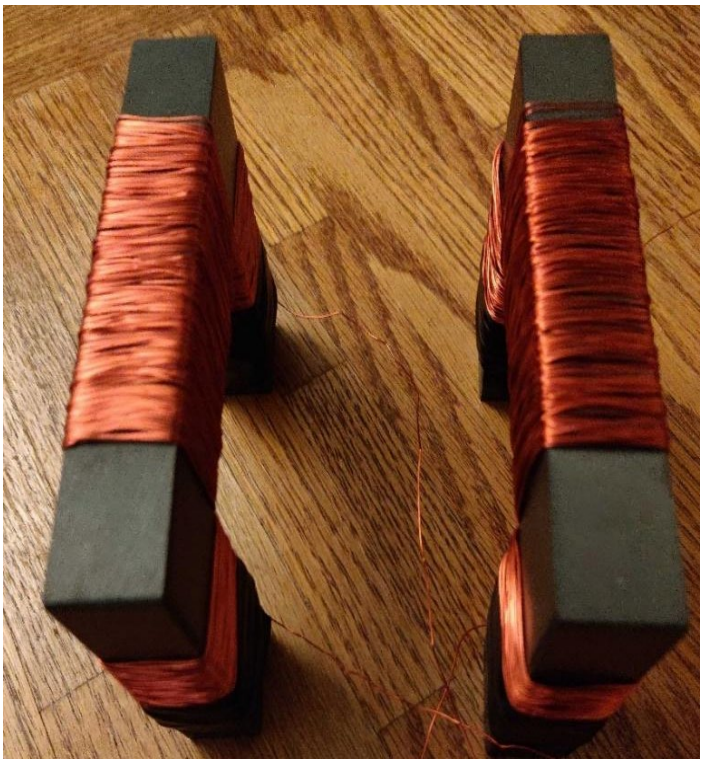

Figure 214: The two magnets used in the sensor setup that consists of 210 turns of American wire gauge 25 magnetic wire, with an inductance of 7.5 mH

After the device is turned on and the LCR meters are set as previously described, the software is started on the computer and run while the device is being held in air, to get the baseline measurements. The device is then placed on the surface of the specimen that has been cleared of debris, making sure the wheels and the encoder can move as smoothly as possible on the specimen's surface. The device was slowly wheeled along the surface to be scanned using the handle shown in Figure 211. The device collects inductance data, and the encoder collects the positional data so that the inductance can be mapped to location. After measurements were taken at a particular location, the device was moved to the next location and the process was repeated until all chosen locations had been tested.

12.3.3. Version 3: Dual Sensor System in 3D Printed Enclosure

Version 3, while very similar to version 2, consists of some changes. Figure 212 shows this version of the system. First, the number of turns was increased to 400 turns of the same AWG 25 wire. The dustpan was replaced with a 3D printed enclosure with four wheels to make the system more compact and easier to handle. The 3D printed enclosure measures 16 in. × 10 in. × 6 in., the wheels can be mounted to the enclosure, and the encoder has a slot in the enclosure to make it more compact. The enclosure was printed using polylactide (PLA) with a dense fill to make it as sturdy as possible. However, the handles were replaced with wood because the 3D printed plastic handle could not hold the weight of all the electromagnets, encoder, and the data acquisition system. The enclosure showed some areas of delamination, which will be corrected for in future designs.

The dual sensor system with the printed enclosure operates much like the Dual sensor system with the dustpan, the only difference in operation is that the device is pushed using the wooden handle on the 3D printed system while the Dual sensor system with the dustpan is pushed using the long plastic handle. The dual sensor system with the printed enclosure has the advantage of being easier to pick up and easier to scan a vertical wall than with the dustpan version. The inductance readings from the two LCR meters and the encoder data are collected as the concrete member is scanned.

12.3.4. Automated, Robotic Version

The automated version consists of a robot system with two electromagnets inside to calculate the inductance change of the specimen shown in Figure 213. The system also consists of a mapping system that uses a positioning system that can be calibrated to calculate the position it is at all times and then map this position to the inductance change calculated. The goal of the vehicle is to be able to run remotely on many different sizes of concrete. To accomplish this, the chassis chosen was modified to minimize the width. The Andymark Configurable TileRunner chassis was chosen because it can be configured to meet the system needs. The motor NeveRest 60 with a 9:7 gear ratio was chosen. The NeveRest 60 has a free speed of 105 rpm and with the 9:7 gear ratio the rpm drops to 135 rpm; with the wheel diameter of 4 in, the drive train speed under load is 1.91 fps (0.58 m/s). To further decrease the speed, a 6V battery is used on the 12V DC motors, dropping the speed to .955 fps (0.29 m/s). In the center of the chassis, a box for housing the detection circuit is installed such that it can be easily removed for analyzing surfaces smaller than the width of the chassis. This allows for a more flexible testing apparatus. The box was 3-D printed with drop-down slots for the detection coils on the bottom so the coils can get as close to

the concrete as possible. A perforated polycarbonate sheet is mounted on the top so the electronics and positioning equipment can be secured. To access the detection coils the top can be removed and the coils taken out.

This robotic device's detection system is controlled by a Launchpad microprocessor. The microprocessor communicates with an induction-to-digital converter integrated circuit (IC), which is connected directly to the detection coil circuit. Measurements are returned to the microprocessor at regular timer intervals. The microprocessor simultaneously receives data requests from the host computer and responds with packets of induction data at the relevant time intervals. The central beacon of the robotic device's positioning system, which is mounted on the vehicle, collects real time positional data and uses the detection system's microprocessor to relay the positional data to the host computer. The vehicle is designed to drive at a consistent speed and take measurements at regular intervals. This results in a relatively even distribution of data points over the scanned area. The robotic system interfaces with the MATLAB code written for the acquisition and processing of the acquired data, and it also displays a 3D plot representation of the position in x and y coordinates. The inductance values are represented by a color gradient of their magnitudes in the z coordinate of the 3D plot. The raw data is also stored so that it can be accessed later and used in any desired way.

12.3.5. Software Interface

The software interface was designed in LabVIEW, a graphical programming environment made by National Instruments (NI). The backend consists of the acquisition and data saving loops for the encoder and the inductance, capacitance, and resistance (LCR) devices. The data acquisition rate, sampling rate, and buffer size in the software backend were set to be consistent with the system data storage capacity. The front end, shown in Figure 215, consists of the interface to start and stop the acquisition of data. It also contains chart plotters to visualize the acquired data in real time. The interface consists of three waveform charts that allow observation of the data in real time and to visualize the data and make needed decisions as the element is scanned. On the left there is the sections where the name of the files can be saved. There are different file names for the encoder, the first and second LCRs also. On the right, there are three individual boxes that display error if there is one, and it gives a brief description of the error. On the top left corner, there is the run button in the shape of an arrow that is used to run the application, and beside this button, there is a stop button which can be used to stop acquisition when done. There are also two other stop buttons that can be used to stop either the encoder loop or the LCR loop in case there is a need.

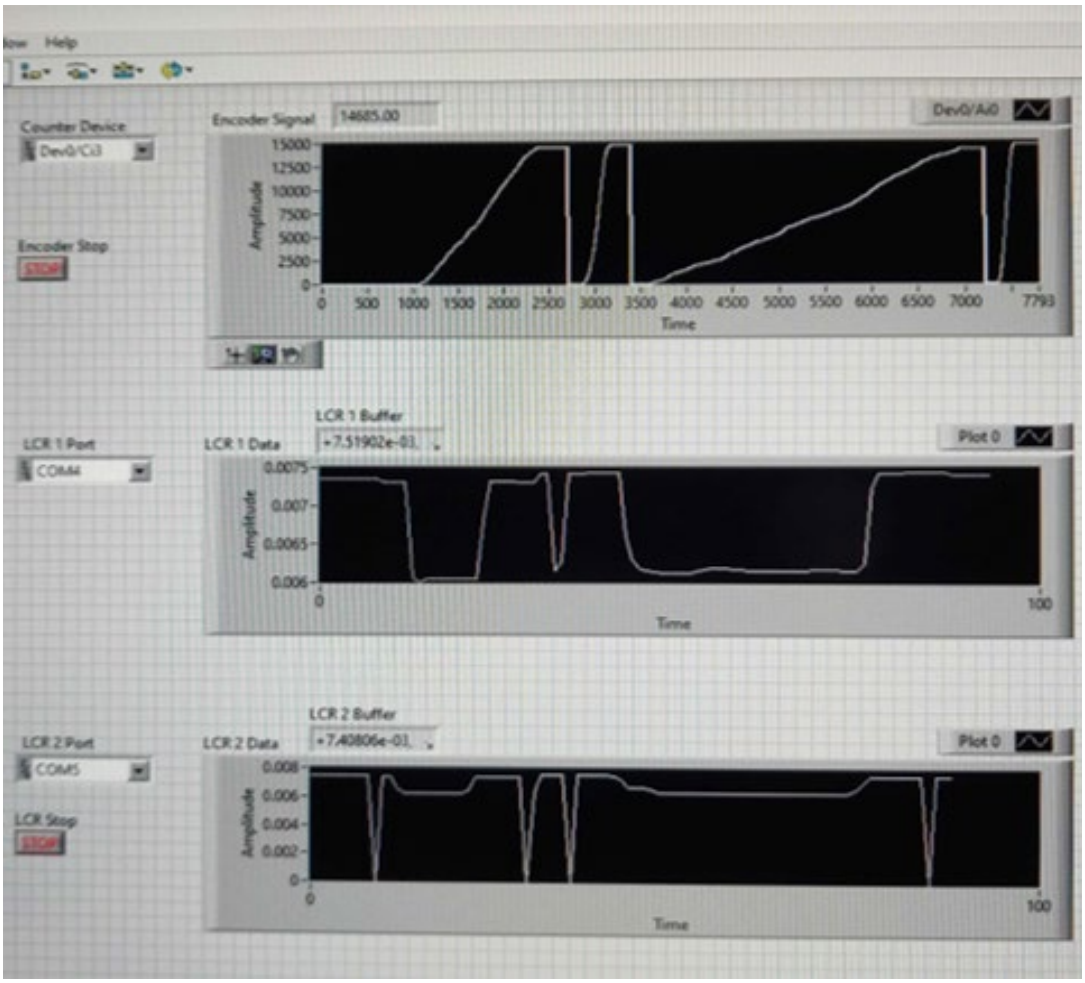

Figure 215: The LabVIEW interface for the software

12.4. Experimental Methods

Described in this section is the detailed experimental setup, including the fabricated UHPC members used in the lab and field tests. Figure 216 details the laboratory experimental setup using a single magnet.

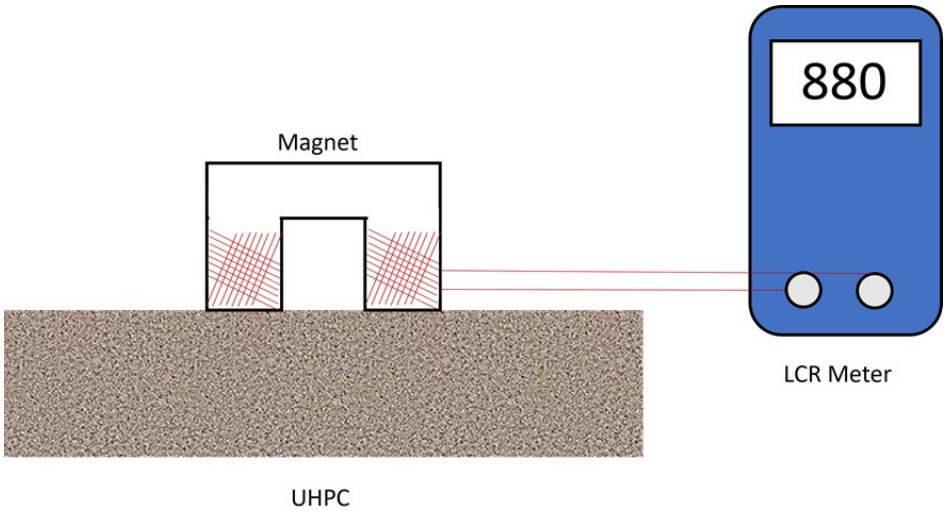

Figure 216: Experimental setup showing the sensor (magnet), the LCR meter which is a BK Precision 880 Dual-Display Handheld LCR Meter, and the UHPC test specimen containing steel fibers

12.4.1. Laboratory UHPC Members

Multiple UHPC prisms measuring 4 in. × 4 in. × 14 in. that contained steel fibers ranging from 1% to 3% by volume were used in lab tests. A specimen with 0% fibers was used as a control specimen to determine whether the device would give a false negative, and to test the level of noise in the measurements.

The lab specimens shown in Figure 217 were made using steel molds. Sample sides were labeled using the configuration in Figure 217(a). The naming is only applied to the four long sides of the prisms, with the rough side being the finished side of the UHPC (the side of the UHPC at the top of the mold), the smooth side being the formed side (the side of the UHPC at the bottom of the mold), and sides A and B for the rough and the smooth sides.

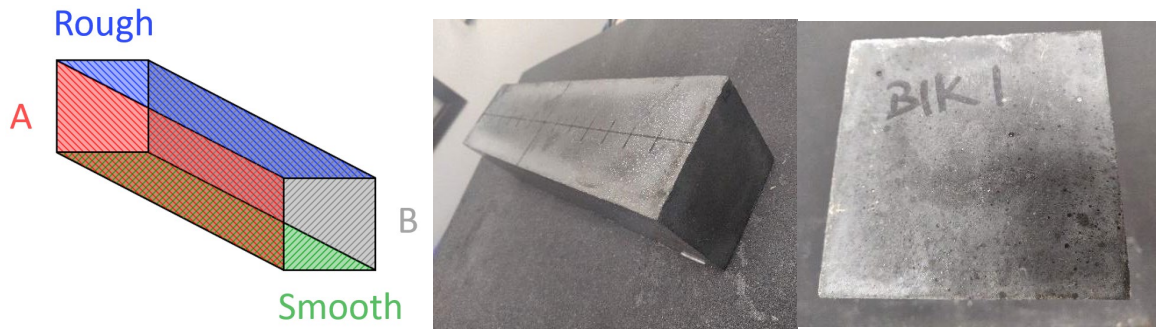

(a) (b) (c)

Figure 217: (a) The UHPC sides were named according to their relative placement in the mold. The side labels are color coordinated here to match the sides being depicted. (b) showing the smooth side of the prism along the length and (c) showing the top of the UHPC prism showing the labeling of the UHPC specimen from the long ends

A UHPC prism measuring 14 in. × 14 in. × 3 in. was used to evaluate the ability to estimate fiber orientation in the lab. The large prism was made using six UHPC prisms measuring 14 in. × 2 in. × 2 in. that have the steel fibers aligned along the length. Each member was placed in a mold and a 2% by volume UHPC was placed to fill in any gaps, ensuring relative alignment of the fibers along the length of the initial six UHPC prisms. This resulted in a specimen that has its fibers mostly aligned in a particular direction as shown in Figure 218. Stripes on the slab correspond to the direction of the relative alignment of the fibers. The lighter stripes are the UHPC prisms, while the darker stripes correspond to the newer 2% mix that was placed to fill in the gaps.

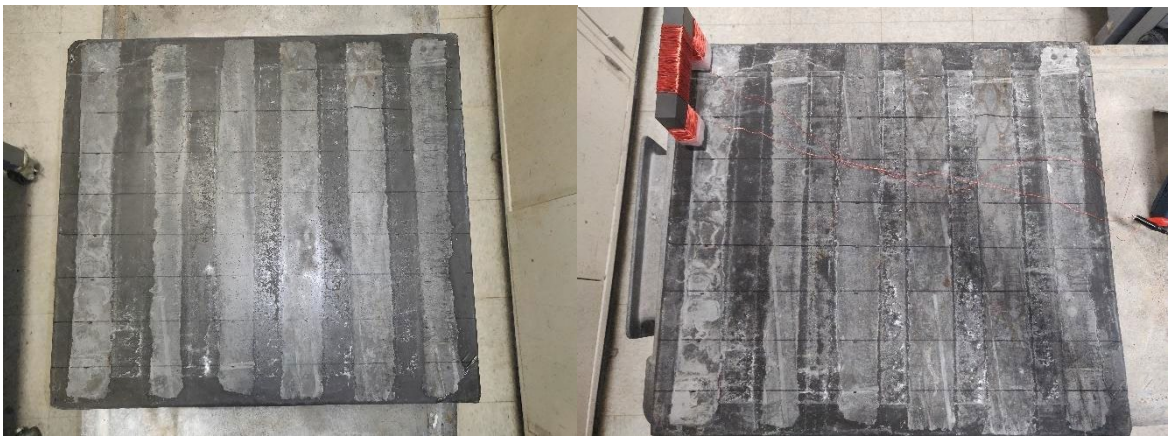

Figure 218: (a) The UHPC slab that is used for the orientation test, the stripes show the approximate preferred orientation of the steel fiber alignment. (b) shows the specimen with the magnet sensor on it taking incremental measurements to measure the orientation. The black marker lines are visible and were used to measure the inductance in the perpendicular direction to the striped direction

12.4.2. Device Calibration

Before each use, the magnetic sensor system was calibrated to determine how the inductance change mapped to fiber density in the UHPC. The term "inductance change" describes the difference in the inductance measured in air and that measured on a UHPC or another type of specimen. Before every lab or field test was done, an air measurement was taken before continuing with specimen measurement to establish a measurement baseline.

The inductance of air was measured followed by observation of how the field deteriorated with lift-off distance. These measurements define the effective penetration depth of the sensor. These measurements were used to weight CT scans readings during validation of the readings. Inductance change was obtained as a function of lift-off distance by placing the magnet on the UHPC specimen and taking readings while slowly increasing the height/separation distance by 5 mm at a time. A non-ferromagnetic material was used between the sensors and UHPC so as to not interfere with the accuracy of the result. The distance was increased until a reading was obtained that was indistinguishable from the noise/baseline. Measurements were made at 100 Hz, 120 Hz, 1000 Hz, and 10,000 Hz. The mean values are shown in Figure 219 because the behaviors were similar at the low frequencies used. In Figure 219, an exponential decay in the field was observed as the distance increased, with a high R^2 correlation coefficient of 0.9883. Based on these measurements, the inductance changes can be measured at approximately 1 in. from the sensor.

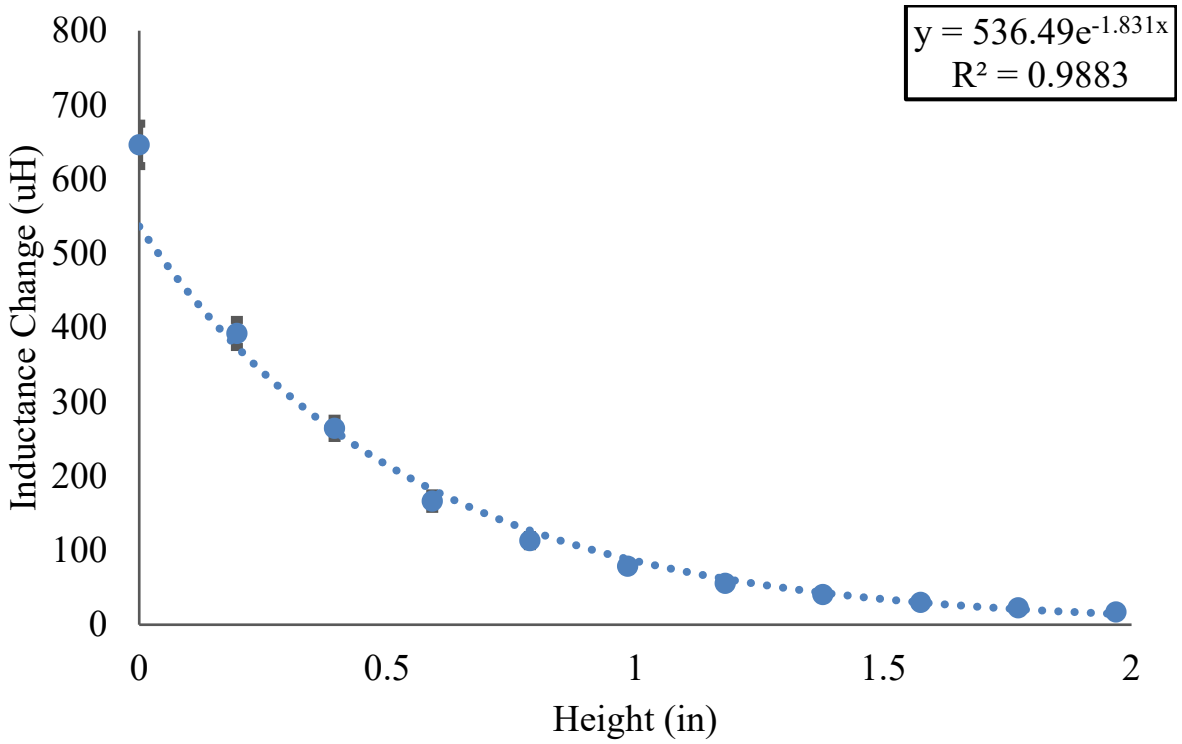

Figure 219: A plot of the inductance change against the height of the magnet from the specimen. Measurements were taken at 5 mm increments, starting from the point where the magnet was touching the specimen as 0 cm, to 5 cm. The standard error is also shown on the graph

The sensor was calibrated to map fiber percentage to inductance change. UHPC prisms were made (as shown in Figure 217**)** in the lab containing 1%, 2%, 2.5%, and 3% fiber percentage by volume. Figure 220 shows the relationship between the fiber percentage and the measured inductance change. A linear curve is fitted to the measurement. It is observed that the measurements provided an excellent linear relationship ($R^2 = 0.9965$). The optimal linear curve has a small negative bias. This is most likely due to the noise effect. This relationship can be used to identify the fiber percentages that are observed in field tests.

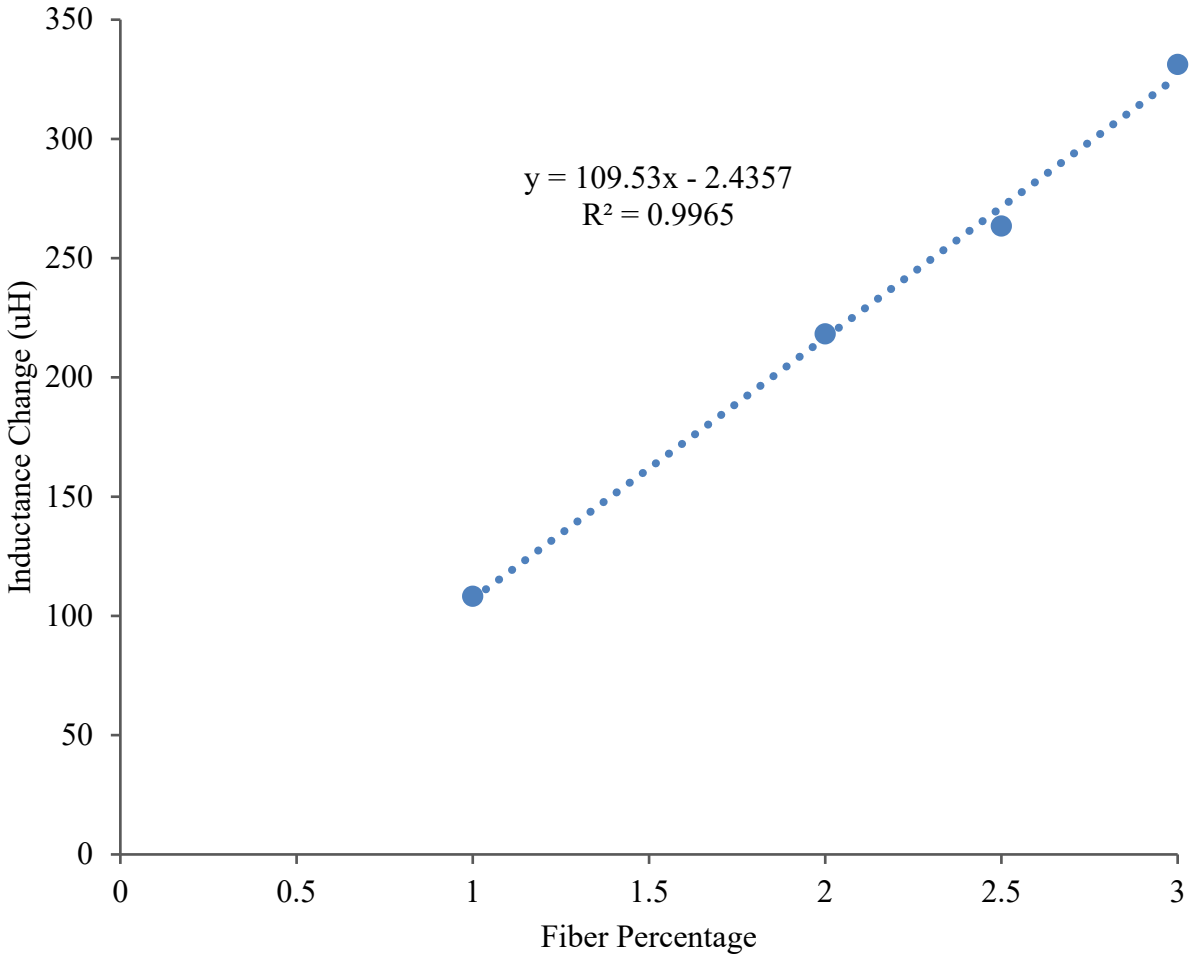

Figure 220: A plot of the inductance change versus the fiber percentage

12.4.3. Field Test Experiments

Field test measurements were taken at the Marcus H. Ansley Structures Research Center located at Innovation Park in Tallahassee, Florida. It is a structural research and testing facility for the FDOT. Several UHPC structural members were stored in the storage area behind the laboratory and were available for use in the project. This provided an opportunity of having a varied set of structures of testing and evaluation of these methods.

The fiber content and orientation of five (5) different UHPC members were evaluated at the test site. The samples were measured twice. The first test used version 2 of the sensor system and was performed on March 4, 2021. The second test used version 3 of the sensor system and was performed on December 9, 2021. An H-pile, I-beam, square pile, box-beam, and an octagonal pile that is hollow on the inside were scanned on each visit. The tests performed during each visit are detailed in Table 79 and

Table 80, respectively. Each member was designed to include approximately 1.5 to 2 % of fibers by volume.

Table 79: List of tests performed during field site visit on March 4, 2021

Shape	Region Scanned	Number of times Cored	Thickness [cm]	Notes
H-beam	Web	3 times	13	One of the cores contained steel strands that had to be cut out because it was affecting the CT scan
I-beam	Flange	2 times	14	
Box Beam	Surface	3 times	11	
Octagonal Pile	Surface	2 times	11.7 - 12.6	
Bridge Member	Web	0	-	

Table 80: List of tests performed during field site visit on 28th of January 2022

Shape	Region Scanned	Number of times Cored	Thickness [cm]
H-beam	Web	2 times	13
I-beam	Flange	4 times	14
Box Beam	Surface	4 times	11
Octagonal Pile	Surface	0	-

For the field tests, the specimens were first prepared, making sure no debris or loose metals on the specimen to be tested were present. Then a calibration air measurement was made four or five times to establish a steady baseline was taken. Then gently scanning along the specimen surface, taking measurements continuously as illustrated in Figure 221. Repeated measurements were taken to study the repeatability of the results. Multiple paths were taken to study fibers

varying across the surface of the member. After taking these measurements, regions of interests were marked off using an oil-based marker from which 2-in. diameter cores were taken, drilling through the entire material thickness as illustrated in Figure 222. With the markings, the directionality of scans relative to the specimen were signified. The oil-based marker was used because it had better durability during the coring process. The cores were then analyzed with an x-ray computed tomography (CT) system to obtain a measure of fiber density throughout the core. Calibrated magnetic readings were then compared to these CT scan results.

Figure 221: The field setup with the device on the H-pile

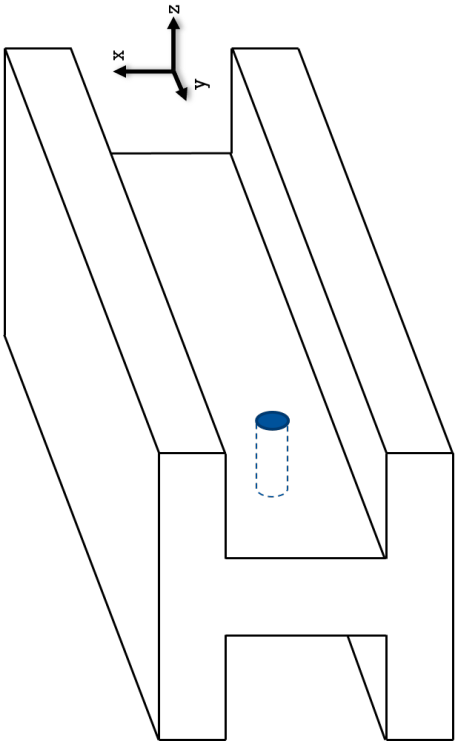

Figure 222: The process of taking out a core from the pile

12.4.4. CT Scanning Process

X-ray CT was used to assess the internal structure of the concrete cores. This system penetrates the cores using high voltage x-rays and measures the variations in these x-rays to compute the internal structure as a three-dimensional volume. The three-dimensional volume can then be analyzed to determine the density and orientation of the steel fiber. Due to the challenges with fabricating UHPC in the field, the fiber density and orientation will vary as a function of location within the core. In the analysis, averages over set thickness were considered when comparing the fiber density or orientation observed by the CT with the magnetic inductance readings measured by the sensor.

The process for preparing and scanning each core is briefly discussed here. Before performing the x-ray CT scan, an aluminum strip was placed on the markings to enable axes identification after scanning the material. An example of this is shown in Figure 223. Aluminum was used because it is dense enough to show up in the CT scan. Figure 224 shows the alignment of the core and axes labeling so that the orientation after scanning could be determined. This prepared sample was then placed into a plastic holder that could fit into the specimen holder in the CT scanner. A plastic holder was used due to its low density to allow the x-rays to easily penetrate through the holder and not produce any artifacts within the scan. It was ensured that the sample was stable and did not shift during the scan by add packing peanuts on the sides. Next, the holder with the sample in it was placed into the chuck holder and ensured it sat properly and was tightened securely.

Figure 223: Picture of the core with markings made before taking it out (orange double-headed arrow) and the ones made right after taking the cores (single-headed black and orange arrows)

Figure 224: The aluminum strip held by tapes placed on the double-headed arrow signifying the direction of the magnetic scan

The voltage was set between 200 and 230 kV and the current between 90 and 110 µA. A higher voltage provides better contrast and penetration depth at the cost of energy consumption and greater x-ray production. Higher currents improve signal-to-noise-ratios (SNR) and can reduce the effect of noise and artifacts. The voltage and current were limited because of machine limitations and because higher voltage and current increases the heating of the x-ray tubes, shortening their life. Higher voltages and currents than would typically be used to scan concrete were used because of the high cementitious material density and steel fibers. Higher voltages and currents enabled sufficient penetration of the samples with fine resolution, as shown in Figure 225. With this configuration, resolutions as high as 70 µm can be obtained. A high-resolution scan is necessary because the small diameter of the steel fibers (~ 200 µm in diameter) must be distinguishable from the cementitious materials to measure fiber density and orientation.

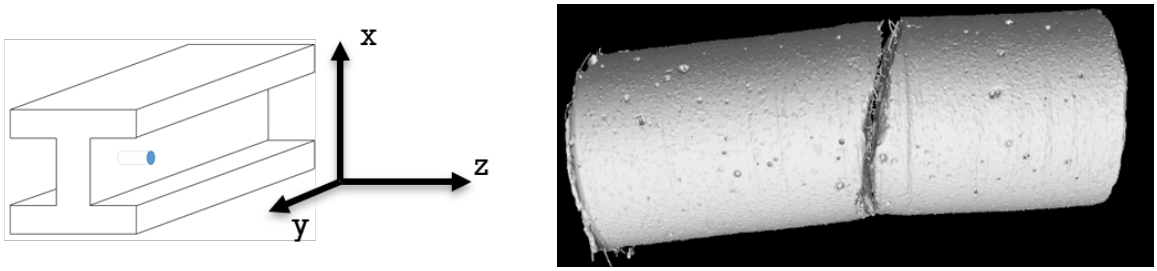

Figure 225: CT Scanning of H Pile Core for Fiber analysis. The core was scanned and oriented as shown so the z axis is perpendicular to the cored surface and y axis is lengthwise for the H pile

12.5. Results

12.5.1. Qualitative Field Test Results

In this section, the results of the field tests are qualitatively described, focusing on the regions of the scans that were not specifically validated with cores. Coring at the same frequency and resolution as the scanning would be overly impractical and time consuming. Hence, these results are described as qualitative since they cannot be directly validated without corresponding cores.

Figure 226 shows the measurements taken from scanning of the web of the H-pile. The results illustrate a sine-wave-shaped behavior. This behavior was found to be consistent with repeated measurements. It is hypothesized that the sine-wave measure is the result of the rheological behavior of the concrete and where the concrete was placed. This will result in some portions of the H-pile with a higher inductance change at the peaks of the sinewave because of a higher concentration of the steel fibers there. Some portions with a lower inductance change occur at the troughs of the sinewave because of lower concentration of steel fibers, possibly because of fiber segregation.

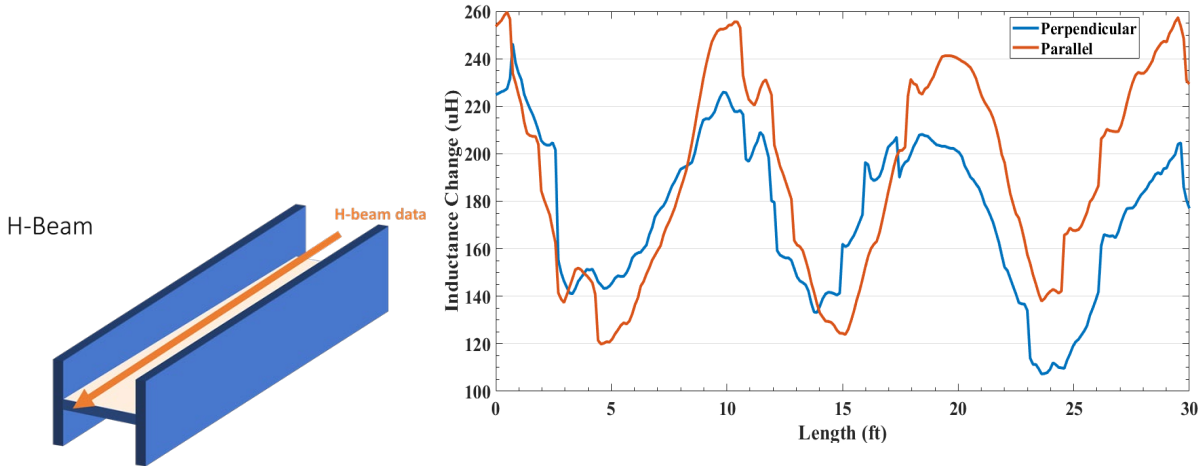

Figure 226: (a) The direction of scan along the web of the H-pile. (b) The result from the two magnets, the parallel and the perpendicular scans are shown. It can be seen that the sine-wave-like results, showing high inductance and low inductance points in the H-pile corresponding to high and low relative fiber concentrations

Figure 227 shows the square pile during scanning, while Figure 228 shows the results of a scan across the top of the square pile. When the pile was made, it was cast with a form joint, which has visible steel fibers protruding from the surface as shown in Figure 229. This visually confirmed a higher concentration of steel fibers in this location. These results confirm this high concentration of steel fibers. In Figure 230, a spike in the inductance change at the exact location of the joint in the square pile can be observed. Both the whole top and side of the square pile were scanned. Both scans showed the high inductance change caused by high steel fiber concentrations. A higher concentration of the steel fibers in one of the two sensors can be seen, indicating preferential alignment along the length of the square pile. Specifically, it can be seen that the parallel (corresponding to the length of the square pile) direction had a higher inductance change compared to the perpendicular (corresponding to the width of the square pile) direction of the square pile.

Figure 227: Square pile during scanning

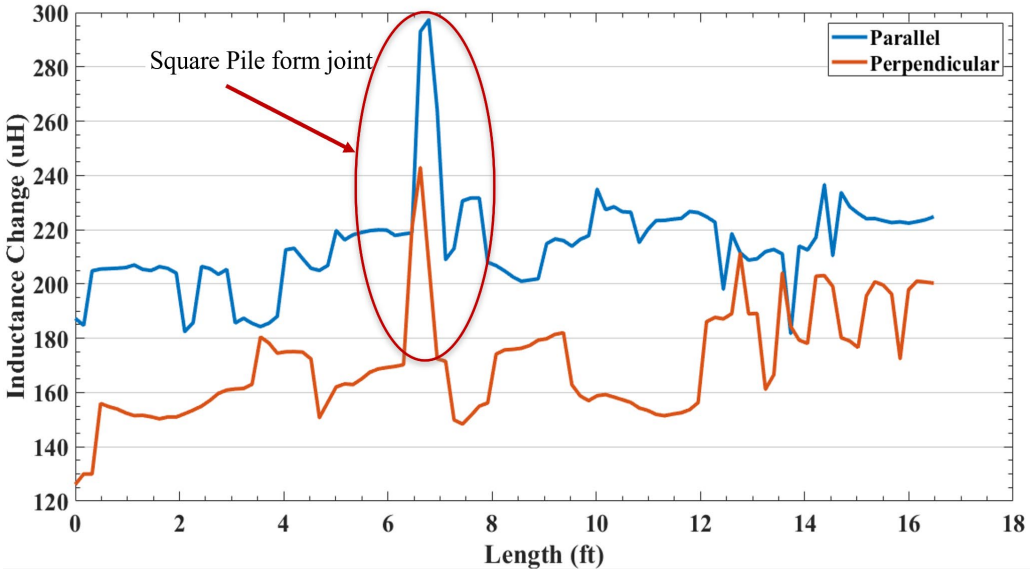

Figure 228: Inductance change for the square pile showing an unusual concentration of steel fibers along the form joint on the top of the pile

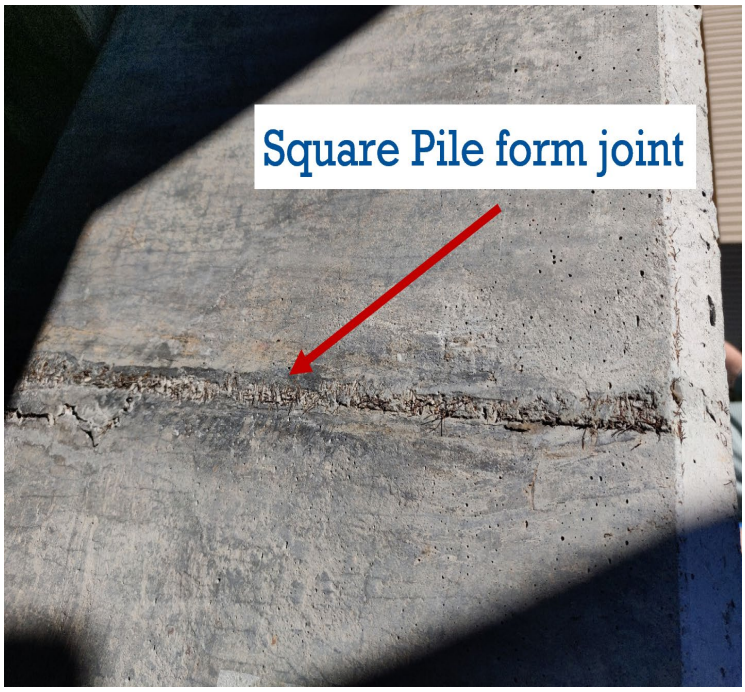

Figure 229: Photograph of concrete at location of form joint

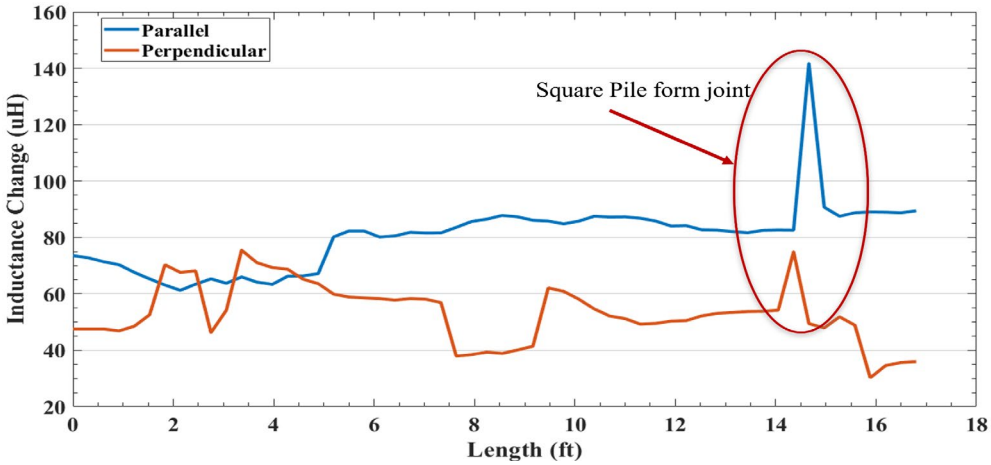

Figure 230: Inductance change for the square pile showing an unusual concentration of steel fibers along the form joint on the side of the pile

Figure 231 shows a picture of the octagonal pile scanned. The surfaces of the octagonal pile had an imprinted texture from form liners used during placement, as shown in Figure 232. Figure 233 shows the magnetic scan of the pile. The surface texture from the form liner had a significant effect on the readings. The region without the form pattern had a significantly higher inductance change when compared to the region with the form pattern. The form pattern likely pushed the

steel fibers farther into the concrete. As a result, the fibers had a weaker effect on the magnetic readings in regions with the form pattern.

Figure 231: Longitudinal view of the octagonal pile scanned

Figure 232: Octagonal pile highlighting region without surface texture imparted by form liner

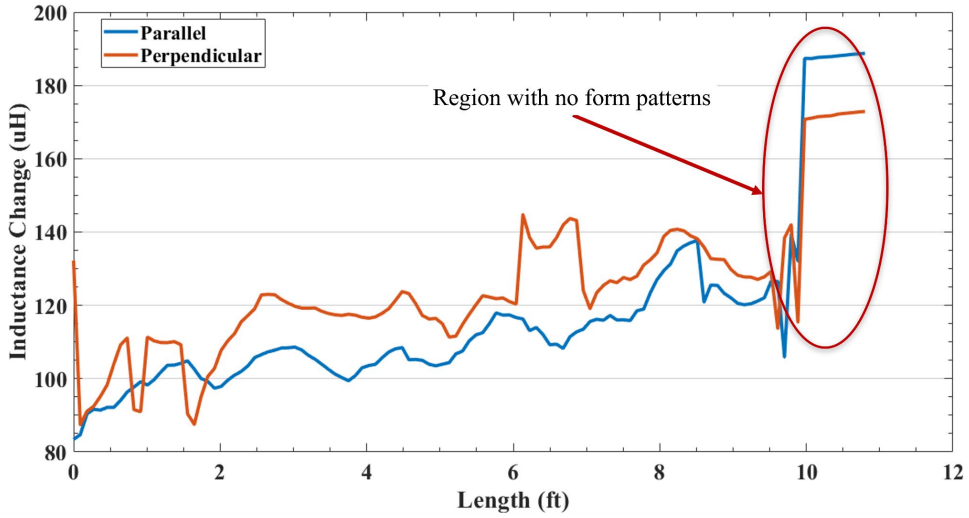

Figure 233: The form pattern on the surface of an octagonal pile and the corresponding inductance changes

A bridge member that was designed with self-compacting concrete (SCC), no steel fibers in the beam center, and steel fiber-reinforced UHPC at the ends of the bridge member was tested. This is illustrated in Figure 234. The scans indicate that the two regions of the member, the SCC without fibers and the UHPC with fibers, can be successfully distinguished. Figure 235 shows that the inductance change in the regions with SCC was close to zero, confirming the absence of steel fibers in the SCC regions when compared with the UHPC regions.

Figure 234: The result of scanning a bridge member (G6E1) containing self-compacting concrete (SCC) with no fibers, and UHPC with fibers. The top figure shows the bridge member G6E1 with the darker portions (end portion) as the UHPC and the lighter portion (remaining portion) as the SCC without fibers

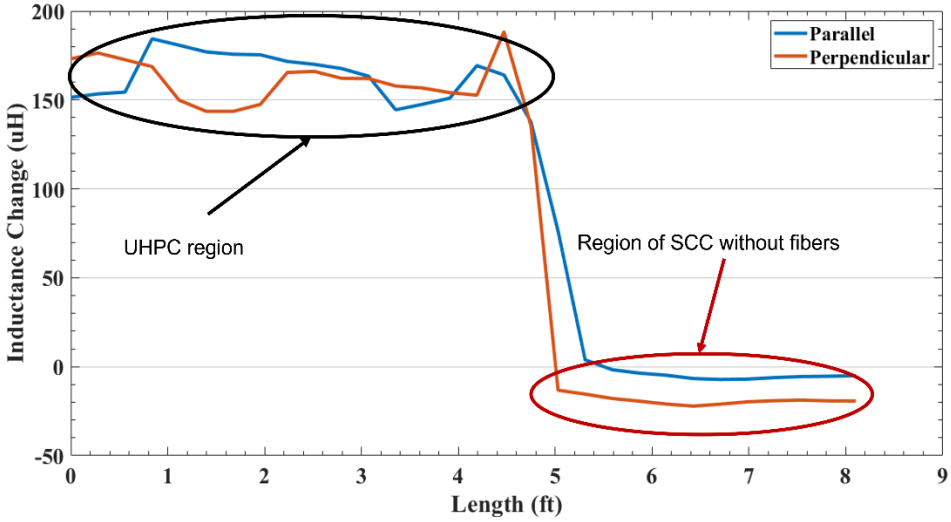

Figure 235: Shows the result of the scan of the first portion of the bridge member showing the clearly delineated UHPC - SCC regions clearly marked by the inductance change going to zero or slightly below zero

12.5.2. Quantitative Field Test Results

For each core taken in the field tests, the CT data was extracted, preprocessed using the Phoenix Datos-X software, and then exported to a 3D file to be analyzed using VGStudio Max [331]. The fiber analysis was performed in VGStudio Max to determine the fiber percentage and the fiber alignment of a region or entirety of the core. The voxel grayscale threshold for the fibers was set, so that every voxel with a grayscale value above this threshold was considered to be part of a steel fiber. The threshold was determined from a fiber thickness analysis, in which the ray method of wall thickness analysis in VGStudio Max was used. This fiber thickness analysis provides the average fiber thickness across the core. Figure 236 shows the results for a core from H-pile.

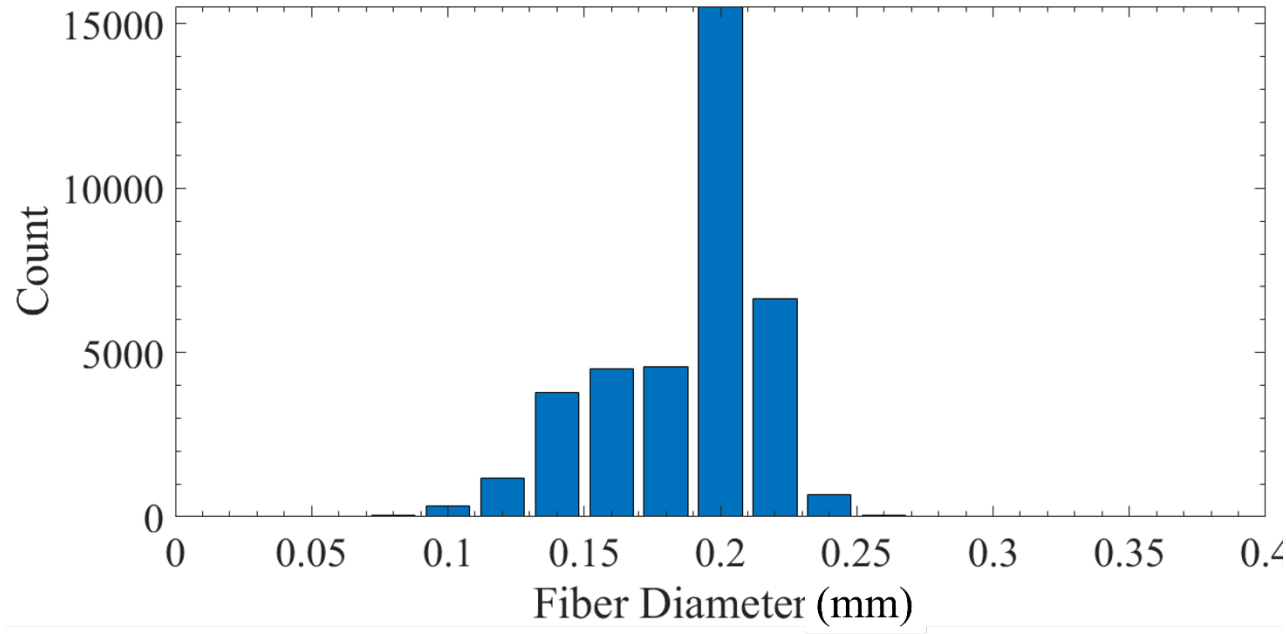

Figure 236: Fiber thickness distribution in a core, with a mean thickness of 200 µm, which is in line with the expected thickness value

The software's estimate was validated by measuring steel fiber diameters with an optical microscope to digitally measure and record the thickness of 50 individual steel fibers. The fiber thickness histogram is shown in Figure 237. The microscope used and a close-up picture of a typical steel fiber used are shown in Figure 238 and Figure 239 respectively. A picture of the measurement on a typical steel fiber is shown in Figure 240. The average thickness was 210 µm and the standard deviation was 3.14.

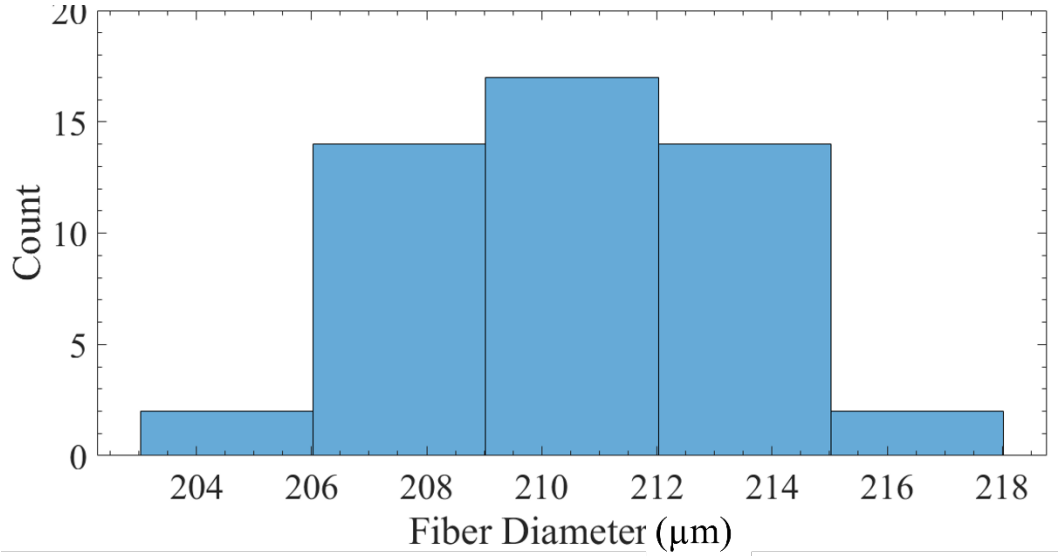

Figure 237: A histogram of the steel fiber diameters was plotted, giving the average thickness as 210 μm

Figure 238: The microscope that was used to scan and determine the thickness of the steel fibers, the microscope is attached with a tablet computer to digitally measure and record the thickness of the steel fibers

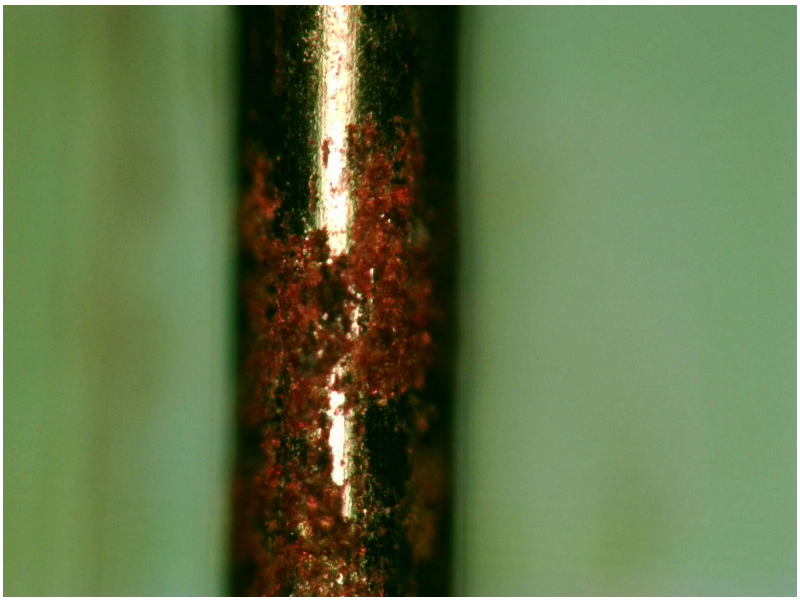

Figure 239: The typical steel fiber under the microscope magnification

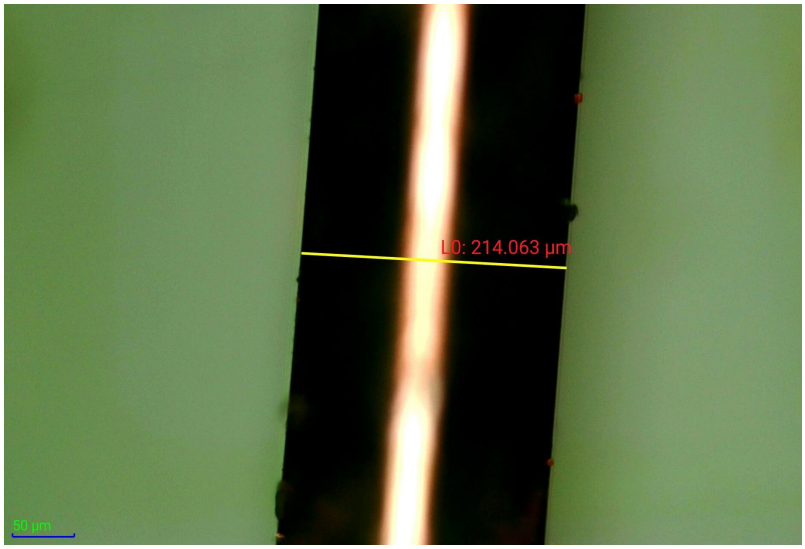

Figure 240: The thickness measurement and the scale of the measurement

Based on the fiber distribution measured in the microscope, a threshold average fiber diameter was chosen as 200 µm. This threshold value was then used in the remaining volumetric analysis to determine the fiber percentage and fiber orientation. The fiber percentage was obtained by calculating the number of voxels that were just steel fibers as a percentage of the total number of voxels that comprised the whole UHPC specimen. The orientation was calculated by determining the number of voxels of steel fibers that were oriented along each of the predefined axes, defined by the aluminum strip on top to the core, plotted against the angular displacement of these voxels

from the respective axes. For example, from an x-axis reference point, all the fibers along the 0^0 axis are perfectly parallel to the x-axis and all the fibers shown at 90^0 were perfectly perpendicular to the x-axis.

Figure 241 shows the orientation of the fibers in each of the axes. Scans with more blue fibers show more fibers in the direction of the respective axis. From these scans, it can be seen that there were distinct layers of concrete with preferentially oriented fibers. To measure fiber orientation, the ratio of the values for the x-axis to the values for the y-axis were calculated to measure the relative orientation. If the value was greater than 1, the fibers were more aligned towards the x-axis. If the value was less than 1, they were more aligned towards the y-axis. A similar approach to the magnetic inductive sensor data was applied.

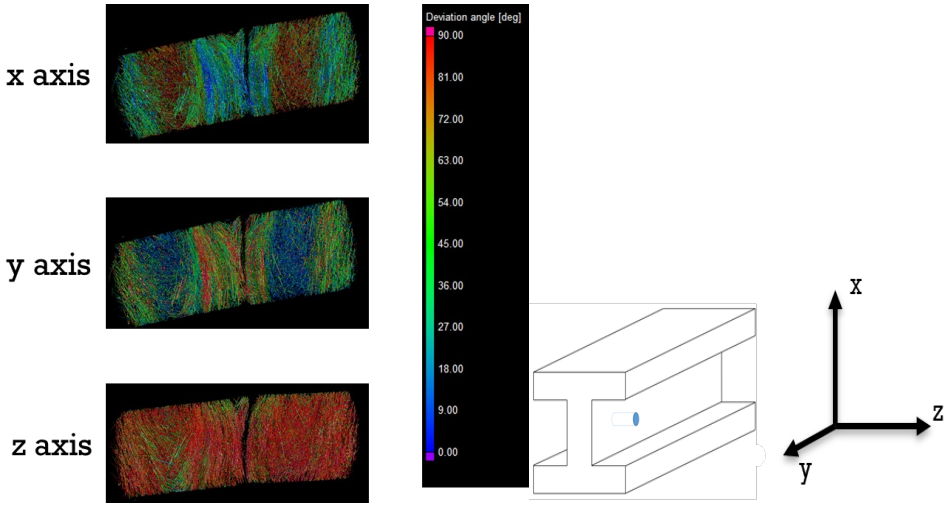

Figure 241: The fiber orientation analysis with CT Scanner. Fiber orientation was analyzed in the three directions: x, y, and z. For each of the axes, blue means the fibers are aligned with the axis. red means that the fibers are roughly perpendicular to the axis, and green means that the fibers are in intermediate range

12.5.3. CT Scan and Magnetic Sensor Comparison Results

For the magnetic fiber percentage, the fiber percentage to the inductance change was calibrated using lab specimens. This served as the calibration for the field results. Based on this calibration, the results of the magnetic scan and the CT core scans were compared. Figure 242 and Figure 243 show the result of comparison of the magnetic readings with those of the CT scan. Figure 242 shows the comparison between the relative orientation of the fibers by representing it as a ratio of their inclination between two axes, in this case defined as perpendicular and parallel, for the orientation towards the direction of scan. The results show a good agreement between the magnetic results and the CT scan results, with an R-squared value of 0.978. The best linear fit line nearly passes through (1,1), where both directions experience the same inductance change (i.e., there is likely no preferred orientation). While the results are not the same, they are proportional, allowing the magnetic results to be used with a proportionality constant in the field.

Figure 243 shows the comparison between the fiber percentages computed by the magnetic sensor and the CT scan result. It had a R^2 value of 0.21 and shows that the magnetic readings can detect fiber presence, but more work is needed to measure fiber content more accurately.

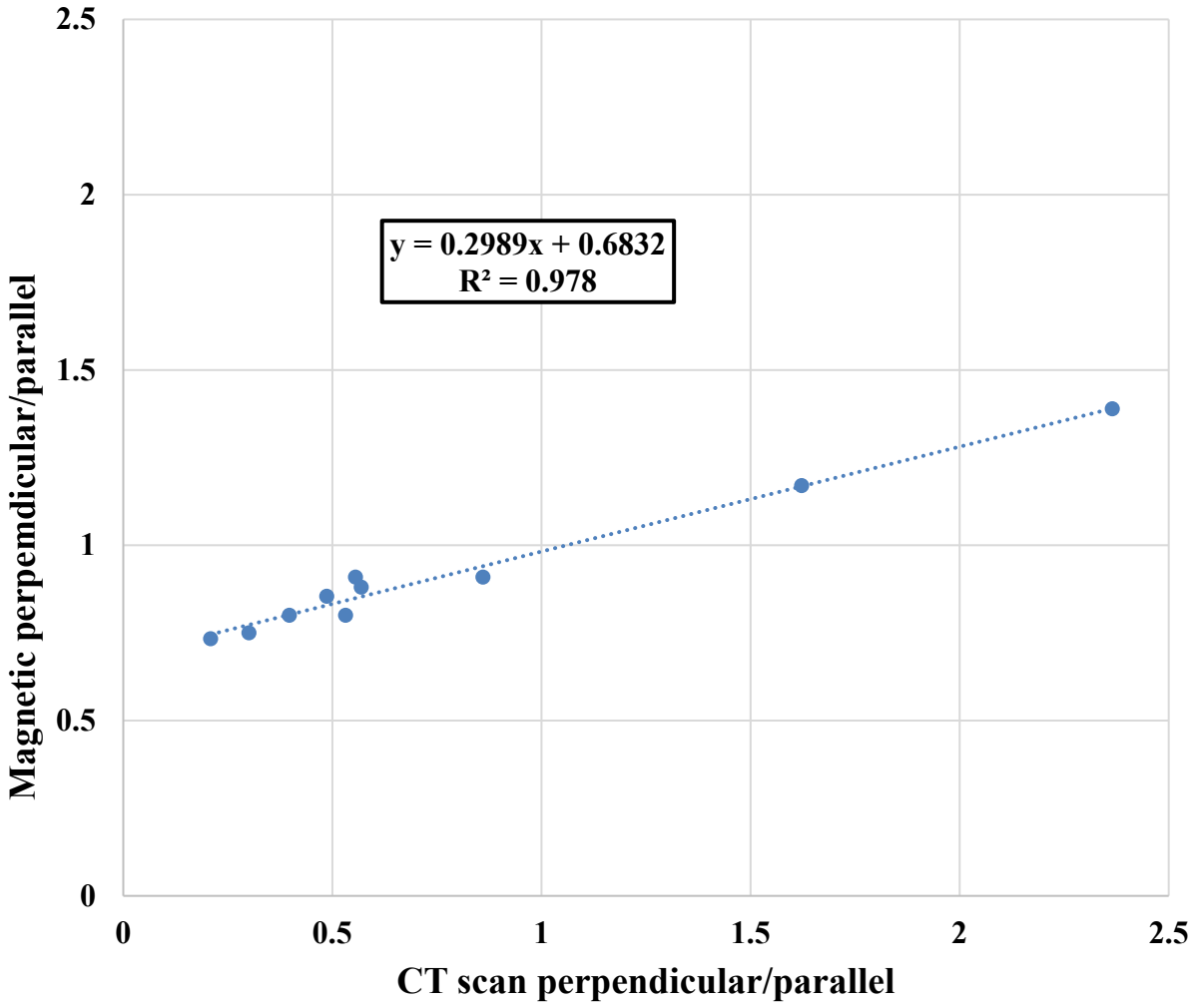

Figure 242: The comparison between the magnetic orientation result versus the CT scan orientation result

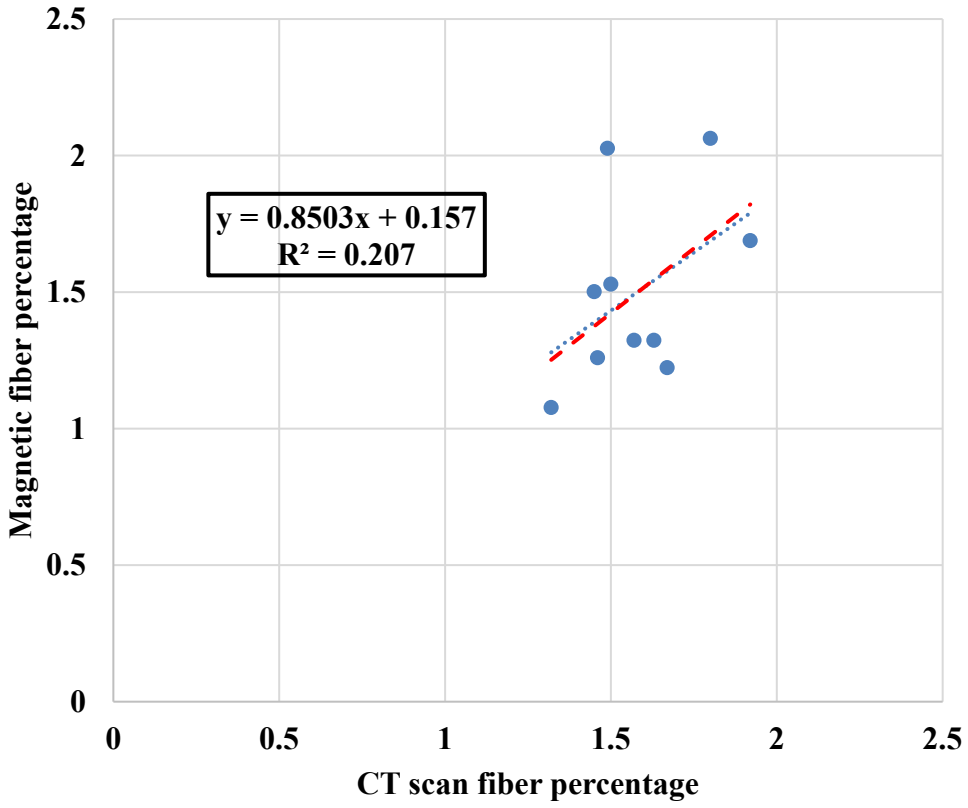

Figure 243: The comparison between the magnetic fiber percentages of the cores taken versus the fiber percentage obtained from the CT scans

12.5.4. Custom CT Analysis

The previous analysis described in section 12.5.3 was achieved using VGStudio Max's software for computing fiber density and orientation. However, the algorithms used to compute these quantities are a black box, aside from a few inputs (such as the threshold value) that hint at the process. These algorithms can have a relatively large effect on the values estimated from the CT scans. There are also fewer capabilities to modify the analysis of the CT when constrained to commercial software. For example, the strength of the change in inductance varies as a function of distance. This information should be incorporated into the analysis of the CT scan data to determine any causes of results that deviate from those expected. To accomplish this, an open-source CT analysis system in MATLAB was created.

The analysis system extracts distinct elements of the CT scan step-by-step, as shown in Figure 244. The first step was to distinguish the background air from the core. This was accomplished first by computing the histogram of the values throughout the CT scan. The histogram exhibited two peaks, corresponding to the two highest-volume materials present, air, and cementitious material. Air had the lower value, and the cementitious material had the higher value. A two-term Gaussian curve was then fit to the histogram to identify the range of values that represented these dominating components. The background air was initially computed to be all voxels that

were three or more standard deviations below the mean value for the cementitious material. The binary map representing the background air was then eroded and dilated [332] with kernel sizes of 20 pixels to remove anomalously small values within the core (such as air voids). The "Background" image in Figure 244 illustrates the result of this process. In Figure 244, the "Background" represents areas outside of the concrete core. "Voids" represent areas low in density and small in size (i.e., distinguishing themselves from the background). Note that these may not necessarily be air voids, but regions of the mixture that have locally lower densities. "Fibers" represent the highest density voxels in the CT based on a user-supplied threshold. "Cementitious" represents the remaining medium-density voxels in the CT system

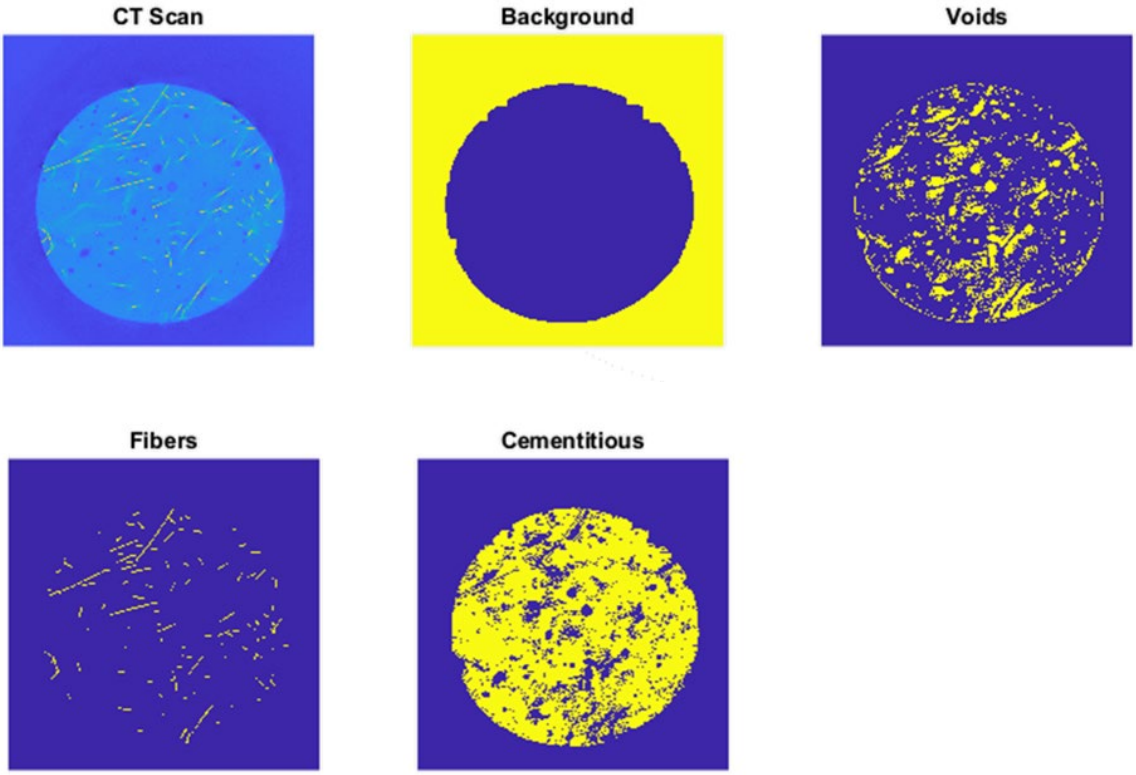

Figure 244: Illustration slice of a three-dimensional core for each step in the custom CT analysis software.

The voxels within the core (i.e., the voxels that were not defined as part of the "Background" were then exclusively processed. The goal was to distinguish cementitious material (the primary density) from the fibers (higher density voxels) and voids or other low-density areas (low-density voxels). Note that while the voids and low-density areas were extracted, this information was not utilized in the report. Based on empirical observations, the distribution of voxel values within the core approximately followed a Laplacian distribution. For a Laplacian distribution, the measure of central tendency is a median and the measure of variation is the mean absolute deviation from the median value. Therefore, the defined voids and low-density areas as one or more mean absolute deviations below the median. The fibers were defined as nine mean absolute deviations

above the median. These ranges were determined empirically by calibrating with the expected fiber percentages. Note that these threshold values changed from CT scan to CT scan, probably because of differences in the x-ray intensity from tube wear, sample thickness, or other sample variations. These regions are illustrated by the “Voids” and “Fibers” images in Figure 244.

The fiber percentage was then computed for each circular slice of the CT core. The fiber percentage was calculated as the ratio of the number of voxels classified as fibers versus the number of voxels classified as not air (i.e., the number of voxels in the core). This may give a slightly higher fiber percentage than expected because entrained and entrapped air is part of the concrete. The air was not included in these calculations because of the difficulty in separating the air outside of the concrete in the scan from that inside the concrete. The orientation was computed by applying first-order derivative edge detection filters [333] in the vertical and horizontal directions. For example, a vertically oriented filter will only retain components of fibers in the vertical detection. Fibers exclusively in the horizontal direction were removed. Fibers aligned in multiple directions will be reduced in amplitude. The absolute values of all filtered voxels for the horizontal and vertical filtered volumes were then summed. The ratio of these sums was then computed to represent the average fiber orientation. In addition, for computing the average fiber percentage or orientation, the weighted average across the thickness of the core was computed. That is, fibers near the sensor were weighted stronger than fiber far from the sensor. The weighting was proportional to exp(-1.831x) where x is the distance from the sensor in inches. This corresponds to the sensor’s calibrated spatial decay and is defined from the calibration in Figure 219, where 0.721 cm^{-1} converts to 1.831 $inch^{-1}$. This was done to determine if the fiber height from the surface and preferential orientation near the surface was causing errors in the fiber percentage readings.

The magnetic fiber percentage values were calibrated from the lab data, as with the other analyses. The fiber percentage was computed as the average readings from the two sensors. Figure 245 and Figure 246 illustrate the sensor measurements vs. CT scan estimates of fiber orientation and fiber percentage while applying the analysis from the custom CT analysis algorithms. The fiber orientation results show a strong relationship between the average fiber orientation from the CT scan and the average fiber orientation from the sensor systems. The relationship with orientation was not as strong as observed from the VGStudio Max software, which may imply that the commercial software tool is utilizing a more effective estimation strategy. Like the results from VGStudio Max however, a line with a slope of one was not obtained. The estimate of fiber percentage (which now weights the fiber percentages as a function of height in the core) is now in line with the results from the magnetic inductive sensor because the distance from the surface for the CT results were corrected for. While this does not help with measurements taken in the field, it does show that the cause is fiber vertical preferential orientation. The slope of the best fit linear line is 1.01, indicating a good calibration between the two analysis methods. The root mean square error is 0.23%.

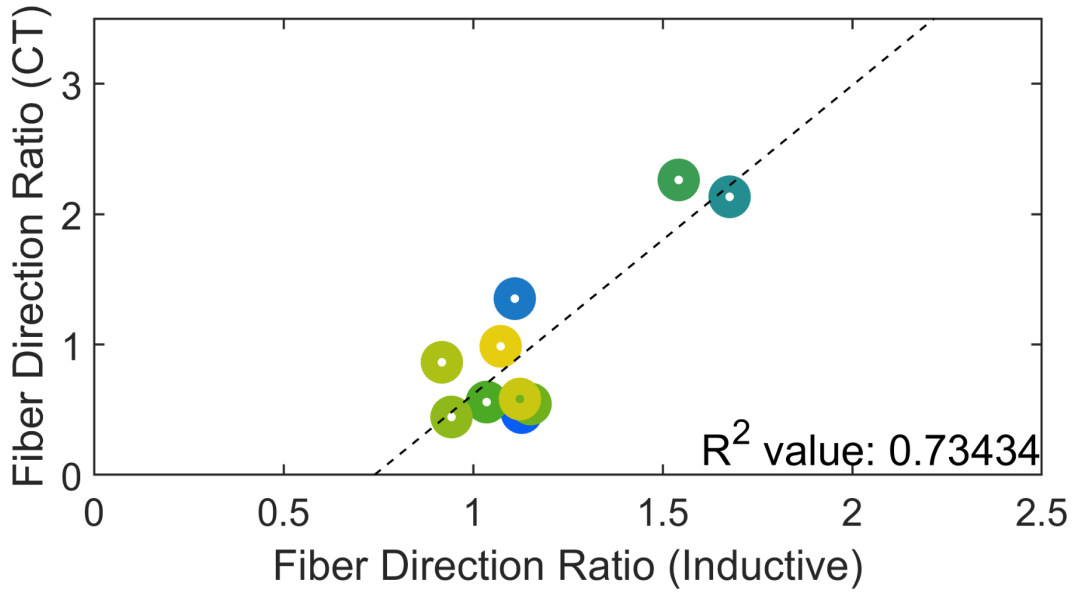

Figure 245: The correlations between magnetic readings and CT fiber percentage estimate for average fiber orientation measured as the ratio of fibers in orthogonal directions

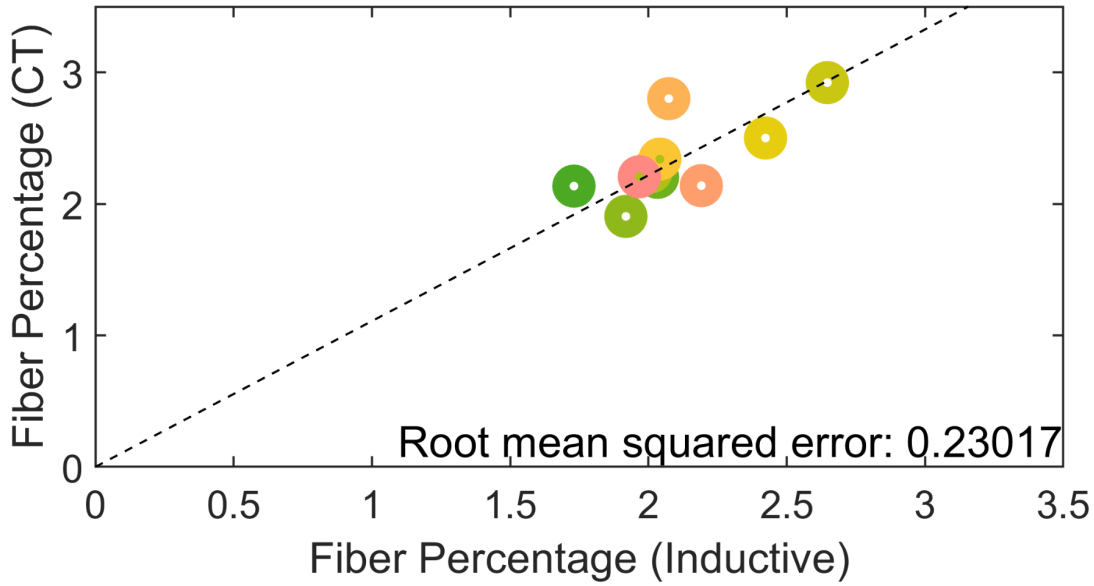

Figure 246: The correlations between magnetic readings and CT fiber percentage estimate for average fiber percentage for ten measurements and cores taken from field data

12.5.5. System Reliability and Robustness Assessment

A system reliability and robustness assessment by comparing the results of the multiple scans to see how repeatable the measurements are reported. The version 2 results are also here compared against the version 3 results to see if updating the sensor gave a repeatable result, taking into consideration operator variability and properties changing with sample age.

12.5.5.1. Measurement Repeatability

For the different field specimens scanned, it was decided to take repeated measurements to see how repeatable the measurements are, while bearing in mind that these might have a lot of errors from the operator, the paths taken etc. Figure 247 shows the repeated measurements taken over the Box Beam that was taken on the 28th of January, 2022 using the version 3 system. The differences observed that could be due to a number of reasons, from difference in acquisition paths, to overall noise in the system were also noted.

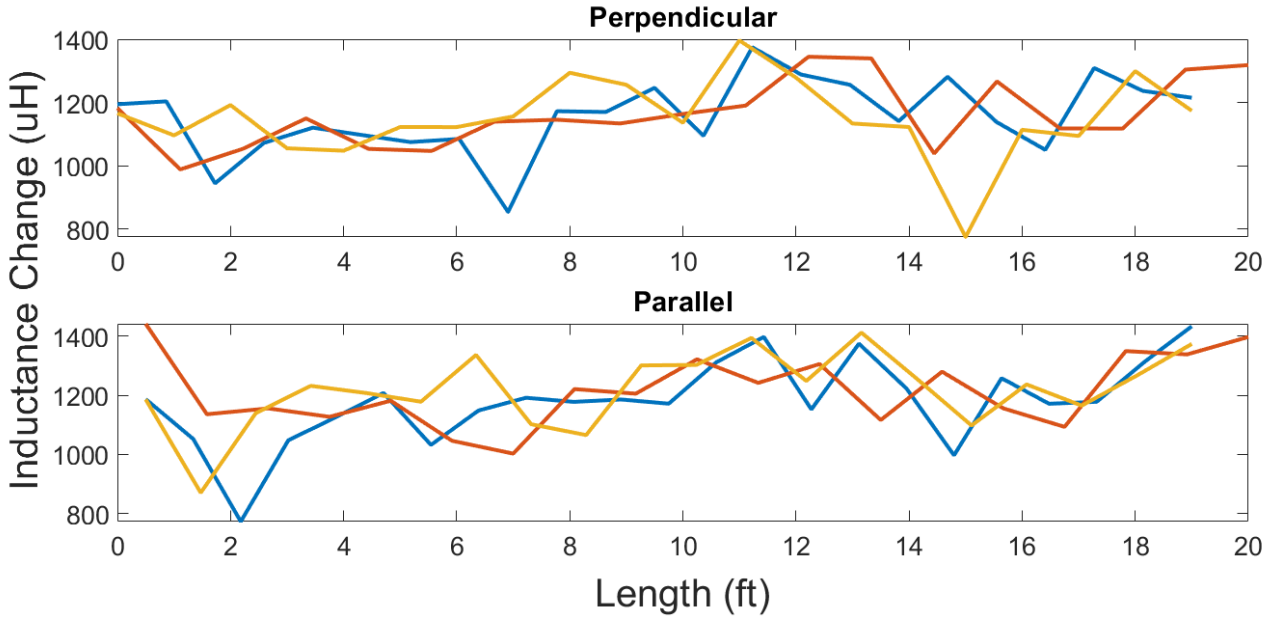

Figure 247: Showing 3 repeated measurements over the same path on the Box Beam. The measurements were each taken and repeated while trying to follow the same path as closely as possible.

12.5.5.2. Version 2 vs. Version 3 of Sensor System

Data was collected over different days using versions 2 and 3 in the field, and it is shown here how the data compares with each other. There was a desire to see if there are similar trends while using the different versions of the sensor system on the same specimen. Figure 248 shows a comparison between the data collected over the octagonal pile using the version 2 and version 3 sensor systems. Note here that the data collected using version 3 was collected after two (2) cores were taken from the pile. In Figure 248 (A) and (B), cores have been taken from the member, one around the 9-ft. mark, and the other around the 11-ft. mark, accounting for the sharp dips around these points.

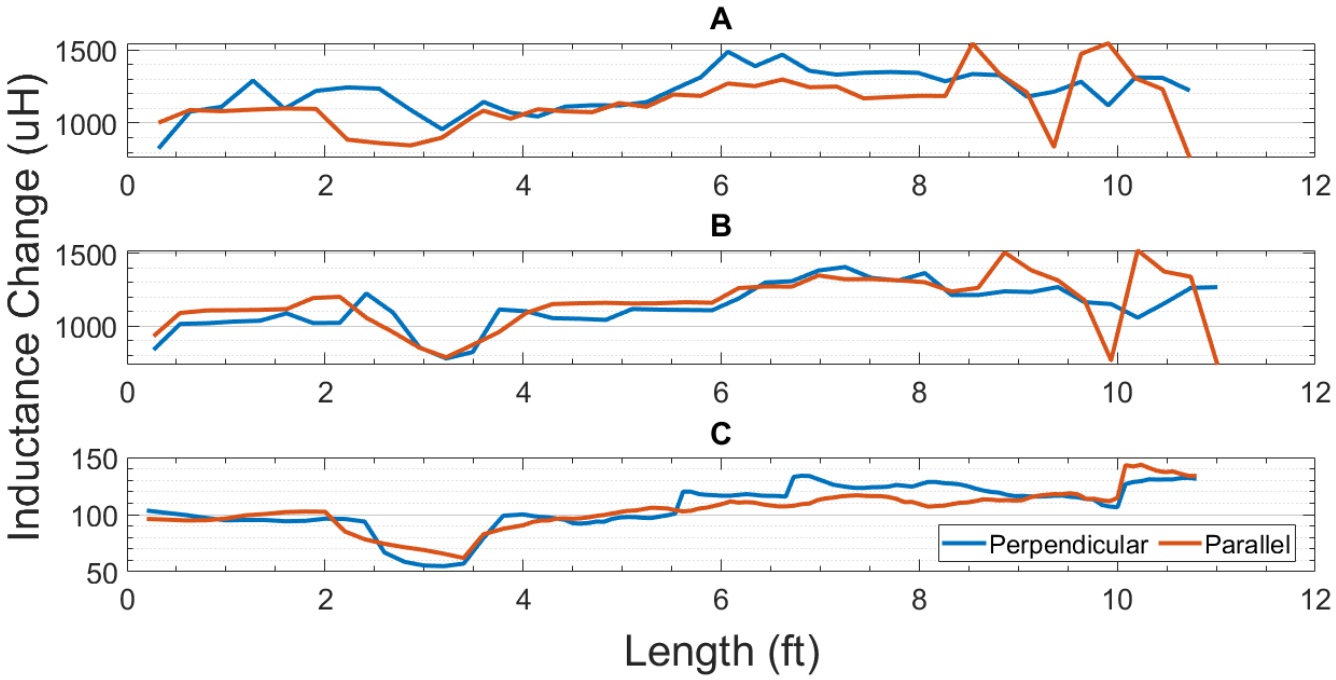

Figure 248: Showing the data acquired over the octagonal pile with the form liner pattern. (A) and (B) were taken using the sensor system three, while (C) was taken using the sensor system 2

From Figure 248, it can be seen that there is repeatability of results using both the versions 2 and 3, and the main difference is the 10-times gain in the inductance change from version 2 to version 3 which will potentially help in having a better inductance change resolution.

12.6. Summary

In this report, the design and construction of a working prototype for an electromagnetic sensor based on inductive principles to characterize and quantify the steel fiber percentages and orientation in ultra-high-performance concrete (UHPC) was detailed. The system was tested both in the lab and in the field. With sufficient calibration, the results demonstrated excellent capability to distinguish medium to severe variations in fiber percentage and orientation. This was demonstrated both through qualitative observations with the system as well and quantitative analyses, comparing the magnetic readings with values extracted from CT scans of cores from the field tests.

For future work, the portability of the design is desired to be improved on so that it can be easily produced for mass markets. It is also desired to be able to make it very easy to carry and operate by technicians out on the field. In addition, future optimizations can be made to the sensor design (e.g., switching to a soft iron core) and circuitry/analysis algorithms (e.g., leveraging multiple frequency information) that should allow for better penetration depths and more reliable measurements. Sensor calibration can also be done to output the same values as seen in the CT scans.

13. SPECIFICATION RECOMMENDATIONS

13.1. Introduction

Ultra-high-performance concrete (UHPC) has the potential to increase the durability of concrete transportation infrastructure, enable new structural member shapes, and increase bridge member spans. UHPC has traditionally been sold as a prebagged material. Considerable cost savings can be realized if nonproprietary concrete mixtures can be used in lieu of prebagged materials. For these benefits to be realized for the Florida Department of Transportation (FDOT), specifications are needed to allow the use of non-proprietary UHPC. Recommended specifications for UHPC materials and construction were made and use some language from the FDOT development specifications 349 and 927 and from the PCI model UHPC specification. The recommended specifications reference two test methods that would need to be adopted as Florida Methods. Draft test specification language for the Modified Double Punch Test is included in Appendix A, while draft test specification language for the Modified Rapid Chloride Migration Test is included in Appendix B. The Modified Rapid Chloride Migration Test is based on NT Build 492 [13], with a few modifications for sample curing, applied voltage, and test duration.

SECTION 349

NON-PROPRIETARY ULTRA-HIGH-PERFORMANCE CONCRETE CONSTRUCTION AND QUALITY CONTROL

349-1 Description.

Use ultra-high-performance concrete (UHPC) composed of an optimized gradation of granular constituents, cementitious materials, and reinforcing fibers with a water-to-cementitious materials ratio of no greater than 0.25.

Use a UHPC mix design that meets the criteria in Section 928.

349-2 Materials.

349-2.1 General: Meet the following requirements:

Manufacturer Material Certification and APL……... Section 6
Non-Proprietary High-Performance Concrete Material Design and Approval. Section 928
Water/Ice…….…... Section 923*

*Use potable water.

349- 3 Onsite Supervision of Ultra-High-Performance Concrete (UHPC) Production.

349- 3.1 General: Arrange for the qualified Contractor's supervisor to be onsite during the production of all UHPC structural elements.

349- 3. 2 Qualified Contractor's Supervisor: Provide a qualified onsite supervisor during UHPC production and work activities; including mixing, batching, placement, and curing. Evidence of training completed by the supervisor and competence to accomplish the supervision of the UHPC related construction in a satisfactory and safe manner may be given. This shall include procedures to batch, place, and cure the concrete. The supervisor shall have experience with at least two successful UHPC mockups or members fabricated, with evidence provided of the date, time, location, member type, and concrete properties.

349-4 Construction Work Plan.

Submit a detailed work plan to the Engineer for review and approval prior to UHPC pre-pour meeting. As a minimum, include the following items in the work plan:

1. Quality Control Plan (QCP) in accordance with Section 105.
2. Member plans with dimensions showing element dimensions and layout of mild steel and prestressing reinforcement.
3. Proposed forming materials and details for ensuring forms are watertight.
4. Details of all equipment to be used to batch and place UHPC materials.

5. UHPC mix design including raw materials, mix proportions, water-to-cementitious materials ratio, flow, working time, and set time.
6. Storage plan of UHPC materials ingredients per manufacturer's/contractor's recommendation.
7. When applicable, the method to provide a roughened surface or exposed aggregate finish for all hardened concrete or UHPC surfaces in contact with a subsequent UHPC or concrete placement.
8. Detailed mixing instructions including order of addition of batch components and mixing times of each mixing stage.
9. Table of approximate working times as a function of UHPC temperature.
10. Placement plan that will enable placement and finishing within the estimated working time for the anticipated UHPC temperature and environmental conditions. Placement plan shall include at least the following:
    a. UHPC delivery method
    b. Type and number of test samples
    c. Placement procedure
    d. Finishing procedure
    e. Curing procedure
    f. QC procedure to use
    g. If required by engineer, detailed mockup procedure to demonstrate the ability to properly cast UHPC in accordance with the design plans and specifications.
11. Hardened mechanical properties including tensile strength properties and compressive strength properties at different ages.
12. Submit the qualification testing of the UHPC at least 60 days prior to casting UHPC. Perform the sampling and testing by a qualified testing laboratory meeting the laboratory qualification requirements of Section 105.
13. Pre-pour meeting agenda, including manufacturer's recommended topics.

349-5 UHPC Mockup Pre-Pour Meeting.

Conduct a pre-pour meeting prior to the UHPC mockup demonstration. Pre-Pore meeting should discuss placement and finishing plan for mockup, testing plan for mockup, experience with previous similar UHPC placements, and engineer expectations for successful mockup placement.

349-6 UHPC Element Mockup.

349-6.1 General: Construct a UHPC element mockup in accordance with the design plans, approved shop drawings, pre-pour meeting discussions, and as recommended by the UHPC manufacturer.

Cast a mockup that is large enough to be representative of the proposed element at least 30 calendar days prior to placement of UHPC in concrete member.

Evaluate uniformity of UHPC fiber at locations specified by the Engineer of Record using one of the following methods.

1. Cut a minimum of six rectangular prisms for direct tension testing at locations specified by the Engineer, with dimensions as required by AASHTO T 397. Perform the AASHTO T 397 direct tension test at the designated age in accordance with AASHTO T 397. The peak stress and stress at 0.0035 strain shall be no less than 75% of the values specified in Table 927-2 for the concrete's tensile strength class. Cut or core specimens from the concrete at locations specified by the Engineer of Record. Characterize the fiber density and alignment using techniques approved by the Engineer of Record. (PCI)
2. Non-destructive testing that demonstrates fiber orientation and volume in the bottom and top of the structure.
3. Cut or core specimens from the concrete at locations specified by the Engineer of Record. Characterize the fiber density and alignment using techniques approved by the Engineer of Record. (PCI)

349-6.2 Mix Workability: Perform the flow loss testing described in this section during mockup casting to determine the duration that the UHPC will remain workable. Perform the flow tests in accordance with the test method described in Table 349-1 while the ambient temperature is between 50°F and 90°F and concrete temperature is maintained between 60°F and 90°F.

Perform the following workability procedure during the casting of the mockup:

1. Take initial samples prior to the start of the discharge of UHPC and perform the flow tests. Record the time of sampling and initial flow value.
2. Measure and record the UHPC and ambient temperatures.
3. Continue sampling at every 10-minute intervals and determine the flow of each sample, until flow measure is below 4 inches.
4. Plot the flow versus time for the duration of the test. From the plot of the flow vs. time curve, determine the time when the flow is 8 inches, which is considered the mixture placement cutoff time.
5. For the production concrete, complete the placement of UHPC in less than or equal to cutoff time.

The determined working time shall only be used for concrete mixes with the same or lower ambient and UHPC temperatures as those recorded during the mix workability test. It is recommended that the mix workability test be repeated with different UHPC and ambient temperatures so there can be a more accurate estimate of a mix's working time at different temperatures.

349-6.3 Set Times: Perform the Time of Setting test of UHPC in accordance with test method described in Table 349-1.

349-7 Construction Methods and Requirements.

1. Determine the range of estimated working times of the UHPC by performing workability testing for the range of temperatures expected for the UHPC at the time of placement.
2. Perform forming, batching, placing, and curing in accordance with the detailed construction work plan and Article 349-4, as approved by the Engineer.
3. Construct formwork from nonabsorbent materials that are properly sealed and capable of resisting the hydrostatic pressures of unhardened UHPC. Do not remove formwork until the UHPC achieves a minimum compressive strength of 10,000 psi or 50% of the specified 28-day compressive strength, whichever is lower.
4. Prior to UHPC placement, prewet precast concrete surfaces that will be in contact with UHPC. Continuously wet the concrete contact area with fresh water for at least 24 hours prior to the UHPC placement.
5. Remove all standing surface water just prior to UHPC placement.
6. Ensure that the fibers are fully distributed, without clumping.
7. During batching, keep the temperature of the UHPC below 85°F. Replacing mix water with ice to reduce temperature and improve flow is allowable, but do not exceed the approved material's water-to-cement ratio.
8. Place UHPC in accordance with the approved placement plan. Keep UHPC temperature above 60°F until it has achieved a minimum compressive strength of 10,000 psi or 50% of the specified 28-day strength, whichever is lower.
9. Place the UHPC in a continuous, non-stop pour, unless otherwise approved by the Engineer. Placement of UHPC shall follow the leading edge of the flow of previously placed UHPC to avoid weak cold joints. For members requiring more than one batch of concrete to fill the formwork, submit a plan including the UHPC placement sequence and any planned joints for the engineer's approval. Overlapping fronts of fresh UHPC shall be mixed by puncturing through both layers of UHPC with a tamping rod at least once per 16 square inches of overlap area.
10. Internal vibration shall not be used for any UHPC element containing fibers. External vibration of the forms may be used to achieve a smooth surface texture and minimize the entrapped air and bugholes on the surface of the element.
11. If required, finishing with hand tools for a flat, smooth finish should be done immediately after consolidation to avoid tearing the UHPC surface. Spiked rollers may be helpful and are permitted for achieving a level surface without tearing the surface.

12. Cure and cover member until the UHPC has achieved a compressive strength of at least 10,000 psi or 50% of the specified 28-day strength, whichever is lower.
13. If grinding is specified, perform grinding of the UHPC surface after a minimum compressive strength of 50% of the specified 28-day strength or 10,000 psi, whichever is lower, has been achieved. Suspend grinding if significant fiber pullout is observed during grinding operations. Take corrective action to prevent the recurrence of the problem. Such action must be approved by the Engineer.
14. The member can be loaded with prestressing strand release when the compressive strength has reached the compressive strength specified by the engineer required for strand release. Compressive strength for prestressing release shall be verified through laboratory testing of match-cured specimens cast at the same time as the structural element.

349-8 Sampling and Testing.

349-8.1 UHPC Quality Control Sampling and Testing: During field demonstration of mockups and construction, perform sampling and testing of UHPC at the frequencies described in Tables 349-1 and 349-2, respectively. Perform the following quality control sampling and testing during casting of the mockup and field casting of UHPC placement:

1. Measure the flow of each batch of UHPC. The allowable flow range is between 8 and 10 inches. Flow shall be measured for each batch within 15 minutes of placement.
2. Record UHPC flow, ambient air, and mix temperature for each batch. Include the time and date, amounts of water/ice and admixtures corresponding to the UHPC batch and LOT numbers for traceability. A LOT of UHPC is defined as 15 yd^3 or one day's production, whichever comes first.
3. As part of the As-Built records, track and show the placement locations of UHPC LOTs on the contract plans. Submit a copy of the as-built records to the Engineer.
4. Compressive Strength Cylindrical Specimens:
   From every LOT, take 3 sets of three 3-in. × 6-in. compressive strength test cylinders according to ASTM C1856. One set will be taken at the beginning and one set at the end of the LOT. In an evenly distributed manner, take one intermediate set from the middle portion of the LOT. Cure all sets in an environment like the placed UHPC. For traceability, track all sets to LOT numbers.
5. Tensile Strength Specimens:
   From every LOT, take 1 set of three tensile strength test cylinders according to FM XXX Modified Double Punch Test. Cure all sets in an environment like the placed UHPC. For traceability, track all sets to LOT numbers.

Table 349-1: UHPC- Sampling and Testing Frequencies During Field Demonstration of Mockup		
Material Characteristic Description	**Test Method**	**Minimum Sampling and Testing Frequency**
Flow of UHPC	ASTM C 1437 (Using Modifications Described in ASTM C1856)	Required number of tests per Sub-article 349-6.2 Mix Workability
Time of Setting of UHPC	ASTM C 191 (Using Modifications Described in ASTM C1856)	One test during mix design verification or field demonstration
Temperature of Freshly Mixed Hydraulic Cement Concrete	ASTM C1064	One test per batch
Compressive Strength of Cylindrical Concrete Specimens	Make test specimens in accordance with ASTM C31 and test them in accordance with ASTM C39 (Using Modifications Described in ASTM C1856)	Cast 5 sets of three cylinders during field demonstration. Test them at the ages of 2, 4, 7, 14, and 28 days
Tensile strength and toughness of concrete	Modified double punch test (Florida test method)	1 set of three cylinders during field demonstration. Test at 28 days
Chloride content	FM 5-516	One test during mix design verification or field demonstration
Mix Workability	349-6.2 Mix Workability	One test per mix design during field demonstration of mockup

Table 349-2: UHPC- Sampling and Testing Frequencies During Construction		
Material Characteristic Description	**Test Method**	**Minimum Sampling and Testing Frequency**
Flow of UHPC	ASTM C 1437 (Using Modifications Described in ASTM C1856)	Two tests per batch: one when mixing is finished and one at the end of placement
Temperature of Freshly Mixed Hydraulic Cement Concrete	ASTM C1064	One test per batch
Compressive Strength of Cylindrical Concrete Specimens	Make test specimens in accordance with ASTM C31 and test them in accordance with ASTM C39 (Using Modifications Described in ASTM C1856)	3 sets of three cylinders per LOT of 25 yd^3 or one day's production, whichever comes first
Chloride content	FM 5-516	One test per month of UHPC production
Tensile strength and toughness of concrete	Modified double punch test (Florida test method)	1 set of three cylinders per LOT of 25 yd^3 or one day's production, whichever comes first

349-8.2 UHPC Quality Control Compressive Strength Testing: For each LOT, test the compressive strength cylinders at the times that are described below:

1. Test three 3-in. × 6-in. cylinders prior to the removal of forms and release of prestressing strands (if applicable) to ensure that the UHPC has achieved the required compressive strength as used for design of prestressing.
2. Test three cylinders at 28 days to verify final strength.
3. Maintain the remaining three cylinders for resolution testing, if needed.

Ensure that the tests are performed by Department qualified testing laboratory meeting the lab qualifications of 105-7. Cure the cylinders onsite in an environment similar to that of the UHPC element material and ship them to the Department qualified testing laboratory for testing. Cure the 28-day test cylinders and resolution test cylinders initially in the field in accordance with ASTM C31 and ship them to the laboratory for final curing and testing. Cylinder ends shall be ground prior to testing to ensure even contact with testing heads.

Ensure that the Quality Control (QC) testing laboratory enters the compressive strength test results into the Department's Materials Acceptance and Certification (MAC) system within 24 hour of their testing. Notify the Engineer when results cannot be entered into MAC.

349-8.3 UHPC Chloride Content Limits for Concrete Construction: Perform the chloride content test at a frequency of one sample per month of UHPC production. The maximum allowable chloride content is 0.50 lb / yd^3.

349-8.4 UHPC Tension Requirements for Concrete Construction: Perform the FM XXX Modified Double Punch Test obtaining three 6-in. × 6-in. cylinders per LOT at 28 days. The average of the three tests must meet the peak strength and toughness values as shown in Table 349-3.

Table 349-3: UHPC Tensile Properties by Tensile Strength Class

Material Characteristic Description	Test Method	Strain-hardening Class	Enhanced Ductility Class
Maximum tensile stress (psi)	Modified double punch test (Florida test method)	1000	1200
Toughness (psi·in.)	Modified double punch test (Florida test method)	130	180

349-9 Quality Assurance Program: Verification Sampling and Testing: The Engineer will observe the UHPC placement and take verification samples for concrete temperature, flow, and compressive strength tests at a frequency of one sample per four LOTs.

For UHPC, the compressive strength verification samples consist of six cylinders; three cylinders for the 28-day tests and three "hold" cylinders for resolution testing, if needed.

Notify the Engineer at least 48 hours prior to the anticipated UHPC placement. Final acceptance will be based upon 28-day compressive strength. Field coring of UHPC for dispute resolution is not allowed.

Meet the requirements of 349-8.1 related to acceptance of UHPC test results. The results of quality control tests are used, when they compare favorably with the verification test results. Consider the quality control and verification tests as favorable when the results of both tests are, either passing

or failing. The test results are not favorable, when one of the test results passes and the other one fails. Proceed to the resolution inspection and testing if the comparison is not favorable.

Provide an adequate location to place acceptance specimens for initial curing prior to transport to the laboratory. Equip the curing boxes with supplemental heat or cooling as necessary to cure specimens in accordance with ASTM C31.

Remove the UHPC and replace or remediate to the satisfaction of the Engineer, if the UHPC does not meet the minimal material properties as described herein.

349-10 Visual Quality Assurance

After removal of the molds, the structural element shall be inspected visually for defects. Prestressed elements must be free of defects according to 450-12.

349-11 Method of Measurement.

The quantities of UHPC to be paid for will be the volume in cubic yards, in place, completed and accepted.

349-12 Basis of Payment.

349-12.1 General: The quantity of UHPC to be paid for will be volume shown in the plans, in place, completed and accepted at the Contract unit price per cubic yards. Price and payment will constitute full compensation for surface preparation, supplying, mixing, transporting, placing, finishing, curing, grinding, and for furnishing all equipment, tools, labor, and incidentals required to complete the work. Include in the measurement the volume of element mockup.

Additional quantity of material used in the determination of material properties and for acceptance testing as described herein will be furnished at no additional cost to the Department.

349-12.2 Reinforcing: Reinforcing bars and reinforcement of mechanical connectors (where required), will be paid for as provided in Section 415.

349-12.3 Pay Items: Payment will be made under:

Item No. 918-349 – Ultra High-Performance Concrete – per cubic yard.

SECTION 928
NON-PROPRIETARY HIGH-PERFORMANCE CONCRETE MATERIAL DESIGN AND APPROVAL

928-1 Description.

This Section covers non-proprietary Ultra-High-Performance Concrete (UHPC) products.

928-2 Approved Mix Design.

UHPC Producers must submit mix designs and certified test reports from an independent laboratory showing that the product meets the requirements of this Section.

Any change of materials or material sources requires new testing and certification of the conformance of the UHPC with this Specification.

928-3 General Requirements.

928-3.1 Meet the requirements of 349-2 with the following additions and modifications:

1. Fibers: Provide the type, diameter, length, and tensile strength, including the percentage of the mix's dry volume. Steel fibers must comply with the source of supply requirements of Section 6.

928-4 Storage.

The manufacturer's instructions shall indicate any required storage temperatures, covering methods, and delivery considerations for the raw materials to protect them from moisture ingress, seepage, corrosion, and UV exposure. The shelf life of the material shall be noted on manufacturer's instructions. The age of all materials used must be within the manufacturer's recommended shelf life.

928-5 Material Data Sheet.

Provide a material data sheet for each UHPC mix design that includes its application and instructions and recommendations for the following:

1. Storage of product components at batch plant.
2. Mix proportions and yield in cubic yards. For each product, provide a mix design with a maximum allowable water-to-cementitious materials ratio no greater than 0.25
3. Allowable ambient and mixture temperatures during batching, mixing, and placement.
4. Batching, mixing, transportation, placement, finishing, and curing methods.

5. Product properties listed in Tables 928-1 Class 17 UHPC or Class 21 UHPC, 928-2 Strain Hardening or Enhanced Ductility, and 928-3.
6. The typical fresh properties of the UHPC mix design, including density, flow, working time, and set time of the mix.

Table 928-1: Plant Batched UHPC Properties			
Material Characteristic Description	**Test Method**	**Class 17 UHPC Acceptance Criteria**	**Class 21 UHPC Acceptance Criteria**
Temperature of freshly mixed hydraulic cement concrete	ASTM C1064	Specified by the Producer	Specified by the Producer
Flow of UHPC	ASTM C1437 (Using modifications Described in ASTM C1856)	Specified by the Producer	Specified by the Producer
Time of setting of UHPC	ASTM C191 (Using modifications Described in ASTM C1856)	Specified by the Producer	Specified by the Producer
Concrete Cylinder Compressive Strength (Non-Heat Treated)	ASTM C39 (Using modifications described in ASTM C1856)	≥ 14,000 psi at 7 days ≥ 17,400 psi at 28 days	≥ 16,000 psi at 7 days ≥ 21,000 psi at 28 days
Static Modulus of Elasticity of Concrete in Compression	ASTM C469 (Using modifications described in ASTM C1856)	≥ 6,500,000 psi at 28 days	≥ 6,500,000 psi at 28 days
Length Change of Hardened Concrete	ASTM C157 (Using modifications described in ASTM C1856)	≤ 800 microstrain at 28 days	≤ 800 microstrain at 28 days

Table 928-2: UHPC Tensile Properties			
Material Characteristic Description	**Test Method**	**Strain-hardening**	**Enhanced Ductility**
Effective Cracking Strength	AASHTO T 397	1,000 psi at 28 days	1,200 psi at 28 days
Crack Localization Strength	AASHTO T 397	1,000 psi at 28 days	1,200 psi at 28 days
Crack Localization Strain	AASHTO T 397	≥ 0.0035	≥ 0.0035
Maximum tensile stress (psi)	Modified double punch test (Florida test method)	1000	1200
Toughness	Modified double punch test (Florida test method)	130	180

Table 928-3: UHPC Durability Properties		
Material Characteristic Description	Test Method	Acceptance Criteria
Chloride content	FM 5-516	≤ 0.5 lb/yd^3
Chloride ion permeability	FM XXX Modified Rapid Chloride Migration Test	≤ 5 mm
Alkali-Silica Reaction	ASTM C1567	Innocuous (at 28-day Test)

14. CONCLUSIONS AND RECOMMENDATIONS

14.1. Conclusions

The research presented in this project shows that non-proprietary mixes with lower compressive strengths than conventional UHPC can exhibit desirable behavior in tension and creep. While mix designs with lower w/cm and more fines performed better in mechanical tests, the cost savings associated with lower cement contents and fewer specialized filler materials must be weighed against the benefits. The curing method used had a large effect on concrete creep behavior but only a very small effect on tensile behavior for mixes with higher w/cm. The effect of heat treatment on compressive strength was much stronger at 2 days than at 28 days and had a larger effect on mixes of higher strengths, closer to the UHPC compressive strength requirements.

Tensile test methods currently in use for UHPC should use post-cracking characteristics such as toughness in addition to peak strength to describe the overall tensile behavior of the concrete. Simplified test methods such as the modified double punch test presented in Chapter 5 and the ASTM C1609 flexure test are useful methods for quality control, but the stress vs. strain relationship measured from a direct tension test is ideal for initial mix qualification.

In field applications, UHPC elements that must be cast using more than one batch should have time intervals between placements of 20 minutes or less. Rodding the interface between the layers can help improve the bond strength.

All mixtures with compressive strength above 15 ksi performed excellent in freeze-thaw testing. Steam curing was found to negatively affect the freeze-thaw performance at the lowest strength level tested.

Significant chloride leaching was found to occur in EN 480-14 during curing and testing, resulting in misleading chloride threshold values. The fresh chloride limit was recommended to be raised by 25% from 0.4 lb/yd^3 to 0.5 lb/yd^3. The ACI 318 water-soluble chloride limits as a % by mass of cementitious materials were found to be higher than that required for corrosion initiation for two of the UHPC mixtures tested and should be re-examined for UHPC.

The steel fibers did not noticeably affect the chloride ingress in bulk diffusion experiments and had only a small effect on the chloride ingress measured in the modified rapid chloride migration test due the disconnected pore structure of the UHPC samples. The modified rapid chloride migration test was found to work for UHPC samples with fibers up to 2% by volume. A limit of 5 mm of chloride intrusion after 7 days was found to be a good limit to differentiate chloride diffusion performance. Steam-curing provided accelerated curing at 28 days that compared well to long-term test results and is recommended for acceptance testing purposes.

A nondestructive electromagnetic sensor based on inductive principles to characterize and quantify the steel fiber percentages and orientation in UHPC can be used in both the lab and field.

14.2. Recommendations

Based upon the findings from this study, the following recommendations are made:

- It is recommended that direct tension tests be used for mix design acceptance.
- The modified double-punch test is recommended for use as a quality-control test for UHPC.
- The modified rapid chloride migration test recommended to be used as quality-control test for the long-term durability of UHPC. For steam-cured samples, a chloride intrusion less than 5 mm for 7 days of testing could be used as an acceptance criterion.
- The fresh chloride limit was recommended to be raised by 25% from 0.4 lb/yd^3 to 0.5 lb/yd^3
- The nondestructive electromagnetic sensor developed to quantify the steel fiber percentages and orientation in UHPC is recommended.

14.3. Future work

- A quantitative method should be developed to determine if the results of a direct tension test were affected by eccentricity of the sample loading in the test frame
- Research should be undertaken to develop procedures to minimize or eliminate the formation of a stiffened surface layer (elephant skin) before surface finishing can be completed or before the placement of another layer on top of the first.
- Development of a resistivity meter with a range sufficient to measure the resistivities of all UHPC samples.
- The modified rapid chloride migration test used in this research shows potential as a quality-control test for UHPC durability. This test should be investigated further by testing samples with steel fibers above 2% at one year and compare the results to bulk diffusion test results
- Improve the protability of the electromagnetic so that it can be easily produced for mass markets. It is also desired to be able to make it very easy to carry and operate by technicians out in the field. In addition, future optimizations can be made to the sensor design (e.g., switching to a soft iron core) and circuitry/analysis algorithms (e.g., leveraging multiple frequency information) that should allow for better penetration depths and more reliable measurements. Sensor calibration can also be done to output the same values as seen in the CT scans.

REFERENCES

1] Y. Kusumawardaningsih, E. Fehling, M. Ismail, A.A.M. Aboubakr, Tensile strength behavior of UHPC and UHPFRC, in: Procedia Eng., Elsevier Ltd, 2015: pp. 1081–1086. https://doi.org/10.1016/j.proeng.2015.11.166.

[2] I.H. Yang, J. Park, T.Q. Bui, K.C. Kim, C. Joh, H. Lee, An Experimental Study on the Ductility and Flexural Toughness of Ultrahigh-Performance Concrete Beams Subjected to Bending, Mater. 2020, Vol. 13, Page 2225. 13 (2020) 2225. https://doi.org/10.3390/MA13102225.

[3] B. Keierleber, D. Bierwagen, F. Fanous, B. Phares, I. Couture, Design of Buchanan County, Iowa, bridge using ultra high performance concrete and PI girders, in: Proc. 2007 Mid-Continent Transp. Res. Symp., Iowa State University, Ames, Iowa, 2007.

[4] R.G. Helou, B.A. Graybeal, Flexural Behavior and Design of Ultrahigh-Performance Concrete Beams, J. of Struct. Eng., 2022,Vol. 148, No. 4, 1-20. https://doi.org/10.1061/(ASCE)ST.1943-541X.0003246

[5] H.G. Russell, B.A. Graybeal, Ultra-High Performance Concrete : A State-of-the-Art Report for the Bridge Community, FHWA-HRT-13-060, 2013, 1-176.

[6] K.H. Khayat, W. Meng, K. Vallurupalli, L. Teng, Rheological properties of ultra-high-performance concrete — An overview, Cem. Concr. Res. 124 (2019) 105828. https://doi.org/10.1016/j.cemconres.2019.105828.

[7] A.B. Groeneveld, T.M. Ahlborn, C.K. Crane, C.A. Burchfield, E.N. Landis, Dynamic strength and ductility of ultra-high performance concrete with flow-induced fiber alignment, Int. J. Impact Eng. 111 (2018) 37–45. https://doi.org/10.1016/J.IJIMPENG.2017.08.009.

[8] E. Wagner, J.S. Lawler, Evaluation of Fiber Distribution and Alignment in Structural UHPC Elements, Int. Interact. Symp. Ultra-High Perform. Concr. 2 (2019). https://doi.org/10.21838/UHPC.9676.

[9] B.A. Graybeal, F. Baby, Development of direct tension test method for ultra-high-performance fiber-reinforced concrete, ACI Mater. J. 110 (2013) 177–186. https://doi.org/10.14359/51685532.

[10] B.A. Graybeal, F. Baby, Tension Testing of Ultra-High Performance Concrete FWHA-HRT-17-053, (No. FHWA-HRT-17-053). United States. Fed. Highw. Adm. Off. Infrastruct. Res. Dev. (2019) 210.

[11] ASTM C1609, Standard Test Method for Flexural Performance of Fiber-Reinforced Concrete (Using Beam With Third-Point Loading) 1, (2012) 1–9. https://doi.org/10.1520/C1609.

[12] UNE 83515, Fiber Reinforced Concrete. Determination of Cracking Strength, Ductility and Residual Tensile Strength. Barcelona Test, (2010) 1–10.

[13] NT Build 492, Chloride migration coefficient from non-steady-state migration experiments, 1999.

[14] AASHTO TP 119, Standard Method of Test for Electrical Resistivity of a Concrete Cylinder Tested in a Uniaxial Resistance Test, Am. Assoc. State Highw. Transp. Off. (2015) 1–11.

[15] AASHTO T 358, Standard Method of Test for Surface Resistivity Indication of Concrete's Ability to Resist Chloride Ion Penetration., AASHTO Provisional Stand. 2011 Ed. (2015) 1–8. https://doi.org/10.1520/C1202-12.2.

[16] ASTM C1202, Standard Test Method for Electrical Indication of Concrete's Ability to Resist Chloride Ion Penetration, Am. Soc. Test. Mater. (2019) 8. https://doi.org/10.1520/C1202-12.2.

[17] ASTM C1556, Standard Test Method for Determining the Apparent Chloride Diffusion Coefficient of Cementitious Mixtures by Bulk Diffusion, (2016) 1–7. https://doi.org/10.1520/C1556-11AR16.2.

[18] European Committee for Standardization, EN 480-14: Admixtures for Concrete, Mortar and Grout – Test Methods – Part 14: Determination of the Effect on Corrosion Susceptibility of Reinforcing Steel by Potentiostatic Electro-Chemical Test, (2008) 1–14.

[19] ASTM C666, Standard Test Method for Resistance of Concrete to Rapid Freezing and Thawing, West Conshohocken, Pennsylvania, 2015.

[20] ASTM C512, Standard Test Method for Creep of Concrete in Compression, West Conchohocken, PA, United States, 2015.

[21] J. Dils, V. Boel, G. De Schutter, Influence of cement type and mixing pressure on air content, rheology and mechanical properties of UHPC, Constr. Build. Mater. 41 (2013) 455–463. https://doi.org/10.1016/j.conbuildmat.2012.12.050.

[22] E.M. Williams, S.S. Graham, P.A. Reed, T.S. Rushing, E.M. Williams, S.S. Graham, P.A. Reed, T.S. Rushing, Laboratory Characterization of Cor-Tuf Concrete With and Without Steel Fibers, Tech. Rep. No. ERDC/GSL TR-02-22, U.S. Army Corps Eng. Eng. Res. Dev. Center, Washington, DC. (2009).

[23] T. Nuruddin, M. F., Khan, S. U., Shafiq, N., & Ayub, Strength Development of High-Strength Ductile Concrete Incorporating Metakaolin and PVA Fibers, Sci. World J. (2014) 11. https://doi.org/10.1155/2014/387259.

[24] Z.B. Haber, I. De la Varga, B.A. Graybeal, B. Nakashoji, R. El-Helou, Properties and Behavior of UHPC-Class Materials, (No. FHWA-HRT-18-036). United States. Fed.

Highw. Adm. Off. Infrastruct. Res. Dev. (2018).

[25] W. Meng, M. Valipour, K.H. Khayat, Optimization and performance of cost-effective ultra-high performance concrete, Mater. Struct. Constr. 50 (2017). https://doi.org/10.1617/s11527-016-0896-3.

[26] K.H. Meng, W., & Khayat, Effect of Hybrid Fibers on Fresh Properties, Mechanical Properties, and Autogenous Shrinkage of Cost-Effective UHPC, J. Mater. Civ. Eng. 30 (2018) 1–8. https://doi.org/10.1061/(ASCE)MT.1943-5533.0002212.

[27] K. Wille, D. Joo, K. Antoine, Strain-hardening UHP-FRC with low fiber contents, Mater. Struct. 44 (2011) 583–598. https://doi.org/10.1617/s11527-010-9650-4.

[28] S.H. Park, D.J. Kima, G.S. Ryub, K.T. Koh, Tensile behavior of Ultra High Performance Hybrid Fiber Reinforced Concrete, Cem. Concr. Compos. 34 (2012) 172–184. https://doi.org/10.1016/j.cemconcomp.2011.09.009.

[29] Q. Song, R. Yu, X. Wang, S. Rao, Z. Shui, A Novel Self-Compacting Ultra-High Performance Fibre Reinforced Concrete (SCUHPFRC) Derived from Compounded High-Active Powders, Constr. Build. Mater. 158 (2018) 883–893. https://doi.org/10.1016/j.conbuildmat.2017.10.059.

[30] M. Alkaysi, S. El-Tawil, Structural Response of Joints Made with Generic UHPC, Struct. Congr. (2015) 1435–1445.

[31] L. Felipe, M. Duque, B.A. Graybeal, Fiber Reinforcement Influence on the Tensile Response of UHPFRC, (2016) 1–10.

[32] W. Meng, K.H. Khayat, Improving flexural performance of ultra-high-performance concrete by rheology control of suspending mortar Improving fl exural performance of ultra-high-performance concrete by rheology control of suspending mortar, Compos. Part B. 117 (2017) 26–34. https://doi.org/10.1016/j.compositesb.2017.02.019.

[33] L. Ferrara, M. Prisco, M.G.L. Lamperti, Identification of the stress-crack opening behavior of HPFRCC : the role of flow-induced fiber orientation, (2010).

[34] P. Sta, J.G.M. Van Mier, Manufacturing, fibre anisotropy and fracture of hybrid fibre concrete, 74 (2007) 223–242. https://doi.org/10.1016/j.engfracmech.2006.01.028.

[35] CSA 23.3, Design of Concrete Structures - Draft, (2018).

[36] D. Yoo, G. Zi, S. Kang, Y. Yoon, Biaxial flexural behavior of ultra-high-performance fi ber-reinforced concrete with different fi ber lengths and placement methods, Cem. Concr. Compos. 63 (2015) 51–66. https://doi.org/10.1016/j.cemconcomp.2015.07.011.

[37] L. Felipe, M. Duque, B. Graybeal, Fiber orientation distribution and tensile mechanical response in UHPFRC, Mater. Struct. 50 (2017) 1–17. https://doi.org/10.1617/s11527-016-

0914-5.

[38] K. Wille, G.J. Parra-montesinos, Effect of Beam Size, Casting Method, and Support Conditions on Flexural Behavior of Ultra-High-Performance Fiber-Reinforced Concrete, (2013) 379–388.

[39] H. Huang, X. Gao, L. Li, H. Wang, Improvement effect of steel fiber orientation control on mechanical performance of UHPC, 188 (2018) 709–721. https://doi.org/10.1016/j.conbuildmat.2018.08.146.

[40] D. Yoo, S. Kang, Y. Yoon, Effect of fiber length and placement method on flexural behavior , tension-softening curve, and fiber distribution characteristics of UHPFRC, Constr. Build. Mater. 64 (2014) 67–81. https://doi.org/10.1016/j.conbuildmat.2014.04.007.

[41] M. Roy, C. Hollmann, K. Wille, Influence of volume fraction and orientation of fibers on the pullout behavior of reinforcement bar embedded in ultra high performance concrete, 146 (2017) 582–593. https://doi.org/10.1016/j.conbuildmat.2017.04.081.

[42] J. Park, Y.J. Kim, J. Cho, S. Jeon, Early-Age Strength of Ultra-High Performance Concrete in Various Curing Conditions, (2015) 5537–5553. https://doi.org/10.3390/ma8085261.

[43] K.-T. Koh, J.-J. Park, G.-S. Ryu, S.-T. Kang, Effect of the compressive strength of ultra-high strength steel fiber reinforced cementitious composites on curing method, J. Korean Soc. Civ. Eng. 27 (2007) 427–432.

[44] H. Yazıcı, M.Y. Yardımcı, S. Aydın, S. Anıl, Mechanical properties of reactive powder concrete containing mineral admixtures under different curing regimes, Constr. Build. Mater. 23 (2009) 1223–1231. https://doi.org/10.1016/j.conbuildmat.2008.08.003.

[45] A.. & Vigneshwari.M, Experimental investigation on ultra high strength concrete containing mineral admixtures under different curing conditions, 2 (2011) 33–42.

[46] G.U. Chunping, Effect of Curing Conditions on the Durability of Ultra- high Performance Concrete under Flexural Load, 31 (2016) 278–285. https://doi.org/10.1007/s11595-016-1365-0.

[47] D. Wang, C. Shi, Z. Wu, J. Xiao, Z. Huang, Z. Fang, A review on ultra high performance concrete : Part II . Hydration , microstructure and properties, Constr. Build. Mater. 96 (2015) 368–377. https://doi.org/10.1016/j.conbuildmat.2015.08.095.

[48] M. Richard, P.; Cheyrezy, Composition of reactive powder concretes, Cem. Concr. Res. 25 (1995) 1501–1511. https://doi.org/10.1016/0008-8846(95)00144-2

[49] U. Mueller, P. Fontana, C. Lehmann, Effects of Autoclaving on the Nano structure and Phase composition of Ultra High Performance Concrete, 12th Euroseminar on Microscopy

Applied to Building Materials, 15-19 September 2009, Dortmund, Germany (2009) 1-9.

[50] M. Cheyrezy, V. Maret, L. Frouin, Microstructural Anaylsis of RPC (Reactive Powder Concrete), Cem. Concr. Res. 25 (1995) 1491–1500. https://doi.org/10.1016/0008-8846(95)00143-Z

[51] O.H. Wallevik, J.E. Wallevik, Rheology as a tool in concrete science: The use of rheographs and workability boxes, Cem. Concr. Res. 41 (2011) 1279–1288. https://doi.org/10.1016/j.cemconres.2011.01.009.

[52] K. Hsu, J. Chiu, S. Chen, Y. Tseng, Effect of addition time of a superplasticizer on cement adsorption and on concrete workability, Cem. Concr. Comp. 21 (1999) 425-430. https://doi.org/10.1016/S0958-9465(99)00030-X

[53] J. Plank, C. Schröfl, M. Gruber, Use of a Supplemental Agent to Improve Flowability of Ultra-High- Performance Concrete, Ninth ACI International Conference on Superplasticizers and Other Chemical Admixtures, Oct. 13-17, Seville, Spain (2012) 1-16.

[54] M. Courtial, M. De Noirfontaine, F. Dunstetter, M. Signes-frehel, P. Mounanga, Effect of polycarboxylate and crushed quartz in UHPC: Microstructural investigation, Constr. Build. Mater. 44 (2013) 699–705. https://doi.org/10.1016/j.conbuildmat.2013.03.077.

[55] K. Wille, A.E. Naaman, G.J. Parra-montesinos, Ultra-High Performance Concrete with Compressive Strength Exceeding 150 MPa (22 ksi): A Simpler Way, ACI Mat. J. Vol 108 No. 1 (2011) 46-54.

[56] A.Feylessoufi, M.Crespin, P.Dion, F.Bergaya, H.Van Damme, P.Richard, Controlled Rate Thermal Treatment of Reactive Powder Concretes, Adv. Cem. Based Mat. Vol. 6 No. 1 (1997) 21-27.

[57] F. Hirschi, T., & Wombacher, T. Hirschi, F. Wombacher, Influence of different superplasticizers on UHPC, in: S.S. E. Fehling, M. Schmidt (Ed.), Ultra High Perform. Concr. Proc. Second Int. Symp. Ultra High Perform. Concr., Kassel University Press, Kassel, Germany, 2008: pp. 77–84.

[58] A. Yahia, M. Tanimura, Rheology of belite-cement – Effect of w / c and high-range water-reducer type, Constr. Build. Mater. 88 (2015) 169–174. https://doi.org/10.1016/j.conbuildmat.2015.03.029.

[59] ASTM C1856, Standard Practice for Fabricating and Testing Specimens of Ultra-High, West Conshohocken, PA; ASTM Int. i (2017) 15–18. https://doi.org/10.1520/C1856.

[60] ASTM C1437, Standard Test Method for Flow of Hydraulic Cement Mortar 1, (2019) 18–19. https://doi.org/10.1520/C1437-15.2.

[61] N. Roussel, C. Stefani, R. Leroy, From mini-cone test to Abrams cone test: measurement of cement-based materials yield stress using slump tests, Cem. Concr. Res. 35 (2005)

817–822. https://doi.org/10.1016/j.cemconres.2004.07.032.

[62] S.P. Tregger, N., Ferrara, L., & Shah, Identifying viscosity of cement paste from mini-slump-flow test, ACI Mater. J. 105 (2008) 558.

[63] M. Sung, J. Soo, K. Seong, K. Koh, S. Hee, Estimation of rheological properties of UHPC using mini slump test, Constr. Build. Mater. 106 (2016) 632–639. https://doi.org/10.1016/j.conbuildmat.2015.12.106.

[64] K.A. Riding, C.C. Ferraro, H.R. Hamilton, M.S. Voss, R.S. Alrashidi, Requirements for Use of Field-Cast, Proprietary Ultra-High-Performance Concrete in Florida Structural Applications Final report, Univ. Florida, Draft Tech. Memo. BDV-31 TWO 977-94. (2019).

[65] J.P.P. Binard, UHPC: A Game-Changing Material for PCI Bridge Producers, PCI J. (2017) 34–46. https://doi.org/10.15554/pcij62.2-01

[66] H.S. Lee, H.O. Jang, K.H. Cho, Evaluation of bonding shear performance of ultra-high-performance concrete with increase in delay in formation of cold joints, Materials (Basel). 9 (2016) 362. https://doi.org/10.3390/ma9050362.

[67] C.K. Crane, L.F. Kahn, Interface Shear Capacity of Small UHPC / HPC Composite T-Beams, Proc. Hipermat 2012 3rd Int. Symp. UHPC Nanotechnol. High Perform. Constr. Mater. Kassel. (2012).

[68] ASTM C403, Standard Test Method for Time of Setting of Concrete Mixtures by Penetration Resistance, ASTM International, 2019. https://doi.org/10.1520/C0403.

[69] ASTM C191, Standard Test Methods for Time of Setting of Hydraulic Cement by Vicat Needle, (2019) 1–8. https://doi.org/10.1520/C0191-19.2.

[70] Li, P. P., Yu, Q. L., Brouwers, H. J. H., & Yu, R. (2016). Fresh behaviour of ultra-high performance concrete (UHPC) : an investigation of the effect of superplasticizers and steel fibres. In Proceedings of the 9th International Concrete Conference 2016, Environment, Efficiency and Economic Challenges for Concrete, July 4-6, 2016, Dundee, Scotland, United Kingdom (pp. 635-644).

[71] D.B. Valentim, S. Aaleti, A. Amirkhanian, M.E. Kreger, Experimental Evaluation of Test Methods to Characterize Tensile Behavior of Ultra-High Performance Concrete, in: Second Int. Interact. Symp. UHPC, Iowa State University, Albany, NY, 2019: pp. 1–10.

[72] C. Molins, A. Aguado, S. Saludes, Double punch test to control the energy dissipation in tension of FRC (Barcelona test), Mater. Struct. Constr. 42 (2009) 415–425. https://doi.org/10.1617/s11527-008-9391-9.

[73] ASTM C1018, Standard Test Method for Flexural Toughness and First-Crack Strength of Fiber-Reinforced Concrete (Using Beam With Third-Point Loading), ASTM International,

1997.

[74] F. Baby, B. Graybeal, P. Marchand, F. Toutlemonde, Proposed Flexural Test Method and Associated Inverse Analysis for Ultra-High-Performance Fiber-Reinforced Concrete, ACI Mat. J. (2012) 545–556.

[75] ASTM C496, Standard Test Method for Splitting Tensile Strength of Cylindrical Concrete Specimens, Vol. 109 No. 5 (2017) 545-555. https://doi.org/10.1520/C0496.

[76] B.A. Graybeal, Practical Means for Determination of the Tensile Behavior of Ultra-High Performance Concrete, J. ASTM Intern. Vol. 3 No. 8 (2006) Paper JAI100387. https://doi.org/10.1520/JAI100387

[77] H.A. Goaiz, T. Yu, M.N.S. Hadi, R. Online, H.A. Goaiz, T. Yu, M.N. S Hadi, Quality evaluation tests for tensile strength of reactive powder concrete, J. Mat. Civ. Eng. Vol. 30 No. 5 (2018) Paper 04018070. https://doi.org/10.1061/(ASCE)MT.1943-5533.0002257

[78] C. Ozyildirim, Evaluation of Ultra-High-Performance Fiber-Reinforced Concrete, Virginia DOT Final Report VCTIR 12-R1, http://www.virginiadot.org/vtrc/main/online_reports/pdf/12-r1.pdf

[79] M. Prisco, M.G.L. Lamperti, S. Lapolla, Double-edge wedge splitting test: preliminary results, in FraMCoS-7 - Seventh International Conference Fract. Mech. Concr. Concr. Struct. (2010) 1579–1586.

[80] W.F. Chen, T. Colgrove, Double-Punch Test for Tensile Strength of Concrete, Transp. Res. Rec. J. Transp. Res. Board. 504 (1974) 43–50.

[81] S. Tuladhar, A standard tensile testing procedure for fiber-reinforced concrete (FRC) and UHPFRC based on double punch test(DPT), University of Texas at Arlington, 2017.

[82] P. Pujadas, A. Blanco, S. Cavalaro, A. de la Fuente, A. Aguado, New Analytical Model to Generalize the Barcelona Test Using Axial Displacement, J. Civ. Eng. Manag. 19 (2013) 259–271. https://doi.org/10.3846/13923730.2012.756425.

[83] E. Galeote, A. Blanco, S.H.P. Cavalaro, A. de la Fuente, Correlation between the Barcelona test and the bending test in fibre reinforced concrete, Constr. Build. Mater. 152 (2017) 529–538. https://doi.org/10.1016/j.conbuildmat.2017.07.028.

[84] D. Choumanidis, E. Badogiannis, P. Nomikos, A. Sofianos, Barcelona test for the evaluation of the mechanical properties of single and hybrid FRC, exposed to elevated temperature, Constr. Build. Mater. 138 (2017) 296–305. https://doi.org/10.1016/j.conbuildmat.2017.01.115.

[85] S.H. Chao, N.B. Karki, J.S. Cho, R.N. Waweru, Use of double punch test to evaluate the mechanical performance of fiber reinforced concrete, in: Proc. 6th Int. Work. High Perform. Fiber Reinf. Cem. Compos., 2011: pp. 27–34.

[86] K. Wille, S. El-tawil, A.E. Naaman, Properties of strain hardening ultra high performance fiber reinforced concrete (UHP-FRC) under direct tensile loading, Cem. Concr. Compos. 48 (2014) 53–66. https://doi.org/10.1016/j.cemconcomp.2013.12.015.

[87] ASTM C39, Standard Test Method for Compressive Strength of Cylindrical Concrete Specimens, ASTM Stand. (2018) 1–7. https://doi.org/10.1520/C0039.

[88] N. Roux, C. Andrade, M.A. Sanjuan, Experimental Study of Durability of Reactive Powder Concretes, J. Mat. Civ. Eng. Vol. 8, No. 1 (1996) 1–6.

[89] O. Bonneau, C. Vernet, M. Moranville, P. Aitcin, Characterization of the granular packing and percolation threshold of reactive powder concrete, Cem. Concr. Res. Vol. 30 No. 12 (2000) 1861-1867. https://doi.org/10.1016/S0008-8846(00)00300-8

[90] C. Vernet, UHPC microstructure and related durability perfor-mance laboratory assessment and field experience examples, in: Proc. 2003 Int. Symp. High Perform. Concr., Orlando, FL, 2003.

[91] T. Ahlborn, D.K. Harris, D.L. Misson, E.J. Peuse, Durability and Strength Characterization of Ultra-High Performance Concrete Under Variable Curing Regimes, in: S.S. E. Fehling, M. Schmidt (Ed.), Ultra High Perform. Concr. Proc. Second Int. Symp. Ultra High Perform. Concr., Kassel University Press, 2008: pp. 197–204.

[92] P. Acker, M. Behloul, M. Acker, P., & Behloul, Ductal® Technology: A Large Spectrum of Properties, A Wide Range of Applications, in: C.G. M. Schmidt, E. Fehling (Ed.), Proc. Int. Symp. Ultra High Perform. Concr., Kassel, Germany, 2004: pp. 11–23.

[93] J. Piérard, B. Dooms, N. Cauberg, Durability evaluation of different types of UHPC, RILEM-Fib-AFGC Int. Symp. Ultra-High Perform. Fibre-Reinforced Concr. UHPFRC 2013 –. (2013) 275–284. http://demo.webdefy.com/rilem-new/wp-content/uploads/2016/10/f44eafb7c62b85f77bb95f4880434a80.pdf.

[94] M. Lee, K. Lee, M. Tia, UHPC Precast Product under Severe Freeze-Thaw Conditions, 13th International Conference on Fracture, June 16–21, 2013, Beijing, China (2013) 1–8.

[95] Z. Zhou, Development, Characterization, and Modeling of Ultra-High Performance Concrete (UHPC) with Locally Available Materials, Doctoral Thesis, Washington State University, (2018). https://doi.org/10.13140/RG.2.2.24787.63522.

[96] C. P. Vernet, Ultra-Durable Concretes: Structure at the Micro- and Nanoscale, MRS Bulletin Vol. 29 (2012) 324–327.

[97] M. Thomas, B. Green, E. O'Neal, V. Perry, S. Hayman, A. Hossack, Marine performance of UHPC at Treat Island, in: S.P. M. Schmidt, E. Fehling, C. Glotzbach, S. Frohlich (Ed.), Proc. Hipermat 2012 3rd Int. Symp. UHPC Nanotechnol. High Perform. Constr. Mater., Kassel University Press, 2012: pp. 365–370.

[98] J.J. Valenza, G.W. Scherer, Mechanism for Salt Scaling, J. Am. Ceram. Soc. Vol. 89 No. 4 (2006) 1161-1179. https://doi.org/10.1111/j.1551-2916.2006.00913.x

[99] B.A. Graybeal, Material Property Characterization of Ultra-High Performance Concrete, Publication No. FHWA-HRT-06-103 (2006) 1-188.

[100] M. Schmidt, E. Fehling, T. Teichmann, K. Bunje, Durability of Ultra High Performance Concrete, in: T. and F. G. König, F. Dehn (Ed.), Proc. 6th Int. Symp. High Strength/High Perform. Concr., Leipzig, Germany, 2002: pp. 1367–1376.

[101] S. El-tawil, M. Alkaysi, A.E. Naaman, W. Hansen, Z. Liu, Development, Characterization and Applications of a Non Proprietary Ultra High Performance Concrete for Highway Bridges, Final Report RC-1637 (2016) 1-60.

[102] Z. Li, K. Afshinnia, P.R. Rangaraju, Effect of alkali content of cement on properties of high performance cementitious mortar, Con. Build Mat. Vol. 102 (2016) 631–639. https://doi.org/10.1016/j.conbuildmat.2015.10.110

[103] ASTM C1567, Standard Test Method for Determining the Potential Alkali-Silica Reactivity of Combinations of Cementitious Materials and Aggregate (Accelerated Mortar-Bar Method), (2021) 6 pp. https://doi.org/10.1520/C1567-13.2

[104] B. Möser, C. Pfeifer, J. Stark, Durability and microstructural development during hydration in ultra-high performance concrete, Concrete Repair, Rehabilitation and Retrofitting II, CRC Press (2009) 87–88.

[105] J. Sawab, I. Lim, Y. Mo, M. Li, H. Wang, M. Guimaraes, Ultra-High-Performance Concrete and Advanced Manufacturing Methods for Modular Construction, FY-ID-13-5282 CA-13-TX-UH-0606-0122, 2016.

[106] J. Pitroda, F.S. Umrigar, Evaluation of Sorptivity and Water Absorption of Concrete with Partial Replacement of Cement by Thermal Industry Waste (Fly Ash), Int. J. Eng. Innov. Technol. 2 (2013) 245–249.

[107] K.A. Snyder, The relationship between the formation factor and the diffusion coefficient of porous materials saturated with concentrated electrolytes: Theoretical and experimental considerations, Concr. Sci. Eng. 3 (2001) 216–224. https://doi.org/10.1017/CBO9781107415324.004.

[108] G.E. Archie, The Electrical Resistivity Log as an Aid in Determining Some Reservoir Characteristics, Trans. AIME. 146 (1942) 54–62. https://doi.org/10.2118/942054-G.

[109] R. Spragg, Y. Bu, K. Snyder, D. Bentz, J. Weiss, Electrical Testing of Cement-Based Materials: Role of Testing Techniques, Sample Conditioning, Publication FHWA/IN/JTRP-2013/28. Joint Transportation Research Program, Indiana Department of Transportation and Purdue University, West Lafayette, Indiana, 2013. https://doi.org/10.5703/1288284315230

[110] Y. Bu, J. Weiss, The influence of alkali content on the electrical resistivity and transport properties of cementitious materials, Cem. Concr. Compos. 51 (2014) 49–58. https://doi.org/10.1016/j.cemconcomp.2014.02.008.

[111] R. Spragg, L. Montanari, I. Varga, B.A. Graybeal, Using Formation Factor to Define the Durability of Ultra-High Performance Concrete, 2nd International Interactive Symposium on Ultra-High Performance Concrete (2019). DOI: 10.21838/uhpc.9696

[112] Proceq SA, The world's most accurate concrete surface resistivity meter, (2016).

[113] ASTM C1202, Standard Test Method for Electrical Indication of Concrete's Ability to Resist Chloride, (2019) 8. https://doi.org/10.1520/C1202-19.2.

[114] J.D. Shane, C.D. Aldea, N.F. Bouxsein, T.O. Mason, H.M. Jennings, S.P. Shah, Microstructural and pore solution changes induced by the rapid chloride permeability test measured by impedance spectroscopy, Concr. Sci. Eng. 1 (1999) 110–119.

[115] K.A. Riding, J.L. Poole, A.K. Schindler, M.C.G. Juenger, K.J. Folliard, Simplified concrete resistivity and rapid chloride permeability test method, ACI Mater. J. 105 (2008) 390–394.

[116] Z. Li, Proportioning and Properties of Ultra-High Performance Concrete Mixtures for Application in Shear Keys of Precast Concrete Bridges, Doctoral Thesis, Clemson University (2015).

[117] NT Build 492, Concrete, mortar and cement-based repair materials: Chloride migration coefficient from non-steady-state migration experiments, Measurement. (1999) 1–8. https://doi.org/UDC 691.32/691.53/691.54

[118] J.P. Vincler, T. Sanchez, V. Turgeon, D. Conciatori, L. Sorelli, A modified accelerated chloride migration tests for UHPC and UHPFRC with PVA and steel fibers, Cem. Conc. Res. 117 (2019) 38–44. https://doi.org/10.1016/j.cemconres.2018.12.006

[119] S.H.G. Mosavinejad, M. Alimohammad, J. Barandoust, A. Ghanizadeh, Electrical and microstructural analysis of UHPC containing short PVA fibers, Constr. Build. Mater. 235 (2020) 117448. https://doi.org/10.1016/j.conbuildmat.2019.117448.

[120] A. Rafiee, Computer Modeling and Investigation on the Steel Corrosion in Cracked Ultra High Performance Concrete, Doctoral Thesis, Kassel University (2012).

[121] M. Jooss, H.W. Reinhardt, Permeability and diffusivity of concrete as function of temperature, Cem. Conc. Res. 32 (2002) 1497–1504. https://doi.org/10.1016/S0008-8846(02)00812-8

[122] ASTM C1152, Standard Test Method for Acid-Soluble Chloride in Mortar and Concrete, ASTM International, 2020. https://doi.org/10.1520/C1152.

[123] J. Piérard, B. Dooms, N. Cauberg, Evaluation of Durability Parameters of UHPC Using Accelerated Lab Tests, (2012).

[124] M.A. Roux, N., Andrade, C., & Sanjuan, Experimental Study of Durability of Reactive Powder Concrete J. Mat. Civ. Eng. Vol. 8 No. 1 (1996) 1–6. https://doi.org/10.1061/(ASCE)0899-1561(1996)8:1(1)

[125] ASTM C1585, Standard Test Method for Measurement of Rate of Absorption of Water by Hydraulic Cement Concretes, (2013) 6. https://doi.org/10.1520/C1585-13.2.

[126] BS EN 12390-8, Testing hardened concrete. Depth of penetration of water under pressure, (2009).

[127] J. Castro, D. Bentz, J. Weiss, Effect of sample conditioning on the water absorption of concrete, Cem. Concr. Compos. 33 (2011) 805–813. https://doi.org/10.1016/j.cemconcomp.2011.05.007.

[128] S. Zhutovsky, R.D. Hooton, Role of sample conditioning in water absorption tests, Con. Build. Mat. Vol. 215 (2019) 918–924. https://doi.org/10.1016/j.conbuildmat.2019.04.249.

[129] E. Ghafari, H. Costa, E. Júlio, A. Portugal, Enhanced Durability of Ultra High Performance Concrete by Incorporating Supplementary Cementitious Materials, in: 2nd Int. Conf. Microstruct. Relat. Durab. Cem. Compos. 11-13 April 2012, Amsterdam, Netherlands, 2012: pp. 1–8.

[130] E.F. O'Neil, C.E. Dauriac, S.K. Gililand, Development of Reactive Powder Concrete (RPC) Products in the United States Construction Market, High- Strength Concr. An Int. Perspect. Pap. Present. Three Halfday Sess. ACI Conv. Montr. SP-167. (1997) 249–261.

[131] C.G. M. Schmidt, E. Fehling, Ultra High Performance Concrete (UHPC) Proceedings of the International Symposium on Ultra High Performance Concrete, 2004.

[132] P. Smarzewski, D. Barnat-hunek, Effect of Fiber Hybridization on Durability Related Properties of Ultra-High Performance Concrete, Int. J. Concr. Struct. Mater. 11 (2017) 315–325. https://doi.org/10.1007/s40069-017-0195-6.

[133] H. Giesche, Mercury Porosimetry : A General (Practical) Overview, Part. Part. Syst. Charact. 23 (2006) 9–19. https://doi.org/10.1002/ppsc.200601009.

[134] K. Tanaka, K. Kurumisawa, Development of technique for observing pores in hardened cement paste, Cem. Conc. Res. 32 (2002) 1435–1441. https://doi.org/10.1016/S0008-8846(02)00806-2

[135] A.B. Abell, K.L. Willis, D.A. Lange, Mercury Intrusion Porosimetry and Image Analysis of Cement-Based Materials, J. Coll. Inter. Sc. Vol. 44 No. 1 (1999) 39–44. https://doi.org/10.1006/jcis.1998.5986

[136] R.A. Cook, K.C. Hover, Mercury porosimetry of hardened cement pastes, Cem. Conc. Res. Vol. 29 No. 6 (1999) 933–943. https://doi.org/10.1016/S0008-8846(99)00083-6

[137] Sung-Hoon Kang, J.-H. Lee, S.-G. Hong, J. Moon, Microstructural Investigation of Heat-Treated Ultra-High Performance Concrete for Optimum Production, Materials (Basel) (2017). https://doi.org/10.3390/ma10091106

[138] M. Zhang, H. Li, Pore structure and chloride permeability of concrete containing nano-particles for pavement, Constr. Build. Mater. 25 (2011) 608–616. https://doi.org/10.1016/j.conbuildmat.2010.07.032

[139] D. Daniel, M. Kouril, N. Radka, P. Petr, P. Radka, Measurement of Chloride Permeability in UHPC by Accelerated Method, Solid State Phenomena Vol. 259 (2017) 80–84. https://doi.org/10.4028/www.scientific.net/SSP.259.80

[140] N. Roux, C. Andrade, M.A. Sanjuan, Experimental Study of Durability of Reactive Powder Concretes, J. Mat. Civ. Eng. Vol. 8, No. 1 (1996) 1–6.

[141] A. Carmen Andrade, E. Torroja, Long Term Carbonation of UHPC, RILEM-fib-AFGC Int. Symposium on Ultra-High Performance Fibre-Reinforced Concrete, UHPFRC 2013 – October 1-3, 2013, Marseille, France (2013) 249–256.

[142] ACI 201.2, A.C.I. 201.2R-16, Guide to Durable Concrete, ACI International, Farmington Hills, MI, 2016.

[143] Elzbieta Horszczaruk, Abrasion resistance of high-strength concrete in hydraulic structures, Wear Vol. 259 (2005) 62–69. https://doi.org/10.1016/j.wear.2005.02.079

[144] L.A. Sbia, A. Peyvandi, P. Soroushian, A.M. Balachandra, Optimization of ultra-high-performance concrete with nano- and micro-scale reinforcement, Cogent Eng. 43 (2014) 1–11. https://doi.org/10.1080/23311916.2014.990673

[145] E. J. Van Dam, Abrasion Resistance of Concrete and the Use of High Performance Concrete Railway Crossties, Master Thesis, Univ. Illinois Urbana-Champaign. (2014) 103.

[146] J. Sustersic, E. Mali, S. Urvancic, Erosion-Abrasion Resistance of Steel Fiber Reinforced Concrete, ACI Spec. Publ. 126. (1991) 729–744.

[147] ASTM C418, Standard Test Method for Abrasion Resistance of Concrete by Sandblasting, (2012) 4. https://doi.org/10.1520/C0418-12.

[148] ASTM C1138, Standard Test Method for Abrasion Resistance of Concrete (Underwater Method), (2019) 5. https://doi.org/10.1520/C1138M-19.2.

[149] ASTM C944, Standard Test Method for Abrasion Resistance of Concrete or Mortar Surfaces by the Rotating-Cutter Method, (2019) 5. https://doi.org/10.1520/C0944.

[150] M. Lee, Y. Wang, C. Chiu, A preliminary study of reactive powder concrete as a new repair material, Con. Build. Mat. Vol. 21 (2005) 182–189. https://doi.org/10.1016/j.conbuildmat.2005.06.024

[151] B. Graybeal, J. Tanesi, Durability of an Ultra high-Performance Concrete Durability of an Ultrahigh-Performance Concrete, J. Mat. Civ. Eng. Vol. 19 No. 10 (2007) 848-854. https://doi.org/10.1061/(ASCE)0899-1561(2007)19:10(848)

[152] S. Pyo, S. Yihune, H. Kim, Abrasion resistance of ultra high performance concrete incorporating coarser aggregate, Con. Build. Mat. Vol. 165 (2018) 11–16. https://doi.org/10.1016/j.conbuildmat.2018.01.036.

[153] M. Blais, P. & Couture, Precast, Prestressed Pedestrian World's First Reactive Powder Concrete Structure, PCI J. (1999) 60-71.

[154] J. Hola, K. Schabowicz, State-of-the-art non-destructive methods for diagnostic testing of building structures – anticipated development trends, Arch. Civ. Mech. Eng. 10 (2012) 5–18. https://doi.org/10.1016/s1644-9665(12)60133-2.

[155] D.. McCann, M.. Forde, Review of NDT methods in the assessment of concrete and masonry structures, NDT E Int. 34 (2001) 71–84. https://doi.org/10.1016/S0963-8695(00)00032-3.

[156] J.L. Rose, Ultrasonic guided waves in solid media, Cambridge University Press, 2014. https://doi.org/10.1017/CBO9781107273610

[157] Y. Dong, F. Ansari, Non-destructive testing and evaluation (NDT/NDE) of civil structures rehabilitated using fiber reinforced polymer (FRP) composites, in: Serv. Life Estim. Ext. Civ. Eng. Struct., Woodhead Publishing, 2010: pp. 193–222. https://doi.org/10.1016/B978-1-84569-398-5.50007-9.

[158] ASTM C1740, Standard Practice for Evaluating the Condition of Concrete Plates Using the Impulse-Response Method, (2016) 10.

[159] A.G. Davis, M.K. Lim, C.G. Petersen, Rapid and economical evaluation of concrete tunnel linings with impulse response and impulse radar non-destructive methods, NDT E Int. 38 (2005) 181–186. https://doi.org/10.1016/J.NDTEINT.2004.03.011.

[160] D. Streicher, D. Algernon, J. Wöstmann, M. Behrens, H. Wiggenhauser, Automated NDT of port- tensioned concrete bridges using imaging echo methods, in: 9th Eur. Conf. NDT, 2006: pp. 1–8.

[161] ASTM C1383, Standard Test Method for Measuring the P-Wave Speed and the Thickness of Concrete Plates Using the Impact-Echo Method, (2015) 11.

[162] G.E. Stavroulakis, Impact-echo from a unilateral interlayer crack. LCP–BEM modelling and neural identification, Eng. Fract. Mech. 62 (1999) 165–184.

https://doi.org/10.1016/S0013-7944(98)00107-6.

[163] J.-K. Zhang, W. Yan, D.-M. Cui, J.-K. Zhang, W. Yan, D.-M. Cui, Concrete Condition Assessment Using Impact-Echo Method and Extreme Learning Machines, Sensors. 16 (2016) 447. https://doi.org/10.3390/s16040447.

[164] ASTM B548, Standard Test Method for Ultrasonic Inspection of Aluminum-Alloy Plate for Pressure Vessels, (2017) 5.

[165] K. Hoegh, L. Khazanovich, H.T. Yu, Ultrasonic Tomography for Evaluation of Concrete Pavements, Transp. Res. Rec. J. Transp. Res. Board. 2232 (2011) 85–94. https://doi.org/10.3141/2232-09.

[166] J. Martin, K.. Broughton, A. Giannopolous, M.S.. Hardy, M.. Forde, Ultrasonic tomography of grouted duct post-tensioned reinforced concrete bridge beams, NDT E Int. 34 (2001) 107–113. https://doi.org/10.1016/S0963-8695(00)00035-9.

[167] S.R. Doctor, T.E. Hall, L.D. Reid, SAFT — the evolution of a signal processing technology for ultrasonic testing, NDT Int. 19 (1986) 163–167. https://doi.org/10.1016/0308-9126(86)90105-7.

[168] J.E. Michaels, Detection, localization and characterization of damage in plates with an in situ array of spatially distributed ultrasonic sensors, Smart Mater. Struct. 17 (2008) 035035. https://doi.org/10.1088/0964-1726/17/3/035035.

[169] I. Lawson, F.K. Quashie, Non-Destructive Evaluation of Concrete using Ultrasonic Pulse Velocity The design of a multisource americium-beryllium (Am-Be) neutron irradiation facility using MCNP for the neutronic performance calculation View project IAEA coordinated research project, 2011.

[170] ASTM C597, Standard Test Method for Pulse Velocity Through Concrete, (2016) 4.

[171] M.A. Kewalramani, R. Gupta, Concrete compressive strength prediction using ultrasonic pulse velocity through artificial neural networks, Autom. Constr. 15 (2006) 374–379. https://doi.org/10.1016/J.AUTCON.2005.07.003.

[172] P. Wiciak, G. Cascante, M.A. Polak, Sensor and Dimensions Effects in Ultrasonic Pulse Velocity Measurements in Mortar Specimens, Procedia Eng. 193 (2017) 409–416. https://doi.org/10.1016/J.PROENG.2017.06.231.

[173] G. Karaiskos, A. Deraemaeker, D.G. Aggelis, D. Van Hemelrijck, Monitoring of concrete structures using the ultrasonic pulse velocity method, Smart Mater. Struct. 24 (2015) 113001. https://doi.org/10.1088/0964-1726/24/11/113001.

[174] O.I. Lobkis, R.L. Weaver, Coda-Wave Interferometry in Finite Solids: Recovery of P - to- S Conversion Rates in an Elastodynamic Billiard, Phys. Rev. Lett. 90 (2003) 254302. https://doi.org/10.1103/PhysRevLett.90.254302.

[175] J. Zhu, J. Popovics, Non-contact detection of surface waves in concrete using an air-coupled sensor, AIP Conf. Proc. 615 (2002) 1261. https://doi.org/10.1063/1.1472940.

[176] E. Hwang, G. Kim, G. Choe, M. Yoon, N. Gucunski, J. Nam, Evaluation of concrete degradation depending on heating conditions by ultrasonic pulse velocity, Constr. Build. Mater. 171 (2018) 511–520. https://doi.org/10.1016/J.CONBUILDMAT.2018.03.178.

[177] F. Mielentz, Phased Arrays for Ultrasonic Investigations in Concrete Components, J. Nondestruct. Eval. 27 (2008) 23–33. https://doi.org/10.1007/s10921-008-0032-6.

[178] A. E2700, Standard Practice for Contact Ultrasonic Testing of Welds Using Phased Arrays, (2014) 9.

[179] A. V Bishko, A.A. Samokrutov, V.G. Shevaldykin, Ultrasonic Echo-Pulse Tomography of Concrete Using Shear Waves Low-Frequency Phased Antenna Arrays, 17th World Conference on Nondestructive Testing, Shanghai, China, 25-28 Oct 2008 (WCNDT 2008) 2008.

[180] H. Hu, X. Zhu, C. Wang, L. Zhang, X. Li, S. Lee, Z. Huang, R. Chen, Z. Chen, C. Wang, Y. Gu, Y. Chen, Y. Lei, T. Zhang, N. Kim, Y. Guo, Y. Teng, W. Zhou, Y. Li, A. Nomoto, S. Sternini, Q. Zhou, M. Pharr, F.L. di Scalea, S. Xu, Stretchable ultrasonic transducer arrays for three-dimensional imaging on complex surfaces, Sci. Adv. 4 (2018) eaar3979. https://doi.org/10.1126/sciadv.aar3979.

[181] A.A. Shah, Y. Ribakov, Non-linear ultrasonic evaluation of damaged concrete based on higher order harmonic generation, Mater. Des. 30 (2009) 4095–4102. https://doi.org/10.1016/J.MATDES.2009.05.009.

[182] P. Antonaci, C.L.E. Bruno, A.S. Gliozzi, M. Scalerandi, Monitoring evolution of compressive damage in concrete with linear and nonlinear ultrasonic methods, Cem. Concr. Res. 40 (2010) 1106–1113. https://doi.org/10.1016/J.CEMCONRES.2010.02.017.

[183] P. Antonaci, C.L.E. Bruno, P.G. Bocca, M. Scalerandi, A.S. Gliozzi, Nonlinear ultrasonic evaluation of load effects on discontinuities in concrete, Cem. Conc. Res. Vol. 40 No. 2 (2009). 340-346. https://doi.org/10.1016/j.cemconres.2009.09.014

[184] C.L.E. Bruno, A.S. Gliozzi, M. Scalerandi, P. Antonaci, Analysis of elastic nonlinearity using the scaling subtraction method, Phys. Rev. B - Condens. Matter Mater. Phys. 79 (2009) 1–13. https://doi.org/10.1103/PhysRevB.79.064108.

[185] M. Scalerandi, A.S. Gliozzi, C.L.E. Bruno, D. Masera, P. Bocca, A scaling method to enhance detection of a nonlinear elastic, Appl. Phys. Lett. 92 (2008) 101912. https://doi.org/10.1063/1.2890031

[186] T.R. Hay, L. Wei, J.L. Rose, T. Hayashi, Rapid Inspection of Composite Skin-Honeycomb Core Structures with Ultrasonic Guided Waves, J. Compos. Mater. 37 (2003) 929–939. https://doi.org/10.1177/0021998303037010005.

[187] H. Chan, B. Masserey, P. Fromme, High frequency guided ultrasonic waves for hidden fatigue crack growth monitoring in multi-layer model aerospace structures, Smart Mater. Struct. 24 (2015). https://doi.org/10.1088/0964-1726/24/2/025037.

[188] M. Hirao, H. Ogi, H. Fukuoka, Resonance EMAT system in sheet metals for acoustoelastic stress measurement, 64 (1993) 3198–3205.

[189] P. Wilcox, M. Lowe, P. Cawley, Omnidirectional guided wave inspection of large metallic plate structures using an EMAT array, IEEE Trans. Ultrason. Ferroelectr. Freq. Control. 52 (2005) 653–665. https://doi.org/10.1109/TUFFC.2005.1428048.

[190] S. Guide, Standard Guide for Electromagnetic Acoustic Transducers (EMATs) 1, Significance. 03 (2002) 1–8. https://doi.org/10.1520/E1774-12.1.4.

[191] C.B. Thring, Y. Fan, R.S. Edwards, Multiple focused EMAT designs for improved surface breaking defect characterization, AIP Conf. Proc. 1806 (2017). https://doi.org/10.1063/1.4974560.

[192] ASTM E1962, Standard Practice for Ultrasonic Examinations Using Electromagnetic Acoustic Transducer (EMAT) Techniques, Society. (2019) 10. https://doi.org/10.1520/E1816-12.

[193] J. Maser, A. Osanna, Y. Wang, C. Jacobsen, J. Kirz, S. Spector, B. Winn, D. Tennant, Soft X-ray microscopy with a cryo scanning transmission X-ray microscope: I. Instrumentation, imaging and spectroscopy, J. Microsc. 197 (2000) 68–79. https://doi.org/10.1046/j.1365-2818.2000.00630.x.

[194] A. Rundquist, C.G. Durfee, Z. Chang, C. Herne, S. Backus, M.M. Murnane, H.C. Kapteyn, Phase-matched generation of coherent soft X-rays, Science. 280 (1998) 1412–5. https://doi.org/10.1126/science.280.5368.1412.

[195] Z. Chang, A. Rundquist, H. Wang, M.M. Murnane, H.C. Kapteyn, Generation of Coherent Soft X Rays at 2.7 nm Using High Harmonics, Phys. Rev. Lett, Vol. 79 (1997). https://doi.org/10.1103/PhysRevLett.79.2967

[196] J.M. Rodenburg, A.C. Hurst, A.G. Cullis, B.R. Dobson, F. Pfeiffer, O. Bunk, C. David, K. Jefimovs, I. Johnson, Hard-X-Ray Lensless Imaging of Extended Objects, Phys. Rev. Lett. Vol. 98 (2007). https://doi.org/10.1103/PhysRevLett.98.034801

[197] E.J. Hall, D.J. Brenner, Cancer risks from diagnostic radiology, Br. J. Radiol. 81 (2008) 362–378. https://doi.org/10.1259/bjr/01948454.

[198] R.D. Owen, Portable linear accelerators for X-ray and electron-beam applications in civil engineering, NDT E Int. 31 (1998) 401–409. https://doi.org/10.1016/S0963-8695(98)00042-5.

[199] L. Peng, J. Bai, X. Zeng, Y. Zhou, Comparison of isotropic and orthotropic material

property assignments on femoral finite element models under two loading conditions, Med. Eng. Phys. 28 (2006) 227–233. https://doi.org/10.1016/J.MEDENGPHY.2005.06.003.

[200] T.S. Oesch, E.N. Landis, D.A. Kuchma, Conventional Concrete and UHPC Performance–Damage Relationships Identified Using Computed Tomography, J. Eng. Mech. 142 (2016) 04016101. https://doi.org/10.1061/(ASCE)EM.1943-7889.0001168.

[201] T. Ruan, A. Poursaee, Fiber-Distribution Assessment in Steel Fiber–Reinforced UHPC Using Conventional Imaging, X-Ray CT Scan, and Concrete Electrical Conductivity, J. Mater. Civ. Eng. 31 (2019) 04019133. https://doi.org/10.1061/(ASCE)MT.1943-5533.0002733.

[202] T. Oesch, E. Landis, D. Kuchma, A methodology for quantifying the impact of casting procedure on anisotropy in fiber-reinforced concrete using X-ray CT, Mater. Struct. Constr. 51 (2018) 1–13. https://doi.org/10.1617/s11527-018-1198-8.

[203] H. Saleh, R. Livingston, Experimental Evaluation of a Portable Neutron-Based Gamma-Spectroscopy System for Chloride Measurements in Reinforced Concrete, J. Radioanal. Nucl. Chem. 244 (2000) 367–371. https://doi.org/10.1023/A:1006787626016.

[204] K. Karhunen, A. Seppänen, A. Lehikoinen, P.J.M. Monteiro, J.P. Kaipio, Electrical Resistance Tomography imaging of concrete, Cem. Concr. Res. 40 (2010) 137–145. https://doi.org/10.1016/J.CEMCONRES.2009.08.023.

[205] F. Wenner, A method for measuring Earth resistivity, Bulletin of the Bureau of Standards, (1915) 469-478.

[206] B. Shafei, B. Phares, M. Najimi, T. Hosteng, Laboratory and Field Evaluation of an Alternative UHPC Mix and Associated UHPC Bridge, Ames, IA, 2019. http://publications.iowa.gov/31049/1/TR-684_Final Report_Laboratory_and_field_eval_of_alternative_UHPC_mix_and_bridge_w_cvr.pdf.

[207] B. Elsener, C. Andrade, J. Gulikers, R. Polder, M. Raupach, Half-cell potential measurements—Potential mapping on reinforced concrete structures, Mater. Struct. 36 (2003) 461–471. https://doi.org/10.1007/BF02481526.

[208] ASTM C876, ASTM C 876 Standard Test Method for Corrosion Potentials of Uncoated Reinforcing Steel in Concrete, (2016) 8. https://doi.org/10.1520/C0876-15.2.

[209] M.F. Md Jaafar, H. Mohd Saman, N.F. Ariffin, K. Muthusamy, S. Wan Ahmad, N. Ismail, Corrosion monitoring on steel reinforced nano metaclayed-UHPC towards strain modulation using fiber Bragg grating sensor, in: IOP Conf. Ser. Mater. Sci. Eng., Institute of Physics Publishing, 2018. https://doi.org/10.1088/1757-899X/431/12/122006.

[210] B. Elsener, O. Klinghoffer, T. Frolund, E. Rislund, Y. Schiegg, H. Böhni, Assessment of reinforcement corrosion by means of galvanostatic pulse technique, Int.Conf. Repair of

Concrete Structures, Svolvær, Norway (1997) 1-10.

[211] ASTM C876-91, Standard test method for half-cell potentials of uncoated reinforcing steel in concrete, (2015) 8.

[212] J.M. Torrents, A. Blanco, P. Pujadas, A. Aguado, P. Juan-García, M.Á. Sánchez-Moragues, Inductive method for assessing the amount and orientation of steel fibers in concrete, Mater. Struct. Constr. 45 (2012) 1577–1592. https://doi.org/10.1617/s11527-012-9858-6.

[213] H. Kim, D. Kang, S.J. Oh, C. Joo, Nondestructive evaluation on dispersion of steel fibers in UHPC using THz electromagnetic waves, Constr. Build. Mater. 172 (2018) 293–299. https://doi.org/10.1016/j.conbuildmat.2018.03.238.

[214] A. Robert, Dielectric permittivity of concrete between 50 Mhz and 1 Ghz and GPR measurements for building materials evaluation, J. Appl. Geophys. 40 (1998) 89–94. https://doi.org/10.1016/S0926-9851(98)00009-3.

[215] C. Maierhofer, Nondestructive evaluation of concrete infrastructure with ground penetrating radar, J. Mater. Civ. Eng. 15 (2003) 287–297. https://doi.org/10.1061/(ASCE)0899-1561(2003)15:3(287).

[216] L.D. Favro, R.L. Thomas, X. Han, Z. Ouyang, G. Newaz, D. Gentile, Sonic infrared imaging of fatigue cracks, Int. J. Fatigue. (2001). https://doi.org/10.1016/s0142-1123(01)00151-7.

[217] ASTM C1609, Standard Test Method for Flexural Performance of Fiber-Reinforced Concrete (Using Beam With Third-Point Loading), (2019). https://doi.org/10.1520/C1609_C1609M-19A.

[218] ACI Committee 318, Building Code Requirements for Structural Concrete, (2019).

[219] Florida Department of Transportation, Prepackaged Ultra-High-Performance Concrete (UHPC) Section 927, (2019).

[220] Idaho Department of Transportation, S501-40A SP Bridge, UHPC (Ultra High Performance Fiber Reinforced Concrete), (n.d.).

[221] Colorado Department of Transportation, Revision of Section 601 Ultra High Performacne Concrete, (2018).

[222] CSA A23.3, Design of Concrete Structures (Draft), (2018).

[223] E. Brühwiler, Recommendation: Ultra-High Performance Fibre Reinforced Cement-based composites (UHPFRC), Constr. Mater. Dimens. Appl. Lausanne, Switz. (2016).

[224] NMDOT Section 512-A, Special Provisions for Ultra High Performance Concrete, (2018).

[225] DelDOT 618XXX, Ultra High Performance Concrete Overlay, 2018.

[226] S. Qian, V.C. Li, Simplified inverse method for determining the tensile properties of strain hardening cementitious composites (SHCC), J. Adv. Concr. Technol. 6 (2008) 353–363. https://doi.org/10.3151/jact.6.353.

[227] F. Baby, B.A. Graybeal, P. Marchand, F. Toutlemonde, Proposed flexural test method and associated inverse analysis for UHPFRC, ACI Mater J. 109 (2012) 545–555.

[228] T. Kanakubo, Tensile characteristics evaluation method for ductile fiber-reinforced cementitious composites, J. Adv. Concr. Technol. 4 (2006) 3–17. https://doi.org/10.3151/jact.4.3.

[229] F. Baby, B. Graybeal, P. Marchand, F. Toutlemonde, UHPFRC tensile behavior characterization: Inverse analysis of four-point bending test results, Mater. Struct. Constr. 46 (2013) 1337–1354. https://doi.org/10.1617/s11527-012-9977-0.

[230] N.J. Carino, H.S. Lew, Re-examination of the Relation Between Splitting Tensile and Compressive Strength of Normal Weight Concrete, ACI J. 79 (1982) 214–218.

[231] K.A. Riding, J.L. Pool, A.K. Schindler, M.C.G. Juenger, K.J. Folliard, Statistical Determination of Cracking Probabiliby for Mass Concrete, J. Mater. Civ. Eng. 26 (2014).

[232] J.M. Raphael, Tensile Strength of Concrete, ACI J. 81 (1984) 158–165.

[233] AFNOR, Concrete - Ultra-High Performance Fiber-Reinforced Concrete - Specifications, Performance, Production, and Conformity, (2016).

[234] CSA A23.1:19, Concrete materials and methods of concrete construction, (2019) 379–409.

[235] ASTM C136, Standard Test Method for Sieve Analysis of Fine and Coarse Aggreate, (2019) 5.

[236] ASTM C31, Standard Practice for Making and Curing Concrete Test Specimens in the Field, (2021) 1–8. https://doi.org/10.1520/C0031.

[237] S. Yousuf, P. Shafigh, Z. Ibrahim, H. Hashim, M. Panjehpour, Crossover Effect in Cement-Based Materials: A Review, Appl. Sci. 9 (2019). https://doi.org/doi:10.3390/app9142776.

[238] ASTM C469, Standard Test Method for Static Modulus of Elasticity and Poisson's Ratio of Concrete in Compression, West Conchohocken, PA, United States, 2014.

[239] V.Y. Garas, K.E. Kurtis, L.F. Kahn, Creep of UHPC in tension and compression: Effect of thermal treatment, Cem. Concr. Compos. 34 (2012) 493–502. https://doi.org/https://doi.org/10.1016/j.cemconcomp.2011.12.002.

[240] ASTM C1365, Standard Test Method for Determination of the Proportion of Phases in Portland Cement and Portland-Cement Clinker Using X-Ray Powder Diffraction Analysis, West Conchohocken, PA, United States, 2018. https://doi.org/10.1520/C1365-18.

[241] ASTM C802, Standard Practice for Conducting an Interlaboratory Test Program to Determine the Precision of Test Methods for Construction Materials 1, (2021) 1–24. https://doi.org/10.1520/C0802-14.2.

[242] K.K. Walsh, N.J. Hicks, E.P. Steinberg, H.H. Hussein, A.A. Semendary, Fiber Orientation in Ultra-High-Performance Concrete Shear Keys of Adjacent-Box-Beam Bridges, ACI Mater. J. 115 (2018) 227–238.

[243] Ç. Yalçınkaya, O. Çopuroğlu, Elephant skin formation on UHPC surface: Effects of climatic condition and blast furnace slag content, Constr. Build. Mater. 268 (2021). https://doi.org/https://doi.org/10.1016/j.conbuildmat.2020.121126.

[244] Miguel A. Carbonell Muñoz, Devin K. Harris, Theresa M. Ahlborn, David C. Froster, Bond Performance between Ultra-high-Performance Concrete and Normal-Strength Concrete, J. Mater. Civ. Eng. 26 (2014) 4014031. https://doi.org/10.1061/(ASCE)MT.1943-5533.0000890.

[245] P. Ganesh, A. Ramachandra Murthy, Simulation of surface preparations to predict the bond behaviour between normal strength concrete and ultra-high performance concrete, Constr. Build. Mater. 250 (2020). https://doi.org/https://doi.org/10.1016/j.conbuildmat.2020.118871

[246] B. Graybeal, Design and construction of field-cast UHPC connections, FHWA-HRT-14-084 (2014) 1-36.

[247] ASTM C595, Standard Specification for Blended Hydraulic Cements, ASTM Int. (2019) 1–8. https://doi.org/10.1520/C0595.

[248] ASTM C1583, Standard Test Method for Tensile Strength of Concrete Surfces and the Bond Strength or Tensile Strength of Concrete Repair and Overlay Materials by Direct Tension (Pull-off Method), West Conchohocken, PA, United States, 2020.

[249] J.C. Flietstra, Creep and shrinkage behavior of ultra high-performance concrete under compressive loading with varying curing regimes, Master's Thesis, Michigan Technological University, 2011. https://doi.org/https://doi.org/10.37099/mtu.dc.etds/236

[250] G.M. Gapinski, J. Scanlon, Silica Fume, (2006). https://www.norchem.com/pdf/technical-papers-articles-gapinksi-scanlon.pdf

[251] M. Kakizaki, H. Edahiro, T. Tochigi, T. Niki, Effect of Mixing Method on Mechanical Properties and Pore Structure of Ultra High-Strength Concrete, ACI Special Publication 132 (1992) 997–1015.

[252] ACI 363, State of the Art Report on High Strength Concrete, American Concrete Institute, Farmington Hills, MI, 1992.

[253] J. Ma, F. Dehn, N.V. Tue, M. Orgass, D. Schmidt, Comparative Investigations on Ultra-High Performance Concrete with and without Coarse Aggregates, in: M. Schmidt, E. Fehling, C. Geisenhansllüke (Eds.), Proceedings, Int. Symp. Ultra-High Perofrmance Concr., kassel university press GmbH, Kassel, Germany, 2004: pp. 205–212.

[254] A. Mohebbi, B. Graybeal, Prestress loss model for ultra-high performance concrete, Eng. Struct. 252 (2022). https://doi.org/https://doi.org/10.1016/j.engstruct.2021.113645.

[255] ASTM C150-18, Standard Specification for Portland Cement, ASTM Int. (2007) 6–7.

[256] ASTM C989, Standard Specification for Slag Cement for Use in Concrete and Mortars, (2018) 1–7. https://doi.org/10.1520/C0989.

[257] ASTM C1240, Standard Specification for Silica Fume Used in Cementitious Mixtures, West Conshohocken, PA; ASTM Int. (2015) 1–7. https://doi.org/10.1520/C1240-14.2.

[258] ASTM C511, Standard Specification for Mixing Rooms, Moist Cabinets, Moist Rooms, and Water Storage Tanks Used in the Testing of Hydraulic Cements and Concretes, ASTM Int. (2019) 1–3. https://doi.org/10.1520/C0511-19.2.

[259] ASTM C305, Standard Practice for Mechanical Mixing of Hydraulic Cement Pastes and Mortars of Plastic Consistency, (2020) 1–3.

[260] ASTM C215, Standard Test Method for Fundamental Transverse, Longitudinal, and Torsional Resonant Frequencies of Concrete Specimens, (2019) 1–7.

[261] Z. Sun, G.W. Scherer, Pore size and shape in mortar by thermoporometry, Cem. Concr. Res. 40 (2010) 740–751. https://doi.org/10.1016/j.cemconres.2009.11.011.

[262] B. Li, J. Mao, T. Nawa, T. Han, Mesoscopic damage model of concrete subjected to freeze-thaw cycles using mercury intrusion porosimetry and differential scanning calorimetry (MIP-DSC), Constr. Build. Mater. 147 (2017) 79–90. https://doi.org/10.1016/j.conbuildmat.2017.04.136.

[263] D.N. Winslow, S. Diamond, A Mercury Porosimetry Study of the Evolution of Porosity in Portland Cement : Technical Publication. Publication FHWA/IN/JHRP-69/31. Joint Highway Research Project, Indiana Department of Transportation and Purdue University, West Lafayette, Indiana, 1969. https://doi.org/10.5703/1288284314510

[264] H.G. Midgley, J.M. Illston, Some comments on the microstructure of hardened cement pastes, Cem. Concr. Res. 13 (1983) 197–206. https://doi.org/10.1016/0008-8846(83)90102-3.

[265] A.C.A. Muller, K.L. Scrivener, A reassessment of mercury intrusion porosimetry by

comparison with 1 H NMR relaxometry, Cem. Concr. Res. 100 (2017) 350–360. https://doi.org/10.1016/j.cemconres.2017.05.024.

[266] M. Yousuf, S., Shafigh, P., Ibrahim, Z., Hashim, H., & Panjehpour, Crossover Effect in Cement-Based Materials: A Review, Appl. Sci. 9 (2019).

[267] J. Tanesi, B. Graybeal, M. Simon, M. di Prisco, R. Felicetti, G. Plizzari, Effects of curing procedure on freeze–thaw durability of ultra-high performance concrete, Proc., Int. RILEM Symp., Fiber Reinf. Concr. (2004) 603–613.

[268] C. Foy, M. Pigeon, N. Banthia, Freeze-thaw durability and deicer salt scaling resistance of a 0.25 water-cement ratio concrete, Cem. Concr. Res. 18 (1988) 604–614.

[269] S. Jacobsen, E.J. Sellevold, Self healing of high strength concrete after deterioration by freeze/thaw, Cem. Concr. Res. 26 (1996) 55–62. https://doi.org/10.1016/0008-8846(95)00179-4.

[270] M.-G. Lee, Preliminary study for strength and freeze-thaw durability of microwave-and steam-cured concrete, J. Mater. Civ. Eng. 19 (2007) 972–976. https://doi.org/10.1061/(ASCE)0899-1561(2007)19.

[271] M.J. Lee, M.G. Lee, Y.C. Wang, Y. Huang, W.C. Wang, Study of steam and microwave curing of concretes containing slag, fly ash, or silica fume, J. Test. Eval. 43 (2015) 248–254. https://doi.org/10.1520/JTE20140107.

[272] B. Graybeal, J. Tanesi, Durability of an Ultra high-Performance Concrete, J. Mater. Civ. Eng. 19 (2007) 848–854. https://doi.org/10.1061/(asce)0899-1561(2007)19:10(848).

[273] M. An, Y. Wang, Z. Yu, Damage mechanisms of ultra-high-performance concrete under freeze–thaw cycling in salt solution considering the effect of rehydration, Constr. Build. Mater. 198 (2019) 546–552. https://doi.org/10.1016/j.conbuildmat.2018.11.175.

[274] P. Halamickova, R.J. Detwiler, D.P. Bentz, E.J. Garboczi, Water Permeability and Chloride Ion Diffusion in portland cement mortars: relationship to sand content and critical pore diameter, Cem. Concr. Res. 25 (1995) 790–802.

[275] A. Arora, M. Aguayo, H. Hansen, C. Castro, E. Federspiel, B. Mobasher, N. Neithalath, Microstructural packing- and rheology-based binder selection and characterization for Ultra-high Performance Concrete (UHPC), Cem. Concr. Res. 103 (2018) 179–190. https://doi.org/10.1016/j.cemconres.2017.10.013.

[276] P.P. Li, H.J.H. Brouwers, W. Chen, Q. Yu, Optimization and characterization of high-volume limestone powder in sustainable ultra-high performance concrete, Constr. Build. Mater. 242 (2020) 118112. https://doi.org/10.1016/j.conbuildmat.2020.118112.

[277] S.S. E. Fehling, M. Schmidt, Ultra High Performance Concrete (UHPC), 2008.

[278] Y. Cao, C. Gehlen, U. Angst, L. Wang, Z. Wang, Y. Yao, Critical chloride content in reinforced concrete — An updated review considering Chinese experience, Cem. Concr. Res. 117 (2019) 58–68. https://doi.org/10.1016/j.cemconres.2018.11.020.

[279] U. Angst, B. Elsener, C.K. Larsen, Ø. Vennesland, Critical chloride content in reinforced concrete - A review, Cem. Concr. Res. 39 (2009) 1122–1138. https://doi.org/10.1016/j.cemconres.2009.08.006.

[280] I.G. Ogunsanya, C.M. Hansson, Detection of the critical chloride threshold of carbon steel rebar in synthetic concrete pore solutions, RILEM Tech. Lett. 3 (2018) 75–83. https://doi.org/10.21809/rilemtechlett.2018.70.

[281] C. Boschmann Käthler, S.L. Poulsen, H.E. Sørensen, U.M. Angst, Investigations of accelerated methods for determination of chloride threshold values for reinforcement corrosion in concrete, Sustain. Resilient Infrastruct. (2021). https://doi.org/10.1080/23789689.2021.1905221.

[282] R. Pernicová, Chloride Transport in Ultra High Performance Concrete, Int. J. Mater. Metall. Eng. 8 (2014) 1192–1195.

[283] C. Chalhoub, R. François, M. Carcasses, Critical chloride threshold values as a function of cement type and steel surface condition, Cem. Concr. Res. 134 (2020) 1–18. https://doi.org/10.1016/j.cemconres.2020.106086.

[284] ACI 318-19, Building Code Requirements for Structural Concrete (ACI 318-19) and Commentary on Building Code Requirements for Structural Concrete (ACI 318R-19), 2019.

[285] ACI 222R, Guide to Protection of Metals in Concrete Against Corrosion, Farmington Hills, MI, 2019.

[286] U.A. Birnin-Yauri, F.P. Glasser, Friedel's salt, Ca2Al (OH) 6 (Cl, OH)· 2H2O: its solid solutions and their role in chloride binding, Cem. Concr. Res. 28 (1998) 1713–1723.

[287] G.K. Glass, N.R. Buenfeld, The influence of chloride binding on the chloride induced corrosion risk in reinforced concrete, Corros. Sci. 42 (2000) 329–344. https://doi.org/10.1016/S0010-938X(99)00083-9.

[288] FDOT, Florida Department of Transportation (FDOT), FDOT, Standard Specifications for Road and Bridge Construction, (2021).

[289] ASTM C1218, Standard Test Method for Water-Soluble Chloride in Mortar and Concrete, West Conshohocken, PA; ASTM Int. (2020) 9–11. https://doi.org/10.1520/C1218.

[290] FM 5-516, Florida Method of Test For Determining Low-Levels of Chloride in Concrete and Raw Materials, (2018) 1–11. https://fdotwww.blob.core.windows.net/sitefinity/docs/default-

source/materials/materials/administration/resources/library/publications/fstm/methods/fm5-516.pdf?sfvrsn=58645143_2.

[291] ASTM C33, Standard Specification for Concrete Aggregates, (2018) 1–8. https://doi.org/10.1520/C0033.

[292] E.D. Rodríguez, L. Soriano, J. Payá, M.V. Borrachero, J.M. Monzó, Increase of the reactivity of densified silica fume by sonication treatment, Ultrason. Sonochem. 19 (2012) 1099–1107. https://doi.org/10.1016/j.ultsonch.2012.01.011.

[293] E.G. Moffatt, M.D.A. Thomas, A. Fahim, R.D. Moser, Performance of ultra-high-performance concrete in Harsh marine environment for 21 years, ACI Mater. J. 117 (2020) 105–112. https://doi.org/10.14359/51727022.

[294] M.N. Haque, O.A. Kayyali, Free and water soluble chloride in concrete, Cem. Concr. Res. 25 (1995) 531–542. https://doi.org/10.1016/0008-8846(95)00042-B.

[295] M.D.A. Thomas, E.G. Moffatt, The Performance of Concrete in a Marine Environment, in: Proc. Sixth Int. Conf. Durab. Concr. Struct., Leeds, UK, 2018: pp. 1–15.

[296] R.S. Mikhail, S.A. Selim, Adsorption of organic vapors in relation to the pore structure of hardened Portland cement pastes, Spec. Report-Highw. Res. Board 90-95. (1966) 123–134.

[297] J.I. Escalante-García, J.H. Sharp, The microstructure and mechanical properties of blended cements hydrated at various temperatures, Cem. Concr. Res. 31 (2001) 695–702. https://doi.org/10.1016/S0008-8846(01)00471-9.

[298] L. Fan, W. Meng, L. Teng, K.H. Khayat, Effects of lightweight sand and steel fiber contents on the corrosion performance of steel rebar embedded in UHPC, Constr. Build. Mater. 238 (2020) 117709. https://doi.org/10.1016/j.conbuildmat.2019.117709.

[299] M. Horňáková, P. Lehner, Relationship of surface and bulk resistivity in the case of mechanically damaged fibre reinforced red ceramic waste aggregate concrete, Materials (Basel). 13 (2020) 1–13. https://doi.org/10.3390/ma13235501.

[300] V. Afroughsabet, L. Biolzi, T. Ozbakkaloglu, High-performance fiber-reinforced concrete: a review, Springer US, 2016. https://doi.org/10.1007/s10853-016-9917-4.

[301] R.P. Spragg, B. Graybeal, Spragg, Robert, et al. Electrical Resistivity Testing to Rapidly Assess the Durability of UHPC-Class Materials, No FHWA-HRT-21-095. (2022).

[302] H. Ma, Mercury intrusion porosimetry in concrete technology: Tips in measurement, pore structure parameter acquisition and application, J. Porous Mater. 21 (2014) 207–215. https://doi.org/10.1007/s10934-013-9765-4.

[303] S. Abbas, M.L. Nehdi, M.A. Saleem, Ultra-High Performance Concrete : Mechanical

Performance , Durability , Sustainability and Implementation Challenges, Int. J. Concr. Struct. Mater. 10 (2016) 271–295. https://doi.org/10.1007/s40069-016-0157-4.

[304] M.G. Sohail, R. Kahraman, N. Al Nuaimi, B. Gencturk, W. Alnahhal, Durability characteristics of high and ultra-high performance concretes, J. Build. Eng. 33 (2021) 101669. https://doi.org/10.1016/j.jobe.2020.101669.

[305] S. Diamond, Mercury porosimetry. An inappropriate method for the measurement of pore size distributions in cement-based materials, Cem. Concr. Res. 30 (2000) 1517–1525. https://doi.org/10.1016/S0008-8846(00)00370-7.

[306] J.B. Elise Berodier, and A.C.A. Muller, Mercury intrusion porosimetry, in: A Pract. Guid. to Microstruct. Anal. Cem. Mater., 2017: pp. 419–444. https://doi.org/10.1201/b19074.

[307] ACI Committee 201, Guide to Durable Concrete, American Concrete Institute, 2016.

[308] J. Chen, J. Wang, R. He, H. Shu, C. Fu, Experimental study on effective chloride diffusion coefficient of cement mortar by different electrical accelerated measurements, Crystals. 11 (2021) 1–13. https://doi.org/10.3390/cryst11030240.

[309] F.J. Luna, Fernández, M.C. Alonso, The influence of curing and aging on chloride transport through ternary blended cement concrete, Mater. Constr. 68 (2018). https://doi.org/10.3989/mc.2018.11917.

[310] E. Vivas, A.J. Boyd, H.R. Hamilton, M. Bergin, Permeability of Concrete - Comparison of Conductivity and Diffusion Methods, FDOT Final Report, 2007.

[311] ASTM C33, Standard Specification for Concrete Aggregates, Constr. Build. Mater. 25 (2011) 2472–2479. https://doi.org/10.1016/j.conbuildmat.2010.11.069.

[312] F. Saint-Pierre, A. Philibert, B. Giroux, P. Rivard, Concrete Quality Designation based on Ultrasonic Pulse Velocity, Constr. Build. Mater. 125 (2016) 1022–1027. https://doi.org/10.1016/j.conbuildmat.2016.08.158.

[313] D.J. McClements, P. Fairley, Ultrasonic pulse echo reflectometer, Ultrasonics. 29 (1991) 58–62. https://doi.org/10.1016/0041-624X(91)90174-7.

[314] A.M.T. Hassan, S.W. Jones, Non-destructive testing of ultra high performance fibre reinforced concrete (UHPFRC): A feasibility study for using ultrasonic and resonant frequency testing techniques, Constr. Build. Mater. 35 (2012) 361–367. https://doi.org/10.1016/J.CONBUILDMAT.2012.04.047.

[315] V.G. Haach, F.C. Ramirez, Qualitative assessment of concrete by ultrasound tomography, Constr. Build. Mater. 119 (2016) 61–70. https://doi.org/10.1016/J.CONBUILDMAT.2016.05.056.

[316] A.N. AbdAlla, M.A. Faraj, F. Samsuri, D. Rifai, K. Ali, Y. Al-Douri, Challenges in

improving the performance of eddy current testing: Review, Meas. Control (United Kingdom). 52 (2019) 46–64. https://doi.org/10.1177/0020294018801382.

[317] N.P. de Alcantara, F.M. da Silva, M.T. Guimarães, M.D. Pereira, Corrosion Assessment of Steel Bars Used in Reinforced Concrete Structures by Means of Eddy Current Testing, Sensors 2016, Vol. 16, Page 15. 16 (2015) 15. https://doi.org/10.3390/S16010015.

[318] P. Ripka, A. Lewis, Eddy curent metal detectors - pulse vs. CW, J. Electr. Eng. 57 (2006) 175–177.

[319] K.H. Lee, M.K. Baek, I.H. Park, Estimation of Deep Defect in Ferromagnetic Material by Low Frequency Eddy Current Method, IEEE Trans. Magn. 48 (2012) 3965–3968. https://doi.org/10.1109/TMAG.2012.2202643.

[320] C.G. Berrocal, K. Hornbostel, M.R. Geiker, I. Löfgren, K. Lundgren, D.G. Bekas, Electrical resistivity measurements in steel fibre reinforced cementitious materials, Cem. Concr. Compos. 89 (2018) 216–229. https://doi.org/10.1016/J.CEMCONCOMP.2018.03.015.

[321] S. Cleven, M. Raupach, T. Matschei, Electrical Resistivity of Steel Fibre-Reinforced Concrete—Influencing Parameters, Mater. 2021, Vol. 14, Page 3408. 14 (2021) 3408. https://doi.org/10.3390/MA14123408.

[322] A.O.S. Solgaard, M. Geiker, C. Edvardsen, A. Küter, Observations on the electrical resistivity of steel fibre reinforced concrete, Mater. Struct. Constr. 47 (2014) 335–350. https://doi.org/10.1617/S11527-013-0064-Y/FIGURES/10.

[323] S. Fericean, R. Droxler, New noncontacting inductive analog proximity and inductive linear displacement sensors for industrial automation, IEEE Sens. J. 7 (2007) 1538–1545. https://doi.org/10.1109/JSEN.2007.908232.

[324] Y. Wu, Z. Tian, J. Xu, Y. Cao, C. Yang, The effect of particle shape in particle detection using inductive sensors, Rev. Sci. Instrum. 90 (2019) 105002. https://doi.org/10.1063/1.5099300.

[325] L. Ferrara, M. Faifer, S. Toscani, A magnetic method for non destructive monitoring of fiber dispersion and orientation in steel fiber reinforced cementitious composites-part 1: Method calibration, Mater. Struct. Constr. 45 (2012) 575–589. https://doi.org/10.1617/S11527-011-9793-Y/FIGURES/14.

[326] J. Torrents, A. Blanco, P. Pujadas, A. Aguado, P. Juan-Garcia, M. Angel Sanchez-Moragues, Inductive method for assessing the amount and orientation of steel fibers in concrete, Mat. & Struct. Vol. 45 (2012) 1577-1592. https://doi.org/10.1617/s11527-012-9858-6

[327] U.M. Jow, M. Ghovanloo, Geometrical design of a scalable overlapping planar spiral coil array to generate a homogeneous magnetic field, IEEE Trans. Magn. 49 (2013) 2933–

2945. https://doi.org/10.1109/TMAG.2012.2235181.

[328] Y.P. Su, X. Liu, S.Y.R. Hui, Mutual inductance calculation of movable planar coils on parallel surfaces, IEEE Trans. Power Electron. 24 (2009) 1115–1123. https://doi.org/10.1109/TPEL.2008.2009757.

[329] E.B. Rosa, F.W. Grover, Formulas and Tables for the Calculation of Mutual and Self-Inductance, Bulletin of the Bureau of Standards Vol. 8 No. 1 (1912). https://dx.doi.org/10.6028/bulletin.185

[330] S.I. Babic, C. Akyel, Calculating mutual inductance between circular coils with inclined axes in air, IEEE Trans. Magn. 44 (2008) 1743–1750. https://doi.org/10.1109/TMAG.2008.920251.

[331] V.G. Gmbh, Industrial Computer Tomography-A Universal Inspection Tool, Conf. Nondestruct. Test. Proceeding (2008) 25–28.

[332] R.M. Haralick, S.R. Sternberg, X. Zhuang, Image Analysis Using Mathematical Morphology, IEEE Trans. Pattern Anal. Mach. Intell. PAMI-9 (1987) 532–550. https://doi.org/10.1109/TPAMI.1987.4767941.

[333] J. Shen, S. Castan, Towards the unification of band-limited derivative operators for edge detection, Signal Processing. 31 (1993) 103–119. https://doi.org/10.1016/0165-1684(93)90060-N.

APPENDIX A: TEST RESULTS FROM SAMPLES TESTED USING MODIFIED DOUBLE PUNCH, ASTM C1609, AND DIRECT TENSION

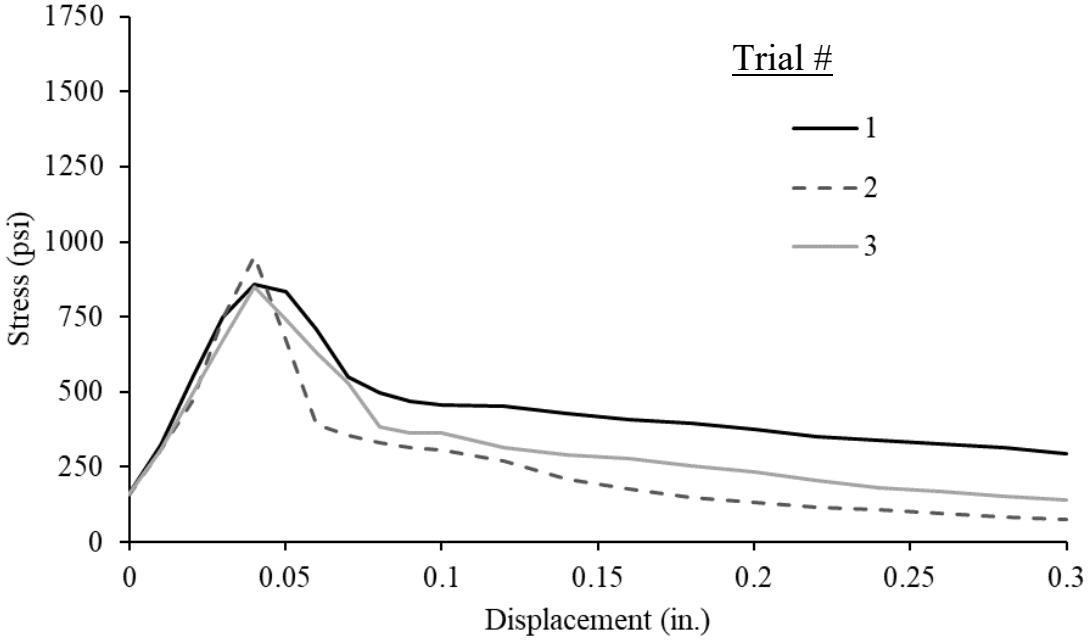

Figure A-1: Double-punch results for 1% straight fiber specimens

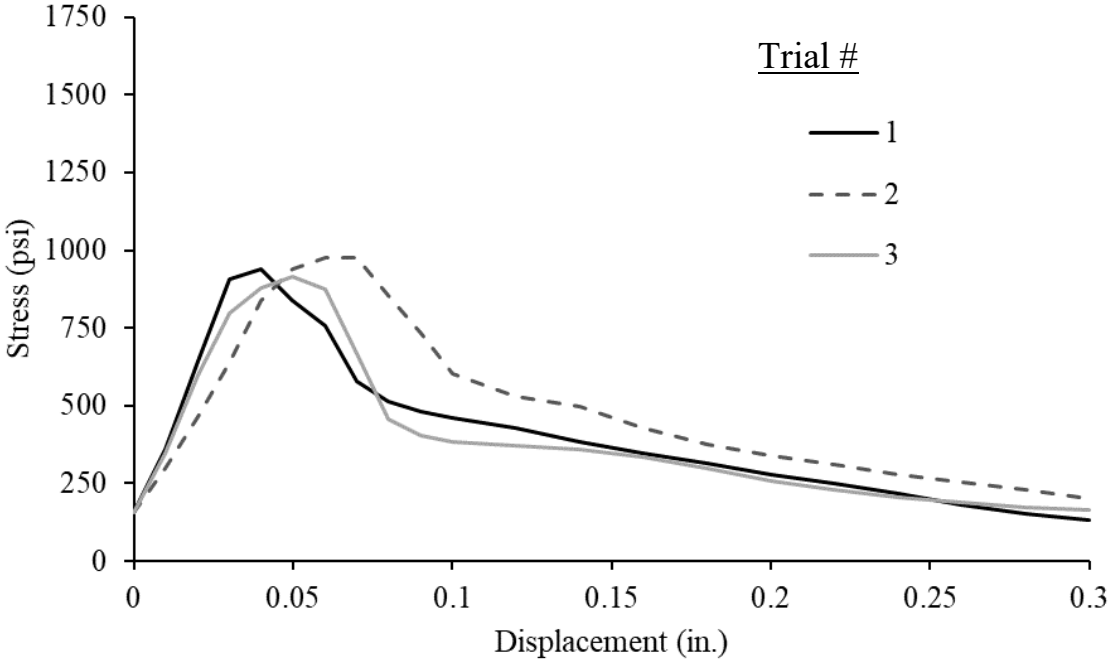

Figure A-2: Double-punch results for 1.5% straight fiber specimens

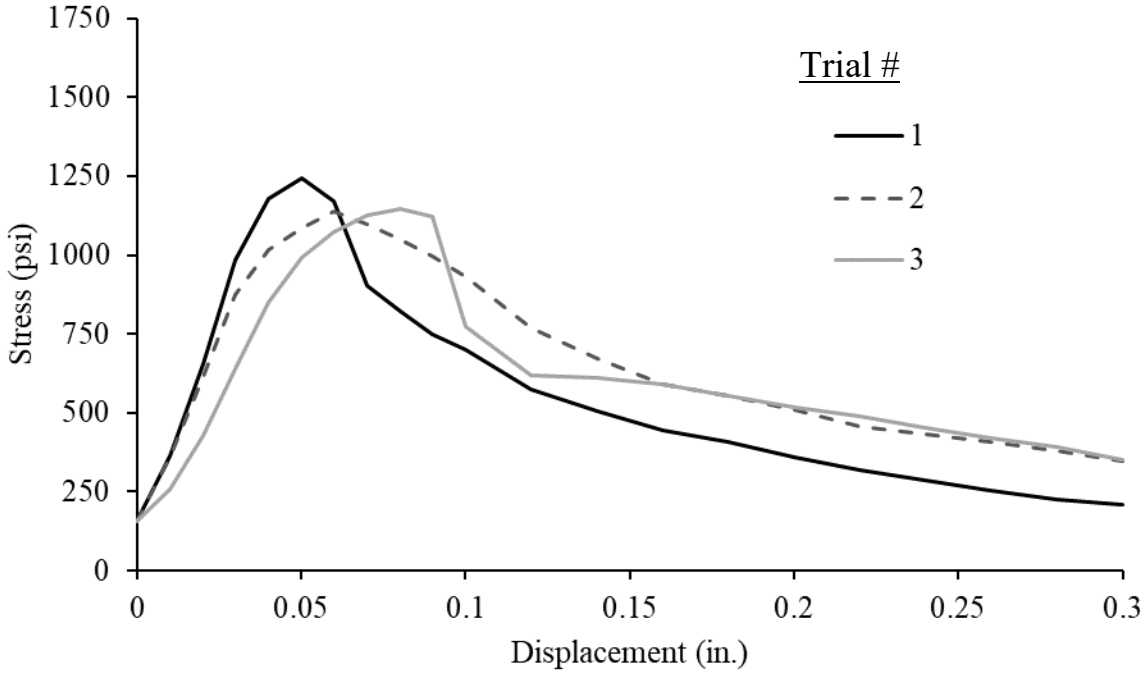

Figure A-3: Double-punch results for 2% straight fiber specimens

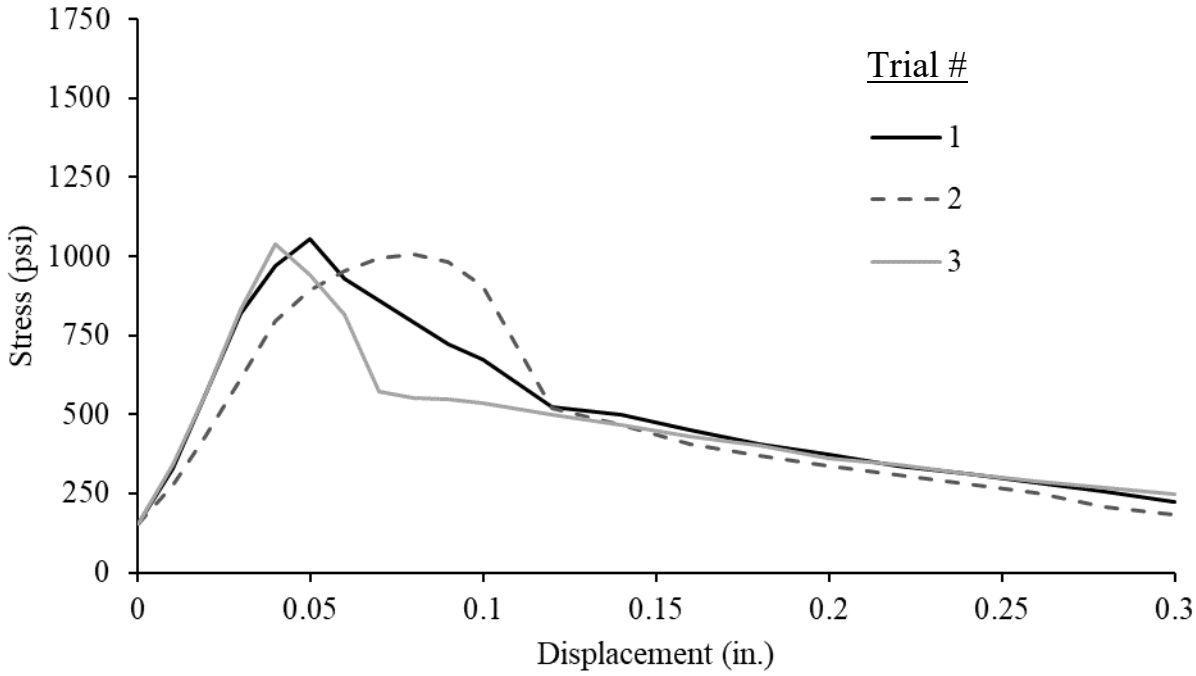

Figure A-4: Double-punch results for 2.5% straight fiber specimens

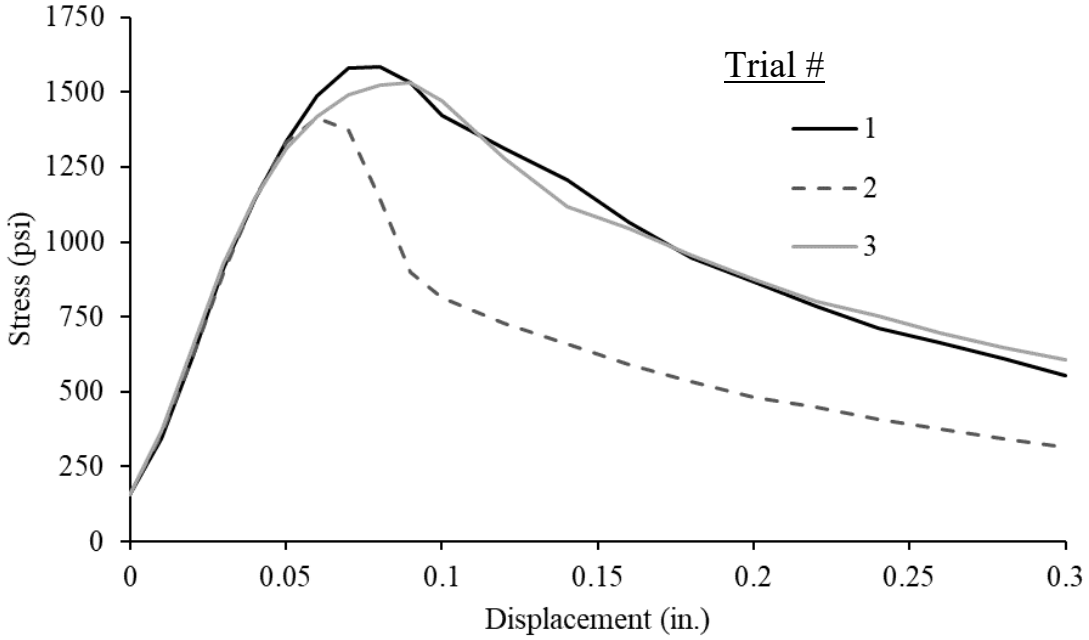

Figure A-5: Double-punch results for 3% straight fiber specimens

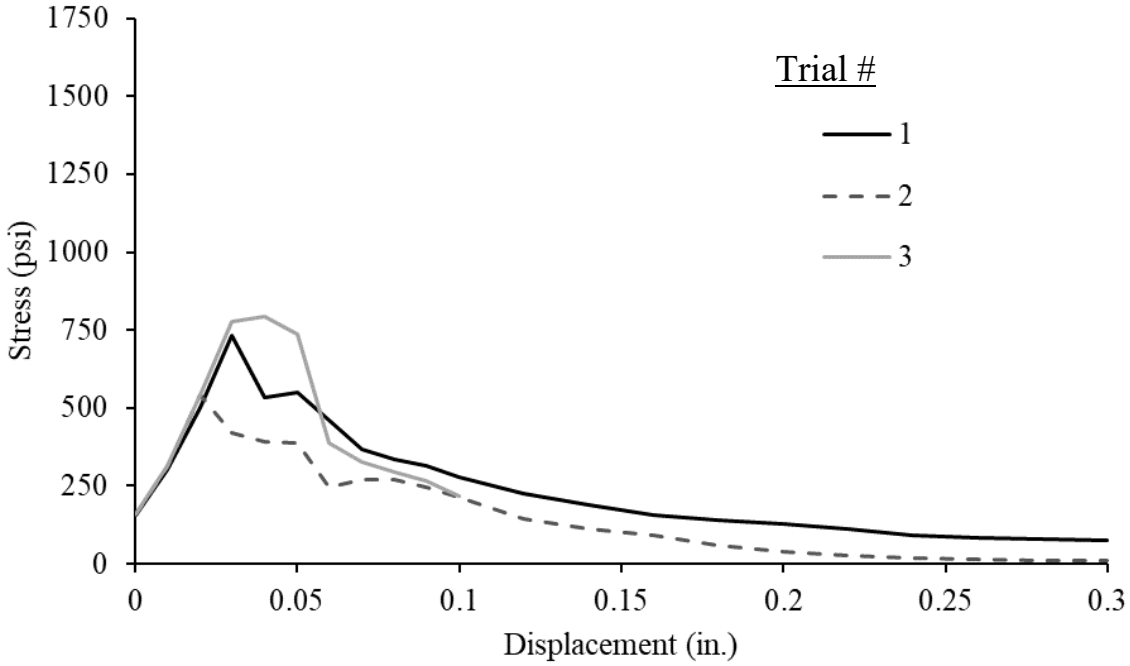

Figure A-6: Double-punch results for 1% twisted fiber specimens

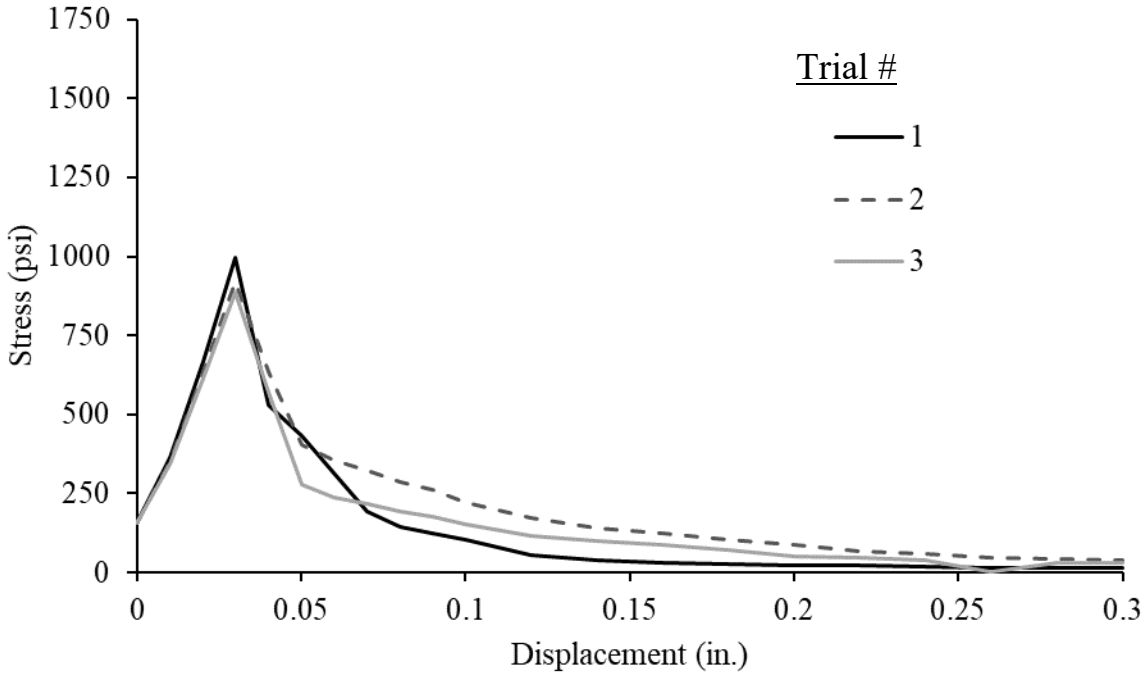

Figure A-7: Double-punch results for 1.5% twisted fiber specimens

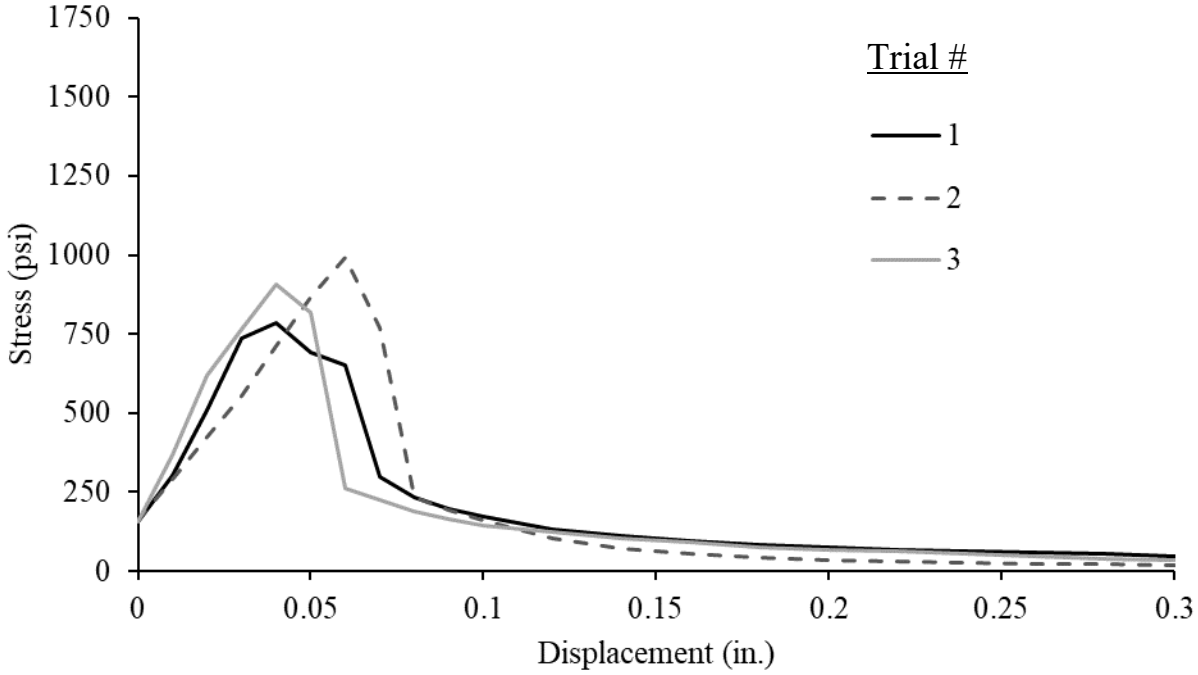

Figure A-8: Double-punch results for 2% twisted fiber specimens

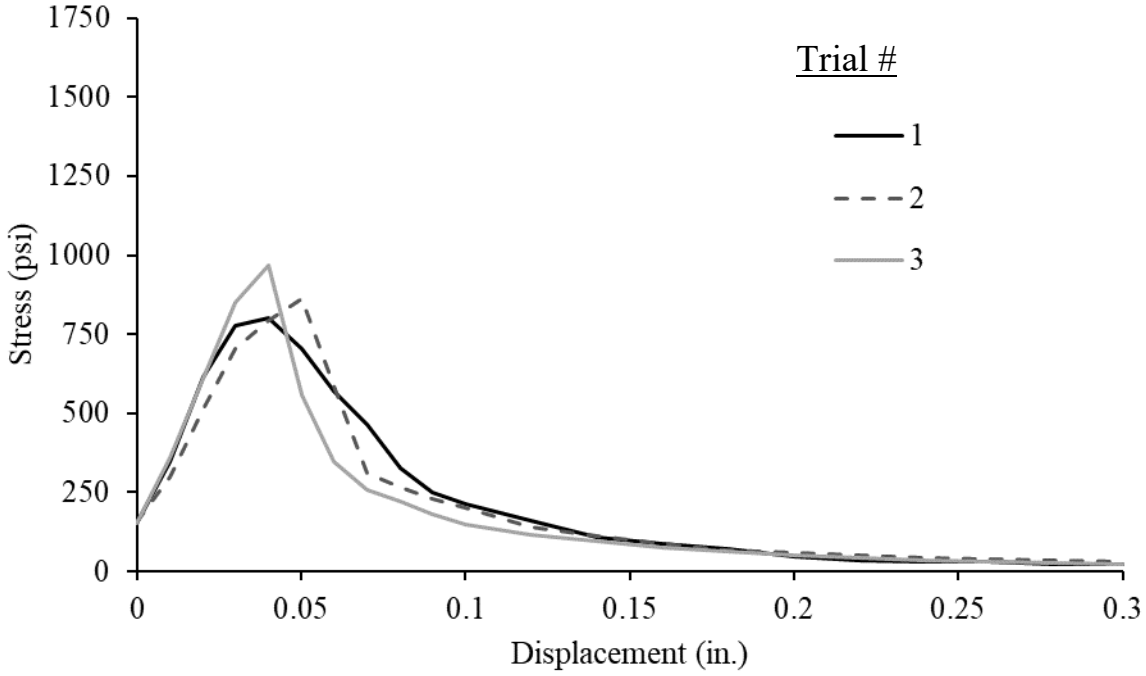

Figure A-9: Double-punch results for 2.5% twisted fiber specimens

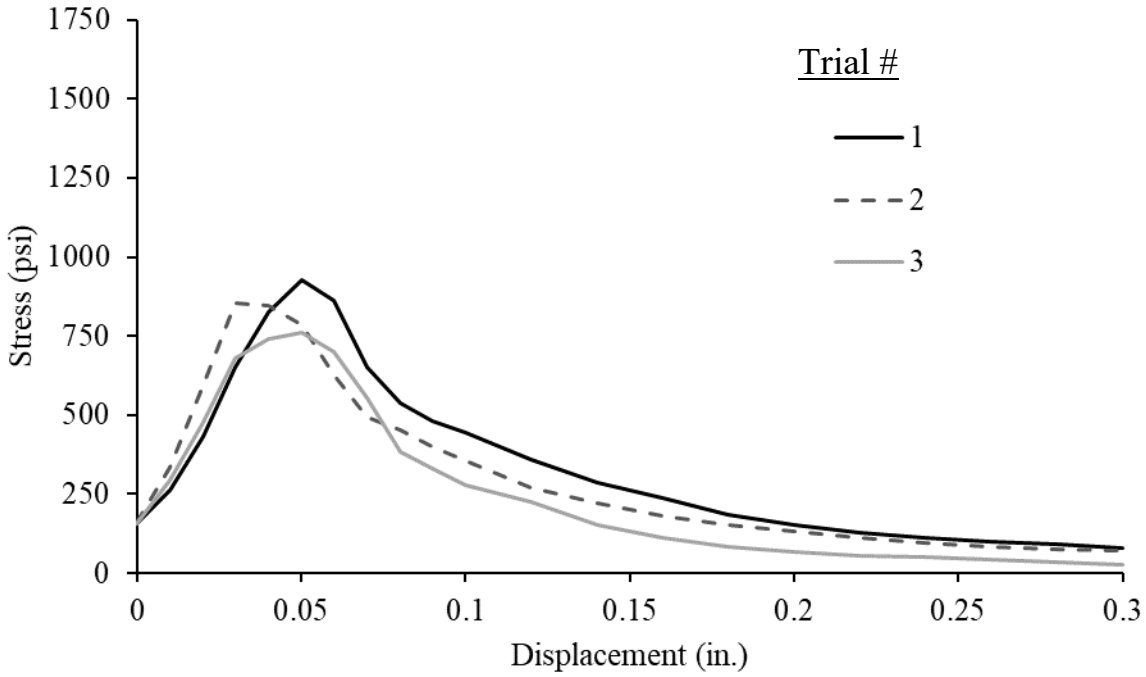

Figure A-10: Double-punch results for 3% twisted fiber specimens

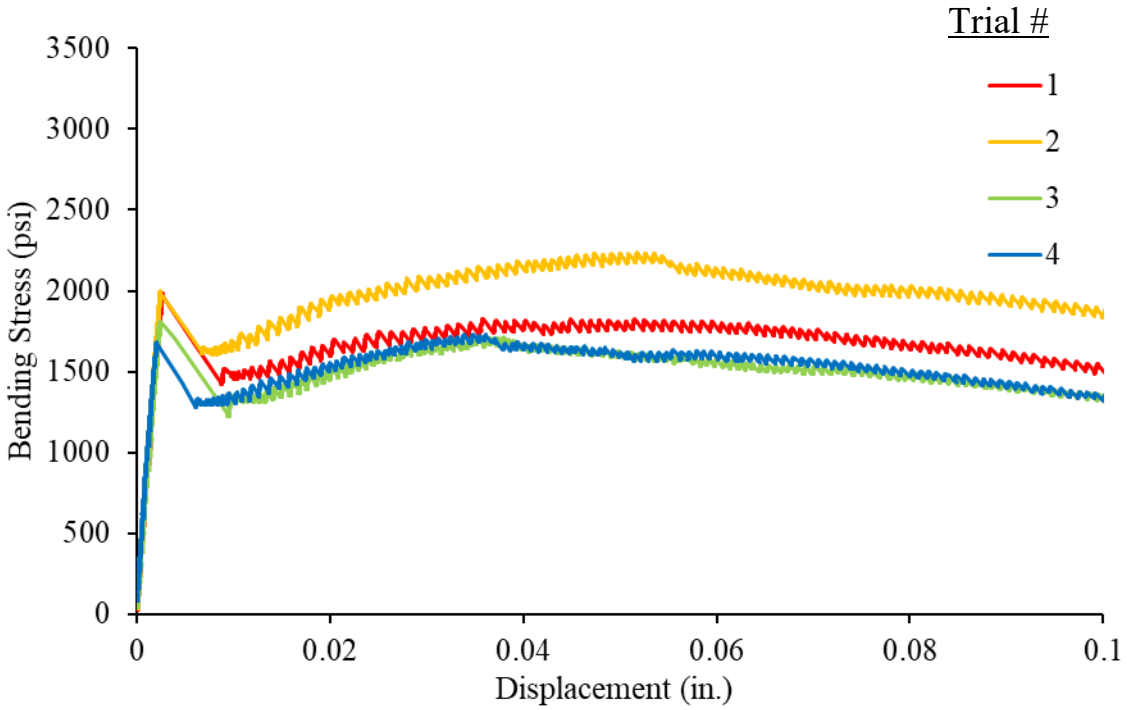

Figure A-11: Flexure results for 1% straight fiber specimens

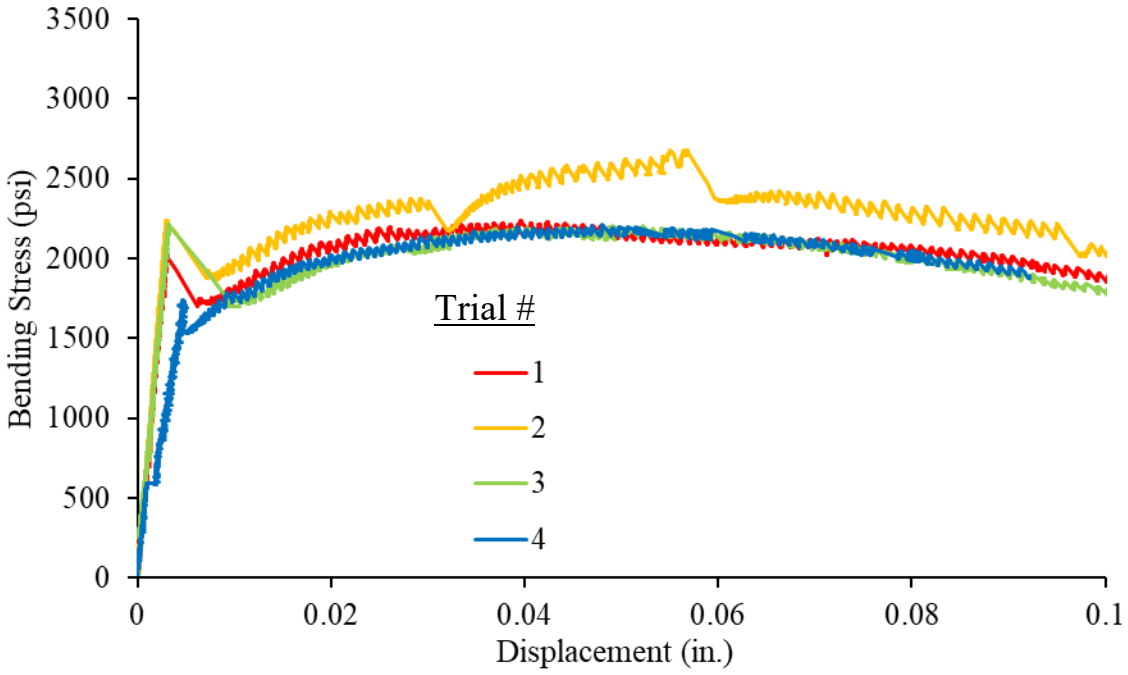

Figure A-12: Flexure results for 1.5% straight fiber specimens

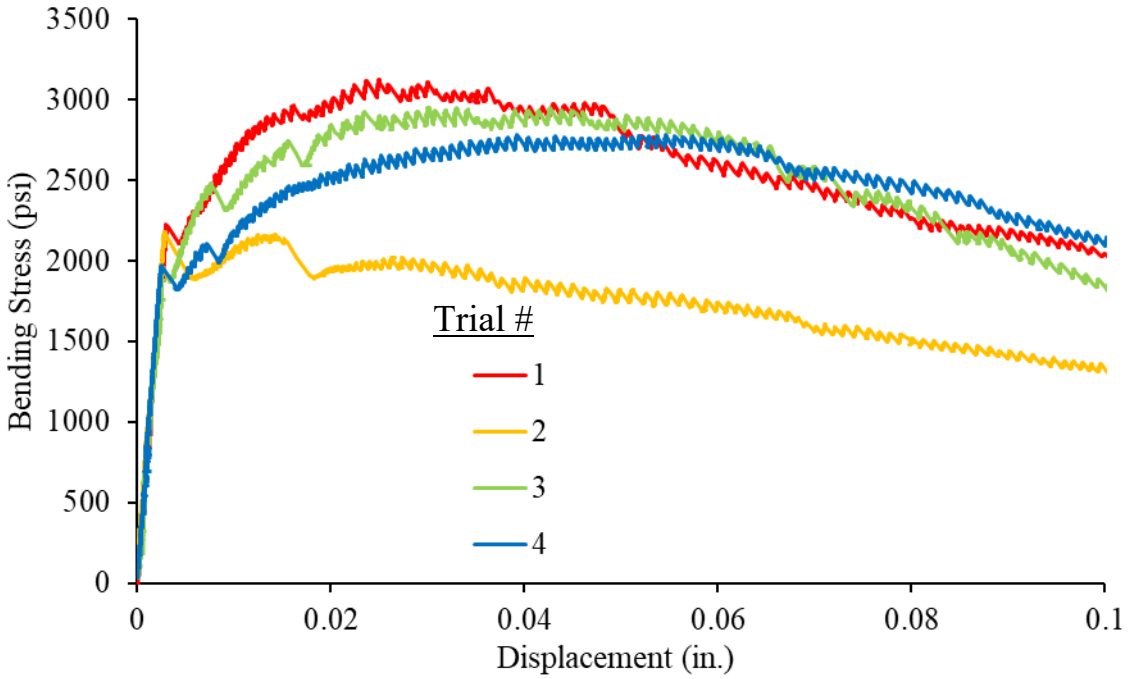

Figure A-13: Flexure results for 2% straight fiber specimens

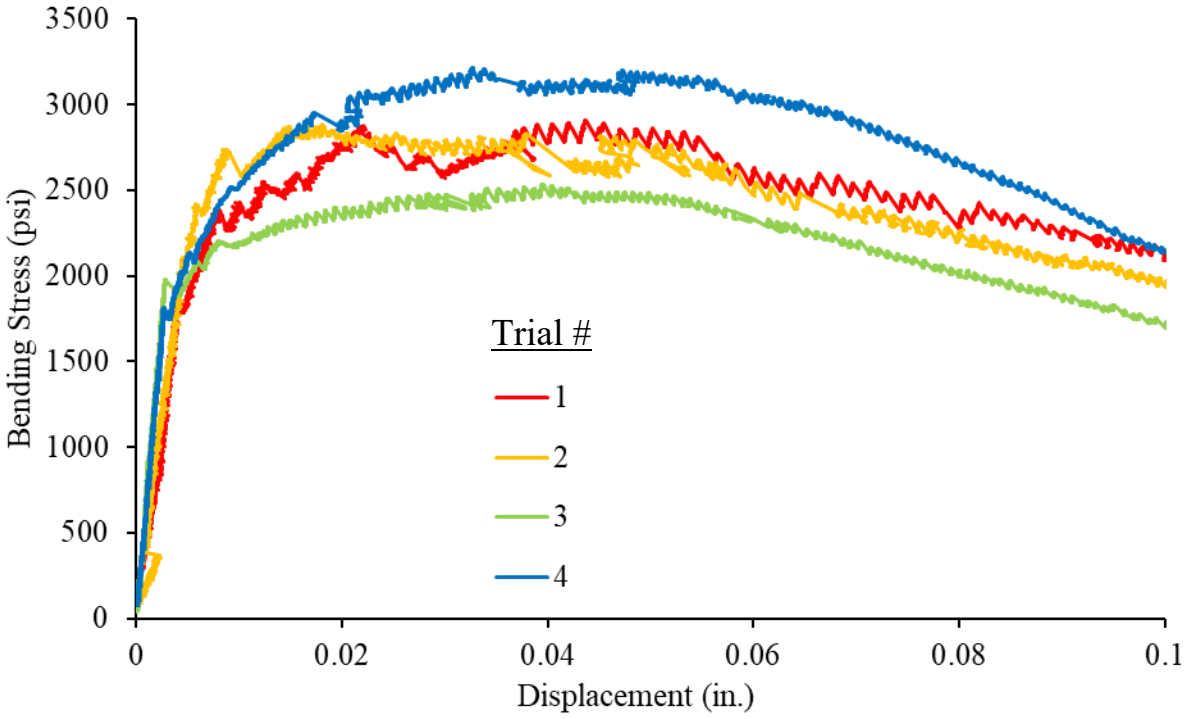

Figure A-14: Flexure results for 2.5% straight fiber specimens

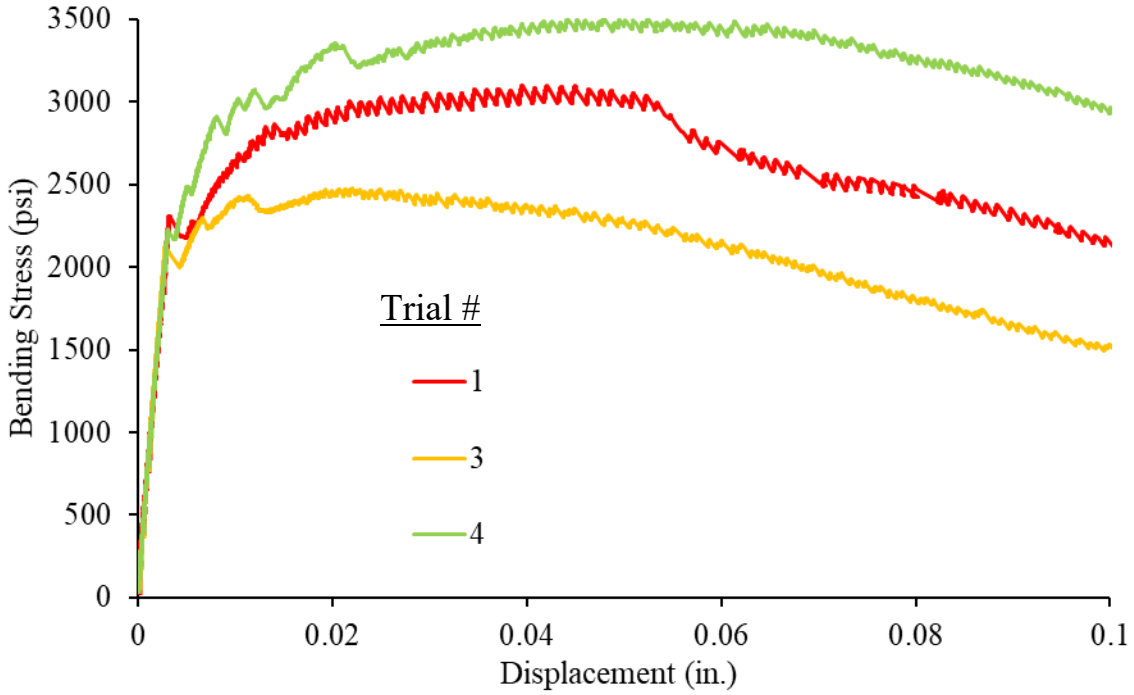

Figure A-15: Flexure results for 3% straight fiber specimens

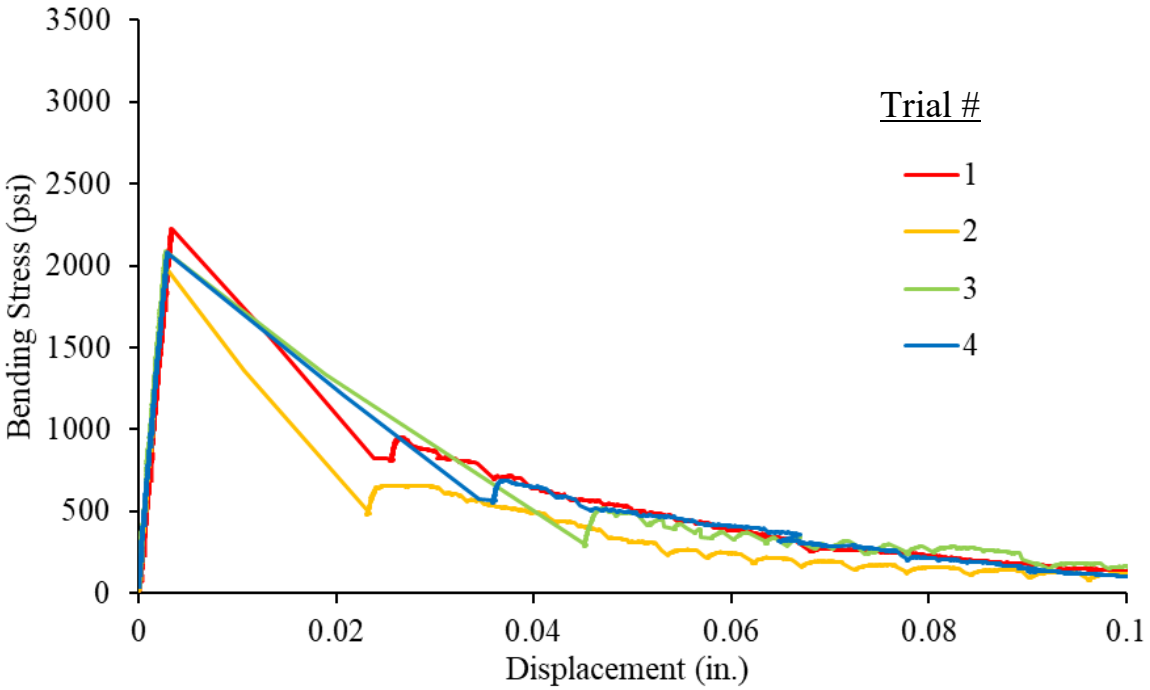

Figure A-16: Flexure results for 1% twisted fiber specimens

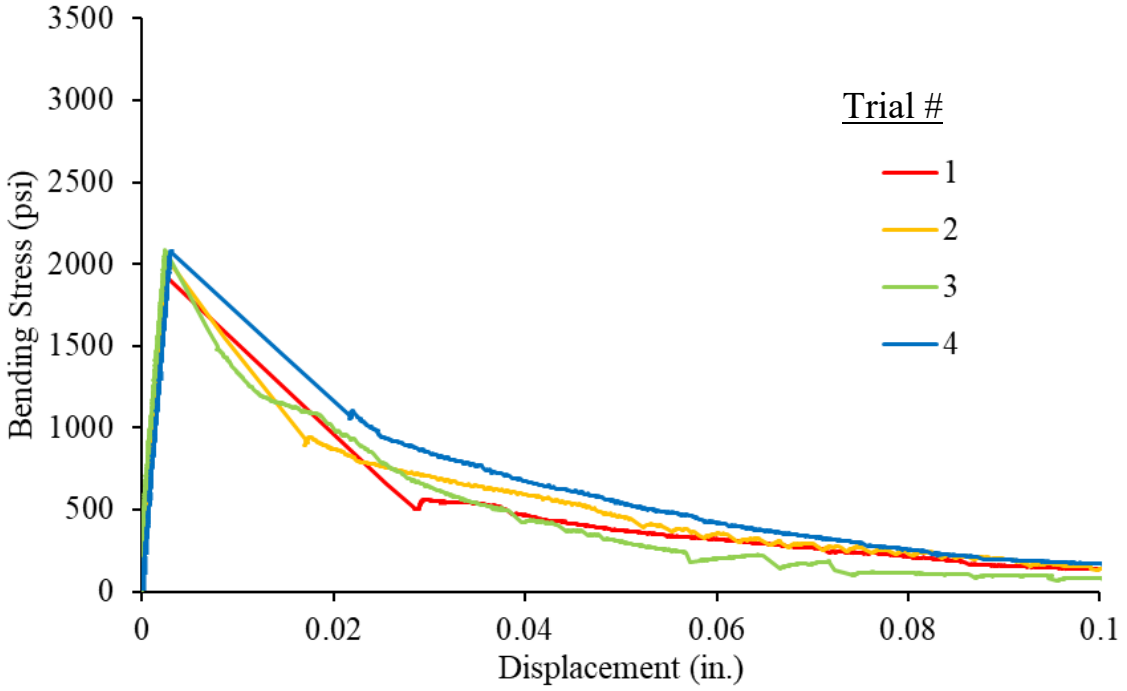

Figure A-17: Flexure results for 1.5% twisted fiber specimens

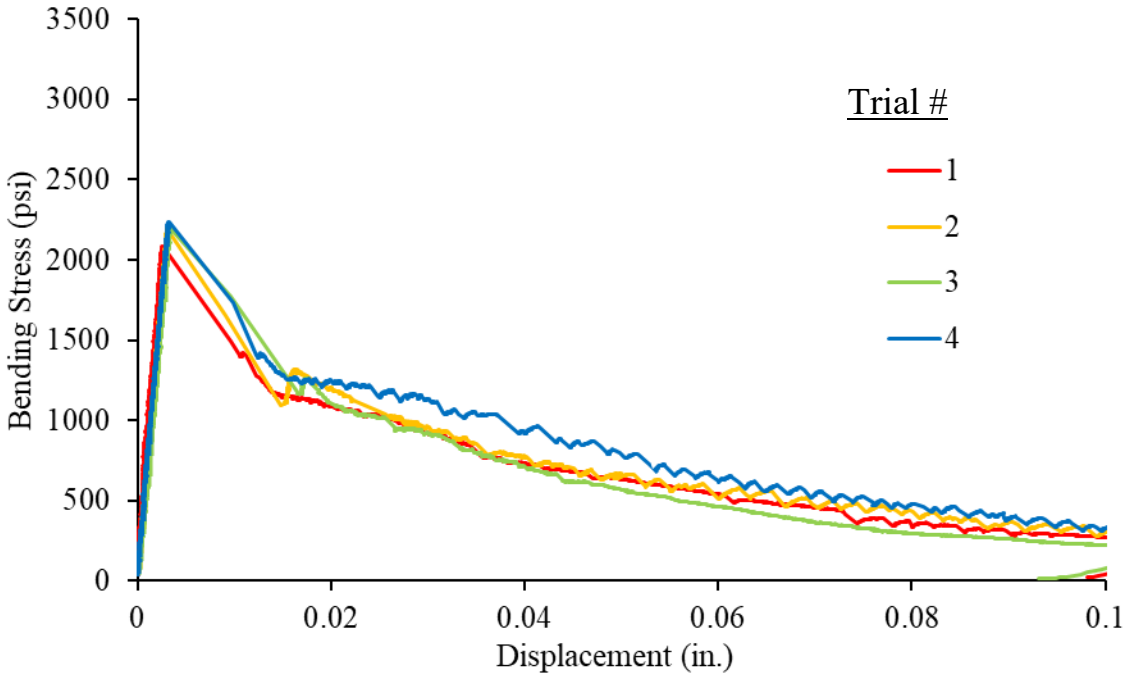

Figure A-18: Flexure results for 2% twisted fiber specimens

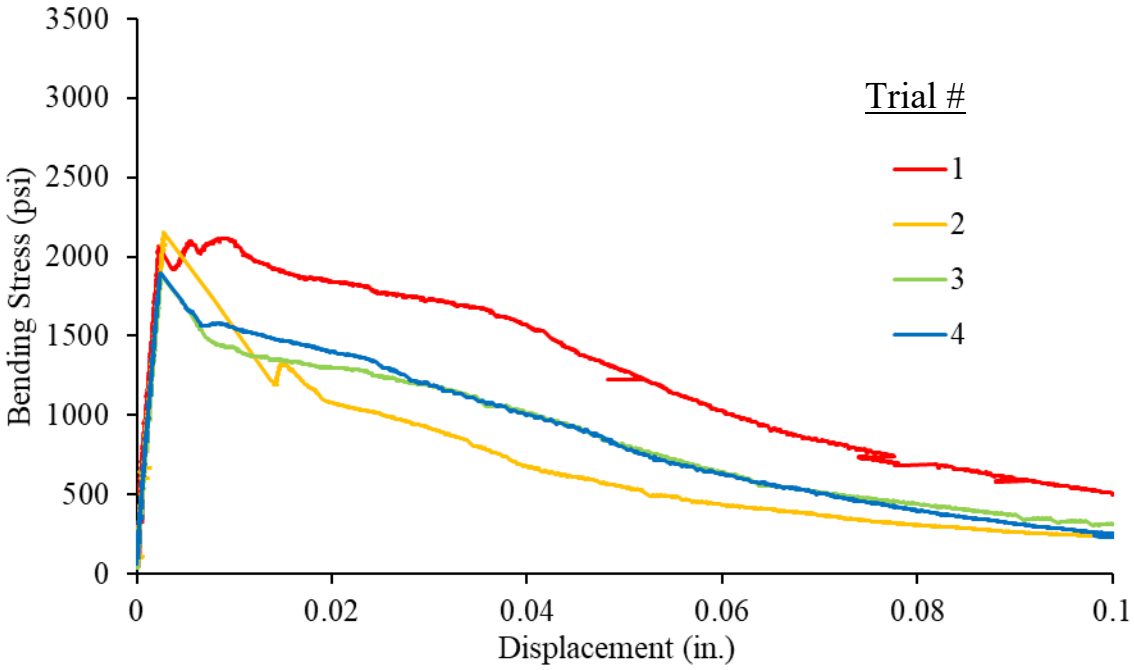

Figure A-19: Flexure results for 2.5% twisted fiber specimens

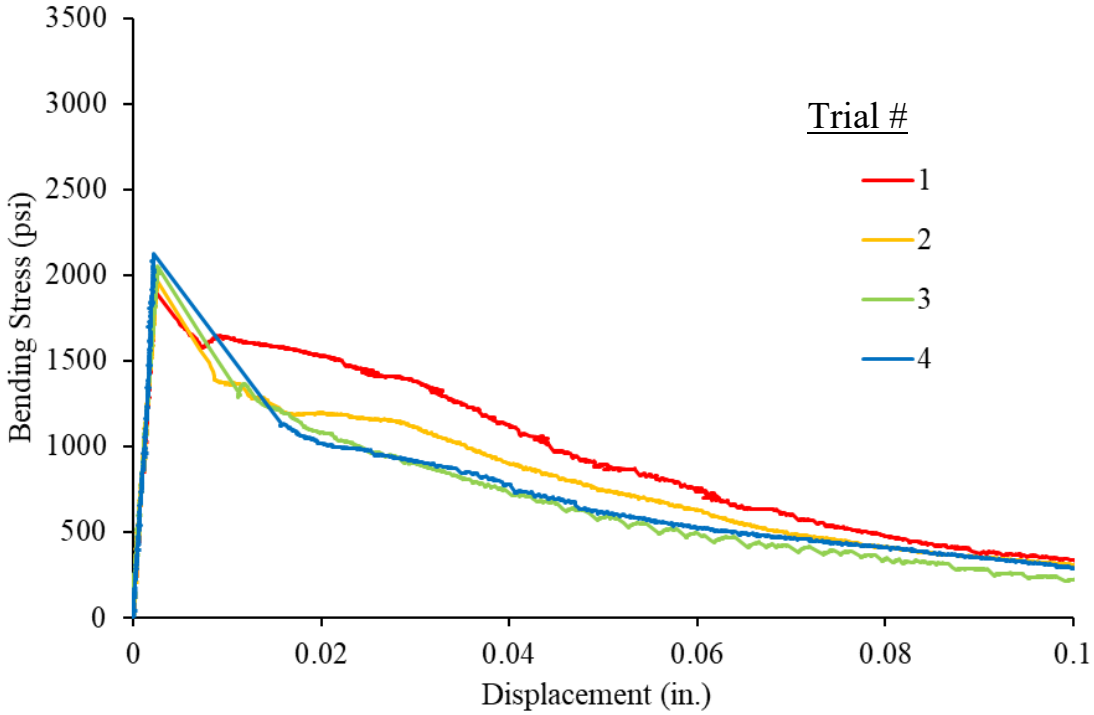

Figure A-20: Flexure results for 3% twisted fiber specimens

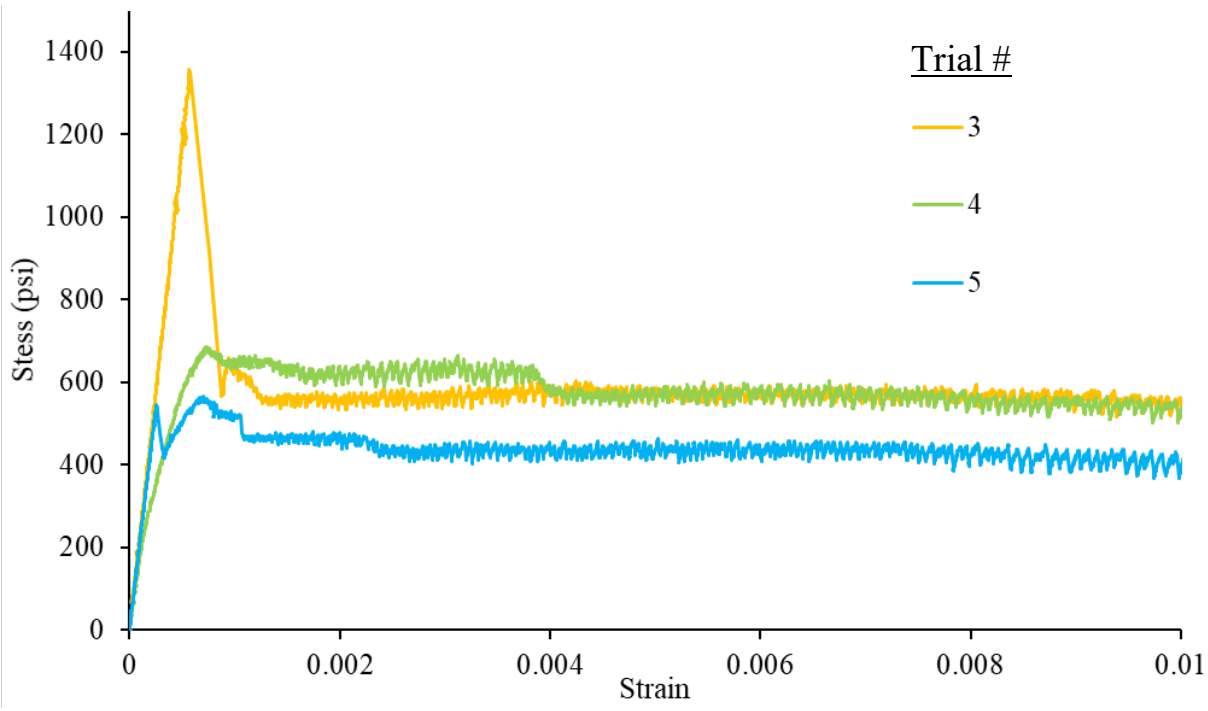

Figure A-21: Direct tension results for 1% straight fiber specimens

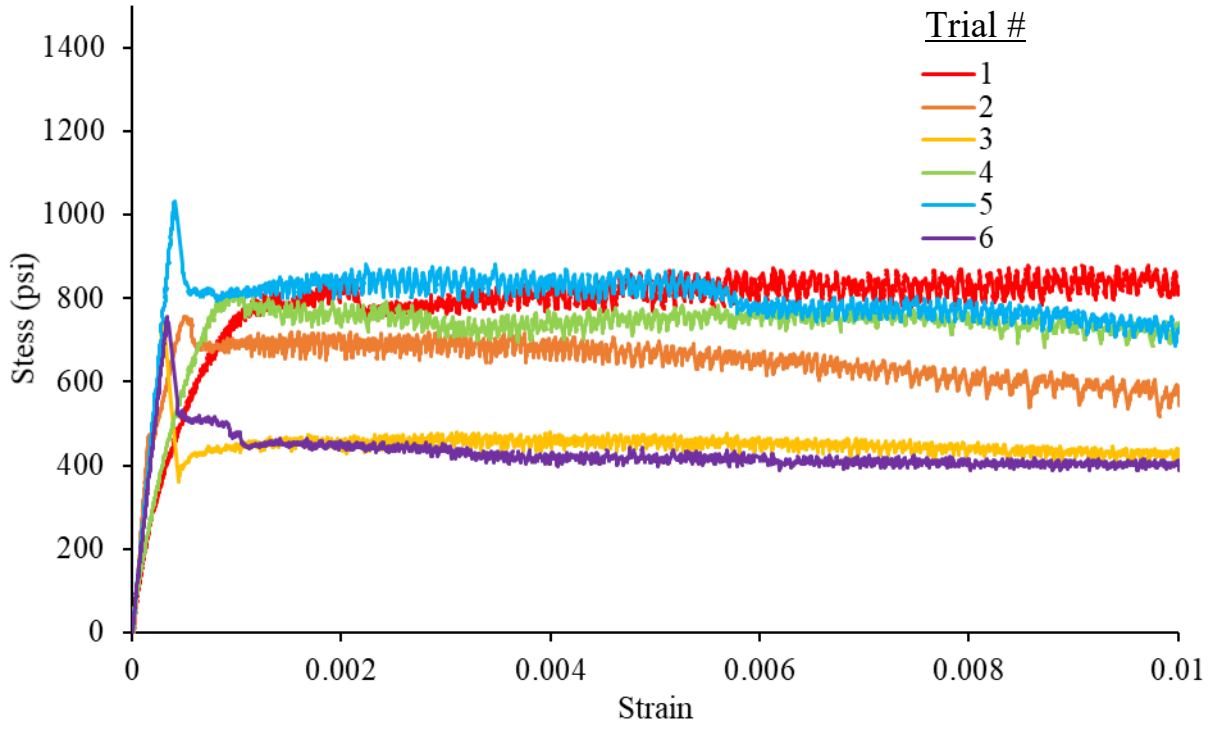

Figure A-22: Direct tension results for 1.5% straight fiber specimens

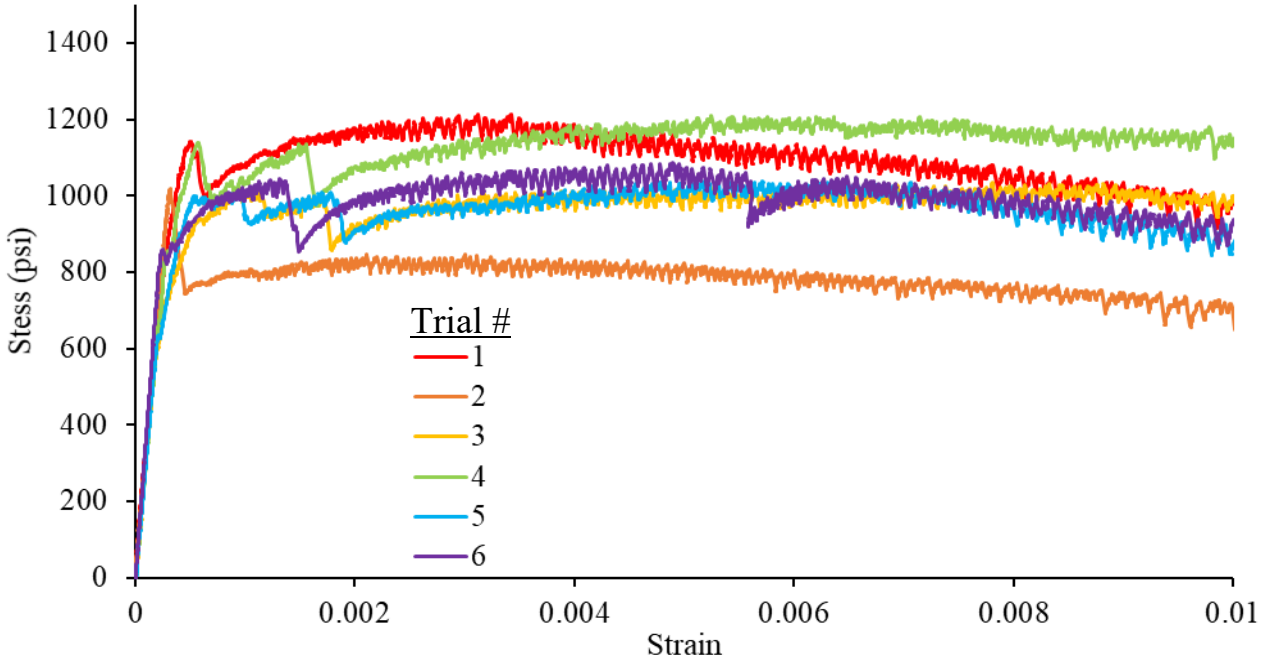

Figure A-23: Direct tension results for 2% straight fiber specimens

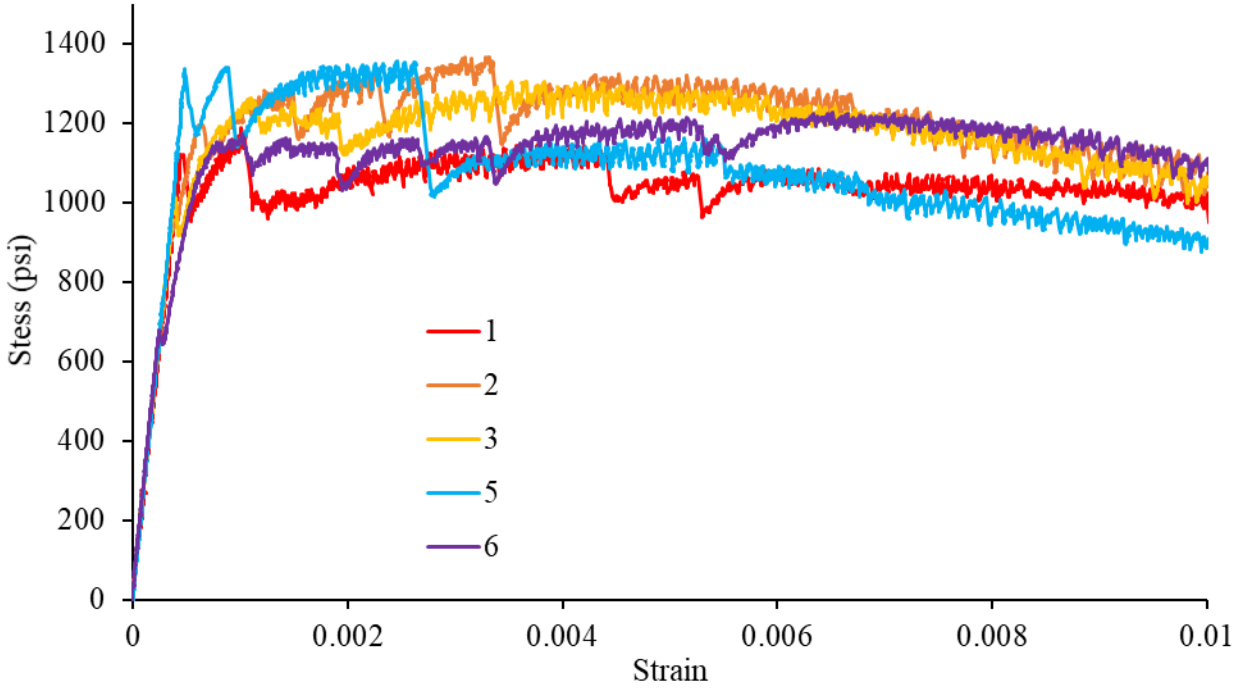

Figure A-24: Direct tension results for 2.5% straight fiber specimens

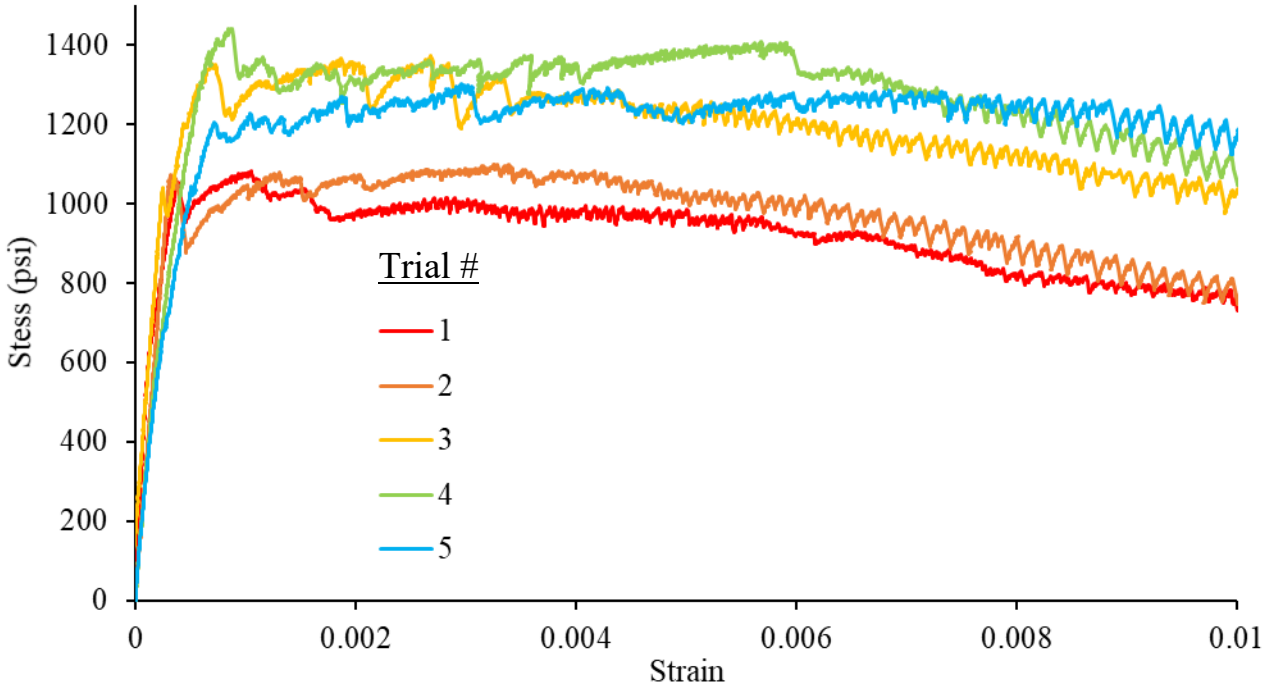

Figure A-25: Direct tension results for 3% straight fiber specimens

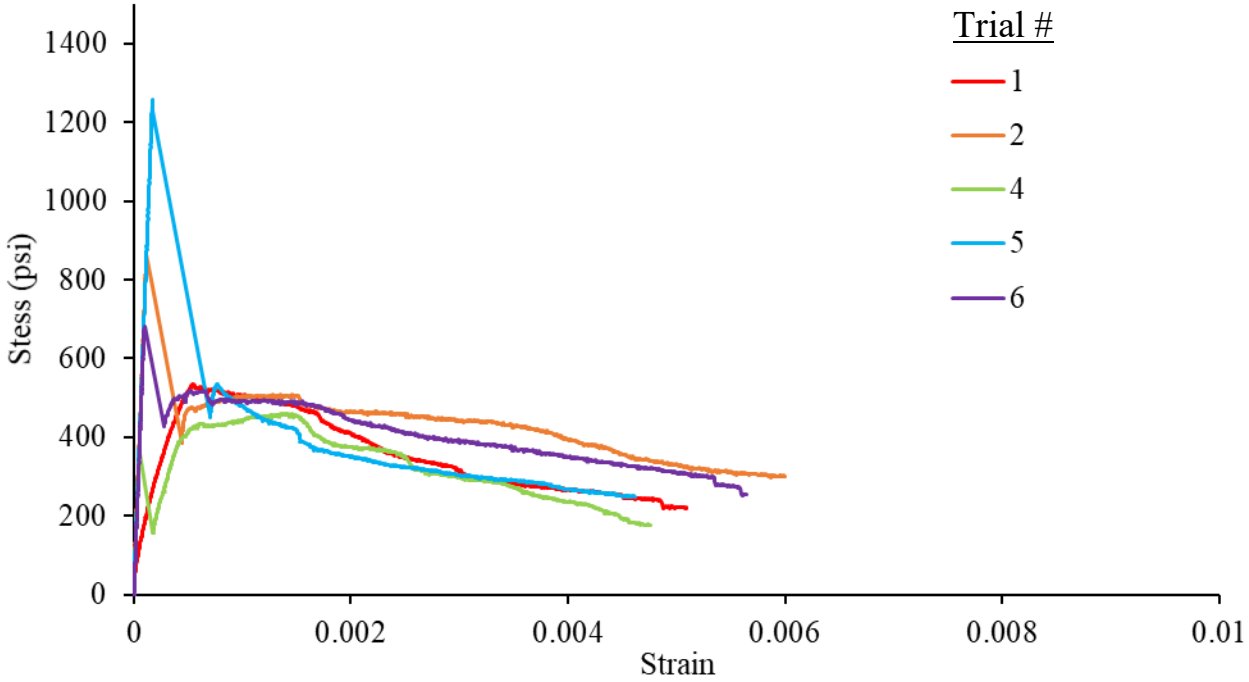

Figure A-26: Direct tension results for 1% twisted fiber specimens

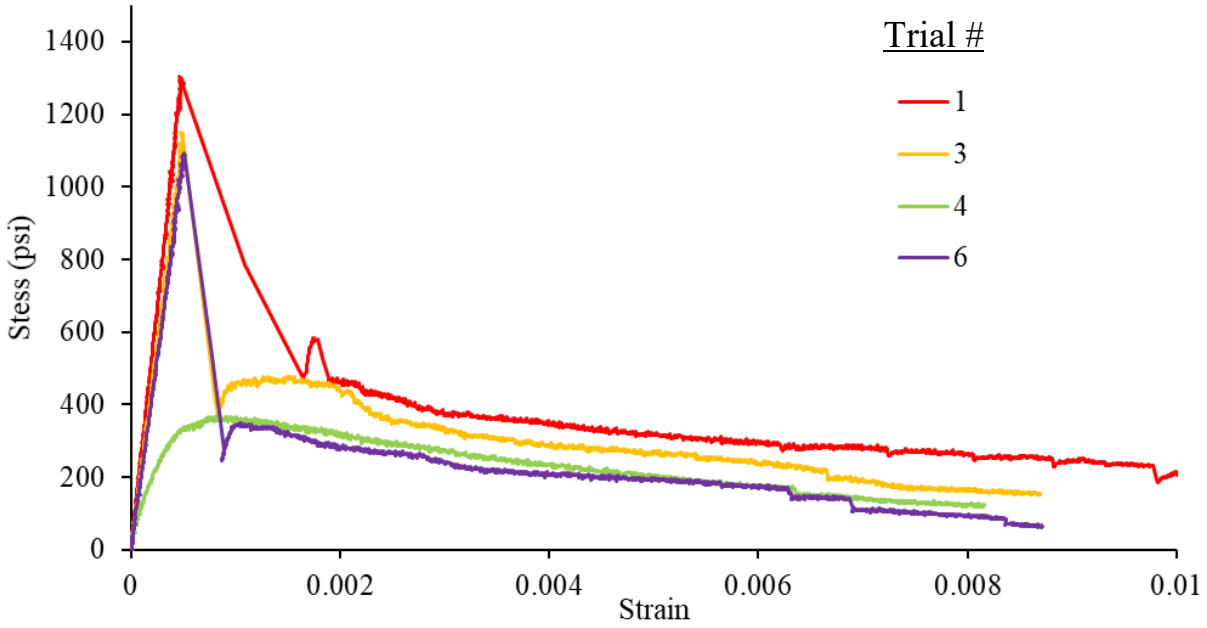

Figure A-27: Direct tension results for 1.5% twisted fiber specimens

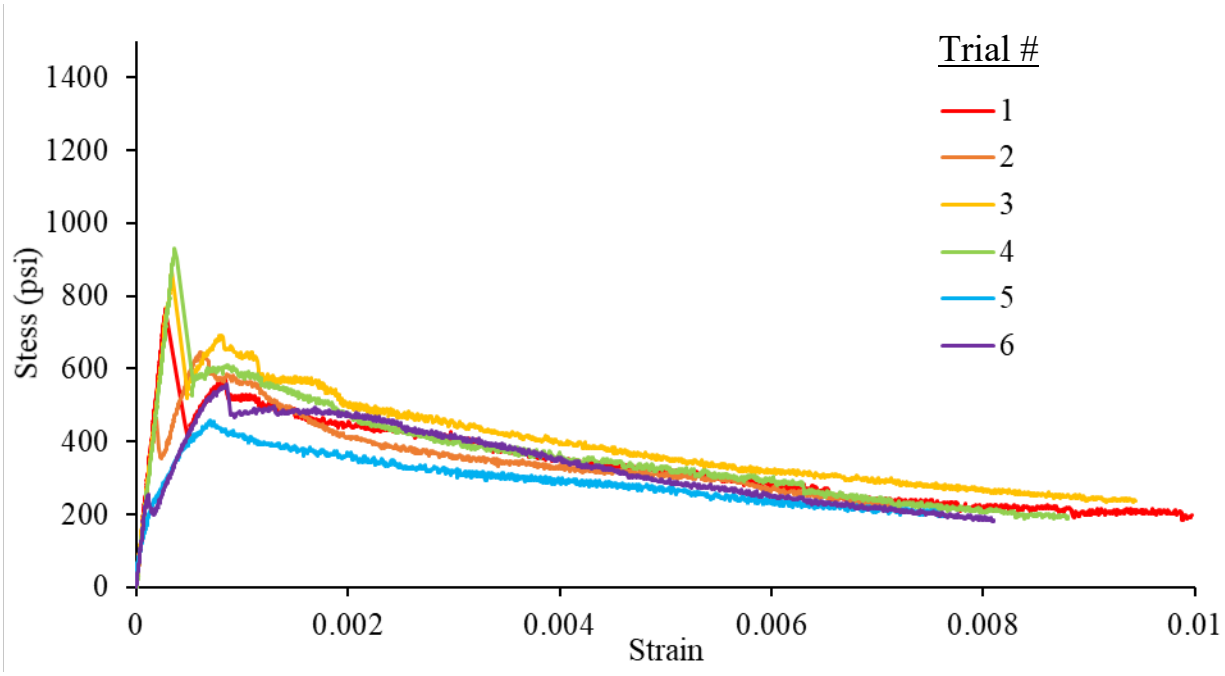

Figure A-28: Direct tension results for 2% twisted fiber specimens

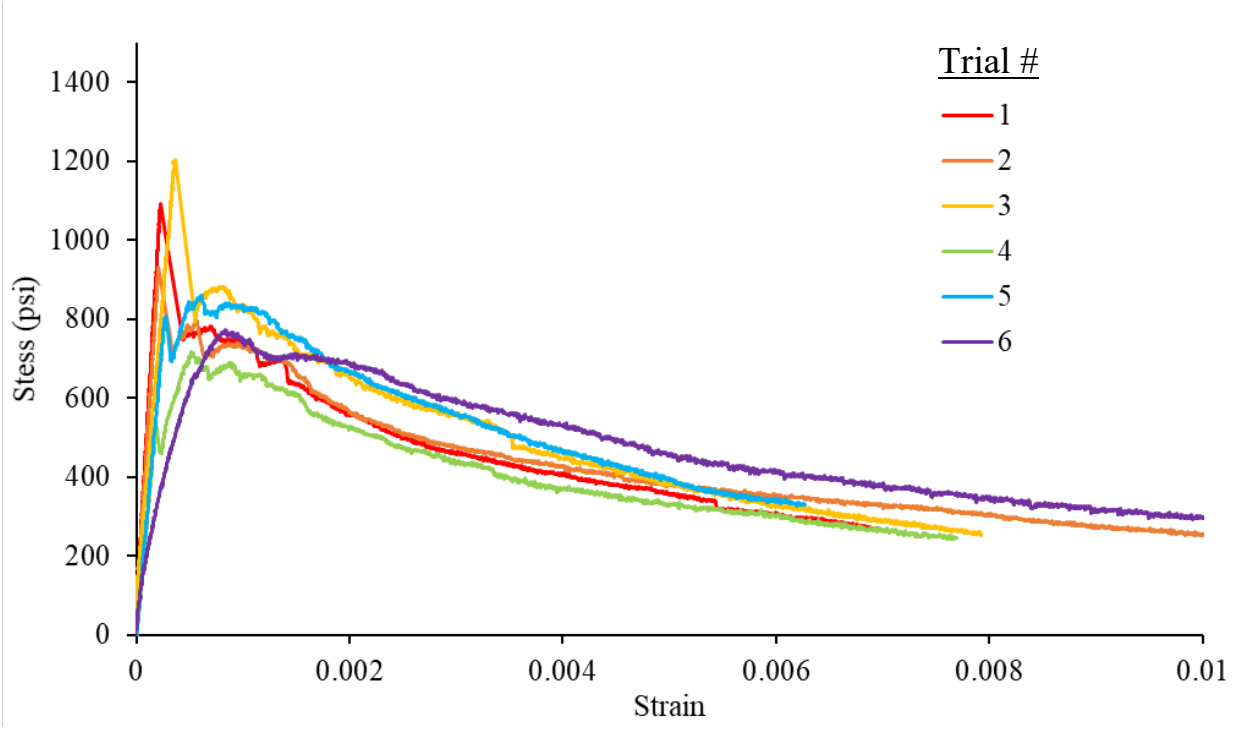

Figure A-29: Direct tension results for 2.5% twisted fiber specimens

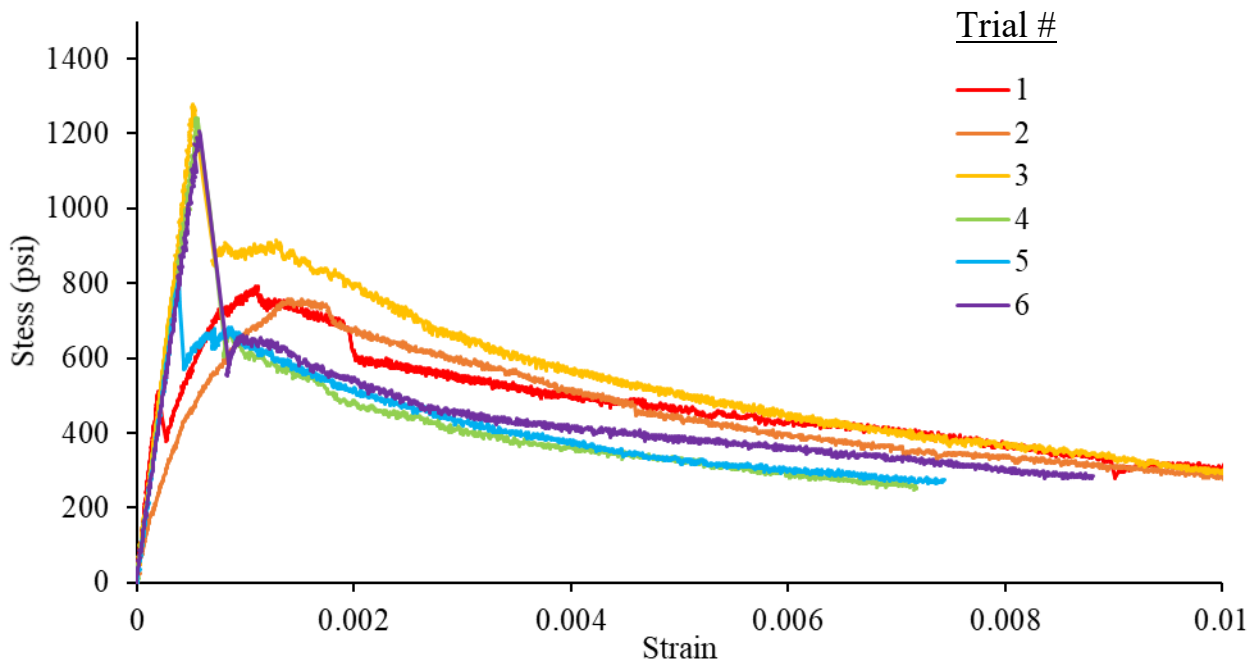

Figure A-30: Direct tension results for 3% twisted fiber specimens

APPENDIX B: DIRECT TENSION RESULTS

Table B-1. Averages and Standard Deviations for each sample group

Mix Design	Curing	E (psi)	f_{cr} (psi)	f_{max} (psi)	Toughness (psi*in.)	stress at 0.005 (psi)
12+	Steam	4.06E+06	714	922	4.00	778
	Std. Dev.	1.30E+06	91	100	0.32	65
12+	Precast	3.11E+06	775	976	4.21	904
	Std. Dev.	4.04E+05	59	117	0.36	91
12+	Fog	3.55E+06	917	1116	4.83	1020
	Std. Dev.	5.92E+05	191	187	0.94	217
15+	Steam	4.48E+06	1005	1272	5.37	1021
	Std. Dev.	1.39E+06	186	168	0.97	181
15+	Precast	5.19E+06	1176	1305	5.07	877
	Std. Dev.	1.38E+06	130	81	0.36	68
15+	Fog	3.53E+06	819	1031	4.43	911
	Std. Dev.	3.45E+05	87	106	0.42	103
18+	Steam	4.57E+06	1061	1227	5.24	966
	Std. Dev.	1.40E+06	213	182	0.33	71
18+	Precast	3.25E+06	1052	1203	5.12	970
	Std. Dev.	1.00E+05	81	105	0.47	131
18+	Fog	7.35E+06	971	1310	5.31	1080
	Std. Dev.	1.93E+05	201	181	0.40	105
21+	Steam	5.03E+06	1582	1806	7.64	1457
	Std. Dev.	1.39E+06	173	154	0.64	195
21+	Precast	3.56E+06	1365	1603	7.08	1394
	Std. Dev.	2.33E+05	155	126	0.65	192
21+	Fog	6.23E+06	1364	1616	6.50	1264
	Std. Dev.	1.70E+06	107	221	0.67	202

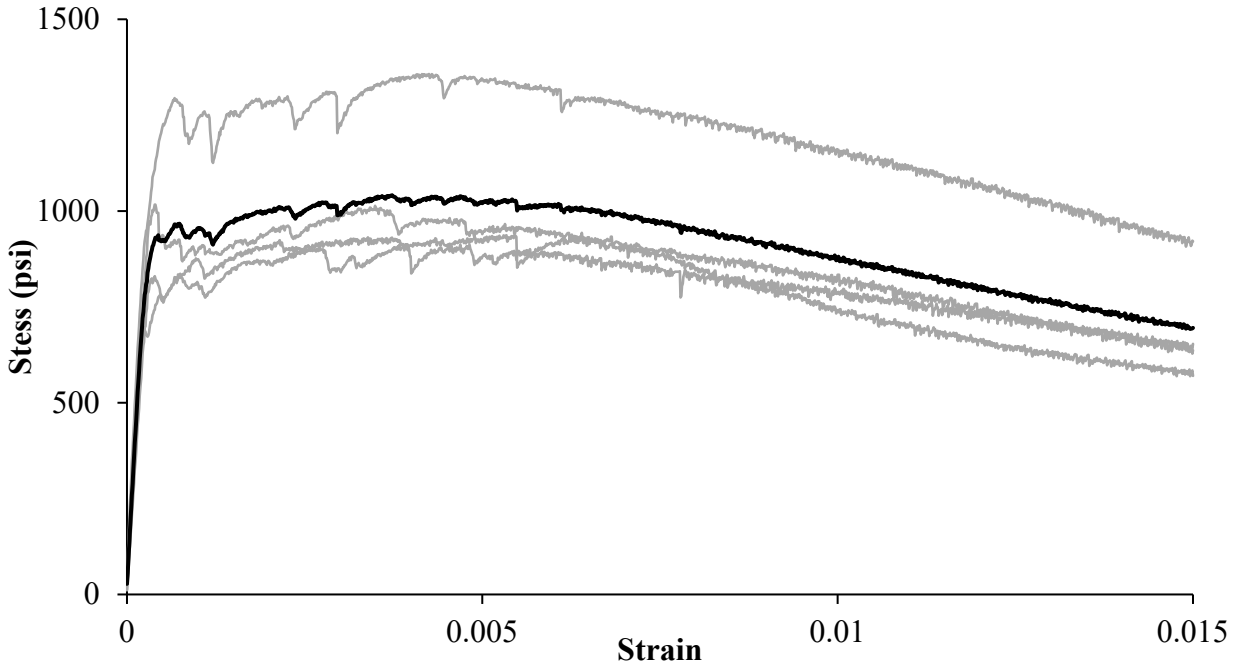

Figure B-1: 12+ Fog direct tension results

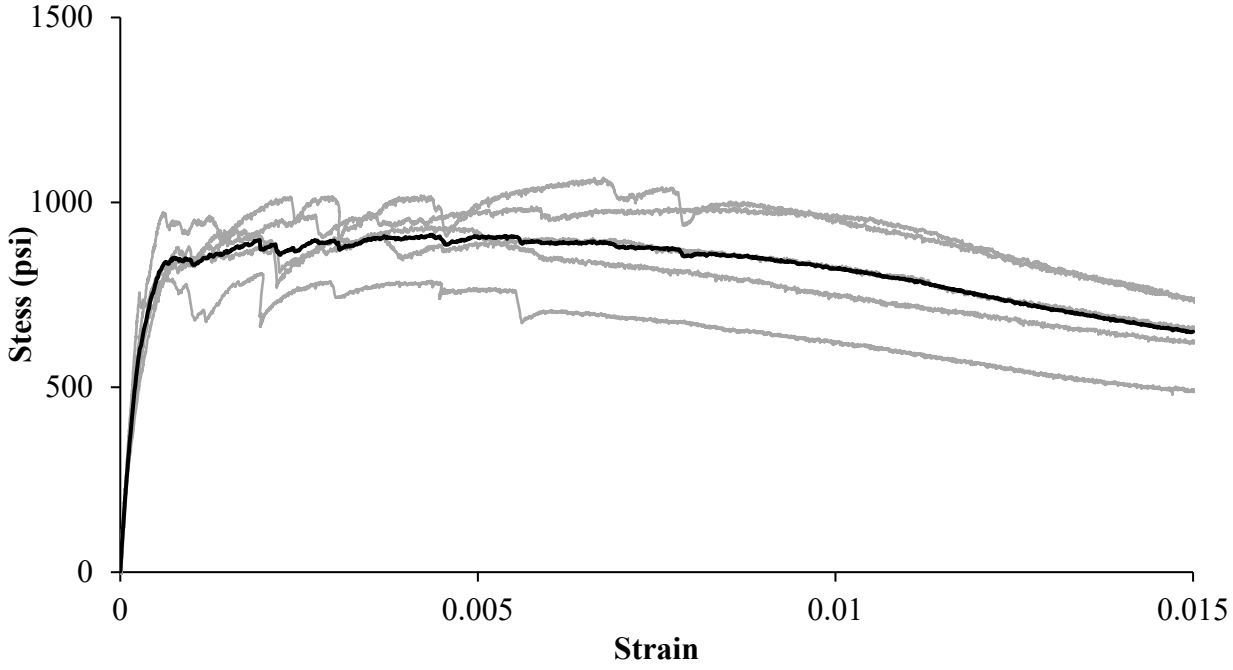

Figure B-2: 12+ Precast direct tension test results

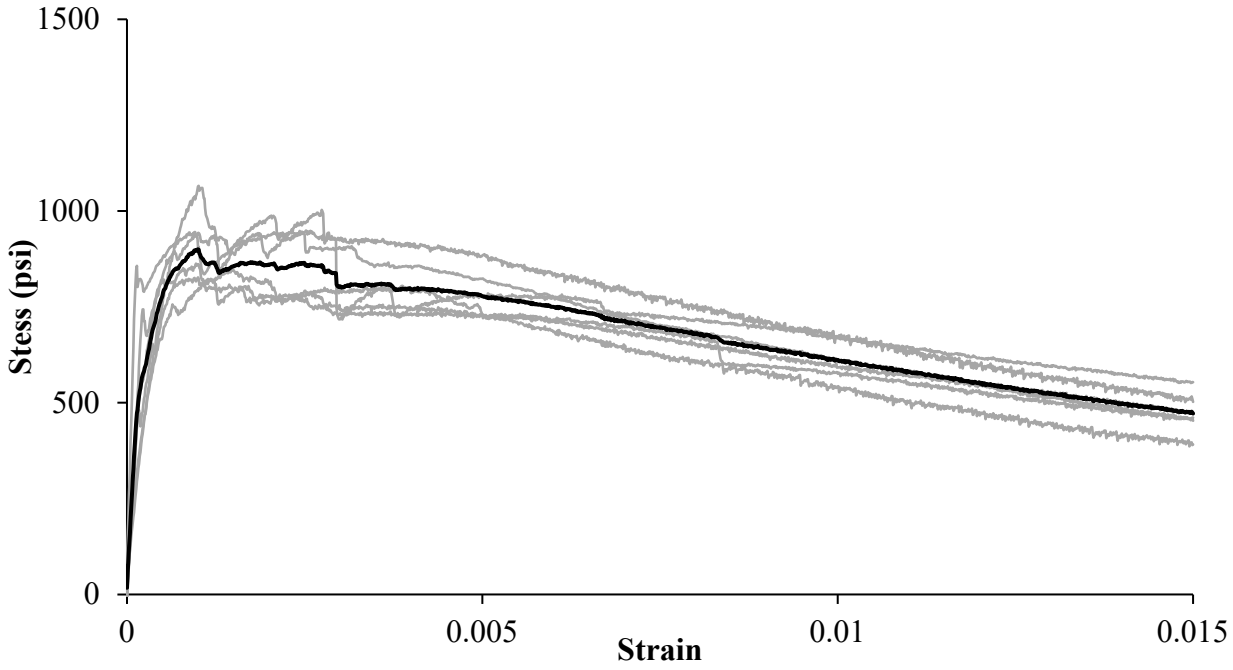

Figure B-3: 12+ Steam direct tension results

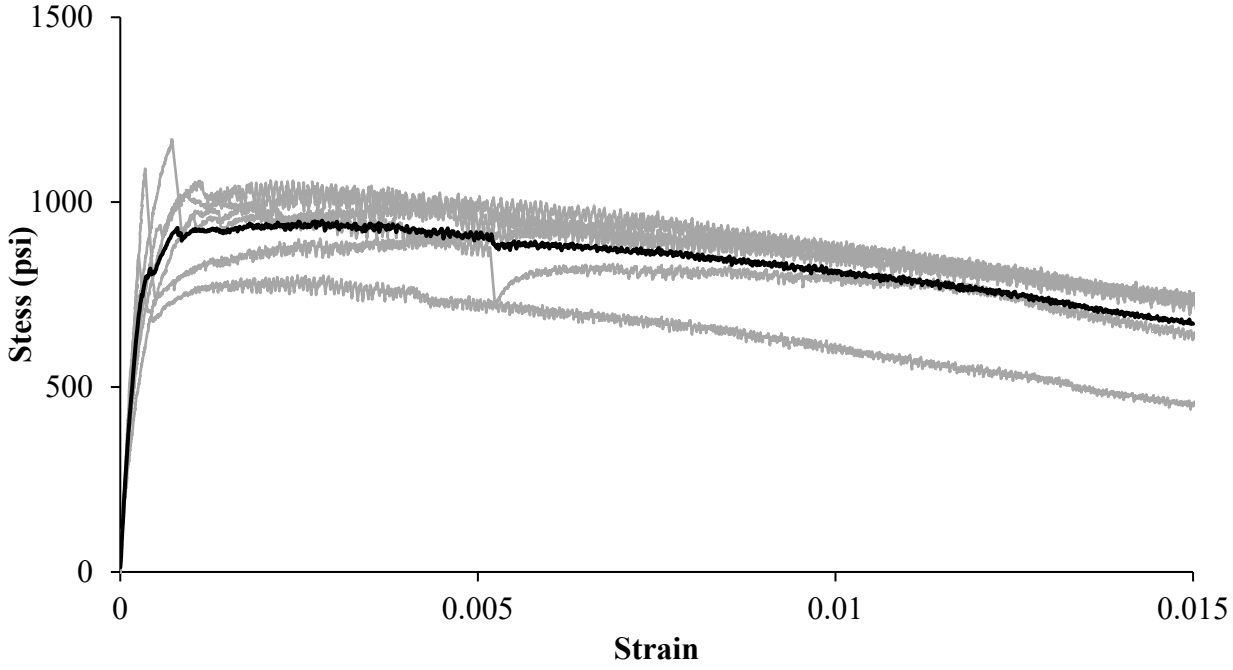

Figure B-4: 15+ Fog direct tension results

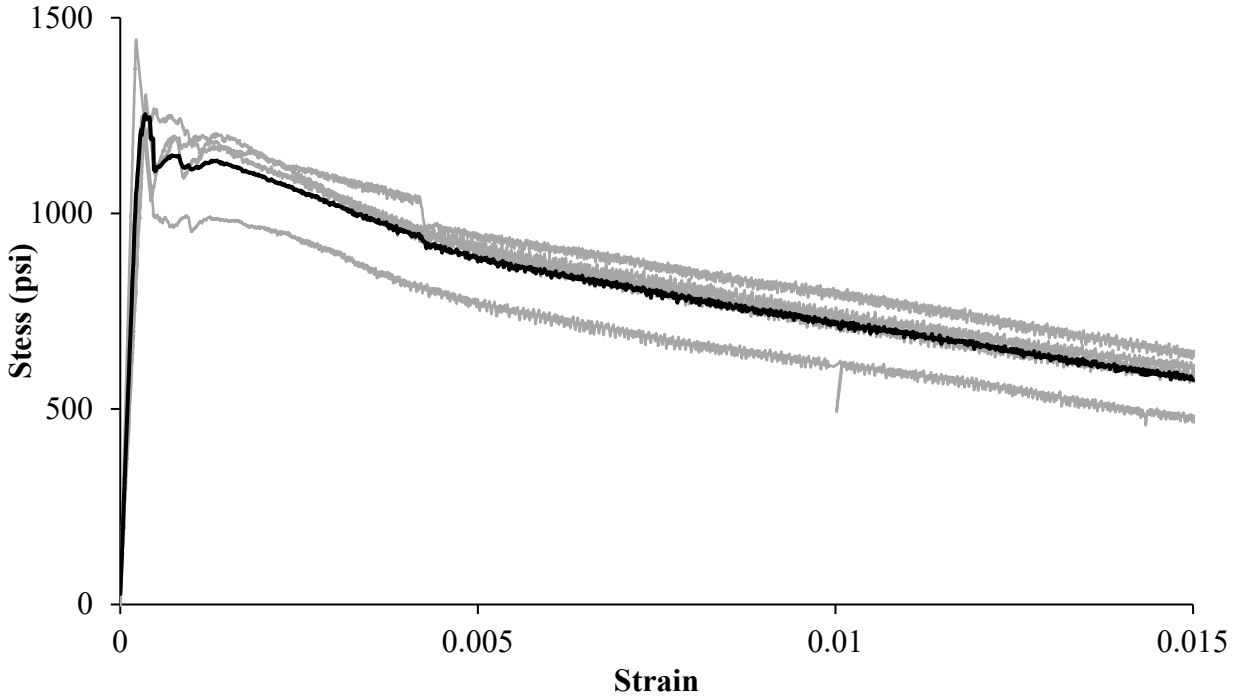

Figure B-5: 15+ Precast direct tension results

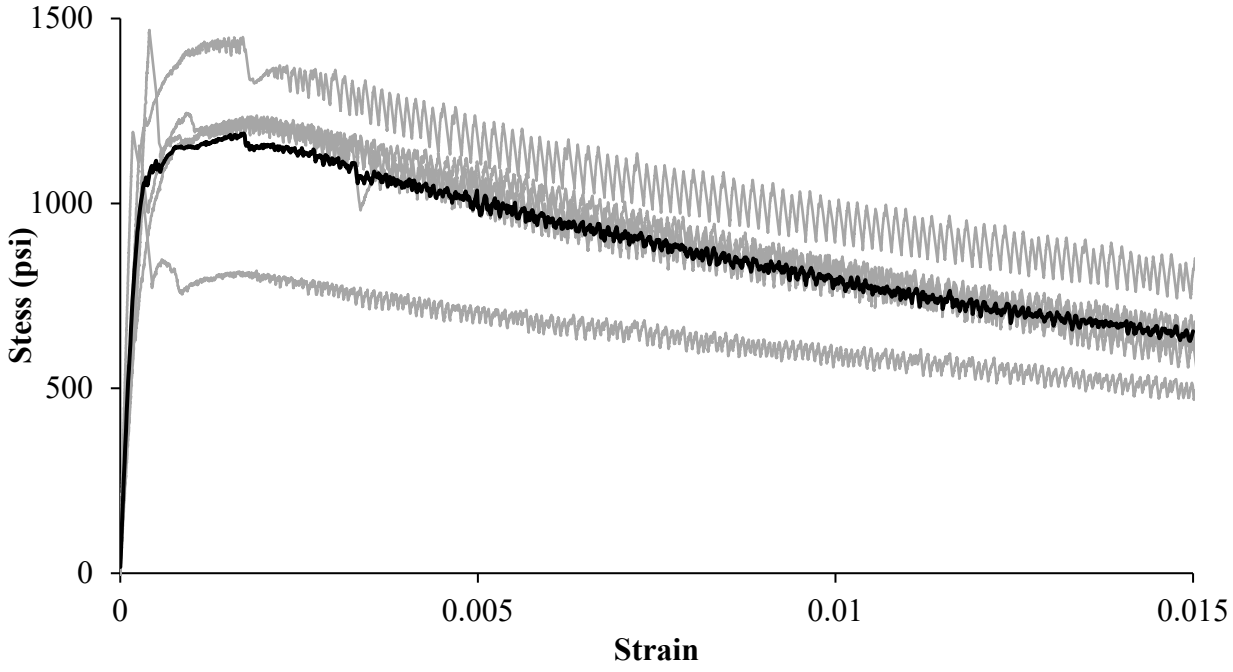

Figure B-6: 15+ Steam direct tension results

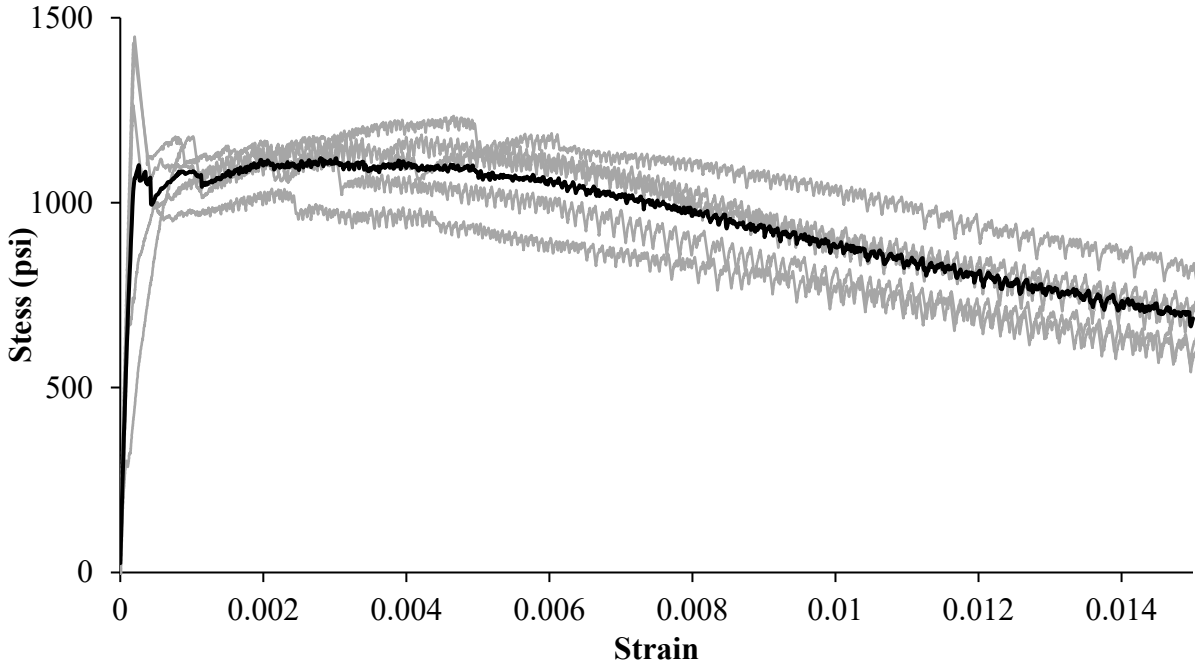

Fi Figure B-7: 18+ Fog direct tension test results

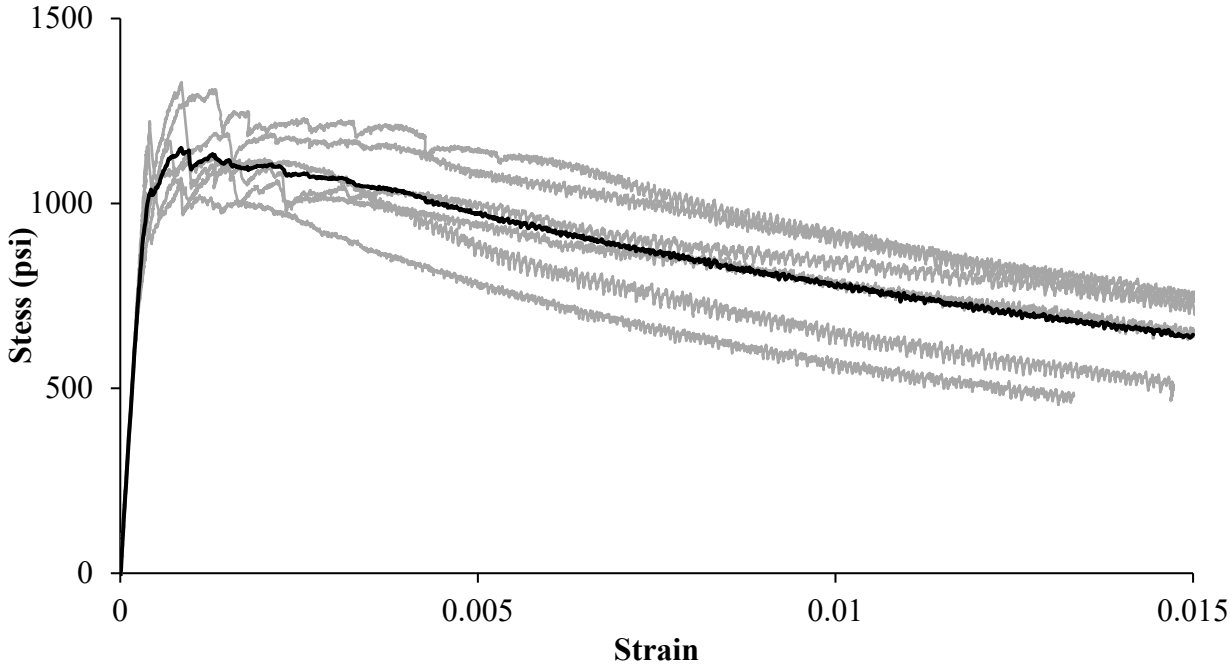

Figure B-8: 18+ Precast direct tension test results

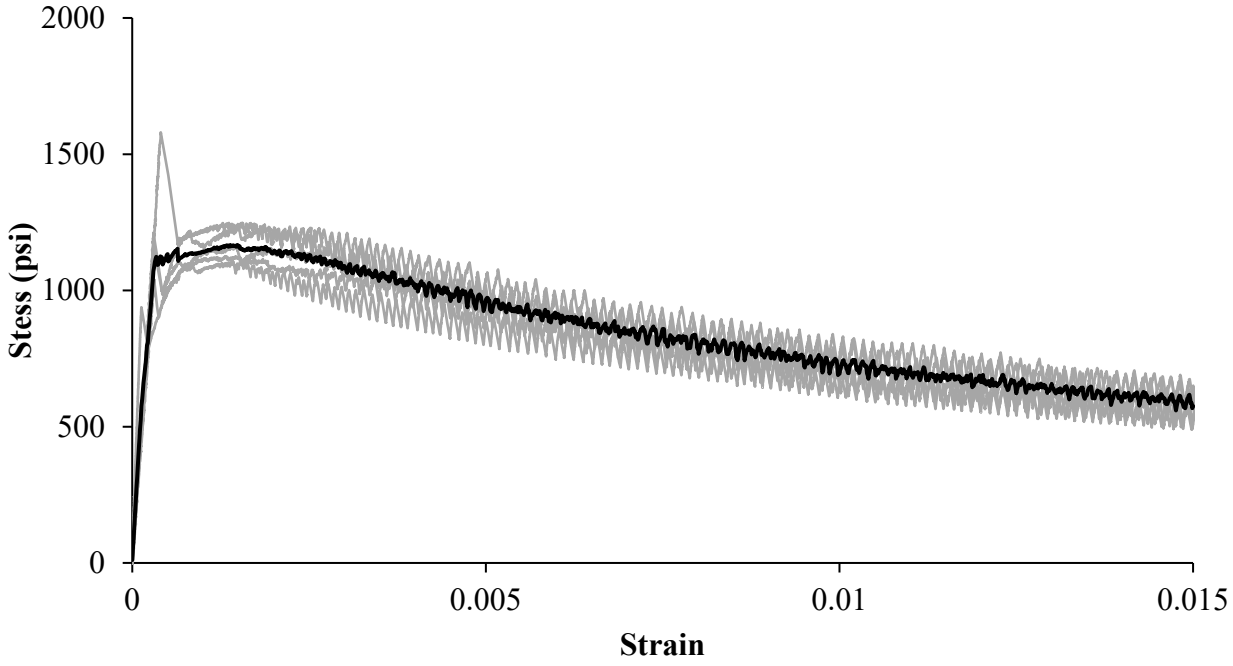

Figure B-9: 18+ Steam direct tension results

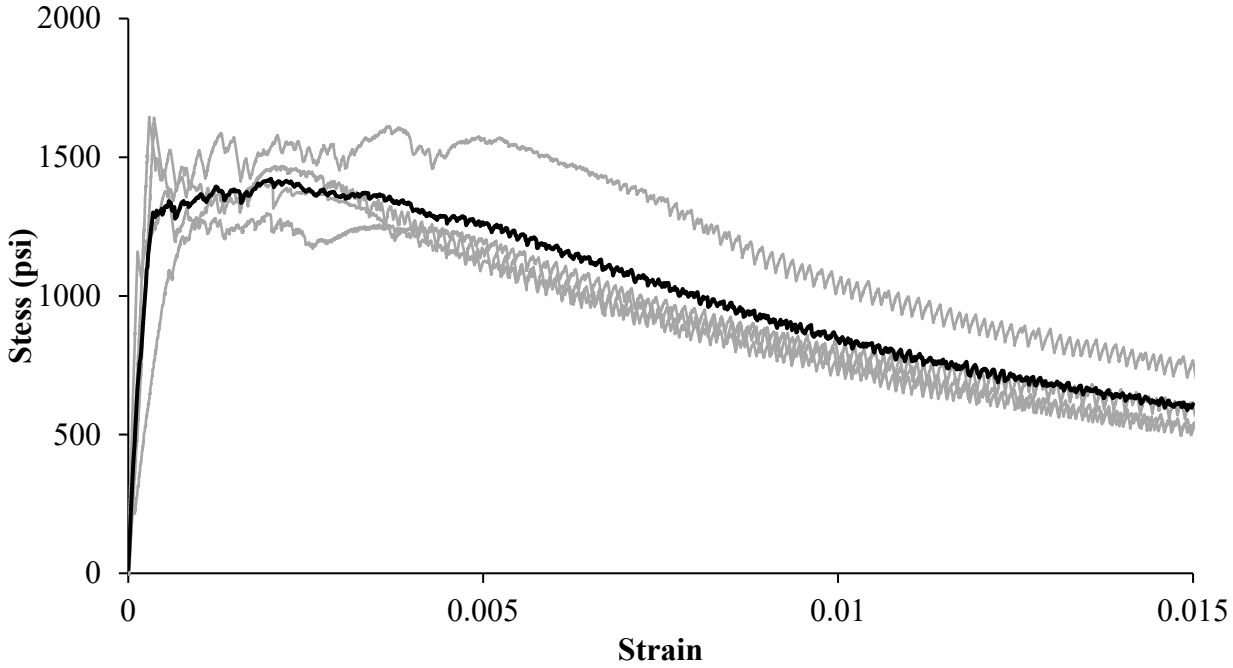

Figure B-10: 21+ Fog direct tension results

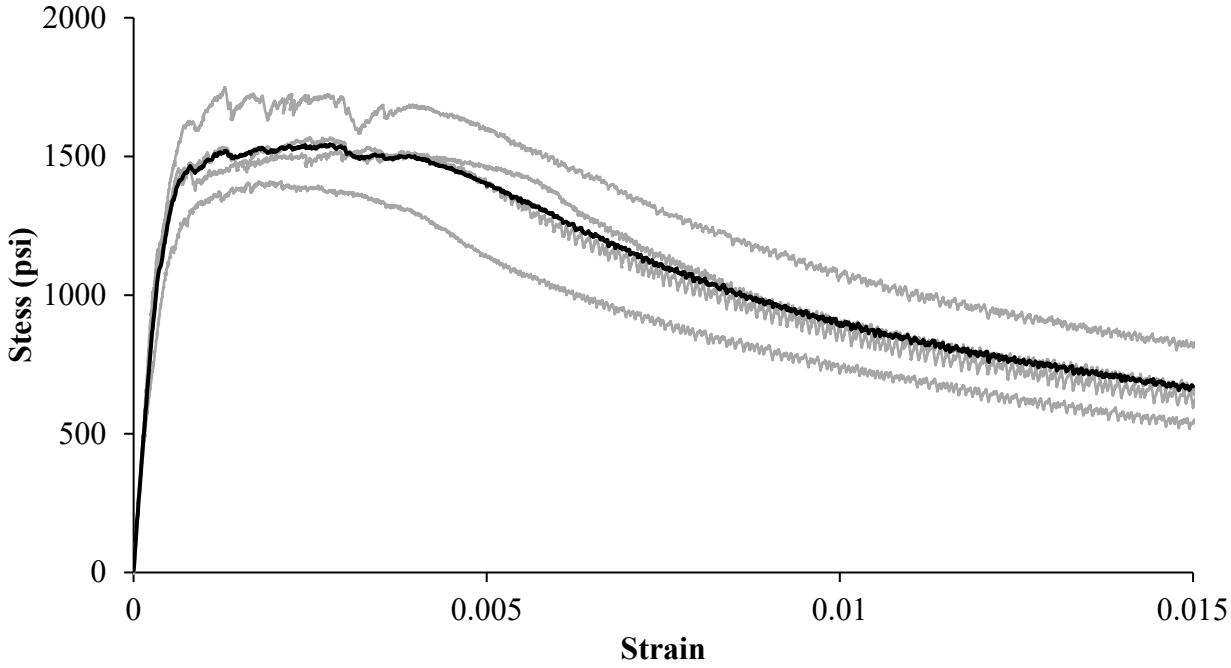

Figure B-11: 21+ Precast direct tension results

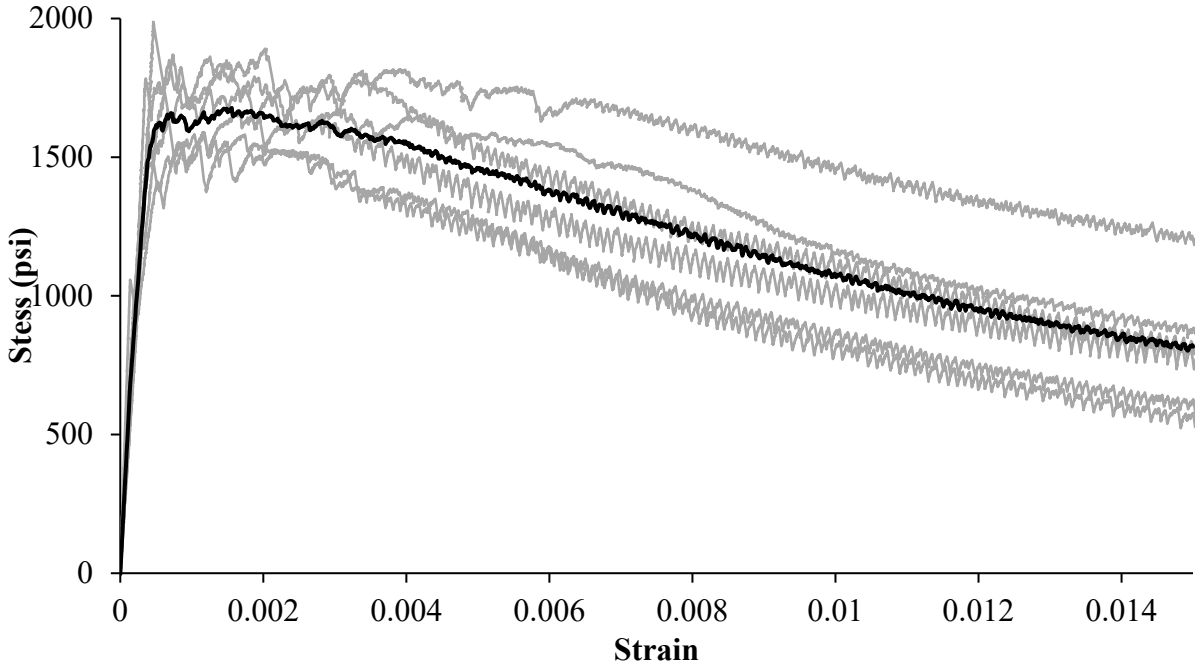

Figure B-12: 21+ Steam direct tension results

APPENDIX C: FREEZE-THAW COMPANION SAMPLE MIP RESULTS

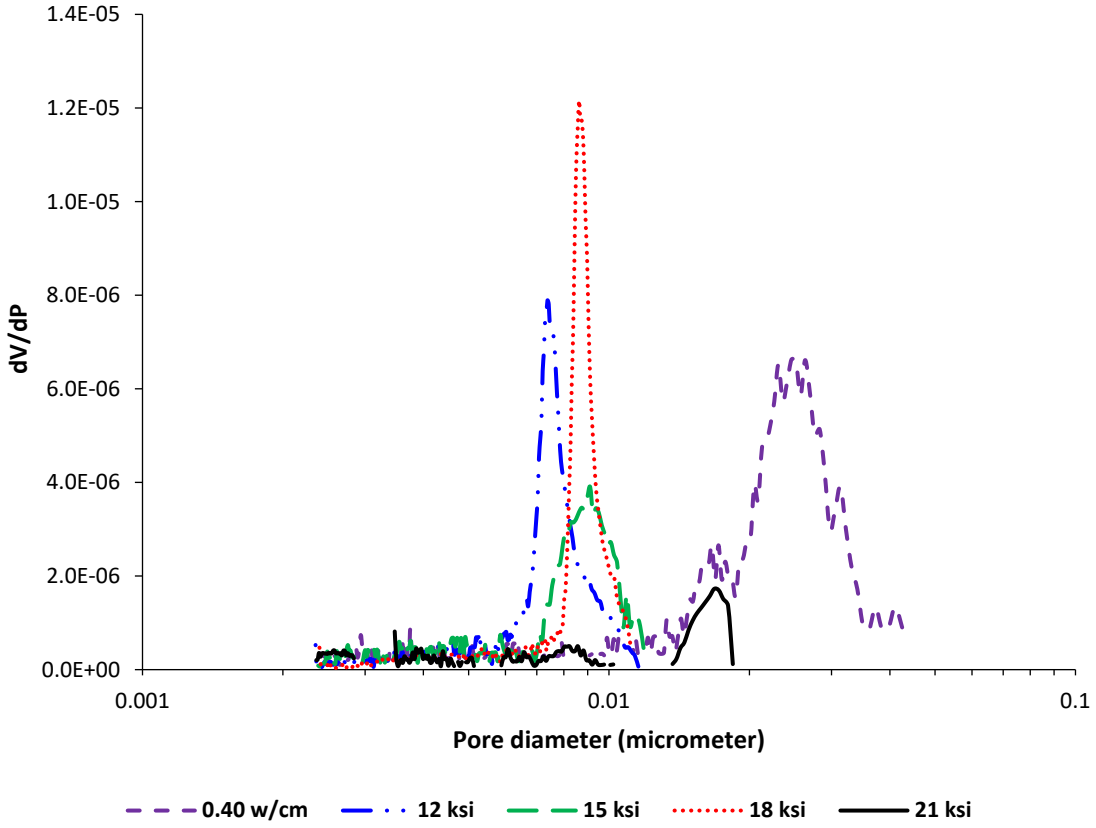

Figure C-1: Differential curve of the limewater cured samples measured by MIP at 14 days

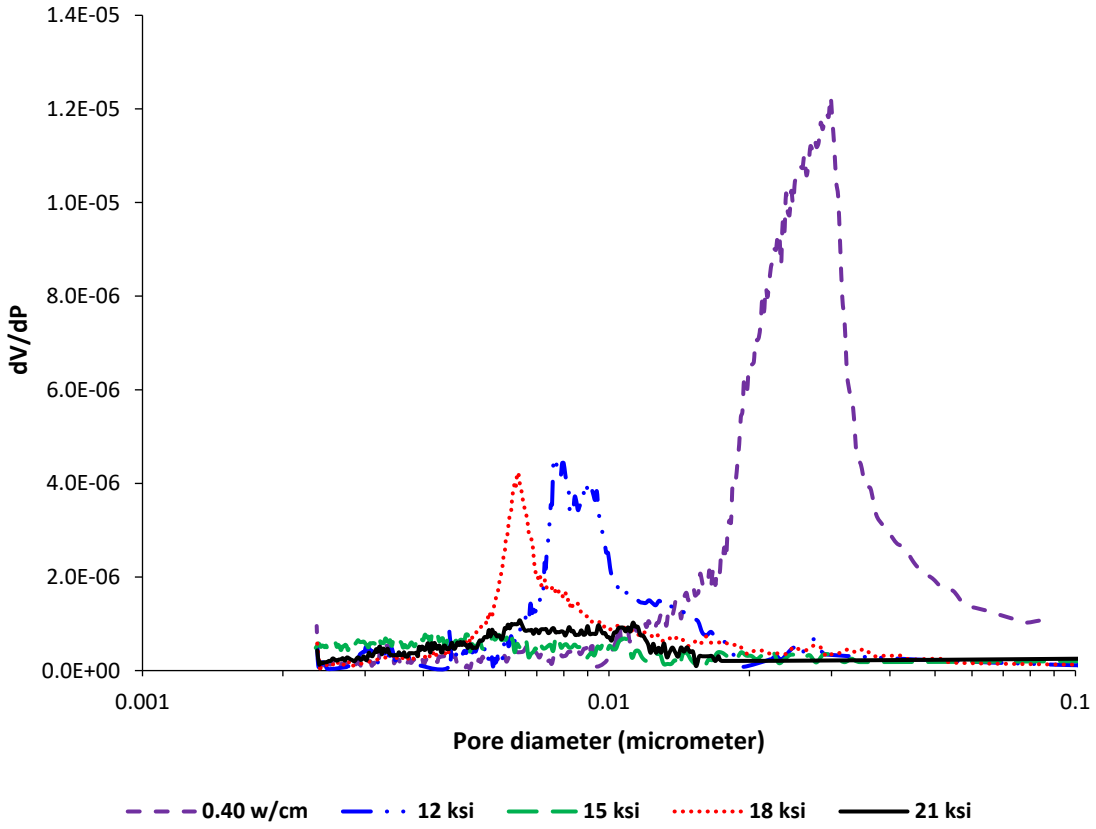

Figure C-2: Differential curve of the precast cured samples measured by MIP at 14 days

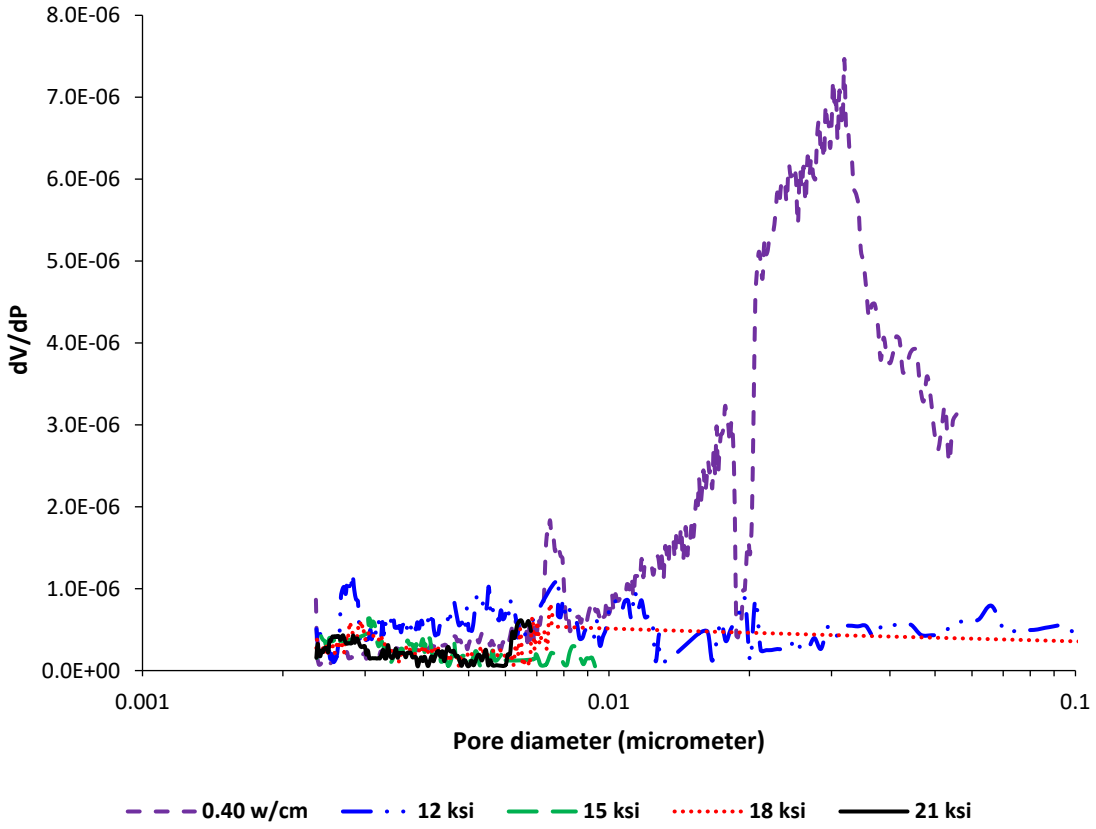

Figure C-3: Differential curve of the steam cured samples measured by MIP at 14 days

APPENDIX D: MODIFIED DOUBLE-PUNCH TEST METHOD

FM XXX: Modified Double Punch Test

1. Scope
   1.1 This test method covers the determination of the tensile strength and relative toughness of cylinders cast with fiber-reinforced concrete.

2. Reference Documents

   UNE 83515 Fiber Reinforced Concrete. Determination of Cracking Strength, Ductility and Residual Tensile Strength. Barcelona Test.

   ASTM C39 Standard Test Method for Compressive Strength of Cylindrical Concrete Specimens

   ASTM C192/C192M Practice for Making and Curing Concrete Test Specimens in the Laboratory

3. Terminology

4. Summary of Test Method
   4.1 This Test method consists of situating a concrete cylinder with equal height and diameter (to within 5%) between two cylindrical steel punches with diameters of ¼ the concrete diameter centered on the parallel surfaces of the concrete specimen. A compressive force is then applied to the steel punches at a constant load rate to produce tensile stresses on the concrete cylinder. A load vs. punch displacement curve is plotted from visual observance of a dial gauge and the compression machine output. The tensile stress is then calculated based on specimen height and load applied to produce a stress vs. displacement curve, from which a relative toughness is calculated.

5. Significance and Use
   5.1 This test method has been designed for use as a quality control test to ensure fiber quantity and distribution in the mix is consistent with that of the specifications and approved mix design.
   5.2 The results of this test method may be affected not only by the materials and proportions used in mix design, but also by the methods of mixing, placing, molding, and curing.
   5.3 The age of the specimen will affect the results of this test.

6. Apparatus
   6.1 Testing machine (Figure D-1)
   6.1.1 The testing machine must meet all requirements of Section 6 of ASTM C39
   6.2 Platens

6.2.1 Platens shall be steel with hardened bearing faces.
6.2.2 Platens shall have a diameter or a length and width of at least 3.0 inches.
6.2.3 Platens shall be solid.
6.2.4 The bearing faces shall not depart from a plane by more than 0.02 mm [0.001 in.] along any 150 mm [6 in.] length for bearing blocks with a diameter of 150 mm [6 in.] or larger, or by more than 0.02 mm [0.001 in.] in any direction of smaller bearing blocks. New bearing blocks shall be manufactured within one half of this tolerance.
6.2.5 The top and bottom surfaces of the platens shall be parallel to each other.
6.2.6 The upper platen shall be in full contact with the upper bearing block that conforms to the requirements of 6.2.4 Upper Bearing Block in ASTM C39. The upper steel punch shall be in full contact with the platen.
6.2.7 The lower platen shall be fully supported by the lower bearing block of the testing machine or by any spacers used. The lower steel punch shall be in full contact with lower platen.
6.3 Steel Punches
6.3.1 Two steel disks shall be used to apply loading to the top and bottom faces of the test specimen.
6.3.2 Disks should have a hardness of at least 90 HRB and a yield strength of 100,000 psi
6.3.3 The surfaces of the two disks should be plane and parallel to each other. The error in surface planeness shall be less than 0.02 inches.
6.3.4 The diameter of the two disks shall be 1.5 inches with a tolerance of 0.01 inches.
6.3.5 The height of the disks shall be at least 0.60 inches, with a maximum 1.20 inches.
6.4 Load Indication
6.5 Displacement Indication - A dial gauge or other real-time displacement indicator must be used to measure the distance the punches have moved over the duration of the test.
6.5.1 The indicator display may be analog or digital
6.5.2 The display on the indicator must be visible to the technician while the test is being performed.
6.5.3 The gauge must be situated so the plunger is within 2° of vertical.
6.5.4 The gauge must be able to be adjusted in height, either by use of an adjustable stand, by raising or lowering the entire stand on a pile of spacers, or by a combination of the two, to within 0.10” of a target height.
6.5.5 The gauge must have a range of at least 0.50 inches.
6.5.6 The gauge must have a precision of at least 0.001 inches.

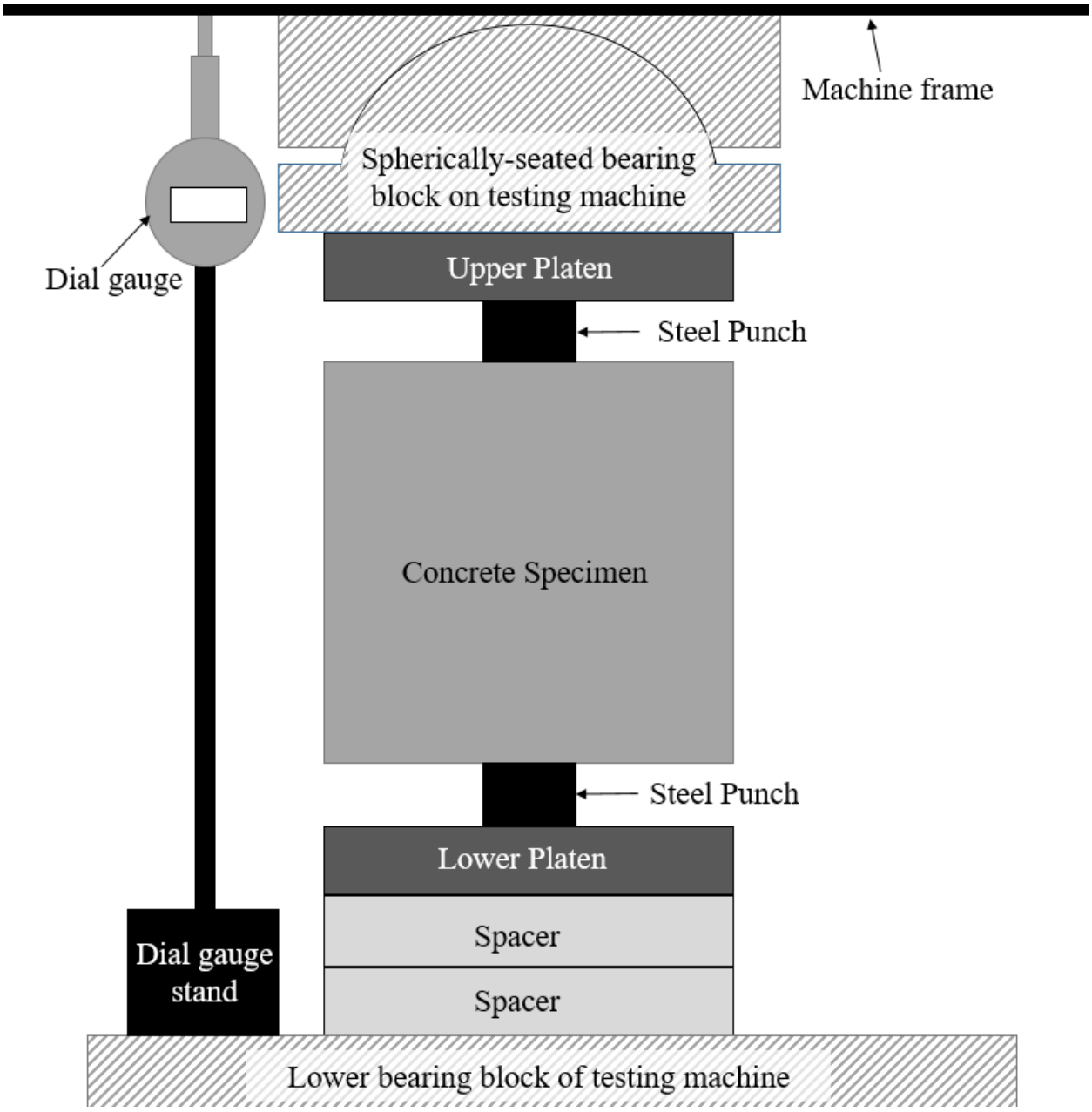

Figure D-1 Compression Testing Setup for the Modified Double-Punch Test

7. Test Specimens
   - 7.1 The test specimen shall be cylinders 6.00 ± 0.50 inches tall and 6.00 ± 0.10 inches in diameter.
   - 7.2 The test specimens shall be made per 7.2.1 or 7.2.2:
   - 7.2.1 Casting vertically in a mold 6 inches in diameter and 6 inches high.
   - 7.2.2 Casting vertically in a mold 6 inches in diameter and 12 inches high, with later cutting at half of the height for a perpendicular plane at the axis of symmetry of the specimen.

The cut shall be plane within 0.125 in. and perpendicular to the longitudinal axis within a 0.5° deviation. If this method of specimen fabrication is used, the samples tested must include at least the same number of samples taken from the top portion of the cylinder as specimens taken from the bottom portion of the cylinder.

7.3 Place concrete into cylinder molds in one continuous layer. The duration of placement time shall not exceed 10 seconds for a 6-inch-tall cylinder or 20 seconds for a 12-inch-tall cylinder.

7.4 Rodding or vibration may not be used during fabrication of the specimens.

7.5 Consolidation of the concrete will consist of tapping specimens 30 times with a mallet around the circumference of the specimen mold.

7.6 Perform finishing with the minimum manipulation necessary to produce a flat even surface that is level with the rim or edge of the mold. After consolidation, finish the top surfaces by striking them off with a handheld float or trowel.

7.7 Test specimens shall be moist-cured in accordance with ASTM C192/192M unless they are cured with heat treatment in accordance with ASTM C1856. Report the type and procedures used for curing the specimens.

8. Procedure

8.1 Prior to testing, measure the height of the specimen at 3 locations evenly distributed around the circumference of the cylinder. Record the heights.

8.2 Prior to testing, determine the diameter of the specimen by averaging two measurements taken at right angles to each other at midheight of the specimen.

8.3 Place the specimen between the two steel punches so that each punch is located in the center of the concrete's circular face. To ensure the correct centering, it is recommended to use a disk made of cardboard, plastic, or thick paper with an external diameter of 6 inches and an internal diameter of 1.55 inches. Place the specimen and punches centrally in the testing machine.

8.4 Prior to testing the specimen, verify that the load indicator on the compression machine is set to zero. If it is not, adjust the indicator.

Note: an uneven top surface of the specimen can result in a steel punch and upper platen that are not level with the test machine's spherically seated bearing block. This is acceptable as the steel punch will seat itself evenly during the initial loading.

8.5 Place the dial gauge in the machine to measure the change in distance between the upper machine frame and the lower bearing block. Ensure the dial gauge has a minimum of 0.40 inches of available displacement in compression.

8.6 Load the specimen slowly and without shock, at a rate below 200 lb/s until the load reaches 10,000 pounds.

8.7 When the load reaches 10,000 pounds, record the reading on the dial gauge.

8.8 Adjust the load rate on the machine to be within 200-400 lb/second. Make no adjustment in the rate of movement (platen to crosshead) as the ultimate load is being approached and the stress rate decreases due to cracking in the specimen.

8.9 While loading the concrete specimen, collect data pairs of load vs. displacement by recording the displacement displayed on the dial gauge indicator and the load displayed by the testing machine at the same time. Data pairs shall be recorded using increments of no greater than 0.01 inches for the first 0.10 inch of displacement and increments no greater than 0.02 inches for the next 0.20 inches of displacement.

8.10 Testing may be discontinued after the dial gauge has shown at least 0.30 inches of displacement.

Note: Some machines may include settings that will stop testing after the load drops a certain percentage from the peak load. It is recommended to adjust this setting so the machine will continue up until a decrease of 90% of peak load.

8.11 In addition to the loads recorded at specified displacements, record the maximum load carried by the specimen during the test.

9. Calculations

9.1 Calculate the tensile stress from the loads recorded at each crosshead displacement and for the maximum load using Equation 1.

$$f_t = \frac{4\,P_f}{9\,\pi\,a\,H} \qquad [1]$$

Where: P_f is the load (in lb)

a is the diameter of the loading disk (in in.), equal to 1.5 in.

H is the height of the specimen (in in.)

9.2 Plot the data pairs of stress vs. specified displacements as shown in Figure D-2.

9.3 Calculate the toughness as the area under the stress vs. crosshead displacement curve up until the endpoint of 0.30 inches by using Equation 2.

$$T = \sum \frac{f_{t,n-1} + f_{t,n}}{2} \times (y_n - y_{n-1}) \qquad [2]$$

Where: T is the specimen's toughness (in psi•in.)

$f'_{t,n}$ is the stress for data point n (in psi)

$f'_{t,n-1}$ is the stress at the data point directly preceding n (in psi)

y_n is the axial displacement of the machine for data point n (in in.)

y_{n-1} is the axial displacement of the machine for the data point directly preceding n (in in.)

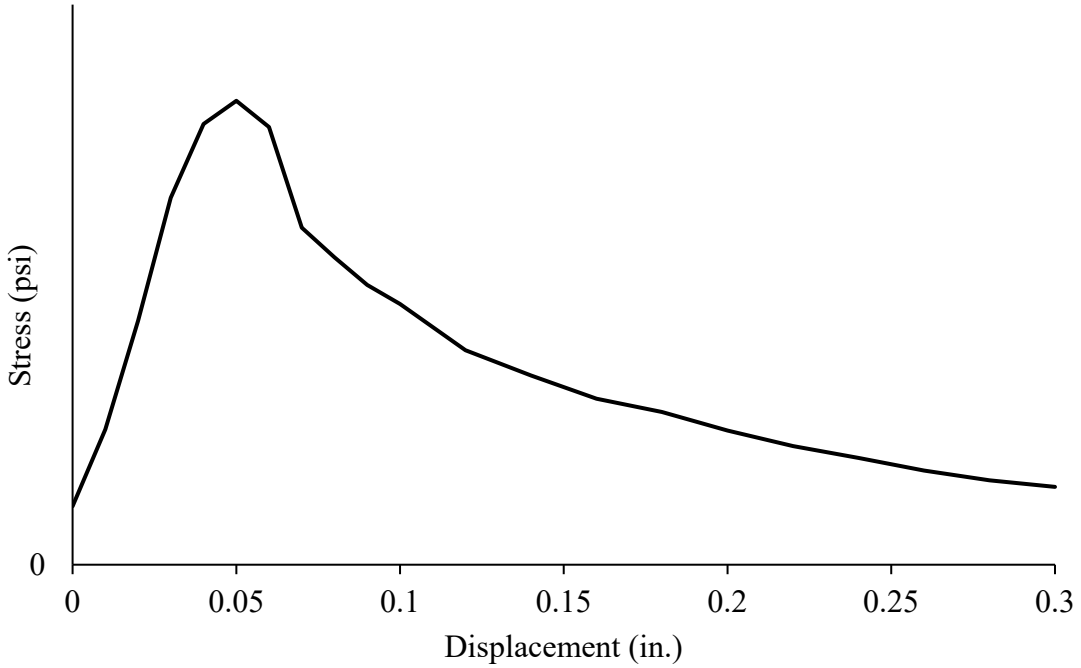

Figure D-2 – Plot of Stress vs. crosshead displacement

10. Report
    - 10.1 Report the following information:
    - 10.1.1 Specimen Identification, ie. Project number, date sampled, lot number.
    - 10.1.2 Specimen curing conditions, if different from moist curing specified in ASTM C192/C192M
    - 10.1.3 Specimen configuration. Whether specimen was cast as a 6-inch-long cylinder, was the top of a cut 12-inch-long cylinder, or the bottom of a cut 12-inch-long cylinder.
    - 10.1.4 Average measured height and diameter of specimen to the nearest 0.01 inches
    - 10.1.5 Raw data pairs of displacement (in inches, to the nearest 0.001 inch) and loads (in pounds, to the nearest 100 pounds)
    - 10.1.6 Calculated stresses (in psi) at the measured displacements from 10.1.5.
    - 10.1.7 Maximum load (in pounds) and calculated maximum stress (in psi).
    - 10.1.8 Plot of calculated stress in psi vs. crosshead displacement in inches.
    - 10.1.9 Toughness (*T*), in psi•inches.

APPENDIX E: MODIFIED RAPID CHLORIDE MIGRATION TEST FOR UHPC

FM XXX: Modified Rapid Chloride Migration Test for Ultra-High-Performance Concrete (UHPC) Cylinders

This test method follows NT Build 492, with the following modifications:

1. Steam-cure the 4-inch × 8-inch concrete cylinders for 24 hours, remove and demold the cylinders, and place them in a steam bath at 194 ± 1.8°F for 48 hrs. Allow the cylinders to gradually cool in a moist environment over a 2-hour period, remove them from the steam bath, and place them in a moist-curing room until 27 days of age. Sawcut and precondition the cylinders as described in NT Build 6.3.2 Preconditioning.

   Note: The steam bath can be made using a large stainless-steel pot or another suitable stainless-steel container with a tight-fitting lid. Place 1 to 2 inches of water in the bottom of the container to provide the steam. Provide a perforated platform to support the cylinders above the water. Use duct tape to seal the lid and container to prevent moisture loss, while preventing pressure build up in the container. Remove the container from the oven after 48 hours and place it on a benchtop at room temperature with the lid still on to allow the concrete to cool. Water must still be in the bottom of the container after cooling, otherwise the sample experienced drying during curing and shall not be tested.

2. Instead of adjusting the test voltage and time as specified in NT Build 6.4.4, all UHPC tests shall use a 30V DC electrical potential applied to the concrete for 168 ± 0.5 hours. The current at this voltage is very low due to the very high resistance of UHPC, resulting in minimal I^2R heating of the samples, and no voltage reductions are needed to offset temperature rise.

3. Test results reported in NT Build 6.7 l) shall include the initial current, final current, maximum sample temperature during test, migration coefficient, and the average depth penetrated for the samples after 7 days of applied voltage.